ANALYSIS OF DEEP EXCAVATIONS IN CLAY

by

YOUSSEF M.A. HASHASH

B.S. Civil Engineering, MIT 1987

M.S. Civil Engineering, MIT 1988

SUBMITTED TO THE DEPARTMENT OF CIVIL
ENGINEERING IN PARTIAL FULFILLMENT OF
THE REQUIREMENTS FOR THE DEGREE OF

DOCTOR OF PHILOSOPHY IN CIVIL ENGINEERING

at the

MASSACHUSETTS INSTITUTE OF TECHNOLOGY

APRIL 1992

Signature of Author_____
Department of Civil Engineering
April 23,1992

Certified by_____
Professor Andrew J. Whittle
Thesis Supervisor

Accepted by_____
Professor Eduardo Kausel
Chairman, Departmental Committee on Graduate Students

ANALYSIS OF DEEP EXCAVATIONS IN CLAY

BY
YOUSSEF M.A. HASHASH

Submitted to the Department of Civil Engineering on April 23, 1992 in partial fulfillment of the requirements for the degree of Doctor of Philosophy in Civil Engineering

Abstract

This dissertation describes the application of non-linear finite element analyses for predicting and interpreting ground deformations associated with deep, braced excavations in clays.

The first part of this research reviews algorithms for the implementation of elasto-plastic constitutive equations in non-linear finite element analyses. Robust and efficient numerical convergence characteristics are achieved for the Modified Cam Clay soil model through the formulation of an implicit numerical integration scheme, together with a consistent tangent stiffness matrix. A second soil model, MIT-E3, has shown excellent capabilities for predicting complex aspects of the measured behavior of soft clays including a) anisotropic stress-strain-strength, b) small strain non-linearity and c) hysteretic and path dependent behavior for overconsolidated clays. The numerical implementation of MIT-E3 in the ABAQUS finite element code uses explicit integration with a quasi-consistent tangent stiffness matrix.

Part two presents an extensive program of numerical experiments to evaluate the mechanisms controlling the performance of excavations in clay. The analyses focus on the short term behavior for deep excavations in Boston Blue Clay, supported by structural diaphragm walls and braced internally using techniques of top down construction. The principal parameters considered in the study include the stress history and modelling of clay behavior, wall length and support spacing. The results show that the excavation sequence induces small strains in the surrounding soil, and imposes complex loading on soil elements, characterized by principal stress rotation and stress reversals. These loading paths generate earth pressures, acting over the excavated height of the diaphragm wall, which can exceed the initial lateral stresses. Improved modelling of this behavior using MIT-E3 leads to more realistic predictions of wall deflections, surface settlements and failure mechanisms in the soil than can be obtained using simple elasto-plastic models. Wall length has negligible effect on pre-failure deformations but affects the mechanism of failure. Summary charts describe the expected wall deflections and ground movements as functions of the support conditions and excavation depth. Further predictions show that excavation response for clay deposits with variable stress history can be interpreted from results obtained using simplified soil profiles.

The third part describes a detailed simulation of the real time construction sequence for the seven-storey, underground garage at Post Office Square in Boston. Model predictions are evaluated through comparisons with extensive field data, including wall deflections, soil deformations, surface settlements and piezometric elevations. Differences between predicted and measured wall movements are attributed primarily to post-construction shrinkage of the roof and floor system, which brace the structure, while predicted settlements are affected by modelling of piezometric elevations in the underlying rock. The results demonstrate that reliable and consistent predictions of soil deformations and transient groundwater flow can be achieved by advanced methods of analysis, without recourse to parametric iteration. The study also emphasizes the need for adequate characterization of engineering properties for all pertinent soils in the profile.

Thesis Supervisor: Dr. **Andrew John Whittle**
Title: Assistant Professor of Civil Engineering

Acknowledgments

This work marks the end of a long journey that was not possible without the help of many individuals and organizations.

I am first indebted to my thesis committee members:
Professor Andrew J. Whittle for his tremendous support of my work, for spending many long days discussing, reviewing and arguing with me about various facets of my research and for his meticulous review of my thesis. He has been an advisor and a mentor. It has been a pleasure working with him.
Professor Robert V. Whitman for involving me with the Post Office Square Garage case history and keeping me in touch with the practical side of the research.
Professor Charles C. Ladd for his input and careful review of my thesis.

I would like to thank Dr. John Germaine, Professor Antonio Gens and Professor Scott Sloan for their help and feedback during the various stages of this research.

I would like to acknowledge Mr David Schoenwolf and Mr Chris Eriksson from Haley & Aldrich, Mr. Eldon Abbot from Parsons Brinkerhoff Quade and Douglas, Inc. and Mr. James M. Becker, Friends of Post Office Square for providing much of the data on the Post Office Square Garage case study.

I would like to thank the Friends of Post Office Square, MIT Sea Grant College Program, and Moh & Associates for their partial financial support of this research.

I would like to express my appreciation to the Hariri Foundation for giving me the opportunity to come to the United States and pursue my studies and who have been my sponsors since then.

I would have not been able to survive without the many friends who put up with me during my ups and downs. Doug Larson for being such a good friend over the past few years. Charles Aubeny (office mate) for the lengthy discussions we had. Anne Williamson (ex-office mate) who is enjoying life in Australia. (Prof) Tom 'Tim' Sheehan, and Dede (yummy cookies!). Juan Pestana and Fu Shu Jeng. Anne Estabrook (author of the finite elephant method) and Ute Sheran for the many long lunches in the sun. Delaine Thompson for the TV Dinners and rented movies. Paul Thompson for all those good Summer's of butterfly collecting, and Winter e-mails.

Special thanks to my two sisters. Naila for her e-mail support that kept me going through hard times and all those goodies that she made. Mariam for being patient with me during her visits, I owe her a lot of entertainment time.

To my father and mother I owe the most. This would have not been possible without their vision, support and sacrifice under very difficult circumstances.

Youssef M.A.Hashash

Table of Contents

List of Tables

List of Figures

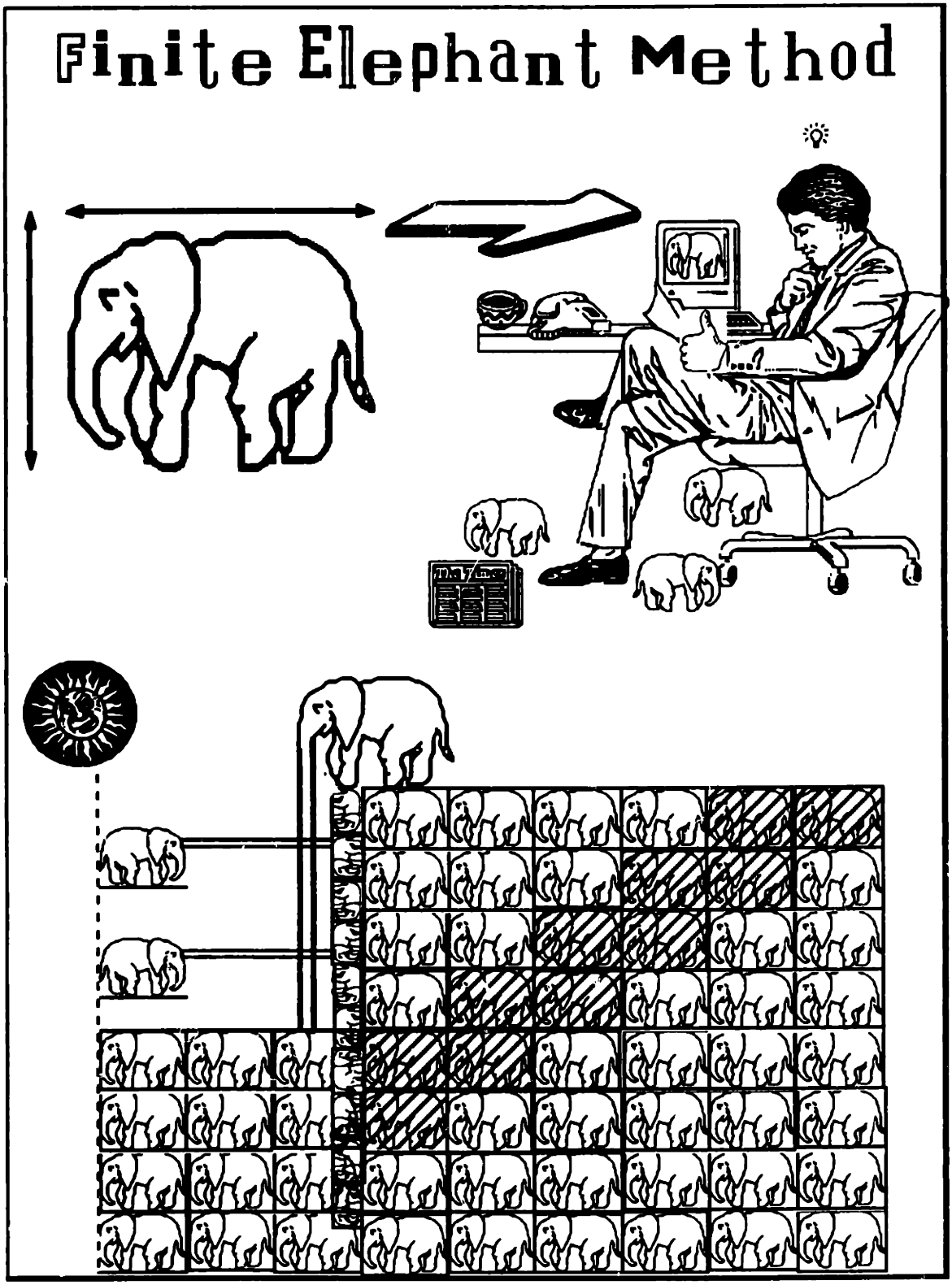
Finite Elephant Method

1. Introduction

The demand for underground space, for use as transport tunnels, parking garages, storage spaces, etc., in many heavily urbanized areas requires the construction of deep excavations in close proximity to sensitive structures. Advanced excavation techniques, including the use of thick structural diaphragm walls and top-down construction procedures, are effective methods to reduce deformations in the surrounding soil and damage to adjacent structures. However, in deep excavations and walls embedded in deep clay deposits, soil movements are difficult to control. The prediction of these movements, in such situations, becomes an important part of the design stage of the support structure as well as the construction monitoring stage. Numerical methods (for example, the finite element method, FEM, and the boundary element method, BEM) are the only methods available to predict deformations caused by complex construction activities. The usefulness of these methods is determined, in large part, by the accuracy of the characterization of the mechanical behavior of the soil material and the availability of procedures to model complex construction sequences. In this thesis, a new capability is developed to model deep supported excavations in soft clay deposits using accurate numerical techniques and an advanced soil model.

This thesis is divided into three main sections: 1) the development of numerical procedures to integrate advanced constitutive soil models (Modified Cam Clay, MCC, Roscoe and Burland, 1968, and MIT-E3, Whittle, 1990) in the FEM and procedures to accurately model various excavation construction activities; 2) the application of the numerical techniques for understanding some of the fundamental mechanisms controlling movements in excavations in deep clay deposits; and 3) the analyses of the performance of an excavation for a seven story underground garage in Boston, Massachusetts. The thesis represents the first use of the MIT-E3 model in the solution of a boundary value problem.

1.1. Development of Numerical Techniques

In this thesis, the displacement based finite element method is used to solve the excavation boundary value problem. The general purpose finite element code ABAQUS[1] is used as the shell for solving the excavation problem numerically. ABAQUS provides a versatile capability for performing numerical analyses, including large element and

[1]Hibbitt, Karlsson and Sorensen. ABAQUS is made available to MIT under an academic license agreement.

material model libraries, a variety of procedures to perform effective stress analyses, and a facility for user supplied material models.

Soil elements inside and outside an excavation undergo complex loading paths during excavation construction. Accurate numerical predictions of ground movements associated with braced excavations therefore require the use of realistic constitutive models to describe soil behavior under these conditions. The MIT-E3 model (Whittle 1987), is the principal clay model used in this thesis. The model captures important aspects of soil behavior such as nonlinearity at small strains, stress-strain-strength anisotropy and irrecoverable strains regardless of the position of the state of stress with respect to the yield surface.

The incorporation of constitutive models in the solution of boundary value problems using the finite element method requires the development of specific numerical techniques to ensure that the problem is solved accurately and efficiently. Chapter 2 describes the general framework for integrating elasto-plastic soil models in the displacement based finite element method. The framework is then applied in the integration of the MCC and MIT-E3 models in ABAQUS.

Chapter 3 reviews some of the previous FE codes and other numerical methods presented in the literature for modelling the excavation boundary value problem. A discussion of the limitations of some of the earlier numerical techniques is presented. The chapter describes the procedures adopted and developed to perform a variety of construction activities in ABAQUS. The chapter discusses the methods used to simulate soil removal, brace installation, and the mixing of effective stress analyses for the soil and the total stress analyses for the support wall.

The capabilities developed in Chapters 2 and 3 provide a versatile tool for simulating complex excavation construction activities using a realistic mechanical description of the in-situ soil.

1.2. Behavior of Braced Diaphragm Walls in Deep Clay Deposits

Major transportation construction projects currently underway, such as the Central Artery/Tunnel (CA/T) in Boston, Massachusetts and the Rapid Transit System in Taipei, Taiwan, involve the construction of deep excavations in deep soft clay deposits. There is very limited experience available for designing these types of excavations and a general lack of understanding of the influence of various construction activities, excavation geometry and soil properties on predictions of deformations (as well as failure) of supported excavations. Many of the published numerical studies on

excavations focus on specific case studies and offer little guidance on 'generalized' excavation performance. As a result, there is great interest in understanding some of the fundamental mechanisms which control the behavior of such excavations.

Chapter 4 describes a numerical study aimed at understanding the fundamental behavior of braced excavations. The study assumes an idealized excavation geometry, construction sequence and soil profile. The discussion focuses on examining the influence of a variety of parameters (e.g., wall length, support condition and soil stress history) on excavation response. Chapter 4 presents, in detail, the global excavation response including soil and wall deformations and system failure; as well as soil stress and strain history at selected points in the clay deposit. The results of the study are synthesized in a simple framework that incorporates the influence of the parameters considered in the study.

1.3. Excavation Case Study

The construction of the new seven story underground garage at Post Office Square included a very deep excavation in a soil profile with a substantial layer of Boston Blue Clay. The site is located in close proximity to many sensitive structures in downtown Boston, Massachusetts. Accurate predictions of movements were required during the design and construction monitoring stages of the project to avoid damage to surrounding utilities and structures. Extensive monitoring of soil deformation and pore pressure changes throughout the site was conducted during construction.

The development of the numerical capabilities in this thesis was motivated, in part, by this project. Chapter 5 presents the details of the numerical simulation of the construction activity for the garage. Many details of the construction sequence such as floor installation, berm construction, temporary dewatering, etc., are included in the numerical model. The influence of specific construction details such as floor shrinkage are simulated. The chapter presents comprehensive, systematic comparisons between model predictions and field observations.

1.4. References

Roscoe,K.H., and Burland,J.B., 1968, On the Generalized Stress-Strain Behavior of 'wet' Clay. *Engineering Plasticity*, pp. 535-609.

Whittle,A.J., 1987, "A Constitutive Model for Overconsolidated Clays with Application to the Cyclic Loading of Friction Piles." *Sc.D. Thesis* , Dept. of Civil Engineering, MIT, Cambridge, MA., 641p.

Whittle, A.J., 1990, "A Constitutive Model for Overconsolidated Clay," *MIT Sea Grant Report*, MITSG90-15.

2. Integration of Elasto-Plastic Soil Models in Finite Element Analyses

2.1. Introduction

Constitutive equations which model accurately the behavior of soils are essential if reliable numerical predictions of performance are to be achieved for practical geotechnical problems. Significant difficulties in developing such models are associated with the complexity of soil behavior observed from both laboratory tests and field observations. The most widely used generalized models for soil behavior are formulated using the theoretical framework of rate independent, elasto-plasticity (e.g., Drucker et al. 1957, Hashiguchi, 1985) and relate deformations to changes in effective stresses (Terzaghi, 1925). This approach achieved prominence through the formulation of the Cam Clay (Roscoe et al. 1963) and Modified Cam Clay (MCC; Roscoe and Burland, 1968) models which describe an idealized conceptual framework of soil behavior referred to as Critical State Soil Mechanics (Schofield and Wroth, 1968; Atkinson and Bransby, 1978; Wood, 1990).

Significant research efforts over the last twenty years have attempted to develop constitutive models which describe more complex aspects of real soil behavior including a) anisotropic stress-strain-strength, b) non-linear and inelastic properties of overconsolidated clays, and c) material response under cyclic loading. This work has produced a plethora of soil models whose predictive capabilities and limitations have been evaluated primarily through comparisons with laboratory test data (i.e., at the 'element' level).

In order to apply these models in the solution of boundary value problems, the constitutive equations must be implemented in non-linear finite element analyses. In general, elasto-plastic soil models describe material behavior which is path dependent and hence is characterized by 'rate constitutive equations' (relating infinitesimal increments of strains and effective stresses). However, when the constitutive model is used in non-linear finite element analyses, the constitutive equations must be integrated numerically over a discrete sequence of time steps[1]. Recent works (e.g., Ortiz and Popov, 1985; Simo and Taylor, 1985 and 1986; de Borst and Vermeer, 1984) have shown that the

[1]In a static analysis, without time dependent behavior or pore water movement, time is only a convenient variable which denotes different intensities of load application and hence different configurations in the finite element model.

procedures used to integrate the constitutive equations have a direct impact on the overall accuracy, stability and convergence properties of non-linear finite element analyses.

This chapter summarizes the role played by rate independent elasto-plastic equations in non-linear finite element computations. Section 2.2 describes numerical algorithms used to integrate the constitutive relations and introduces the concept of consistent linearization in estimating the tangent stiffness in the finite element equilibrium equations. Section 2.3 describes the implementation of the Modified Cam Clay (MCC; Roscoe and Burland, 1968) model in the general purpose finite element code ABAQUS[1] (HKS, 1989) using a fully implicit integration scheme and a consistent constitutive matrix. Numerical examples are presented to illustrate the accuracy and robustness of the algorithm.

Finally, Section 2.4 presents algorithms used to implement a complex elasto-plastic constitutive model, MIT-E3 (Whittle, 1987, 1990), in ABAQUS. The MIT-E3 model includes: a) non-linear paraelastic equations[2] (Nova and Huekel, 1979) to describe small strain non-linearity and hysteretic behavior; b) bounding surface plasticity (Dafalias, 1982; Hashiguchi, 1985) for inelastic behavior of overconsolidated clays; c) non-associated flow rules; and d) complex hardening functions. These components present a formidable challenge for efficient model implementation. The proposed algorithm uses explicit integration of the rate equations together with a consistent constitutive stiffness matrix. Numerical verification of the proposed procedure demonstrates that this algorithm is stable and accurate.

2.2. Rate Independent Plasticity in Finite Element Computations

2.2.1. Solution of Non-Linear Finite Element Equations

For most practical geotechnical applications, non-linear system response is attributed primarily to the constitutive behavior of the soils, while geometric non-linearities are of secondary importance (e.g., Vermeer and van Langen, 1989). As a result, this chapter focuses exclusively on materially non-linear finite element analyses (e.g., Bathe, 1982) in which the continuum behavior is described by infinitesimal deformations and strains.

In the (displacement based) non-linear finite element formulation, it is assumed

---

[1]ABAQUS is commercially available from Hibbitt, Karlsson and Sorensen, RI, and is made available to the MIT geotechnical group through an academic license.

[2]There is no linear range of behavior in MIT-E3.

that the solution is known[1] at time t_n, such that the finite element equilibrium equations can be written:

$$f({}^{n}U) = {}^{n}R - {}^{n}F = 0 \tag{2.1}$$

where ${}^{n}U$ are the nodal point displacements, ${}^{n}R$ is the vector of the applied nodal forces and ${}^{n}F$ are the nodal point forces due to stresses in the elements at time, t_n.

The solution (i.e. nodal point displacements, U*) is then required at time t_{n+1} ($=t_n+\Delta t$) at which the new configuration is defined by a known set of applied forces ${}^{n+1}R$:

$$f(U^*) = 0 \tag{2.2}$$

where $f(U^*) = {}^{n+1}R - {}^{n+1}F(U^*)$.

Assuming that values of U* are obtained by iteration, then f(U*) can be determined from a Taylor series approximation using the displacements estimated at iteration [i-1]:

$$f(U^*) = f\left({}^{n+1}U^{[i-1]}\right) + \left(U^* - {}^{n+1}U^{[i-1]}\right)\left.\frac{\partial f}{\partial U}\right|_{[i-1]}^{n+1} + \ldots \tag{2.3}$$

where ${}^{n+1}U^{[i-1]}$ are the displacements at t_{n+1} from iteration [i-1]. Neglecting the higher order terms in the expansion (i.e. linearizing the problem), the finite element equilibrium equations (2.2) can be re-expressed as:

$$\left.\frac{\partial f}{\partial U}\right|_{[i-1]}^{n+1}\left(U^* - {}^{n+1}U^{[i-1]}\right) = {}^{n+1}R - {}^{n+1}F^{[i-1]} \tag{2.4}$$

where ${}^{n+1}F^{[i-1]}$ are obtained from the element stresses (using the displacements ${}^{n+1}U^{[i-1]}$). Equation 2.4 can be simplified by the following definitions:

$$\Delta U^{[i-1]} = U^* - {}^{n+1}U^{[i-1]} \tag{2.5}$$

where $\Delta U^{[i-1]}$ is the displacement increment correction, and:

$$\left.\frac{\partial f}{\partial U}\right|_{[i-1]}^{n+1} = \left.\frac{\partial F}{\partial U}\right|_{[i-1]}^{n+1} = {}^{n+1}K^{[i-1]} \tag{2.6}$$

where ${}^{n+1}K^{[i-1]}$ is the tangent (global) stiffness matrix evaluated in iteration [i-1].

The direct (full Newton) iteration procedure to solve the equilibrium equations can then be summarized as follows:

$${}^{n+1}K^{[i-1]}\Delta U^{[i-1]} = {}^{n+1}R - {}^{n+1}F^{[i-1]} \tag{2.7a}$$

$${}^{n+1}U^{[i]} = {}^{n+1}U^{[i-1]} + \Delta U^{[i-1]} \tag{2.7b}$$

with initial conditions (in the first iteration) given by:

$${}^{n+1}K^{[0]} = {}^{n}K \; ; \; {}^{n+1}F^{[0]} = {}^{n}F \; ; \; {}^{n+1}U^{[0]} = {}^{n}U \tag{2.7d}$$

Equations 2.7 solve the non-linear response of the system through a sequence of

---

[1] i.e. the nodal point displacements satisfy the global equilibrium requirements.

linear problems (i.e., solving for $\Delta U^{[i]}$, Equation 2.7). Convergence of the Newton scheme is evaluated by ensuring that force residuals (right hand side of Equation 2.7a) and/or displacement residuals ($\Delta U^{[i-1]}$, Equation 2.7a) are sufficiently small.

The iterative (Newton) scheme is being applied to a history dependent problem when the material behavior is non-linear and path dependent. Therefore, the intermediate, non-converged solution obtained during the iteration process is usually not on the actual solution path (HKS, 1989). Hence, the integration of history dependent variables must be performed completely over the load increment at each iteration, and not obtained as the sum of integrations associated with $\Delta U^{[i-1]}$ increments of the Newton iteration (Equations 2.7).

At each iteration, the constitutive relations are invoked by the incremental nodal point displacements ${}^{n+1}\Delta U^{[i-1]} = {}^{n+1}U^{[i-1]} - {}^{n}U$ (at all nodes of the finite element model). For isoparametric elements, standard interpolation functions are used to estimate incremental strains at the Gauss points; ${}^{n+1}\Delta\varepsilon_g^{[i]} = B_g {}^{n+1}\Delta U^{[i]}$ (where B_g is the interpolation matrix evaluated at the gauss point g).

At each Gauss point, the constitutive model computes the increments of stress and state variables (see Section 2.2.2) given a) the initial state of the material (stresses and state variables), and b) the applied strain increments. For elasto-plastic models, the constitutive equations are described in rate (differential) form. The material response over finite increments of strain is then obtained by integrating the equations numerically (Section 2.2.2). The constitutive model supplies two pieces of information for the global finite element equilibrium calculations (Equations 2.7):

1. The updated stress state determines the nodal point force vector, ${}^{n+1}F^{[i-1]}$ (Equation 2.7a; through isoparametric interpolation and volume integration).
2. The global tangent stiffness matrix (${}^{n+1}K^{[i-1]}$; Equation 2.7a) is assembled from the local tangent moduli of the constitutive model. The global tangent stiffness matrix can be re-written as:

$$ {}^{n+1}K^{[i-1]} = \left.\frac{\partial F}{\partial U}\right|_{[i-1]}^{n+1} = \frac{\partial\left({}^{n}F + {}^{n+1}\Delta F^{[i-1]}\right)}{\partial\left({}^{n}U + {}^{n+1}\Delta U^{[i-1]}\right)} = \frac{\partial\left({}^{n+1}\Delta F^{[i-1]}\right)}{\partial\left({}^{n+1}\Delta U^{[i-1]}\right)} \qquad (2.8) $$

then at the Gauss point level, using the interpolation functions, the matrix becomes the constitutive matrix (Jacobian):

$$ {}^{n+1}J^{[i-1]} = \frac{\partial\left({}^{n+1}\Delta\sigma_g^{[i-1]}\right)}{\partial\left({}^{n+1}\Delta\varepsilon_g^{[i-1]}\right)} \qquad (2.9) $$

Section 2.2.2 describes the various methods by which these moduli are determined.

Figure 2.1 shows schematically the solution scheme of the finite element method using a full Newton iteration scheme. The major computational cost is in the calculation and factorization of the tangent stiffness matrix at each iteration. Other iterative schemes including the 'initial stress', 'modified' and 'quasi-Newton' solutions are widely reported in the finite element literature. These schemes attempt to reduce computational cost by re-calculating the tangent stiffness matrix less frequently. However, they also tend to degrade the convergence characteristics of the solution[1]. Then, the effectiveness of an individual iterative scheme depends on the specific problem of interest and the user must select an appropriate solution strategy (i.e. automatic step control should be used with severe caution)[2].

2.2.2. Integration of Elasto-Plastic Equations

The general equations of rate independent elasto-plasticity are well established in the literature (see for example, Rice, 1976; Prévost, 1978; Hashiguchi, 1985; or Ortiz and Simo, 1986) and can be summarized as follows:

$$\dot{\varepsilon}_{ij} = \dot{\varepsilon}^{e}_{ij} + \dot{\varepsilon}^{p}_{ij} \tag{2.10a}$$

$$\dot{\sigma}_{ij} = C_{ijkl}\left(\dot{\varepsilon}_{kl} - \dot{\varepsilon}^{p}_{kl}\right) = C_{ijkl}\,\dot{\varepsilon}^{e}_{kl} \tag{2.10b}$$

$$\dot{\varepsilon}^{p}_{ij} = \dot{\Lambda}\, P_{ij}(\sigma, q) \tag{2.10c}$$

$$\dot{q}_{\alpha} = \dot{\Lambda}\, h_{\alpha}(\sigma, q) \tag{2.10d}$$

where $\dot{\varepsilon}_{ij}$, $\dot{\varepsilon}^{e}_{ij}$ and $\dot{\varepsilon}^{p}_{ij}$ denote the total, elastic and plastic strain rate tensors, $\dot{\sigma}_{ij}$ are the components of the (Cauchy) stress rate and $\dot{q}_{\alpha}$ correspond to a set of internal variables which characterize the in-elastic history of loading. Equation 2.10a represents the standard additive decomposition of the strain rate tensor into elastic and plastic components. The fourth order tensor C_{ijkl}, are the elastic moduli that characterize the hypo-elastic[3] relation between stress and strain rates. Conservative elastic behavior is ensured by the existence of a strain energy potential. In this case, the elastic stress-strain relations are 'hyper-elastic' and equations 2.10a, b can be re-written:

$$\varepsilon_{ij} = \varepsilon^{e}_{ij} + \varepsilon^{p}_{ij} \tag{2.11a}$$

$$\sigma_{ij} = \overline{C}_{ijkl}\,\varepsilon^{e}_{kl} \tag{2.11b}$$

---

[1]For the full Newton iteration, the solution converges quadratically as long as the tangent moduli are obtained by consistent linearization (Simo and Taylor, 1985).

[2]In ABAQUS, the user has the choice of using different iteration schemes and automatic step control. In this thesis, the full Newton iteration is used with no automatic step control.

[3]A material is hypo-elastic if the stress rate is an homogeneous, linear function of the rate of deformation.

where the components of $\bar{C}_{ijkl}$ can be non-linear function of elastic strain.

Equation 2.10c expresses a general (non-associated) flow rule in which the strain directions are functions of the current material state (i.e., current values of σ,$\mathbf{q}$), while Equation 2.10d describes hardening functions (h_α) controlling the evolution of the internal variables. The plastic multiplier $\dot{\Lambda}$ is obtained from the loading criterion through the definition of a yield surface, $f(\sigma,\mathbf{q}) \leq 0$. The loading criterion is written:

$$\frac{\partial f}{\partial \sigma_{ij}} \dot{\sigma}_{ij} > 0 \text{ Loading}$$

$$= 0 \text{ Neutral Loading} \qquad (2.12)$$

$$< 0 \text{ Unloading (elastic)}$$

The neutral loading condition is satisfied by writing $\dot{\Lambda} = 1/H\left(Q_{ij}\,\dot{\sigma}_{ij}\right)$, where $Q_{ij} = \partial f/\partial \sigma_{ij}$ (Mróz, 1980)[1].

During loading, the stress state must remain in contact with the yield surface, and hence $\dot{\Lambda}$ can be obtained from the plastic consistency condition (Prager, 1956):

$$\dot{f} = Q_{ij}\dot{\sigma}_{ij} + \frac{\partial f}{\partial q_\alpha}\dot{q}_\alpha = 0 \qquad (2.13a)$$

$$\dot{\Lambda} = \frac{Q_{ij}\, C_{ijkl}\, \dot{\varepsilon}_{kl}}{H + Q_{ij}\, C_{ijkl}\, P_{kl}} \qquad (2.13b)$$

where, $H = -\dfrac{\partial f}{\partial q_\alpha} h_\alpha$

Equations 2.10 to 2.13 describe the path dependent elasto-plastic material response for infinitesimal increments of strain. In finite element analyses, global load steps (or changes in configuration) control the deformation increments experienced at the individual Gauss points. The material response must then be found for finite strain increments $\Delta\varepsilon = ({}^{n+1}\varepsilon - {}^{n}\varepsilon)$, where ${}^{n}\varepsilon$ and ${}^{n+1}\varepsilon$ are the strains at times t_n and t_{n+1} respectively. It is assumed that the material experiences a holonomic strain path (i.e., proportional increments of strain) over the time interval $[t_n, t_{n+1}]$:

$$\Delta\varepsilon_{ij} = \int_{t_n}^{t_{n+1}} \dot{\varepsilon}_{ij}\, dt \qquad (2.14)$$

---

[1]For associated flow rule: $P_{ij} = Q_{ij}$

Ortiz and Popov (1985) describe a general class of integration algorithms[1] for integrating the elasto-plastic constitutive equations (2.10 to 2.13):

$$\sigma_{n+1} = \overline{C} : (\varepsilon_{n+1} - \varepsilon^p_{n+1}) \tag{2.15a}$$

$$\varepsilon^p_{n+1} = \varepsilon^p_n + \Delta\Lambda\,[(1-\alpha)\mathbf{P}_n + \alpha\mathbf{P}_{n+1}] \tag{2.15b}$$

$$\mathbf{q}_{n+1} = \mathbf{q}_n + \Delta\Lambda\,[(1-\alpha)\mathbf{h}_n + \alpha\mathbf{h}_{n+1}] \tag{2.15c}$$

$$f_{n+1} = 0 \tag{2.15d}$$

where the symbol ':' signifies the double contraction of the tensors (i.e, $\overline{C}:\varepsilon = \overline{C}_{ijkl}\,\varepsilon_{kl}$), $(\mathbf{P}_n, \mathbf{P}_{n+1})$ and $(\mathbf{h}_n, \mathbf{h}_{n+1})$ are the flow and hardening directions evaluated at t_n and t_{n+1}, respectively. The conditions at time t_n (σ_n, ε_n, ε^p_n, $\mathbf{q}_n$) are fully defined, while ε_{n+1} corresponds to the imposed strains at t_{n+1}. The unknown variables σ_{n+1}, ε^p_{n+1}, $\mathbf{q}_{n+1}$ are solved from equations 2.15a,b,c, while $\Delta\Lambda$ satisfies the integrated consistency condition (Equation 2.15d).

The algorithmic parameter, α ($0 \le \alpha \le 1$) controls the type of integration scheme. For α=0, the updated variables are obtained by 'forward marching' or 'explicit' integration based on conditions at t_n. When α=1, the updated variables depend on the flow and hardening directions at t_{n+1} and, therefore, the equations are integrated implicitly by iteration. The integration schemes are unconditionally stable for $\alpha \ge 1/2$, and achieve second order accuracy for α=1/2 (Ortiz and Popov, 1985)[2]. However, in practice, most implicitly integrated elasto-plastic equations use α=1.

The following paragraphs summarize explicit and implicit integration methods.

2.2.2.1. Explicit Integration

Explicit integration methods are used extensively in integrating elasto-plastic constitutive equations (see for example, Nayak and Zienkiewiczs, 1972; and Potts and Gens, 1985) and generally assume the following approximation to equations 2.15b,c:

$$\varepsilon^p_{n+1} = \varepsilon^p_n + \dot{\Lambda}\,\mathbf{P}_n \tag{2.16a}$$

$$\mathbf{q}_{n+1} = \mathbf{q}_n + \dot{\Lambda}\,\mathbf{h}_n \tag{2.16b}$$

In this procedure, the plastic consistency condition (Equation 2.12d) is not imposed directly, and the plastic multiplier $\Delta\Lambda = \dot{\Lambda}$ ($\dot{\Lambda}$, for infinitesimal strain is calculated using Equation 2.13b).

This type of integration is 'first order' accurate (i.e. accuracy depends on the size of the strain increment) and can become unstable for large strain increments (conditionally

---

[1]Equations 2.15 represent a general trapezoidal rule. Other integration schemes involve the plastic strains at intermediate time $t_{n+\alpha}$ where $0 \le \alpha \le 1$ (see Kreyzig, 1983).

[2]For $\alpha \ne 1/2$, the integrated equations are first order accurate.

stable). In order to achieve accurate, stable solutions, the algorithm should be used in conjunction with the following:

1. Sub-stepping (subincrementation). The explicit integration scheme only converges to the 'exact' solution for $\Delta\varepsilon/\Delta t \rightarrow \dot{\varepsilon}$. However, numerical accuracy can be evaluated by comparing the response (stress path) for integration over n substeps, $d\varepsilon$, where $\Delta\varepsilon = n d\varepsilon$ (e.g Hermann et al., 1987; Pasternack and Timmermann, 1987; Faruque and Desai, 1985). Thus, for a given soil model, the user can estimate the maximum allowable step size[1] $|d\varepsilon|_{max}$ to achieve numerically accurate solution (i.e., within prescribed tolerance). However, experience reported in the literature shows that there is no general prescriptive method for estimating $|d\varepsilon|_{max}$ a priori.
2. Drift correction. If the plastic consistency is not imposed in the integration algorithm (i.e. using equations 2.15a, 2.16a,b only), the stress point tends to 'drift' away from the yield surface[2], even for small (substepping) strain increments, $|d\varepsilon| < |d\varepsilon|_{max}$. In order to avoid accumulating errors, a drift correction is applied after each substep to ensure that the stress point always remains in contact with the yield surface. Potts and Gens (1985) compare the relative merits of a number of drift correction algorithms in conjunction with a density hardening Cam Clay model. Their results confirm the ad-hoc nature of the drift correction and hence emphasize the importance of using small substepping strain increments.

A number of authors (Simo and Ortiz, 1985; Simo and Hughes, 1987) have shown that the drift correction is not necessary if the explicit integration scheme includes the plastic consistency condition (Equation 2.15d). Figure 2.2 shows the explicit integration algorithm proposed by Simo and Hughes (1987) and is based on the concept of an elastic predictor-plastic corrector method:

In the first step (k=0), it is assumed that $\varepsilon_{n+1}^{p[0]} = \varepsilon_n$ (no plastic strains) and $q_{n+1}^{[0]} = q_n$ (no hardening). The updated 'elastic predictor' stress state is obtained by integrating the (hyper)elastic stress-strain relations:

$$\sigma_{n+1}^{[0]} = \overline{C} : (\varepsilon_{n+1} - \varepsilon_n^p) \tag{2.17a}$$

and the updated yield function is then determined as:

$$f_{n+1}^{[0]} = f\left(\sigma_{n+1}^{[0]}, q_{n+1}^{[0]}\right) \tag{2.17b}$$

---

[1] $|d\varepsilon|$ is a norm of the tensor.

[2] Higher order schemes (Sloan 1987) do not require drift correction.

The ultimate goal of the algorithm is to satisfy the yield function, $f_{n+1} = 0$. At intermediate stages, k, the yield function can be written $\left(f_{n+1}^{[k]} + df_{n+1}^{[k]}\right) = 0$, where $df_{n+1}^{[k]}$ is the residual/error in the estimate of f_{n+1}. The estimate of the yield function can be improved by considering the Taylor series expansion of the residual:

$$df = \left[\frac{\partial f}{\partial \sigma} d\sigma + \frac{\partial f}{\partial \mathbf{q}} d\mathbf{q}\right]_{n+1}^{[k]} = - f_{n+1}^{[k]} \tag{2.18}$$

where the variations $d\sigma$ and dq are functions of the plastic multiplier:

$$\frac{d\sigma}{d\Lambda} = \frac{d\sigma}{d\varepsilon^p}\frac{d\varepsilon^p}{d\Lambda} = \mathbf{C}:\mathbf{P} \; ; \; \frac{d\mathbf{q}}{d\Lambda} = \mathbf{h} \tag{2.19}$$

and the residual is computed:

$$df_{n+1}^{[k]} = \left[-\mathbf{Q}_{n+1}^{[k]}:\mathbf{C}:\mathbf{P}_{n+1}^{[k]} + \left(\frac{\partial f}{\partial \mathbf{q}}\right)_{n+1}^{[k]} \mathbf{q}_{n+1}^{[k]}\right] d\Lambda^{[k]} \tag{2.20}$$

where $\mathbf{Q} = \partial f / \partial \sigma$.

The plastic consistency parameter can then be obtained at the intermediate stage:

$$d\Lambda_{n+1}^{[k]} = \frac{f_{n+1}^{[k]}}{\left[\mathbf{Q}_{n+1}^{[k]}:\mathbf{C}:\mathbf{P}_{n+1}^{[k]} - \left(\frac{\partial f}{\partial \mathbf{q}}\right)_{n+1}^{[k]} \mathbf{h}_{n+1}^{[k]}\right]} \tag{2.21}$$

Hence, the incremental plastic strains and hardening parameters are computed starting from the trial state. The algorithm (Figure 2.2) describes a sequence of explicit steps[1] characterizing the plastic correction (return mapping) of the stress point. The algorithm falls within the class of convex cutting plane methods (see Figure 2.2) of constrained optimization.

It is important to emphasize that: a) the algorithm is explicit and is only conditionally stable (i.e. sub-stepping may still be necessary for large $\Delta\varepsilon$); and b) the main advantage of the method is to eliminate the need for drift corrections.

This section focuses on first order integration methods. Sloan (1987) and Gens and Potts (1987) describe higher order integration schemes such as the Runga-Kutta-England method. These methods are more accurate than the simple explicit Euler scheme.

2.2.2.2. Implicit Integration

The principal advantage of implicit integration schemes (i.e. α=1; Equations 2.15) is that they are unconditionally stable (i.e. will converge on a unique solution for all $\Delta\varepsilon$) and hence are generally more robust in numerical computations than first order explicit integration schemes. However, it is important to emphasize that the step size ($\Delta\varepsilon$)

[1]Calculations involve only function evaluations.

generally controls the numerical accuracy of the analysis for two reasons: 1) the numerical integration linearizes the (non-linear) constitutive equations over the imposed strain step ($\Delta\varepsilon$); 2) the strain step linearizes the non-linear load-displacement behavior at the global level. The net result is that improved accuracy can always be achieved by substepping (either at the local or global level).

Implicit integration of elasto-plastic constitutive equations was first proposed by Wilkins (1964) for a von Mises yield criterion with associated perfect plasticity[1]. Simo and Ortiz (1985) and Simo and Taylor (1985) have presented generalized return mapping algorithms for implicit integration of rate independent elasto-plastic constitutive equations. These techniques are now widely used, especially in large strain problems associated with metal plasticity. (e.g. Lush et al., 1989; Eterovic and Bathe, 1990), and have recently been proposed for effective stress soil models (e.g. De Borst and Vermeer, 1984; Runesson, 1987; Borja and Lee, 1990). The computational algorithm includes the following steps:

1. An elastic predictor gives the first estimate of the updated stress and internal variables at t_{n+1}, $\left(\sigma_{n+1}^{[0]}\ ,\ \mathbf{q}_{n+1}^{[0]}\right)$.
2. Solve the plastic corrector problem by an implicit backward Euler difference scheme.
3. Solve the consistency requirement iteratively using a (full) Newton scheme.

Figure 2.3 summarizes the complete implicit integration algorithm (adopted from Simo and Hughes, 1987)[2] in which $\left(\varepsilon_{n+1}^{p},\ \mathbf{q}_{n+1}\right.$ and $\left.\Delta\Lambda_{n+1}\right)$ are solved by iteration:

1. The residuals $\left\{\mathbf{R}_{n+1}^{[k]}\right\}$, at iteration k, correspond to the errors in the flow and hardening rules due to the approximations in $\left(\varepsilon_{n+1}^{p},\ \mathbf{q}_{n+1}\right.$ and $\left.\Delta\Lambda_{n+1}\right)$.
2. Assuming that the residuals are functions of the current state variables (i.e. $\mathbf{R}\left(\sigma_{n+1}^{[k]},\ \mathbf{q}_{n+1}^{[k]}\right)$), then better estimates of the actual state variables can be obtained using a Newton-Raphson scheme (item iii, Figure 2.3):

$$\begin{bmatrix} \dfrac{\partial \mathbf{R}_1}{\partial \sigma_{n+1}} & \dfrac{\partial \mathbf{R}_1}{\partial \mathbf{q}_{n+1}} \\ \dfrac{\partial \mathbf{R}_2}{\partial \sigma_{n+1}} & \dfrac{\partial \mathbf{R}_2}{\partial \mathbf{q}_{n+1}} \end{bmatrix} \begin{Bmatrix} \delta\sigma_{n+1} \\ \delta\mathbf{q}_{n+1} \end{Bmatrix} = \begin{Bmatrix} \mathbf{R}_1 \\ \mathbf{R}_2 \end{Bmatrix} \tag{2.22}$$

where $\mathbf{R}_1\left(\varepsilon_{n+1}^{p}\ ,\ \mathbf{P}_{n+1}\right)$; $\mathbf{R}_2\left(\mathbf{q}_{n+1}\ ,\ \mathbf{h}_{n+1}\right)$ are the current values of the flow rule and hardening rule residuals, respectively.

---

[1]For perfect plasticity, integration requires a two step algorithm of elastic predictor and radial return mapping (plastic corrector).

[2]Figure 2.3 allows for generai non-linear hardening and non-associated flow rules. A similar scheme is used by the ABAQUS (See ABAQUS Theory Manual).

3. The consistency parameter is also corrected concurrently by computing the residual on the yield function, $R_f(\Delta\Lambda)$ (item iv) and then solving for $\delta\Lambda^{[k]}\left(= \Delta\Lambda^{[k+1]} - \Delta\Lambda^{[k]}\right)$ using a second Newton scheme.
4. Corrections for $\delta\varepsilon_{n+1}^{p[k]}$ and $\delta q_{n+1}^{[k]}$ are obtained by combining the two results (item iii and iv) and the updated values are applied to obtain an improved solution by iteration (item vi). Numerical accuracy is prescribed by separate tolerance criteria on the flow/ hardening rule residuals and on the yield function (item ii).
   A modified version of this procedure is presented in Section 2.3.

2.2.2.3. Incremental Stiffness Matrix

The preceding paragraphs have summarized integration methods for computing accurately the local updated stress and state variables at time t_{n+1} (σ_{n+1}, q_{n+1}) given the initial state (σ_n, q_n) and the applied strain increment ($\Delta\varepsilon$). The updated stresses are used directly in the global equilibrium calculations (Equation 2.7a), while the incremental (global) stiffness matrix ${}^{n+1}\mathbf{K}$ is assembled from the local tangent stiffness or 'Jacobian' $\mathbf{J}\left(= \partial\sigma/\partial\varepsilon\right)$ evaluated at the Gauss points (Equations 2.8 and 2.9). For infinitesimal strain steps, $\Delta\varepsilon/\Delta t \rightarrow \dot{\varepsilon}$, the Jacobian is defined unambiguously from the rate constitutive equations and consistency condition (Equations 2.10a,b,c,d and 2.13a,b):

$$\dot{\sigma}_{ij} = C_{ijkl}\left[\dot{\varepsilon}_{kl} - \dot{\Lambda}P_{kl}\right] = C_{ijkl}\left[\dot{\varepsilon}_{kl} - \frac{Q_{ab}\,C_{abcd}\,\dot{\varepsilon}_{cd}\,P_{kl}}{H + Q_{ab}\,C_{abcd}\,P_{cd}}\right] \qquad (2.23)$$

from which, $\mathbf{J} = \left(\partial\dot{\sigma}_{ij}/\partial\dot{\varepsilon}_{ij}\right)$ can be obtained.

The components of this 'continuum Jacobian' operator are most clearly expressed by subdividing all tensorial quantities (in Equation 2.23) into octahedral and deviatoric components:

$$\sigma_{ij} = \sigma_{oct}\delta_{ij} + s_{ij} \qquad (2.24a)$$

$$\varepsilon_{ij} = \varepsilon_{vol}\delta_{ij} + e_{ij} \qquad (2.24b)$$

where $\sigma_{vol} = \frac{1}{3}\sigma_{kk}$ is the mean stress, $\varepsilon_{vol}=\varepsilon_{kk}$ is the volumetric strain, s_{ij} and e_{ij} are the deviatoric stress and strain tensors, respectively. The algebra is further simplified using transformed measures of the deviatoric components S_i and E_i (i=1,2,3,4,5) as defined in Table 2.1 (Kavvadas, 1982; Whittle, 1987)[1]. The general stress-strain relations

---

[1]Notation Convention: Up to this point in the chapter, σ and ε are the tensorial stress and strain quantities respectively. With the introduction of the transformed measures (Table 2.1), σ' is the mean effective stress, $\underline{\sigma}$ is the stress tensor, ε is the volumetric strain and $\underline{\varepsilon}$ is the strain tensor. This convention will be adopted through the rest of the chapter.

quation 2.10b) are now:

$$\dot{\sigma}' = K\left(\dot{\varepsilon} - \dot{\Lambda}P\right) \tag{2.25a}$$

$$\dot{S}_i = 2G\left(\dot{E}_i - \dot{\Lambda}P'_i\right) \tag{2.25b}$$

$$\dot{\Lambda} = \frac{KQ\dot{\varepsilon} + 2GQ'_jE_j}{H + KQP + 2GQ'_jP'_j} \tag{2.25c}$$

here K and G are the hypo-elastic bulk and shear moduli and the remaining terms are ecified in Table 2.1.

The continuum Jacobian, $\mathbf{J_c}$ has components:

$$\mathbf{J_c} = \begin{bmatrix} \frac{\partial\sigma'}{\partial\varepsilon} & \frac{\partial\sigma'}{\partial E_i} \\ \frac{\partial S_j}{\partial\varepsilon} & \frac{\partial S_j}{\partial E_i} \end{bmatrix} = \begin{bmatrix} K\left(1 - P\frac{\partial\dot{\Lambda}}{\partial\dot{\varepsilon}}\right) & -KP\frac{\partial\dot{\Lambda}}{\partial\dot{E}_i} \\ -2GP'_j\frac{\partial\dot{\Lambda}}{\partial\dot{\varepsilon}} & 2G\left(\delta_{ij} - P'_j\frac{\partial\dot{\Lambda}}{\partial\dot{E}_i}\right) \end{bmatrix} \tag{2.26}$$

ith

$$\frac{\partial\dot{\Lambda}}{\partial\dot{\varepsilon}} = \frac{KQ}{\Omega} \; ; \; \frac{\partial\dot{\Lambda}}{\partial\dot{E}_i} = \frac{2GQ'_i}{\Omega}$$

and $\Omega = (H + KQP + 2GQ'_kP'_k)$

and i = 1,2 ... 5

For an elastic material, $\dot{\Lambda} = 0$ and the continuum Jacobian is:

$$\mathbf{J_c} = \begin{bmatrix} K & 0 \\ 0 & 2G\delta_{ij} \end{bmatrix} \tag{2.27}$$

For finite load steps (i.e., given $\Delta\underset{\sim}{\varepsilon}$), the continuum Jacobian is not uniquely efined, as it can be evaluated at any point along the integration path (e.g., at $(\underset{\sim}{\sigma}_n, \mathbf{q}_n)$ or $(\underset{\sim}{\sigma}_{n+1}, \mathbf{q}_{n+1})$ etc)[1]. Furthermore, Nagtegaal (1982) and Simo and Taylor (1985) show at the use of the continuum Jacobian causes a deterioration in the convergence rate of e global Newton iteration scheme, and can reduce very significantly the efficiency (i.e. crease computation times) of the non-linear finite element analysis. These authors troduce the concept that the Jacobian must be consistent with integration algorithm. The nsistent Jacobian, $\mathbf{J} = \partial\Delta\underset{\sim}{\sigma}/\partial\Delta\underset{\sim}{\varepsilon}$, (where $\Delta\underset{\sim}{\sigma} = (\underset{\sim}{\sigma}_{n+1} - \underset{\sim}{\sigma}_n)$, $\Delta\underset{\sim}{\varepsilon} = (\underset{\sim}{\varepsilon}_{n+1} - \underset{\sim}{\varepsilon}_n)$) ensures that e global iteration scheme converges quadratically (using full Newton iteration).

For implicit integration schemes (without subincrementation, such as the closest oint algorithm, Section 2.2.2.2), the consistent Jacobian can be linearized exactly in osed form (Simo and Taylor, 1985; Simo and Hughes, 1987). For explicit integration,

---

[1] Existing finite element codes in geotechnical engineering rarely describe the particular procedure for evaluating $\mathbf{J_c}$.

the consistent Jacobian is approximated, assuming a linear response over the strain step $\Delta\underline{\varepsilon}$. Although this is numerically more cumbersome, the consistent Jacobian does improve significantly the convergence of the global iterative scheme (especially compared to solutions using $\mathbf{J}_c$).

The robust (unconditionally stable), efficient algorithms for implicit integration of elasto-plastic equations and calculation of the consistent Jacobian have gained widespread popularity and have been implemented for a wide variety of constitutive models (e.g. Benalla et al., 1988; Borja and Lee, 1990; De Borst and Feenstra, 1990; Dodds, 1987; Lush et al., 1989; Simo and Ju, 1987; Simo and Pister, 1984; Szabo and Kovacs, 1987).

2.3. Integration of the Modified Cam Clay Model

2.3.1. Model Formulation

The Modified Cam Clay model (MCC; Roscoe and Burland, 1968) is the most widely used effective stress soil model for non-linear finite element analyses of practical geotechnical problems (c.f. Potts and Gens, 1988). The MCC model describes an idealized behavior of soils which is characterized by the framework of Critical State Soil Mechanics (Schofield and Wroth, 1968, Atkinson and Bransby, 1976). The model is formulated around two major observations of soil behavior:

1. It unifies observations of: a) 'volumetric behavior' of soils (characterized by relations between mean effective stress, σ', and void ratio, e; and b) shear behavior, relating σ' to the shear stress[1], S_1. Normally consolidated states of soil form a unique state boundary surface, $\mathbb{S}(\sigma', S_1, e)=0$. Large irrecoverable plastic strains occur only for stress states located on the state boundary surface. Stress states $\mathbb{S}(\sigma', S_1, e)<0$ are referred to as overconsolidated and exhibit elastic, recoverable behavior.
2. When soils are sheared, under general drainage conditions, they tend asymptotically to a critical state, $h(\sigma', S_1, e)=0$, where continued shear distortions can occur at constant effective stress, σ', with no further change in void ratio (i.e., no further volumetric strains).

The generalized constitutive equations of the MCC model can be summarized as follows:

1. The yield function has the form of an ellipsoid:

$$f\{\underline{\sigma},\alpha'(e)\} = S_iS_i - c^2\sigma'(2\alpha'-\sigma') = 0 \qquad (2.28)$$

[1]Where S_1 is the deviatoric stress in triaxial space, Table 2.1.

where α is a hardening parameter describing the maximum hydrostatic pressure (hydrostatic pre-consolidation pressure), and c is the slope of the critical state line[1] (Figure 2.4). Equation 2.28 assumes a von Mises generalization of the yield function and critical state failure criterion (Whittle, 1987). The constant c is calculated from large strain frictional angle in triaxial compression shear tests, ϕ'_{TC}:

$$c = \sqrt{\frac{2}{3}}\, M = \sqrt{\frac{2}{3}}\, \frac{6 \sin \phi'_{TC}}{3 - \sin \phi'_{TC}} \tag{2.29}$$

2. The plastic strains follow an associated flow rule:

$$P = Q = \frac{\partial f}{\partial \sigma'} = 2c^2 (\sigma' - \alpha') \tag{2.30a}$$

$$P'_i = Q'_i = \frac{\partial f}{\partial S_i} = 2S_i \tag{2.30b}$$

3. The elastic moduli are estimated from the slope of a 1-D swelling line, κ, in e-$\log_e\sigma$ space (Figure 2.4):

$$K = \frac{\dot{\sigma}'}{\dot{\varepsilon}} = \left(\frac{v_0}{\kappa}\right) \sigma' \tag{2.31a}$$

where $v_0=(1+e_0)$ is the initial specific volume.

In this version of the model, a constant Poisson's ratio, ν', is used and hence:

$$2G/K = 3\,(1-2\nu')\,/\,(1+\nu') = \text{constant.} \tag{2.31b}$$

4. The yield surface exhibits density hardening which is proportional to the rate of plastic volumetric strain $\dot{\varepsilon}^p$:

$$\dot{\alpha}' = \left(\frac{v_0}{\lambda - \kappa}\right) \dot{\Lambda}\, P \tag{2.32a}$$

where λ is the measured slope of the virgin consolidation line (VCL) in e-$\log_e\sigma'$ space (Figure 2.4). It should be noted that changes in void ratio are controlled by the rate of volume change:

$$\dot{e} = -\,(1 + e_0)\,\dot{\varepsilon} \tag{2.32b}$$

5. Overall, the MCC model uses four input material constants (ϕ'_{TC}, κ, λ, 2G/K) and two state variables (α',e).

2.3.2. Integration Algorithm

This section describes an implicit integration algorithm for the MCC model based on the *General Closest Point Projection Algorithm* (Simo and Hughes, 1987; Section

[1] c also describes the ratio of the major to minor semi-axes of the ellipsoid.

.2.2.2)[1].

. Elastic Predictor:

In the first estimate for the updated stress, $\left(\sigma'^{[0]}_{n+1}\ ,\ S^{[0]}_{i,n+1}\right)$, the plastic strains and ardening function assume the following:

$$\Delta\varepsilon^{p[0]}_{n+1} = \Delta E^{p[0]}_{i,n+1} = \Delta\alpha'^{[0]}_{n+1} = 0 \tag{2.33a}$$

The updated stress state:

$$\sigma'^{[0]}_{n+1} = \sigma'_n + \overline{K}\,\Delta\varepsilon_{n+1}\ ;\ S^{[0]}_{i,n+1} = S_{i,n} + 2\overline{G}\,\Delta E_{i,n+1} \tag{2.33b}$$

The hyperelastic moduli $\overline{K}$, $2\overline{G}$ are evaluated by integrating the non-linear elastic ate equations 2.25a,b and 2.31a,b:

$$\sigma'^{[0]}_{n+1} = \sigma'_n \exp\left[v_0\,\kappa^{-1}\,\Delta\varepsilon_{n+1}\right] \tag{2.34a}$$

$$S^{[0]}_{i,n+1} = S_{i,n} + \left(\frac{2G}{K}\right)\sigma'_n\left(\frac{\Delta E_{i,n+1}}{\Delta\varepsilon_{n+1}}\right)\left(\exp\left[v_0\,\kappa^{-1}\,\Delta\varepsilon_{n+1}\right] - 1\right) \tag{2.34b}$$

For the special case when $\Delta\varepsilon_{n+1}\rightarrow 0$ (undrained deformation or isotropic hearing) equations 2.34a,b reduce to the form:

$$\sigma'^{[0]}_{n+1} = \sigma'_n \tag{2.34c}$$

$$S^{[0]}_{i,n+1} = S_{i,n} + \left(\frac{2G}{K}\right)\frac{v_0}{\kappa}\,\sigma'_n\,\Delta E_{i,n+1} \tag{2.34d}$$

These equations are imposed separately to avoid division by zero errors. They do not affect the formulation of the local Newton iteration scheme or the consistent Jacobian perator.

The elastic predictor (equations 2.34a,b) assumes that there is no change in void atio accurring over the applied increment of strain ($\Delta\underset{\sim}{\varepsilon}$). This approximation simplifies ntegration of the non-linear elastic relations but has negligible effect on the solution ccuracy (or convergence characteristics).

. Plastic Corrector

If the trial stress state is located outside the yield surface (i.e., $\left(\underset{\sim}{\sigma}^{[0]}_{n+1}\ ,\ \alpha'^{[0]}_{n+1}\right) > 0$) then plastic strains occur. The 'plastic corrector' imposes the flow nd hardening rules together with the consistency requirement. For the MCC model, ıese equations can be summarized as follows:

MCC was previously integrated within ABAQUS. However, details of this formulation are propriety to IKS. A similar formulation has also recently been presented independently by Borja and Lee (1990).

$$
\begin{aligned}
\sigma'_{n+1} &= \sigma'_n \exp\left[v_0\,\kappa^{-1}\left(\Delta\varepsilon_{n+1} - \Delta\varepsilon^p_{n+1}\right)\right] \\
\Delta\varepsilon^p_{n+1} &= \Lambda_{n+1}\, 2\, c^2 \left(\sigma'_{n+1} - \alpha'_{n+1}\right) \\
S_{i,n+1} &= S_{i,n} + \left(\frac{2G}{K}\right)\sigma'_n \left(\frac{\Delta E_{i,n+1} - \Delta E^p_{i,n+1}}{\Delta\varepsilon_{n+1} - \Delta\varepsilon^p_{n+1}}\right)\left\{\exp\left[v_0\,\kappa^{-1}\left(\Delta\varepsilon_{n+1} - \Delta\varepsilon^p_{n+1}\right)\right] - 1\right\} \\
\Delta E^p_{i,n+1} &= \Lambda_{n+1}\, 2\, S_{i,n+1} \\
\alpha'_{n+1} &= \alpha'_n \exp\left[v_0\left(\lambda - \kappa\right)^{-1}\Delta\varepsilon^p_{n+1}\right] \\
\left(S_i\, S_i\right)_{n+1} &- c^2\,\sigma'_{n+1}\left(2\alpha'_{n+1} - \sigma'_{n+1}\right) = 0
\end{aligned}
\qquad (2.35)
$$

where $i=1,2,\ldots,5$, $\Delta\varepsilon^p_{n+1} = \left(\varepsilon^p_{n+1} - \varepsilon^p_n\right)$ and $\Delta E^p_{i,n+1} = \left(E^p_{i,n+1} - E^p_{i,n}\right)$.

Figure 2.5 summarizes the algorithm for solving these equations using an implicit Euler integration scheme with full Newton iteration (c.f. Figure 2.3). The void ratio can be updated at the end of each step in accordance with Equation 2.32b.

2.3.3. Consistent Tangent Stiffness Matrix

Simo and Taylor (1985), Section 2.2.2.3, show that the definition of the tangent stiffness matrix affects the convergence characteristics of the global finite element equilibrium equations. For Newton iteration schemes, quadratic convergence can be achieved using a tangent stiffness matrix which is consistent with the integration algorithm of the constitutive model, and is referred to as the consistent Jacobian, **J**:

$$
\mathbf{J} = \begin{bmatrix} \dfrac{\partial\Delta\sigma'}{\partial\Delta\varepsilon} & \dfrac{\partial\Delta\sigma'}{\partial\Delta E_i} \\ \dfrac{\partial\Delta S_i}{\partial\Delta\varepsilon} & \dfrac{\partial\Delta S_i}{\partial\Delta E_i} \end{bmatrix} \qquad (2.36)
$$

for implicit integration of the MCC model, analytical expressions can be derived for the components of **J** for a) non-linear elastic and b) elasto-plastic stress-strain response.

The MCC model exhibits a non-linear elastic behavior for all stress states within the yield surface. Elastic stress-strain behavior (equations 2.34) leads to the following consistent stiffness matrix:

$$
\begin{aligned}
\mathbf{J} &= \begin{bmatrix} \dfrac{v_0}{\kappa}\,\sigma'_n \exp\left[v_0\,\kappa^{-1}\,\Delta\varepsilon_{n+1}\right] & 0 \\ 0 & \delta_{ij}\left(\dfrac{2G}{K}\right)\dfrac{v_0}{\kappa}\,\sigma'_n \exp\left[v_0\,\kappa^{-1}\,\Delta\varepsilon_{n+1}\right] \end{bmatrix} \\
&= \begin{bmatrix} K_{n+1} & 0 \\ 0 & \delta_{ij}\, 2\, G_{n+1} \end{bmatrix}
\end{aligned}
\qquad (2.37)
$$

where K_{n+1} and G_{n+1} are the hypo-elastic moduli evaluated at the end of the strain increment $\Delta\varepsilon_{n+1}$.

For elasto-plastic behavior, equations 2.35a to 2.35f can be rewritten in ifferential form:

$$\begin{aligned}
\delta\sigma'_{n+1} &= K_{n+1}\left(\delta\varepsilon_{n+1} - \delta\varepsilon^{p}_{n+1}\right)\\
\delta\varepsilon^{p}_{n+1} &= \Lambda_{n+1}\, 2c^2\left(\delta\sigma'_{n+1} - \delta\alpha'_{n+1}\right) + P_{n+1}\,\delta\Lambda_{n+1}\\
\delta S_{i,n+1} &= 2G_{n+1}\left(\delta E_{i,n+1} - \delta E^{p}_{i,n+1}\right)\\
\delta E^{p}_{i,n+1} &= \Lambda_{n+1}\, 2\delta S_{i,n+1} + P'_{i,n+1}\,\delta\Lambda_{n+1}\\
\delta\alpha'_{n+1} &= \alpha'_{n+1}\, v_0\left(\lambda-\kappa\right)^{-1}\,\delta\Delta\varepsilon^{p}_{n+1}\\
\delta f &= s_{i,n+1}\,\delta s_{i,n+1} - c^2\left(\alpha'_{n+1} - \sigma'_{n+1}\right)\delta\sigma'_{n+1} - c^2\,\sigma'_{n+1}\,\delta\alpha'_{n+1} = 0
\end{aligned} \tag{2.38}$$

here $(P,P'_i)_{n+1}$ and Λ_{n+1} are the flow direction and plastic multiplier at t_{n+1}. The nearized plastic multiplier $\delta\Lambda_{n+1}$ is evaluated by solving equations 2.38:

$$\delta\Lambda_{n+1} = \frac{\dfrac{K_{n+1}}{\beta_1}\left\{Q_{n+1} - 2c^2\,\sigma'_{n+1}\, z\,\dfrac{\beta_6}{\beta_3}\right\}\delta\varepsilon_{n+1} + \dfrac{2G_{n+1}}{\beta_2}\left(Q'_i\,\delta E_i\right)_{n+1}}{2c^2\,\sigma'_{n+1}\, z\,\dfrac{\beta_7}{\beta_3}\,P_{n+1} + \dfrac{1}{\beta_3}\,\dfrac{K_{n+1}}{\beta_3}\,Q_{n+1}\,P_{n+1} + \dfrac{2G_{n+1}}{\beta_2}\left(Q'_i\,P'_i\right)_{n+1}} \tag{2.39}$$

here:

$$\begin{aligned}
z &= v_0\left(\lambda - \kappa\right)\alpha'_{n+1}\\
\beta_1 &= 1 + K_{n+1}\,\frac{2c^2\,\Lambda_{n+1}}{\beta_3}\\
\beta_2 &= 1 + 4G_{n+1}\,\Lambda_{n+1}\\
\beta_3 &= 1 + 2c^2\,\Lambda_{n+1}\,\alpha'_{n+1}\,v_0\left(\lambda - \kappa\right)\\
\beta_4 &= 2c^2\,\Lambda_{n+1}\left(1 - \frac{z}{\beta_3}\,2c^2\,\Lambda_{n+1}\right)\\
\beta_6 &= 2c^2\,\Lambda_{n+1}\,\frac{K_{n+1}}{\beta_1}\\
\beta_7 &= 1 - \left(\frac{2c^2\,\Lambda_{n+1}}{\beta_3}\right)\frac{K_{n+1}}{\beta_1}
\end{aligned} \tag{2.40}$$

Table 2.2 summarizes the consistent Jacobian for elasto-plastic material response. lthough the analytical expressions for **J** are cumbersome, the use of the consistent acobian provides important benefits of numerical efficiency. The following points hould be noted from Table 2.2:

1. For infinitesimal strain increments, $\Lambda_{n+1} \rightarrow 0$ and hence $\beta_1, \beta_2, \beta_3, \beta_7 \rightarrow 1$ while $\beta_4, \beta_6 \rightarrow 0$. The consistent tangent stiffness matrix reduces to the continuum Jacobian expression (Equation 2.26).
2. Non-symmetric terms in the consistent Jacobian are due to the density hardening of the MCC model. From a computational perspective, this non-symmetry is of

relatively minor importance. Similar convergence of the global equilibrium equation can be achieved using either symmetric or non-symmetric matrix solvers.

2.3.4. Model Verification

This section describes results a number of numerical experiments which demonstrate the accuracy, stability and convergence properties for implicit integration of the MCC model with the consistent Jacobian formulation. Table 2.3 list input parameters for the MCC model corresponding to the behavior of Boston Blue Clay.

Figure 2.6 shows the effective stress paths and shear stress-strain response for undrained triaxial compression and extension tests[1] computed by the MCC model for a single finite element[2]. In this example, the sample is consolidated hydrostatically to an initial OCR ($=\sigma'_p/\sigma'_{vo}$)=1.5, and the undrained shear strains are applied in N finite steps of size $\Delta\varepsilon_a$ (N.B. $\Delta\varepsilon_h = -1/2\ \Delta\varepsilon_a$) up to a total axial strain $|\varepsilon_a|$=20%. Numerically accurate solutions can always be obtained using a large number of steps. Thus, the results for N=1000 correspond to the 'correct' integration of the MCC constitutive equations. The figure shows that a very similar response is obtained using much larger strain steps (N = 20 , 5). These results confirm that the implicit integration algorithm is robust (stable) and can give accurate solutions without sub-stepping.

Figure 2.7 shows further results for a drained triaxial compression shear test performed at a constant confining (horizontal) stress for a clay sample consolidated to OCR=8. In this case, yielding of the clay induces significant dilation of the sample and the MCC model predicts strain softening behavior which approaches critical state conditions at large shear strains. Even for this more complex example, numerically accurate solutions can be achieved using relatively large strain steps. The non-linearity in the pre-peak portion of the stress strain curve (i.e., the elastic response, Figure 2.7b) is a result of assuming a constant Poisson's ratio, ν', in the MCC model formulation (Equation 2.31b). This assumption is widely used in the literature on the MCC model (see for example, Wood, 1990; Gens and Potts, 1987; Borja and Lee, 1990). An alternative formulation of the elastic functions would be to use a constant shear modulus, G, which would lead to a linear elastic pre-peak response in Figure 2.7b. Using a

---

[1]Note: In triaxial space $S_1 = \frac{2}{\sqrt{6}}(\sigma_a - \sigma_h)$, while for undrained shear, $E_1 = \frac{2}{\sqrt{6}}(\Delta\varepsilon_a - \Delta\varepsilon_h) = \frac{\sqrt{3}}{\sqrt{2}}\Delta\varepsilon_a$. σ'_p is the effective preconsolidation pressure.

[2]Eight node isoparametric element with pore pressure degrees of freedom at the corner nodes.

constant G may result in unrealistic (and even negative) values of the Poisson's ratio of the soil skeleton.

Figure 2.8 summarizes results from a simple boundary value problem which illustrates the importance of the consistent Jacobian formulation. The analysis simulates the drained triaxial shearing of normally consolidated BBC at constant confining stress with rigid rough end platens (Figure 2.8d). Figure 2.8e compares the convergence of solutions using the continuum (J_c, Equation 2.26) and consistent Jacobian (Table 2.2) formulations. The results show that the consistent Jacobian reduces significantly the number of iterations required to achieve a prescribed solution accuracy. Figure 2.8f shows the force residuals computed at successive iterations in selected steps of the analysis using the consistent Jacobian. These results confirm the quadratic convergence of the equilibrium equations using the consistent Jacobian (N.B. The tolerance on force residuals is used in this calculation).

2.4. Integration of the MIT-E3 model

This section summarizes the formulation of MIT-E3 (Whittle 1987, 1990) and describes the procedures used to integrate this model in the ABAQUS finite element code.

2.4.1. Model Formulation[1]

The MIT-E3 model was developed to describe the behavior of overconsolidated clays and clays under cyclic loading. The model is based on a simple conceptual framework which attempts to unify important aspects of non-linear, in-elastic and anisotropic behavior of overconsolidated clays.

Experimental data indicate that the unloading and reloading characteristics of a clay in drained shearing (σ'=constant) and hydrostatic compression exhibit similar features: a) much stiffer response than the primary loading curve; b) hysteretic stress-strain behavior; c) small irrecoverable deformations on completion of the unload-reload cycle; and d) reloading transition to the primary loading curve (normally consolidated condition). These observations are modelled in MIT-E3 using a simple mechanical model. Figure 2.9 shows the conceptual framework used by the model for the hydrostatic unloading and reloading. It is assumed throughout that the soil can be modelled as a rate independent material (i.e., creep effects are not considered). The measured behavior of a clay is most closely described by A-B-C (Figure 2.9b). For modelling purposes, MIT-E3 subdivides this behavior into two components:

---

[1]For complete details of the model formulation refer to Whittle (1990).

1. A closed, symmetric, hysteresis loop (Figure 2.9a) which matches the observed behavior during unloading. This response is referred to as 'Perfectly Hysteretic' and is described through a formulation similar to that proposed by Hueckel and Nova (1979).
2. For reloading, plastic (irrecoverable) strains are assumed to develop as the Virgin Consolidation Line (VCL) is approached, resulting in residual plastic strains, Δ^p, at A. The magnitude of plastic strains is determined by the proximity of the current stress state to the VCL. Thus the plasticity is conveniently described using a bounding surface (Dafalias and Herrmann, 1980) or subloading surface (Hashiguchi, 1980) model.

Within this subdivision, MIT-E3 implicitly contains a number of important assumptions concerning the behavior of overconsolidated clays:

1. The behavior of overconsolidated clays can not be fully described by the overconsolidation ratio (OCR) of the soil. Additional information of the loading history is also required to distinguish between 'unloading' and 'reloading' at a particular overconsolidated stress state, i.e., extra state variables must be included in the material description.
2. A load cycle in stress space always involves some plastic strains, so that there is no purely reversible (elastic) range of behavior.
3. Inclusion of plastic strains, using bounding surface plasticity, provides the means of coupling volumetric and shear behavior and is also the mechanism by which anisotropic properties are described for overconsolidated clays. Bounding surface plasticity also insures a smooth transition to normally consolidated behavior, so that 'yielding' is smoothed out (hence the classical role of the 'yield surface' is no longer of critical importance).

Finally, the generalized behavior of K_0-normally consolidated clays is described using an elasto-plastic formulation (extending an earlier model developed by Kavvadas, 1982). This model describes; a) the anisotropic properties of K_0-normally consolidated clays, and b) strain softening behavior which is observed experimentally for certain modes of deformation.

2.4.1.1. Normally Consolidated Clay

The mechanical behavior of soil elements normally consolidated along radial effective stress paths (S/σ' = constant) is described by a yield surface which is initially oriented along the direction of consolidation. The yield function is written (Kavvadas, 1982):

$$f = (\mathbf{S} - \sigma' \mathbf{b}) : (\mathbf{S} - \sigma' \mathbf{b}) - c^2 \sigma' (2\alpha' - \sigma') = 0 \tag{2.41}$$

where, α' controls the size of the yield surface, $\mathbf{b}$ is a second order tensor describing the orientation of the yield surface in effective stress space (σ', $\mathbf{S}$) and c is the ratio of the semi-axes of the ellipsoid (Figure 2.10). For the case when $\mathbf{b}=\mathbf{0}$, the yield surface reduces to the same form as that used in the Modified Cam Clay model (MCC; Roscoe and Burland, 1968).

A 'virgin normally consolidated' soil element (i.e., one consolidated from a slurry along a radial effective stress path) is described by the stress state at the tip of the yield surface such that:

$$\begin{aligned} \sigma' &= 2\,\alpha' \\ \mathbf{S} &= 2\,\alpha'\,\mathbf{b} \end{aligned} \tag{2.42}$$

The load direction, $\mathbf{Q}$, for stress states located on the yield surface is given by the gradient of the yield surface:

$$\begin{aligned} \mathbf{Q} &= 2\,c^2 (\sigma' - \alpha') - 2\,(\mathbf{S} - \sigma'\,\mathbf{b}) : \mathbf{b} \\ Q'_i &= 2\,(S_i - \sigma'\,b_i) \end{aligned} \tag{2.43}$$

Failure conditions are represented by an anisotropic failure criterion:

$$h = \left(\mathbf{S} - \sigma' \underset{\sim}{\xi}\right) : \left(\mathbf{S} - \sigma' \underset{\sim}{\xi}\right) - k^2 \sigma'^2 = 0 \tag{2.44}$$

where h describes a cone in effective stress space, with apex at the origin and axes along the direction $(\mathbf{I} + \underset{\sim}{\xi})$ (Figure 2.10).

In general, the components of $\underset{\sim}{\xi}$ cannot be determined from standard laboratory tests. Instead, it is assumed that the orientation tensor is fully defined by the friction angles measured in triaxial compression and extension tests (ϕ'_{TC} and ϕ'_{TE}, respectively) at large strain conditions (typically $\varepsilon_a \approx 10\%$ in undrained shear tests). The failure condition can then be written using the transformed stress measures (Tables 2.1):

$$h = S_i\,S_i - 2\,S_1\,\sigma' \xi_1 + \sigma'^2 \left(\xi_1^2 - k^2\right) = 0 \tag{2.45}$$

where $\xi_1 = \frac{1}{2}(C_c - C_e)$ $\qquad k = \frac{1}{2}(C_c + C_e)$

$$C_c = \sqrt{\frac{2}{3}}\,\frac{6 \sin \phi_{TC}}{3 - \sin \phi_{TC}} \qquad C_e = \sqrt{\frac{2}{3}}\,\frac{6 \sin \phi_{TE}}{3 + \sin \phi_{TE}}$$

The model assumes two hardening rules to describe changes in the size and orientation of the yield surface respectively:

$$\dot{\alpha}' = \alpha'\,\zeta\,\dot{\varepsilon}^p \tag{2.46a}$$

$$\dot{\mathbf{b}} = \psi_o \langle r_x \rangle \frac{1}{\alpha'} (\mathbf{S} - \sigma \mathbf{b})\,\dot{\varepsilon}^p \tag{2.46b}$$

where ζ is a dimensionless function of the state variables which is obtained by invoking

e consistency requirement ($\dot{f} = 0$), ψ_0 is a material constant controlling the rate of ıtation of the yield surface, and r_x is a scalar which describes the relative orientation of e yield surface to the critical state cone (Figure 2.10, algebraic definition of r_x is derived Appendix A).

Equation 2.46a corresponds to density hardening similar to that used by the MCC ıodel, while Equation 2.46b describes the rotational hardening of the yield surface and ɜnce controls the rate of change of anisotropy of the clay. The general form of the ıuation is such that the principal axes of anisotropy rotate towards the principal stress ‹es. For the specific case when the principal axes of stress ($\underline{\sigma}$) and anisotropy (**b**) ɔincide, there are no further rotations of the principal directions of anisotropy (**b=0**). he variable r_x imposes limits on the principal directions of anisotropy. The form of r_x is ɜlected such that a K_0-normally consolidated material (i.e., a sample with anisotropic ructure due to its consolidation history) changes its anisotropic structures more slowly ıan a hydrostatically consolidated sample (which is isotropic due to the stress history) ɔaded under the same conditions.

A non-associated flow rule is used in order to generate: a) critical state failure conditions; and b) K_0 conditions for a 'virgin normally consolidated clay' (K_{0NC}). The flow rule is defined as follows:

$$\begin{aligned} \mathbf{P} &= 2\, c^2\, \alpha'\, r_c \\ \mathbf{P}' &= c^2\, x\, (\mathbf{Q}' + \langle r_c \rangle\, \mathbf{S}) \end{aligned} \tag{2.47}$$

'here x is a constant which defines the K_{0NC} condition:

$$x = \left(\frac{\lambda}{\lambda - \kappa}\right)\left\{\frac{1 + 2\,K_{0NC}}{3\,(1 - K_{0NC})} - \frac{K}{2G}\left(\frac{\kappa}{\lambda}\right)\right\} \tag{2.48}$$

The parameter r_c is a scalar variable (Figure 2.10; Appendix A) which describes ıe location of the current stress state relative to the failure surface.

The elasto-plastic modulus, H, is defined by detailed consideration of the ɜhavior of K_0-normally consolidated clays. The functional form of H is selected in order ɔ describe: a) virgin consolidation lines (VCL) with slope λ in e-$\log_e\sigma'$ space for all ıdial consolidation paths in effective stress (σ',**S**) space; and b) strain hardening, peak ɜrength, strain softening and critical state conditions for undrained shearing of K_0-ɔrmally consolidated clays:

$$H = 2\, c^2 \left(\frac{\kappa}{\lambda - \kappa}\right) K \left\{\alpha'\, P - S_t\, 2\, c^2\, \alpha'\, x\, \langle r_c \rangle (\mathbf{Q}' : \mathbf{b})\right\} \tag{2.49}$$

'here S_t is a material constant.

Having selected the functional form of the elasto-plastic modulus, the model ɔrmulation is completed by invoking the consistency requirement that the stress state

remains in contact with the yield surface for loading of a normally consolidated clay:

$$\dot{f} = \frac{\partial f}{\partial \underline{\sigma}} : \dot{\underline{\sigma}} + \frac{\partial f}{\partial \alpha'} : \dot{\alpha}' + \frac{\partial f}{\partial \mathbf{b}} : \dot{\mathbf{b}} \tag{2.50}$$

This equation can be satisfied by solving for the constant ζ (Equation 2.46a) (Kavvadas, 1982):

$$\zeta = \frac{1}{\alpha'} \left\{ \frac{1}{2\, c^2\, \alpha'} \frac{H}{P} - \psi_0 \langle r_x \rangle \frac{\sigma'}{\alpha'} (2\,\alpha' - \sigma') \right\} \tag{2.51}$$

2.4.1.2. Hysteretic Model

For a load cycle in stress space, the perfectly hysteretic model describes a closed symmetric hysteresis loop in the stress-strain response of the material. This behavior is obtained using a formulation which is piecewise continuous (i.e., the moduli vary smoothly) between stress reversal points as suggested by Hueckel and Nova (1979). The model requires a) the definition of a 'stress reversal point', and b) the development of suitable expressions to describe the (secant or tangent) moduli relative to the stress reversal point.

It is assumed that the perfectly hysteretic response is based on the incremental isotropic relations between effective stress and elastic strain rates (Equation 2.25). Furthermore, the Poisson's ratio for the soil skeleton, ν', is assumed to be constant, (i.e. 2G/K = constant). Thus, there is no coupling between volumetric and shear behavior in the perfectly hysteretic equations. The perfectly hysteretic model is constructed by dimensionless distances (in stress space), which relate the current stress state to the stress reversal state:

$$\xi = \begin{cases} \sigma' / \sigma'_{rev} & \text{if } \sigma' > \sigma'_{rev} \\ \sigma'_{rev} / \sigma' & \text{if } \sigma' < \sigma'_{rev} \end{cases} \qquad \xi_s = \left(\bar{\eta}_i\, \bar{\eta}_i\right)^{1/2} \tag{2.52}$$

where, σ'_{rev} is the mean effective stress at the stress reversal point, and $\bar{\eta}_i = \omega_i \times \eta_i = \omega_i \times \left(\frac{S_i}{\sigma'} - \frac{S_{i,\,rev}}{\sigma'_{rev}} \right)$ is the change in shear stress ratio from the last stress reversal state. The parameters ω_i are material constants. For K_0-normally consolidated clays, values of ω_i can be obtained from triaxial shear data assuming that $\omega_1 = \omega$, $\omega_2 = \omega_3 = \omega_4 = \omega_5 = 10\omega_1$.

The volumetric response is described by a tangential bulk modulus:

$$K = \frac{1+e_0}{(1+\delta)\,\kappa_0}\,\sigma' \qquad \delta = C\, n \left(\log_e \xi + \xi_s\right)^{n-1} \tag{2.53}$$

where e_0 is the void ratio, κ_0 defines the initial unloading slope in e-$\log_e\sigma'$ space, and C

and n are material constants to describe non-linearity at small strain levels.

Equations 2.52 and 2.53 show that:

1. The variation of moduli are described using the two measures of stress amplitude ξ and ξ_s corresponding to volumetric and shear behavior. This takes advantage of the uncoupled nature of the incremental stress-strain relations (Equation 2.25).
2. The moduli are related to the most recent stress reversal state. This implies that the small strain behavior of an overconsolidated clay is controlled by the most recent stress history as suggested by Hight et al (1983).

The major assumption of the perfectly hysteretic model is that strains are only recovered in a stress cycle if the cycle begins from a stress reversal point. In this sense, the perfectly hysteretic model may be classed as a para-elastic constitutive law (Huekel and Nova, 1979). In the proposed formulation, the moduli are described relative to the most recent stress reversal point. Thus there is a strong similarity between the stress reversal point and the concept of unloading in plasticity. However for the perfectly hysteretic model, the effective stress $(\dot{\sigma}' , \dot{S})$ and strain rates $(\dot{\varepsilon} , \dot{E})$ are proportional and the stress reversal point is defined in the direction of the strain rates. Hight et al. (1983) present data which further suggest that the initiation of undrained shearing always involves high stiffness at small strain levels irrespective of the past consolidation (or strain) history. This implies that it may be more useful to separate the loading criterion into volumetric and deviatoric components and take advantage of the lack of coupling between volumetric and shear behavior in the perfectly hysteretic model. The definition of the load reversal point is achieved by introducing a scalar strain amplitude parameter which describes the strain history relative to (the strain state at) the most recent stress reversal point as follows:

$$\chi = \begin{cases} \Delta l_{\varepsilon} & \text{for } \dot{\varepsilon} \neq 0, \quad \text{Drained Behavior} \\ \left(\Delta l_E : \Delta l_E \right)^{1/2} & \text{for } \dot{\varepsilon} = 0, \text{ Undrained Behavior} \end{cases} \tag{2.54}$$

where, $\Delta l_{\underset{\sim}{\varepsilon}} = \int_{rev} d\underset{\sim}{\varepsilon} = \underset{\sim}{\varepsilon} - \underset{\sim}{\varepsilon}_{rev}$; and E are the deviatoric strains.

The implication of Equation 2.54 is that the volumetric strains are predominantly important in determining the non-linearity of the soil. 'Loading' is then defined from the sign of the rate of the strain amplitude; $(\dot{\chi} = {}^{t+\Delta t}\chi - {}^{t}\chi)$.

2.4.1.3. Bounding Surface Plasticity

In the modelling of overconsolidated clays, the development of plastic strains plays a crucial role for three main reasons. Firstly, plastic strains introduce coupling

between volumetric and shear behavior, so that shear induced pore pressures are obtained for undrained (montonic and cyclic) shearing. Secondly, within the MIT-E3 formulation, plastic strains enable the incorporation of anisotropic response for overconsolidated clays and provide a smooth transition to the normally consolidated behavior. The bounding surface model (Dafalias and Herrmann, 1980) relates the plastic strains of overconsolidated clays to the plastic behavior previously defined for the normally consolidated material. Difficulties lie in the formulation of these mapping relations and the physical meaning of material constants to describe them.

In the proposed model, the bounding surface of normally consolidated clay behavior is described by the yield function (Equation 2.41). For overconsolidated stress states, a radial mapping rule is used to define a unique image point in the bounding surface (Figure 2.10). Plastic behavior at the current (overconsolidated) stress state, P, is linked to the plastic behavior at the image point, I. The occurrence of plastic strains at P is contingent on the loading condition defined as:

$$K\,Q_I\,\dot{\varepsilon} + 2G\,(\mathbf{Q'_I}:\dot{\mathbf{E}}) \begin{cases} \geq 0 \text{ loading} \\ < 0 \text{ unloading} \end{cases} \tag{2.55}$$

where, Q_I and $\mathbf{Q'_I}$ are the volumetric and deviatoric components of the gradient of the bounding surface at the image point I.

For stress states within the bounding surface, plastic strains are defined by specifying the elasto-plastic modulus, H, and flow direction, **P**, for loading at the current stress state. In the bounding surface formulation, functions are developed to relate H and **P** to the corresponding values at the current image point, H_I and $\mathbf{P_I}$. The MIT-E3 model introduces separate mapping rules for the elasto-plastic modulus and the flow direction which can be expressed in general form:

$$\begin{aligned} \mathbf{P} &= \mathbf{P_I} + \mathbf{P_0}\, g_1 \\ H &= H_I + H_o\, g_2 \end{aligned} \tag{2.56}$$

where $\mathbf{P_0}$, H_0 are the values of **P** and H at the first yield (i.e. at first loading for stress states within the bounding surface); and g_1, g_2 are mapping functions described by the relative position of the current stress and image stress states.

The selection of suitable expressions for H_0, $\mathbf{P_0}$, g_1 and g_2 is a difficult process, especially in view of the joint effects of the two mapping functions. However, this task can be achieved by observing clay behavior in a) hydrostatic unloading and reloading, and b) undrained triaxial shearing of overconsolidated clays. After a number of iterations, a consistent set of equations has been adopted as follows:

$$
\begin{aligned}
P_0 &= -\left\{2\, c^2\, \alpha'\, r_c + (\eta_I : Q'_I)\right\} \\
P'_0 &= 0 \\
g_1 &= \{(\alpha' - \alpha'_o)/(\alpha' - \alpha'_{oi})\}^{\gamma} \\
H_0 &= \frac{1}{\kappa_0}(1+e_0)\{(\alpha' - \alpha'_0)\, h\, |Q_I|\, |P_I|\} \\
g_2 &= \{(\alpha' - \alpha'_0)/(\alpha'_0 - \alpha'_{0i})\}
\end{aligned}
\qquad (2.57)
$$

In these equations, h,g are dimensionless material constants which are established from parametric studies; α'_{0i} is the size of the load surface at first yield.

2.4.1.4. Model Input Parameters

Table 2.4 summarizes the input parameters used by the MIT-E3 model together with their physical significance and proposed laboratory tests from which these properties can be determined (Whittle, 1990). In addition to these 15 material constants, the MIT-E3 model uses the following state variables:

1. The effective stress tensor (σ', S).
2. The size and orientation of the bounding surface (α', **b**).
3. Effective stresses at the most recent reversal state (σ'_{rev}, S_{rev}).
4. The strains accumulated since the last reversal state (Δl_ε, Δl_E).
5. The size of the bounding surface at the last reversal state, α'_{rev}; and the size of the load surface at first yield, α'_{0i}.

Initial values of these state variables must be specified at the start of an analysis:

1. For virgin K_0-normally consolidated clays, the initial values can be defined unambiguously:

$$
\begin{aligned}
&\sigma' = \frac{1}{3}(1 + 2\,K_{0NC})\,\sigma'_{v0},\quad S_1 = \frac{2}{\sqrt{6}}(1 - K_{0NC})\,\sigma'_{v0},\quad S_2 = S_3 = S_4 = S_5 = 0 \\
&\alpha' = \frac{1}{2}\sigma', \qquad b_1 = \frac{1}{2\,\alpha'}\,S_1, \qquad b_2 = b_3 = b_4 = b_5 = 0 \\
&\sigma'_{rev} = \sigma', \qquad S_{rev} = S \\
&\Delta l_\varepsilon = \Delta l_E = 0, \qquad \alpha'_{rev} = \alpha'_{0i} = \alpha'
\end{aligned}
$$

Equations 2.58

2. For overconsolidated clays, ambiguity can arise due to lack of information on the past stress history of the clay (Whittle, 1990). For practical calculations, this thesis assumes that the current (initial) stress state is a stress reversal state and hence:

$$\sigma' = \frac{1}{3}(1 + 2\,K_0)\,\sigma'_{v0}, \qquad S_1 = \frac{2}{\sqrt{6}}(1 - K_0)\,\sigma'_{v0}, \qquad S_2 = S_3 = S_4 = S_5 = 0$$

$$\alpha' = \alpha'_{rev} = \frac{1}{6}(1 + 2\,K_{0NC})\,\sigma'_p, \qquad b_1 = \frac{1}{\alpha'\sqrt{6}}(1 - K_{0NC})\,\sigma'_p, \qquad b_2 = b_3 = b_4 = b_5 = 0$$

$$\sigma'_{rev} = \sigma', \qquad S_{rev} = S$$

$$\Delta l_E = \Delta l_E = 0, \qquad \alpha'_{0i} = \frac{1}{2}\sigma'$$

Equations 2.59

2.4.2. Model Implementation in ABAQUS

Section 2.2 has demonstrated the advantages of a) implicit integration of constitutive equations for stability[1] (robustness) in local stress computations and b) consistent tangent stiffness formulations which insure quadratic convergence of non-linear equilibrium calculations by Newton iteration. For the Modified Cam Clay model (Section 2.3) the components of the consistent Jacobian can be expressed analytically by exact[2] linearization of the (implicitly integrated) constitutive equations. Unfortunately, the same approach cannot be used for the MIT-E3 model due to the following:

1. The hypo-elastic effective stress-strain equations are complex functions which cannot be integrated analytically[3]:

$$\dot{\sigma}' = \frac{1+e_0}{(1+\delta)\,\kappa_0}\,\sigma'\,\dot{\varepsilon}$$
$$\dot{S}_i = \left(\frac{2G}{K}\right)\frac{1+e_0}{(1+\delta)\,\kappa_0}\,\sigma'\,\dot{E}_i \qquad (2.60)$$

   where $\delta = C\,n\left(\log_e \xi(\sigma') + \xi_s(S_i\,,\,\sigma')\right)^{n-1}$, thus, parameter δ couples the non-linear volumetric and shear behavior.

   The elastic predictor must then be obtained by accurate numerical integration and can only be achieved using small strain increments (sub-steps), $d\varepsilon \cong 0.001\%$ (Whittle, 1987). This restriction eliminates the possible benefits of an implicit integration scheme.

2. The scalar parameters r_c and r_x used in the flow and hardening rules are functions of the current stress state which must be evaluated numerically (Appendix A). Thus, it is not possible to derive closed form expressions for the coefficients in a consistent Jacobian.

---

[1]Implicit integration avoids the need for substepping and hence greatly enhances computational efficiency at the local level.

[2]However, note that the implicit integration does contain a small approximation for the void ratio (see Section 2.3)

[3]Analytic integration is only possible for $\xi_s = 0$.

In order to overcome these difficulties, the following strategy is adopted for ıplementing MIT-E3 in the ABAQUS code: 1) the constitutive equations are integrated ;plicitly using simple Euler type integration with substepping and 2) the consistent ;cobian is estimated numerically from the explicit stress calculations.

Figure 2.11 shows the flow chart of the computational procedure used in explicit :uler) integration of the MIT-E3 model. In order to achieve numerically accurate)lutions, the maximum substep size, $d\varepsilon_{max}$= 0.001%. A radial return drift correction is)plied at the end of each substep to ensure that plastic consistency is satisfied (Section .2.2.1).

The continuum Jacobian (tangent stiffness matrix) represents the material :havior at each sub-step (i.e. $d\underset{\sim}{\varepsilon} \approx \dot{\underset{\sim}{\varepsilon}}$) and hence:

$$d\underset{\sim}{\sigma} = \mathbf{J}_c : d\underset{\sim}{\varepsilon} \tag{2.61}$$

here components of $\mathbf{J}_c$ can be computed from equations 2.26 and 2.27. For m sub-eps over the applied strain increment, the computed effective stresses can be written:

$$\Delta\underset{\sim}{\sigma}_{n+1} = \sum_{i=1}^{m} {}_iC\ {}_i\mathbf{J}_c : {}_id\underset{\sim}{\varepsilon} \tag{2.62}$$

where ${}_iC$ are the drift correction factors at each sub-step. The drift corrections impose and additive error in computing the stress increments and affect the evaluation of the consistent tangent stiffness matrix.

Assuming that the material response is linear over imposed strain increment, an)proximate expression for the consistent Jacobian can then be written:

$$\mathbf{J} = \frac{\partial\Delta\underset{\sim}{\sigma}_{n+1}}{\partial\Delta\underset{\sim}{\varepsilon}_{n+1}} \cong \frac{1}{m}\sum_{i=1}^{m} {}_iC\ {}_i\mathbf{J}_c \tag{2.63}$$

This approach is conceptually similar to schemes adopted by Hermann et al .987) for bounding surface plasticity models. Although the consistent Jacobian is not :act, the proposed formulation (Equation 2.63) greatly improves the convergence ıaracteristics of the global Newton iteration scheme. Since the MIT-E3 model has a non-;sociated flow rule, the corresponding Jacobian (Equations 2.26 and 2.63) is)nsymmetric.

.4.3. Model Verification

This section describes a number of numerical experiments which demonstrate the :curacy, stability and convergence properties of the explicit integration algorithm of the IIT-E3 model in ABAQUS. Table 2.4 lists input parameters of the MIT-E3 model)rresponding to the behavior of Boston Blue Clay.

Figure 2.12 shows the effective stress paths and the shear stress-strain response for undrained triaxial compression and extension tests computed by the MIT-E3 model for a single finite element[1]. In these examples the sample is consolidated to various OCR levels, then undrained shear strains are applied up to a total axial strain $|\varepsilon_a|=10\%$. The predicted response matches the response predicted by Whittle (1987) using the explicit integration algorithm of MIT-E3 without the ABAQUS code.

The explicit integration algorithm and the approximate nature of the Jacobian stiffness matrix used for MIT-E3 in ABAQUS cause a deterioration in the convergence characteristics of the global FE equations using the full Newton scheme. It is no longer possible to impose stringent tolerance requirements on force residual calculations. Convergence under these conditions is achieved by imposing a tolerance criterion on maximum displacements residuals. At a given time step Δt (step n to n+1), convergence is achieved if in two successive iterations (i-1 and i) in the global Newton scheme the maximum displacement residual is below a specified tolerance:

$$\left[\frac{{}^{n+1}\Delta U^{[i]} - {}^{n+1}\Delta U^{[i-1]}}{{}^{n+1}\Delta U^{[i]}}\right]_{max} \leq TOL \qquad (2.64)$$

This approach has been used by several published FE schemes utilized in the solution of geotechnical problems (Gunsallas et al., 1989; Finno and Harahap, 1990; Chan, 1986; Chan and Morgenstren, 1989)

Figure 2.13 summarizes results for a simple boundary value problem which illustrates the use of the convergence criteria represented by Equation 2.64. The analysis simulates the undrained triaxial shearing of a BBC sample at OCR=2 with rough rigid platens. The sample is sheared up to a total axial strain of 2% using 8 and 32 analysis steps at the global FE level. Figure 2.13a plots the total shear stress-strain curve of the sample. Figure 2.13b plots the shear stress-strain curve at the center of the sample. Relatively accurate solution can be obtained even when only 8 steps are used. The accuracy of the solution deteriorates with increasing strain softening. Figure 2.13d shows the displacement residuals for the two analyses. The residuals decrease slowly (i.e., no quadratic convergence) because of the approximate nature of the tangent stiffness matrix.

2.5. Summary

This chapter described the numerical issues related to integrating constitutive models in non-linear finite element analysis. The chapter achieved the following:

1. The chapter clarified many of the strategies required to numerically implement

[1]Eight node isoparametric element with pore pressure degrees of freedom at the corner nodes.

rate independent plasticity models (Section 2.2). It described the advantages of using implicit integration schemes with corresponding consistent Jacobian (tangent stiffness matrix) over explicit integration schemes in the solution of FE boundary value problems using a full Newton solution strategy.

2. The implicit integration technique was applied successfully to the Modified Cam Clay model. Examples presented in Section 2.3.4 show excellent robust and accurate convergence characteristics of this technique.
3. The MIT-E3 model, with highly non-linear (and non-integrable) incremental elastic and hardening functions, was implemented using an explicit integration scheme. A consistent Jacobian (Equation 2.63), which is physically meaningful, was used in the FE implementation. Examples presented in Section 2.4.4 show the technique to give reasonably accurate results.

2.6. References

Atkinson, J.H., and Bransby, P.L., 1978, *The Mechanics of Soils: An Introduction to Critical Soil Mechanics*. McGraw Hill, London, 375p.

Benallal, A., Billardon, R., and Doghri, I. 1988, "An Integration Algorithm and the Corresponding Consistent Tangent Operator for Fully Coupled Elastoplastic And Damage Equations." *Communications in Applied Numerical Methods*, Vol. 4, pp 731-740.

Borja, R.L. and Lee, S.R., 1990, "Cam-Clay Plasticity, Part I: Implicit Integration of Elasto-Plastic Constitutive Relations." *Computer Methods in Applied Mechanics and Engineering*, 78, pp 49-72.

Bathe, K-J., 1982, *Finite Element procedures in Engineering Analysis*, 735p.

Dafalias, Y.F., 1982, "Bounding Surface Elastoplasticity-Viscoplasticity for Particulate Cohesive Media." Proc. Int. Union for Theoretical and Applied Mechanics *Conf. on Deformation and Failure of Granular Materials*, Delft, pp. 97-107.

Dafalias , Y.F., and Herrmann, L.R., 1980, "A Generalized Bounding Surface Constitutive Model for Clays." *Proc., Symposium on Limit Equilibrium and Generalized Stress-Strain in Geot. Engrg*, Florida, pp. 78-95.

De Borst, R., and Feenstra,P.H., 1990, "Studies in Anisotropic Plasticity with Reference to the Hill criterion." *Int. J. for Numerical Methods in Engineering*, Vol.29, pp 315-336.

De Borst, R. and Vermeer, P.A., 1984, "Possibilities and Limitations of Finite Elements for Limit Analysis." *Géotechnique*, 34, No. 2, pp 199-210.

Dodds, R.H., 1987, "Numerical Techniques for Plasticity Computations in Finite Element Analysis." *Computer & Structures*, Vol. 26, No. 5, pp 767-779.

Drucker, D.C., Gibson, R.E., and Henkel, D.J., 1957, "Soil Mechanics and

Work Hardening Theories of Plasticity." *ASCE Transactions*, Vol. 122, pp. 338-346.

Eterovic, A.L. and Bathe, K.J., 1990, "A Hyperelastic-based Large Strain Elasto-Plastic Constitutive Formulation with Combined Isotropic-Kinematic Hardening using the Logarithmic Stress and Strain Measures." *Int. J. Numerical and Analytical Methods in Engineering*, 30, pp. 1099-1114.

Faruque, M.O. and Desai, C.S., 1985, "Implementation of a General Constitutive Model for Geological Material." *Int'l J. for Numerical and Analytical Methods in Geomechanics*, Vol. 9, pp 415-436.

Finno, R.J., Harahap, I.S., and Sabatini, P.J. (1991), "Analysis of Braced Excavations with Coupled Finite Element Formulation, Part 1: Formulation." *Submitted for Publication.*

Gens, A., and Potts,D.M., 1987, "Critical State Models in Computational Geomechanics." *Engrg. Comput.*, Vol. 5, Sept, pp. 178-197.

Hashiguchi, K., 1980, "Constitutive Equations of Elasto-Plastic Materials with Anisotropic Hardening and Elastic Plastic Transition." ASME, *J. of Applied Mech.*, Vol. 48, pp. 297-301.

Hashiguchi, K., 1985, "Constitutive Laws for Soils: II Macrometric Approaches-Static Intrinsically Time Dependent." State-of-the-Art Report, *Proc. XIth Int. Conf. Soil. Mech. Fndn. Engrg.*, San Francisco, pp. 25-65.

Herrmann, L.R., Kaliakin, V., Shen, C.K., Mish, K., and Zhu, Z-Y., 1987, "Numerical Implementation of Plasticity Model for Cohesive Soils." *ASCE, J. Engrg Mech.*, Vol. 113,No. 4, pp. 500-519.

Hight, D.W., Gens, A. and Jardine, R.J., 1985, "Evaluation of Geotechnical Parameters from Triaxial Tests on Offshore Clay." *Proc. Soc. for Underwater Tech. Conf. on Offshore Site Investigation,* Soc. for Underwater Tech., London, pp.253-268.

Hueckel, T. and Nova, R., 1979, "Some Hysteresis Effects of the Behavior of Geological Media." *Int. J. of Solids and Structures*, Vol. 15, pp. 625-642.

HKS, 1989, "ABAQUS Version 4.8 User's Manual," *Hibbitt, Karlsson & Sorensen, Inc.*, Providence, RI.

Kavvadas, M., 1982. Non-Linear Consolidation around Driven Piles in Clays. *Ph.D. Thesis*, Dept. of Civil Engineering, MIT, Cambridge, MA., 666p.

Kreyzig,E. 1983, *Advanced Engineering Mathematics*, John Wiley and Sons, 988p.

Lush, A.M., Weber, G., and Anand, L., 1989, "An Implicit time-Integration Procedure for a Set of Internal Variable Constitutive Equations for Isotropic Elasto-Viscoplasticity." *International Journal of Plasticity*, Vol. 5, pp 521-549.

Mróz, Z., 1980, "On Hypo-elasticity and Plasticity Approaches to Constitutive Modelling of Inelastic Behavior of Soils." *Int. J. Numerical and Analytical Methods in Geomechanics*, Vol. 4, pp. 45-55.

Nagtegaal, J.C., 1982, "On the Implementation of Inelastic Constitutive Equations with Special Reference to Large Deformation Problems." *Computer Methods in Applied Mechanics and Engineering*, 33, pp 469-484.

Nayak, G.C., and Zienkiewiczs, O.C., 1972, "Elasto-Plastic Stress Analysis. A Generalization for Various Constitutive Relations Including Strain Softening." *Int. J. Numerical Methods in Geomechanics*, Vol. 5, No. 1, pp. 113-135

Nova, R., and Hueckel, T., 1979, "An Engineering Theory of Soil Behavior in

nloading and Reloading." *Meccanica,* Vol. 16, No. 3, pp. 136-148.

révost, J.H., 1978, "Plasticity Theory for Soil Stress-Strain Behaviour." ASCE, *J. ngrg Mech. Div.,* Vol. 104, EM5, pp. 1177-1194.

rtiz, M., and Popov, E.P., 1985, "Accuracy and Stability of Integration lgorithms for Elastoplastic Constitutive Relations." *Int. J. for Numerical Methods in ngineering,* Vol. 21, pp. 1561-1576.

rtiz, M., and Simo, J.C., 1986, "An Analysis of a New Class of Integration lgorithms for Elastoplastic Constitutive Relations." *Int. J. for Numerical Methods in ngineering,* Vol. 23, pp. 353-366.

asternack, S.C. and Timmerman, D.H., 1987, "Numerical Implementation of a wo Surface Elasto-Plastic Material Model." *Constitutive Laws for Engineering laterials. Theory and Application,* Volume II, pp 1281-1288.

otts, D.M. and Gens, A., 1985, "A Critical Assessment of Methods of Correcting r Drift from Yield Surface in Elasto-Plastic Finite Element Analysis." *Int'l J. for umerical and Analytical Methods in Geomechanics,* Vol. 9, pp. 149-159.

rager, W., 1956, "A New Method of Analyzing Stresses and Strains in Work ardened Plastic Solids." ASME, *J. Applied Mechanics,* Vol. 23, Series E., pp. 493-96.

ice, J.R., 1976, "The Localization of Plastic Deformation." Proc. 14th *Int. Congress n Theoretical and Applied Mechanics,* Delft, Vol. I, pp. 207-221.

..oscoe, K.H., and Burland, J.B., 1968, On the Generalized Stress-Strain Behavior of 'Wet' Clay. *Engineering Plasticity,* pp. 535-609.

Roscoe, K.H., Schofield, A.N. and Thurarajah, A, 1963, "Yielding of Clays in States Wetter than Critical." *Géotechnique,* Vol. 13, No. 3, pp. 211-240.

Runesson,K., 1987, "Implicit Integration of Elastoplastic Relations with Reference to ils." Short Communication, *Int. J. for Numerical and Analytical Methods in eomechanics,* Vol. 11, pp 315-321.

chofield, A.N. and Wroth, C.P., 1968, *Critical State Soil Mechanics.* McGraw ill, London, 310p.

imo, J.C., and Hughes, T.J.R., 1987, "General Return Mapping Algorithms for ate-Independent Plasticity." *Constitutive Laws for Engineering Materials: Theory and pplications,* pp 221-231.

imo, J.C., and Ju, J-W., 1987, Strain- and Stress-Based Continuum Damage lodels-II. Computational Aspects. *Int. J. Solids Structures,* Vol. 23, No.7, pp. 841-69.

imo, J.C., and Ortiz, M., 1985, "A Unified Approach to Finite Deformation lastoplastic Analysis based on the Use of Hyperelastic Constitutive Equations." *omputer Methods in Applied Mechanics and Engineering,* 49, pp 221-245.

imo, J.C., and Pister, K.S., 1984, "Remarks on Rate Constitutive Equations for inite Deformation Problems: Computational Implications." *Computer Methods in pplied Mechanics and Engineering,* 46, pp. 201-215.

imo, J.C., and Taylor, R.L., 1985, "Consistent Tangent Operator for Rate-ıdependent Elastoplasticity." *Computer Methods in Applied Mechanics and ngineering,* 48, pp 101-118.

imo, J.C., and Taylor, R.L., 1986, "A Return Mapping Algorithm for Plane

tress Elastoplasticity." *Int. J. for Numerical Methods in Engineering*, Vol. 22, pp. 649-70.

loan, S.W., 1987, " Substepping Schemes for the Numerical Integration of lastoplastic Stress-Strain Relations." *Int. J. for Numerical Methods in Engineering*, 'ol. 24, pp. 893-911.

zabo, L., and Kovacs, A., 1987, "Numerical Implementation of Prager's :inematic Hardening Model in Exactly Integrated form for Elasto-Plastic Analysis." *'omputers and Structures*, Vol. 26, No. 5, pp 815-822.

'erzaghi, K., 1925, Erdbaumechanik, Fraz Deuticke, Vienna.

'ermeer, P.A. and Van Langen, H., 1989, "Soil Collapse Computations with inite Elements." *Ingenieur-Archiv*, 59, pp. 221-236.

Vilkins, M.,1964, "Calculation of Elastic-Plastic Flow." *Methods of Computational hysics 2*, Academic Press, N.Y.

Vhittle, A.J., 1987, "A Constitutive Model for Overconsolidated Clays with .pplication to the Cyclic Loading of Friction Piles." *Sc.D. Thesis* , Dept. of Civil ngineering, MIT, Cambridge, MA., 641p.

Vhittle, A.J., 1990, "A Constitutive Model for Overconsolidated Clays." *MIT Sea 'rant College Program, MITSG 90-15*, Cambridge, MA..

Vood, D.M., 1990, *Soil Behavior and Critical State Soil Mechanics*, Cambridge 'niversity Press, England, 462p.

Effective Stress	Strain	Yield Surface Gradient	Plastic Flow Direction	Anisotropy
$\underset{\sim}{\sigma} = (\sigma', \mathbf{S})$	$\underset{\sim}{\varepsilon} = (\varepsilon, \mathbf{E})$	$\mathbf{Q} = (Q, Q')$	$\mathbf{P} = (P, P')$	$(1, \mathbf{b})$
$\sigma' = \frac{1}{3}(\sigma_x + \sigma_y + \sigma_z)$	$\varepsilon = \varepsilon_x + \varepsilon_y + \varepsilon_z$	$Q = Q_x + Q_y + Q_z$	$P = P_x + P_y + P_z$	1
$S_1 = \frac{1}{\sqrt{6}}(2\sigma_y - \sigma_x - \sigma_z)$	$E_1 = \frac{1}{\sqrt{6}}(2\varepsilon_y - \varepsilon_x - \varepsilon_z)$	$Q'_1 = \frac{1}{\sqrt{6}}(2Q_y - Q_x - Q_z)$	$P'_1 = \frac{1}{\sqrt{6}}(2P_y - P_x - P_z)$	$b_1 = \frac{1}{\sqrt{6}}(2b_y - b_x - b_z)$
$S_2 = \frac{1}{\sqrt{2}}(\sigma_z - \sigma_x)$	$E_2 = \frac{1}{\sqrt{2}}(\varepsilon_z - \varepsilon_x)$	$Q'_2 = \frac{1}{\sqrt{2}}(Q_z - Q_x)$	$P'_2 = \frac{1}{\sqrt{2}}(P_z - P_x)$	$b_2 = \frac{1}{\sqrt{2}}(b_z - b_x)$
$S_3 = \sqrt{2}\,\sigma_{xy}$	$E_3 = \sqrt{2}\,\varepsilon_{xy}$	$Q'_3 = \sqrt{2}\,Q_{xy}$	$P'_3 = \sqrt{2}\,P_{xy}$	$b_3 = \sqrt{2}\,b_{xy}$
$S_4 = \sqrt{2}\,\sigma_{yz}$	$E_4 = \sqrt{2}\,\varepsilon_{yz}$	$Q'_4 = \sqrt{2}\,Q_{yz}$	$P'_4 = \sqrt{2}\,P_{yz}$	$b_4 = \sqrt{2}\,b_{yz}$
$S_5 = \sqrt{2}\,\sigma_{zx}$	$E_5 = \sqrt{2}\,\varepsilon_{zx}$	$Q'_5 = \sqrt{2}\,Q_{zx}$	$P'_5 = \sqrt{2}\,P_{zx}$	$b_5 = \sqrt{2}\,b_{zx}$

Table 2.1 Transformed Measures (Kavvadas, 1982).

$J = \frac{\partial \Delta \underline{\sigma}_{n+1}}{\partial \Delta \underline{\varepsilon}_{n+1}}$	$/\partial \Delta \varepsilon$	$/\partial \Delta E_1$	$/\partial \Delta E_2$	$/\partial \Delta E_3$	$/\partial \Delta E_4$	$/\partial \Delta E_5$
$\partial \Delta \sigma'$	$K\left(1 - K\frac{QP}{b}\right)$	$-2KG\frac{PQ'_1}{b}$	$-2KG\frac{PQ'_2}{b}$	$-2KG\frac{PQ'_3}{b}$	$-2KG\frac{PQ'_4}{b}$	$-2KG\frac{PQ'_5}{b}$
$\partial \Delta S_1$	$-2KG\frac{\hat{Q}P'_1}{b}$	$2G\left(1-2G\frac{P'_1Q'_1}{b}\right)$	$-4G^2\frac{P'_1Q'_2}{b}$	$-4G^2\frac{P'_1Q'_3}{b}$	$-4G^2\frac{P'_1Q'_4}{b}$	$-4G^2\frac{P'_1Q'_5}{b}$
$\partial \Delta S_2$	$-2KG\frac{\hat{Q}P'_2}{b}$	$-4G^2\frac{P'_2Q'_1}{b}$	$2G\left(1-2G\frac{P'_2Q'_2}{b}\right)$	$-4G^2\frac{P'_2Q'_3}{b}$	$-4G^2\frac{P'_2Q'_4}{b}$	$-4G^2G\frac{P'_2Q'_5}{b}$
$\partial \Delta S_3$	$-2KG\frac{\hat{Q}P'_3}{b}$	$-4G^2\frac{P'_3Q'_1}{b}$	$-4G^2\frac{P'_3Q'_2}{b}$	$2G\left(1-2G\frac{P'_3Q'_3}{b}\right)$	$-4G^2\frac{P'_3Q'_4}{b}$	$-4G^2\frac{P'_3Q'_5}{b}$
$\partial \Delta S_4$	$-2KG\frac{\hat{Q}P'_4}{b}$	$-4G^2\frac{P'_4Q'_1}{b}$	$-4G^2\frac{P'_4Q'_2}{b}$	$-4G^2\frac{P'_4Q'_3}{b}$	$2G\left(1-2G\frac{P'_4Q'_4}{b}\right)$	$-4G^2\frac{P'_4Q'_5}{b}$
$\partial \Delta S_5$	$-2KG\frac{\hat{Q}P'_5}{b}$	$-4G^2\frac{P'_5Q'_1}{b}$	$-4G^2\frac{P'_5Q'_2}{b}$	$-4G^2\frac{P'_5Q'_3}{b}$	$-4G^2\frac{P'_5Q'_4}{b}$	$2G\left(1-2G\frac{P'_5Q'_5}{b}\right)$

$$b=2c^2\sigma'_{n+1}z\frac{\beta_7}{\beta_3}P_{n+1}+\frac{1}{\beta_3}\frac{K_{n+1}}{\beta_1}Q_{n+1}P_{n+1}+\frac{2G_{n+1}}{\beta_2}(Q'_iP'_i)_{n+1}$$

$$K=\frac{K_{n+1}}{\beta_1}\ ;\ 2G=\frac{2G_{n+1}}{\beta_2}$$

$$\hat{Q} = Q_{n+1}-2c^2\sigma'_{n+1}z\frac{\beta_6}{\beta_3}$$

$$P=P_{n+1}\ ,\ Q=Q_{n+1}$$

$$z = v_0(\lambda - \kappa)\,\alpha'_{n+1}$$

$$\beta_1 = 1 + K_{n+1}\frac{2c^2\,\Lambda_{n+1}}{\beta_3}$$

$$\beta_2 = 1 + 4G_{n+1}\,\Lambda_{n+1}$$

$$\beta_3 = 1 + 2c^2\,\Lambda_{n+1}\,\alpha'_{n+1}\,v_0(\lambda - \kappa)$$

$$\beta_4 = 2c^2\,\Lambda_{n+1}\left(1 - \frac{z}{\beta_3}2c^2\,\Lambda_{n+1}\right)$$

$$\beta_6 = 2c^2\,\Lambda_{n+1}\frac{K_{n+1}}{\beta_1}$$

$$\beta_7 = 1 - \left(\frac{2c^2\,\Lambda_{n+1}}{\beta_3}\right)\frac{K_{n+1}}{\beta_1}$$

Table 2.2 Linearized Jacobian Consistent with the MCC Implicit Integration Algorithm (Figure 2.5).

Input Property	Value for BBC
κ	0.034
λ	0.17
2G/K (ν')	0.9231 (0.3)
c (ϕ'_{TC})	1.101 (33.4^0)
v_0 (e_0)	2.12 (1.12)

Table 2.3 Input Parameters for the MCC Model.

Test Type	Parameter/ Symbol	Physical contribution/ meaning	Boston Blue Clay
1-D Consolidation (Oedometer, CRS etc.)	e_0	Void ratio at reference stress on virgin consolidation line	1.12
	λ	Compressibility of virgin normally consolidated clay	0.184
	C	Non-linear volumetric swelling behaviour	22.0
	n		1.6
	h	Irrecoverable plastic strain	0.2
K_0 -oedometer or K_0 -triaxial	K_{0nc}	K_0 for virgin normally consolidated clay	0.48
	2G/K	Ratio of elastic shear to bulk modulus (Poisson's ratio for intial unload)	1.05
Undrained Triaxial Shear Tests: OCR=1; CK_0UC OCR=1; CK_0UE OCR=2; CK_0UC	ϕ'_{TC}	Critical state friction angles in triaxial compression and	33.4^0
	ϕ'_{TE}	extension (large strain failure criterion)	45.9^0
	c	Undrained shear strength (geometry of bounding surface)	0.86
	s_t	Amount of post-peak strain softening in undrained triaxial compression	4.5
	ω	Non-linearity at small strains in undrained shear	0.07
	γ	Shear induced pore pressure for OC clay	0.5
Resonant Column*	κ_0	Small strain compressibility at load reversal	0.001
Drained Triaxial	ψ_0	Rate of evolution of anisotropy (rotation of bounding surface)	100.0

* Alternatively use shear wave velocity from cross-hole tests.

Table 2.4 Input Parameters for the MIT-E3 Model (Whittle, 1990).

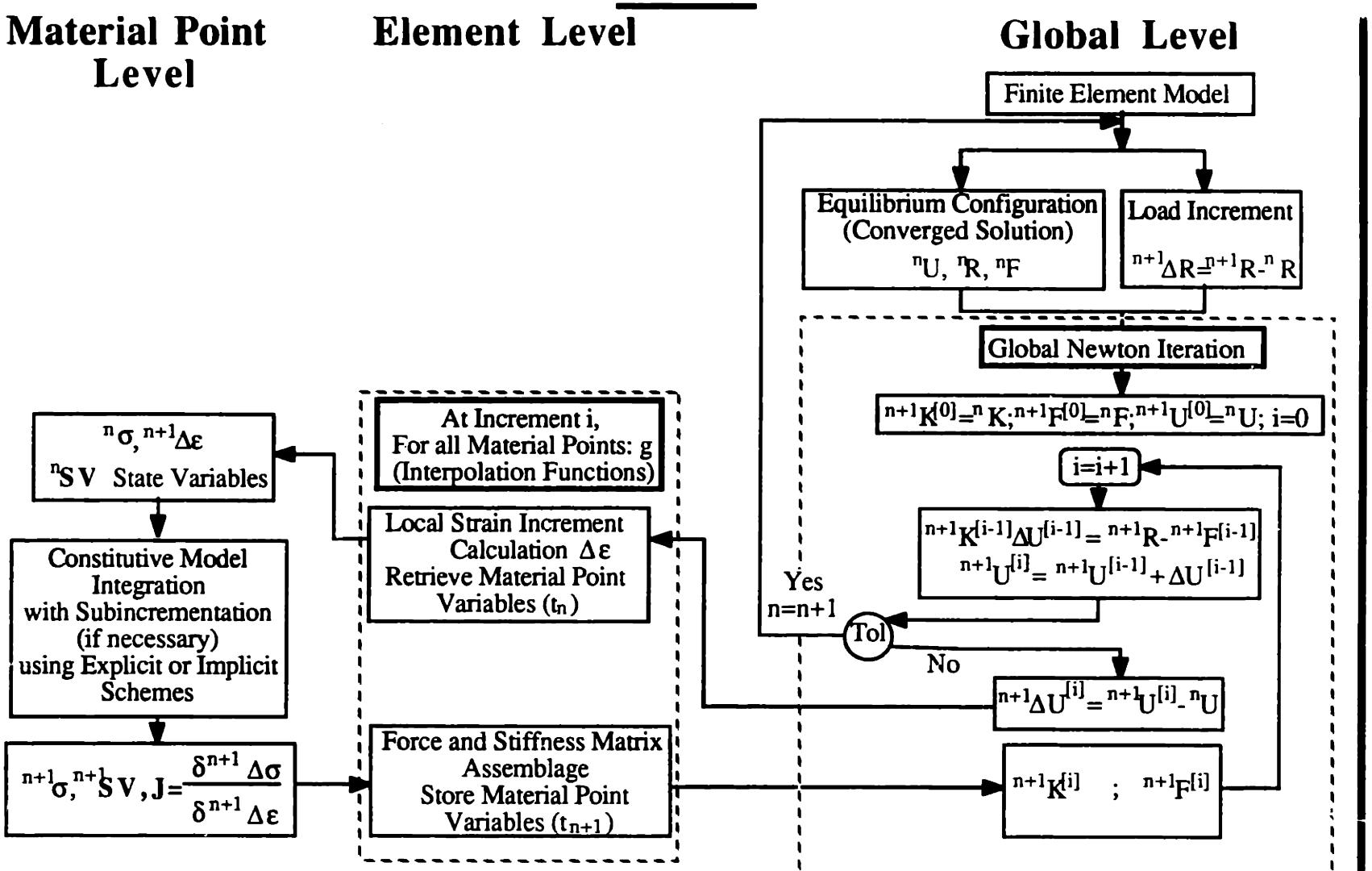

Figure 2.1 Materially Non-Linear Finite Element Method Solution Strategy

i) Initialize:

$$k=0\ ;\ \varepsilon_{n+1}^{p[0]} = \varepsilon_n^p\ ;\ q_{n+1}^{[0]} = q_n\ ;\ \Delta\Lambda=0$$

ii) Compute stresses, hardening moduli and yield function:

$$\sigma_{n+1}^{[k]} = \overline{C}\left(\varepsilon_{n+1} - \varepsilon_{n+1}^{p[k]}\right)$$
$$h_{n+1}^{[k]} = h\left(\sigma_{n+1}^{[k]}\ ,\ q_{n+1}^{[k]}\right)$$
$$f_{n+1}^{[k]} = f\left(\sigma_{n+1}^{[k]}\ ,\ q_{n+1}^{[k]}\right)$$

IF $\left(f_{n+1}^{[k]} \le TOL\right)$ THEN EXIT, ELSE

iii) Compute plastic consistency parameter:

$$d\Lambda_{n+1}^{[k]} = \frac{f_{n+1}^{[k]}}{\left[Q_{n+1}^{[k]} : C : P_{n+1}^{[k]} - \left(\frac{\partial f}{\partial q}\right)_{n+1}^{[k]} h_{n+1}^{[k]}\right]}$$

iv) Update state variables:

$$\varepsilon_{n+1}^{p[k+1]} = \varepsilon_{n+1}^{p[k]} + d\Lambda_{n+1}^{[k]}\ P_{n+1}^{[k]}$$
$$q_{n+1}^{[k+1]} = q_{n+1}^{[k]} + d\Lambda_{n+1}^{[k]}\ h_{n+1}^{[k]}$$
$$\Delta\Lambda_{n+1}^{[k+1]} = \Delta\Lambda_{n+1}^{[k]} + d\Lambda_{n+1}^{[k]}$$

set k=k+1 and GOTO (ii)

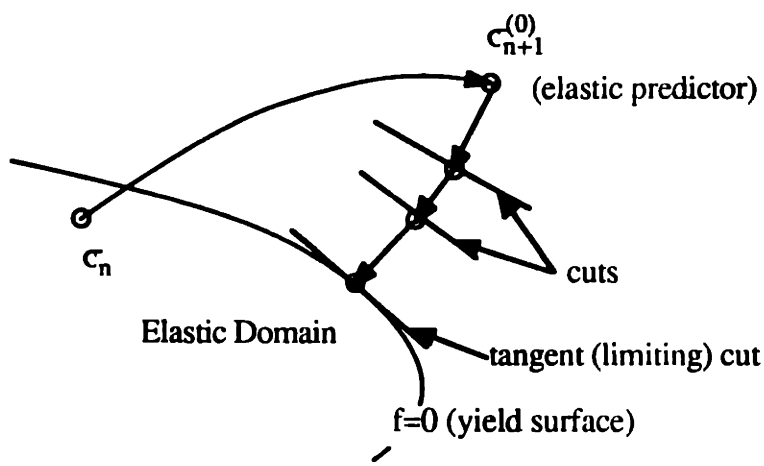

Figure 2.2 General Convex Cutting Plane Algorithm
(after Simo and Hughes, 1987).

Initialize:

$$k=0\ ;\ \varepsilon_{n+1}^{p[0]} = \varepsilon_n^p\ ;\ q_{n+1}^{[0]} = q_n\ ;\ \Delta\Lambda=0$$

Check yield condition and evaluate flow rule/hardening law residuals:

$$\sigma_{n+1}^{[k]} = \overline{C}\left(\varepsilon_{n+1} - \varepsilon_{n+1}^{p[k]}\right)$$

$$f_{n+1}^{[k]} = f\left(\sigma_{n+1}^{[k]}\ ,\ q_{n+1}^{[k]}\right)$$

$$\left\{R_{n+1}^{[k]}\right\} = \begin{Bmatrix} -\varepsilon_{n+1}^{p[k]} + \varepsilon_n^p \\ -q_{n+1}^{[k]} + q_n \end{Bmatrix} + \Delta\Lambda_{n+1}^{[k]} \begin{Bmatrix} P_{n+1}^{[k]} \\ h_{n+1}^{[k]} \end{Bmatrix}$$

$\left\langle f_{n+1}^{[k]} \le TOL1 \text{ and } \left|R_{n+1}^{[k]}\right| \le TOL2\right\rangle$ THEN EXIT, ELSE

) Calculate correction terms ($\delta\sigma$, δq):

$$\delta\sigma_{n+1}^{[k]} = \sigma_{n+1}^{[k+1]} - \sigma_{n+1}^{[k]}\ ;\ \delta q_{n+1}^{[k]} = q_{n+1}^{[k+1]} - q_{n+1}^{[k]}$$

$$\begin{Bmatrix} \delta\sigma_{n+1}^{[k]} \\ \delta q_{n+1}^{[k]} \end{Bmatrix} = -\left[A^{[k]}\right]\left\{R_{n+1}^{[k]}\right\}$$

ıere;

$$\left[A^{[k]}\right]^{-1} = \begin{bmatrix} \left(C_{n+1}^{[k]-1} + \Delta\Lambda_{n+1}^{[k]} \dfrac{\partial P_{n+1}^{[k]}}{\partial\sigma_{n+1}^{[k]}}\right) & \Delta\Lambda_{n+1}^{[k]} \dfrac{\partial P_{n+1}^{[k]}}{\partial q_{n+1}^{[k]}} \\ \Delta\Lambda_{n+1}^{[k]} \dfrac{\partial h_{n+1}^{[k]}}{\partial\sigma_{n+1}^{[k]}} & \left(-1 + \Delta\Lambda_{n+1}^{[k]} \dfrac{\partial h_{n+1}^{[k]}}{\partial q_{n+1}^{[k]}}\right) \end{bmatrix}$$

iv) Calculate correction to consistency parameter, $\delta\Lambda$:

$$\delta\Lambda_{n+1}^{[k]} = \Delta\Lambda_{n+1}^{[k+1]} - \Delta\Lambda_{n+1}^{[k]}$$

$$\delta\Lambda_{n+1}^{[k]} = \frac{f_{n+1}^{[k]} - \left(\dfrac{\partial f_{n+1}^{[k]}}{\partial\sigma_{n+1}^{[k]}}\delta\sigma_{n+1}^{[k]} + \dfrac{\partial f_{n+1}^{[k]}}{\partial q_{n+1}^{[k]}}\delta q_{n+1}^{[k]}\right)}{\left(\dfrac{\partial f_{n+1}^{[k]}}{\partial\sigma_{n+1}^{[k]}}\dfrac{\partial\sigma_{n+1}^{[k]}}{\partial\varepsilon_{n+1}^{p[k]}}\dfrac{\partial\varepsilon_{n+1}^{p[k]}}{\partial\Delta\Lambda_{n+1}^{[k+1]}} + \dfrac{\partial f_{n+1}^{[k]}}{\partial q_{n+1}^{[k]}}\dfrac{\partial q_{n+1}^{[k]}}{\partial h_{n+1}^{p[k]}}\dfrac{\partial h_{n+1}^{p[k]}}{\partial\Delta\Lambda_{n+1}^{[k+1]}}\right)} = \frac{R_{f,\,n+1}^{[k]}}{\left(\partial R_{f,\,n+1}^{[k]}/\partial\Delta\Lambda_{n+1}^{[k+1]}\right)}$$

ıere;

$$\left(\frac{\partial R_{f,\,n+1}^{[k]}}{\partial\Delta\Lambda_{n+1}^{[k+1]}}\right) = \left[\frac{\partial f_{n+1}^{[k]\ T}}{\partial\sigma_{n+1}^{[k]}}\ \frac{\partial f_{n+1}^{[k]\ T}}{\partial q_{n+1}^{[k]}}\right]\left[A_{n+1}^{[k]}\right]\begin{Bmatrix} P_{n+1}^{[k]} \\ h_{n+1}^{[k]} \end{Bmatrix}$$

Obtained correction terms ($\delta\varepsilon^p$, δq):

$$\begin{Bmatrix} \delta\varepsilon_{n+1}^{p[k]} \\ \delta q_{n+1}^{[k]} \end{Bmatrix} = \begin{bmatrix} C_{n+1}^{[k]-1} & 0 \\ 0 & -1 \end{bmatrix}\left[A_{n+1}^{[k]}\right]\left[\left\{R_{n+1}^{[k]}\right\} + \delta\Lambda_{n+1}^{[k]}\begin{Bmatrix} P_{n+1}^{[k]} \\ h_{n+1}^{[k]} \end{Bmatrix}\right]$$

) Update state variables and consistency parameter:

$$\varepsilon_{n+1}^{p[k+1]} = \varepsilon_{n+1}^{p[k]} + \delta\varepsilon_{n+1}^{p[k]}$$

$$q_{n+1}^{[k+1]} = q_{n+1}^{[k]} + \delta q_{n+1}^{[k]}$$

$$\Delta\Lambda_{n+1}^{[k+1]} = \Delta\Lambda_{n+1}^{[k]} + \delta\Lambda_{n+1}^{[k]}$$

t k=k+1 and GOTO (ii)

Figure 2.3 General Closest Point Algorithm (after Simo and Hughes, 1987).

The Modified Cam Clay Model

(after Roscoe and Burland, 1968)

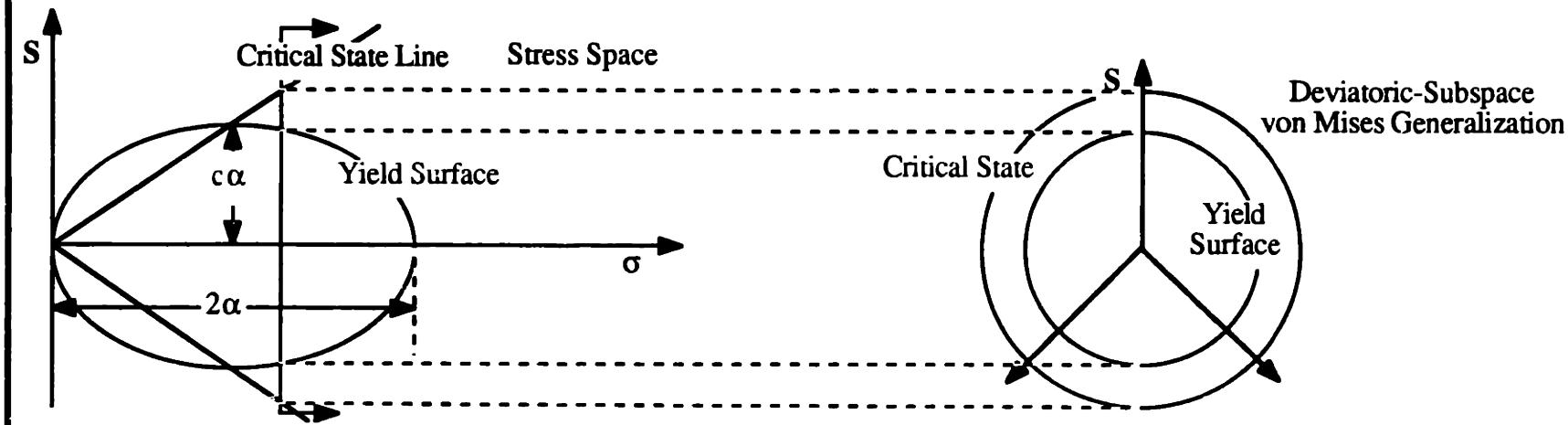

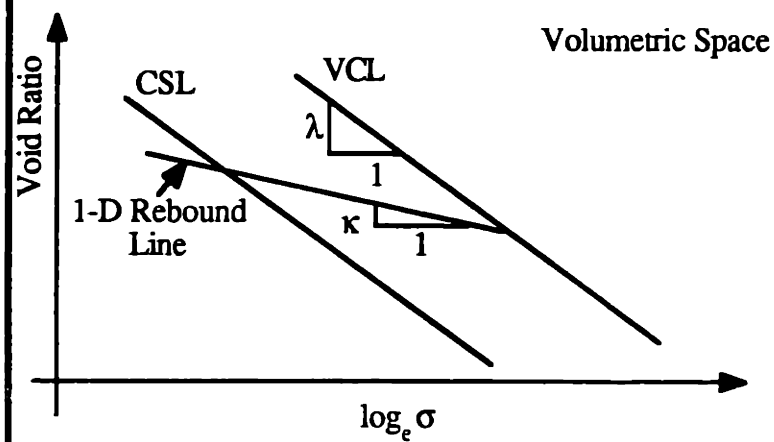

Symbol	Physical Meaning
Material Properties	
ϕ'_{TC}	Critical State Friction Angle in Triaxial Compression
κ	Slope of 1-D Swelling line
λ	Slope of Consolidation line
2G/K	Poisson Ratio
State Variables	
α	Size of Yield Surface
e	Void Ratio

Figure 2.4 The Modified Cam Clay Model

1) Initialize:

$$m=0,\ \Delta\varepsilon^{p[0]}_{n+1}=0,\ \Delta E^{p[0]}_{n+1}=0,\ \alpha'^{[0]}_{n+1}=0,\ \Lambda^{[0]}_{n+1}=0$$

2) Calculate elastic predictor and check yield condition:

$$\sigma'^{[0]}_{n+1} = \sigma'_n \exp\left[v_0\,\kappa^{-1}\,\Delta\varepsilon_{n+1}\right]$$

$$S^{[0]}_{i,n+1} = S_{i,n} + \left(\frac{2G}{K}\right)\sigma'_n\left(\frac{\Delta E_{i,n+1}}{\Delta\varepsilon_{n+1}}\right)\left\{\exp\left[v_0\,\kappa^{-1}\,\Delta\varepsilon_{n+1}\right] - 1\right\}$$

$$f^{[0]}_{n+1} = S^{[0]}_i S^{[0]}_{i,n+1} - c^2\sigma'^{[0]}_{n+1}\left(2\alpha' - \sigma'^{[0]}_{n+1}\right)$$

IF $f^{[0]}_{n+1} \le$ TOL1 THEN GOTO 5 (elastic increment), ELSE

3) Calculate plastic corrector, i.e. find the solution vector **U** by solving Equations 2.35 using a local (full) Newton scheme:

$$\mathbf{U}^{-1} = \left[\sigma'_{n+1}\ ,\ \Delta\varepsilon^{p}_{n+1}\ ,\ S_{j,n+1}\ ,\ \Delta E^{p}_{j,n+1}\ ,\ \alpha'_{n+1}\ ,\ \Lambda_{n+1}\right]$$

i) Calculate Residuals:

$$\mathbf{R}^{m}_{n+1} = \begin{bmatrix} \sigma'^{[m]}_{n+1} - \sigma'_n \exp\left[v_0\,\kappa^{-1}\left(\Delta\varepsilon_{n+1} - \Delta\varepsilon^{p[m]}_{n+1}\right)\right] \\ \Delta\varepsilon^{p[m]}_{n+1} - \Lambda^{[m]}_{n+1}\,2c^2\left(\sigma'^{[m]}_{n+1} - \alpha'^{[m]}_{n+1}\right) \\ S^{[m]}_{i,n+1} - S_{i,n} - \left(\frac{2G}{K}\right)\sigma'_n\left(\frac{\Delta E_{i,n+1} - \Delta E^{p}_{i,n+1}}{\Delta\varepsilon_{n+1} - \Delta\varepsilon^{p}_{n+1}}\right)\left\{\exp\left[v_0\,\kappa^{-1}\left(\Delta\varepsilon_{n+1} - \Delta\varepsilon^{p[m]}_{n+1}\right)\right] - 1\right\} \\ \Delta E^{p[m]}_{i,n+1} - \Lambda^{[m]}_{n+1}\,2S_{i,n+1} \\ \alpha'^{[m]}_{n+1} - \alpha'_n \exp\left[v_0\left(\lambda - \kappa\right)^{-1}\Delta\varepsilon^{p[m]}_{n+1}\right] \\ s^{[m]}_{i,n+1}s^{[m]}_{i,n+1} - c^2\,\sigma'^{[m]}_{n+1}\left(2\alpha'^{[m]}_{n+1} - \sigma'^{[m]}_{n+1}\right) \end{bmatrix}$$

IF $\left|R^{[m]}_{k,n+1}\right| \le$ TOL2 , $\forall$ k THEN GOTO 5, ELSE

Figure 2.5 Algorithm for Implicit Integration of the Modified Cam Clay Model (continued on next page).

ii) Calculate consistent tangent matrix $\mathbf{T}^{[m]}_{n+1} = \dfrac{\partial \mathbf{R}^{[m]}_{n+1}}{\partial \mathbf{U}^{[m]}_{n+1}}$ for the local Newton scheme:

$$\begin{bmatrix}
 & /\partial\sigma'^{[m]}_{n+1} & /\partial\Delta\varepsilon^{p[m]}_{n+1} & /\partial S^{[m]}_{j,n+1} & /\partial\Delta E^{p[m]}_{j,n+1} & /\partial\alpha'^{[m]}_{n+1} & /\partial\Lambda^{[m]}_{n+1} \\
\partial & 1 & K^{[m]}_{n+1} & 0 & 0 & 0 & 0 \\
\partial & -\Lambda^{[m]}_{n+1}2c^2 & 1 & 0 & 0 & \Lambda^{[m]}_{n+1}2c^2 & -P^{[m]}_{n+1} \\
\partial & 0 & 0 & \delta_{ij} & \delta_{ij}2G^{[m]}_{n+1} & 0 & 0 \\
\partial & 0 & 0 & -\delta_{ij}2\Lambda^{[m]}_{n+1} & \delta_{ij} & 0 & -2S^{[m]}_{i,n+1} \\
\partial & 0 & -\alpha_n v_0(\lambda-\kappa)^{-1} \exp\left\{v_0(\lambda-\kappa)^{-1}\Delta\varepsilon^{p[m]}_{n+1}\right\} & 0 & 0 & 1 & 0 \\
\partial & Q^{[m]}_{n+1} & 0 & Q'^{[m]}_{j,n+1} & 0 & -2c^2\sigma'^{[m]}_{n+1} & 0
\end{bmatrix}$$

iii) Solve $\mathbf{T}\,\delta\mathbf{U}=-\mathbf{R}$ using Gauss Elimination. Where:

$$\delta\mathbf{U}^{-1} = \left[\delta\sigma'^{[m]}_{n+1}\,,\ \delta\Delta\varepsilon^{p[m]}_{n+1}\,,\ \delta S^{[m]}_{j,n+1}\,,\ \delta\Delta E^{p[m]}_{j,n+1}\,,\ \delta\alpha'^{[m]}_{n+1}\,,\ \delta\Lambda^{[m]}_{n+1}\right]$$

iv) Update the solution vector $\mathbf{U}^{[m+1]}_{n+1} = \mathbf{U}^{[m]}_{n+1} + \delta\mathbf{U}^{[m]}_{n+1}$:

$$\sigma'^{[m+1]}_{n+1} = \sigma'^{[m]}_{n+1} + \delta\sigma'^{[m]}_{n+1}, \qquad S^{[m+1]}_{i,n+1} = S^{[m]}_{i,n+1} + \delta S^{[m]}_{i,n+1}$$

$$\Delta\varepsilon^{p[m+1]}_{n+1} = \Delta\varepsilon^{p[m]}_{n+1} + \delta\Delta\varepsilon^{p[m]}_{n+1}, \qquad \Delta E^{p[m+1]}_{i,n+1} = \Delta E^{p[m]}_{i,n+1} + \delta\Delta E^{p[m]}_{i,n+1}$$

$$\alpha'^{[m+1]}_{n+1} = \alpha'^{[m]}_{n+1} + \delta\alpha'^{[m]}_{n+1}, \qquad \Lambda^{[m+1]}_{n+1} = \Lambda^{[m]}_{n+1} + \delta\Lambda^{[m]}_{n+1}$$

4) m=m+1, GOTO 3

5) Converged Solution

$$\sigma'_{n+1} = \sigma'^{[m]}_{n+1}, \qquad S_{i,n+1} = S^{[m]}_{i,n+1}$$

$$\Delta\varepsilon^{p}_{n+1} = \Delta\varepsilon^{p[m]}_{n+1}, \qquad \Delta E^{p}_{i,n+1} = \Delta E^{p[m])}_{i,n+1}$$

$$\alpha'_{n+1} = \alpha'^{[m]}_{n+1}, \qquad \Lambda_{n+1} = \Lambda^{[m]}_{n+1}$$

Figure 2.5 Algorithm for Implicit Integration of the Modified Cam Clay Model (cont'd).

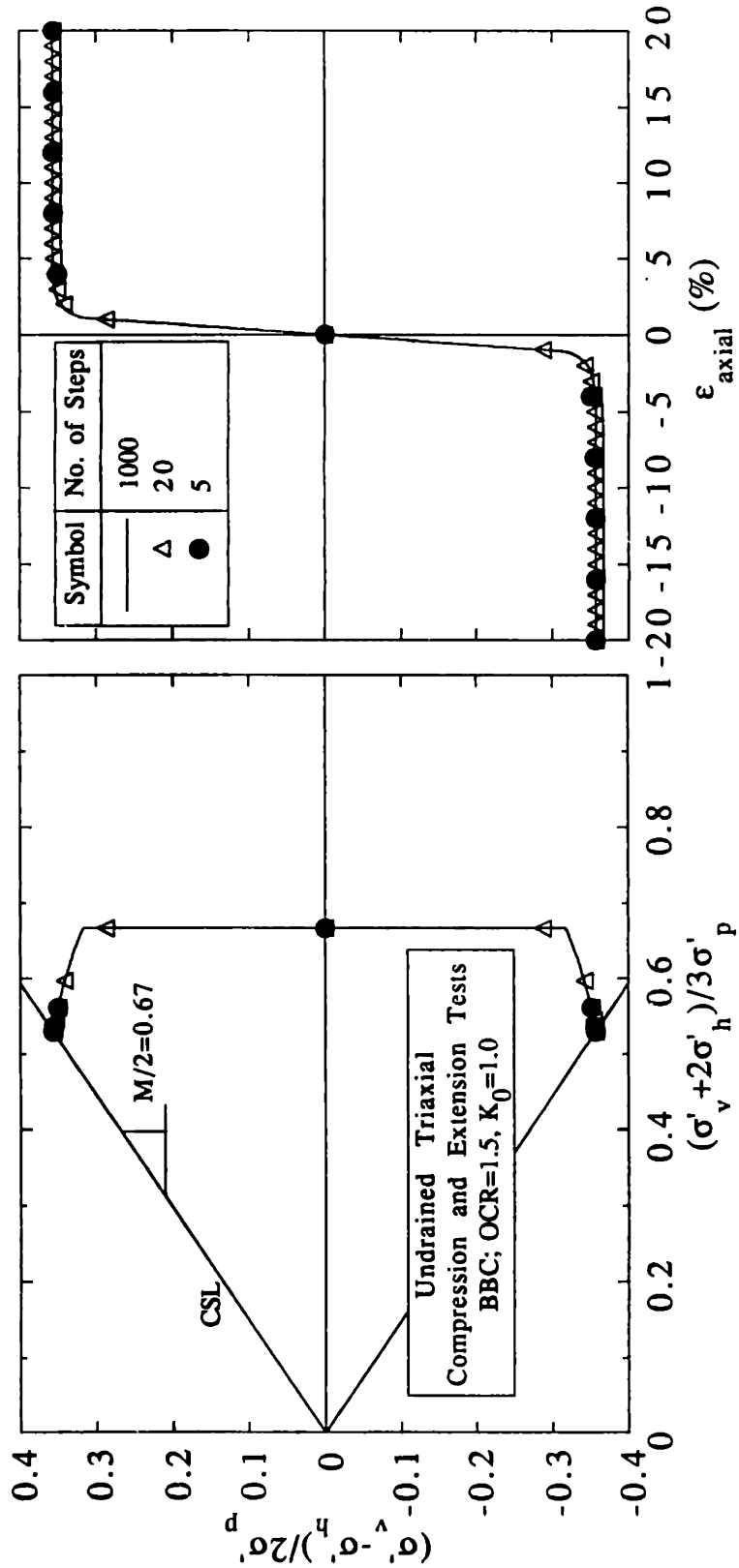

Figure 2.6 Evaluation of the MCC Model Integration Algorithm, Single Element Undrained Triaxial Test Simulation.

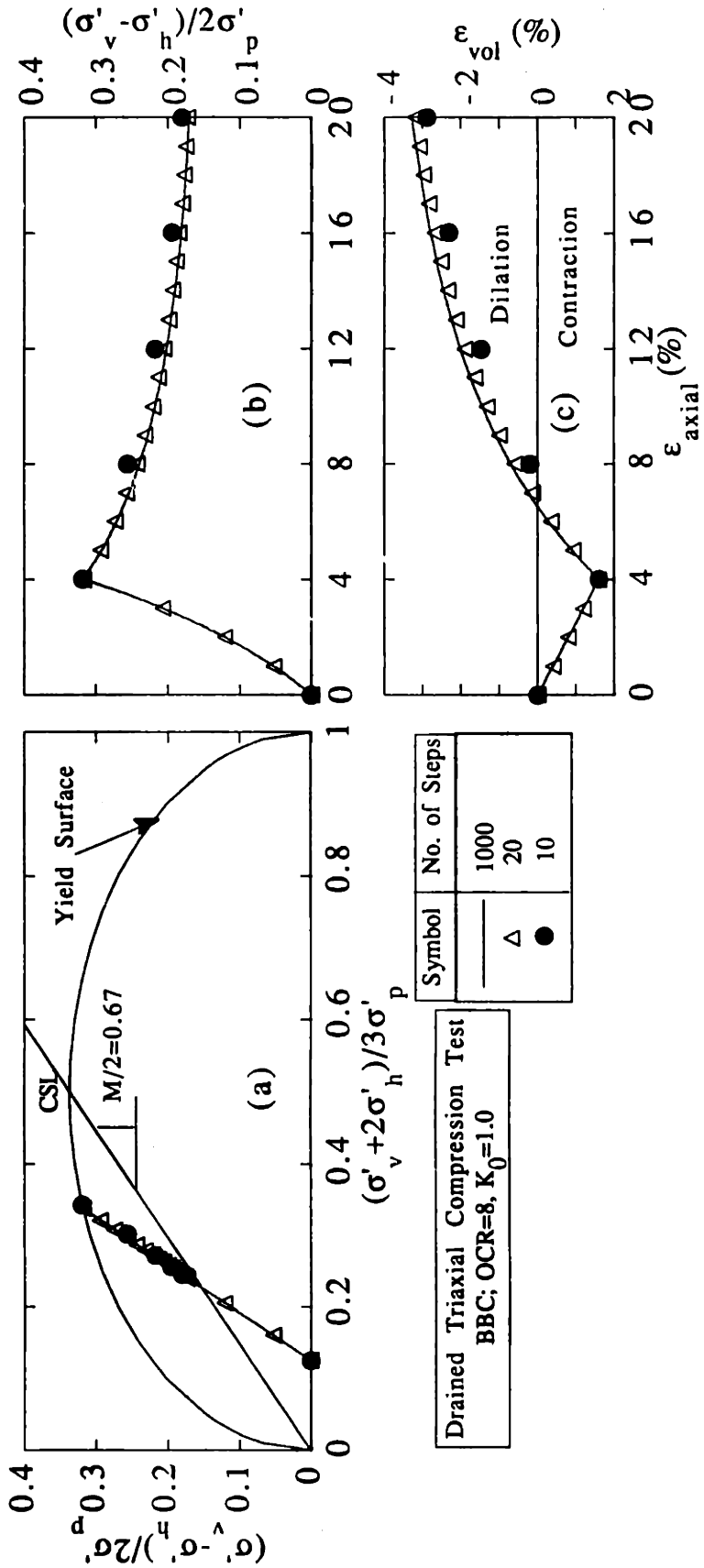

Figure 2.7 Evaluation of the MCC Model Integration Algorithm, Single Element Drained Triaxial Compression Test Simulation.

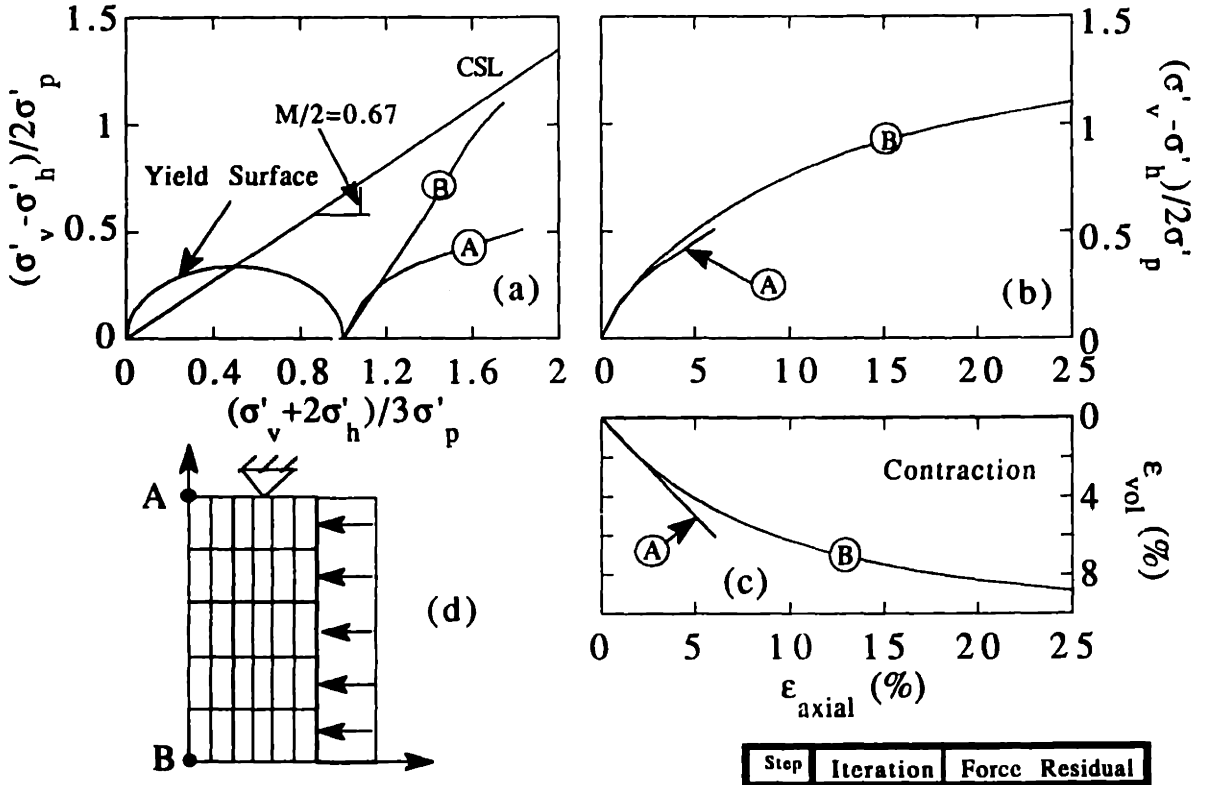

Step or ε_a(%) Total	Continuum Jacobian		Consistent Jacobian	
	Iterations per Step	Total Iterations	Iterations per Step	Total Iterations
1	13	13	5	5
2	13	26	4	9
4	13	52	5	19
6	13	78	5	29
8	13	104	6	40
10	14	132	6	52
12	14	160	6	64
14	14	188	6	76
16	14	216	8	92
18	14	244	8	108
20	14	272	8	124

(e)

Drained Triaxial Compression Test
BBC; OCR=1, K_0=1.0

Step	Iteration	Force Residual
8	1	0.717
	2	2.064×10^{-2}
	3	$7.\times10^{-3}$
	4	1.6×10^{-4}
	5	1.223×10^{-4}
	6	3.487×10^{-6}
20	1	0.188
	2	3.010×10^{-2}
	3	1.745×10^{-2}
	4	3.644×10^{-3}
	5	2.782×10^{-3}
	6	5.389×10^{-4}
	7	4.567×10^{-4}
	8	8.557×10^{-5}

Force Residuals of Typical Nodal Forces

(f)

Figure 2.8 Evaluation of the MCC Model Integration Algorithm
30 Element Drained Triaxial Compression Test Simulation with Frictional Ends.

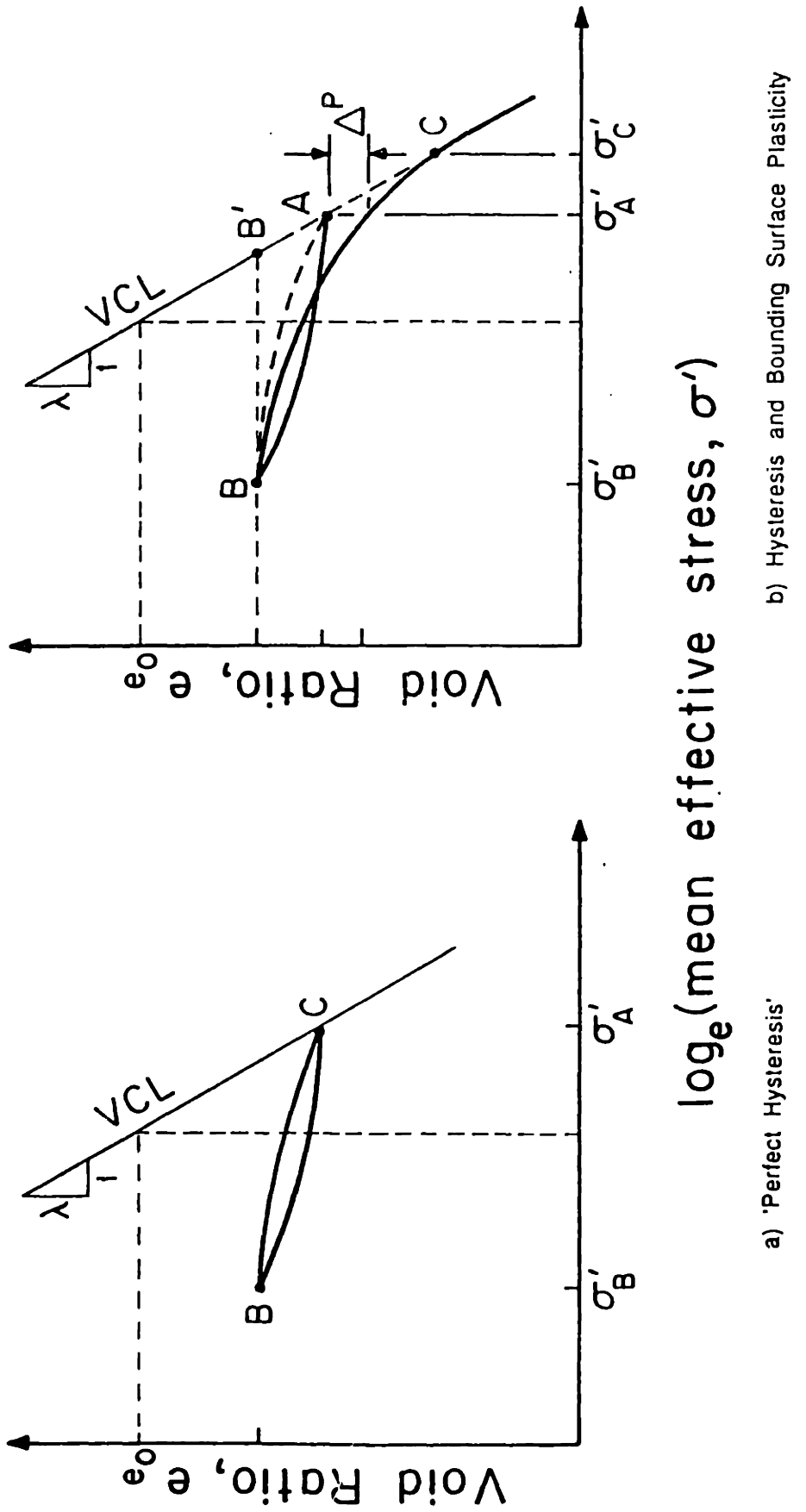

Figure 2.9 Conceptual Model of Unload-Reload Used by MIT-E3 for Hydrostatic Compression (Whittle, 1990).

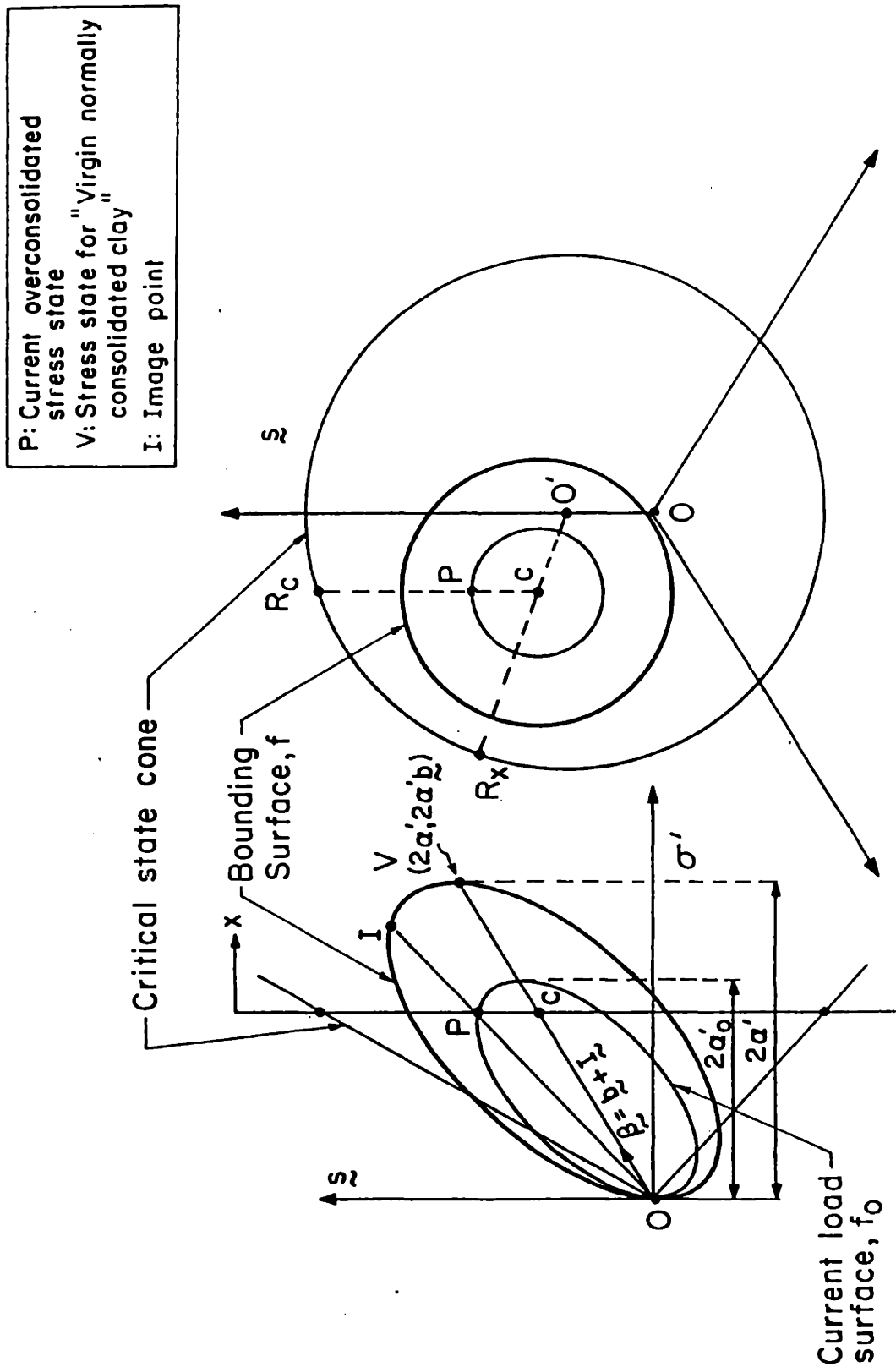

Figure 2.10 Yield and Failure Surface for Normally Consolidated Clay (Whittle, 1990).

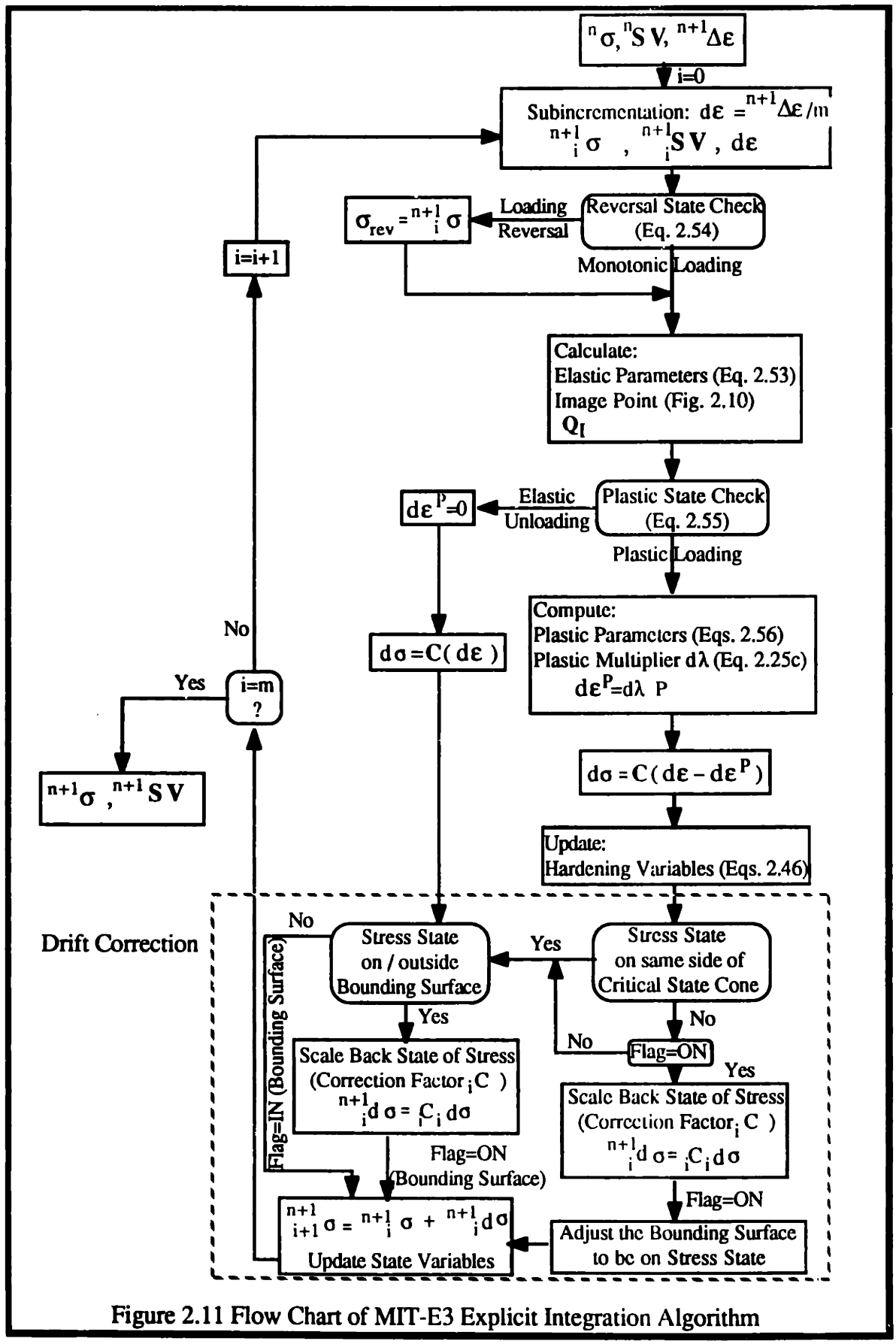

Figure 2.11 Flow Chart of MIT-E3 Explicit Integration Algorithm

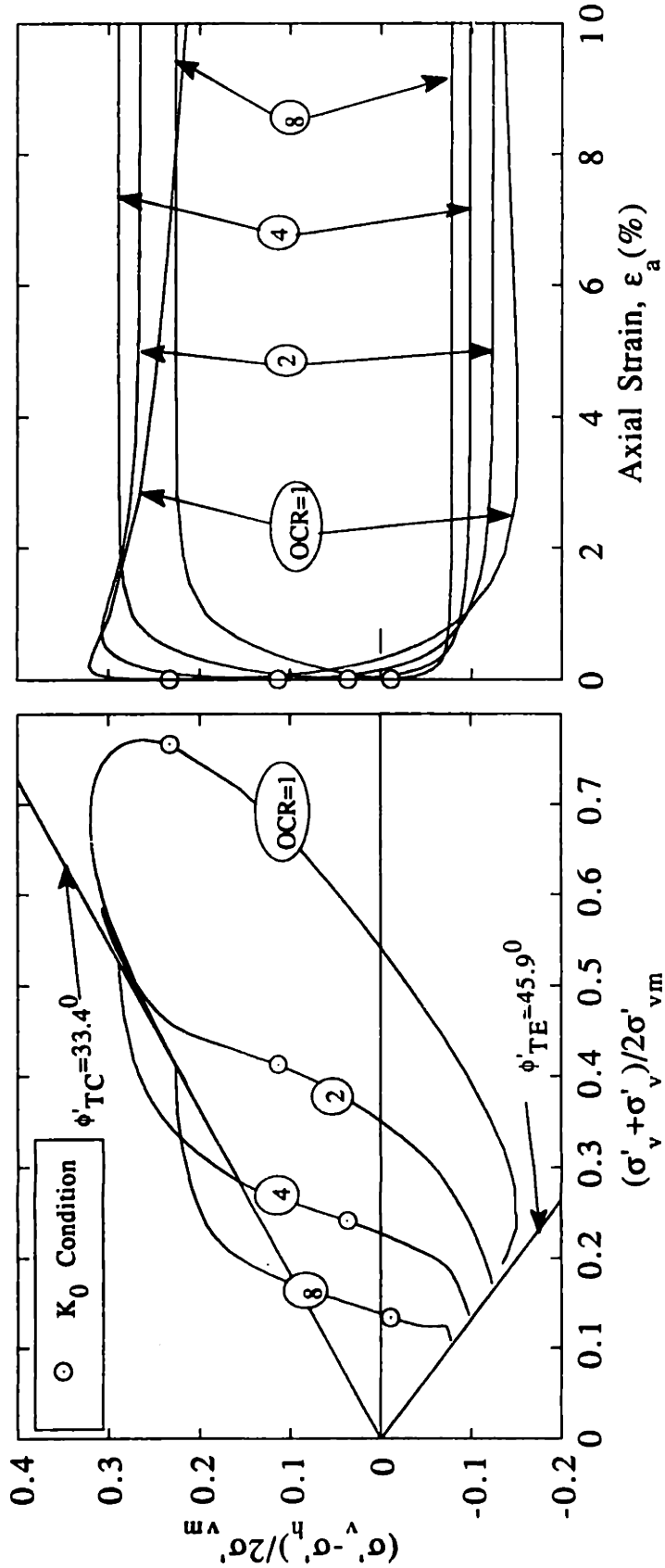

Figure 2.12 Evaluation of the MIT-E3 Explicit Integration Algorithm in ABAQUS, Single Element Undrained Triaxial Test Simulation.

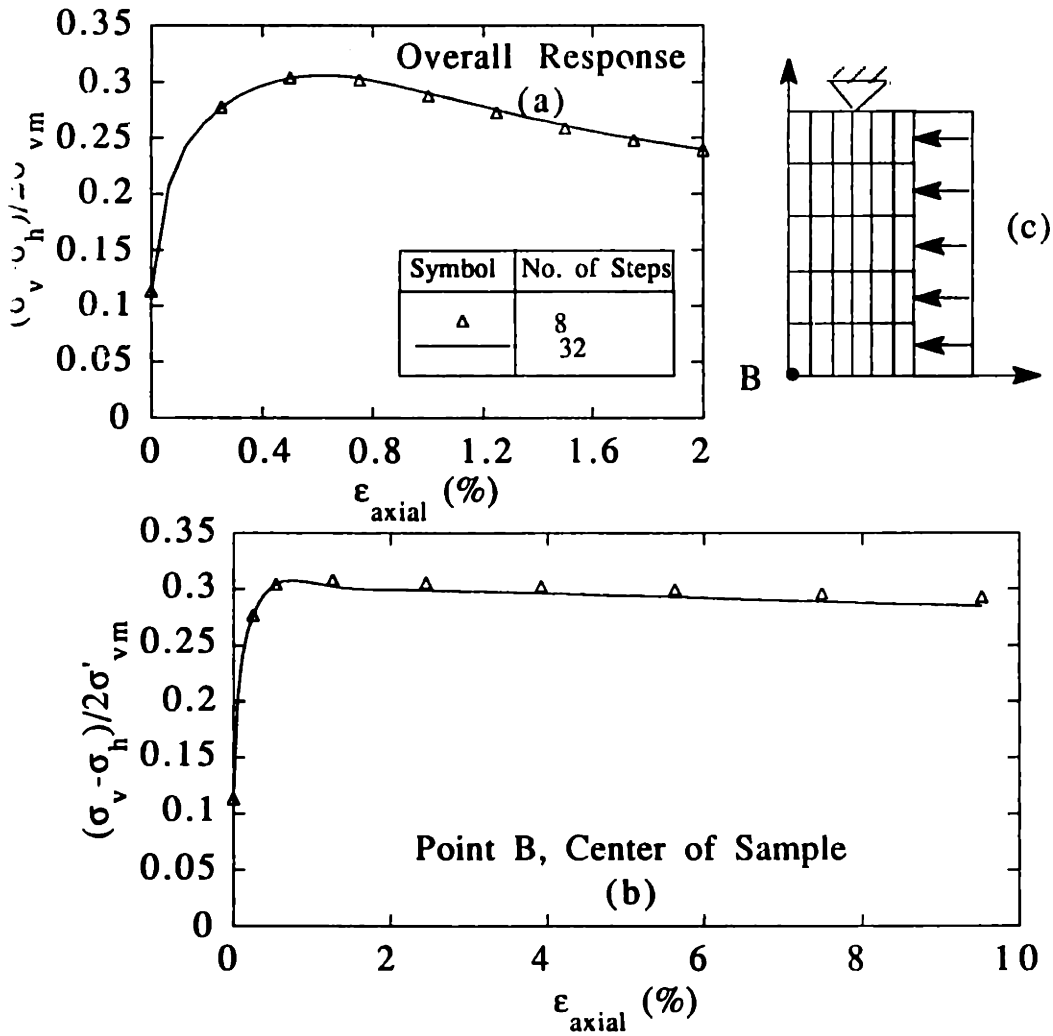

Total ε_a (%)	8 Step Analysis			32 Step Analysis		
	Step	Iteration	Maximum Disp. Residual	Step	Iteration	Maximum Disp. Residual
1.0	4	9	1.39×10^{-3}	16	6	8.28×10^{-4}
		10	6.95×10^{-4}		7	5.52×10^{-4}
		11	6.94×10^{-4}		8	$2. \times 10^{-4}$
		12	$<1 \times 10^{-4}$		9	$2. \times 10^{-4}$
2	8	17	6.25×10^{-3}	32	17	1.26×10^{-3}
		18	3.73×10^{-3}		18	7.57×10^{-4}
		19	7.47×10^{-4}		19	5.05×10^{-4}
		20	6.2×10^{-4}		20	2.53×10^{-4}

(d)

Figure 2.13 Evaluation of the MIT-E3 Explicit Integration Algorithm in ABAQUS, 30 Element Undrained Triaxial Compression Test Simulation with Frictional Ends, OCR=2.

3. Finite Element Modelling of Excavations

3.1. Introduction

Conventional design methods for supported excavations are based on limit equilibrium calculations, which consider a base heave failure mechanism in the soil (e.g., Terzaghi 1943). However, in many urban environments, the main design constraint is the allowable magnitude of adjacent soil movements, rather than system failure. The estimation of potential ground movements due to a given excavation is difficult to quantify as there are many variables in the construction process:

1- Initial in-situ soil conditions:

Characterization of stratigraphy, soil properties and their spatial variability is a major challenge in all geotechnical problems. Plasticity theory has been used extensively to describe stress-strain-strength behavior of the soil.

2- Construction details and sequence:

Excavations represent complex soil-structure interaction problems. There are many diverse construction activities associated with excavations which can affect ground movements. These include:

a) Pre-excavation wall installation (e.g., driving of sheet or soldier pile, or slurry wall construction)

b) Pre-construction site preparation including, dewatering, utility relocation, demolition of preexisting structures, etc...

c) Soil removal and stability berm construction (changing geometry).

d) Excavation dewatering using shallow sumps and/or deep wells.

e) Support installation (bracing, floors, tiebacks, etc...)

These activities occur over a continuous and overlapping time periods. Different construction activities may also occur at various locations around the site at the same time.

There are no simple analytical methods for estimating ground movements associated with these activities, and hence, predictions must be based either on empirical observations (e.g., Peck 1969, O'Rourke and Clough 1990), or on numerical simulations using finite element methods.

The finite element method is a powerful tool for modelling excavation problems and can incorporate factors such as: 1) details of soil stratification and properties; 2) structural properties of the support system; and 3) construction activities related to soil removal, berm construction and excavation. The FEM is attractive as the numerical analysis is generalized and independent of the particular excavation problem under

consideration. The modelling of excavations using finite element methods was first reported by Clough and Duncan (1971), and are currently very popular for the design of complex excavations. Significant developments in FEM techniques, computer hardware technology and soil modelling have led to important advances in predictive capabilities. Table 3.1 summarizes the capabilities of some of the FE excavation programs published in the literature. Limitations of these earlier works can be summarized as follows:

1- Approximate solution of finite element equations: Many of the earlier implementations of the FE method for excavations use the 'initial stress method' to solve the FE equations. The initial stress method corresponds to a linearization of the response about the initial configuration of the FE system, and may result in a very slowly convergent or even divergent solution (Bathe, 1982). The method is used because it requires the calculation of the stiffness matrix only once for each loading increment. This is advantageous given the limited computer capacity available. However, the technique requires the use of very small loading increments to obtain an accurate solution (infinitesimal increments). Discrete 'relatively large' loading steps commonly used in FE analyses lead to substantial errors in the calculation and unreliable predictions. Solving the FE equations using an iterative scheme such as the Newton-Raphson method (e.g., Section 2.2.1) gives more efficient and accurate solutions for non-linear analyses.

2-The soil model: Hyperbolic elastic models and simple elastic-perfectly plastic models (Table 3.1) are used extensively in earlier implementations of the FE method for excavations. Recent advances in soil modelling provide the analyst with more realistic models of soil behavior (Sections 2.3, 2.4).

3- Element types: Isoparametric elements, used in recently published works (Table 3.1) are sometimes preferred over subparametric elements because they use the same degree of interpolation for coordinates and displacements (subparametric elements use a lower degree of interpolation for the coordinates).

4- Soil removal procedures: A basic postulate that must be satisfied when simulating an excavation process is the principle of uniqueness of the cutting process (Ishihara 1970) in a linear elastic medium. The principle states that for an excavation in a linearly elastic material, the final state of stress and deformation is independent of the number of excavation steps needed to reach the final configuration. This principle derives from the fact that response of a linear elastic material is path independent. Earlier finite element codes (some of which widely used in practice) do not satisfy this basic principle (Tsui 1974, Hansen 1980). The error in these procedures propagates and increases with the increase in the

number of excavation steps. Christian and Wong (1973) present a discussion of the sources of these errors and numerical schemes proposed to correct the excavation procedure.

The error[1] occurs during element removal, when forces applied on the freshly excavated surface do not satisfy global equilibrium equations and is due to the incorrect application of the FE equations in the remaining part of the numerical model. Ghaboussi and Pecknold (1984), Brown and Booker (1985) show an example of the correct application of FEM for the simulation of the excavation process. Aubery and Modaressi (1989) and Borja et al. (1989) describe a formulation to model the excavation process as a domain continuously changing (shrinking) in time. However, once this algorithm is discretized in the FEM it appears to be identical to the conventional formulation.

5- Total stress analysis: Although it is widely recognized that soil behavior is controlled by effective stresses, the majority of previous analyses rely on total stress methods of analysis. As a result, predictions of soil deformations are limited to simplified drainage conditions (fully drained or undrained) while separate analyses must be used to calculate ground water flow.

The finite difference method provides another alternative for modelling excavations. However, the method is severely limited compared to the FEM as the numerical coding required is problem specific (Bathe, 1982).

The boundary element method is being promoted as a method superior to FEM (Beskos, 1988). The method is efficient for modelling large domains with predominantly linear response. Booker et al (1989) present an application of the BEM to excavations. Girija Vallabhan (1987) combines the FEM and BEM where the FEM is used to model the domain where significant changes in geometry and loads occur, while BEM is used to model the far field. However, BEM cannot, by itself, replace FEM for modelling excavations.

Regardless of the numerical model used to simulate the excavation process, the analyst should be aware of the limitations of the model and its predictions. It is unrealistic to expect the numerical model to predict exactly all aspects of observed excavation behavior. The model is best used to understand the contribution of various construction activities to excavation response.

---

[1]Error in this context is that the FE excavation procedure doesn't satisfy superposition.

3.2. Numerical Issues and Procedures

Figure 3.1 is a schematic of a simplified excavation problem, modelled using FEM. Starting from an initial configuration, at an intermediate stage in the construction sequence, soil is removed, supports installed, and temporary dewatering implemented. At the final/long term stage, permanent supports and dewatering system are installed. Simulating these activities using FEM requires the adoption of specific numerical techniques. This section discusses the various numerical issues encountered in the FE modeling of excavations in this thesis.

1. Geometric Approximation

Most excavations have geometries and construction sequences that are three dimensional in nature. Performing a 3-D analysis of an excavation using a complex soil model is prohibitively expensive given available computer capabilities. The excavation problem is, therefore, simplified using a 2-D geometry. Many analyses assume a plane strain geometry. This assumption can be a good approximation for linear excavations (e.g., subway construction) and for wall sections located midway along the longer edge of a rectangular excavation, but will overestimate movements at corners of an excavation.

Naylor and Pande (1981) report on a study by St. John (1975) regarding the differences between 2-D and 3-D models. For an unsupported excavation which is square in plan, 3-D and axisymmetric solutions give similar results. A plane strain analysis gives similar settlements but greater horizontal deformations up to 100% larger than predicted in a 3-D or an axisymmetric analysis.

2. Soil Modelling

The ABAQUS finite element code can incorporate generalized effective (or total) stress soil models through the user material subroutine UMAT. This thesis uses the following material models to describe soil response:

- •Linear Elastic Model: with constant or increasing stiffness with depth.
- •Elastic-perfectly plastic model: which allows for a dilatant or non-dilatant behavior, friction angle and cohesion.
- •Modified Cam Clay Model: an isotropically hardening plasticity model.
- •MIT-E3 model: a bounding surface plasticity model with isotropic and kinematic hardening.

3. Simulation of the Support Wall

The simulation of the support wall in an excavation problem involves: 1) the

modelling of the physical wall; 2) the modelling of wall installation; and 3) the modelling of wall-soil interaction.

Bending behavior of the support walls in the excavation problem is the most important aspect that needs to be captured correctly in a model. Two types of elements can be used to model the wall:

a) One-Dimensional beam elements model wall bending correctly. Tsui (1974) and Christian (1989) describe problems of incompatibility between bending elements and adjacent soil elements. This occurs if the order of deformation in the bending elements and the soil elements are different. The problem is avoided using beam elements with quadratic interpolation of deformations in conjunction with 8-node isoparametric plane elements for the soil (also with quadratic interpolation of deformations).

b) Solid elements can be used to describe the wall, providing they model the bending action described by simple beam theory. Tsui (1974) shows that a minimum of two rows of solid elements are required to model bending of the wall.

While bending action is the most important behavior that needs to modelled accurately, there are other factors that have to be taken into consideration when modelling *concrete diaphragm (slurry) walls*. These factors (listed below) make it necessary to use solid isoparametric elements instead of beam elements:

Wall Thickness: Slurry walls have a characteristic thickness, t=0.75-2m, which is non-negligible compared to other dimensions in the excavation problems. Two dimensional solid elements are necessary to model the wall thickness.

Wall Weight::The equivalent weight of the wall in beam elements will produce a concentrated load at the bottom of the wall. The concentrated load at the bottom will increase during excavation due to loss of frictional resistance from the excavated soil. Solid elements will model more realistically the bearing capacity aspect of the analysis due to self weight of wall during excavation.

Cracked section, Concrete, and Rebar Modelling: The response of the support wall is usually assumed to be linear elastic. However, in situations where large wall deflections are expected to occur, inelastic behavior of the reinforced concrete is expected. Beam elements are limited in that capacity. Solid elements can incorporate more realistic elasto-plastic models of concrete behavior and can model rebar reinforcement.

Pore Pressure: For some types of wall (e.g., sheet piles, soldier pile and lagging), water seepage through the wall is important. In this case, mixed finite elements

(i.e., displacement and pore pressure degrees of freedom) should be used to model wall behavior.

In this thesis, the concrete diaphragm (slurry) wall is modelled using two columns of 8-node isoparametric plane elements. The wall is characterized as a linear elastic material whose response is governed by total stresses.

Wall installation generally causes disturbance of the surrounding soil and alters the local state of stress and soil properties. For example, driving of sheet pile walls in soft clays induces significant excess pore pressures in the surrounding soil (e.g., Finno and Harahap 1991). The mechanics of wall penetration can be modelled using techniques such as the Strain Path Method (e.g., Whittle et al. 1991), or other approximate procedures (Finno and Harahap 1991). Diaphragm wall installation by the slurry method does induce small ground movements (e.g., Cowland and Thorley 1984) but generally causes less disturbance of the surrounding soil. For this reason, it is convenient to assume that the wall is 'wished into place' for all the analyses presented in this thesis.

Explicit modelling of soil-wall interface behavior is generally necessary in order to limit the friction which is mobilized between the soil and the wall. Interface elements include and generally assume a Mohr-Coulomb slip criterion. More elaborate elements use hyperbolic models and allow for a peak, as well as, residual interface friction angle. Some elements are also capable of forming a gap upon specifying a minimum contact pressure. Such elements are useful in situations where one expects some tension to develop between the soil and the structure which may produce undesirable or unrealistic results.

The in-situ construction of diaphragm walls produces a rough interface between the concrete wall and the soil. No slippage is expected to occur between the soil and the concrete providing the deformations remain relatively small. Potts and Fourier (1984), Fourie and Potts (1989) have computed the mobilized wall friction angle for a variety of excavation geometries and show that there is no need to introduce interface elements. Interface behavior only becomes a significant factor in collapse calculations (Desai 1988, Bakker and Vermeer 1986). Interface elements are not used in the present study.

4. Establishing Initial Conditions

Determining the initial, in-situ state of stress is an integral part of an excavation analysis. In many FE excavation procedures, an analysis step is performed to establish the initial state of stress. The body forces are applied in order to obtain the vertical stresses, while horizontal stresses are computed using appropriate values of K_0 (e.g., Gunsallus et al. 1989, Tsui 1974). The material is assumed to behave elastically in this

step. Strains generated in the mesh are ignored in subsequent analysis steps.

This procedure is laborious and difficult to implement in some cases. Parrish and Labreche (1988) describe an elaborate procedure to establish the initial, in-situ stress state for cases of complex geologic conditions and variable topography. The procedure leads to better evaluation of the in-situ state of stress than the procedure described previously.

In ABAQUS the initial state of stress (such as a geostatic state of stress) as well as body forces are provided as an input for the code. The program allows for an arbitrary initial state of stress. The first step in the analysis checks the equilibrium between the applied forces and pressures and the specified state of stress using the true material properties of the different model components. The required input is relatively easy to provide for a level ground surface and horizontal soil layers.

Determining the initial state of stress of soil elements directly underneath the wall is more difficult.as the unit weight of the wall is usually larger than that of the soil surrounding it. These problems are ameliorated in the present study by assuming similar total unit weights for the soil and wall materials. This approximation has negligible effect in subsequent analyses.

5. Soil Removal

Soil removal was discussed above. The excavation procedure in ABAQUS satisfies the principal of uniqueness for excavation in an elastic medium (Ishihara, 1970).

6. Modelling of the Bracing System

The bracing system is commonly modelled as elastic spring elements with no moment connection to the wall. This is a reasonable assumption even when bracing is provided by internal floor slabs (Chapter 5) as the supports provide relatively little resistance in bending. Some form of non-linear behavior may be needed to simulate certain aspects of support behavior such as shrinkage, due to temperature changes or curing of concrete. Displacements due to these factors can be significant, as shown in Chapter 5.

In ABAQUS, the activity of installing a strut is performed instantaneously, in a single step. From the numerical/programming point of view, the procedure of simulating strut installation is not performed by adding a spring element at the desired position. Instead, when initially constructing the F.E. model, all spring elements representing supports are specified at the desired position (Figure 3.2). The boundary condition at node B is specified such that the degrees of freedom (DOF) at node B are equal to those at node A. This means that the spring is not allowed to stretch or compress, and the strut

is not activated (installed). When the strut is to be installed, node B is fixed in its position, while node A is allowed to move in response to the loading in the system. The spring is, therefore, allowed to change in length and carry load, just as if a strut has been installed.

7. Coupled Analysis of Excavations in ABAQUS

The ABAQUS program formulates coupled analysis[1] using the following definitions:

"The formulation is defined in terms of excess pore pressures, so that the weight of the pore fluid should not be included in the loading definition, and the static pore pressure should not be included in the boundary condition definitions"[2]

The term *excess pore pressure* is used in a different context from that used in the geotechnical engineering literature, and can be deceiving if taken out of the context of the entire paragraph. It is important to understand clearly how pore pressures are handled in ABAQUS as they have a significant impact on the way various excavation activities are simulated. In order to understand the concept, it is useful to define some of the terminology used (Lambe and Whitman, 1969):

Static Pore Pressure, u_s:

This is the hydrostatic pore pressure. $u_s = \gamma_w(z-z_w)$ (Figure 3.3).

Steady State Pore Pressure, u_{ss}:

This is the pore pressure when steady state conditions are achieved after a loading step has been applied. If there is no flow in the system, $u_{ss} = u_s$.

Excess Pore Pressure, u_e:

Transient flow occurs in a system if the excess pore pressure is different from zero, $u_e = (u-u_{ss}) \neq 0$. The pore pressure in excess of steady state controls the change in effective stresses in the system.

ABAQUS's Pore Pressure, u_{es}:

In ABAQUS only pore pressures in excess of hydrostatic pore pressures are used, $u_{es} = (u-u_s)$. The gradient of u_{es} controls the flow in the system. In terms of pressure head (Figure 3.3) the definitions become:

Pore pressure head: $h_p = u/\gamma_w$

Total Head : $h_t = h_p + h_{el}$ (h_{el} is the elevation head)

---

[1]The analyses couple (effective) stresses and pore pressures.

[2]The equilibrium and pore fluid equations of the coupled analysis are solved simultaneously in ABAQUS, as opposed to using a staggered approach whereby the two sets of equations are solved in succession until negligible changes in the solutions are obtained (See ABAQUS Theory Manual).

Under hydrostatic pore pressure conditions, the total head throughout the system is constant: $h_{t,s} = h_{p,s} + h_{el} = \text{constant}$.

At any point in time, after applying a loading step:

$$h_t = \frac{u}{\gamma_w} + h_{el} = \frac{u_e + u_{ss}}{\gamma_w} + h_{el} = h_{t,ss} + \frac{u_e}{\gamma_w}$$

$$\text{or, } h_t = \frac{u_{es} + u_s}{\gamma_w} + h_{el} = h_{t,s} + \frac{u_{es}}{\gamma_w}$$

If the datum is chosen such that $h_{t,s} = 0$, then $u_{es} = h_t \gamma_w$. Therefore contours of u_{es} represent contours of total head.

Gibson et al (1989) present a clear discussion of the various terminology used to describe pore pressures. In the terminology of their paper, u_{es} equals the excess pore pressure as defined by Terzaghi (1943).

When imposing pore pressure boundary conditions in ABAQUS, the pore pressure must be expressed in terms of u_{es}. Later chapters of this thesis indicate clearly pore pressure definitions used.

In order to perform a coupled analysis of a supported excavation, three components have to be modeled, the soil, the support structure, and soil removal process.

The behavior of the soil is described by effective stresses. The saturated soil removal (which includes both the solid and fluid parts) is a total stress process. The support wall/strut response is governed by total stresses being applied to the wall. Therefore, the excavation procedure mixes effective stress and total stress analyses. Special provisions need to be made in order to apply the correct pressures around the wall and to simulate the saturated soil removal.

Figure 3.4 illustrates these procedures assuming that the water table is located at the ground surface and that pore pressures are hydrostatic. Figure 3.5 extends the method to cases where the water table is below the ground surface, and there is full capillarity in the overlying soil.

1. In ABAQUS, initially, the stresses applied by the soil on the wall are effective stresses. Therefore, an additional distributed load should be applied to account for the hydrostatic water table (Figure 3.4). A simple calculation shows that the resulting stresses in the wall are correct.
2. When soil elements are removed, there is no compensation for the removal of water. Therefore, to simulate properly the water removal, additional distributed loads have to be applied (Figure 3.5). It can be proved that in the final analysis, the newly excavated surface is stress free. Consider a point along the center line,

point 1 (Figure 3.5):

a) Initial State of stress: $\gamma_b z$

b) Unloading Stresses: $-(\gamma_b+\gamma_w) z$

c) The final state of stress: $(\gamma_b-\gamma_b-\gamma_w)z$

3. However, since the static water pressure is not included in the FE model the static water pressure has to be added in order to compute the final state of stress $\gamma_b z-\gamma_b z-\gamma_w z-\gamma_w z=0.0$. This means that the surface is stress free, which is the objective of the excavation process.
4. The reasoning in the previous section can be further extended to model a situation where a capillary pressure exists above the hydrostatic water table. Again in this case, no flow conditions exist initially and all initial pore pressures are hydrostatic pore pressures. The total stress at the ground surface is zero, and the effective stress is $-\gamma_b z_w$. In order to input the correct initial state of stress into the F.E. mesh, a distributed load equal to the effective stress at the surface has to be added. This will lead to a non-zero effective stress at the surface, as required. Modifications to the distributed loads applied to the wall and the freshly excavated surface have to be made. Actually, the modifications are simple. For the wall, an all around (unloading) distributed load equal to the capillary pressure at the surface should be applied. This will lead to correct total stresses in the wall. Along the freshly excavated surface, a distributed load equal to the capillary pressure at the surface should be applied. Again, this will result in a correct stress free surface. Figure 3.6 shows the additional loads that have to be applied.

8. Free Water Surface

Dewatering within the excavation may cause a lowering of the water table in the retained soil. Modelling of a moving free water surface in FEM is difficult and requires special treatment (see for example Bathe and Khoshgoftaar 1979, Borja 1992). ABAQUS cannot model the development of a moving free water surface. The code assumes that the soil remains saturated and that capillary (negative) pore pressures develop above the water table. While this procedure imposes limitations for situations where there is significant lowering of the water table, the procedure is reasonable for deep excavations in clay described in this thesis.

3.3. References

Aubery, D. and Modaressi, A., 1989, "A Rational Approach to the Analysis of Construction Filling or Excavation." *Int. Symposium on Numerical Models in Geomechanics*, NUMOG III, Niagara Falls, Canada, pp. 455-462.

Bakker, K.J. and Vermeer, P.A., 1986, "Finite Element Analysis of Sheet Pile Walls." *2nd Int. Symposium Numerical Models in Geomechanics*, Ghent, pp. 409-416.

Barbas, F., 1982, "Contribution a l'utilization de la M.E.F. en Mécanique des Sols dans le domain del l'élastoplasticité." *Rapport no. 116 du L.C.P.C.*, France.

Bathe, K-J., 1982, *Finite Element procedures in Engineering Analysis*, Prentice-Hall, Inc., 735p.

Bathe, K-J. and Khoshgoftaar, M.R., 1979, "Finite Element Free Surface Seepage Analysis without Mesh Iteration." *Int J. for Numerical and Analytical Methods in Geomechanics*, Vol. 3, pp. 13-22.

Beskos, D.E., 1988, "Boundary Element Methods in Geomechanics." *Boundary Elements X*, Vol. 4: Geomechanics, Wave Propagation and Vibrations, Computational Mechanics, Springer-Verlag, pp. 3-28.

Booker, J.R., Carter, J.P., Small, J.C., Brown, P.T., and Poulos, H.G., 1989, "Some Recent Applications of Numerical Methods to Geotechnical Analysis." *Research Report No.598*, School of Civil and Mining Engineering, The University of Sydney, Australia, 34p.

Borja, R.I., 1992, "Free Boundary, Fluid Flow, and Seepage Forces in Excavations." *J. of Geotechnical Engrg.*, Vol. 118, No. 1, pp. 125-146.

Borja, R.L., Lee, S.R., and Seed, R.B., 1989a, "Numerical Simulation of Excavation in Elastoplastic Soils." *Int. J. For Numerical and Analytical Methods in Geomechanics*, Vol. 13, pp. 231-249.

Borja, R.L., Lee, S.R., and Seed, R.B., 1989b, "Excavation in Cohesive Soils: Modelling the Effects of Creep on Long-Term Performance." *Int. Symp. Numerical Models in Geomechanics*, NUMOG III, Niagara Falls, Canada, pp. 585-592.

Britto, A.M., and Gunn, M.J., 1987, *Critical State Soil Mechanics via Finite Elements*, Halsted Press, 488p.

Broms, B.B., Wong, I.H., and Wong, K.S., 1986, "Experience with Finite Element Analysis of Braced Excavations in Singapore." *Int. Symp. Numerical Models in Geomechanics*, Ghent, pp. 309-324.

Brown, P.T. and Booker, J.R., 1985, "Finite Element Analysis of Excavation." *Computers and Geotechnics*, Vol. 1, pp. 207-220.

Chan, D.H, 1986, "Finite Element Analysis of Strain Softening Material." *Ph.D. Thesis*, Department of Civil Engineering, The University of Alberta, 345p.

Chan, D.H, and Morgenstern, N.R., 1989, "An Effective Stress Approach to Undrained Analysis." *Int. Symposium on Numerical Models in Geomechanics*, NUMOG III, Niagara Falls, Canada, pp. 740-750.

Christian, J.T. and Wong, I.H., 1973, "Errors in Simulating Excavations in Elastic Media by Finite Elements." *Soils and Foundations*, Vol. 13, No. 1, pp. 1-10.

Christian, J.T., 1989, "Design of Lateral Support Systems." *Proc. BSCE Symposium Design Construction and Performance of Deep Excavations in Urban Areas*, MIT, November, 32p.

Clough, G.W. and Duncan, J.M., 1971, "Finite Element Analysis of Retaining Wall Behavior." *J. of Soil Mechanics and Foundation Engrg,* ASCE, Vol. 97, SM12, pp. 1657-1673.

Clough, G.W. and Hansen, L.A., 1981, "Clay Anisotropy and Braced Wall Behavior." *ASCE J. of Geotechnical Division,* GT7, pp. 893-913.

Clough, G.W., Smith, E.M. and Sweeney, B.P., 1989, "Movement Control of Excavation Support Systems by Iterative Design." *Foundation Engrg Proceedings Congress,* ASCE, Colorado Division, Evanston, Ill, pp. 869-884.

Cowland, J.W. and Thorley, C.B., 1984, "Ground and Building Settlement Associated with Adjacent Slurry Trench Excavation," *Proc. of Third Int. Conference on Ground Movements and Structures*, Cardiff, pp. 723-738.

Desai, C.S., 1988, "Case Studies Through Material Modelling and Computation." *Case Histories in Geotechnical Engrg*, 2nd Int. Conference, St. Louis, Vol. II, pp. 1551-1565.

Duncan, J.M., and Chang, C.S., 1977, "EXCAV: A Computer Program for Analyses of Stresses and Movements in Excavations." *Geotechnical Engrg, Research Reptort No. TE 77-4,* University of California, Berkeley, CA.

Dysli, M., and Fontana, A., 1982, "Deformations around the Excavations in Clayey Soils" *Int. Symp. Numerical Models in Geomechanics*, Zurich, pp. 634-642.

Finno, R.J. and Harahap, I.S., 1991, "Finite Element Analysis of HDR-4 Excavation." *J. Geotechnical Engrg.*, Vol. 117, No. 10, pp. 1590-1609.

Folic, R., and Pavlovic, P., 1986, "Numerical Analysis of Anchored Reinforced Concrete Diaphragm Walls." *Proc. 2nd Int. Symp. Numerical Methods in Geomechanics,* Ghent, pp. 423-431.

Fourie, A.B., and Potts, D.M., 1989, "Comparison of Finite Element and Limiting Equilibrium Analysis for an Embedded Cantilever Retaining Wall." *Géotechnique*, Vol. 39, No. 2, pp. 175-188.

Genna, F., and Gioda, G., 1985, "An Approach for Undrained Geotechnical Problems Accounting for the Development of Partial Saturation." *Int. J. Numerical Methods in Engrg,* Vol. 21, pp. 2169-2187.

Ghaboussi, J., and Pecknold, D.A., 1984, "Incremental Finite Element Analysis of Geometrically Altered Structures." *Int. J. for Numerical and Analytical Methods in Engrg*, Vol. 20, pp. 2051-2064.

Gibson, R.E., Schiffman, R.L. and Whitman, R.V., 1989, "On the Two Definitions of Excess Pore Water Pressure." *Géotechnique,* 39, No. 1, pp. 169-171.

Gioda, G., and Jurina, L., 1981, "Numerical Identification of Soil-Structure Interaction Pressures." *Int. J. Numerical and Analytical Methods in Geomechanics*, Vol. 5, pp. 33-56.

Girijia Vallabhan, C.V., 1987, "Coupling of BEM/FEM Technology: An Overview." *Boundary Element Techniques:* Applications in stress Analyses and Heat Transfer, eds. C.A. Brebbia and W.S. Venturini, pp. 15-30.

Gunsallus, K.L., Kulhawy, F.H., and Ingraffea, A.R., 1989, "A Geotechnical Analysis system with Applications for Drilled Shaft Foundations." *Foundation Engrg: Current Principles and Practice*, Vol. 1, Proc. of ASCE Congress, Evanston Illinois, pp. 640-653.

Hansen, L.A., 1980, Prediction of the Behavior of Braced Excavation in Anistropic

Clay. *PhD Thesis*, Stanford University, 379p.

Hata, S., Ohta, H., Yoshida, S., Kitamura, H., and Honds, H., 1985, "A Deep Excavation in Soft Clay Performance of an Anchored Diaphragm Wall." *Fifth Int. Conf. Numerical Methods in Geomechanics*, Nagoya, pp. 725-730.

Ishihara, K., 1970, "Relations Between Process of Cutting and Uniqueness of Solution." *Soils and Foundations*, Vol. 10, No. 3, pp. 50-65.

Jardine, R.J., Potts, D.M., Fourie, A.B. and Burland, J.B., 1986, "Studies of the Influence of Non-Linear Stress-Strain Characteristics in Soil-Structure Interaction." *Géotechnique*, Vol. 6, No. 3, pp. 377-396.

LNEC, 1982, "Estudio de Equilibrios tridimensionais em estruturas laminares e maciças utilizando elementos finitos subparametrico." *Relatorio, Proc. 46/11/7302*. Lisboa.

Matos Fernandes, M., 1986, "Three Dimensional Analysis of Flexible Earth-Retaining Structures." *2nd Int. Symp. Numerical Models in Geomechanics*, Ghent, pp. 433-438.

Matsui, M., 1982, "Two-Dimensional Elasto-Plastic Consolidation Analysis by Finite Elements Method." *Annual Report of Maeda Institute of Construction Technology*, Vol. 23, pp. 9-18.

Monnet, J., Kastner, R., Laréal, P., and Bouyat, C., 1985, "Finite Element Calculation and Experimenting on the Saxe-Gambetta Station." *Fifth Int. Conf. Numerical Methods in Geomechanics*, Nagoya, pp. 747-753.

Naylor, D.J., and Pande, G.N., 1981, *Finite Elements in Geotechnical Engineering*. Pineridge Press, 245p.

Parrish, D.K., and Labreche, D.A., 1988, "Initializing the Equilibrium Stress State for Stress Analysis in Geomechanics." *Proc. 29th US Symposium, Key Questions in Rock Mechanics*, Cundall et al (eds), Balkema, pp. 303-310.

Potts, D.M. and Burland, J.B., 1983, "A Numerical Investigation of the Retaining Walls of the Bell Common Tunnel." *Transport and Road Research Laboratory*, TRRL Supplementary Report 783.

Potts, D.M., and Fourie, A.B., 1984, "The Behavior of a Propped Retaining Wall: Results of a Numerical experiment." *Géotechnique*, Vol. 34, No. 3, pp. 383-404.

Poulos, H.G., and Davis, E.H., 1974, *Elastic Solutions for Soil and Rock Mechanics*, Wiley, 411p.

Sekiguchi, H., and Ohta, H., 1977, "Induced Anisotropy and Time Dependency in Clays." *Constitutive Equations of Soils, Proc. Specialty Session 9, Ninth Int. Conf. Soil Mechanics and Foundation Engrg*, pp. 229-238.

Small, J.C., 1986, *User Manual, Program FLEA, (Finite Layer Elastic Analysis).* School of Civil and Mining Engineering, The University of Sydney.

Small, J.C., 1986, *User Manual, Program FLAC, (Finite Layer Analysis of Consolidation).* School of Civil and Mining Engineering, The University of Sydney.

St. John, H.D., 1975, "Field and Theoretical Studies of the Behavior of Ground Around Deep Excavations in London Clay." *Ph.D. Thesis*, University of Cambridge.

Terzaghi, C., 1943, *Theoretical Soil Mechanics*, J. Wiley and Sons, 510p.

Tsui,Y., 1974, "A Fundamental Study of Tied-Back Wall Behavior." *PhD Thesis*, School of Engineering, Duke University, 259p.

Van Langen, H., 1991, "Analysis of Soil Structure Interaction." *Ph.D. Thesis*, Delft Technical University, 142p.

Vermeer, P.A. and Van Langen, H., 1989, "Soil Collapse Computations with Finite Elements." *Ingenieur-Archiv*, Vol. 59, pp. 221-236.

Whittle, A.J., Aubeny, C.P., Rafalovich, A., Ladd, C.C. and Baligh, M.M., 1991, "Interpretation of In-Situ Tests in Cohesive Soils using Rational Methods." *MIT Research Report, R91-01*, 226p.

Wong, K.S., and Broms, B.B., 1989, "Lateral Wall Deflections of Braced Excavations in Clay." *ASCE Journal of Geotechnical Engrng*, Vol. 115, No. 6, pp.853-870.

Program Name	Stress Analysis	FE Solution Method	Geometry (2-D or 3-D)	Soil Models	Element Type	Correct Excavation procedure	References	Institution
SoilStruct	Total	Initial Stress	2-D	Hyperbolic	Subparametric	No	Tsui (1974) Clough & Hansen (1981) Clough et al (1989)	Widely used in geotechnical practice in US.
EXCAV	Total	Initial Stress	2-D	Hyperbolic	Subparametric	?	Duncan and Chang (1977) Broms et al (1986) Wong and Broms (1989)	University of California, Berkeley
STRUPL-2	Effective	?	2-D	Elasto-Plastic	Isoparametric	Yes	Genna & Gioda (1985) Gioda & Jurina (1981)	Technical University of Milan
Adina AdinaT	Effective	Newton-Raphson	3-D	Elasto-Plastic Drucker-Praguer	Isoparametric	Yes	Dysli & Fontana (1982)	Laboratory of Swiss Institute of Technology
	Effective	?	2-D	Sekiguchi & Ohta (1977)	?	?	Matsui (1982) Hata et al (1985)	Maeda Institute of Construction Technology
	Total	Initial Stress?	3-D	Elastic	Subparametric	?	LNEC (1982) Matos Fernandes (1986)	Nacional Civil Engineering Laboratory of Lisbon
ROSALIE	Total?	?	2-D?	?	8-node	?	Barbas (1982) Monnet et al (1985)	Laboratoire Cenntral des Ponts et Chausées
ICFEP	Effective	Initial Stress	3-D?	Elasto-Plastic	?	?	Potts and Burland (1983) Potts and Fourie (1984) Jardine et al (1986)	Imperial College
?	Effective		2-D	Hyperbolic w/ Strain Softening	Isoparametric	Yes	Chan (1986) Chan & Morgenstern (1989)	University of Alberta
FLEA FLAC	Total/ Consolidation	Initial Stress ?	2-D	Elasto-Plastic	Isoparametric	Yes	Small (1986a,b) Brown and Booker (1985) Booker et al (1989)	The University of Sydney

Table 3.1 Finite Element Programs for Excavation Analysis (continued on next page)

Program Name	Stress Analysis	FE Solution Method	Geometry (2-D or 3-D)	Soil Models	Element Type	Correct Excavation procedure	References	Institution
CRISP	Effective	Initial Stress	2-D	MCC	Isoparametric	Yes	Britto & Gunn (1987)	Cambridge University
GNOME	Total	Newton-Raphson	3-D	Hyperbolic, Bounding Surface	Isoparametric	Yes	Gunsallas et al (1989)	Cornell University
PLAXIS	Effective	Initial Stiffness	3-D	Elasto-Plastic	Isoparametric	Yes	Vermeer & van Langen (1989) van Langen (1991)	Delft Technical University
DIGDIRT	Effective	Newton-Raphson	3-D	Cam Clay w/ Creep	Isoparametric	Yes	Borja & Lee (1989a,b)	Stanford University
JFEST	Effective	Newton-Raphson	2-D	Elastic, Hyperbolic, MCC, Bounding Surface	Isoparametric	Yes	Finno and Harahap (1991)	Northwestern University
ABAQUS	Effective	Newton-Raphson	3-D	Elastic, MCC, MIT-E3 (UMAT)	Isoparametric	Yes	This Thesis	HKS. Massachusetts Institute of Technology

Table 3.1 Finite Element Programs for Excavation Analysis (continued from previous page)

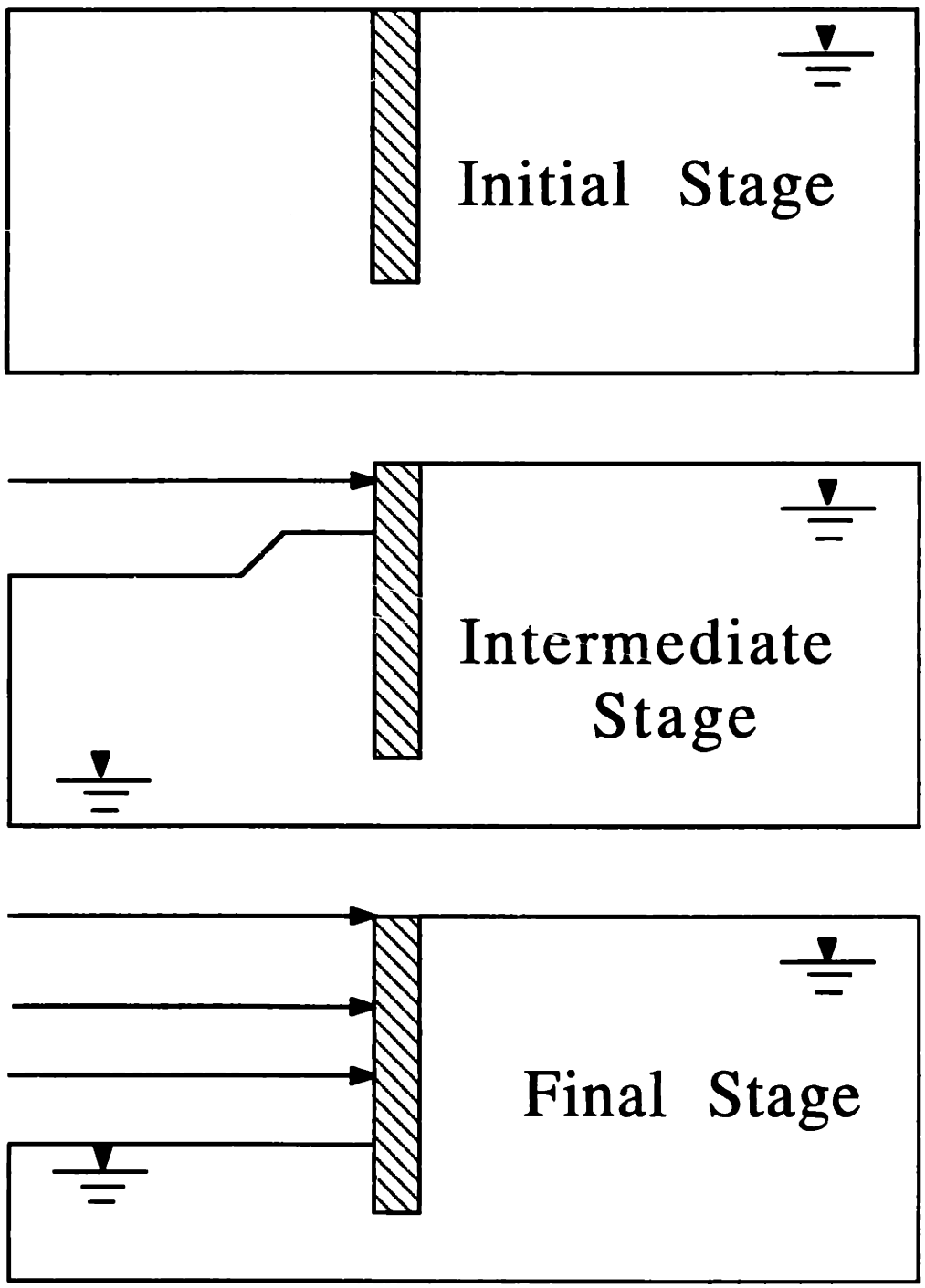

Figure 3.1. Typical Excavation Sequence

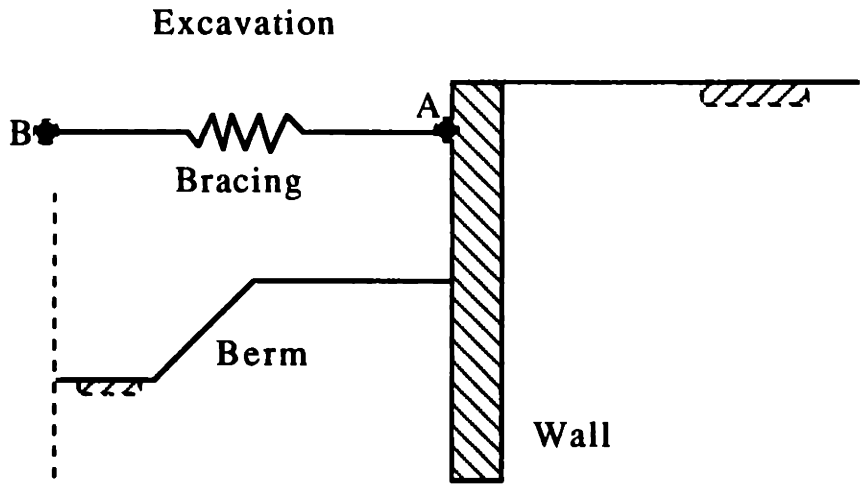

Figure 3.2 Strut Installation Procedure

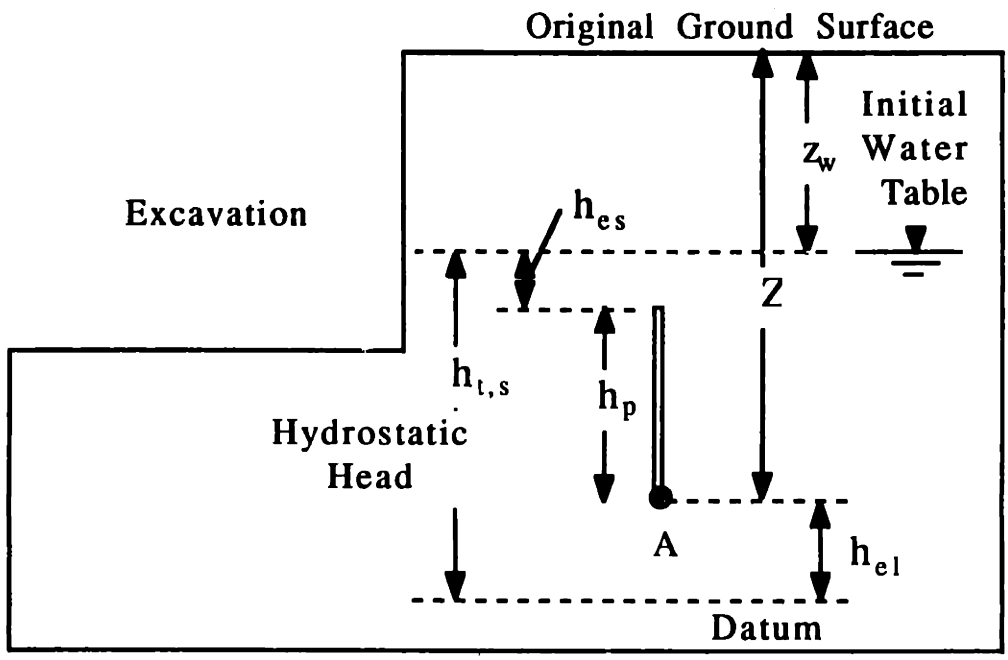

Figure 3.3 Pore Pressure Terms

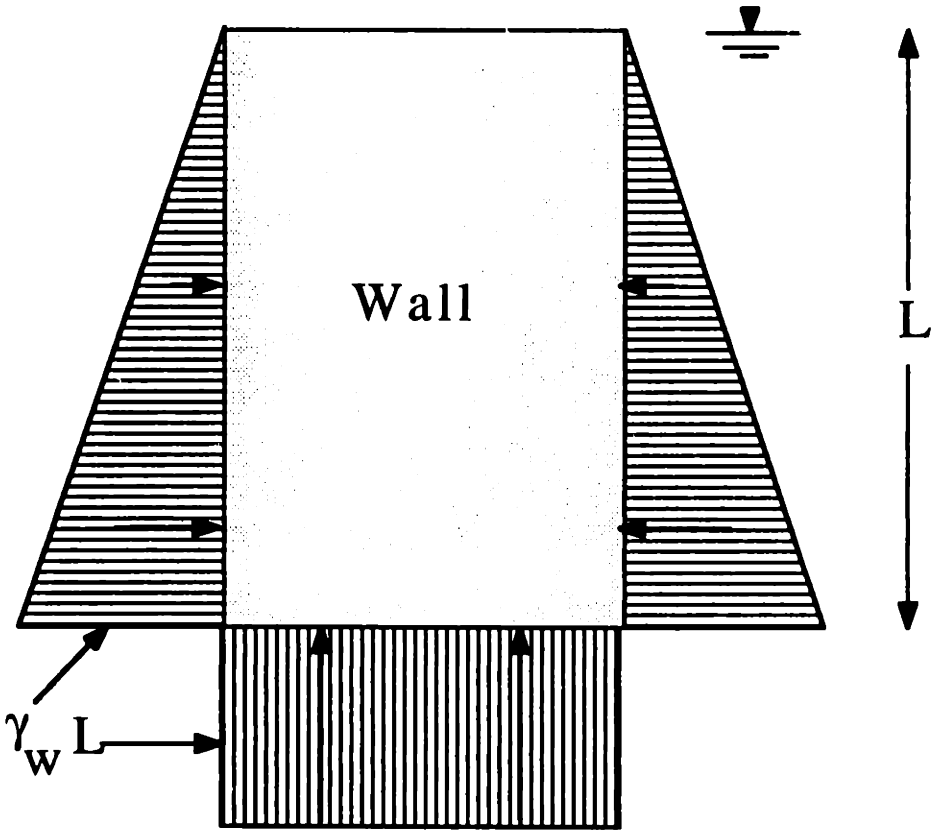

Figure 3.4.Distributed Loads on the Wall, Coupled Analysis (Water Table at Ground Surface, Hydrostatic Pore Water Pressure)

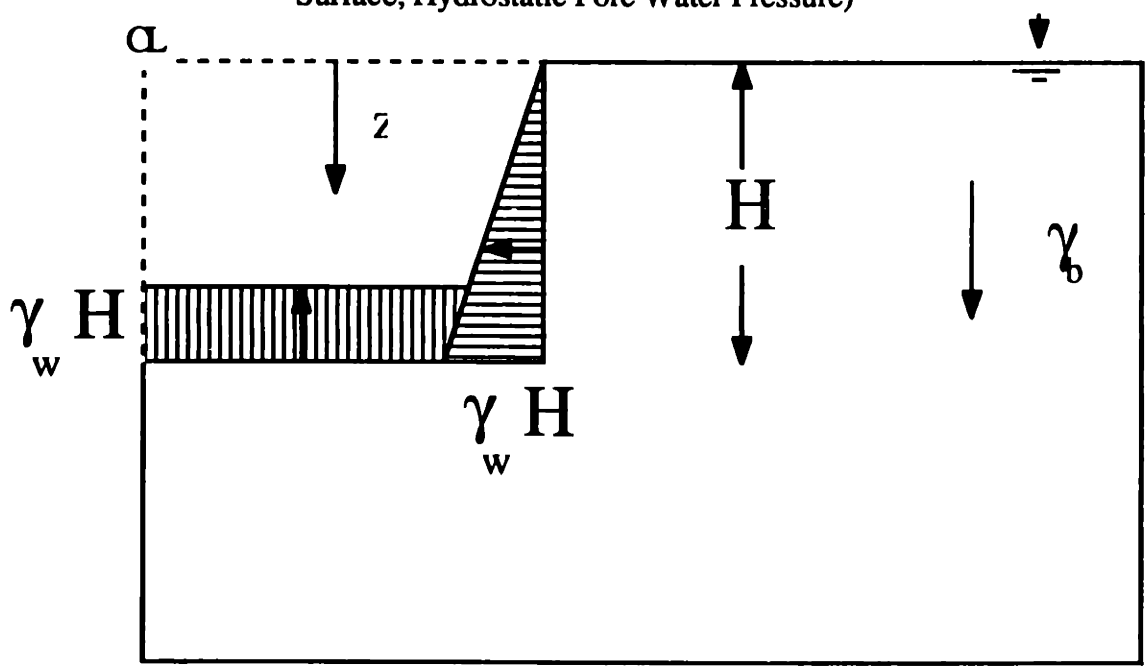

Figure 3.5 Loads Applied During Excavation, Coupled Analysis Water Table at Ground Surface, Hydrostatic Pore Water Pressure).

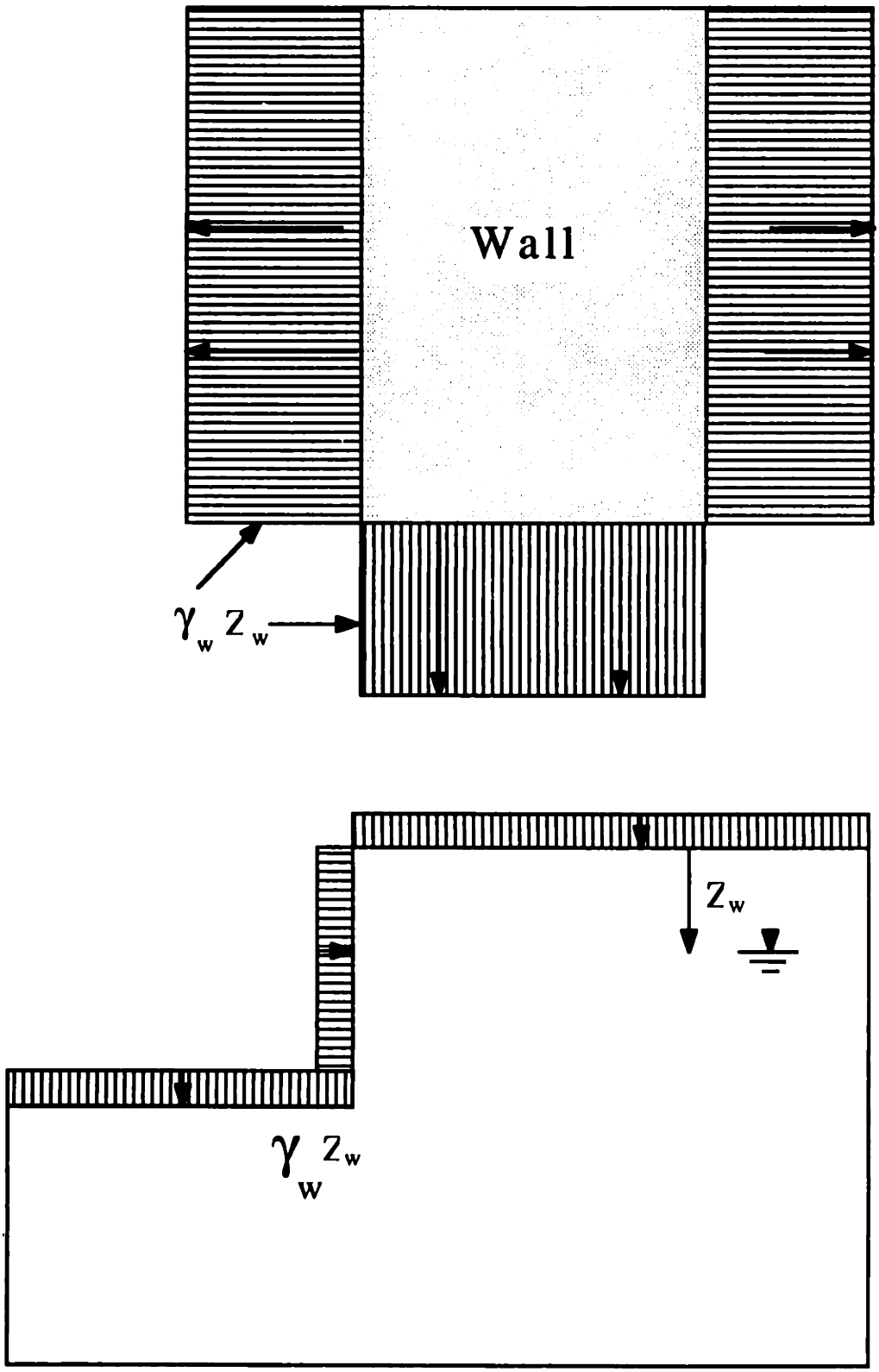

Figure 3.6 Loads in Addition to Figure 3.4 and 3.5, Capillary Conditions.

4. Analysis of the Behavior of Braced Diaphragm Walls in Deep Deposits of Clay

4.1. Introduction

Modern techniques of excavation, including the use of structural diaphragm walls and top-down construction, provide effective methods for minimizing deformations in the surrounding soil. However, for deep excavations and walls embedded in deep layers of soft clays, it is difficult to control soil movements. In these situations, reliable predictions of deformations are important both in the design of the earth support system and in assessing the effects of the excavation on adjacent facilities.

There are no standard design methods (e.g., comparable to those used in the estimate of settlement of shallow foundations) for estimating soil deformations caused by the staged construction of a braced excavation. Existing techniques[1] for estimating wall deflections and soil settlements involve (see Chapter 3) either a) interpolation from the published empirical data base (Peck, 1969; Mana and Clough, 1981; O'Rourke, 1981; Clough and O'Rourke, 1990), or b) numerical analyses[2] using finite element (Mana and Clough, 1981; Potts and Fourie, 1984; Finno and Harahap, 1991) or boundary element methods (Stolle, 1989).

Peck (1969) compiled measurements of surface settlement profiles, lateral wall deflections and strut loads for sheet pile and soldier pile walls with cross-lot bracing. For excavations in soft clays, these data show settlements extending to lateral distances of 3-4 times the excavated depth, H, and achieving maximum values greater than 0.02H at locations close to the wall. In subsequent studies, Mana and Clough (1981) and Clough and O'Rourke (1990) show that measurements of maximum lateral wall deflections, δ_{Hmax}, can be closely correlated with the factor of safety against basal heave, as defined by Terzaghi (1943). They report large deflections ($\delta_{Hmax} > 0.02H$ to $0.03H$) for walls embedded in soft clays with factors of safety less than 1.5. Although these results provide initial guidance on the expected magnitudes of deformations, most of the existing data were obtained from excavations less than 15m deep with relatively flexible lateral earth support systems[3] (i.e., sheet pile and soldier pile walls). There are significant uncertainties in extrapolating the empirical observations to situations of current interest

---

[1] "Beam on-elastic-foundation" and other simplified structural analyses do not explicitly provide information on soil deformations and hence are not considered in this discussion.

[2] Simplified analytical procedures have been proposed recently by Bolton et al (1990a,b) for propped diaphragm walls in stiff clays.

[3] Typical bending stiffness for a sheet pile wall, EI≈50-80MPa/m compared to EI≈1,800MPa/m for a 1m thick diaphragm wall.

involving much deeper excavations (up to H=30m) supported by structural diaphragm walls.

Finite element analyses were first applied to braced excavations by Clough et al. (1972), Clough and Mana (1976), Wong (1970) and Christian and Wong (1973) and are now widely used to estimate deformations for a variety of lateral earth support systems (Hubbard et al., 1986, Desai, 1988, and Caliendo et al., 1990). The principal advantage of the finite element method in these applications is the capability to model complex construction/excavation sequences, and to incorporate detailed properties of the structural system and surrounding soils. As a consequence, however, the numerical predictions are affected by a large number of parameters and it is difficult to interpret fundamental mechanisms controlling the development of deformations due to excavation. Thus, although there are many papers describing finite element predictions for particular case studies, there are very few which interpret results from parametric analyses (notable exceptions include Mana and Clough 1981; Clough and Hansen 1981; Potts and Fourie 1984).

This chapter describes results of numerical experiments designed to analyze the behavior of braced diaphragm walls in deep deposits of clay. The calculations are performed using the finite element procedures described in Chapter 2 and Chapter 3, which provide numerically accurate, effective stress analysis of excavations in non-linear soils (with the ABAQUS program). The analyses also incorporate the MIT-E3 model (Chapter 2) which describes accurately many features of the behavior of normally and overconsolidated clays ($1 \leq OCR \leq 8$) observed in laboratory element tests including a) anisotropic stress-strain-strength; b) small strain non-linearity; and c) strain softening in certain modes of shear deformations.

The work is motivated, in part, by two large construction projects currently in progress; 1) the Central Artery and Third Harbor Tunnel (CA/T) project in Boston; and 2) the Taipei Rapid Transit (TRT) System in Taiwan. Both projects will include deep excavations (greater than 20m) supported by diaphragm walls and embedded in deep layers of soft clay. Reliable predictions of soil deformations are particularly important in these projects due to the proximity of adjacent structures.

Section 4.2 outlines the scope of the parametric study. Section 4.3 illustrates the importance of soil modelling in the performance of deep excavations in clay. Sections 4.4 through 4.6 summarize how wall embedment, support spacing and stress history affect predictions of wall deflections and soil deformations. These results are combined in Section 4.7 to form a simplified framework for estimating wall deflections and ground movements as functions of excavation depth. The predictions from this study are

compared with existing empirical and semi empirical methods in Section 4.8. Section 4.9 shows how results of analyses based on the measured stress history at a site in South Boston (with properties typical of the CA/T project) can be evaluated from the previous parametric studies. Finally, in Section 4.10 a discussion of the practical implications of this study is presented.

4.2. Scope of the Parametric Study

The main aim of the numerical experiments in this chapter is to develop a fundamental understanding of deformations for braced diaphragm walls in deep layers of clay. Compilations of measured data (e.g., Goldberg et al. 1976; O'Rourke 1989) and case histories (e.g., Chapter 5) emphasize the large number of factors relating to construction activities (e.g., Table 4.2-1) and soil conditions which can affect ground movements for internally braced and tied back excavations. In contrast, the design of numerical experiments attempts to limit the number of parameters in order to facilitate the interpretation of the analyses, while still maintaining sufficiently realistic conditions such that the results can have practical application. In this study, the principal parameters of interest are the wall length (and embedment), support conditions and soil properties. The analyses include the following assumptions:

1. For deep layers of low permeability clay[1], the excavation process occurs sufficiently rapidly that there is no migration of pore water, hence the soil is subject to undrained shearing. Although this assumption is reasonable in view of the very long time required to achieve steady flow conditions, it should be noted that partial drainage increases the magnitude of soil deformations and hence reduces the operative safety factor. A preliminary analysis of the effects of drainage during excavation is presented separately in Appendix C.
2. Deep excavations for the Central Artery/Tunnel project and Taipei Rapid Transit System will be supported by diaphragm walls and braced internally using techniques of top-down construction. In order to provide results which have direct relevance to those projects, the numerical experiments use plane strain geometry with a fixed excavation half width, w=20m (Figure 4.2-1a) and a standard wall thickness, t=0.9m[2]. The analyses assume that installation of the diaphragm wall does not disturb the surrounding soil (i.e., the wall is 'wished in

[1]The analyses assume the clay layer to be very deep (120m) and to extend up to 220m from the center line of the excavation to reduce 'boundary effects'.

[2]Figure 4.2-1a shows that the analyses assume the same unit weight for the wall and surrounding soil. This assumption simplifies the numerical analysis and has negligible effect on the predicted deformations.

place').

3. The clay is saturated and exhibits normalized engineering properties. The numerical experiments then focus on simplified soil profiles in which the overconsolidation ratio, OCR ($=\sigma'_p/\sigma'_{v0}$), of the clay is constant with depth, and hence the engineering properties are proportional to the effective overburden stress, σ'_{v0}. It is assumed that the pore pressures are initially hydrostatic with the groundwater table located at a depth, d_w=2.5m (typical of conditions in Boston) and full capillarity in the overlying clay (hence, σ'_{v0}=25 kPa at the ground surface). Section 4.9 describes further analyses for stress history profiles more typical of conditions in downtown Boston.
4. Effective stress-strain behavior of the soil is described by the MIT-E3 model, with input parameters corresponding to properties of Boston Blue Clay (Tables 4.2-2a and 2b). Results presented in Whittle (1987) and Chapter 2 show that MIT-E3 describes many aspects of the observed behavior of K_0-normally consolidated and lightly overconsolidated ($1 \leq OCR \leq 8$) clays including: a) small strain non-linearity; b) anisotropic stress-strain-strength; and c) hysteretic and inelastic behavior due to cyclic loading. Section 4.3 evaluates the importance of clay behavior on the predicted performance of braced excavations by comparing results obtained using elastic, Modified Cam Clay (MCC) and MIT-E3 soil models.
5. The excavation is braced by incompressible (rigid) supports spaced at equal intervals, h, as shown in Figure 4.2-1b. Installation of rigid bracing represents an ideal condition in which there is no further lateral deflection of the wall at the elevation of the support. The analyses do not consider support compressibility or other complex aspects of soil-structure interaction associated with different bracing systems such as a) shrinkage and expansion of cast in-situ floor slabs (e.g., Chapter 5), and b) prestressing of cross-lot bracing (Mana and Clough 1981, Finno and Harahap 1991). Further studies are necessary to evaluate the importance of these factors on the performance of braced excavations. In general, the predictions with rigid bracing can be expected to underestimate the magnitudes of wall deflections and soil movements.
6. The analyses assume a simplified construction sequence (Figure 4.2-1b) comprising the following steps: 1) soil is initially excavated to a depth, h_u, without lateral support; 2) the wall is propped at the surface and excavation proceeds to a depth, h_e ; 3) a second level of support is installed at a spacing, h ($h \leq h_e$), and soil is then removed over a further interval, h_e; 4) step 3 is repeated

until either failure occurs (Section 4.4) or the excavation reaches a total depth H=40m. By varying the parameters h, h_e and h_u, it is possible to study a wide range of top down construction sequences. However, all of the analyses described in this chapter assume that the lower support levels are all constructed 'on-grade' (i.e., h_e=h).

Figure 4.2-2 shows the finite element mesh and boundary conditions used in the analyses. The interface between the diaphragm wall and the surrounding soil is assumed to be rough, such that there is no slip[1]. The concrete wall is represented by 8-node isoparametric solid elements (ABAQUS element type CPE8, total stress analysis), and the clay by 8-node isoparametric elements coupled with pore pressures (ABAQUS element type CPE8P, effective stress analysis with pore pressures). The model has a total of 3292 degrees of freedom[2] and uses a full integration procedure. The minimum excavation increment possible using this mesh is 2.5m, which controls the analysis resolution of excavation deformations and failure.

Figure 4.2-1 summarizes the ranges of soil properties (stress history) and principal geometric parameters (L, h, h_u) considered in the study:

1. The wall length varies from a minimum value, L=12.5m, which represents a very short cast in-situ wall, up to a maximum L=60m, which is significantly longer than the diaphragm walls currently proposed for either the CA/T or TRT projects. However, 'super-deep' diaphragm walls up to 100m long have recently been used in the construction of an underground gas storage tank (Goto and Iguro 1989).
2. The minimum support spacing, h=0m, is referred to as the 'perfect wall support' condition. In this case, wall deflections can only occur below the base of the excavation. Predictions of soil deformations associated with perfect wall support represent the minimum disturbance caused by the excavation. At the opposite extreme, the analyses consider walls supported at intervals h=10m, which are referred to as 'minimally-supported'.
3. The initially unsupported height of the wall ranges from h_u=0m (roof slab cast on grade) up to h_u=5m, which is comparable in magnitude to the maximum excavation depth used in the design of cantilevered sheet pile walls (US Steel, 1975).
4. The analyses consider soil profiles having constant value of OCR with depth

---

[1]The maximum shear stress that develops at the interface is controlled by the maximum shear stress allowable in the soil and will not exceed the soil shear strength.

[2]The total number of elements is 442 and the total number of nodes is 1413.

(OCR=1.0, 2.0 and 4.0). Table 4.2-2d summarizes reference values of undrained strength ratio, s_u/σ'_{v0}, predicted by the MIT-E3 model for Boston Blue Clay in plane strain active, direct simple shear and plane strain passive elemental modes of shearing.

Table 4.2-3 lists the soil conditions and geometric parameters used in the numerical experiments.

4.3. Effects of Soil Model

The soil in this study is assumed to be governed by an effective stress-strain relationship. MIT-E3 is used as the primary model to describe clay behavior. At the element level, MIT-E3 accurately describes the most important inviscid aspects of soil behavior (Whittle, 1987; Section 2.4, Section 4.3.1). However, in order to assess the role of MIT-E3 in the excavation boundary value problem, its predictions are compared with those of two simpler soil models[1].

This section demonstrates how modelling of soil behavior affects predictions of the behavior (deformations and failure) for a braced diaphragm wall in a deep clay layer. A 'representative' excavation configuration is assumed in the analysis with the following properties: 1) L=40m (longest expected wall in CA/T), 2) $h=h_u$=2.5m (typical top-down construction), and 3) OCR=1 Boston Blue Clay (most critical case for deformations and failure).

The mechanical behavior of clay is described by one of three material models (Table 4.2-2):

1. Elastic Model: This model uses the same elastic formulation used in the MCC model (Equation 2.25a,b and 2.31a, b). Analyses are performed using two stiffnesses: a) a stiffness equal to the elastic stiffness of MCC (κ=0.034, E_u/σ'_{vo}=71, soft elastic); and b) a stiffness where the initial elastic predictions of wall movements match those of MIT-E3 (κ=0.01, E_u/σ'_{vo}=240, stiff elastic).
2. MCC with BBC properties (E_u/σ'_{vo}=71). MCC is currently one of the most commonly used soil models for the analysis of geotechnical boundary value problems.
3. MIT-E3 with BBC properties (At small strains E_{uMAX}/σ'_{vo}=2413).

Elastic analyses are performed, even though BBC behavior is inelastic, to provide a reference solution of the excavation behavior. The solutions are used to assess the

[1]The comparisons are made, in part, to evaluate (and justify) the additional cost of using MIT-E3 in the prediction of excavation behavior.

deviation of MCC and MIT-E3 predictions from the basic elastic solution of the problem. The elastic solutions will, therefore, provide a base line that is used to estimate the contribution of the varying degrees of plasticity and nonlinearity in MCC and MIT-E3 in the prediction of the braced excavation boundary value problem.

The material properties of MCC and MIT-E3 are chosen such that they have the same reference undrained shear strength in triaxial compression. In the following sections, it will be shown that the triaxial strength is not a sufficient soil property to characterize clay response in a braced excavation. Table 4.2-2 lists the material properties, initial state of stress and state variables for the elastic, MCC and MIT-E3 models.

The influence of the soil model on the global behavior of the excavation (wall deformations, surface settlements, failure, etc), and the stress-strain history throughout the field of the boundary value problem is presented in detail. Comparing[1] the various model predictions will enhance understanding the role of the soil's mechanical description in analytical prediction of braced excavation performance.

4.3.1. Undrained Plane Strain Shear Behavior of Normally Consolidated BBC

The excavation analyses are performed under undrained conditions and assume a plane strain geometry. During the excavation process, soil elements undergo shearing in active and passive modes as well as intermediate modes that involve continuous rotation of principal stress directions. The predictive capabilities of the clay constitutive model, therefore, need to be evaluated at the element level under shear in plane strain. Whittle (1987) presents an extensive comparison of the predictive capabilities of MIT-E3 and MCC relative to laboratory data on BBC in various modes of shearing in triaxial and plane strain spaces. Laboratory data for plane strain shearing of K_0-normally consolidated BBC are available from two sources: a) Ladd et al. (1971), who present results of plane strain active (PSA) and plane strain passive (PSP) shear tests (comparison with these data is presented in Whittle, 1987); and b) Directional Shear Cell (DSC) tests by Seah (1990).

The Directional Shear Cell is a plane strain device in which normal stresses are applied via flexible pressure bags and shear stresses using shear sheets (Arthur and Menzies 1972; Germaine 1982). The applied major principal stress in the DSC can be

[1]The relevant analyses in this section, Table 4.2-3, are st1_40_02, st1mcc_40_02, st1elas_40_02, st1elas_40_02_stiff.

fixed in any desired direction, and/or continuously rotated during shear (Figure 4.3-1). The δ angle (Figure 4.3-1) is defined as the direction of the major principal stress relative to the depositional direction (taken as vertical). Another unique feature of the DSC is that its performance can be verified by performing tests in the isoptropic plane of a specimen, which should have stress-strain relationships independent of the principal stress direction. A series of tests were performed in the DSC on K_0-normally consolidated BBC by applying incremental principal stresses oriented at an angle δ_{inc} to the direction of the principal consolidation stress (σ'_{yc}) (Figure 4.3-2). The data at $\delta_{inc}=0^0,90^0$ correspond to plane strain 'active' and 'passive' modes of shearing, while intermediate values of δ_{inc} produce continuous rotations of principal stresses (i.e., δ varies throughout the test, Figure 4.3-1).

The DSC data are unique because they are the only available laboratory data on clay that include complete principal stress rotation effects and are useful for predicting and interpreting soil response during excavation.

Predictions of MIT-E3 and MCC are compared to both sets of data (Ladd et al. 1971; Seah 1990). Material properties for the two models are chosen using other laboratory data (triaxial and oedometer tests; Whittle 1987). Therefore, the comparisons are true predictions of the models' response in this mode of shearing.

The DSC measures the complete state of stress in the soil and hence, comprehensive comparisons with model predictions can be made. As the DSC tests were conducted under stress control, reliable measurements and predictions can be made only up to the peak strength, beyond which instability due to softening occurs.

MIT-E3 predictions are compared with measured data in Figure 4.3-3.

a) Figure 4.3-3a compares the stress paths in a $\frac{p'_{vh}}{\sigma'_{yc}} = \frac{\sigma'_y + \sigma'_x}{2\,\sigma'_{yc}}$, $\frac{q_{vh}}{\sigma'_{yc}} = \frac{\sigma'_y - \sigma'_x}{2\,\sigma'_{yc}}$ space, which ignores the τ_{xy} shear stress component. At $\delta_{inc}=0^0$, 90^0 there is some scatter between DSC results and PS results reported by Ladd et al (1971). At $\delta_{inc}=0^0$, MIT-E3 adequately predicts the initial part of the stress path. At large strains, MIT-E3 predicts a larger friction angle than calculated from PSA data. At $\delta_{inc}=45^0,60^0$, the match between predictions and measured data is excellent. At $\delta_{inc}=75^0$, MIT-E3 overpredicts the reduction in q_{vh}. At $\delta_{inc}=90^0$, there is a reasonable agreement between MIT-E3 predictions and measured data.

b) Figure 4.3-3b shows the shear stress component, τ_{xy}, versus q_{vh}. In the DSC, δ_{inc}=constant is achieved by applying a constant $\Delta\tau_{xy}/\Delta q_{xy}$ ratio. The figure shows the proportional paths at the various δ_{inc} angles. The large triangles

indicate the locations at which the maximum shear stress $q_{max} = \frac{1}{2}\sqrt{(\sigma_x - \sigma_y)^2 + 4\,\tau_{xy}^2}$ reaches its peak value. The dashed line is the envelope of peak undrained shear strength in plane strain as predicted by MIT-E3. The strengths are calculated assuming proportional strain paths (i.e., $\Delta\varepsilon_{xy}/\Delta\varepsilon_{yy}$=constant). The model predicts accurately the peak shear strength except at $\delta_{inc}=60^0$, where it underpredicts the measurements by 7%.

c) Figure 4.3-3c is a plot of the maximum shear stress versus the maximum shear strain $\gamma = \frac{1}{2}\sqrt{(\varepsilon_x - \varepsilon_y)^2 + 4\,\varepsilon_{xy}^2} = \frac{1}{2}(\varepsilon_1 - \varepsilon_3)$. The measured data show an increase in the shear strain required to mobilize the full shear strength in the soil from $\gamma_f \approx 0.5\%$ at $\delta_{inc}=0^0$, to $\gamma_f \approx 5\text{-}10\%$ at $\delta_{inc}=90^0$. MIT-E3 predictions show excellent agreement with this highly anisotropic stress strain behavior.

d) Figure 4.3-3d is a plot of the maximum undrained shear strength versus orientation of principal stresses at failure. The model accurately predicts measured strength anisotropy. The predicted strength ratio ranges from $q_{max}/\sigma'_{yc}=0.34$ at $\delta=0^0$ to 0.17 at 90^0, and illustrates the importance of anisotropic undrained strength properties of K_0-consolidated Boston Blue Clay.

e) Measurements of the secant modulus (Figure 4.3-3e) show that the clay exhibits non-linear stress-strain behavior for shear strains, $\gamma \geq 0.05\%$. Model predictions agree well with the data for tests with $\delta_{inc}= 60^0, 75^0, 90^0$ but generally overpredict the stiffness at $\delta_{inc}=0^0,45^0$.

The laboratory measurements show that BBC exhibits a significant anisotropic nonlinear stress-strain-strength behavior. MIT-E3 predicts exceptionally well the trends observed in measured data. The results illustrate that MIT-E3 is suited to model the complex stress-strain history of the soil induced by excavation processes, including principal stress rotation.

MCC predictions are compared with DSC and PS data in Figure 4.3-4. MCC is an isotropic model and is not capable of incorporating the significant anisotropic behavior observed for BBC. The influence of the elastic region inside the yield surface is seen clearly in Figure 4.3-4a where MCC predicts no change in the mean effective stress in parts of the stress paths in tests with $\delta_{inc} \geq 45^0$. Regardless of the shearing direction, MCC predicts the same peak strength, $q_{max}/\sigma'_{yc}=0.36$ (Figures 4.3-4b,c,d). MCC and MIT-E3 undrained shear strengths in PSA are different (0.34 for MIT-E3 versus 0.36 for MCC) even though the strengths in triaxial compression are equal. MCC shows a significantly different stress strain behavior than measured in the DSC (Figure 4.3-4c).

The peak strength, in MCC, is mobilized at large shear strains, γ_f>6% regardless of the mode of shearing (no anisotropy). Predictions of the secant modulus, Figure 4.3-4e, do not capture the non-linear behavior measured at shear strains, γ<2-3%. At small strains, MCC predicts a constant stiffness much lower than the measured stiffness.

In summary, BBC exhibits a significant anisotropic behavior with regard to deformation and strength. MIT-E3 captures this anisotropy well, while MCC severely mispredicts this anisotropic behavior. It is shown next that MIT-E3 and MCC give significantly different predictions of the magnitude and distribution of deformations and different estimates of collapse depth in braced excavations.

4.3.2. Wall Deflections and Ground Movements for Normally Consolidated Boston Blue Clay

Excavations in MCC and elastic soil are carried to a depth of 40m (equal to the length of the wall, $h=h_u$=2.5m) with no indication of failure. Excavation in MIT-E3 soil fails[1] at H=22.5m.

Figures 4.3-5 and 4.3-6 show predictions of lateral wall deflections and surface settlements for excavation up to a depth, H=22.5m, using the four different material models for normally consolidated clay (Soft elastic, Stiff elastic, MCC, and MIT-E3). Plots of the deflected wall shape include the excavation geometry at H=22.5m. At H=2.5m, prior to installation of the first lateral support, the wall deforms in a cantilever mode and the maximum deflection occurs at the top of the wall. This observation is independent of the soil model (Figures 4.3-5c,d and 6c,d). For H≥2.5m, bracing is installed and the shape of the wall deflection changes from a cantilever mode to a bulging mode where the maximum bulging occurs below the level of the lowest brace (Figures 4.3-5c,d and 6c,d). Figure 4.3-7a plots the location of the maximum wall deflection versus excavation depth for all the soil models. When (y_{max}-H) is positive, maximum wall deflection is located below the excavated surface. MCC and soft elastic predictions are essentially identical. Beyond an excavated depth of 30m, maximum deflections are located at the toe of the wall (Figure 4.3-7b). MIT-E3 predicts the maximum deflection to be located at a constant depth of 8.75m below the excavated surface regardless of the excavation depth (H) and the failure state. Overall, for H<25m, all four models predict the maximum deflection to be located within a narrow range of depths (6-10m) below the bottom of the excavation.

The two elastic predictions exhibit the same qualitative behavior (Figure 4.3-5).

---

[1] A detailed discussion of failure is presented in Section 4.4.

Even at shallow excavation depths there is a substantial movement of the toe. MCC predictions, Figure 4.3-6c, are quantitatively very similar to the soft elastic response, although MCC predicts slightly larger deflections.

At H≤5m, MIT-E3 deflections, (Figure 4.3-6d) match the stiff elastic model predictions[1] (Figure 4.3-5d). As the excavation depth increases beyond H=5m, a rapid increase in wall deformations is observed until failure occurs (Figure 4.3-9b). Note that MIT-E3 predicts smaller initial movements of the wall than MCC. This is because the initial response is much stiffer than for the MCC model (effect of small strain nonlinearity).

Figure 4.3-7b shows the ratio of the toe movement to maximum wall deflection versus depth for the four models. Initially, the toe movement in MIT-E3 is small compared to the maximum wall deflection, but increases with increasing excavation depth. The elastic and MCC models exhibit similar behavior, whereas MIT-E3 predicts a much lower ratio until failure. The smaller toe movement to maximum deflection ratio in MIT-E3 is due to the small strain formulation in the model. It leads to greater flexure in the wall and greater predicted moments (near failure; this issue is discussed later).

Surface movement (Figures 4.3-5a and 5b; the sign convention is positive for heave and negative for settlement) predictions in the two elastic models are qualitatively similar. The elastic models predict a significant upward movement of the wall (compared to maximum settlement) due to the elastic unloading of the soil within the excavation. The elastic models also predict significant settlements, even up to a distance of 200m away from the excavation center line (an unrealistic result). MCC predictions (Figure 4.3-6a) are similar to the soft elastic response, but now, due to the plasticity in the model, smaller upward wall movements are predicted for H>20m (see Figure 4.3-7d). There is also a slightly greater decrease in the settlement away from the excavation. MIT-E3 (Figure 4.3-6b) predicts a significantly different settlement behavior with minimal upward movement of the wall. Figure 4.3-7d compares vertical displacement of the top of the wall for the four models. For the elastic models the wall initially heaves and then starts to move downward for deep excavations with H≥32.5m. The downward movement is not caused by a failure condition, but is due to the removal of restraint at the toe of the wall and the downward drag applied on the wall by the retained soil above the excavation level. The wall in MCC moves downward at an earlier stage (H=25m) due to yielding of the soil supporting the toe of the wall. For MIT-E3, the wall shows much smaller upward

[1]The stiff elastic model properties are chosen such that the initial stiff elastic wall movement matches that of MIT-E3 initial predictions.

movement followed by downward movement as failure is approached. (see Section 4.4 for further discussion of failure). Settlements predicted by MIT-E3 decrease quickly beyond a distance of 100m from the excavation center line (Figure 4.3-6b).

The significant difference in the shape of the settlement trough predicted by MIT-E3 versus the other models is attributable to small strain nonlinearity introduced in MIT-E3. Jardine et al. (1986), Figure 4.3-8, report a similar (but less pronounced) effect.

Figure 4.3-9 shows the development of maximum wall deflection, wall moment, surface settlement, and center line heave with excavation depth. The curves of maximum deflection for the soft elastic and MCC models (Figure 4.3-9a) initially coincide. At later excavation stages, greater movement is predicted by MCC. MIT-E3 and stiff elastic solutions are initially tangent, but the maximum deflection quickly accelerates for MIT-E3 until failure is reached at 22.5m. For the two elastic models, the initial portions of the maximum deflection curves are approximately linear, but flatten with increasing excavation depth. This nonlinearity in the elastic solution is most likely due to the width/depth ratio of the excavation. The narrow excavation (40 m) limits the wall movement. It is expected that for a very wide excavation, the curves will be almost linear.

Maximum settlement curves (Figure 4.3-9b) and center line heave curves (Figure 4.3-9d) exhibit trends similar to those of the maximum wall deflection curves.

Moments in the wall are calculated from the vertical nodal stresses in the FE analysis. A linear distribution of stress is assumed between the nodes. The torque generated by these stress distributions in a section of the wall (per unit length of wall) about a pivot in the middle of the section is referred to as the bending moment. Figure 4.3-9c shows the development of maximum moments with depth. For all models, the maximum moments reach an initial maximum and then decrease slightly and then increase again (less pronounced for MIT-E3). This is associated with the change in the deflection mode of the wall and the movement of the toe. For MCC and elastic models, the moment reaches a constant value beyond a certain excavation depth. This is related to the change in the location of the maximum moments from the point of maximum wall bulging to about a depth of 5m below the ground surface. The shift is related to the release (outward movement) of the toe of the wall, and hence, the reduction of moments in the lower portion of the wall. For the MIT-E3 model, the maximum moment increases continuously until failure.

The influence of the soil model on maximum deformation and moment predictions is more pronounced when these quantities are divided by κ (compressibility parameter in the elastic equations, inversely proportional to the elastic modulus, Figure 2.4, Table 4.2-2) of the elastic models. MCC predictions are divided by κ of the soft elastic model, and

MIT-E3 predictions are divided by κ of the stiff elastic model. Figure 4.3-10 presents these quantities. In this space the predictions of deformations of the two elastic models are indistinguishable (Figures 4.3-10a,b,d). The MCC model predictions coincide with the elastic solution up to a depth of H=25m, beyond which effects of model plasticity become more pronounced. For MIT-E3 the deviation from the elastic solution starts at a much earlier stage of excavation (H≥7.5m). The nonlinearity and plasticity in MIT-E3 have a more pronounced effect on the behavior than MCC plasticity. Moments in Figure 4.3-10c show that MCC and elastic models give similar predictions. MIT-E3 predicts larger moments. Results of Figure 4.3-10 have great practical significance as they indicate a fundamental difference in the prediction of subsequent behavior between different models. Normalizing by the compressibility parameter essentially removes uncertainties in the initial system stiffness, in this case, MIT-E3 indicates a complete difference in behavior from other models.

Figures 4.3-11a,b present normalized surface settlements (adopted from Peck 1969) for the four models at two excavation depths H=10 and 22.5m. MCC and elastic predictions are almost identical in this space, but differ markedly from the MIT-E3 predictions. MIT-E3 predicts a far more limited zone of settlement than the other models and shows the maximum settlement to occur closer to the wall. The predicted shape of the settlement trough influences the estimated damage to adjacent structures. Figures 4.3-11c and 11d are plots of normalized wall deflection. The normalized depth, (y-H)/L, distorts the depth and location of the wall. The most significant observation in this plot is that at two different depths of excavation the normalized location of maximum deflection for all models is almost unique (this was also indicated in Figure 4.3-7a). MIT-E3 predicts greater flexure in the wall. At H=10m, MIT-E3 predicts smaller toe movements than other models. Even at H=22.5m, just prior to failure, MIT-E3 predicts smaller absolute deflections, of the wall, but greater flexure and bending moments than the MCC or elastic models.

Boscardin and Cording (1989) state that in addition to settlement and angular distortion, lateral wall displacements at the ground surface affect the damage to structures adjacent to excavations. Figure 4.3-12 shows plots of lateral surface movement versus lateral distance from the center line. The difference between the four models is similar to that observed for the corresponding surface settlements (Figures 4.3-5a,b, 4.3-6a,b). MIT-E3 predicts that movements decrease significantly beyond a distance of 100-120m from the center line, while other models do not predict such a steep decrease. A more important factor that affects damage assessment is lateral strain rather than absolute lateral displacement (Figure 4.3-13). MCC and elastic models predict lateral tensile (negative)

strain to extend to a large distance behind the wall, while MIT-E3 predicts localization of these strains within a smaller zone behind the wall, and hence predicts a more limited area of potential damage to surrounding structures. Again, the difference in model predictions can be attributed to small strain nonlinearity introduced in MIT-E3.

4.3.3. Development of Stresses and Strains in the Soil

To gain further insight into the mechanics controlling the development of deformations described in Section 4.3.2, the stress and strain history of the soil during excavation is monitored at select locations around the wall and globally over the entire excavation F.E. mesh. Differences and similarities between the soft elastic, MCC and MIT-E3 models are examined.

In the current analyses the clay soil is undergoing undrained shear in plane strain conditions. Therefore, there are only two independent strain components that describe the complete strain history at a point, $\varepsilon_{yy}=-\varepsilon_{xx}$ and ε_{xy}). In an effective stress model there is a unique relationship between effective stresses and strains. At any point there are four independent stress measures σ'_{xx}, σ'_{yy}, σ'_{zz} and σ'_{xy}. In-plane stresses are of most interest in practice and can be conveniently shown (as before, Figure 4.3-3a,b) in two stress space representations:

$$\left(\frac{q_{vh}}{\sigma'_{v0}}=\frac{\sigma_v-\sigma_h}{2\sigma'_{v0}},\ p'_{vh}=\frac{\sigma'_v+\sigma'_h}{2\sigma'_{v0}}\right)\ \&\ \left(\frac{q_{vh}}{\sigma'_{v0}}=\frac{\sigma_v-\sigma_h}{2\sigma'_{v0}},\ \frac{\tau}{\sigma'_{v0}}=\frac{\sigma'_{xy}}{2\sigma'_{v0}}\right).$$

Stresses are normalized by the initial vertical effective stress as the soil models assume normalized behavior. This approach also avoids difficulties in presenting and scaling results caused by differences in stresses with depth (i.e., geostatic stress gradients).

Figure 4.3-14 shows the locations of points in the excavation at which stress and strain histories are monitored. The goal is to monitor a sufficient number of locations so that the general character of stress-strain behavior can be observed during excavation.

4.3.3.1. Strain Paths

Strain paths of points selected in Figure 4.3-14 are shown in Figure 4.3-15. Positive ε_{yy} indicates vertical compression strains (and equal lateral tensile strains). Relation of the sign of ε_{xy} to the deformation direction of a soil element is shown in Figure 4.3-16. The paths in Figure 4.3-15 are presented in a unique format. A solid line represents the path of the point number listed next to that line. The various symbols indicate the excavation depth at a particular location on the line. For example, the strain path of point 15 in Figure 4.3-15e starts at a point marked by the dotted circle (initially

strains are zero). As the excavation proceeds, point 15 undergoes vertical and shear strains. The solid circle marker indicates the strain level at excavation depth of 5m. Similarly, other symbols indicate excavation depths at other points along the path. The last excavation depth shown in the figure is H=22.5m, which represents the last depth prior to failure in MIT-E3. At points 1 and 5, the strain paths terminate before H=22.5m is reached. Since they are inside the excavation and are in the portion of the soil removed at depths less than 22.5m (Point 1 is located at y=11.25m, point 5 is at y=21.25m (Figure 4.3-14). This format of presentation of strain path data is followed in the presentation of other stress and strain paths throughout this chapter.

Strain paths (Figure 4.3-15) of equivalent points (and to a lesser degree of points 8) for the three models are qualitatively similar. This suggests that the fundamental mechanisms controlling deformations in an excavation are unique and largely independent of the soil model.

Points near the center line (1,5,9, and 13) are primarily sheared in PSP (Plane Strain Passive) mode ($\varepsilon_{yy}<0$ is dominant). The elastic and MCC model paths are very similar because unloading in MCC occurs inside the yield surface. As H increases, there is a reversal in strain direction for elements above the level of maximum wall deflection (Point 5 in Elastic and MCC predictions). The reversal effect is possibly similar to a membrane effect, where the membrane (in the current situation) is restrained against movement at the wall (full friction). The reversal is less pronounced when there is soil plasticity (MCC) and is not seen for MIT-E3.

All points on the retained soil side (behind the wall) exhibit complex strain histories in which rotation of principal strain direction is continuous throughout the excavation process. For these points ε_{xy} is as important as ε_{yy}.

Initially all points in the retained soil undergo positive changes in $\Delta\varepsilon_{yy}$ and $\Delta\varepsilon_{xy}$. The $\Delta\varepsilon_{yy}$ strain is positive (axial compression) as a result of soil removal and lateral wall deflection towards the excavation. $\Delta\varepsilon_{xy}$ is positive because the soil heaves due to soil removal causing an initial upward movement in the wall and soil settlement behind the wall (Figure 4.3-16). As the excavation depth increases there is a reversal in the direction of ε_{xy} and then after a small delay is followed by a reversal in ε_{yy}. The exact point of reversal is dependent on the location of the soil element with respect to the current excavation level. Reversal at a point n, in general, occurs when $H \approx y(n)$, where y(n) is the depth of point n.

The reversal in the sign of ε_{xy} is determined by the relative location of the point to the location of the point of maximum settlement. This is most apparent in MIT-E3 points 7,8 where the settlement trough is narrower and failure is approached (see also Figure

4.3-16).

Strain component ε_{yy} at points 3 and 3A changes from positive to negative, indicating that the load on these points has changed from a compression unloading to extension loading. Other points show a reduction in ε_{yy} after initial compression. The observation is most pronounced for MIT-E3, but is also clearly observed in MCC and Elastic models. The lateral reloading of these soil elements (after initial lateral unloading) is due to additional load shed by soil further away from the excavation as that soil moves laterally towards the excavation and settles. This mechanism will become clearer upon examining stress paths and stress and strain contours.

4.3.3.2. Effective Stress Paths

Figure 4.3-17 from Lambe (1970) presents the current state of knowledge reported in the literature (Christian, 1989) with regard to stress paths of soil elements in an excavation. The basic assumption is that points in the retained soil undergo an active mode of shearing and points inside the excavation undergo a passive mode of shearing. This plot ignores the shear stress components in the soil. The stress paths observed in the current analyses are far more complex.

Figures 4.3-18 (elastic), 19 (MCC) and 20 (MIT-E3) present effective stress path (q_{vh}/σ'_{v0}-p'_{vh}/σ'_{v0}, q_{vh}/σ'_{v0}-τ/σ'_{v0}) for soil elements in the same format presented in Figures 4.3-3a&b. All points start from a K_0-normally consolidated stress state (K_0=0.53, p'_{vh}/σ'_{v0}=0.77, q_{vh}/σ'_{v0}=0.23, τ/σ'_{v0}=0.0).

Points along excavation centerline.

Points 1,5,9 and 13 undergo shearing almost identical to the PSP mode and therefore should exhibit behavior very similar to the elemental behavior shown in Figures 4.3-3a and 4.3-4a (For PSP $\delta_{inc}=90^0$). Passive unloading with MIT-E3 (Figure 4.3-20a) causes plastic behavior (and was shown to give good agreement with experimental data), while MCC (Figure 4.3-18a) exhibits an elastic response until the stress path reaches the yield surface. In the current analysis, no points in MCC inside the excavation reach the yield surface as the strain level is small (ε_1-ε_3<5%).

Points outside the excavation.

Examine MCC stress paths first. Figure 4.3-19b shows the effect of principal stress rotation on the retained soil during excavation. Soil elements are initially sheared in a compression mode ($\Delta\varepsilon_{yy}$ <0) but then exhibit a reversal in the stress path (at H≈y(n), extension mode, $\Delta\varepsilon_{yy}$ >0), for which the model predicts an elastic response (see for example points 3 and 3A in Figure 4.3-19a). At H=22.5m, the shear stresses on these soil elements are far less than their undrained shear strength (Figure 4.3-19b). Much

larger shear strains than those observed in Figure 4.3-15e are required to mobilize the maximum shear strength in the MCC model (Figure 4.3-4). The elastic model exhibits qualitatively similar behavior to the MCC model (Figure 4.3-18). The mean stress in Figure 4.3-18a is constant due to isotropy in the elastic response for undrained shearing. Stress rotation shown in Figure 4.3-18b is similar to that observed in Figure 4.3-19b.

The behavior in the MIT-E3 analysis (Figure 4.3-20) is more complex than MCC (Figure 4.3-19) because of the following reasons: 1) the plasticity and nonlinearity for stress states on and inside the bounding surface; 2) the mobilization of peak strength (especially in compression) occurs at much smaller strain levels than in MCC; and 3) anisotropy. The undrained shear strength envelope shown in Figure 4.3-20b is calculated assuming proportional strain paths, which is not the case for points outside the excavation but provides a reference condition for interpreting model predictions in more complex loading modes. The envelope provides a good upper bound for the stress paths of elements in the retained soil. Most points in the retained soil reach the peak strength envelope, and undergo some strain softening prior to undergoing a major change in the load direction. Points 3 and 3A initially undergo shearing along stress paths which match elemental PSA paths (Figure 4.3-20a), but then reverse to stress paths that approach the elemental PSP stress paths. Points 3 and 3A, therefore, undergo a very large rotation in principal stresses. Even though points 6 and 7 undergo very different initial stress paths, upon loading reversal, they follow stress paths that approach stress paths of points 3 and 3A.

Loading reversal can be further seen by examining the total stress paths at points 3 and 3A (Figure 4.3-20c). Points 3 and 3A initially follow a TSP that is similar to that of a plane strain compression unloading. Upon reversal, they follow a stress path that is similar to that of a plane strain extension loading. Figure 4.3-20d shows that initially points 3 and 3A undergo a net decrease in the total horizontal stress followed by a net increase in the horizontal stress indicating a shift of behavior from an active 'un'loading to a passive loading mode.

The stress paths of figures 4.3-18,19, and 20 show the importance of incorporating anisotropic clay behavior in the soil to model accurately the effect of stress rotation on soil response due to excavation. The figures illustrate the implications of critical state models in which undrained strength is only achieved at large shear strains. The patterns of stress paths are far more complex than previously explained in the literature[1].

---

[1]More details are presented in the following sections

Other points for which the stress paths are plotted (6,7,8,11,15) undergo the same basic loading mechanisms as points 3 and 3A, however, with varying degrees of principal stress rotation (i.e., development of shear stresses on vertical planes) and reversal of loading paths(These are controlled by the relative location of the soil point to the support wall and excavation front).

4.3.3.3. Pore Pressure Paths

Pore pressures are presented in the form of pore pressures in excess of hydrostatic pore pressures and are made up of two components:

$$\frac{\Delta u}{\sigma'_{v0}} = \frac{u-u_0}{\sigma'_{v0}} = \frac{\Delta u_s}{\sigma'_{v0}} + \frac{\Delta \sigma}{\sigma'_{v0}}$$

$\Delta u_s/\sigma'_{v0}$: Shear induced pore pressure (=0 under elastic conditions)

$\Delta \sigma/\sigma'_{v0}$: Pore pressure change due to change in the total mean confining stress.

Figure 4.3-21 presents plots of pore pressure change for points inside the excavation. For 1-D unloading $\Delta u=\Delta\sigma_v=\gamma_t z$, therefore, linear development of excess pore water pressure would be predicted. In the elastic case ($\Delta u_s=0$), the Δu paths are curved and reflect the $\Delta\sigma_v/\Delta\sigma_h$ ratio change as the excavation approaches the stress point. This is a two dimensional effect that is not explicitly reported in the literature.

The elastic and MCC responses are very similar. This indicates that the main component of pore pressure change in MCC is due to the change in the mean total stress. Note that the reversal in loading reported in Figure 4.3-15 for point 5 inside the excavation does not result in a reversal in the direction of pore pressure change.

MIT-E3 shows a less negative change in pore pressures mainly due to the fact that Δu_s is positive for undrained shear in PSP type shearing, which offsets $\Delta\sigma$ changes.

In the retained soil (Figure 4.3-22) negative $\Delta u/\sigma'_{v0}$ is initially generated due to unloading. A reversal in the Δu direction is observed in the three models, which coincides with reversal in q_{vh}/σ'_{v0} observed in figures 4.3-18, 19 and 20. The pore pressure becomes less negative/more positive as the plasticity in the soil model increases (Elastic→MCC→MIT-E3). The increase in $\Delta u/\sigma'_{v0}$ upon reversal is more pronounced in MIT-E3 than MCC due to the stiffer unload response in MIT-E3. Points 3, 3A, 8 develop large positive excess pore pressures with increasing excavation depth. Smaller positive pore pressures are obtained for MCC and elastic models. The positive pore pressures are, in large part, due to pore pressures induced by extension reloading of these elements after load reversal.

4.3.3.4. Stress and Strain Contours

Contour plots of stress and strain at various excavation depths are presented to

gain a global understanding of the load history of the soil during excavation. Comparisons of contours are made between soft elastic and MCC models at H=10, 20, and 30m (no failure in either model), and between MCC and MIT-E3 models at H=10, 20, and 22.5m (failure depth of MIT-E3 analysis).

1) Maximum Shear Strain and Stress Contours

Maximum shear strain is defined in Section 4.3.1 [$\gamma=0.5(\varepsilon_1-\varepsilon_3)$]. Maximum shear strain contours provide a measure of the extent of shearing of the soil independent of the mode of shearing (i.e., orientation of principal strain direction). In the elastic model, Figure 4.3-23a,b,c, soil inside the excavation undergoes the largest amount of shearing caused by the stress release. In the retained soil, points closest to the wall undergo the largest shear strains. The shear strains are caused by the relative movement of the soil and the wall. As the excavation depth increases (H=10m to H=20m to H=30m), there is an increase in the shear strains, mostly near the wall. Throughout the excavation, shear strains do not exceed a maximum of about 1.6% (small strain range).

In MCC, Figure 4.3-23d,e,f, the development and the magnitude of shear strains are similar to those of the elastic model. In some locations near the wall, MCC shear strains are slightly larger than the corresponding elastic strains (see, for example, Figure 4.3-23c,f). The increase is attributable to plasticity in MCC.

MIT-E3 exhibits markedly different patterns of shear strain development (Figure 4.3-24):

1) The zone influenced by shear strains is smaller in MIT-E3 than in MCC. For example at H=10m, γ_{max}=0.1% contour extends to a depth of 90m and a distance of 70m away from the center line in MCC (Figure 4.3-24a). In MIT-E3, Figure 4.3-24d, the same contour level does not extend beyond a depth of 50m and a distance of 40m away from the center line. The same observation can be made at H=20m, 22.5m. The smaller extent of maximum shear strain in MIT-E3 is related to the small strain nonlinearity formulation introduced in the constitutive model.
2) Shear strains localize along a potential shear/slip surface near failure in the MIT-E3 model. At H=22.5m, Figure 4.3-24f, γ_{max}=0.4% contour line in the retained soil follows a surface extending from the bottom of the wall in the shape of a trough almost reaching the ground surface. This effect is not observed in MCC (Figure 4.3-24c).

In MIT-E3 and MCC models, the maximum magnitude of shear strains does not exceed 1.6%. The constitutive model of the soil should, therefore, accurately represent soil behavior in this strain range if reliable predictions are to be made. The shear strain is not sufficient to mobilize the maximum undrained shear strength in MCC (Figure 4.3-

4c), but will mobilize the peak strengths in MIT-E3, for $\delta_{inc} \leq 45^0$ (Figure 4.3-3c).

Figures 4.3-25 and 4.3-26 present normalized maximum shear stress, τ_{max}/σ'_{v0}, contours. Stress contours are normalized by σ'_{v0} for two reasons: 1) the soil exhibits normalized behavior; and 2) in situations where stresses initially are proportional to the unit weight of soil, stresses increase significantly in magnitude with increasing depth. Plotting contours of the absolute magnitude of the stresses will result in contour plots where contour levels increase with depth. This type of contours obscures the effect of soil disturbance (in this case soil excavation) on the stress state in the excavation.

Contours in figures 4.3-25 and 4.3-26 highlight the difference in magnitude of the mobilized maximum shear stress for the different models. MCC and elastic models mobilize similar levels of shear stresses which are every where less than the undrained strength in the model (0.36). In MIT-E3, Figure 4.3-26, larger shear stresses are mobilized. However, it is difficult to determine whether mobilized shear stresses have reached the undrained strength due to anisotropic properties discussed in Section 4.3.1.

The contour plots of the type given in Figure 4.3-25,26 are commonly used in the literature (Potts and Fourie, 1984) to determine yielded regions in the boundary value problem. For an isotropic model, such as MCC, where the undrained strength is constant and independent of principal stress orientation, these plots are very useful. For a model with an anisotropic strength envelope, the contour plots are not very useful as it is very difficult to estimate whether a particular element has reached peak strength, or, how much additional shear stress will cause failure.

Even with an isotropic model, the contour plots have shortcomings. In the excavation problem, where points undergo load reversal, knowing the percentage of shear strength mobilized at a point at a given excavation depth is not an indication of how soon this point will yield. The point may undergo, at a later excavation stage, load reversal resulting in reduction of mobilized shear stresses. Therefore, the maximum shear stress contours are most useful in situations where the loading regime is monotonic.

2) Horizontal Strain Contours

Positive horizontal strains indicate lateral compressive straining in the soil. Figures 4.3-27,28 present horizontal strain contours. In the elastic model, Figure 4.3-27a, soil inside the excavation undergoes positive (compressive) horizontal strains caused by the inward movement of the wall and vertical tensile straining due to soil removal. In the retained soil, below excavation level, tensile horizontal strains are caused by the wall lateral displacement. In a trough bounded by the $\varepsilon_{yy}=0$ contour, extending from the excavation level behind the wall to the ground surface, positive horizontal strains are predicted. As the excavation level increases, the trough of positive strains extends further

downwards (Figure 4.3-27b,c). Zones in the retained soil that initially underwent lateral tensile strains, now undergo lateral positive compressive strains. The contour plots show the strain reversal reported in Figure 4.3-16 on a global scale. The MCC response, Figure 4.3-27d,e,f, is similar to the elastic response. MIT-E3 response, Figure 4.3-28, is quite different from the MCC and elastic responses. The differences in the horizontal strain contours are similar to the differences observed for the maximum shear strain contours: 1) MIT-E3 shows a smaller influence zone, and 2) localization of strains is observed in MIT-E3 near failure.

3) Pore Pressure Contours

Pore pressure contours are presented in the form of $\frac{u - u_0}{\sigma'_{v0}}$ contours. It was explained previously that this quantity includes changes in pore pressures due to shear induced pore pressures and total mean stress changes. In the elastic solution, shear induced pore pressures are zero, and all the pore pressure change is due to changes in the total mean stress. At H=10m, Figure 4.3-29a, negative changes in pore pressures are predicted indicating a general reduction in the total mean stress throughout the excavation. With greater excavation depth, larger negative changes in pore pressure are generated There is a zone (see Figure 4.3-23c for example) near the exterior surface above the $\frac{u - u_0}{\sigma'_{v0}} = 0$ contour where pore pressure change is positive, indicating an increase in the confining stress in this region.

MCC contours, Figure 4.3-29d,e,f, are similar to the elastic contours. In MCC the zone of positive pore pressure change is larger (see Figure 4.3-29c versus 4.3-29f) caused primarily by the positive shear induced pore pressures.

In MIT-E3, Figure 4.3-30, pore pressure changes inside the excavation are less negative than those observed for MCC. Positive shear induced pore pressures occur in this region that partially offset the negative pore pressures caused by soil removal. Positive pore pressures in the retained soil are larger in MIT-E3 and exceed a value of 0.2. The large positive pore pressure changes are due to the larger shear induced pore pressure in MIT-E3 as well as increase in total confining stress. The positive pore pressures imply that there is an increase in piezometric water elevation in this region. Finno and Nerby (1989) report field observations of increase in piezometric water elevation in parts of the retained soil in an excavation.

4) Horizontal Stress Contours

Horizontal stress contours are presented in the form of $\frac{\sigma_h - u_0}{\sigma'_{v0}}$ contours. The

$\frac{\sigma_h - u_0}{\sigma'_{v0}}$ quantity is equivalent to the total normalized horizontal stress. The $\frac{\sigma_h - u_0}{\sigma'_{v0}}$ quantity is made up of the sum of the horizontal effective stress and the pore pressure change. Knowledge of the magnitude of the total horizontal stress is very useful. In practice, horizontal stresses acting on the wall are used to design the wall and bracing system. Active pressures are assumed to act on the retained soil side of the wall. During construction, pressure cells and strain gauges on braces are used to monitor the load acting on the wall.

Prior to any excavation $\frac{\sigma_h - u_0}{\sigma'_{v0}} = K_0 = 0.53$. For the elastic model inside the excavation (Figure 4.3-31), horizontal stresses decrease with increasing excavation depth. In the retained soil below the excavation level, horizontal stresses also decrease. In the retained soil above the excavation level, part of the soil undergoes a decrease in horizontal stress, and other parts of the soil undergo a slight increase. At any excavation level, stresses on the back of the wall do not exceed the initial stresses. MCC results show trends similar to the elastic solution (Figure 4.3-31).

MIT-E3 shows a greater decrease in the horizontal stresses in the retained soil below excavation level (Figure 4.3-32a v.s. d). The stresses in this part of the soil continuously decrease with increasing excavation depth. In the retained soil above the excavation level, there is a net increase in horizontal stresses in a wedge shaped area behind the wall (Figure 4.3-32c). The increase is continuous with increasing excavation depth. The wedge, therefore, develops passive stresses and is a passive wedge. The existence of this passive wedge is not described in the recent literature (active conditions are assumed to exist in the retained soil). The increase in stresses behind the wall has been reported in field observations of excavations (Aas 1985) and is included in empirical design charts (Peck 1969). Lambe and Whitman (1969, p187) describe a similar observation and attribute the stress increase to a development of a passive stress state in the soil.

The observations made from the contour plots can be seen more clearly in plots of horizontal soil stresses against the wall. Horizontal stresses acting on the wall on the retained soil side and on the excavated side are shown in Figures 4.3-33 and 4.3-34 respectively. On the retained soil side, Figure 4.3-33a, above the excavation level, the elastic and MCC models predict similar horizontal stresses. Below the excavation level, MCC predicts slightly higher stresses than the elastic stresses. Above the excavation level, MIT-E3 predicts larger stresses than MCC and elastic stresses. The stresses are larger than the initial stresses acting on the wall. Below the excavation level, MIT-E3

predicts smaller stresses than MCC and elastic stresses. Similar observations can be made for an excavation H=22.5m (Figure 4.3-33b). Inside the excavation[1], Figure 4.3-34, MIT-E3 predicts lower horizontal stresses than the elastic stresses, while MCC predicts larger stresses than predicted by the elastic solution. Further discussion of lateral stresses behind the wall will be given in later sections (Sections 4.5,4.6).

5) Vertical Stress Contours

Contours of the total vertical stress are presented in the form of $\frac{\sigma_v - u_0}{\sigma'_{v0}}$ contours. The contours are presented to evaluate the change in total vertical stresses due to shear stresses acting on vertical planes. Existing interpretations of stress paths of retained soil behind an excavation ignore changes in the vertical stresses. The stress paths are based on changes measured in lateral pressure cells in the wall.

Initially $\frac{\sigma_v - u_0}{\sigma'_{v0}} = 1.0$; at later excavation stages it is equivalent to the total vertical stress. The reduction in vertical stresses in the three models is similar (Figure 4.3-35,36). Inside the excavation, reduction in the vertical stresses are mainly controlled by the stress relief due to soil removal. In the retained soil, above the level of the lowest support level, vertical stresses are in the range of 0.8-1.0. Below the excavation level, large reductions in the vertical stresses are predicted.

The analyses show that it is difficult to estimate vertical stresses behind the wall. The contours show a reduction in the vertical stresses. This is a result of the τ_{xy} shear stress component acting on the wall due to downward movement of the soil. In field situations, it is not accurate to assume that vertical stresses remain constant (particularly near the wall).

4.3.4. Summary

This section summarizes the effects of the constitutive soil model on predictions of excavation behavior. The following observations are made:

1. The MIT-E3 model predicts a significantly different and more realistic surface settlement behavior than the MCC and elastic models (Figure 4.3-5). The difference is a result of introducing small strain non-linearity in the formulation of the MIT-E3 model.

---

[1]The negative $\frac{\sigma_h - u_0}{\sigma'_{v0}}$ values do not mean that tensile horizontal stresses develop. To obtain the total horizontal stress, the initial hydrostatic pore pressure should be added to this quantity.

2. The shear strain levels induced in the soil due to undrained excavation are generally small and do not exceed 2% (Figure 4.3-24). A constitutive model for predicting excavation behavior should be capable of resolving accurately the stress-strain response at these strain levels. The MIT-E3 model is superior to the MCC model in this respect (Figure 4.3-3e,4e).
3. In an excavation, soil elements undergo significant principal stress and strain rotations (Figure 4.3-20a,b). A soil model that properly accounts for the soil response due to such rotation is required. MIT-E3 predicts exceptionally well soil behavior under these modes of shearing at the element level. MIT-E3 predictions of excavation deformations and failure are quite different from MCC and elastic model predictions. In the following sections, MIT-E3 is the only soil model used to represent the clay layer. It will be shown in Section 4.8 that MIT-E3 produces trends that more closely match field observations of excavation behavior.
4. The observed stress and strain reversal (Figure 4.3-20c) implies that loading of soil elements in a braced excavation is not monotonic. The correct modelling of soil response to loading reversal is, therefore, essential in predictions of excavation behavior. MIT-E3 was originally designed, in part, to predict soil response due to cyclic loading of tension piles in offshore oil platforms. The model can accurately predict soil response to cyclic loading involving many cycles of load reversal (Whittle 1987). This additional aspect of the MIT-E3 model makes it a more suitable model for the prediction of excavation behavior than a model such as MCC.
5. Despite the differences between predictions of the three models, the basic mechanisms controlling stress and strain history in the soil are almost model independent. In all three models, stress and strain reversals (Figure 4.3-15) and stress and strain rotations are observed. It will be shown in later sections (Section 4.6, 4.9) that these basic mechanisms are observed in MIT-E3 for OCR>1, where the soil response is less plastic and approaches an elastic response in some strain ranges.
6. Observations of stress and strain history show that the soil in a braced excavation behaves in a far more complex manner than commonly reported in the literature (simple active and passive shearing). Total vertical stresses in the retained soil experience a significant reduction due to the development of shear stresses, τ_{xy}, along the back of the wall (Figure 4.3-36). A passive stress state develops in the retained soil above the excavation manifested, in MIT-E3, by a significant increase in the total horizontal stress along the back of the wall (Figure 4.3-34a,b)

which exceeds the initial total horizontal stress.

.4. Effect of Wall Length

In deep soft clay deposits, where the bedrock is far beneath the surface, it is neconomical to anchor the diaphragm wall in the bedrock. Under these conditions, the 'all length is an important design parameter. There is little existing guidance on the ffects of wall embedment either on deformation or failure of excavations in soft clays.

The previous section, shows that deformations in a braced excavation are far ıore complex than assumed in conventional design practice. This section examines the ffect of wall length (embedment) on braced excavation behavior (deformations and ıilure). The following assumptions and excavation parameters[1] are used:

1. The clay layer is normally consolidated (OCR=1 which represents the most critical case regarding deformations and failure), with properties described by the MIT-E3 model.
2. The unbraced excavation depth is h_u=2.5m.
3. The support spacing is either h=2.5m or h=10m.
4. Wall lengths are L=12.5m (short wall), L=20m, L=40m, or L=60m (very deep wall).

4.4.1. Wall Deformations and Ground Movements

1. Results for h=2.5m:

Figures 4.4-1 and 2 show predictions of wall deflection and surface settlement for ıe four wall lengths considered.

For the shortest wall (L=12.5m, Figure 4.4-1a,c) the last excavation depth prior) failure is H=10m. The actual failure depth is difficult to estimate precisely as the nalysis uses finite excavation steps of 2.5m. At H=2.5m the wall deforms in a cantilever ıode. At H=5m, after brace installation, the wall bulges. The maximum movement evelops at the toe of the wall. Failure develops in the system by the wall toe 'kickout' nd soil moving underneath the wall from the retained soil side to the excavated soil side. 'he shape of the settlement trough, Figure 4.4-1a, is similar to that observed in Section .3.

For L=20m analysis, Figures 4.4-1b and 1d, the last excavated depth prior to ıilure is H=15m. The development of deformations and failure is similar to that

---

[1] The relevant analyses in this section are st1_12_02, st1_20_02, st1_40_02, st1_60_02, st1_12_10, 1_20_10, st1_40_10, and st1_60_10.

bserved for L=12.5m analysis. At H≤5m, wall deformations and surface settlements are ery similar to those of the L=12.5m case. The failure mechanism is also similar to that f L=12.5m. The wall toe 'kicks out' and the soil moves around and underneath the wall.

The last excavation depth prior to failure for L=40m analysis is H=22.5m. Prior › collapse, the wall shape is characterized by wall bulging (Figure 4.4-2c). No toe :ickout' is observed. A similar observation can be made for L=60m wall, Figures 4.4-b and 2d, where the last excavation depth prior to failure is H=30m.

Settlement troughs for all the wall lengths, Figures 4.4-1a,1b,2a,and 2b, have :milar shapes regardless of how close the excavation is to failure.

Figure 4.4-3 shows plots of maximum movements and moments versus xcavation depth for all wall lengths. The maximum deflections for L=40m and 60m 'alls are practically identical (Figure 4.4-3a). At H=22.5m, L=40m maximum deflection ; slightly larger than that for L=60m wall. Maximum deflections for L=20m wall are ıitially similar to those of L=40m wall, but become larger beyond H=10m. For .=12.5m maximum deflections are similar to those of L=20m.

Trends in maximum settlements for the four wall lengths, Figure 4.4-3b, are similar to those observed for maximum wall deflections. However, the difference between L=20m and L=40m curves is much smaller. Maximum heave for all wall lengths is practically identical (Figure 4.4-3d).

Maximum moments, Figure 4.4-3c, for L=40m and L=60m walls are similar. For ıe L=20m wall, maximum moments are initially similar to L=40m moments, but become ırger beyond H=10m. The increase in moments is caused by the change in the mode ıape of the wall and the toe 'kickout'. Similar development of moments can be noted for .=12.5m wall.

Figure 4.4-3 shows that wall length has a limited impact on deformations in the xcavation problem prior to instability in the system. However, the wall length does have significant impact on failure in the excavation as discussed in Section 4.4.2.

Section 4.3 describes the location of maximum wall deflection at a constant depth .75m below the excavated surface (Figure 4.3-7a). This distance appears to be ıdependent of the excavation depth. For L=60m and L=40m analyses, Figure 4.4-4a, eyond H=5m, the maximum deflection is located at about 8.75m below excavation epth. Therefore, if L<H+8.75, the maximum wall deflection will occur at the toe of the 'all. For L=12.5m and L=20m wall toe kickout can be expected at H≈3.75m (12.5-.75), and H≈11.25m (20-8.75) respectively. Figure 4.4-4b shows that in the FE nalysis toe kickout occurs at a slightly smaller excavation depth.

2. Results for h=10m

Another series of numerical experiments where h=10m is performed to confirm the trends observed at h=2.5m[1]. The last excavation depth prior to failure for L=12.5m wall is 5m, for L=20m wall is 10m, for L=40m wall is 15m, and for L=60m wall is 20m. Failure for L=12.5m and 20m walls, Figure 4.4-5, is characterized by toe kickout, while L=40m and 60m walls, Figure 4.4-6, do not show such behavior.

Figure 4.4-7 presents plots of maximum deflections and moments versus excavation depth. The trends observed are similar to those observed for h=2.5m analysis (Figure 4.4-3), but the h=10m curve is not as smooth. In Figure 4.4-7, the bracing is installed at 10m intervals. Therefore, data presented at H=5 and 15m are for intermediate depths between supports where h_e=5m≠h. In contrast, in Figure 4.4-3, all the data points shown are at depths where supports are (or will be) installed (h_e=h). The bending of the wall between supports for h=10m analyses results in the non-smoothness of the curves of Figure 4.4-7[2]. This point will be better understood once the effect of h on deformations is explained in Section 4.5.

For the balance of this section, the discussion will focus on h=2.5m analyses. The main issues that will be discussed are 1) how to identify failure in the numerical analyses and, 2) how to predict the failure depth apriori.

4.4.2. Failure Conditions from Numerical Experiments

Failure in the analysis occurs when, due to an excavation increment (the analysis proceeds in steps of 2.5m), numerical convergence is not achieved (Section 2.4). The lack of such convergence is due to large incremental deformations in the soil[3]. The diaphragm wall is modelled as a linear elastic material. Failure due to wall yielding is not incorporated in the analysis, but can be modelled in ABAQUS using appropriate constitutive relations for the reinforced concrete wall..

Figure 4.4-8 presents plots of strains and deformations, in the F.E mesh of the excavation for wall length L=12.5m, at the two excavation depths prior to failure. Plots of contours of γ_{max}, Figures 4.4-8a and 8b, show an increase in shear straining in the soil around the excavation prior to failure. The soil that is most strained is located just inside the excavation and beneath the wall.

Figures 4.4-8c and d are plots of incremental strains at H=7.5m and H=10m. For H=7.5m, the incremental strains are calculated by subtracting the strains at H=7.5m from strains at H=5m. Similarly, at H=10m, the incremental strains are computed by

---

[1]A full dicussion of the impact of h on excavation behavior is given in Section 4.5.
[2]In later sections, data from intermediate depths will not be included.
[3]Appendix B shows that accurate collapse calculations are possible using MIT-E3 in ABAQUS.

subtracting the strains at H=10m from strains at H=7.5m. The incremental strain contours show large straining of the soil located just inside the excavation and below the wall.

Figures 4.4-8e and 8f show arrows of the incremental deformations at H=7.5m (from H=5m to 7.5m) and H=10m (from H=7.5m to 10m). The orientation of an arrow represents the direction of the incremental displacement. The length of the arrow reflects the relative magnitude of the incremental displacement, at a particular point, compared to the magnitude of maximum displacement at the excavation depth considered. The figures show the soil to be moving underneath the wall into the excavation. Thus, the excavation is approaching a base heave failure condition[1].

Figure 4.4-9 presents a similar set of plots of strain and deformations for L=20m wall (incremental quantities are presented at H=12.5m, from H=10m to 12.5m, and at H=15, from H=12.5m to 15m). Observations similar to L=12.5m case can be made. The soil that is most strained is in a region just inside the excavation and beneath the wall. The soil appears to be failing by a base heave mechanism.

The shear strains for L=40m wall localize along a potential slip surface as failure is approached (Figures 4.4-10a and b, see also Section 4.3). The localization is observed more clearly in the incremental shear strain contours (Figures 4.4-10c and d, incremental quantities are presented at H=20m, from H=17.5m to 20m, and at H=22.5, from H=20m to 22.5m). The arrows of nodal displacement, Figure 4.4-10f, show that the maximum lateral incremental displacement is occurring in the wall and not in the soil underneath. The failure mechanism for L=40m wall is different from that for L=12.5m and 20m walls. As Figure 4.4-10d shows, failure in the excavation is occurring as a result of the development of a slip surface in the retained soil extending from the bottom of the wall to the ground surface.

Development of shear strains and displacements in the L=60m wall, Figure 4.4-11, is similar to that for L=40m wall. The developing shear surface, Figures 4.4-11a and 11b, does not extend to the bottom of the wall, but intersects the wall at a point about 5m above the wall toe. The wall is modelled as a linear elastic material and, therefore, the failure surface cannot propagate through the wall. Figures 4.4-11e and 11f show that the maximum incremental displacement in the wall, prior to failure, occurs above the toe of the wall.

Two failure modes can be identified from the four analyses. For the short walls (L=12.5m, and L=20m), failure in the excavation occurs due to loss of bearing capacity

---

[1]The soil is moving around the wall into the excavation.

in the soil underneath the wall. The failure mode resembles a base heave failure. For the long walls (L=40m and L=60m) failure develops as a result of the formation of a shear/failure surface extending from the ground surface to the lower part of the wall. Failure in the wall becomes an important variable under these conditions[1].

A common observation for all wall lengths is the behavior of the top of wall movement prior to failure (Figure 4.4-12). Initially, the wall moves upwards due to unloading in the system. As the excavation depth increases, plastic deformations develop in the soil. The bottom part of the wall loses bearing support in the soil. The wall moves downwards until failure. However, these observations have limited practical implications because: a) the magnitude of movements involved is very small (This movement is not commonly monitored in field situations); b) the movement does not correlate clearly with the failure depth; and c) the movement is dependent on assumptions of wall-soil interaction (A no slip interface between the soil and the wall is assumed in the analyses, Section 4.2).

The structural failure in the wall, though not considered in the analysis, can be estimated from the magnitude of the maximum moments (Figure 4.4-3c). In conventional practice, a 0.9m thick medium to heavily reinforced concrete wall (Mulvey, 1991), has an ultimate bending moment that ranges between 1-2 MN-m/m. In L=40m wall, Figure 4.4-3c, M_{max} is greater than 1 MN-m/m for H≥10m. It is possible that failure in the wall occurs beyond this depth. Based on Figure 4.4-3c, structural failure in the wall for all four walls potentially occurs prior to the development of a mechanism in the soil (base heave or slip surface). Hence, computed wall moments are critical in the design of an excavation.

4.4.3. Methods for Estimating Failure of Braced Diaphragm Walls

In current practice, failure due to base heave is the mode of failure assumed in braced excavations in soft clays. Terzaghi (1943), Figure 4.4-13a, introduces the notion of factor of safety against basal heave (FSBH). The excavation is treated as a reverse bearing capacity problem. Several variations of FSBH formula are introduced to account for excavation width effect (Bjerrum and Eide, 1956), soil anisotropy (Ladd, 1991), or increasing strength with depth (adaptation of the formula developed by Davis and Booker, 1973, for the bearing capacity problem). In all these calculations the wall

[1]The width of the excavation is expected to affect failure conditions, particularly for the longer walls. This variable is not considered in this study.

embedment does not impact the factor of safety against basal heave. Terzaghi (1943) suggests that "if the excavation of a cut is made between sheet piles which extend to a depth D_1 below the bottom of the cut, the method for estimating the factor of safety with respect to a heave of the bottom must be modified accordingly. The simplest procedure is to compute the vertical pressure on a horizontal section through the lower edge of the sheet piles. The heave of the bottom is resisted not only by the weight of the soil located between the buried parts of the sheet piles but also by the adhesion between this body of earth and the adjoining sheet piles."

The factor of safety against basal heave is, at best, an index measure of the stability of an excavation. Bjerrum and Eide (1956) present a case where failure occurs when FS=1.16 and another where no failure occurs when FS=1.0.

Figure 4.4-13 lists the different computations used in calculating the factor of safety against basal heave for the excavation considered in this study. Plots of factor of safety against basal heave versus excavation depth are given in Figure 4.4-14. The following observation can be made:

1) The classical Terzaghi method using the undrained shear strength in DSS mode predicts failure at H≈17.5m.
2) Introducing anisotropy in the calculation (Ladd, 1991) reduces the factor of safety substantially. Failure is predicted at H≈12m.
3) Bjerrum and Eide calculations[1], if based on the shear strength in DSS, give an FS slightly higher than that given by the classical Terzaghi method. Failure is predicted at H≈22.5m.
4) Davis and Booker's Method (using S_{uDSS}) gives a lower FS than Terzaghi's and Bjerrum and Eide's Methods. The method predicts failure at H≈9m.
5) When the recommendation by Terzaghi (quoted earlier) is followed to account for the effect of wall embedment underneath the excavation in conjunction with the Davis and Booker method (using S_{uDSS}), the estimate of the failure depth greatly improves. For L=12.5m, the method predicts FS=1 at H≈11.5m. For L=20m, FS=1 at H=15m. For L=40m, FS=1 at H≈28m. The symbols on Figure 4.4-14 show the last excavation depth prior to failure in the F.E. analysis for all four wall lengths considered. For the shorter wall lengths (L=12.5m and L=20m) the method gives excellent predictions of failure. For the longer walls, where the failure mechanism is not only a base heave mechanism, but includes a shear surface, the method over predicts failure depth.

---

[1]They commonly use strengths obtained from field vane tests.

These calculations illustrate the difficulty in defining a meaningful FS for braced excavations if one includes the effect of wall embedment and the nonhomogeneous and anisotropic properties of the soil in the numerical model.

Note that all these calculations are compared with h=2.5m analyses where the wall is well braced and the base heave failure mechanism may be a good approximation of failure condition (mainly for short to medium, L=12.5m and 20m, walls). The base heave calculation cannot account for the effect of the support spacing on the failure depth in the excavation. The numerical analysis of an h=10m excavation gives a lower failure depth than an equivalent analysis with h=2.5m. The failure mechanism is very complex and is related to the shear strength mobilized in the soil. However, a base heave calculation (Method 5, Figure 4.4-13) that accounts for wall embedment appears to give very reasonable estimates of failure depths for short to medium length walls.

4.4.4. Development of Stresses and Strains

Stress and strain paths of some of the points shown in Figure 4.3-14 are examined to assess the impact of wall length on stress and strain changes in the soil.

Figure 4.4-15 shows the strain paths of points 3, 6, 7 and 13 for the four wall lengths. Strain paths of L=40m and L=60m walls are very similar at all points. Small differences are observed at H=22.5m, the last excavation stage in the L=40m analysis. Strain paths of L=20m analysis match strain paths of L=40m up to H=5m, but some deviations occur for H=10m, and substantial differences at H=15m reflect the development of failure for L=20m. At point 3, the significant reversal in the shear strain observed in the L=40m analysis is not observed in the L=20m analysis. Similarly, the reversal in the vertical strain for point 7 observed for L=40m is not observed for L=20m. Strain paths for point 13 are similar for L=40m and 20m walls. The strain paths for L=12.5m analysis are similar to those observed for the L=20m analysis.

The similarities and differences identified in the strain paths are reflected in the effective stress path plots presented in Figure 4.4-16 and in the pore pressure change plots (Figure 4.4-17). Wall length has a very limited impact on the stress and strain history of soil elements in the excavation prior to failure (stable conditions).

4.4.5. Summary

This section shows the effect of the wall length on the prediction of excavation behavior which can be summarized as follows:

1. Wall length controls the failure depth in the excavation. The longer the wall, the greater the failure depth.

2. Conventional methods for the prediction of failure provide limited guidance as to when failure will actually occur. FE analysis results give different estimates of failure than those given by conventional design methods (Figure 4.4-14). A new calculation is proposed that gives estimates of failure depths that matches FE predictions for short and medium length walls.
3. Wall length has a limited effect on prefailure deformations (Figure 4.4-3) and stresses and strains (Figure 4.4-15,16) in the soil. This conclusion (wall length has a limited impact on deformations) is consistent with studies performed by Hansen (1981) using a total stress analysis and a hyperbolic soil model. Hansen (1981) describes his results as 'preliminary', and recommends that further investigations of wall length effect on excavation behavior be performed.

In the following sections, the emphasis will be on the study of the effect of other geometric parameters and soil stress history on prefailure deformations in a deep excavation. Given the results of this section, most of the following analyses will use the L=60m wall to achieve the deepest excavation possible and characterize excavation behavior under stable conditions (i.e., far from failure with full convergence of numerical solutions).

4.5. Effect of Support Conditions

Support conditions in an excavation (including support installation sequence and spacing) are very important in controlling movements. Peck (1969) describes settlements observed in excavations and separates them in categories by the quality of workmanship (i.e., support condition). This section examines the effects of the vertical support spacing, h, and the initial unsupported height, h_u, on excavation response. There are many other possible factors to consider in practical problems, such as bracing shrinkage, prestressing of supports, tie-back versus crosslot bracing, temperature changes,... etc. These parameters are too numerous to consider in a single study. Many of these variables are site specific and are difficult to incorporate in a generalized study of excavation behavior.

The following assumptions are made in this section:

1) The wall length, L=60m representing a very deep wall (The rationale for using an L=60m wall is presented in Section 4.4).
2) The analyses do not include the effect of over excavation, i.e., h_e=h (Figure 4.2-1). Section 4.7 proposes a simple method to account for the effects of over-excavation.
3) The soil profile corresponds to OCR=1, BBC with properties described by the

MIT-E3 model.

.5.1. Effect of Support Spacing

The analyses consider five different magnitudes of vertical support spacing, h=0, .5, 5, 7.5 and 10m[1]. These values cover a wide range of possible support conditions. he h=0m case[2] represents a situation where the wall is continuously braced with ıcreasing excavation depth. The bracing of the wall always follows the excavation front, :presenting the case of a 'perfectly supported' wall. Ground movements for a perfectly ıpported wall correspond to the minimum disturbance induced by the excavation[3]. The =10m case represents a 'minimally' supported wall condition. In practical field ɔplications, typical support spacings are h=2.5-5m.

.5.1.1. Wall Deformations and Ground Movements

Figure 4.5-1 compares the behavior of 'perfectly supported' (h=0m) and ıinimally supported' (h=10m), 60m walls. For the perfectly supported case, the :flected shape is similar to that reported in Figure 4.4-2d (h=2.5m). Maximum lateral deflections occur approximately 10m below the base of the excavation. Failure of the perfectly supported wall at H=35m is associated with a deep seated mechanism in the soil (H=32.5m to H=35m; Figure 4.5-1c) and with a vertical 'bearing' failure of the wall itself (observed from the wall settlements; Figure 4.5-1a). Large deformations (in the :nge 200 to 350 mm) develop in the soil prior to failure. In contrast, for the minimally ıpported wall, large lateral deflections develop over the excavated height, with ıaximum deformations located close to the base of the excavation. Failure in the soil is :sisted by bending of the wall. At a given excavation depth, lateral wall deflection for =10m analysis are much larger than those for h=0m analysis. Despite the large :ttlements observed at H=20m for h=10m analysis (Figure 4.5-1b) the zone affected by .e settlements is confined to a distance of 60m from the center line. Beyond a distance of)m the surface settlement for h=10m analysis is similar in magnitude to the surface

---

[1] The relevant analyses in this section are: st1_60_00, st1_60_02, st1_60_05, st1_60_07, st1_60_10.

[2] In the FE analysis ΔH=2.5m is used in each discretized step. The bracing is installed first and then the il is removed. The procedure will give deformations that are slightly smaller than from an idealized ocedure in which the soil is continuously removed and the bracing is immediately applied.

[3] This is true for this specific construction sequence. There are other methods to reduce deformations rther, a stiffer wall can be used or some braces can be installed prior to full scale excavation activity. ɔep narrow trenches can be excavated from the ground surface extending across the excavation. A brace several braces can be installed in a vertical profile. This activity can be repeated at several intervals ɔng the length of the proposed excavation. This procedure can significantly reduce movements during e removal of the bulk of the soil material. (e.g., Foott 1991).

settlement at H=20m in the h=0m analysis.

Figure 4.5-2 shows wall deflections and settlements for h=2.5m and h=5m cases. For h=5m case, maximum wall deflections occur at about 5m below excavation depth (compared with 8.75m for h=2.5m case). Greater settlements occur in the h=5m case. The h=5m analysis reaches failure at H>25m while the h=2.5m analysis reaches failure at H>30m.

Figure 4.5-3 presents plots of maximum deformations and moments versus excavation depths for all magnitudes of h considered. The parameter h clearly has a dominant effect on the magnitude of wall deflections, bending moments and ground movements. The plot of maximum moments, Figure 4.5-3c, shows that yield in the wall (M_{max}>1-2MN-m/m) would occur prior to failure as detected in the finite element analysis (This issue was discussed in Section 4.4).

4.5.1.2. Stresses and Strains

Stress and Strain Contours

Contours of stresses and strains are examined for h=2.5m and h=5m analyses, at three excavation stages, H=10m, H=20m and the last excavation depth prior to failure (H=30m for h=2.5m analysis and H=25m for h=5m analysis).

At H=10m, the two analyses show similar contours of maximum shear strain contours (Figure 4.5-4a). However, at H=20m (Figure 4.5-4c and 4d) larger shear strains occur in the retained soil for the h=5m analysis (see for example γ_{max}=0.4% contour). At the last excavation depth prior to failure, Figure 4.5-4e and 4f, there is a tendency for the shear strain contours to localize along a potential slip surface. Over-all, the patterns of development of maximum shear strains are similar for the h=2.5m and h=5m cases.

Development of horizontal strain contours for the h=2.5m and h=5m are shown in Figure 4.5-5. The pattern of development of horizontal strain ε_h for both cases is similar and corresponds to the behavior reported previously in sections 4.3 and 4.4. Horizontal strains for h=5m are larger than those for h=2.5m at all excavation stages. The larger strains are most clearly observed at H=20m, in the retained soil below excavation level. Strain reversal, explained in section 4.3 for h=2.5m L=40m wall, occur for both h=2.5m and h=5m analyses (Figure 4.5-5), while passive wedge development in the retained soil above the excavation level (Figures 4.5-5d and 5f) can be seen at H=20m, 30m for the h=5m analysis.

Horizontal stresses and pore pressures contours $\left(\frac{\sigma_h - u_0}{\sigma'_{v0}}\right)$, $\left(\frac{u - u_0}{\sigma'_{v0}}\right)$ (Figures 4.5-

6,7) are similar for both the h=2.5m and h=5m analyses. The magnitudes of stress contours are almost identical. The development of a passive wedge in the retained soil above the excavation level is apparent for both support spacings. Inside the excavation, negative excess pore pressures occur due to vertical stress relief (e.g., Figures 4.5-7c and 7d). At failure (Figures 4.5-7e and 7f) positive shear induced excess pore pressures are generated in the retained soil above the excavation level.

Plots of stress and strain contours show that the mechanisms causing the development of stresses, strains and deformations in the excavation problem under consideration are independent of the exact magnitude of h. The mechanisms, identified in section 4.3, are fundamental to the problem and are controlled by the soil model and the equilibrium of the boundary value problem.

Stress and Strain Paths

Figure 4.5-8 presents strain paths at points 3, 6, 7 and 13 (Locations in Figure 4.3-14) for support spacings, h=0, 2.5, 5, 10m. Along the center line, point 13 is sheared in plane strain extension and strain paths are similar for all four spacings.

The behavior at point 3 (Figure 4.5-8b) can also be explained from previous discussions of mechanisms in the retained soil. For h=0, 2.5 and 5m there is a significant reversal in the shear strain. However, at h=10m the excavation fails at a shallow depth prior to reversal of the shear strain.

At point 6 (Figure 4.5-8a) stress paths for h=0m and h=2.5m are similar. For h=5m, the strain paths are similar for excavation depths up to H=10m. For 10m≤H≤25m, point 6 undergoes larger shear strains. At H=25m, the final strains for h=5m case are similar to that for h=0m and h=2.5m. For the h=10m case, point 6 undergoes very large shear strains without any reversal in the vertical strain. The large shear strains in the soil element next to the wall are due to deep settlement troughs generated during excavation (Figure 4.5-1b).

At point 7 (Figure 4.5-8a) strain paths for h=0,2.5 and 5m are similar. At a particular excavation depth, strains are smallest for h=0m and largest for h=5m. Reversal in strains is consistently observed for all three h magnitudes. For h=10m case, point 7 undergoes much larger compressive strains, with reversal delayed until H=15m.

The strain paths for selected points show that varying h has the following effects:

1. Larger strains are observed with increasing h.
2. Strain reversal is delayed further as h increases.
3. The magnitude of h has a qualitatively limited impact on the basic direction of strain paths.

Figure 4.5-9 plots the stress paths of selected points for h=0,2.5,5 and 10m. The

differences observed in the strain paths are reflected in the effective stress paths of the soil elements.

4.5.1.3. Lateral Load on the Wall

Strut Loads

Loads carried by supports in an excavation are of great interest in designing an excavation support system. Peck (1969) proposes envelopes of apparent earth pressure based on measured loads in the supports. In an apparent earth pressure diagram, the load carried by a support is converted to a pressure acting on a tributary area (See insert of Figure 4.5-10a). Figure 4.5-10 plots the calculated apparent earth pressure at H=10 and 20m for h=2.5, 5 and 10m. For H=10m, h=2.5m case, the apparent earth pressure at the top of the wall is tensile, due to reverse bending of the wall at the top support (Figure 4.5-2c). Large compressive stresses are predicted at the lowest support level.

The h=5m analysis shows a similar apparent earth pressure distribution. The top support is subject to tensile stresses. The pressure distribution calculated in the bottom support represents an average of the pressure distribution calculated from the bottom two supports for the h=2.5m analysis. In the h=10m, analysis only one support is installed at H=10m. The apparent earth pressure is approximately an average of all the apparent pressures calculated from the h=2.5m analysis or h=5m analysis. At H=20m, h=2.5m and h=5m have similar apparent earth pressure distributions. For h=10m relatively large stresses are predicted in the bottom support.

Apparent earth pressure diagrams do not reflect the actual horizontal stress distribution acting on the back of the wall. Figure 4.5-11 plots horizontal stresses $\left(\frac{\sigma_h - u_0}{\sigma'_{v0}}\right)$ acting on the back of the wall (Figures 4.5-11a and 11b) and on the side of the wall inside the excavation (Figures 4.5-11c and 11d). Horizontal stresses are plotted for h=0, 2.5, 5 and 10m. Rankine active (σ_v-$2S_{uA}$) and Rankine passive (σ_v+$2S_{uP}$) stresses are also shown on these plots.

In the retained soil above the excavation level, Figure 4.5-11a, the lateral stresses are larger than the initial stresses (i.e., greater than K_0 conditions), and increase with increasing h. For the h=10m analysis the lateral stress slightly exceeds the initial vertical overburden stress $\left(\frac{\sigma_h - u_0}{\sigma'_{v0}} > 1\right)$ near the ground surface. Similar observations can be made at H=20m (Figure 4.5-11b). The lateral stresses differ from the Rankine active stresses

In the retained soil below the excavation level, the reduction in lateral stresses

ɔpears to be slightly affected by the magnitude of h. An exception is observed for h=10, ⁞=20m stage where the wall is approaching a failure condition.

Inside the excavation, Figure 4.5-11c and 11d, lateral stresses appear to be ımilar and almost independent of the magnitude of the support spacing h. For H=20m ıse the stresses are similar to the Rankine passive stresses (Figure 4.5-11d).

.5.2. Initial Unsupported Excavation

In an optimal excavation process, the first support level is installed at an early age in order to minimize cantilever movements in the wall. However, this may not be ossible due to a variety of site conditions, construction sequence, etc. This section valuates the influence of the initial unsupported depth, h_u, on subsequent excavation ehavior for long walls (L=60m) with h=0 and 5m[1]. For h_u=0m, the first support is ıstalled 'on grade' prior to any excavation, h_u=2.5m is typical of top-down excavations here some site preparation work is performed (See for example Chapter 5, Post Office quare Excavation), while h_u=5m analysis represents a relatively deep unsupported xcavation where large cantilever movements may occur. "If a raker and earth berm system is used, large cantilever movements automatically occur since the structural supports in the system cannot be installed until significant excavation is made and significant movements are needed to mobilize the resistance of the earth berm" (Clough et al. 1990).

Figure 4.5-12 compares behavior for h_u=0 and 5m with 'perfectly supported' ı=0m), L=60m long wall. For the h_u=0 analysis, no cantilever movement is allowed in ıe wall. At all excavation depths, the maximum deflection in the wall occurs at about)m below the excavation level. The settlement trough predicted by this analysis shows ıat the maximum settlement occurs at a distance 40-60m away from the excavation center ne (Figure 4.5-12). The last excavation depth prior to failure is H=30m, the same depth ›r h_u=2.5m case discussed earlier. For h_u=5m the wall deforms in a cantilever mode up › H=5m (Figure 4.5-12d). For H>5m the wall deforms by bulging below the excavation vel. At H=15m, the wall bulging becomes dominant, such that the maximum wall eflection is located at the point of maximum bulging. Note that at H=15m, wall eflection below a depth of about of 15m is almost identical to that in the h_u=0m case. A milar observation can be made at H=20m. The cantilever wall movement induces ıaximum ground settlement next to the wall (i.e., for H≤5m). However, after support ıstallation, a trough develops. At H=20m, the settlement trough has a shape and

---

[1]The relevant analyses are: st1_60_00, st1_60_00a, st1_60_00b, st1_60_05, st1_60_05a.

magnitude similar to that of the perfectly supported wall (h_u=0m).

Figure 4.5-13 compares the behavior of an h_u=2.5m and h_u=5m, 60m long wall with h=5m vertical support spacing. Observations of behavior are similar to those observed for h=0m analyses (Figure 4.5-12). Up to H=h_u, the wall deforms in a cantilever mode. The maximum settlement is located next to the wall. For depths, H>h_u , the wall bulges, and a settlement trough develops. The maximum settlement is located 40-60m away from the excavation center line. For H≥15m, wall deflection below a depth of 15m for h_u=5m analysis is almost identical to that for h_u=2.5m analysis. Settlement troughs for h_u=5m and h_u=2.5m analyses, beyond H=15m, are similar.

Figure 4.5-14 presents plots of maximum deformations and moments for the analyses of Figures 4.5-12 and 13. Data are presented up to H=20m. Maximum wall deflections are shown in Figure 4.5-14a. For h_u=0m, h=0m analysis, no cantilever wall deflection occurs, and the resulting maximum deflection curve is labeled 'basic system response'. For the h=0m, h_u=2.5m analysis, cantilever deflection is allowed until H=2.5m. The maximum deflection is initially larger than the movement given by the basic system response. As excavation proceeds, maximum deflection becomes very similar to that of the basic system response. In h_u=5m case (h=0m analysis), this behavior is more pronounced. The portion of the curve that joins the point of last cantilever deflection and the basic response curve is labelled the 'transient response'. The transient response curve is horizontal. The maximum deflection in the wall is located at the top of the wall until a point in the excavation where deflections given by the basic response curve (due to wall bulging) exceed the cantilever movement.

For h=5m spacing, a different basic system response curve is defined. The transient response curve is unique. A similar behavior is observed for the maximum settlements (Figure 4.5-14b). The transient response curve shows a slight decrease in settlements prior to joining the basic response curve. Soil heave due to soil removal pushes the wall upwards after brace installation, Figure 4.5-14b, resulting in slight reduction of settlements. Plots of maximum heave, Figure 4.5-14d, show that heave is very slightly affected by the magnitude of h_u.

Plots of maximum moments reflect the development of wall deflection. The maximum moment curves at various h_u magnitudes for h=0m coincide beyond H=16m. Similarly, the curves coincide for h=5m beyond H=20m.

The analyses presented show that h_u has a limited transient impact on the basic behavior of an excavation. Beyond a particular excavation depth the 'memory' of the previous cantilever movement is erased, and the excavation behaves as if the first support is installed prior to any excavation.

O'Rourke (1981) suggests that the cantilever movements are essentially additive to movements that occur due to wall bulging alone. Clough et al. (1990) further suggest that movements due to the cantilever mechanism and bulging mechanism can be added to obtain the final movement (Figure 4.5-15). These suggestions imply that cantilever movement will affect significantly deformations at later excavation stages.

The method proposed by O'Rourke (1981) and Clough et al. (1990) to account for cantilever movements is applied to the L=60m, h=0m analyses (Figure 4.5-16). According to that method, wall deflections for an h_u=5m analysis can be 'predicted' by summing wall deflections from an h_u=0m (wall bulging movement only) to the cantilever movement at H=5m. The solid-dashed line in Figure 4.5-16 represents wall deflection for h_u=0m analysis. According to the method, deflections at H=15m for h_u=5m case, for example can be obtained by adding the movement for H=15, h_u=0m case to those due to cantilever movement. The dashed lines with solid square symbols represent the 'predicted' deflection in accordance with Clough et al. (1990) recommendations. The solid lines are the deflection curves obtained from h_u=5m FE analysis. The FE results do not match the 'predicted' deflections[1]. The FE analysis shows that cantilever movements have a very limited impact on later wall movement, and that beyond a certain excavation depth, they have practically no effect. The FE analysis contradicts previous assessments of the effect of cantilever movements made by Clough et al. (1990) and O'Rourke (1981).

4.5.3. Summary

This section has described the effects of vertical support spacing and initial unsupported depth on the prediction of excavation behavior which show the following:

1. Vertical support spacing has a very important impact on excavation response. Greater movements and earlier failure result from increasing the magnitude of h (Figure 4.5-3).
2. The vertical support spacing does not alter the basic soil response to excavation including stress and strain reversal (Figure 4.5-8,9) and the generation of passive stresses in the retained soil above the excavation level (Figure 4.5-11a,b).
3. The initial unsupported depth has a limited effect on subsequent excavation behavior (Figure 4.5-14). Beyond some excavation depth, h_u has no effect on deformations in an excavation. This observation disagrees with suggestions made

[1]However, from a practical perspective, these observed differences are small (of the order of 10mm) relative to other uncertainties in predicting wall movements.

by O'Rourke (1981) and Clough et al (1990) (Figure 4.5-16).

4.6. Effect of Soil Stress history

The study has focused, up to this point, on the effect of a variety of excavation parameters in an OCR=1 soil profile. An OCR=1 profile represents the most critical case with respect to deformations and failure. However, in many situations, due to a variety of geologic factors, the clay deposit is overconsolidated. This section examines the effect of soil stress history (OCR) on deformations, failure and excavation response with regard to changes in wall length and support conditions described previously. The analyses compare three soil profiles with OCR=1, 2 and 4.

4.6.1. OCR Effect on Undrained Plane Strain Shear Behavior Predictions in MIT-E3

Section 4.3.1 compares in detail MIT-E3 predictions of the effect of stress rotation in plane strain to measured laboratory data at OCR=1. Figure 4.6-1 presents a comparison of the predicted BBC behavior at OCR=1,2 and 4 in plane strain active and passive shearing modes. The predictions are compared with measurements made in the plane strain device (Ladd et al., 1971) and Directional Shear Cell (O'Neill, 1985).

Figure 4.6-1a shows the stress paths for the three OCR values. The initial state of stress is dependent on the magnitude of the OCR and is obtained by simulating a one dimensional swelling stress path using MIT-E3. The figure shows the following:

1. At OCR=1, there is very good agreement between the predictions and measurements of the shear-stress strain response in both the active and passive shear modes. The MIT-E3 model describes accurately the effective stress paths, undrained shear strengths in the two shear modes ($S_{uPSA}/\sigma'_{vc}=0.34$; $S_{uPSP}/\sigma'_{vc}=0.16$), shear strains to peak resistance ($\varepsilon_{up}\approx 0.3\%$ and $\varepsilon_{up}>5\%$ respectively), and post peak strain softening in the active shear mode. The model tends to overpredict the critical state friction angle, ϕ'_{PSA}, measured in the PSA shear tests. Similar comparisons with passive test data are not reliable due to sample necking and other experimental difficulties.
2. At OCR=2, MIT-E3 also shows good agreement with measured data especially for axial strains $|\varepsilon_a|\leq 2\%$. In the active shear mode, the model overpredicts the measured undrained shear strength by approximately 8% and underestimates the post peak strain softening. For passive shearing, the soil model describes accurately the small strain non-linearity, while discrepancies for $|\varepsilon_a|>2\%$ can be attributed in large parts to sample necking. The predicted and measured effective

stress paths both show negligible shear induced pore pressures (i.e., $\Delta p' \approx 0$) for shear stresses in the range $-0.1 \leq (\sigma'_y - \sigma'_x)/2\sigma'_{yc} \leq 0.5$. These results imply that plastic strains are not significant for small strain shearing at OCR=2.

3. At OCR=4, MIT-E3 gives good predictions of the non-linear stress-strain behavior in both shear modes, but significantly overestimates the undrained shear strength (by 25%) and the pre-peak stress obliquity ($=(\sigma'_x - \sigma'_y)/(\sigma'_x + \sigma'_y)$) in the active tests. This behavior is due, in large parts, to the assumed shape of the bounding surface in the MIT-E3 model (Whittle 1990) and can be addressed through modifications of the yield function (Equation 2.41, Section 2.4).

Figure 4.6-2 compares MIT-E3 predictions with undrained shear tests performed at OCR=4 in the Directional Shear Cell[1] at various orientations, δ ($=\delta_{inc}$), of the major principal stress, σ_1, to the direction of deposition (O'Neill, 1985). The data at $\delta = 0^0, 90^0$ correspond to the plane strain active and passive shear modes described above, while results for intermediate δ angles illustrate the full range of anisotropic behavior associated with one-dimensional consolidation stress history. The results show the following:

1. As the δ angle increases from 0^0 to 90^0 the measured undrained shear strength decreases monotonically from $S_u/\sigma'_{vc}=1.00$ to 0.56, as compared to model predictions which range from 1.56 to 0.44 (c.f. comment (3) above). Thus, MIT-E3 overpredicts the measured shear strengths for $\delta < 45^0$, and overpredicts the behavior for $\delta > 45^0$. Thus, although the model gives very good predictions of the variations in shear strength with δ, it tends to exaggerate the anisotropic stress-strain response at OCR=4.
2. The model gives excellent predictions of the shear strains required to mobilize the peak shear resistance for tests performed at different δ angles, but tends to overpredict the small strain stiffness for $\delta < 45^0$.
3. MIT-E3 overpredicts the effective stress obliquity and shear induced pore pressures for tests performed at $\delta < 45^0$. However, the model describes accurately the trends in the measured data for effective stress conditions at peak shear strength.

Overall, the above evaluations show that although MIT-E3 predictions are less reliable at OCR=4 compared to OCR=1, the model describes accurately the measured trends in anisotropic stress-strain behavior for different modes of plane strain shearing. These results show that MIT-E3 can be used with reasonable confidence to predict

[1]The DSC is a stress controlled device, and hence cannot provide reliable test data of the post-peak behavior.

ground deformations due to excavation in overconsolidated clay (OCR≤4).

4.6.2. Effect of OCR on Predictions of Excavation Behavior

Analyses at OCR=2 and 4 (in addition to that at OCR=1 presented in Section 4.4, Figure 4.4-2) are conducted using an L=60m wall with a vertical support spacing h=2.5m[1]. At OCR=2 and 4 the excavation is carried to a depth H=40m with no indication of failure[2]. At OCR=1, the last excavation depth prior to failure is H=30m. As expected, excavation response is significantly stiffer at OCR=2 and 4 than at OCR=1, and hence the overall magnitudes of ground movements are reduced significantly.

4.6.2.1. Wall Deformations and Settlements

Figure 4.6-3 presents plots of deformations and settlements at OCR=2 and 4. The development of wall deformations is similar to that presented in previous sections. At OCR=2, cantilever movement is predicted up to H=2.5m, beyond which the wall bulges. Maximum wall movements develop at about 5m below the excavation depth. A similar behavior is observed at OCR=4; however, the magnitude of deformations is smaller than that observed at OCR=2.

The shape of the settlement troughs, Figure 4.6-3a, is significantly different from those shown in Figure 4.4-2b. The magnitude of the settlements is much smaller at OCR=2 and 4 than at OCR=1. For the overconsolidated clays, significant settlements occur at locations far from the excavation. For example at a lateral distance, x=200m, the settlement ratio $\delta_{v200}/\delta_{vMAX}$≈0.2-0.25 for OCR=2,4 at H=20m compared to $\delta_{v200}/\delta_{vMAX}$=0.05 at OCR=1 (Figure 4.4-2). The predictions in Figure 4.6-3 also show that the uplift of the diaphragm wall (δ_{wall}=10-15mm) is similar to that observed at OCR=1 (Figure 4.3-7d), but represents a larger percentage of maximum settlements. These results are consistent with the predominance of elastic (recoverable) stress-strain response for small strain shearing of overconsolidated clays[3]. The shape of settlement troughs at OCR=4, Figure 4.6-3c, are similar to those at OCR=2 but of consistently smaller magnitude.

Figure 4.6-4 plots maximum movements and moments at OCR=1, 2 and 4. Maximum wall deflections at OCR=1, Figure 4.6-4a, accelerate with increasing depth

---

[1]The relevant analyses are st1_60_02, st2_60_02 and st4_60_02.

[2]All the methods listed in Figure 4.4-13 give an FS>1 for the range of excavated depths considered in the OCR=2 and 4 analyses.

[3]Wall uplift is much less pronounced in Figure 4.6-3a than that observed for the MCC model (Figure 4.3-6a).

ntil failure is reached beyond a depth of H=30m. At OCR=2 and 4, maximum deflection urves increase linearly with depth and show a response similar to the elastic behavior own in Figure 4.3-9. Similar comments can be made regarding maximum settlement urves, Figure 4.6-4b, maximum heave, Figure 4.6-4d, and maximum moments, Figure .4-4c

.6.2.2. Stress and Strain History

Stress and Strain Paths

Stress and strain paths for the analyses at OCR=1, 2 and 4 are presented for oints 3, 6, 7 and 13 of Figure 4.3-14.

Figure 4.6-5 shows the strain paths at the selected points. The trends observed at)CR=1 (Figure 4.6-5a) have been discussed in Section 4.4. Strain paths for OCR=2 and analyses (Figure 4.6-5b) show consistently smaller magnitudes of the strains at all oints (Note: Figures 4.6-5a and 5b are plotted to different scales). However, the evelopment of strains (including strain reversal) at all three OCR values is very similar at oints 3, 6 and 7. Strain reversal occurs at approximately the same depth for all OCR values. At point 13, the development of strains is similar up to an excavation depth of 30m (The last excavation depth prior to failure for OCR=1 case). At an excavation depth greater than 30m, vertical strain reversal in OCR=2 and 4 cases is predicted, which is similar to the reversal observed in the MCC and Elastic analyses (Figures 4.3-15b and 5c). The reversal is attributed to a 'membrane' effect over the excavated surface (Section .3).

Figure 4.6-6 presents stress paths for the three OCR analyses with initial onditions described by K_0. In Figure 4.6-6a1, a2 the stress paths at OCR=2 and 4 are ifficult to discern. Points 6, 7 exhibit an elastic behavior with negligible generation of ıear induced pore pressures (Figure 4.6-6a1), while points 13 a stress path similar to ıat of an elemental PSP test (Figure 4.6-6a2).

Figure 4.6-6b1 shows the effect of stress rotation at various OCR values. In the)CR=1 analysis, points 6 and 7 reach the peak strength envelope and undergo some rain softening prior to undergoing stress reversal. In the OCR=2,4 analyses all points ndergo stress rotations similar to those in the OCR=1 analysis but exhibit stress :versals prior to reaching the peak strength envelope. Figure 4.6-6c shows total stress aths for points 3 and 7. The figure shows clearly the reversal in stress paths and the ıbsequent increase in the horizontal stresses (Figure 4.6-6d).

Figure 4.6-7 shows the development of excess pore pressures at points 3,6 and 7 ı the retained soil. In the OCR=1 case, negative excess pore pressures develop initially

followed by a reversal in the direction of the development of excess pore pressures. At H=30m, points 3, 6 and 7 have a net positive excess pore pressure. In the OCR=2 and 4 cases, much larger initial negative pore pressures develop. Upon reversal, at H=40m, points 6 and 7 have a net negative excess pore pressure, while point 3 has a small net positive excess pore pressure. At any particular point, as the OCR increases there is a decrease in the magnitude of the excess pore pressure.

Stress and Strain Contours

Contours of stresses and strains are presented for OCR=1, 2 and 4 analyses at H=15m and H=30m (the last excavation depth prior to failure at OCR=1).

Figure 4.6-8 shows contours of maximum shear strain. At OCR=1, as failure is approached, maximum shear strains localize along a potential slip surface. At OCR=2, the pattern of development of shear strains at H=15m is similar to that at OCR=1. However, the magnitude of the shear strains is smaller at all locations. At H=30m no localization of strains is observed in OCR=2 analysis. The magnitude of strains is smaller than those in the corresponding step at OCR=1. At OCR=4, the pattern of development of strains is similar to the pattern observed at OCR=2, but the magnitude of strains is smaller. The maximum shear strain mobilized is smaller than the strain required to mobilize the undrained shear strength in OCR=2 and 4 materials.

Figure 4.6-9 shows contours of horizontal strain. Strain reversal, accompanied by the development of a passive wedge in the retained soil, occurs at OCR=1 (Figures 4.6-9a and 9b, see also Section 4.3). The passive wedge also develops in the OCR=2 analysis (Figures 4.6-9c and 9d). At H=30m, the passive wedge extends to the bottom of the excavation in the OCR=1 case, while it extends to a depth of 20m in OCR=2 case. The development of horizontal strains in the OCR=4 case, Figures 4.6-9e and 9f, is similar to that at OCR=2.

Figure 4.6-10 shows horizontal stress contours $\left(\frac{\sigma_h - u_0}{\sigma'_{v0}}\right)$ at H=15,30m for the analysis at OCR=1,2 and 4. Prior to the excavation, $\frac{\sigma_h - u_0}{\sigma'_{v0}} = K_0$ (=0.53, 0.69 and 1.0 for the three analyses). At H=15m, all the analyses exhibit a passive wedge (where the horizontal stress exceeds its initial value) in the retained soil. The critical extent of this zone decreases with increasing OCR value. There is also a general reduction in the horizontal stress below the excavation level.

Contours of $\left(\frac{u - u_0}{\sigma'_{v0}}\right)$ in Figure 4.6-11 show positive excess pore pressures developing at H=15m and H=30m in the retained soil above the excavation level for the

)CR=1 analysis. At OCR=2, Figures 4.6-11c and 11d show a smaller zone of positive xcess pore pressures while negative pore pressures extend up to 20m behind the toe of ıe wall. In the OCR=4 analysis, excess pores pressures are slightly less positive and ıore negative than those predicted for the OCR=2 case.

Lateral Stress on the Wall

Figure 4.6-12 shows plots of lateral stresses acting on both sides of the wall for)CR=1, 2 and 4. Rankine active and passive stresses are also included in these figures. ı the retained soil (Figures 4.6-12a,b), lateral stresses at all OCR values exceed Rankine ctive stresses. Above the excavation level, the stresses are almost equal to the initial in-itu lateral stresses and even exceed them for OCR=1 (This is due to the developing assive zone). Inside the excavation at H=30m, Figure 4.6-12d, rankine passive stresses ive a good estimate of the predicted soil stresses.

.6.3. Effect of Support Conditions

A series of analyses similar to those presented in section 4.5 are performed ssuming OCR=2 and 4 soil profiles.

4.6.3.1. Effect of Vertical Support Spacing h

Section 4.5.1 shows that the value of h has a significant influence on deformations and failure for an excavation in OCR=1 clay. A similar set of analyses has een performed at OCR=2 and 4 using a wall length, L=60m, and values of h=0, 2.5, 5, .5 and 10m.

Figure 4.6-13 summarizes the maximum deformations and moments in the)CR=2 case[1] (Figure 4.5-3 shows corresponding plots for OCR=1). No Failure occurs ı any of these analyses. The maximum deflection curve (Figure 4.6-13a) is a linear ınction of H, for 0≤h≤10m, while the magnitude of deformations increases with ıcreasing support spacing. Maximum settlements (Figure 4.6-13b) and heave (Figure .6-13d) exhibit similar patterns of development. The value of h has a minor impact on eave along the excavation center line (Figure 4.6-13d). Plots of maximum moments, igure 4.6-13c, show an increase in wall moments with increasing magnitude of h. In the =7.5m and 10m analyses, maximum moments exceed 1.0MN-m/m at H>20m, ıdicating a possible structural failure in the wall.

The effects of support spacing for the OCR=4 soil[2] are summarized in Figure

---

[1]The relevant analyses are st2_60_00, st2_60_02, st2_60_05, st2_60_07 and st2_60_10.
[2]The relevant analyses are st4_60_00, st4_60_02, st4_60_05, st4_60_07 and st4_60_10.

4.6-14, and are qualitatively similar to those described for OCR=2.

4.6.3.2. Effect of Initial Unsupported Excavation h_u

Section 4.5.2 shows that the unsupported excavation depth, h_u, has only a transient effect on the basic system response in an excavation in an OCR=1 soil. A similar series of analyses have been performed in OCR=4 soil for a wall length L=60m[1].

Figure 4.6-15 summarizes the maximum movements and moments (Figure 4.5-14 shows corresponding plots for OCR=1). The scales used in Figure 4.6-15 are different from those used in Figure 4.5-14 as the movements in the OCR=4 soil are significantly smaller than those for the OCR=1 case. The results show that h_u again has only a transient effect on the excavation response. For example, in in a perfectly supported wall (h=0m), maximum wall deflections in the h_u=5m case initially exceed those in the h_u=0m case. However, for H>12m, the two curves of maximum wall deflection become practically identical.

4.6.4. Effect of Wall Length

Section 4.4 observes that the wall length in an OCR=1 material has a very limited impact on prefailure deformations, but significantly affects the failure depth of an excavation. A similar study performed at OCR=4, compares ground movements for walls of lengths L=12.5m, 20m, 40m and 60m[2] at a support spacing, h=10m. No failure develops in any of these analyses.

Figure 4.6-16 summarizes the maximum deformations and moments observed in the four analyses. Maximum wall deflections (Figure 4.6-16a) for L=40, 60m are identical up to an excavation depth of 30m. At H=40m (i.e., where the excavation depth is equal to the wall length for L=40m case), maximum deflections in the L=40m analysis are slightly larger than those for the L=60m case, due to loss of support at the toe of the wall. A similar observation can be made for the L=20m maximum deflection curve. Maximum wall deflections for L=12.5m case are practically identical to those in L=20m analysis.

Similar trends are observed in the maximum settlement curves, Figure 4.6-16b, maximum heave curves, Figure 4.6-16d, and maximum moment curves (Figure 4.6-16c). Therefore, wall length has a very limited effect on excavation deformations in an OCR=4 material.

---

[1]The relevant analyses are st4_60_00, st4_60_00a, st4_60_00b, st4_60_05 and st4_60_05a.
[2]The relevant analyses are st4_12_10, st4_20_10, st4_40_10 and st4_60_10.

4.6.5. Summary

This section has described detailed analyses of the effect of soil stress history (OCR) on the excavation behavior. The following comments can be made:

1. The magnitude of OCR has a significant impact on the magnitude of deformations and failure conditions in an excavation. At OCR=2 and 4 the FE analysis predicts significantly smaller deformations than at OCR=1 (Figure 4.6-4). For the geometry and support conditions used in the analyses, no failure occurs in the OCR=2 and 4 soil profiles (Note: base heave calculations, Figure 4.4-13, also indicate FS>1 for all cases considered).
2. The basic prefailure mechanisms observed at OCR=1 are observed at OCR=2 and 4. Hence, mechanisms of ground movements which are not affected significantly by the OCR value can be summarized as follows:
    a) Stress and strain path reversals are associated with the development of a passive state in the retained soil above excavation level, and are observed at all OCR values (Figure 4.6-12).
    b) Wall length has a very limited impact on prefailure deformations at all OCR levels (Figure 4.6-16).
    c) Support spacing has a significant systematic impact on deformations prior to failure (Figure 4.5-3, 4.6-13,14).
    d) Unsupported excavation depth has a limited transient impact on the basic excavation response (Figure 4.5-14, 4.6-15).

4.7. A Simplified Framework for Interpreting Deformations

The effect of a variety of parameters on excavation behavior was discussed in Sections 4.3 to 4.6. The analyses show that deformations in an excavation follow a 'basic system response' that is altered by transient effects due to initial unsupported excavation depth. The wall length has a very minor effect on prefailure deformations (i.e., basic and transient system responses). This section proposes a framework to characterize the basic system response of an excavation and in terms of maximum deformation quantities (maximum wall deflection, maximum surface settlement, and excavation heave).

4.7.1. Maximum Wall Deflections and Excavation Failure

Maximum deformations, maximum wall moments, and failure mechanisms are some of the more important parameters used in the design of an excavation. These

arameters are not separable. In this section, the three parameters are combined to rovide a unified evaluation of excavation response.

Figure 4.7-1a summarizes the numerical predictions of maximum wall deflection or excavations in normally consolidated BBC as a function of the excavation depth, H, nd support spacing, h. The figure includes loci of the failure conditions obtained for valls of different lengths, L, ranging from 12.5m to 60m, and implicitly incorporates bservations of different failure mechanisms in the soil. Failure of the diaphragm wall an be evaluated from contours of the maximum moment compared to the capacity of the ection (M_u). The figure shows the following for OCR=1 clay:

1. For excavations deeper than about 15m which are perfectly supported (h=0m), the deflection to depth ratio, (δ_{MAX}/H), is greater than or equal to 0.5%. For minimally supported walls, this ratio increases to (δ_{MAX}/H)=1.5 to 2.0% (H>10m).
2. For excavations less than 10m, Section 4.5 shows that predictions of wall deflections are significantly affected by details of the top-down construction sequence (e.g., initial unsupported height, h_u)
3. Excessive bending moments in the wall are the most critical design condition for long walls (L≥40m) with light (widely spaced) bracing (h≥5m).

Figure 4.7-1b summarizes maximum lateral wall deflections in an overconsolidated BBC deposit with an overconsolidation ratio equal to 2 (OCR=2). No oci of failure condition, due to wall length, are included as failure is not detected in the .E. analyses. Contours of maximum moments show that excessive bending moments re most critical for lightly braced walls (h≥5m). Similar results are obtained at OCR=4 Figure 4.7-1c).

Figures 4.7-1 are very important and useful in interpreting/predicting eformations and failure in braced excavations:

1. The figures present maximum wall deflections which are the most commonly reported (and easily measured) index of deformation in an excavation.
2. The figures combine results from all the previous analyses regarding the effect of wall length and vertical support spacing on maximum wall deflection.
3. The figures can be used to estimate the safety of the excavation against failure a) due to the development of a mechanism (function of wall length, L), or b) the yielding of the wall (function of maximum bending moment, M_u).
4. The figures give minimum expected deflections because of the ideal construction sequence assumed in the analyses. In practice, other construction details, not accounted for in the current analyses, may lead to an increase in the maximum

wall deflections. Therefore, the deformations reported in Figures 4.7-1 represent a lower estimate of expected movements.

5. The absolute magnitude of deformations is strongly dependent on the soil profile (OCR in this series of analyses). Similar figures can be constructed for any given soil profile.
6. Figures 4.7-1 can be used to estimate, quantitatively, deformations for excavations in soft clay deposits with properties similar to those of BBC.

.7.2. Interpretation of Maximum Deformations

During the construction of an excavation, deformations throughout the excavation rocess are monitored to evaluate construction impact and predict deformations during ıbsequent excavation steps. A framework to interpret these observations is, therefore, ery useful in assessing the excavation performance.

Maximum deformations are not affected significantly by wall length (Section 4.4) : all OCR values (Section 4.6). Prefailure maximum wall deflections, surface settlements nd heave computed at OCR=1, 2 and 4 can be related to the excavation depth and vertical support spacing by the following empirical equation:

$$\delta = [ae^{bh} + (c + dh)\,H]\,H \qquad 4.7\text{-}1$$

δ = Maximum deformation (Wall deflection, settlement or heave)

H = Excavation depth

h= Vertical support spacing

The constants a, b, c and d depend on the soil profile and the maximum eformation quantity being calculated (i.e., different sets of constants are required for ıch of the three maximum deformation quantities)

Equation 4.7-1 represents the 'basic system response'. Transient effects due to ıitial unsupported depth, h_u, can be incorporated into the equation framework as iscussed in Section 4.5.2.

For non-zero values of a, b, c and d, the relationship is parabolic (for a given ıagnitude h) and deformations are predicted to accelerate with increasing excavation epth. This relationship is representative of conditions in the OCR=1 profile (Figure 4.7-

a). The $\frac{\delta}{H} = [ae^{bh} + (c + dh)\,H]$ relationship is linear (for a given magnitude h).

When a and b are both non-zero, but c=d=0, the relationship is linear and ıaximum deformations are predicted to increase linearly with depth for a given ıagnitude h. This relationship is representative of conditions at OCR=2 and 4 (Figures

4.7-1b and 1c). Then $\frac{\delta}{H} = [ae^{bh}]$ is a constant for a given magnitude of h.

The relationship given in Equation 4.7-1 provides a limited predictive capability which can be used to reduce the number of FE analyses to be performed for a given soil profile and wall properties (including stiffness and geometric dimensions). Two analyses are required to obtain the four constants a, b, c and d: The first analysis should be performed assuming a 'perfectly supported excavation' (h=0m). The maximum deformation curves from this analysis provide the magnitudes of the constants a and c. The second analysis should be performed for a vertical support spacing, h, greater than or equal to the maximum support spacing to be used in the proposed excavation[1]. The maximum deformation curves for this analysis, together with the selected values of a and c, will give the magnitudes of b and d. Equation 4.7-1 can then be used to estimate (interpolate) maximum deformations for other magnitudes of h (without the need to perform further FE analyses). Effect of changing support conditions can, therefore, be easily determined. Small values of h_u should be used to calibrate Equation 4.7-1 (h_u=0 is preferred).

The proposed procedure for calibrating Equation 4.7-1 is applied to the analyses of the three soil profiles considered (OCR=1, 2 and 4). The constants a, b, c and d are determined using maximum deformation data from FE analyses where h=0m and h=5m. Maximum deformations are then 'predicted' for h=2.5, 7.5, and 10m cases using Equation 4.7-1 and are compared to FE analysis results.

Figure 4.7-2 presents comparisons of maximum wall deflections, surface settlements and excavation heave obtained from the procedure described previously (solid lines on the graph) versus FE analysis results (symbols on the same graph) for OCR=1 soil profile. The magnitude of the constants a, b, c and d, determined from h=0 and 5m analyses, are also given.

Figure 4.7-2a plots maximum wall deflections versus excavation depth. For h=0 and 5m cases, the equation predictions and FE results overlap because the equation is calibrated using the results at those h values. For h=2.5m case the equation provides an accurate prediction of maximum deformations. For h=7.5m the equation predicts reasonably well maximum deflections. At h=10m the equation severely underpredicts wall deformations. Similar observations can be made for maximum surface settlements, Figure 4.7-2b, and maximum excavation heave (Figure 4.7-2c).

Figure 4.7-3 presents a similar set of comparisons for OCR=2 profile. The

---

[1]In many excavations the vertical support spacing, h, is not constant throughout the excavation depth.

constants c and d are zero for this profile. Maximum deformations are very well predicted by the equation at h=2.5, 7.5 and 10m.

Figure 4.7-4 presents maximum deformation comparisons for OCR=4 profile. Equation 4.7-1 predictions fit adequately the FE results.

Thus, overall Equation 4.7-1 provides a simple framework for evaluating the effect of support condition on maximum deformations due to excavation. The magnitude of the constants a, b, c and d cannot be correlated directly to properties used in the FE model (including the 15 material properties of MIT-E3, wall properties and dimensions, and excavation width), but are easily obtained using the curve fitting procedure described above.

Equation 4.7-1 is not a substitute for performing non-linear FE analyses of the excavation. It is most useful in limiting the number of analyses required (and hence reducing the cost of the numerical analysis portion of an excavation project) and can be used to estimate the effect of changes in support conditions on excavation performance.

4.8. Comparison of Analytical Predictions with Published Data and Analyses of Excavation Behavior

The excavation problem has been studied extensively over the past 20 to 30 years. Numerous case histories documenting excavation behavior for a wide range of soil profiles, support conditions, wall characteristics, etc, have been published in the literature. Several authors have synthesized results from many case histories to establish trends and correlations that characterize excavation response, while others have performed extensive numerical analyses to gain insights into excavation behavior.

This section compares and contrasts predictions from the analyses (Sections 4.3 to 4.7) with some of the published empirical and semi-empirical relationships of excavation behavior.

Some comparisons with published work have already been made in previous sections. The comparisons can be summarized as follows:

1. In Section 4.3, predicted stress paths show a stress reversal in the retained soil resulting in the development of a passive wedge. This is not described by conventional hypotheses (Lambe 1970, Figures 4.3-17 through 20).
2. Section 4.4 finds that wall length has a limited effect on prefailure deformations and this is consistent with analytical studies performed by Hansen (1980).
3. Section 4.4 predicts that failure mechanisms for short walls are similar to the basal heave mechanism commonly assumed in the literature (Terzaghi, 1943). However, for long walls, FE analyses give a failure mechanism that is controlled

by a deep seated failure wedge which propagates up through the retained soil and is restrained by the wall embedment.

4. Section 4.5.2 shows that the FE analyses contradict the hypothesis proposed by O'Rourke (1981) and Clough et al. (1990), regarding the impact of the unsupported excavation depth on deflections in subsequent excavation stages. This section presents additional comparisons with published data.

.8.1. Apparent Earth Pressure Diagrams

Figure 4.8-1 shows the empirical apparent earth pressure diagrams proposed by 'eck (1969) for estimating strut loads in braced excavations. The diagrams were eveloped using field measurements for a variety of excavation conditions using elatively flexible walls (e.g., sheet pile, soldier beam and lagging). For clays, the agnitude of the apparent earth pressure (Figure 4.8-1) is calculated assuming a constant trength with depth. The apparent earth pressure diagrams for the current numerical xperiments can be computed using an average undrained shear strength in a plane strain ompression over the excavated height. If lower strengths are used to account for strength anisotropy, larger apparent pressures would be calculated.

Figure 4.8-2 compares Peck's design pressures with pressures back calculated from strut loads in the FE analyses[1]. Peck (1969, Figure 4.8-1b) recommends using m=0.4 for soft clays and m=1.0 for stiff clays. Envelopes using both values of m are eported in Figure 4.8-2. The results show the following:

1. Overall, there is good agreement between Peck's design envelope, with m=0.4, and the apparent earth pressures interpreted from the FE analyses. For shallow excavations (H=15m) in normally and lightly overconsolidated clay (OCR=1→2), the Peck method is conservative and predicts strut loads which are up to 50% larger than the numerical predictions. At OCR=4, and for deep excavations (H=30m) the empirical method tends to underestimate the design loads for the lower strut levels.
2. Predictions of strut loads using Peck's method with m=1 are also in good agreement with the numerical experiments at OCR=1,2 but do not give reasonable design loads at OCR=4.

The apparent earth pressures predicted by the FE analyses fit reasonably well with ublished empirical apparent earth pressure data.

---

[1]For a wall length L=60m and support spacing h=2.5m.

.8.2. Surface Settlements

The accurate prediction of surface settlement distribution is important for ;timating potential damage to structures surrounding an excavation.

Figure 4.8-3 plots normalized settlement data for many excavation case histories 'esented by Clough and O'Rourke et al. (1990)[1]. The plot defines three zones based on ıpport condition after Peck (1969). There is very little reliable data beyond d/H=2.0 and .erefore these design recommendations are largely speculative at locations far from the ‹cavation.

Figure 4.8-4 presents FE predictions of settlement troughs in a form similar to .at in Figure 4.8-3. For OCR=1 case, MIT-E3 and MCC predictions are included. For IIT-E3 analysis, most of the settlement is predicted to occur within Zones I and II. The ıagnitude of settlement decreases rapidly beyond a distance d/H equal to 2.5. In the ICC analysis, there is no apparent decrease in settlements even beyond d/H=3.0.

For OCR=2 and 4 cases, very small settlements are predicted to occur. However, e magnitude of settlement doesn't show a substantial decrease beyond d/H=3.0.

A possible cause of the prediction of some settlements even at a large distance behind the excavation is the assumption of undrained conditions during excavation. If drainage is allowed, larger settlements will be predicted near the excavation, but smaller settlements will be predicted further away due to swelling (reduction of negative pore pressures in the far field).

Figure 4.8-5 presents a different normalization of settlement data versus the .stance behind the excavation as proposed by Clough and O'Rourke (1990). The :ttlement troughs predicted by the FE analysis are plotted in Figure 4.8-6 in a form milar to that in Figure 4.8-5. In the OCR=1 case, Figure 4.8-6a, MIT-E3 predictions .ve settlement troughs which show a better match of the envelope proposed in Figure 8-4 than those given by MCC. For the MIT-E3 analyses, the settlement troughs at =25m and 30m better match the envelope than troughs at H=15m.

For OCR=2 and 4 cases, Figure 4.8-6b and 6c, there is a significant mismatch :tween the proposed envelope and the predicted settlement troughs. The mismatch :creases with increasing excavation depth. The mismatch is most probably due to the iff undrained response assumed in the FE analysis.

Figure 4.8-7 presents measured data of maximum settlements versus excavation :pth. Clough and O'Rourke (1990) state that "for those cases with movements that fall

---

'eck (1969) presents a similar plot, inlay of Figure 4.8-3, based on case histories of excavations pported by sheet pile walls, or soldier beam and lagging walls.

ithin the scatter around 0.2%H trend line, it is notable that the data roughly follow a near relationship with depth. This suggests that the soil masses are behaving ɔproximately as elastic material." Predictions at OCR=2 and 4, Figures 4.6-12b and 3b, fit this observation well. For OCR=2 cases the magnitude of maximum settlements ıges between 0.08%H and 0.16%H and for OCR=4 it ranges between 0.05%H and .11%H.

Figure 4.8-8 presents a plot of measured normalized maximum settlements versus

ıaximum wall movements. The figure shows that the ratio $\frac{\delta_v}{\delta_H}$ ranges between 0.5 and .0. Figure 4.8-9 presents a similar plot of the FE predictions. At all OCR values

ɔnsidered, $\frac{\delta_v}{\delta_H}$ is approximately equal to 0.5. At large deformations the ratio approaches .0 for OCR=1 analysis. The ratio predicted by the FE analysis is, in general, smaller ıan that reported in Figure 4.8-8. A possible reason for this behavior is that the FE ıalyses are performed under undrained conditions. If drainage is allowed, further settlement will occur due to consolidation in the retained soil (e.g., Appendix C).

4.8.3. Wall Deflection and System Stiffness

Peck (1969) proposes that the maximum wall movement depends approximately ı the support spacing magnitude raised to the fourth power (based on simply supported : cantilever beam bending theory). Clough et al (1990) extend this concept further and ɔrmalize it in the form of a chart that describes the dependency of maximum deflections ı the vertical support spacing h (Figure 4.8-10). The chart relates the maximum wall eflections to the support system stiffness and the factor of safety against basal heave. he chart is characterized by the following:

1. The chart combines the effect of the support spacing, h, and the wall stiffness, EI, into one factor called the system stiffness ($EI/\gamma_w h^4$). The h^4 factor is based on simply supported or cantilever beam bending theory.
2. The deformations are dependent on the factor of safety against basal heave (FSBH) using Terzaghi's (Figure 4.4-13) base heave calculation. Lines of equal FSBH values, therefore, represent lines of equal excavation depths.
3. The figure is divided into two main regions, one for excavations supported by sheet pile walls and another for excavations supported by concrete diaphragm walls.

The analyses in this study focus on excavations supported by diaphragm walls with constant EI. The main variables considered are the wall length, the vertical support spacing and the soil profile. The framework presented in Figure 4.7-1 integrates the effect of wall and soil failure on excavation response with the effect of vertical support spacing on maximum deformations. The analyses identify two failure mechanisms including basal heave and development of a slip zone in the retained soil. A direct comparison between results of this study and Figure 4.8-10 is not easy to present.

Figure 4.8-11 is generated using some of the FE predictions from this study. Data are presented at OCR=1, 2 and 4. For OCR=1 case, data at a given excavation depth are joined together by a solid line that would represent a line of 'constant FSBH' regardless of its actual magnitude[1]. For OCR=2 and 4 cases $\frac{\delta}{H}$ is constant for a given system stiffness (i.e., support spacing h) and independent of the excavation depth (i.e., FSBH).

The trends in the FE predictions, Figure 4.8-11, are similar to those given in Figure 4.8-10. However, there are other trends in the FE predictions that do not agree with this chart:

1. Section 4.4 shows that failure is dependent on the wall length. This aspect is not taken into account in the FSBH calculation used in Figure 4.8-10. Therefore, FSBH, in this context, is only an index measure and does not represent actual failure in the system. The FE analyses show that basal heave failure is not the only mechanism of failure, development of a shear zone in the retained soil as well as wall failure especially for long wall can be the dominant failure mechanisms.
2. The FE predictions, Equation 4.7-1, show a different dependency on the vertical support spacing h. The h^4 dependency included in the system stiffness factor, Figure 4.8-10, is based on simply supported or cantilever beam bending theory and does not consider the development of movements with increasing excavation depth.
3. The resolution provided in Figure 4.8-10 for concrete diaphragm walls is not sufficient to capture the variations in deformations predicted in this study. Figure 4.7-1 is a more suitable framework for interpreting deformations predicted from the analyses in this study.

[1] Section 4.4 describes the uncertainty in evaluating FSBH.

4.9. Soil Deformations for a Layered Profile of Boston Blue Clay

The discussion in Sections 4.3 to 4.8 has focused on excavations in a soil deposit with a constant overconsolidation ratio throughout the deposit. However, in excavations for the Central Artery/Tunnel (CA/T) and the Taipei Rapid Transit (TRT) the soil profile has a nonuniform OCR value. Realistic profiles of practical interest comprise a deep layer of normally (or lightly overconsolidated) consolidated clay overlain by a desiccated crust of overconsolidated clay (OCR>1) or other fill material.

Extensive geotechnical investigations for the CA/T project have included a comprehensive in-situ and laboratory testing program at two representative sites. Figure 4.9-1a shows the soil profile at one one of these sites in South Boston (Estabrook 1991). A variety of laboratory tests were performed at MIT on soil samples from this site to characterize the soil stress-strain-strength properties (Estabrook, 1991, and de la Beaumelle, 1991). Figure 4.9-1b shows that the upper part of the clay is overconsolidated and that the lower part is nearly normally consolidated. Figure 4.9-1c shows a plot of the measured undrained shear strength in triaxial compression in the marine clay (Boston Blue Clay) from a variety of test procedures. The data shows that the strength of the material decreases with increasing depth.

The undrained shear strength in triaxial compression for the three OCR profiles used in this study are superimposed on the measured strength profile at the South Boston Test Site (Figure 4.9-1b), assuming that the clay layer extends to the ground surface. This section describes a series of FE analyses using a 'combined' soil profile (OCR=C profile) which is chosen based on the measured strength profile (Figure 4.9-1b). The C-profile is idealized as a clay deposit made up of three layers with different magnitudes of OCR: 1) a 15m deep layer of clay with OCR=4, 2) a 10 m layer of OCR=2 and 3) a deep layer of normally consolidated clay (OCR=1). The thickness of the overconsolidated layers is chosen such that the FE model strength profile approximately matches that measured at the test site. Boston Blue Clay properties obtained from tests on resedimented BBC are used in the MIT-E3 model.

The idealized C-profile and soil properties used in this section do not describe accurately the actual conditions at the South Boston test site for the following reasons:

1. The clay layer in the model is assumed to be very deep (120m). The actual profile in Figure 4.9-1a includes glaciomarine deposits at a depth 45m below ground surface.
2. The C-profile assumes that the clay layer extends to the ground surface. In reality, fill and marine sand overlie the clay to a depth of 10m below ground

surface.

3. The measured shear strength profile can be better modelled assuming a soil profile with OCR value decreasing continuously with depth.
4. The measured stress-strain-strength properties of the clay at the test site show significant deviations from those of resedimented BBC (Estabrook, 1991). Thus further refinement of MIT-E3 input parameters is necessary to describe this material.

The analyses in this section are performed, using the combined profile, in order to extend the concepts developed in Sections 4.3 to 4.7 for a nonuniform soil profile while still maintaining as much simplicity as possible in the model[1]. These analyses will pave the way for future research specifically related to the CA/T and TRT projects.

4.9.1. Wall Deflections and Surface Settlements

Figure 4.9-2 compares predictions of wall deflections and surface settlements for the combined soil profile and OCR=1 analyses at a support spacing h=2.5m (L=60m, h_u=2.5m)[2]. In the OCR=1 analysis failure occurs beyond 30m; while the combined profile (OCR=C) failures beyond H=32.5. The mode of development of wall deflections and surface settlements are similar in both analyses. At early excavation stages (H≤20m), wall deflections in the OCR=C analysis (Figure 4.9-2c) are smaller than those in the OCR=1 analysis (Figure 4.9-2d) due to the presence of the stiff OCR=2 and 4 layers. Beyond H=20m, the movements quickly accelerate but remain smaller in magnitude than those in the OCR=1 analysis.

Settlement troughs for the two analyses, Figure 4.9-2a and 2b, are similar in distribution, although the C-profile predicts smaller settlements at a given excavation depth.

Figure 4.9-3 shows plots of maximum deformations and moments for OCR=1, 2, 4 and C analyses (using L=60m, h=2.5m, h_u=2.5m). Initially, maximum wall deflections for the OCR=C analysis (Figure 4.9-3a) are practically identical to those for OCR=4 analysis. As the excavation depth increases, maximum deflections increase rapidly and follow a curve parallel to that for the OCR=1 analysis. Similar observations can be made for surface settlement (Figure 4.9-3b) and excavation heave curves (Figure 4.9-3d) and to a limited extent for maximum moment curves (Figure 4.9-3c).

Figure 4.9-3 shows that, at small excavation depths, the soil and wall response

---

[1]This simplicity is required to keep a measure of 'intellectual' control on the model.
[2]The relevant analyses are stc_60_02 and st1_60_02.

are similar to that for OCR=4 profile analysis. At larger excavation depths, the response resembles that in an OCR=1 profile.

Figure 4.9-4 presents plots of lateral stresses acting on both sides of the wall. Above the excavation level in the retained soil, the predicted stresses are larger than those corresponding to Rankine active stresses but are almost equal to the initial in-situ stresses. The larger stresses are a result of the development of a passive wedge described previously (Section 4.3.3). Inside the excavation, lateral stresses are smaller than the initial in-situ stresses.

4.9.2. Effect of Vertical Support Spacing

A series of analyses is performed in the OCR=C profile using L=60m wall and values of h=0, 2.5, 5 and 10m[1]. Figure 4.9-5 shows plots of maximum deflections and moments for the four h values considered. The effect of h on maximum deformations and moments is similar to that observed in the OCR=1 analysis (Figure 4.5-3). The magnitude of deformations and moments increases with increasing magnitude of h.

Large moments develop in the wall for all values of the support spacing (Figure 4.9-5c, M_{max}>1.0 MN-m/m), indicating the potential for structural failure of the diaphragm wall.

4.9.3. Effect of Wall Length

A series of analyses is performed using the C-profile with a support spacing h=10m, and wall lengths L=60m, 40m, 20m and 12.5m[2]. Figure 4.9-6 summarizes maximum deformations and moments for the four wall lengths considered. The last excavation depth prior to failure for L=60, 40 and 20m walls is 20m. No failure is detected in the L=12.5m analysis (In this case the entire excavation is performed in the OCR=4 material).

Figure 4.9-6 shows that wall length has no significant effect on prefailure deformations and thus similar to observations at OCR=1, 2 and 4.

4.9.4. Framework for Interpreting Deformations

Figure 4.9-7 summarizes the numerical predictions of wall deflections in a format similar to that given in Figure 4.7-1a. For excavation depths less than 20m there is no failure of the excavation and hence no toe embedment is necessary for (undrained)

---

[1]The relevant analyses are stc_60_00, stc_60_02, stc_60_05 and stc_60_10.
[2]The relevant analyses are stc_60_10, stc_40_10, stc_20_10 and stc_12_10.

stability. Contours of maximum moments show that excessive bending in the wall is the most critical design condition for long walls and lightly braced walls.

The procedure described in Section 4.7.2 for estimating the constants of equation 4.7-1 has been applied to OCR=C analyses. The equation is calibrated using results from h=0m and 5m analyses. Figure 4.9-8 shows a comparison of maximum deformations obtained from Equation 4.7-1 with those from FE analyses. Predictions of maximum wall deflections, Figure 4.9-8a, for h=10m analysis match FE results. Predictions of deflections for h=2.5m case initially match FE results but underpredict deflections at larger excavation depths as the excavation approaches failure. Similar observations can be made for maximum settlements, Figure 4.9-8b, and excavation heave (Figure 4.9-8c) for which the constants a and b are equal to zero.

4.9.5. Summary

This section has summarized a series of analyses performed on an idealized profile of the South Boston test site for the CA/T project (Figure 4.9-1). The analyses show the mechanisms of development of soil movement obtained from constant OCR profiles (Sections 4.3 to 4.6) are also observed for a combined profile in which the OCR decreases with depth. For an excavation depth H>15m, the soil behavior is similar to that for an OCR=1 profile (Figure 4.9-3), while at shallower excavation depths the behavior resembles the behavior reported previously for overconsolidated clays. The framework proposed in Section 4.7 represents an adequate description of the behavior observed in the OCR=C analyses (Figures 4.9-7,8) and hence can be used to interpret deformations for more complicated soil profiles.

4.10. Discussion and Summary of Results of the Numerical Study

At the outset of this chapter, the main aim of this research was to characterize excavation response in deep deposits of soft clay. The task was primarily motivated, as indicated, by deep excavations for the Central Artery/Tunnel project (CA/T) in Boston and the Taipei Rapid Transit system (TRT) in Taiwan. There was little guidance in the published literature related to designing such deep excavations. The primary task in this chapter was to design a numerical study with a limited, but relevant, number of parameters to gain an understanding of the fundamentals of deep excavation behavior in soft clays.

This chapter has described an extensive series of numerical experiments, designed to develop a fundamental understanding of the behavior of braced, diaphragm-wall-

supported excavations in deep layers of clay. The experiments focus on a limited number of parameters, while maintaining sufficiently realistic conditions, such that the results can have practical application (Section 4.2).

The main parameters considered in the study are a) the effect of soil modelling, b) wall length, c) the support spacings and d) soil stress history. The analyses assume undrained conditions throughout the construction process. The study does not consider several other parameters such as (partial) drainage, wall thickness, excavation width and support compressibility.

A detailed examination of the results of the numerical analyses shows the following:

1. Section 4.3 describes predictions of excavation performance using three soil models, MIT-E3, MCC and Linear Elastic, for a normally consolidated (OCR=1) soil profile. At the element level, MIT-E3 gives a superior prediction of clay response compared to either MCC or Elastic model predictions (Figure 4.3-3, 4). The analyses show that excavation response using the MCC and Elastic models is similar. The analyses show that MIT-E3 gives a more accurate and realistic prediction of deformation patterns, particularly surface settlements (Figure 4.8-4, 5) and describes the development of failure for deep excavations (not observed in the MCC analysis).
2. Wall length and hence embedment appears to have a very limited impact on pre-failure deformations in an excavation (Sections 4.4, 4.6.4 and 4.9.3, Figure 4.4-3,4.4-7,4.6-16). However, wall length affects the failure depth of the excavation (OCR=1 and C analyses). Failure mechanisms observed for OCR=1 soil profile include basal heave mechanism for short to medium walls (Figure 4.4-8,9), and a deep seated shear surface for long walls (Figure 4.4-10,11). Basal heave calculations (Figure 4.4-13, Equation 5), which incorporate wall length effect, give good estimates of the safety factor for shallow walls ($L \leq 20m$) but do not predict collapse for long wall embedments.
3. The support spacing has a very significant impact on predicted deformations (all OCR values) and failure (OCR=1 and C, Section 4.5, Section 4.9, Figure 4.5-3, 4.6-13, 4.6-14, 4.9-5) and controls the 'basic system response' (Figure 4.5-14, 4.6-15). The initial unsupported excavation depth has only a 'transient' effect on the 'basic system response' (Figure 4.5-14, 4.6-15). The 'transient' effect may produce large deformations in shallow excavations.
4. The soil stress history has a major impact on predicted deformations and failure (Sections 4.5 and 4.9, Figure 4.9-3). As the OCR increases, the magnitudes of

deformations reduce significantly and failure mechanisms do not develop even for very deep excavations (for OCR=2 and 4 analyses). For a combined soil profile (OCR value decreasing with depth), wall movements are significantly influenced by deep seated movements in the clay which are controlled by soil properties below the current excavation depth.

5. The analyses predict large total lateral stresses acting against the wall behind the excavation. The stresses are in some cases equal to or larger than the initial in-situ total lateral stresses. The large stresses are related to the development of a passive wedge in the retained soil above the excavation level. This wedge is associated with reversal in loading direction for soil elements in that region and has been largely ignored in the literature (an exception is Lambe and Whitman, 1969). Total vertical stresses in this wedge are generally smaller than the initial in-situ stresses due to the development of shear stress along the back of the wall.
6. Section 4.8 presents comparisons of some of the results and trends from the FE analyses with published observations of excavation behavior. Predicted apparent earth pressure diagrams, Figure 4.8-2, compare well with empirical envelopes proposed by Peck (1969). Predicted settlement troughs fall within the range of observed settlements reported in the literature (Figure 4.8-4).
7. The trends observed in the analyses are summarized in a simplified framework that accounts for different failure modes in the excavations (Figure 4.7-1, 4.9-7). In addition to soil failure, the framework includes estimates of structural failure of the diaphragm wall which is a significant factor for excavations with long walls or walls which are lightly braced. The framework can be used to estimate/interpret deformations for a wide range of support conditions and wall lengths (The framework is applicable quantitatively for the 0.9m thick diaphragm wall considered in this study). A simple equation (Equation 4.7-1) is proposed to describe the trends observed for maximum movements and a procedure is described that may be helpful in reducing the number of FE analyses required for a given case study (Figure 4.7-2,3,4, 4.9-8).

The results of the numerical experiments have some significant practical implications that should be considered in the design of deep excavations in soft clays:

1. Wall embedment has a very limited impact on pre-failure deformations, but has a large effect on excavation stability (for OCR=1,C, Figure 4.4-3). This implies that during the construction of an excavation, measurements of deformations may not give a clear warning of possible failure in the system. In addition deformations observed at early excavation stages do not necessarily give an

indication of movements at later excavation stages (See for example the transient effects observed in Section 4.5.2, Figure 4.5-3, or the early movements observed in the OCR=C analysis, Section 4.9). Therefore, care should be used in extrapolating deformation data and in adjusting predictions of movements based on early excavation behavior. The observational method (Peck, 1969) is still a very important tool for monitoring excavation performance. However, the study emphasizes the need for good in-situ characterization of soil properties in order to make reliable predictions of ground movements.

2. The conventional factor of safety against basal heave does not represent fully the failure modes observed in the FE analyses. The basal heave mechanism is valid for short and medium well supported walls (Figure 4.4-14).
3. The wall and support system may need to be designed to withstand large lateral stresses. In the analyses, a passive wedge with stresses equal to or higher than in-situ stresses is predicted in the retained soil (Figure 4.6-12). Stresses equal to or higher than the initial in-situ stresses have been measured in the retained soil of some excavations in soft clays (e.g., Aas 1984).
4. Extensive site characterization is required to predict accurately excavation response. Conventional triaxial compression and extension tests do not characterize the stress paths experienced by soil elements during excavation. The analyses have shown clearly the importance of modelling complex aspects of soil behavior including stress-strain response for a) reversals in stress paths, b)rotations of principal stresses, and c) non-linearity for shearing at small strain levels ($\gamma<0.1\%$).

4.11. References

Aas, G., 1984, "Stability Problems in a Deep Excavation in Clay." *Proc. Int. Conf. Case Histories in Geotechnical Engineering*, St. Louis, Vol. 1, pp. 315-323

Arthur, J.R.F. and Menzies, B.K., 1972, "Inherent Anisotropy in a Sand." *Géotechnique*, 22, No. 1, pp. 115-128.

Bjerrum, L. and Eide, O., 1956, "Stability of Strutted Excavations in Clay." *Géotechnique* VI, pp. 32-48.

Bolton, M.D., Powrie, W. and Symons, I.F., 1990a, "The Design of In-Situ Walls Retaining Overconsolidated Clay: Part I Short Term Behaviour." *Ground Engineering*, January/February, pp. 34-40.

Bolton, M.D., Powrie, W. and Symons, I.F., 1990b, "The Design of Stiff In-Situ Walls Retaining Clay: Part II, Long Term Behaviour." *Ground Engineering*, March, pp. 22-28.

Boscardin, M.D. and Cording, E.J., 1989, "Building Response to Excavation-Induced Settlement." *ASCE J. of Geotechnical Engrg.*, Vol. 115, No. 1, pp. 1-21.

Caliendo, J.A., Anderson, L.R. and Gordon, W.J., 1990, "A Field Study of Tiedback Excavation with a Finite Element Analysis." *Proc. ASCE Specialty Conf. on Design and Performance of Earth Retaining Structures*, pp. 747-763.

Christian, J.T. and Wong, I.H., 1973, "Errors in Simulating Excavation in Elastic Media by Finite Elements." *Soils and Foundations*, Vol. 13, No. 1, pp. 1-10.

Christian, J.T., 1989, "Design of Lateral Support Systems." *Design Construction and Performance of Deep Excavations in Urban Areas*, Boston society of Civil Engineers, Proc. of the 1989 Seminar at MIT, 31p.

Clough, G.W. and Hansen, L.A., 1981, "Clay Anisotropy and Braced Wall Behavior." *J. Geotechnical Division*, ASCE, GT7, pp. 893-913.

Clough, G.W. and Mana, A.I., 1976, "Lessons Learned in Finite Element Analyses of Temporary Excavations in Soft Clay." *Proc. 2nd Int. Conf. Numerical Methods in Geomechanics*, Blacksburg, VA., Vol. 1, pp. 496-510.

Clough, G.W. and O'Rourke, T.D., 1990, "Construction Induced Movements of Insitu Walls." *Proc. ASCE Specialty Conf. on Design and Performance of Earth Retaining Structures*, pp. 439-470.

Clough, G.W., Smith, E.M. and Sweeney, B.P., 1989, "Movement Control of Excavation Support Systems by Iterative Design." *Proc. ASCE Foundation Engineering Congress*, ASCE, Colorado Div., Evanston, Ill, pp. 869-884.

Clough, G.W., Weber, P.R., and Lamont, J., 1972, "Design and Observation of a Tied-Back Wall." *Proc. ASCE Spec. Conf. Performance of Earth and Earth-supported Structures*, Lafayette, Ind., Vol. 1, pp. 1367-1390

Davis, E.H., and Booker, J.R., 1973, "The Effect of Increasing Strength with Depth on the Bearing Capacity of Clays." *Géotechnique*, 23, No.4 , pp. 551-563.

De la Beaumelle, A., 1991, "Evaluation of SHANSEP Strength-Deformation Properties of Undisturbed Boston Blue Clay for Automated Triaxial Testing." *SM Thesis*, Department of Civil Engineering, MIT, 499p.

Desai,C.S., 1988, "Case Studies Through Material Modelling and Computation." *Case*

Histories in Geotechnical Engineering, Proc.2nd International Conference, Vol. II, pp. 1551-1565.

Estabrook, A.H., 1991, "Comparison of Recompression and SHANSEP Strength-Deformation Properties of Undisturbed Boston Blue Clay from Automated Triaxial Testing." *SM Thesis*, Department of Civil Engineering, MIT, 370p.

Finno, R.J. and Nerby, S.M., 1989, "Saturated Clay Response During Braced Cut Construction." *ASCE J. Geotechnical Engrg*, Vol. 115, No. 8, pp. 1065-1084.

Finno, R.J. and Harahap, I.S., 1991, "Finite Element Analysis of HDR-4 Excavation." *ASCE J. Geotechnical Engrg.*, Vol. 117, No. 10, pp. 1590-1609.

Foott, R., 1991, *Personal Communication.*

Germaine, J.T., 1982, "Development of the Directional Shear Cell for Measuring Cross-Anisotropic Clay Deposits." *ScD. Thesis*, Massacusetts Institute of Technology.

Goldberg, D.T., Jaworski, W.E. and Gordon, M.D., 1976, "Lateral Support Systems and Underpinning." *Report FHWA-RD-75-128*, Vol. 1, Federal Highway Administration, Washington, D.C.

GCO, 1990, "Review of Design Methods for Excavations," *Publication No. 1/90, Geotechnical Control Office,* Civil Engineering Services Department, Hong Kong, 192p.

Goto, S. and Iguro, M. 1989, "The World's First High Strength, Super Deep Slurry Wall." *Proc. 12th Int'l Conf. Soil Mech. Found. Engrg.*, pp. 1487-1490.

Hansen,L.A., 1980, "Prediction of the Behavior of Braced Excavation in Anistropic Clay." *PhD Thesis*, Stanford University, 379p.

Hubbard, H.W., Potts, D.M, Miller, D. and Burland, J.B., 1986, "Design of the Retaining Wall for the M25 Cut and Cover Tunnel at the Bell Common." *Propped and Cantlileverd Rigid Walls,* pp. 3-20.

Jardine, R.J., Potts, D.M., Fourie, A.B. and Burland, J.B., 1986, "Studies of the Influence of Non-Linear Stress-Strain Characteristics in Soil-Structure Interaction." *Géotechnique,* 6, No. 3, pp. 377-396.

Ladd, C.C., Bovee, R.B., Edgers, L. and Rixner, J.J., 1971, "Consolidated-Undrained Plane Strain Tests on Boston Blue Clay," *MIT Research Report R71-13*, Dept. of Civil Engrg., MIT, Cambridge, MA, 243p.

Ladd, C.C., 1991, *Personal Communication.*

Lambe, T.W., 1970, "Braced Excavations." *Proc. Spec. Conf. Lateral Stresses in the Ground and Design of Earth Retaining Structures,* Ithaca, N.Y., pp. 149-218.

Lambe, T.W. and Whitman, R.V., 1969, *Soil Mechanics,* John Wiley and Sons.

Mana, A.I. and Clough, G.W., 1981, "Prediction of Movements for Braced Cuts in Clay." *ASCE J.of Geotechnical Division,* Vol. 107, GT6, pp. 759-777.

Mulvey, L., 1991, *Personal Communication.*

O'Neill, D.A., 1985, "Undrained Strength Anisotropy of an Overconsolidated Thixotropic Clay." *SM Thesis*, Dept of Civil Engrg., MIT, Cambridge, MA, 359 p.

O'Rourke, T.D., 1981, "Ground Movements Caused by Braced Excavations." *ASCE J.of Geotechnical Division*, Vol. 107, No. GT9, pp. 1159-1178.

O'Rourke, T.D., 1989, "Predicting Displacements of Lateral Support Systems." Proc. Boston Society of Civil Engineers Seminar, *Design, Construction, and Performenace of Deep Excavations in Urban Areas*, MIT, Cambridge MA, 35p.

O'Rourke, T.D. and Jones, C.J.F.P., 1990, "OverView of Earth Retention Systems: 1970-1990" *Proc. ASCE Conf. on Design and Performance of Earth Retaining Structures,* Ithaca, NY, pp. 22-51.

Peck, R.B., 1969, "Deep Excavations and Tunneling in Soft Ground." *Proc. 7th Int. Conf. Soil Mech. Found. Engrg.*, Mexico City, State-of-the-Art Volume, pp. 225-290.

Potts, D.M., and Fourie, A.B., 1984, "The Behavior of a Propped Retaining Wall: Results of a Numerical experiment." *Géotechnique*, Vol. 34, No. 3, pp. 383-404.

Seah, T.H., 1990, "Anisotropy of Resedimented Boston Blue Clay." *ScD Thesis*, Dept. of Civil Engrg., MIT, Cambridge, MA, 1063p.

Stolle, D.F.E., 1989, "Pore Pressure Development in Moving Boundary Problems." *Soils and Foundations*, Vol. 29, No. 2, pp. 141-145.

Terzaghi, C., 1943, *Theoretical Soil Mechanics*, John Wiley and Sons.

US Steel, 1975, *Steel Sheet Piling Design Manual*, United States Steel133p.

Whittle, A.J., 1987, "A Constitutive Model for Overconsolidated Clays with Application to the Cyclic Loading of Friction Piles." *Sc.D. Thesis*, Dept. of Civil Engineering, MIT, Cambridge, MA., 641p.

Whittle, A.J., 1990, "A Constitutive Model for Overconsolidated Clays." *MIT Sea Grant Report, MITSG 90-15*, Cambridge, MA..

Wong, I.H., 1970, "The Prediction of the Performance of Braced Excavations." *Sc.D. Thesis*, Dept. of Civil Engrg, MIT, Cambridge, MA.

A. Activities Performed Separately of Excavation and Support[1]	
• Relocation of Utilities	• Deep Foundation Construction
• Dewatering	• Preaugering or Driving Soldier Piles
• Removal of Existing Basement	• Concrete Diaphragm Wall Construction
• Removal of Existing Piles	• Installation of Sheet Piles
B. Activities Integral to Excavation and Support	
• Preloading Struts, Rakers and Tiebacks	• Sequence of Excavation
• Connections Between Supports and Walls	• Time Between Excavation and Installation of Support
• Excavation Depth When First Level Supports Installed	• Installation of Lagging
• Depth of Excavation Beneath Lowest Support Level	• Augering or Percussive Drilling of Tiebacks
• Use of Berms	• Surcharge Loads Adjacent to Excavation

[1]In-situ wall installation generally is performed before the main excavation activity and installation of internal supports.

Table 4.2-1 Construction Activities Related to Ground Movements at Braced and Tied-Back Excavations (O'Rourke, 1989).

Test Type	Parameters/ Symbol	Physical Contribution/ Meaning	Boston Blue Clay
1-D Consolidation (Oedometer CRS, etc.)	e_0	Void ratio at reference stress on virgin consolidation line	0.957
	λ	Compressibility of virgin normally consolidated clay	0.184
	C	Non-linear volumetric swelling behavior	22.0
	n		1.6
	h	Irrecoverable plastic strain	0.2
K_0-oedomter or K_0-trixial	K_{0nc}	K_0 for virgin normally consolidated clay	0.53
	2G/K	Ratio of elastic shear to bulk modulus (Poisson's ratio for initial unload)	1.05
Undrained Triaxial Shear Tests	ϕ'_{TC}	Critical state friction angle in triaxial compression and	33.4^0
	ϕ'_{TE}	extension (large strain failure criterion)	45.9^0
OCR=1; CK_0UC	c	Undrained shear strength (geometry of bounding surface)	0.866
OCR=1; CK_0UE	S_t	Amount of post-peak strain softening in undrained triaxial compression	4.5
OCR=2; CK_0UC	ω	Non-linearity at small strains in undrained shear	0.07
	γ	Shear induced pore pressure for OC clay	0.5
Resonant Column*	κ_0	Small strain compressibility at load reversal	0.001
Drained Triaxial	Ψ_0	Rate of evolution of anisotropy (rotation of boundaing surface)	100.0

*Alternatively use field data from cross wave velocity type tests

(a)

Input Parameters for Boston Blue Clay using MCC model					
Parameter	e_0	κ	λ	ϕ'_{TC}	2G/K
Value	0.957	0.184	0.034	33.4^0	1.05

(b)

Table 4.2-2a,b Input Parameters, Initial State Variables, and Undrained Strength Ratios for Boston Blue Clay using the MIT-E3 and the MCC models (after Whittle 1987,1990).

		Initial Stresses		Initial State Variables		
				MIT-E3[2]		MCC
OCR	K_0[1]	σ'/σ'_{v0}	s_1/σ'_{v0}	α'/σ'_{v0}	a_1/σ'_{v0}	α'/σ'_{v0}
1	0.53	0.68	0.38	0.34	0.19	0.62
2	0.69	0.79	0.25	0.66	0.36	1.24
4	1.00	1.00	0.00	1.22	0.67	2.48

1 K_0 vs OCR predicted by MIT-E3 model.

2. Other variables: $\sigma_{rev}= \sigma$; $\alpha'_{rev}=\alpha'_{0i}=\alpha'$

All other state variables are initially zero.

(c)

OCR	MIT-E3				MCC
	S_{uPSA}/σ'_{v0}	S_{uDSS}/σ'_{v0}	τ_{DSS}/σ'_{v0}	S_{uPSP}/σ'_{v0}	S_{uPS}/σ'_{v0}
1.0	0.34	0.26	0.21	0.173	0.37
2.0	0.64	0.47	0.43	0.31	0.66
4.0	1.21	0.84	0.77	0.52	1.21

Reference Undrained Shear Strengths for BBC [$S_u=(\sigma_1-\sigma_3)/2$]

(d)

Model	Compressibility Parameter κ	Initial Undrained Modulus E_u/σ'_{vo}
Soft Elastic	0.034	71
Stiff Elastic	0.010	241.0
MCC	0.034	71
MIT-E3	0.001	2410

(e)

Table 4.2-2c,d,e Input Parameters, Initial State Variables, and Undrained Strength Ratios for Boston Blue Clay using the MIT-E3 and the MCC models.

Referene Number	Soil Model	OCR	L (m)	h (m)	h_u (m)	H_{max} (m) (F) Failure
st1_60_10	MIT-E3	1	60.0	10.0	2.5	20.0 (F)
st1_60_07	MIT-E3	1	60.0	7.5	2.5	22.5 (F)
st1_60_05	MIT-E3	1	60.0	5.0	2.5	25.0 (F)
st1_60_05a	MIT-E3	1	60.0	5.0	5.0	25.0 (F)
st1_60_02	MIT-E3	1	60.0	2.5	2.5	30.0 (F)
st1_60_00	MIT-E3	1	60.0	0.0	2.5	32.5 (F)
st1_60_00a	MIT-E3	1	60.0	0.0	5.0	32.5 (F)
st1_60_00b	MIT-E3	1	60.0	0.0	0.0	22.5
st1_40_10	MIT-E3	1	40.0	10.0	2.5	15.0 (F)
st1_40_02	MIT-E3	1	40.0	2.5	2.5	22.5 (F)
st1_20_10	MIT-E3	1	20.0	10.0	2.5	10.0 (F)
st1_20_02	MIT-E3	1	20.0	2.5	2.5	15.0 (F)
st1_12_10	MIT-E3	1	12.5	10.0	2.5	5.0 (F)
st1_12_02	MIT-E3	1	12.5	2.5	2.5	10.0 (F)
st1mcc_40_02	MCC	1	40.0	2.5	2.5	40.0
st1elas_40_02	Elastic	1	40.0	2.5	2.5	40.0
st1elas_40_02_stiff	Elastic (Stiff)	1	40.0	2.5	2.5	40.0
st2_60_10	MIT-E3	2	60.0	10.0	2.5	40.0
st2_60_07	MIT-E3	2	60.0	7.5	2.5	40.0
st2_60_05	MIT-E3	2	60.0	5.0	2.5	40.0
st2_60_02	MIT-E3	2	60.0	2.5	2.5	40.0
st2_60_00	MIT-E3	2	60.0	0.0	2.5	40.0
st4_60_10	MIT-E3	4	60.0	10.0	2.5	40.0
st4_60_07	MIT-E3	4	60.0	7.5	2.5	37.5
st4_60_05	MIT-E3	4	60.0	5.0	2.5	40.0
st4_60_05a	MIT-E3	4	60.0	5.0	5.0	40.0
st4_60_02	MIT-E3	4	60.0	2.5	2.5	40.0
st4_60_00	MIT-E3	4	60.0	0.0	2.5	40.0
st4_60_00a	MIT-E3	4	60.0	0.0	5.0	22.5
st4_60_00b	MIT-E3	4	60.0	0.0	0.0	22.5
st4_40_10	MIT-E3	4	40.0	10.0	2.5	40.0
st4_20_10	MIT-E3	4	20.0	10.0	2.5	20.0
st4_12_10	MIT-E3	4	12.5	10.0	2.5	10.0
stc_60_10	MIT-E3	C	60.0	10.0	2.5	20.0 (F)
stc_60_05	MIT-E3	C	60.0	5.0	2.5	25.0 (F)
stc_60_02	MIT-E3	C	60.0	2.5	2.5	32.5 (F)
stc_60_00	MIT-E3	C	60.0	0.0	2.5	35.0 (F)
stc_40_10	MIT-E3	C	40.0	10.0	2.5	20.0 (F)
stc_20_10	MIT-E3	C	20.0	10.0	2.5	20.0
stc_12_10	MIT-E3	C	12.5	10.0	2.5	10.0

OCR=C: Combined Profile of Boston Blue Clay (Section 4.9).

Table 4.2-3 List of Finite Element Analyses and Principal Parameters in the Numerical Experiments.

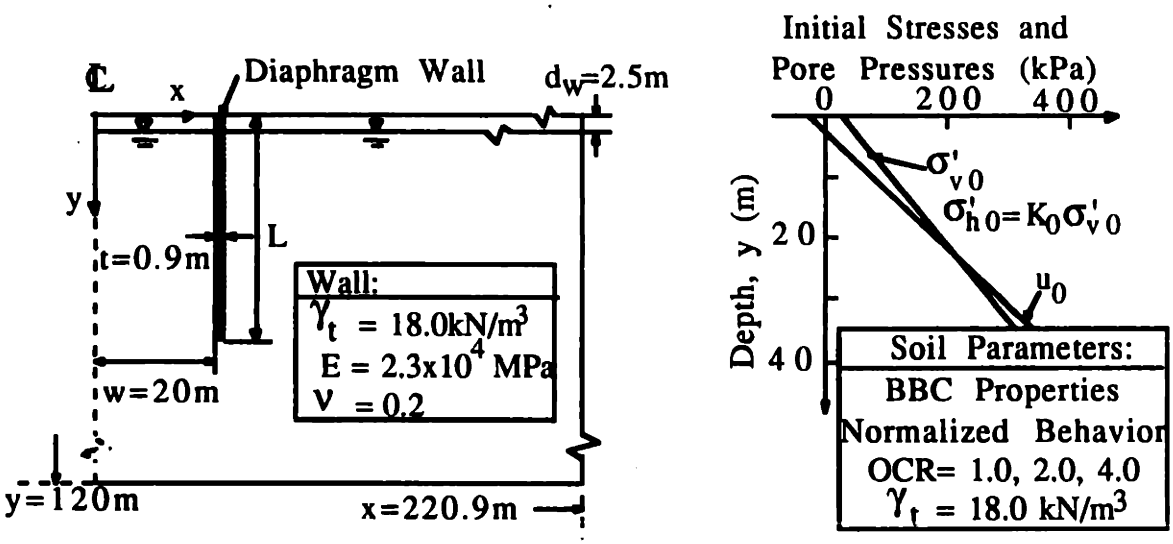

a) Nomenclature, Initial Conditions

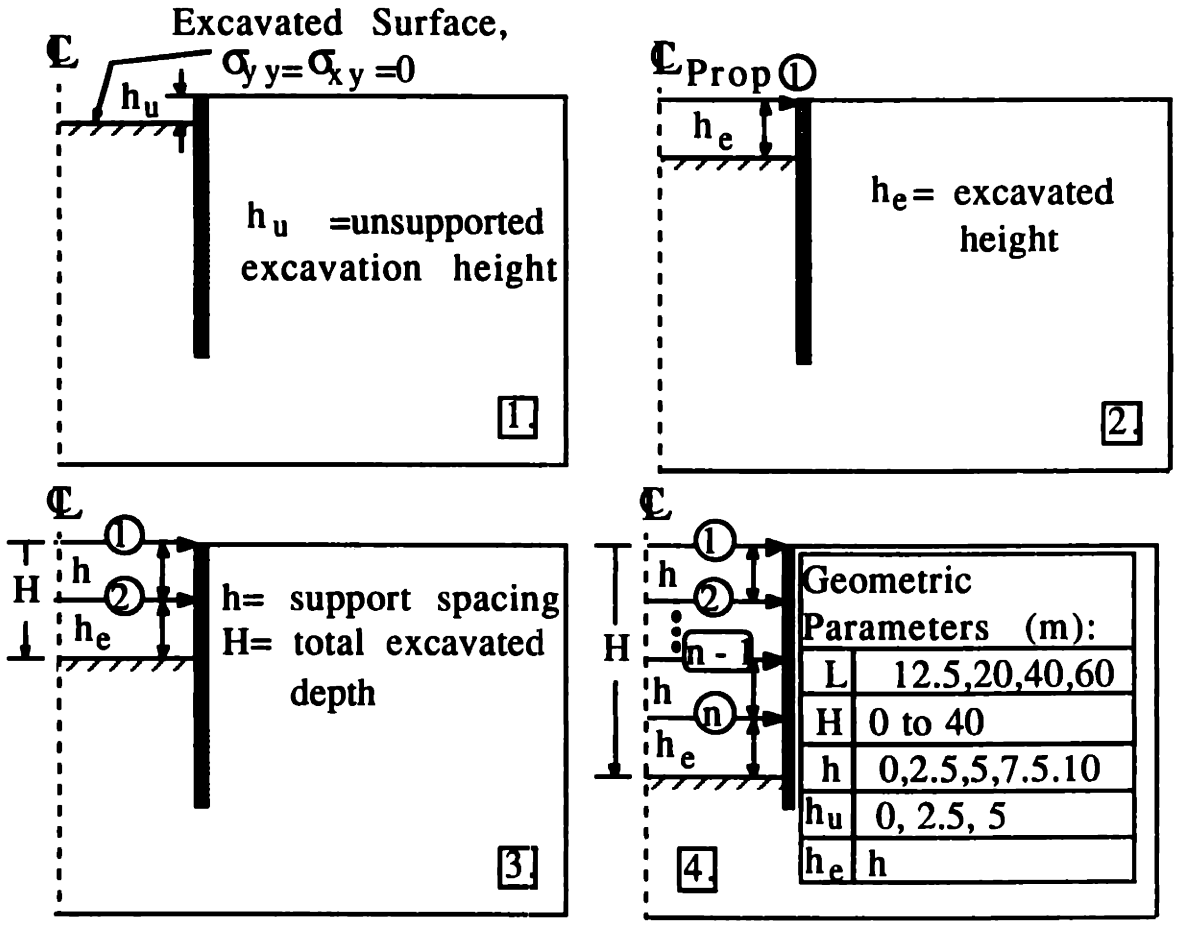

b) Excavation Sequence

Figure 4.2-1 Initial Conditions and FE Model Excavation Sequence

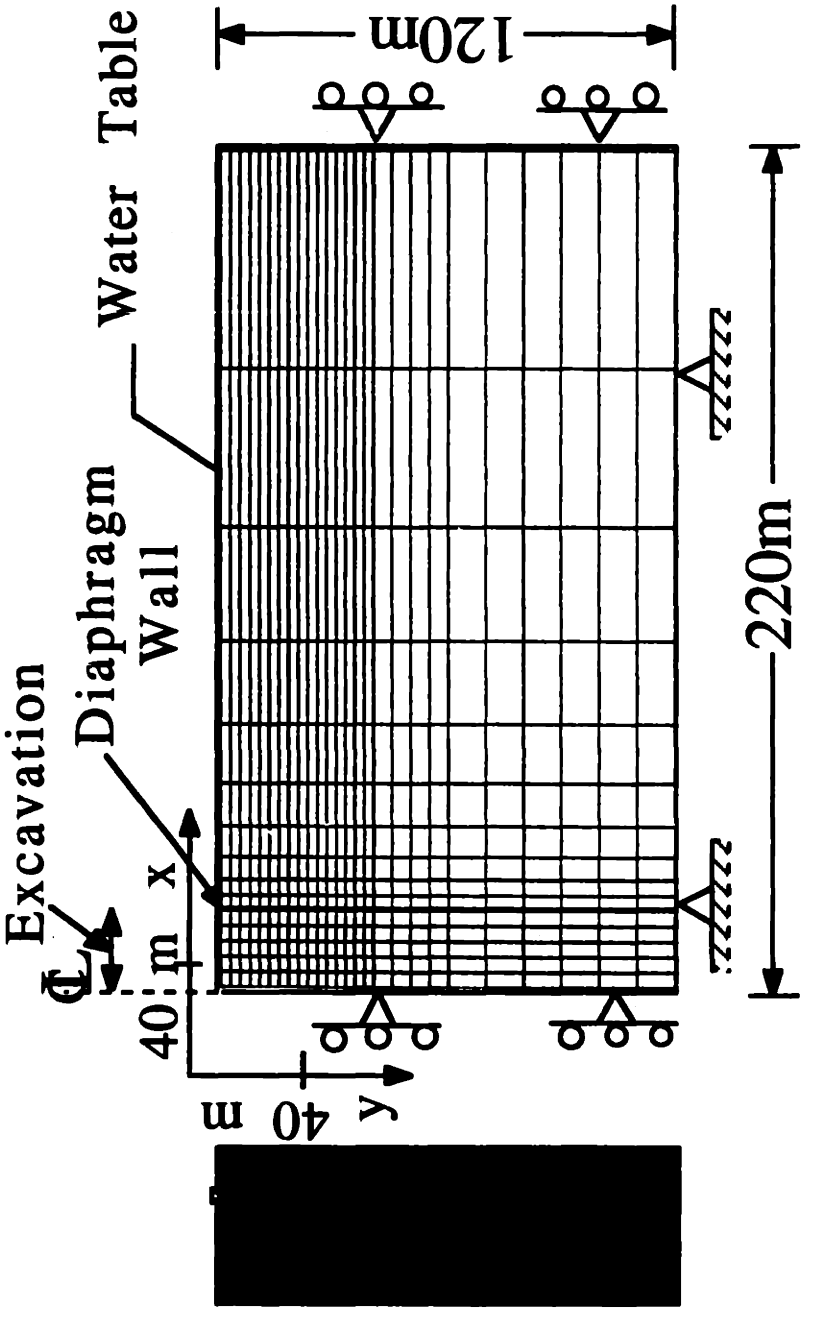

442 Elements, 1413 Nodes, 3292 Degrees of Freedom.

Figure 4.2-2 Finite Element Mesh and Boundary Conditions

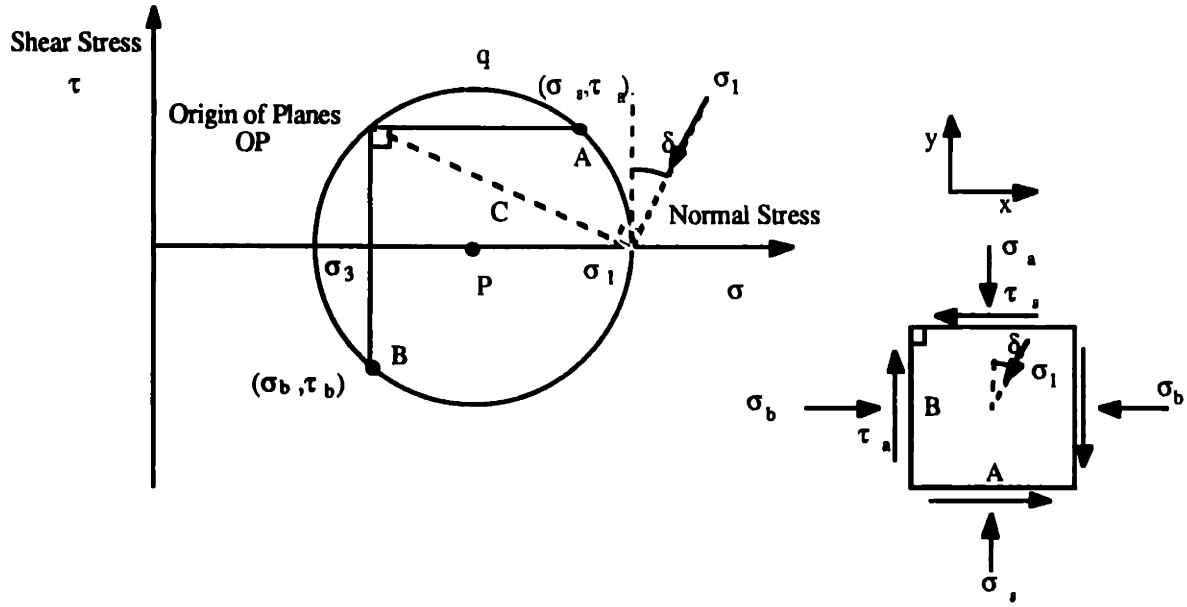

Figure 4.3-1 Mohr Circle of Stress in Directional Shear Cell with no Distortion Correction (Seah, 1990).

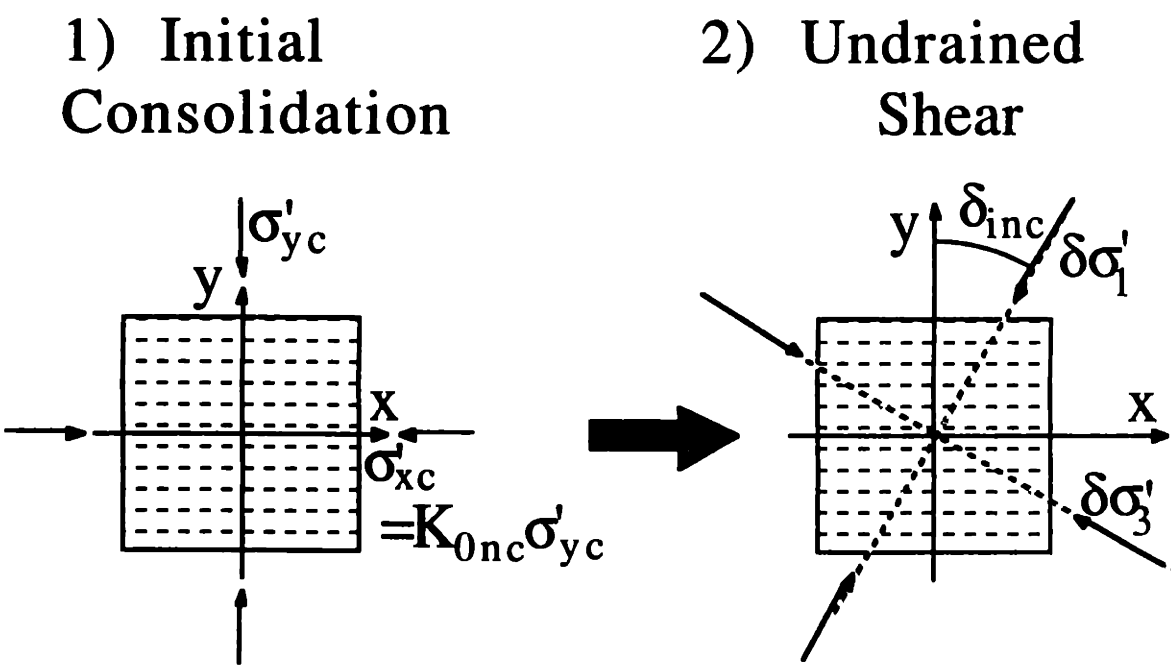

Figure 4.3-2 Directional Shear Cell Test Procedure

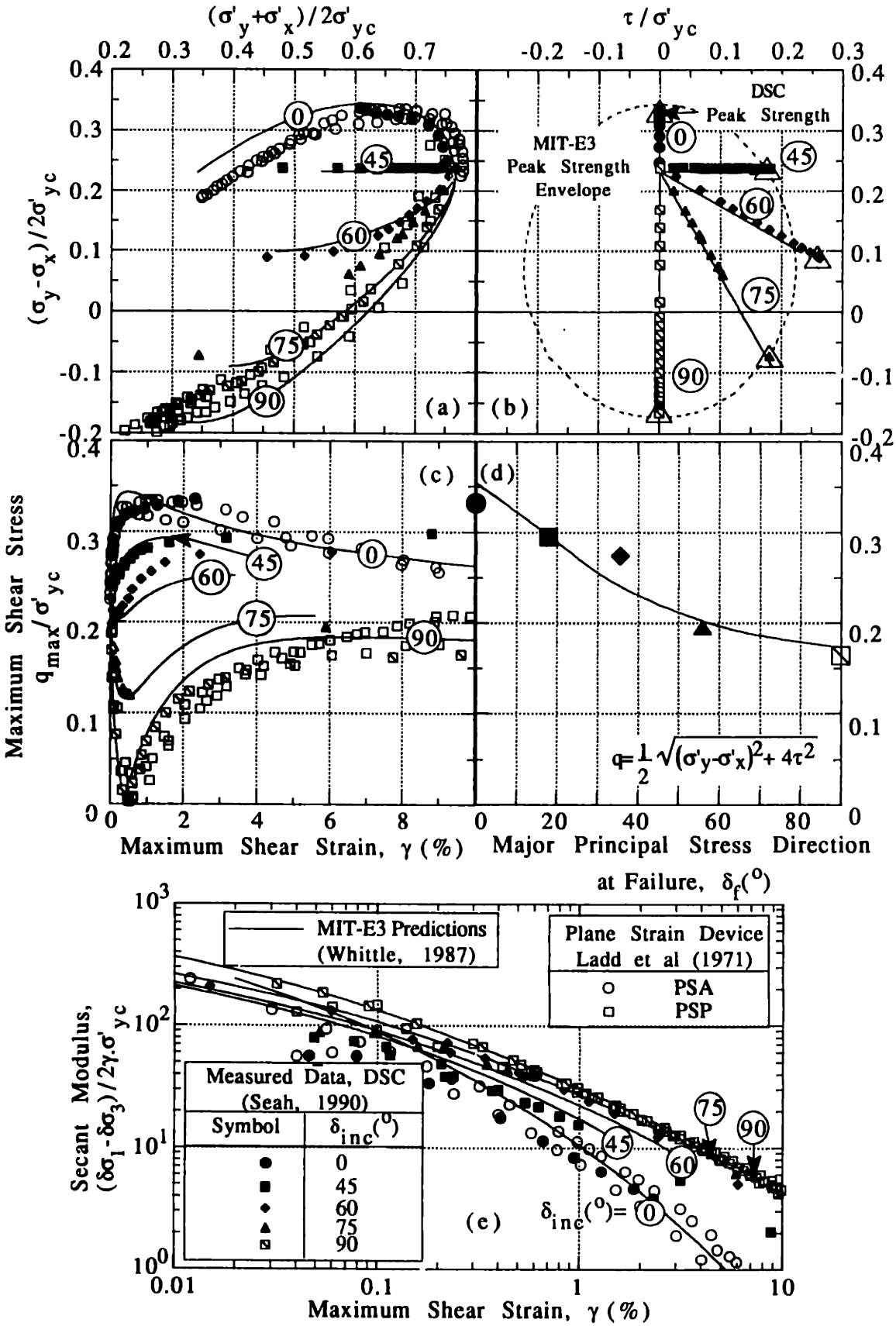

Figure 4.3-3 Measured Laboratory DSC Results versus MIT-E3 Model Predictions

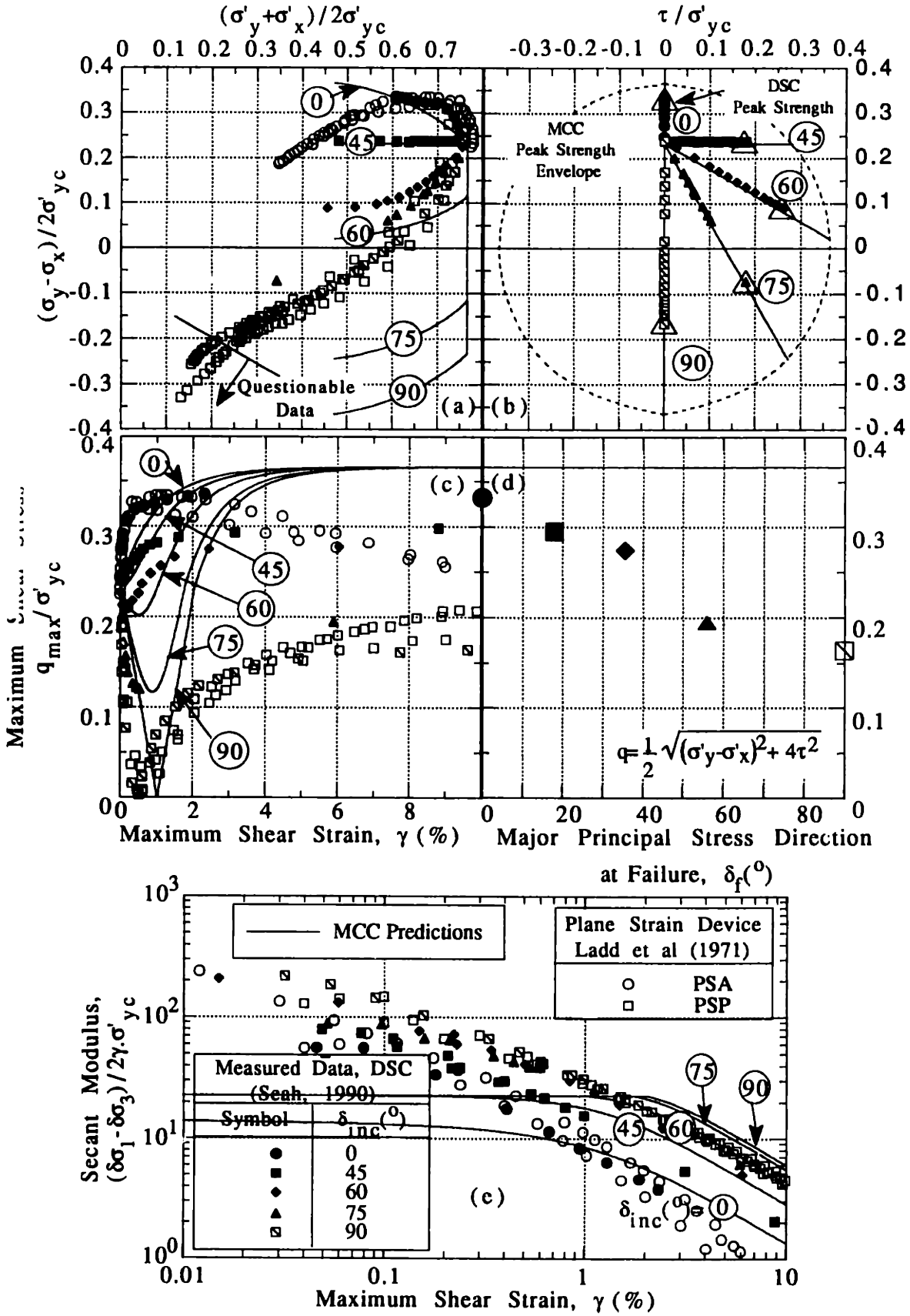

Figure 4.3-4 Measured Laboratory DSC Results versus MCC Model Predictions

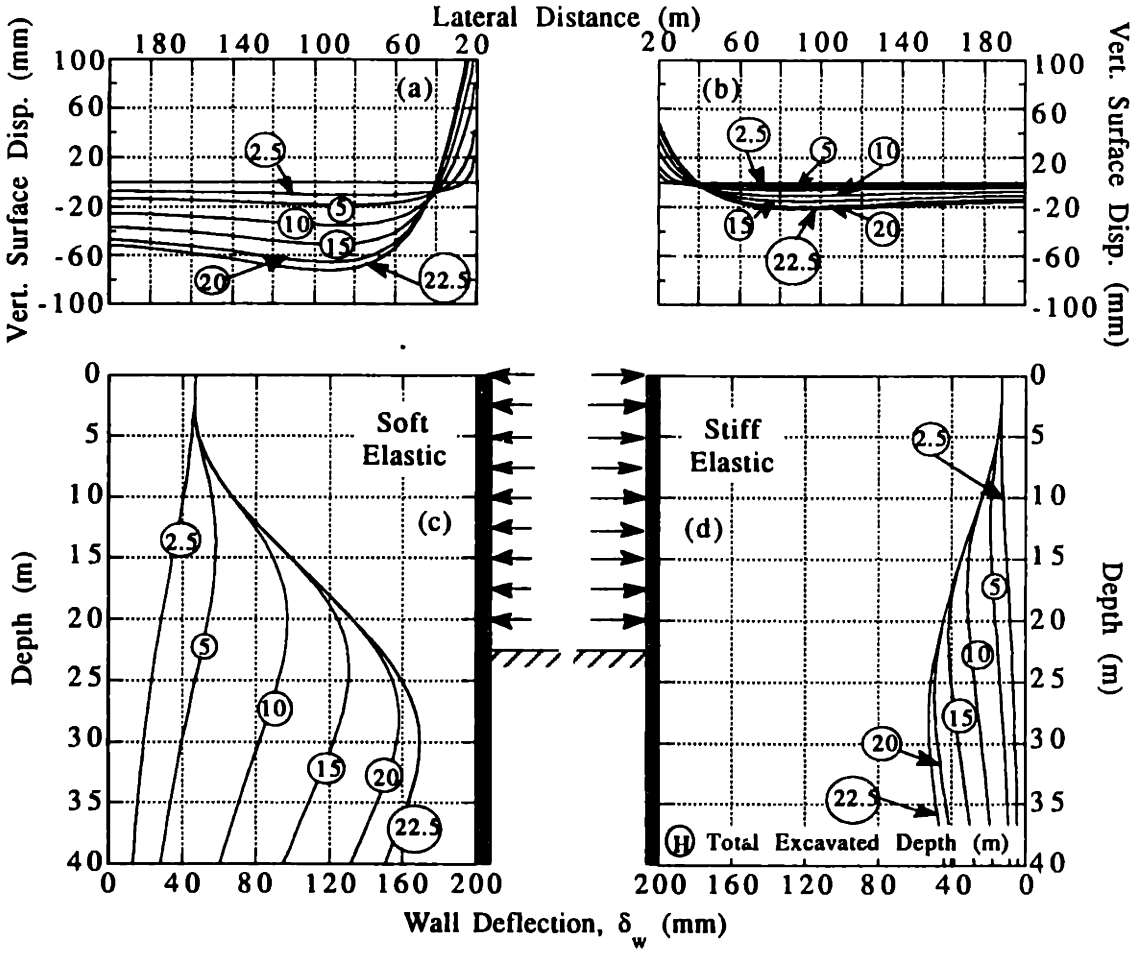

Figure 4.3-5 Comparison of Wall Deflections and Surface Settlements for Soft Elastic and Stiff Elastic Soil Models (h_u=2.5m, h=2.5m, L=40m, OCR=1)

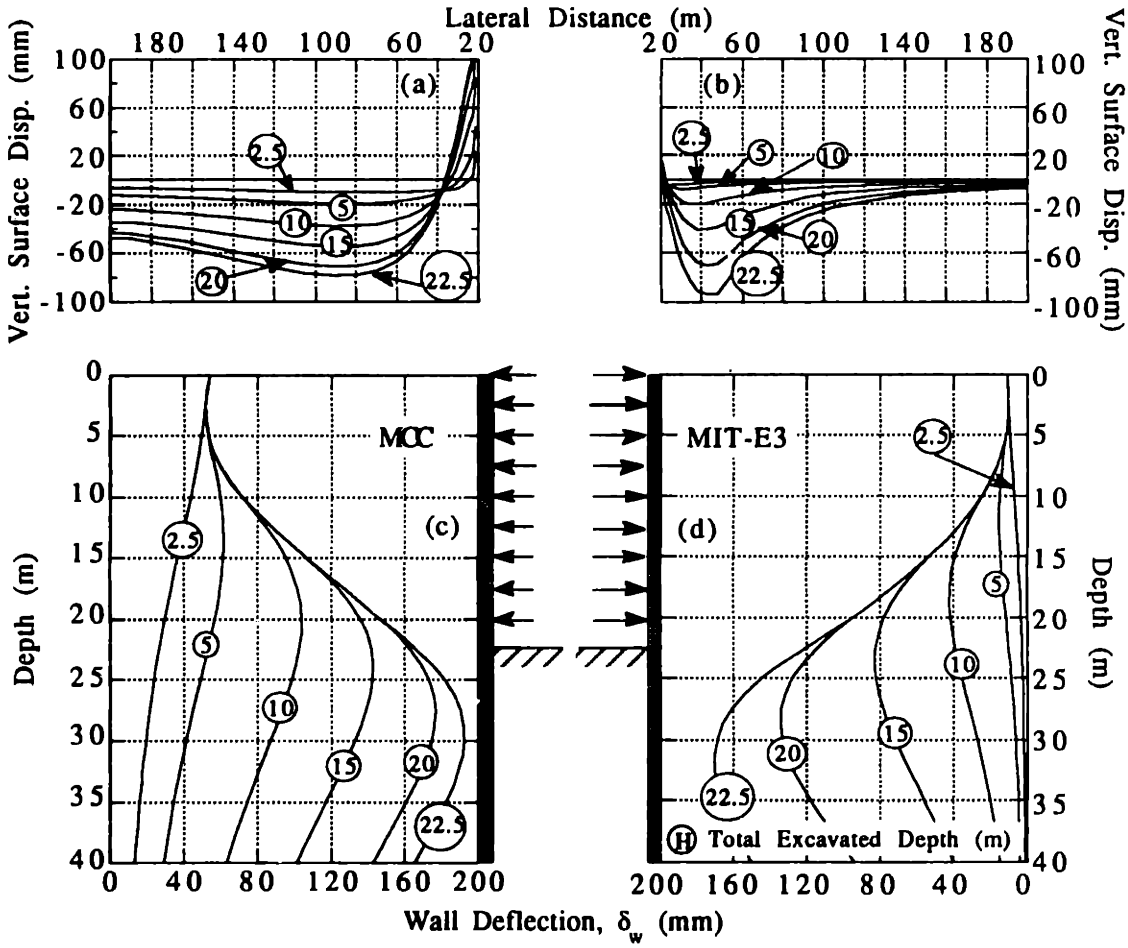

Figure 4.3-6 Comparison of Wall Deflections and Surface Settlements for MCC and MIT-E3 Soil Models (h_u=2.5m, h=2.5m, L=40m, OCR=1)

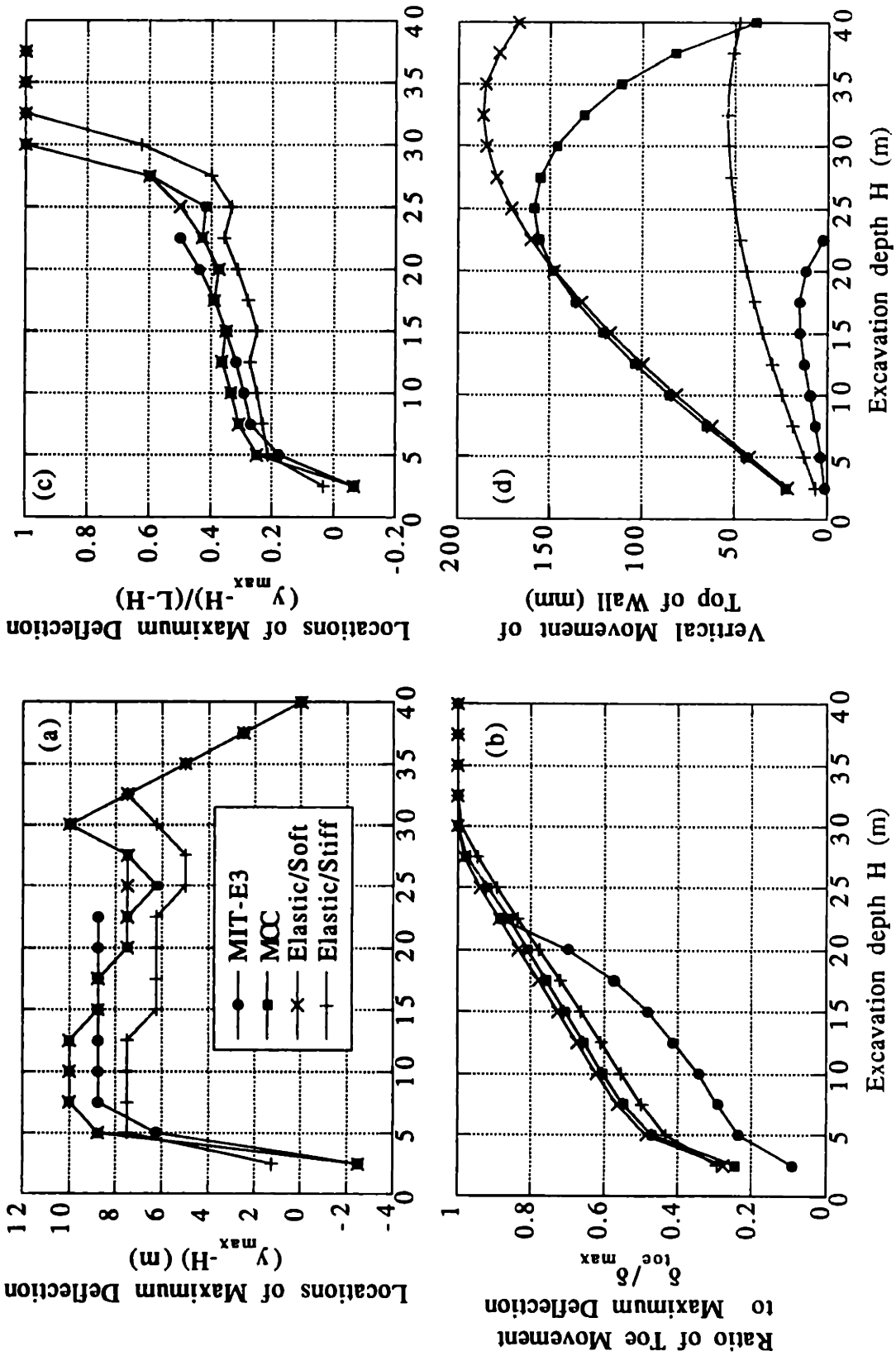

Figure 4.3-7 Effect of Soil Model on Key Wall Movements (h_u=2.5m, h=2.5m, L=40m, OCR=1).

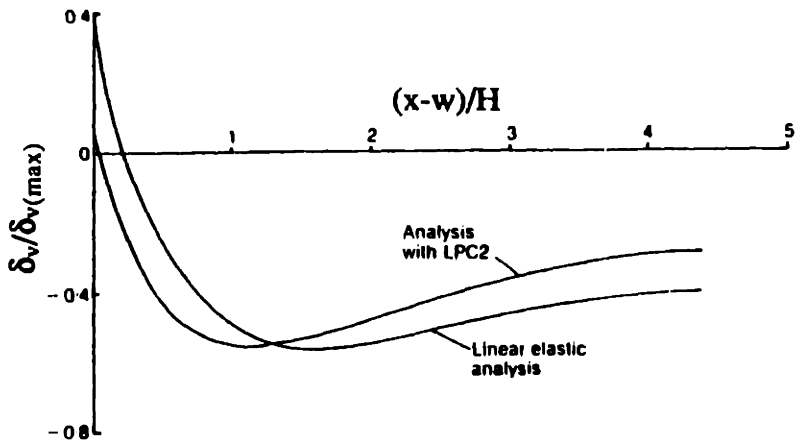

*LPC2 is a model with a small strain non-linearity formulation.

Figure 4.3-8 Vertical Displacement Profiles Adjacent to a Strutted Excavation (Jardine et al., 1988).

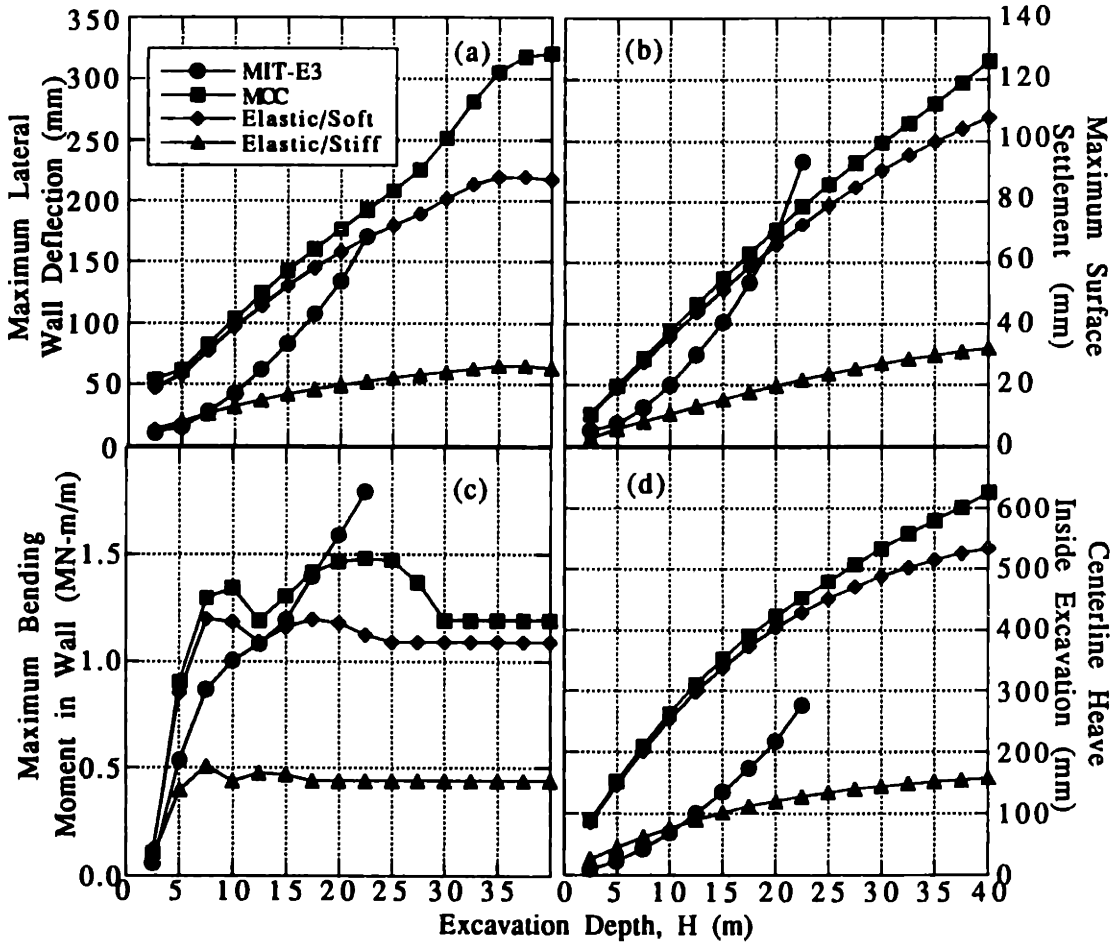

Figure 4.3-9 Effect of Soil Model on Maximum Deformations and Moments (h_u=2.5m, h=2.5m, L=40m, OCR=1).

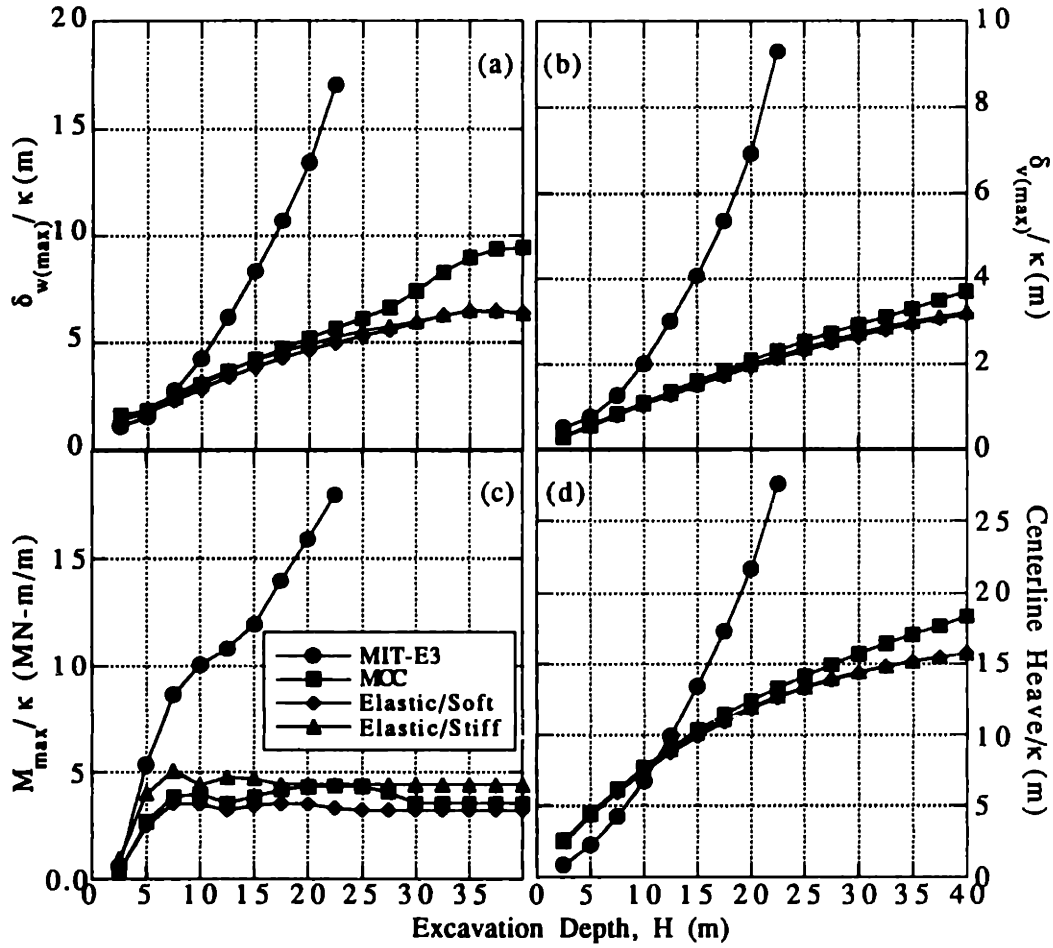

Figure 4.3-10 Effect of Soil Model on Normalized Maximum Deformations and Moments (h_u=2.5m, h=2.5m, L=40m, OCR=1).

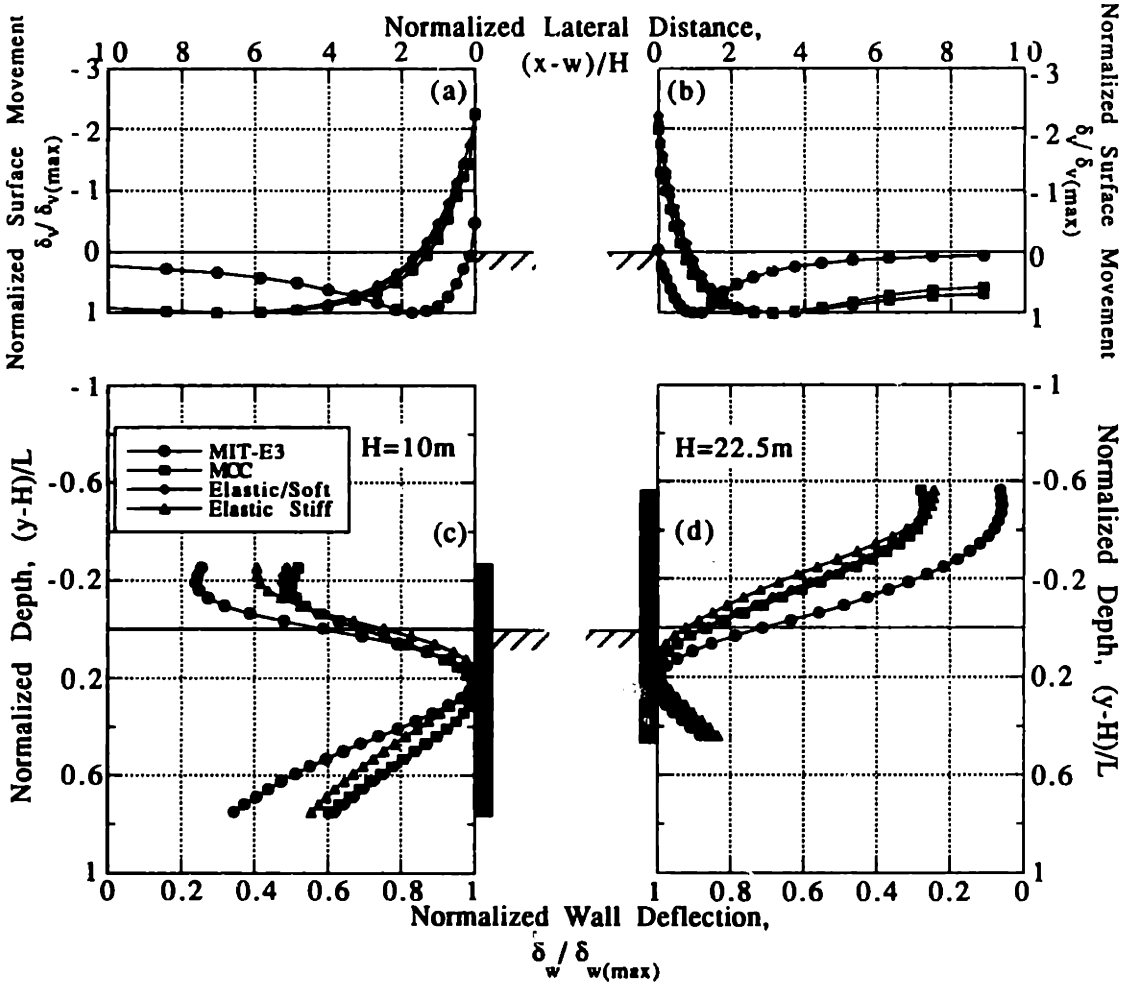

Figure 4.3-11 Effect of Soil Model on Normalized Wall Deflections and Surface Settlements (h_u=2.5m, h=2.5m, L=40m, OCR=1).

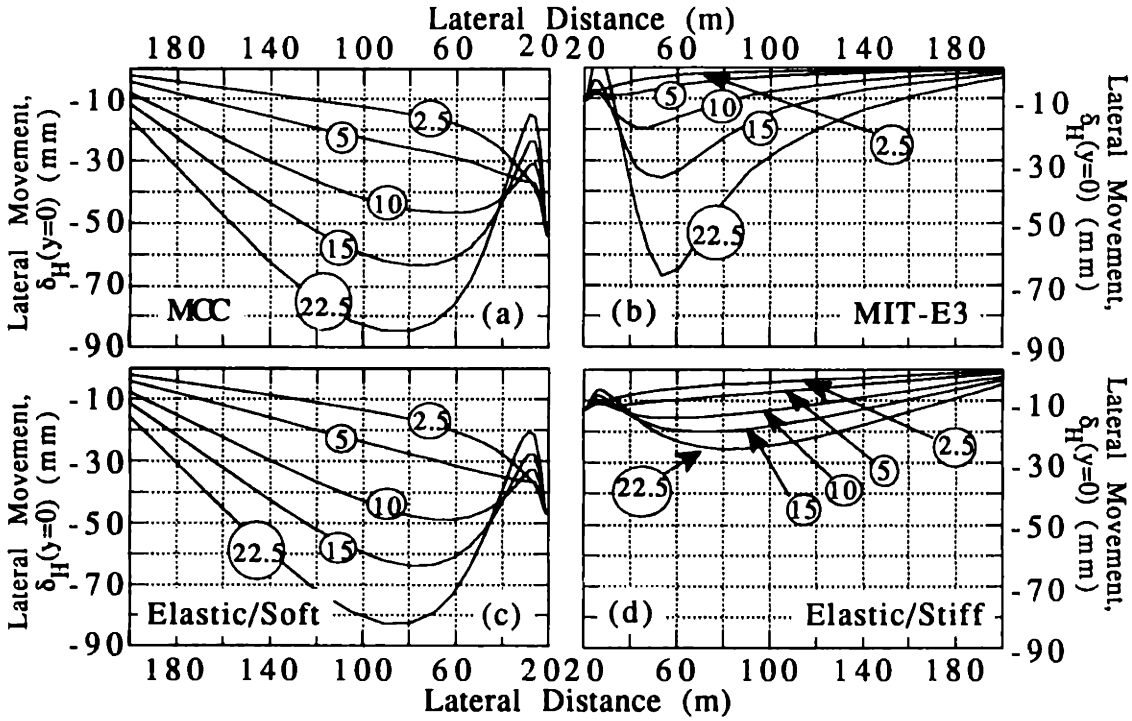

Figure 4.3-12 Effect of Soil Model on Lateral Surface Displacements (h_u=2.5m. h=2.5m, L=40m, OCR=1).

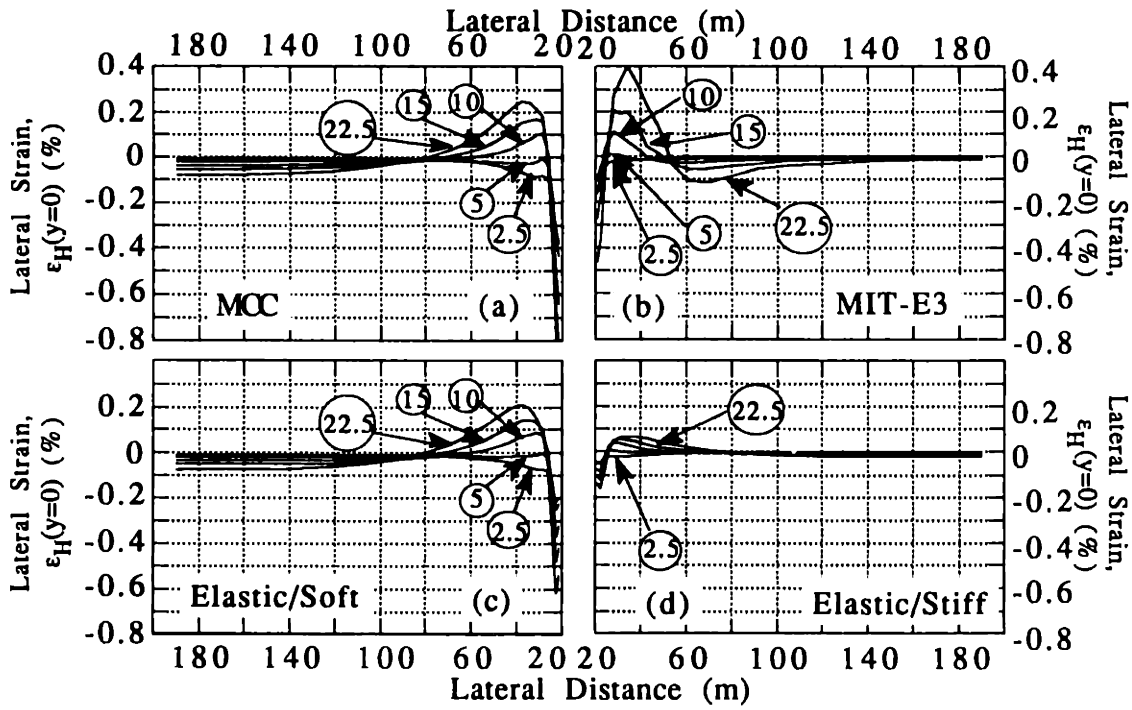

Figure 4.3-13 Effect of Soil Model on Lateral Surface Strain (h_u=2.5m, h=2.5m, L=40m, OCR=1).

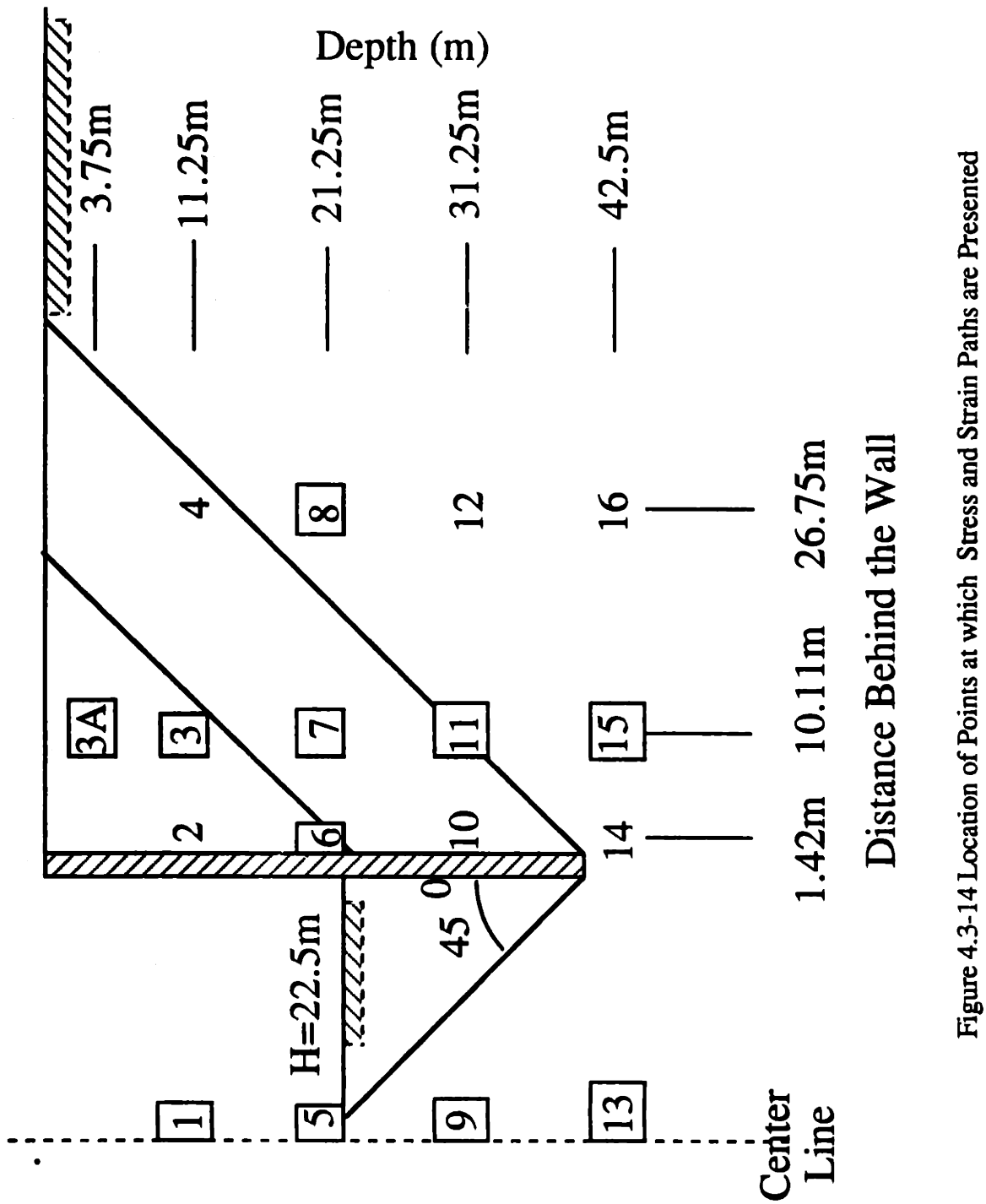

Figure 4.3-14 Location of Points at which Stress and Strain Paths are Presented

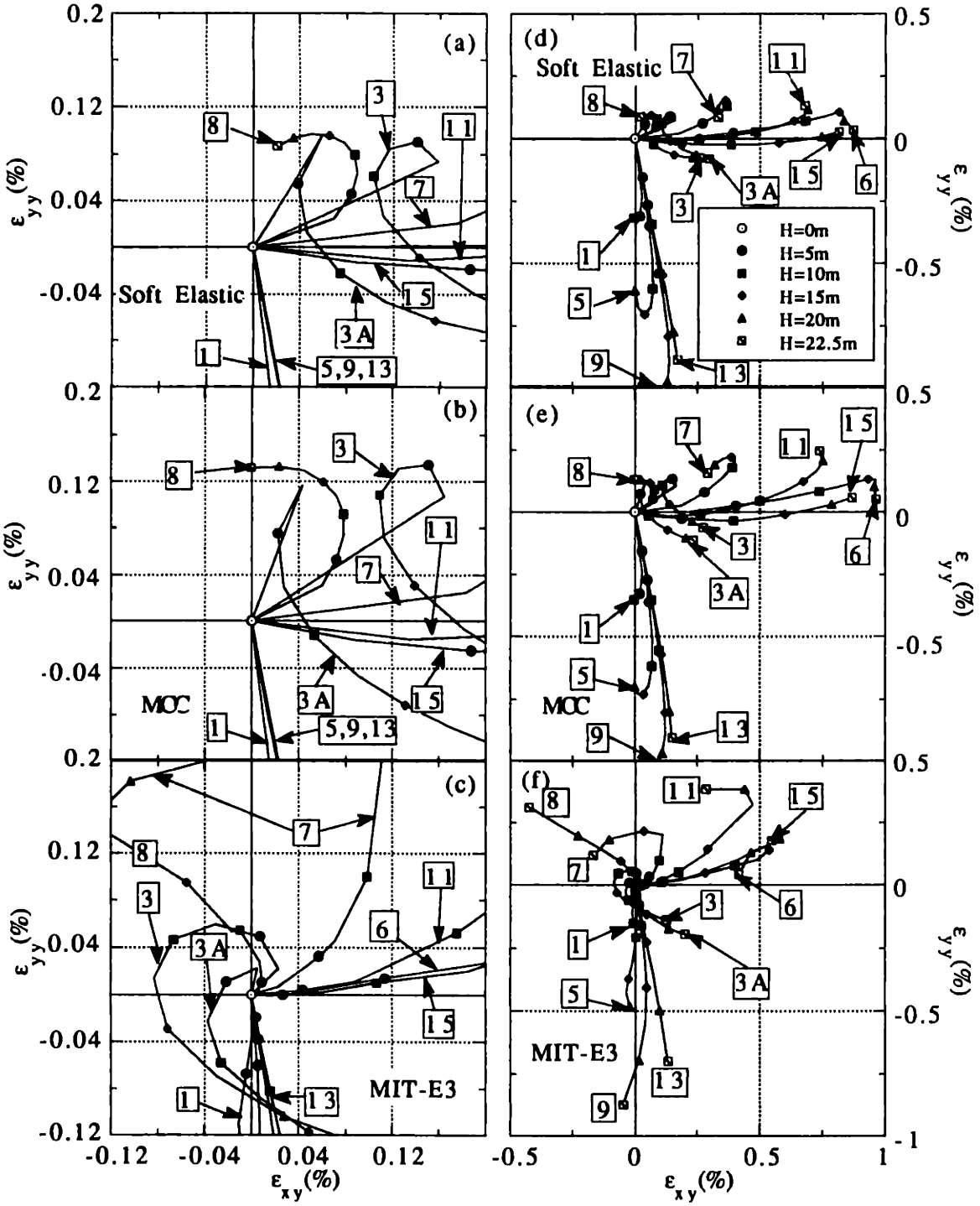

Figure 4.3-15 Effect of Soil Model on Soil Strain Paths (h_u=2.5m, h=2.5m, L=40m, OCR=1).

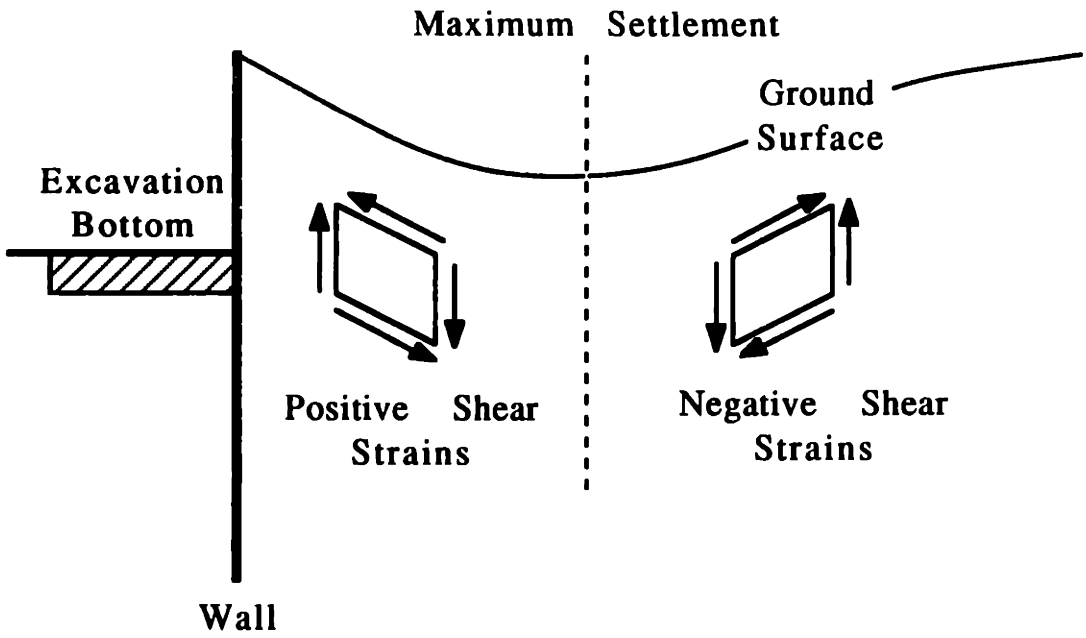

Figure 4.3-16 Schematic of Direction of Soil Shearing due to Surface Settlement.

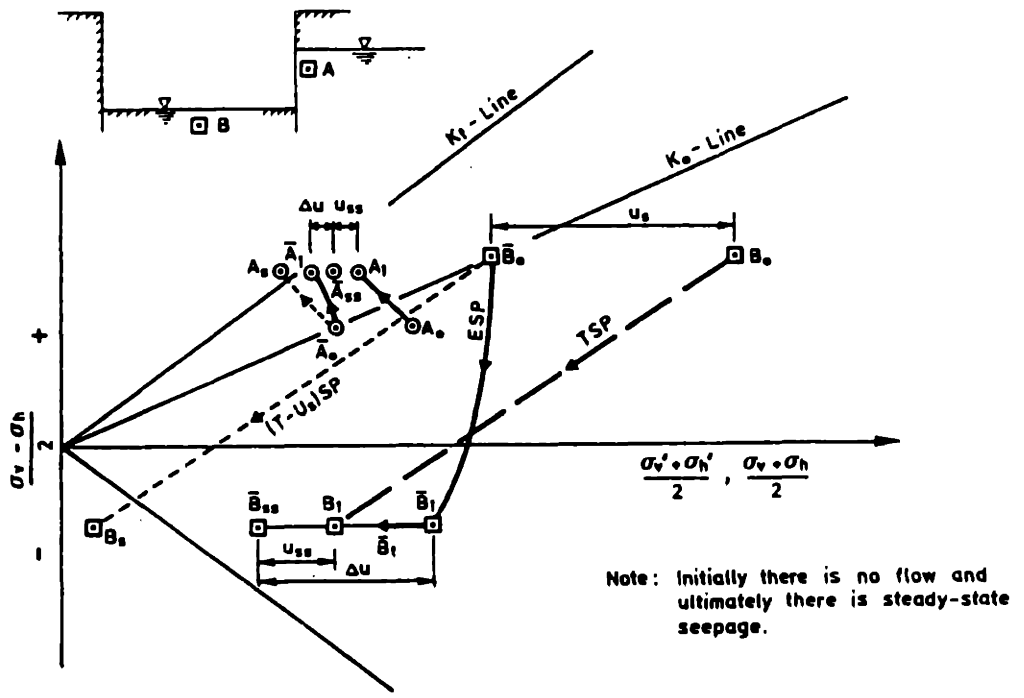

Stresses and Strains for Soil Elements near an Excavation	Soil Element A	Soil Element B
Initial (Static) Pore Pressure, u_s	$A_o\bar{A}_o$	$B_o\bar{B}_o$
Pore Pressure at Steady-state Flow, u_{ss}	$A_1\bar{A}_{ss}$	$B_1\bar{B}_{ss}$
Pore Pressure upon Unloading	Decreases	Decreases
Pore Pressure during Consolidation	Decreases	Increases
Strain upon Unloading	Vertical compression	Vertical extension
Strain during Consolidation	Vertical compression	Vertical extension
Undrained Shear Strength during Consolidation	Increases	Decreases

*Adopted from GCO (1990)

Figure 4.3-17 Stress Paths for Soil Elements near Excavation (Lambe, 1970).

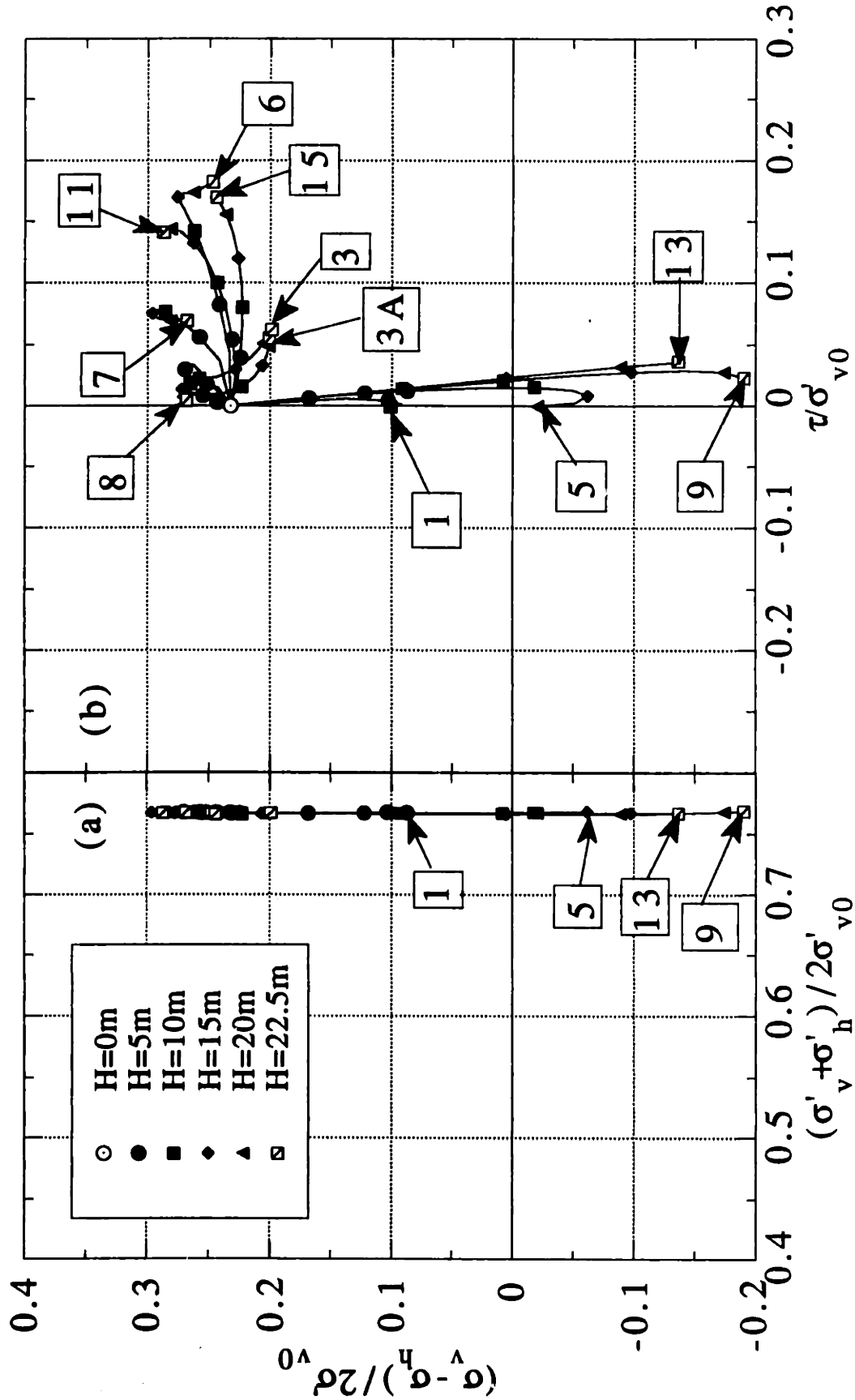

Figure 4.3-18 Stress Paths for Soft Elastic Model Analysis (h_0=2.5m, h=2.5m, L=40m, OCR=1).

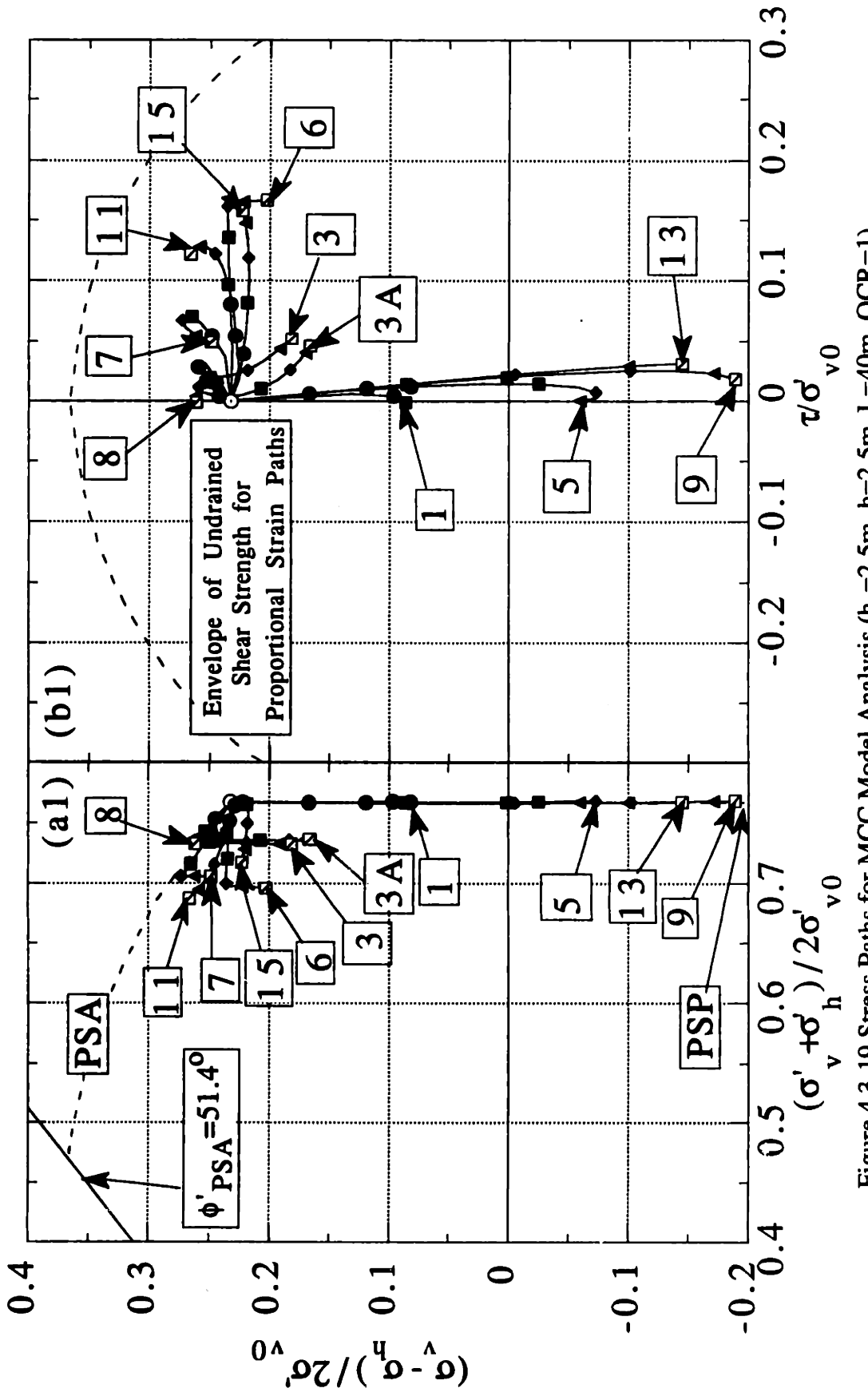

Figure 4.3-19 Stress Paths for MCC Model Analysis (h_u=2.5m, h=2.5m, L=40m, OCR=1).

(continued on next page)

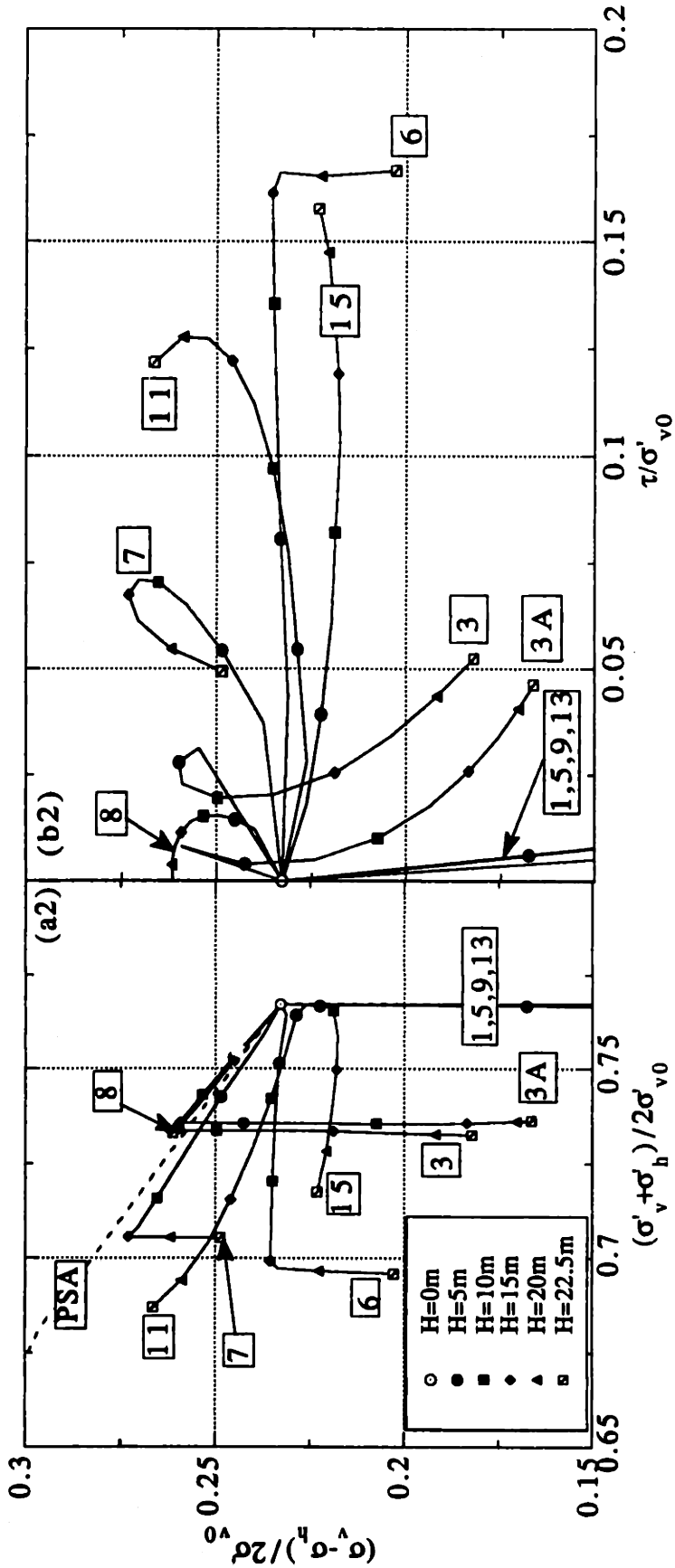

Figure 4.3-19 Stress Paths for MCC Model Analysis (h_u=2.5m, h=2.5m, L=40m, OCR=1).
(continued from previous page)

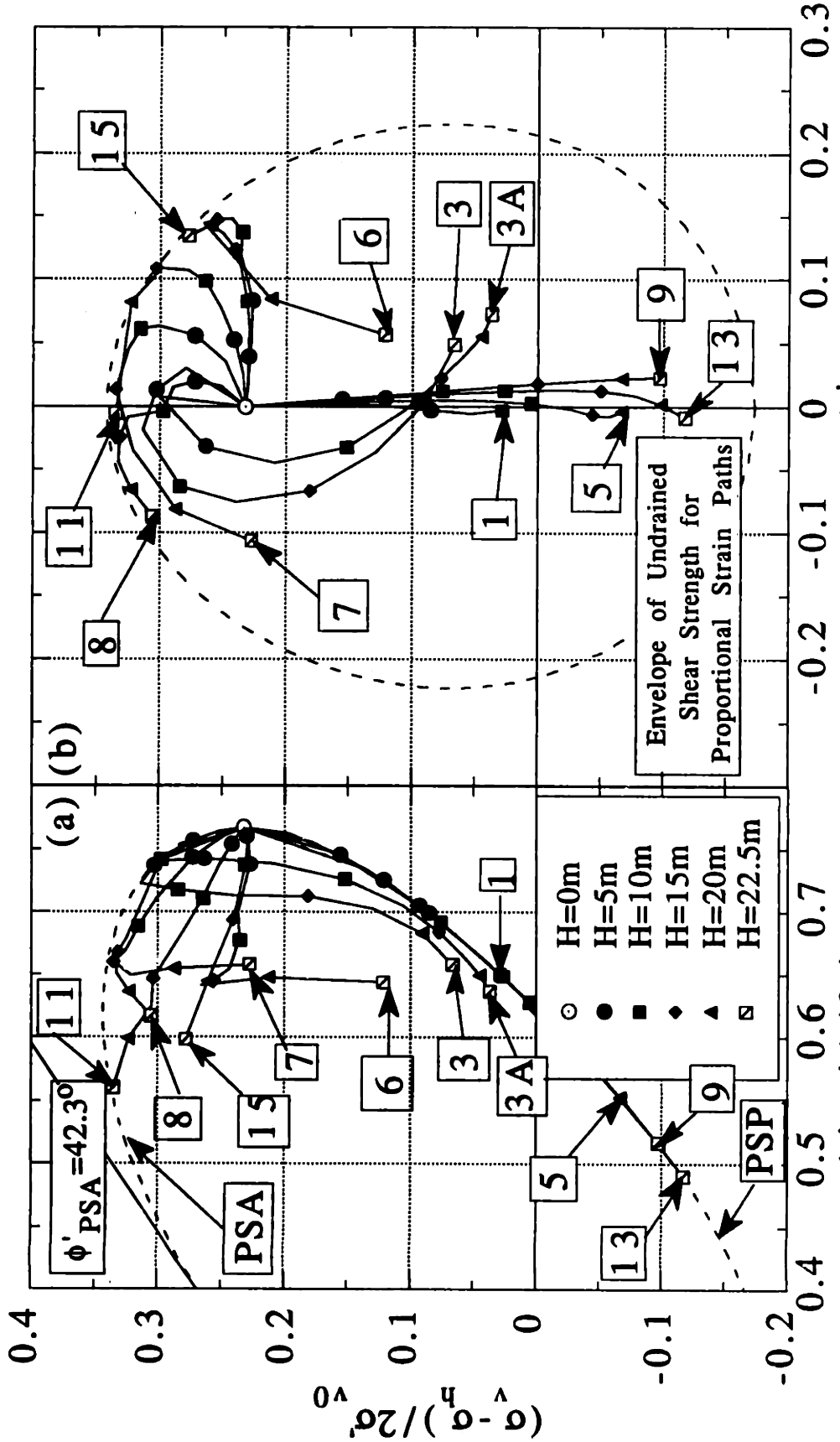

Figure 4.3-20 Stress Paths for MIT-E3 Model Analysis (h_u=2.5m, h=2.5m, L=40m, OCR=1).
(continued on next page)

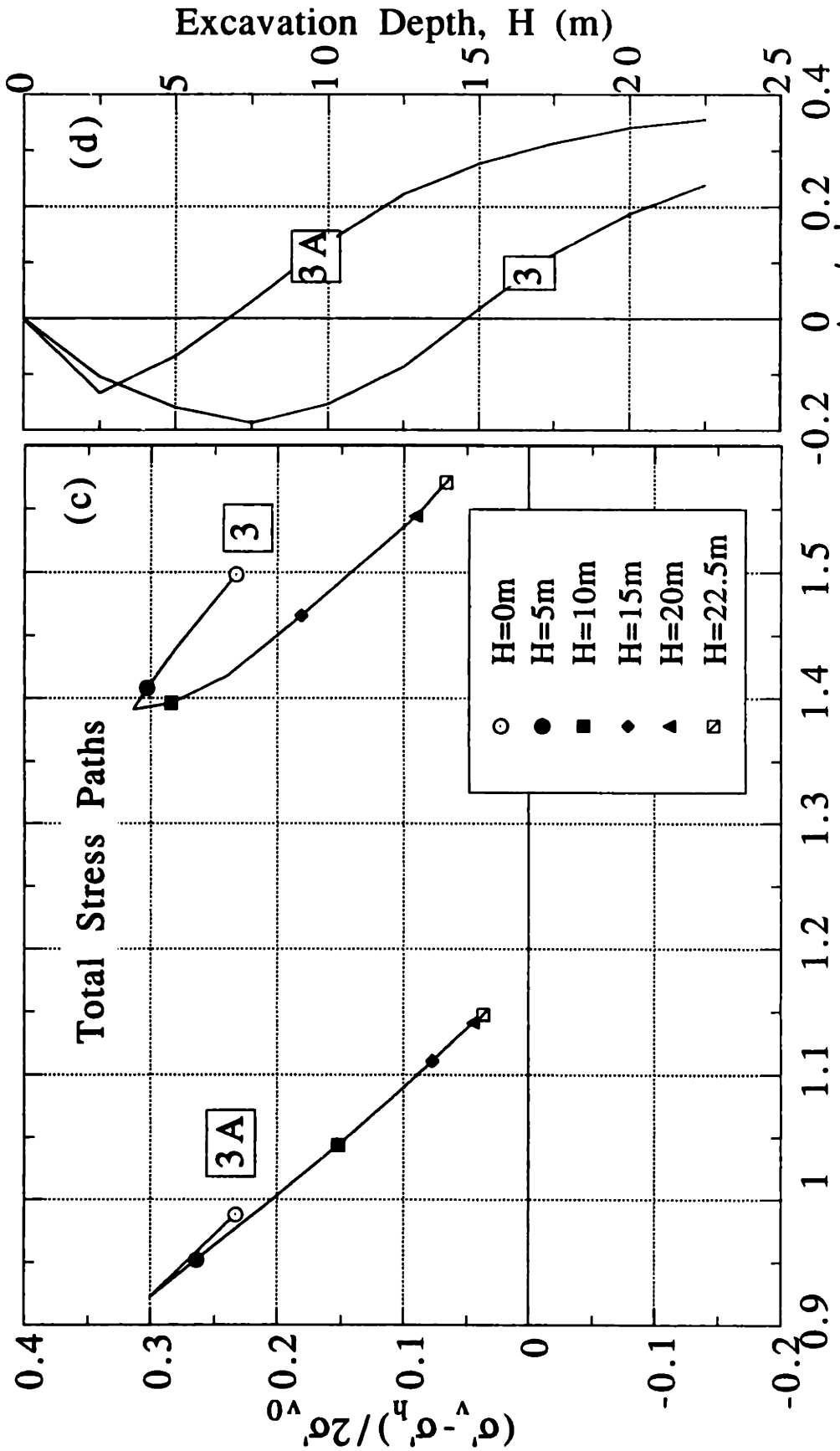

Figure 4.3-20 Stress Paths for MIT-E3 Model Analysis (h_u=2.5m, h=2.5m, L=40m, OCR=1).
(continued from previous page)

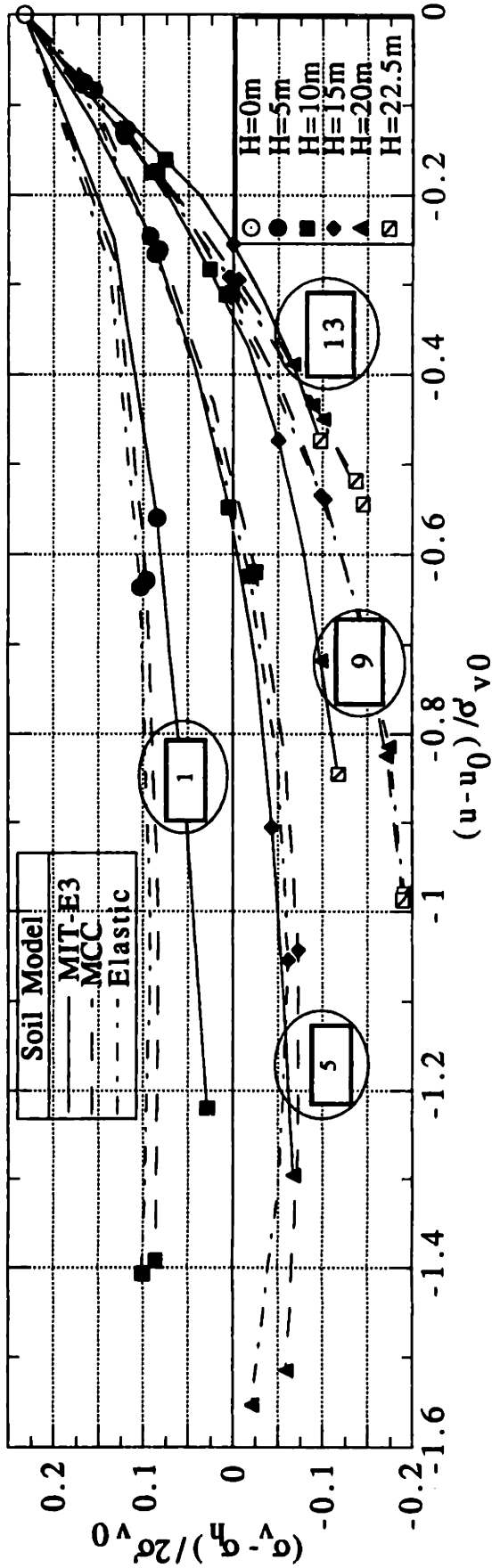

Figure 4.3-21 Effect of Soil Model on Pore Pressure Change for Points Inside the Excavation (h_u=2.5m, h=2.5m, L=40m, OCR=1).

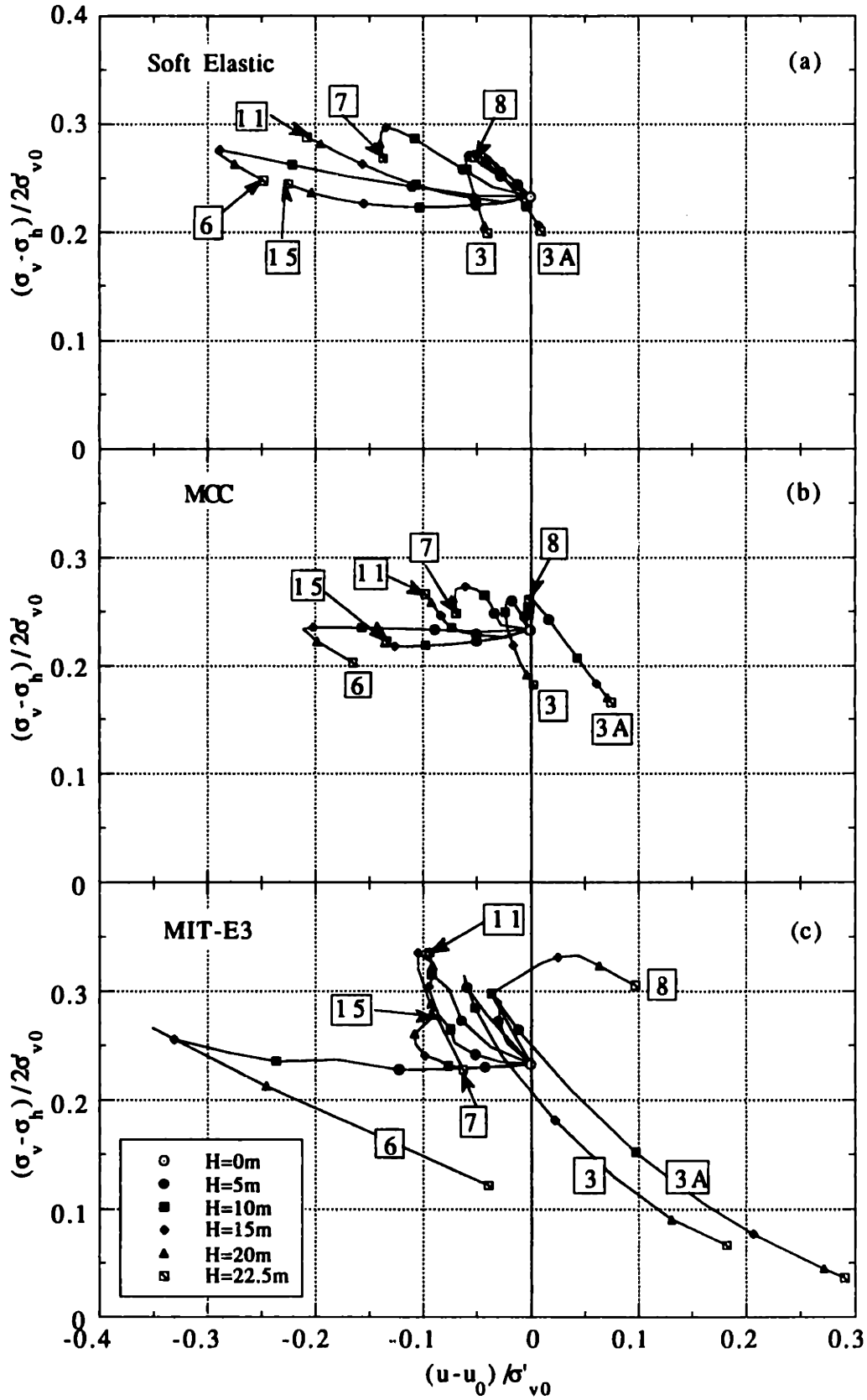

Figure 4.3-22 Effect of Soil Model on Pore Pressure Change for Points in the Retained Soil (h_u=2.5m, h=2.5m, L=40m, OCR=1).

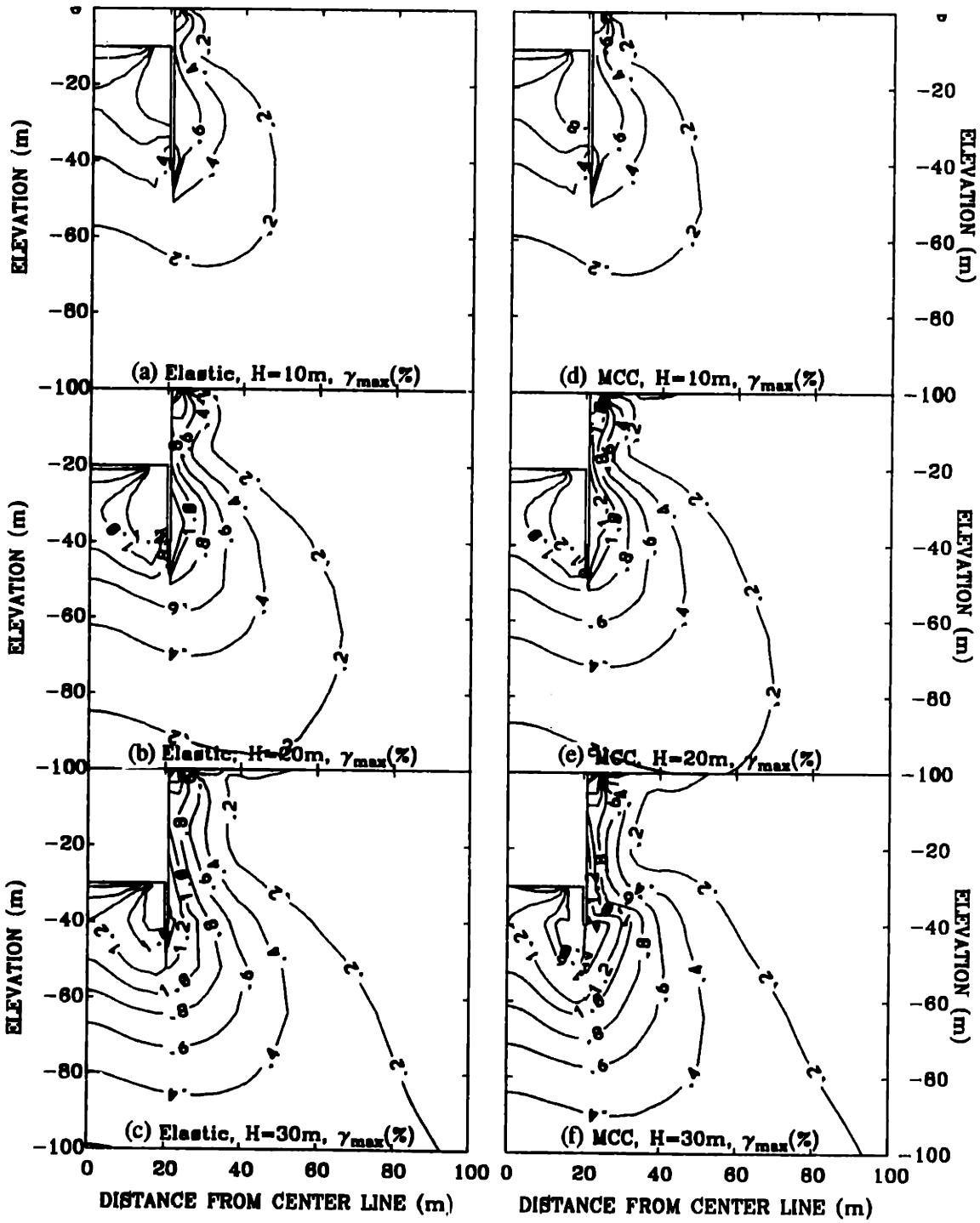

Figure 4.3-23 Contours of Maximum Shear Strain for Soft Elastic and MCC Model Analyses (h_u=2.5m, h=2.5m, L=40m, OCR=1).

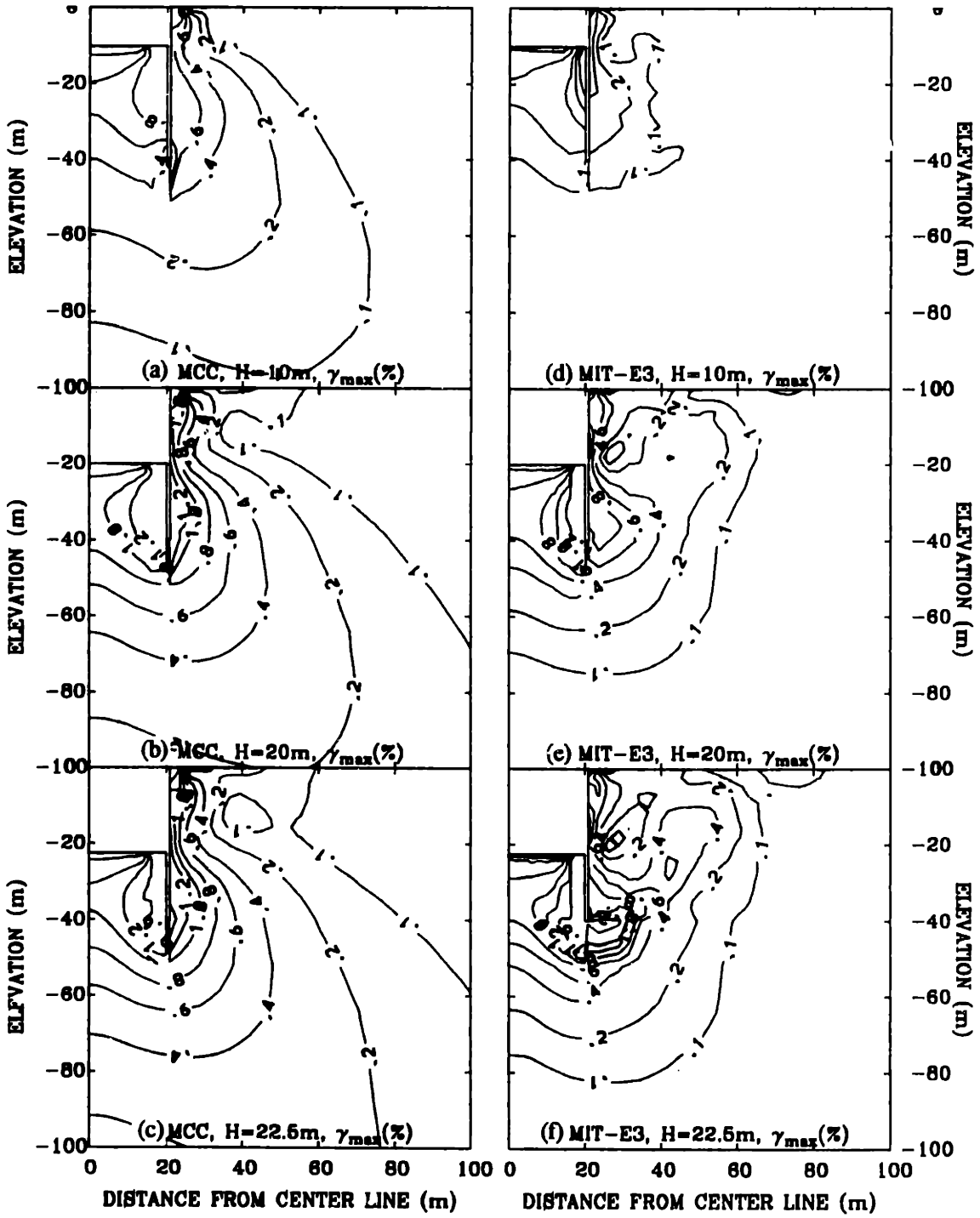

Figure 4.3-24 Contours of Maximum Shear Strain for MCC and MIT-E3 Model Analyses (h_u=2.5m, h=2.5m, L=40m, OCR=1).

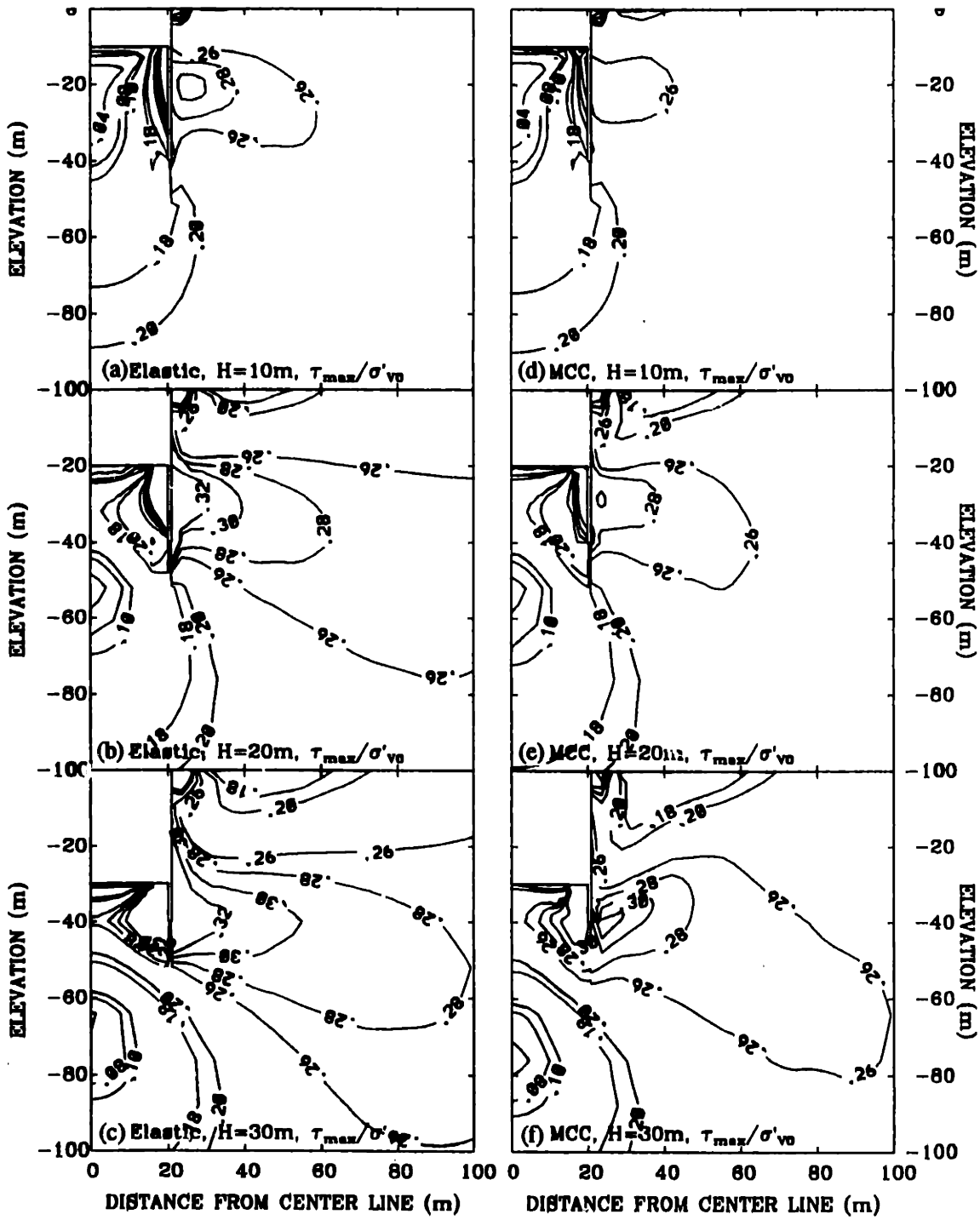

Figure 4.3-25 Contours of Maximum Shear Stress for Soft Elastic and MCC Model Analyses (h_u=2.5m, h=2.5m, L=40m, OCR=1).

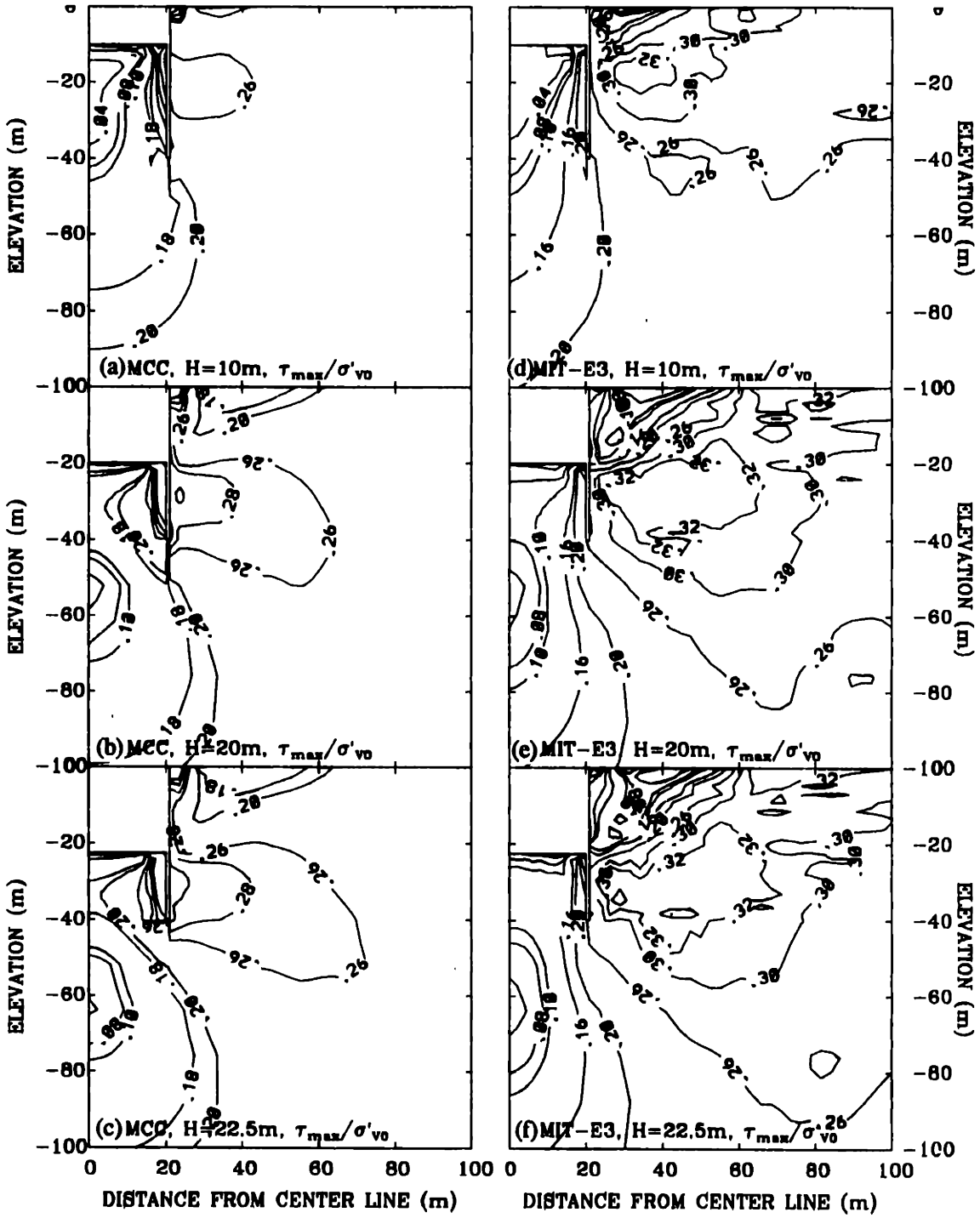

Figure 4.3-26 Contours of Maximum Shear Stress for MCC and MIT-E3 Model Analyses (h_u=2.5m, h=2.5m, L=40m, OCR=1).

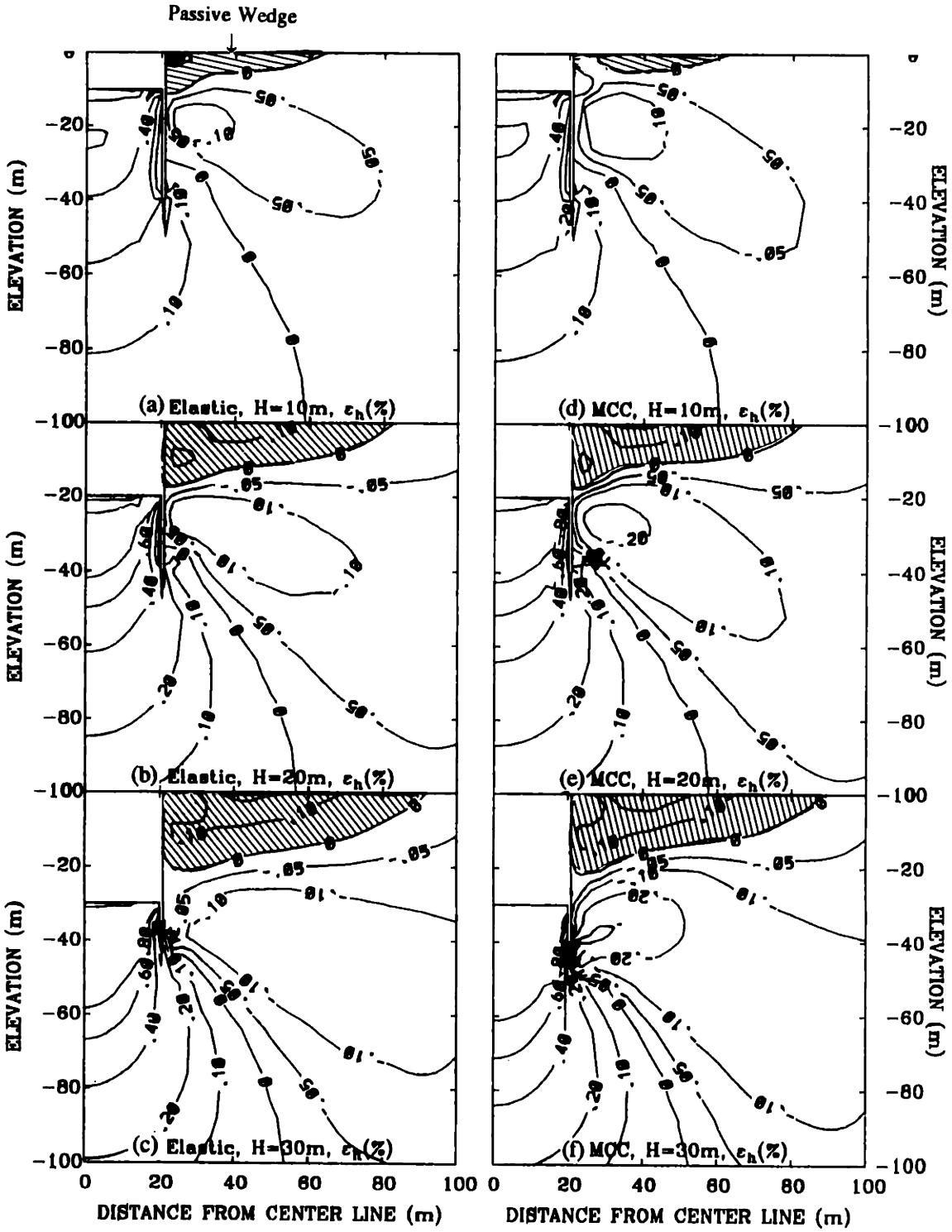

Figure 4.3-27 Contours of Horizontal Strain for Soft Elastic and MCC Model Analyses (h_u=2.5m, h=2.5m, L=40m, OCR=1).

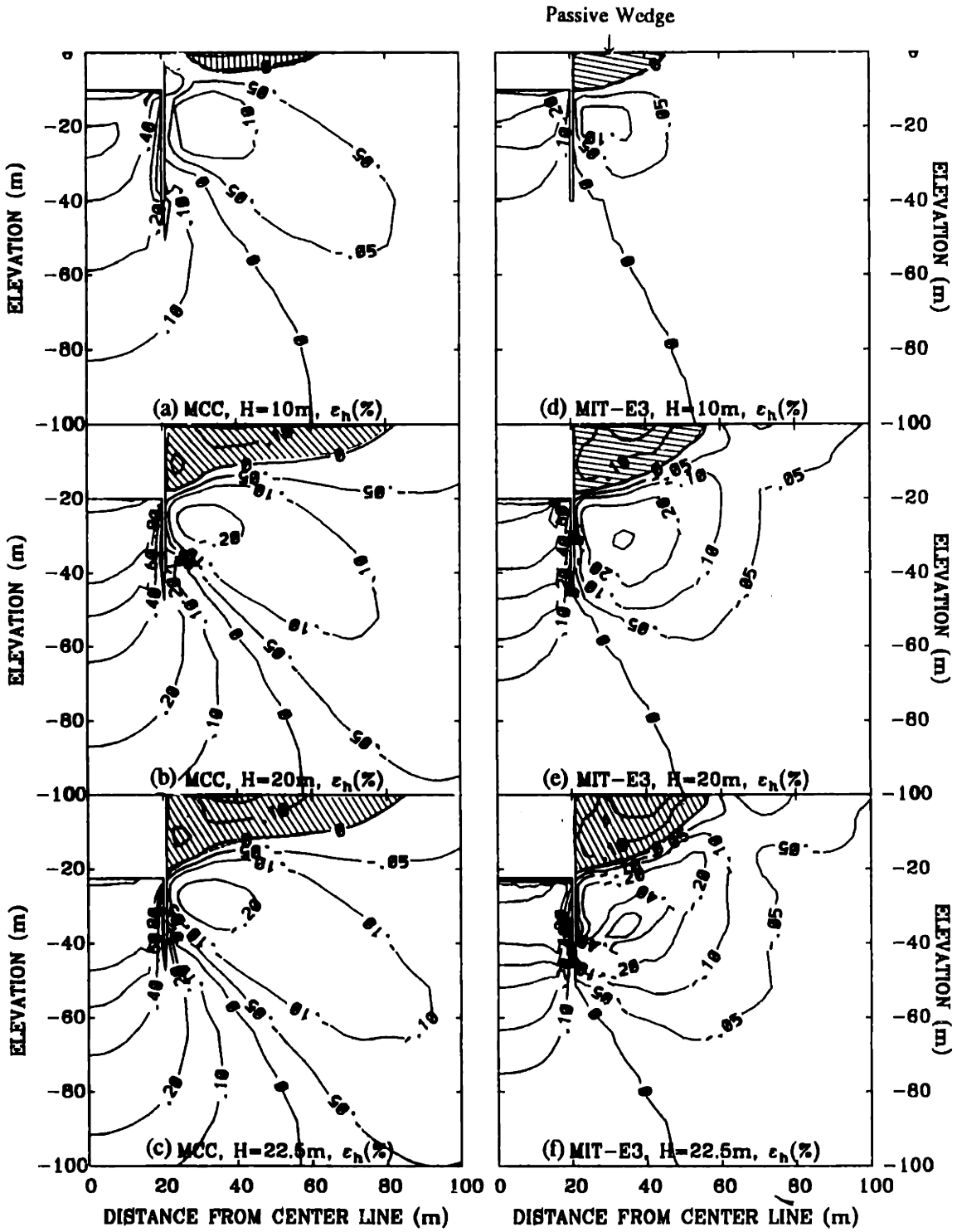

Figure 4.3-28 Contours of Horizontal Strain for MCC and MIT-E3 Model Analyses (h_u=2.5m, h=2.5m, L=40m, OCR=1).

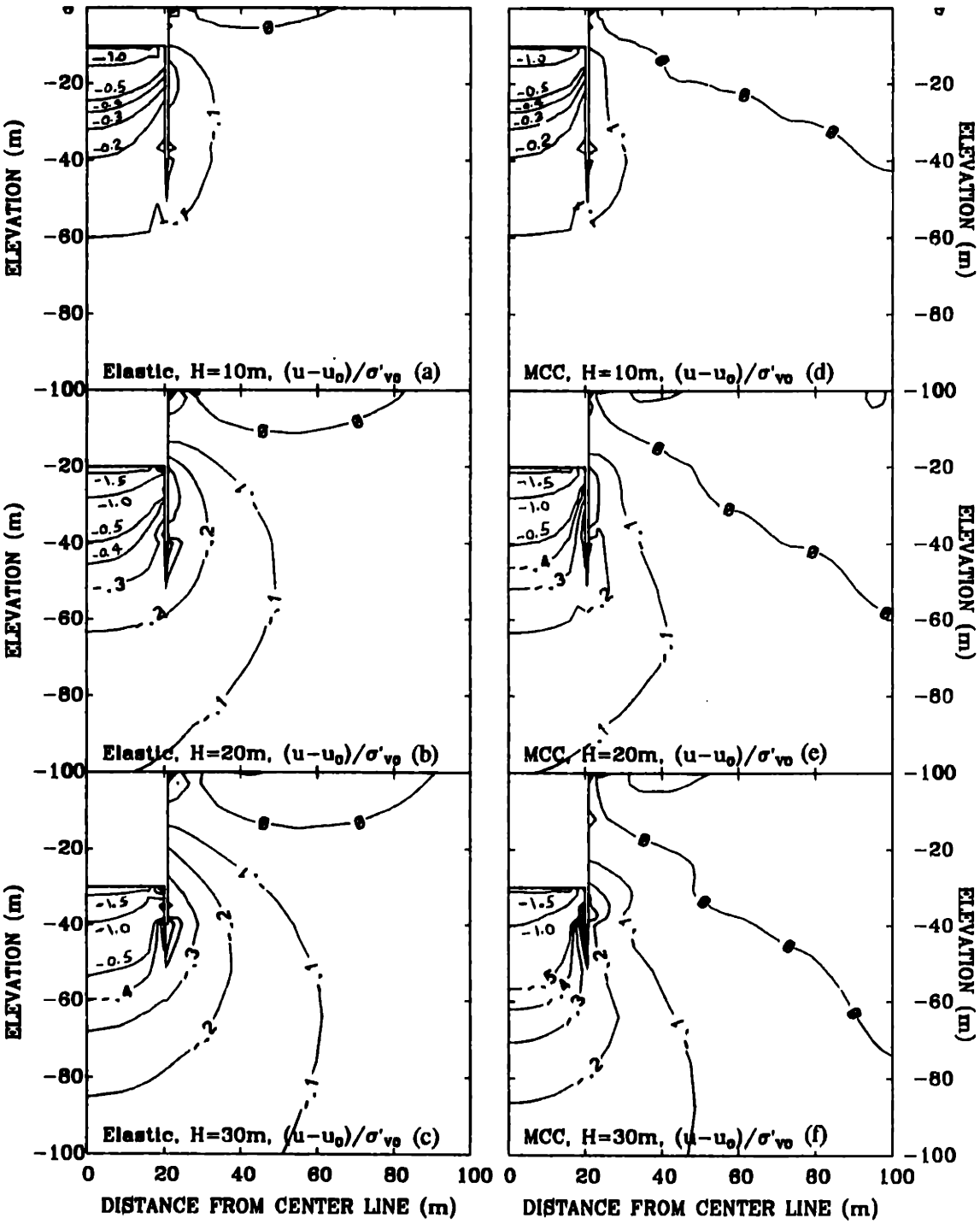

Figure 4.3-29 Contours of Normalized Excess Pore Pressure for Soft Elastic and MCC Model Analyses (h_u=2.5m, h=2.5m, L=40m, OCR=1).

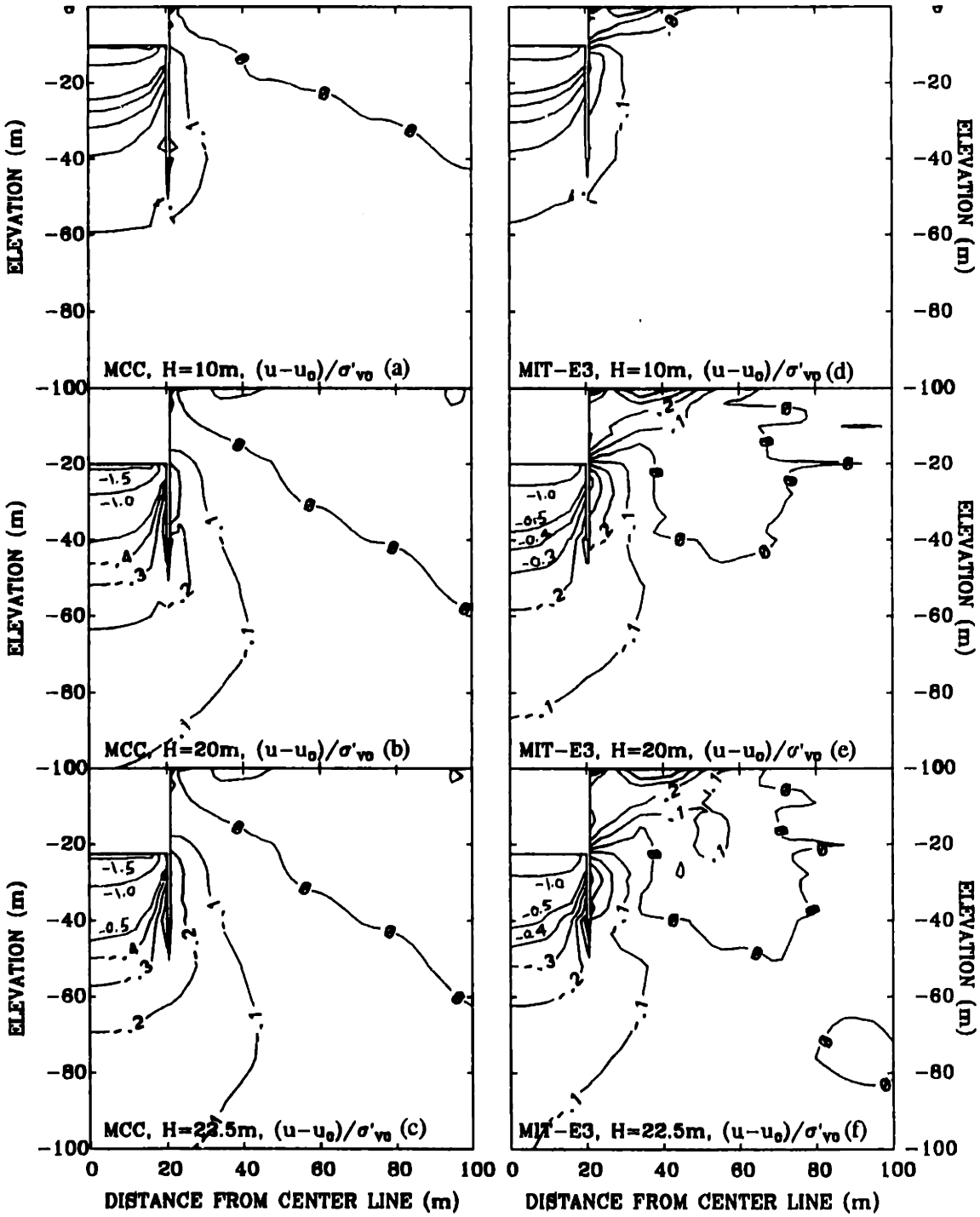

Figure 4.3-30 Contours of Normalized Excess Pore Pressure for MCC and MIT-E3 Model Analyses (h_u=2.5m, h=2.5m, L=40m, OCR=1).

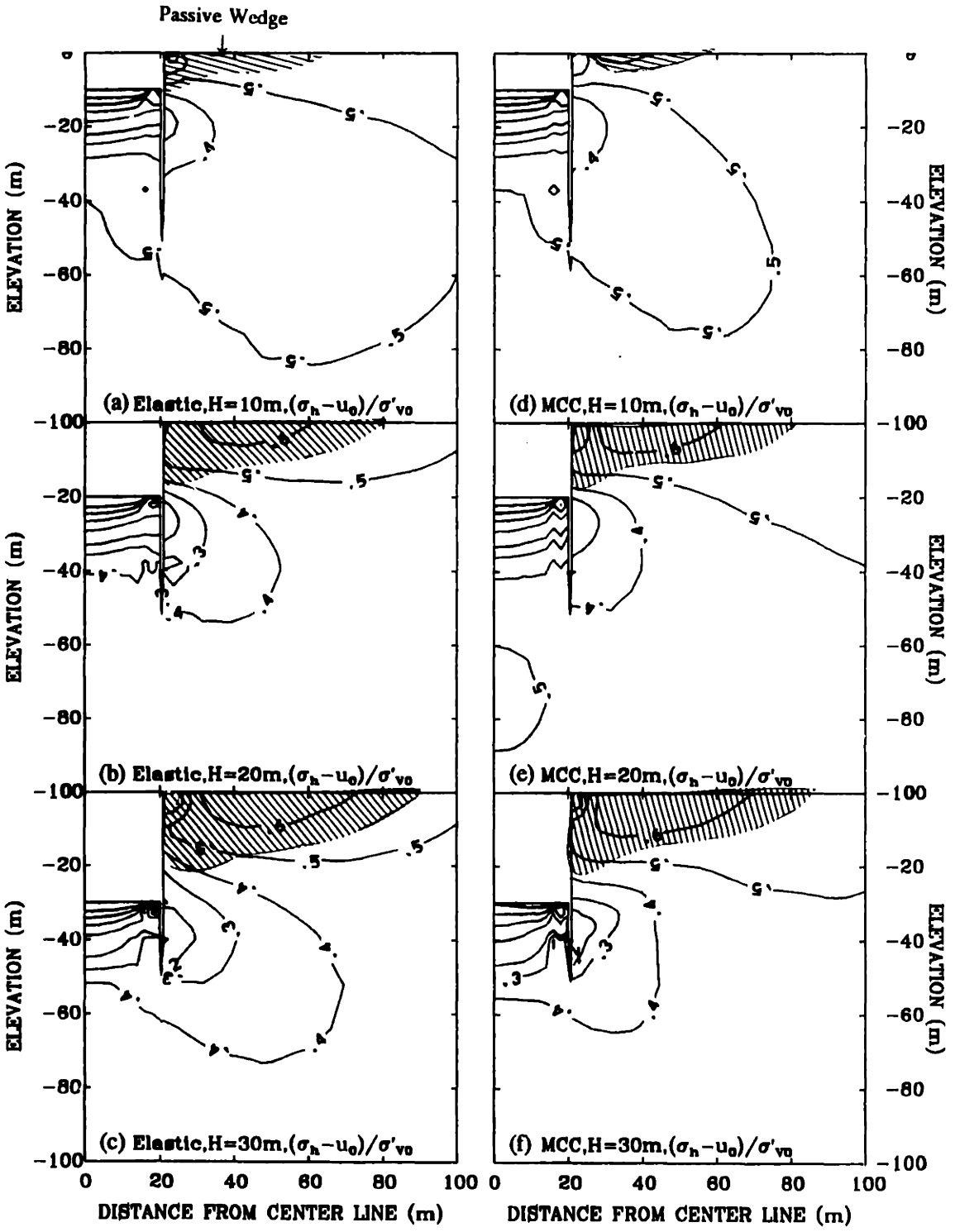

Figure 4.3-31 Contours of Normalized Horizontal Stress for Soft Elastic and MCC Model Analyses (h_u=2.5m, h=2.5m, L=40m, OCR=1).

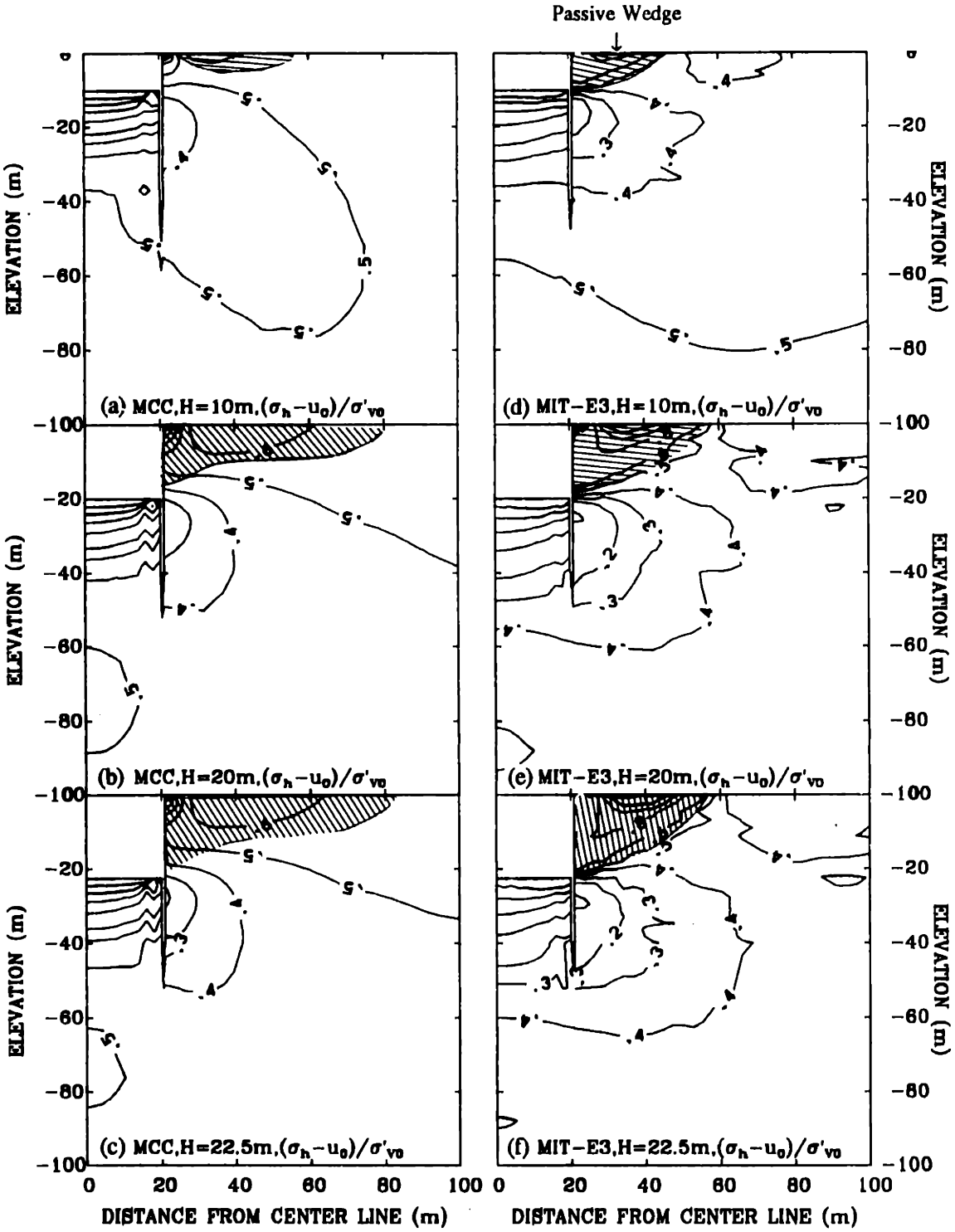

Figure 4.3-32 Contours of Normalized Horizontal Stress for MCC and MIT-E3 Model Analyses (h_u=2.5m, h=2.5m, L=40m, OCR=1).

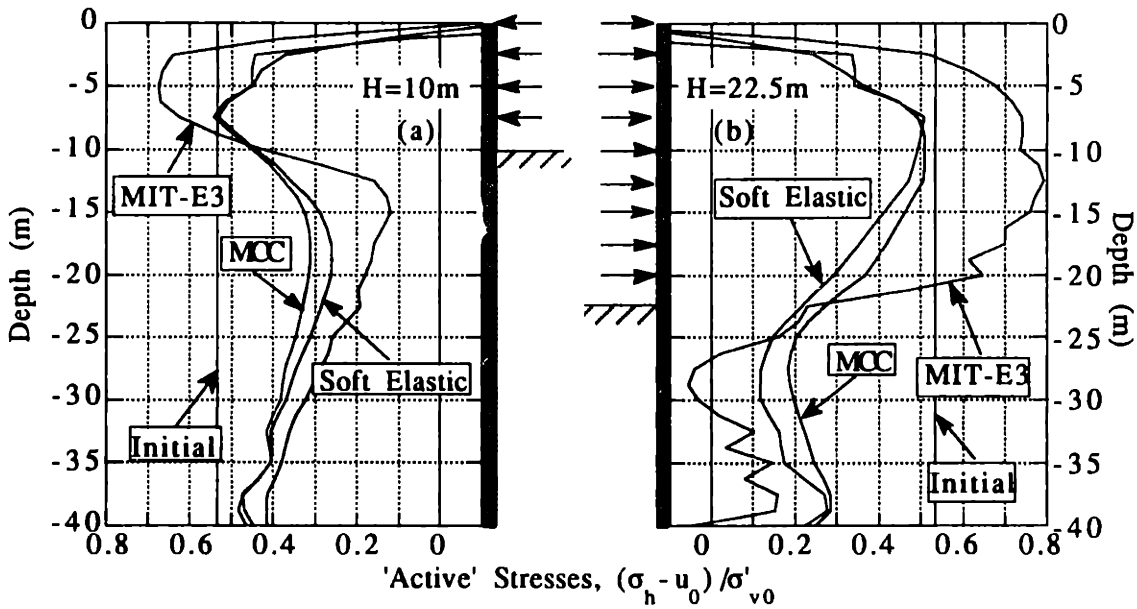

Figure 4.3-33 Effect of Soil Model on Normalized Lateral Stresses Acting on the Wall on the Retained Soil Side (h_u=2.5m, h=2.5m, L=40m, OCR=1).

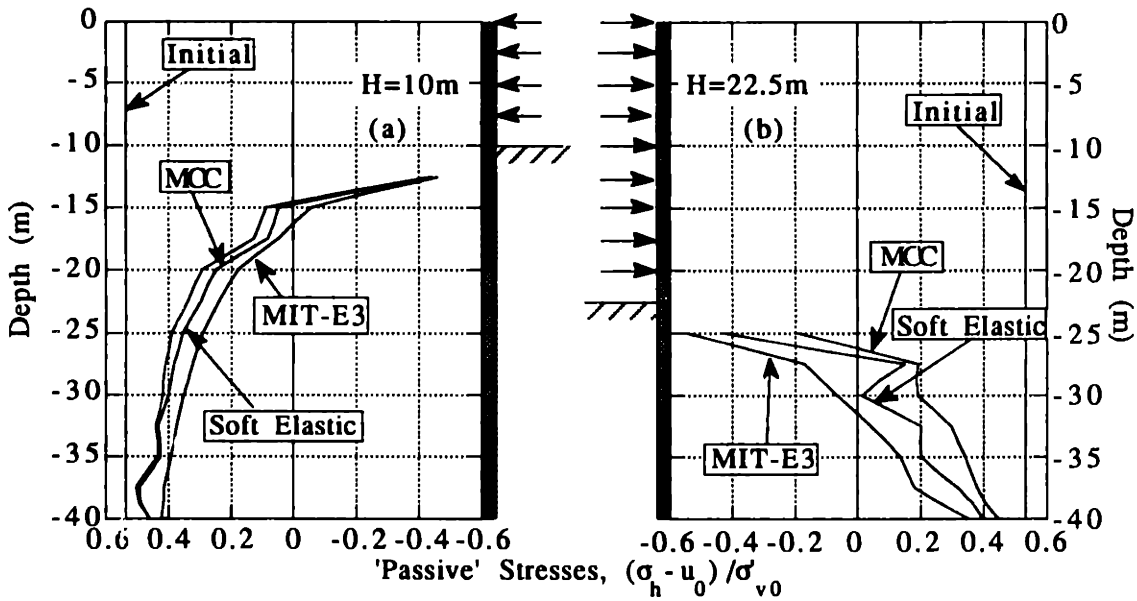

Figure 4.3-34 Effect of Soil Model on Normalized Lateral Stresses Acting on the Wall on the Excavated Soil Side (h_u=2.5m, h=2.5m, L=40m, OCR=1).

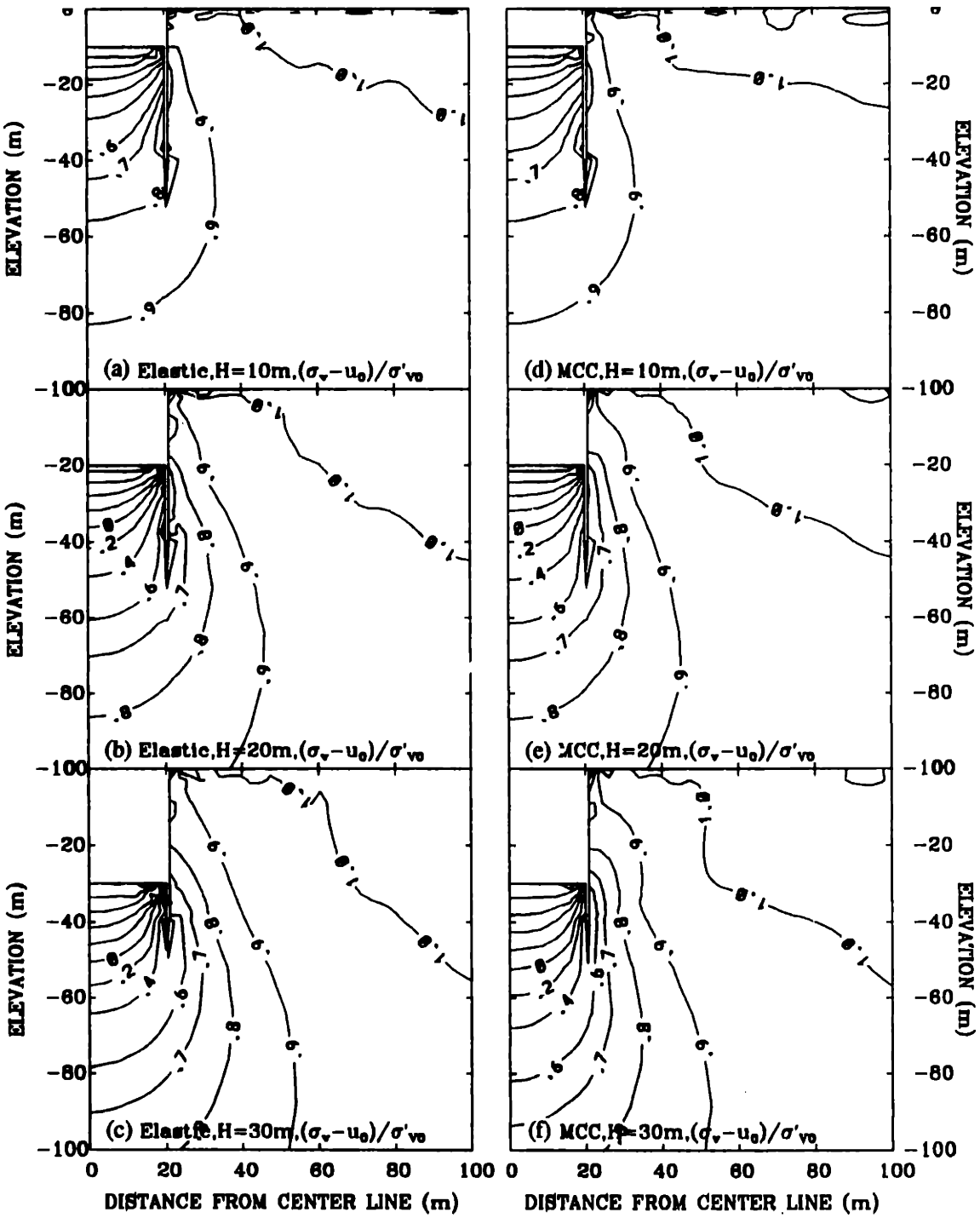

Figure 4.3-35 Contours of Normalized Vertical Stress for Soft Elastic and MCC Model Analyses (h_u=2.5m, h=2.5m, L=40m, OCR=1).

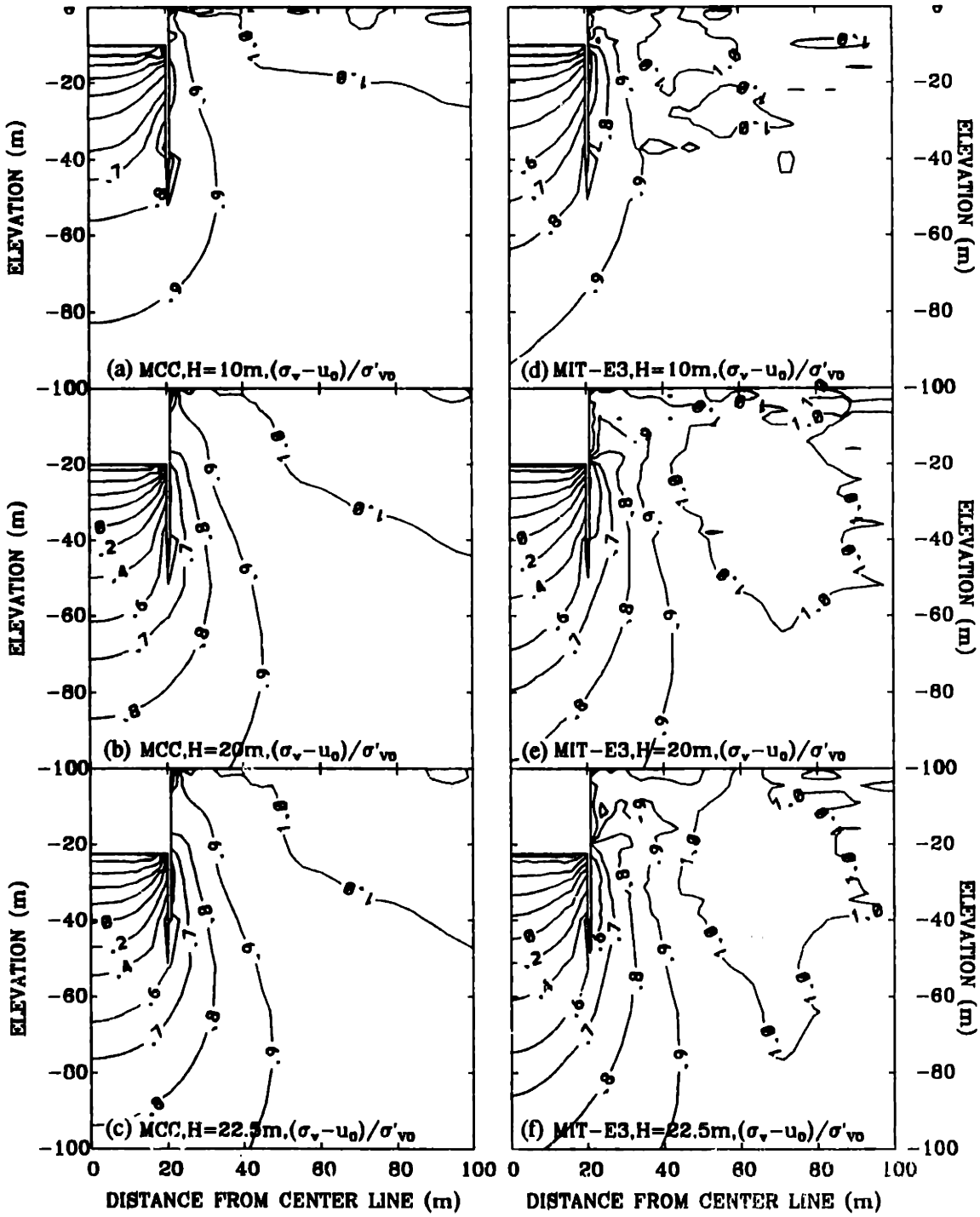

Figure 4.3-36 Contours of Normalized Vertical Stress for MCC and MIT-E3 Model Analyses (h_u=2.5m, h=2.5m, L=40m, OCR=1).

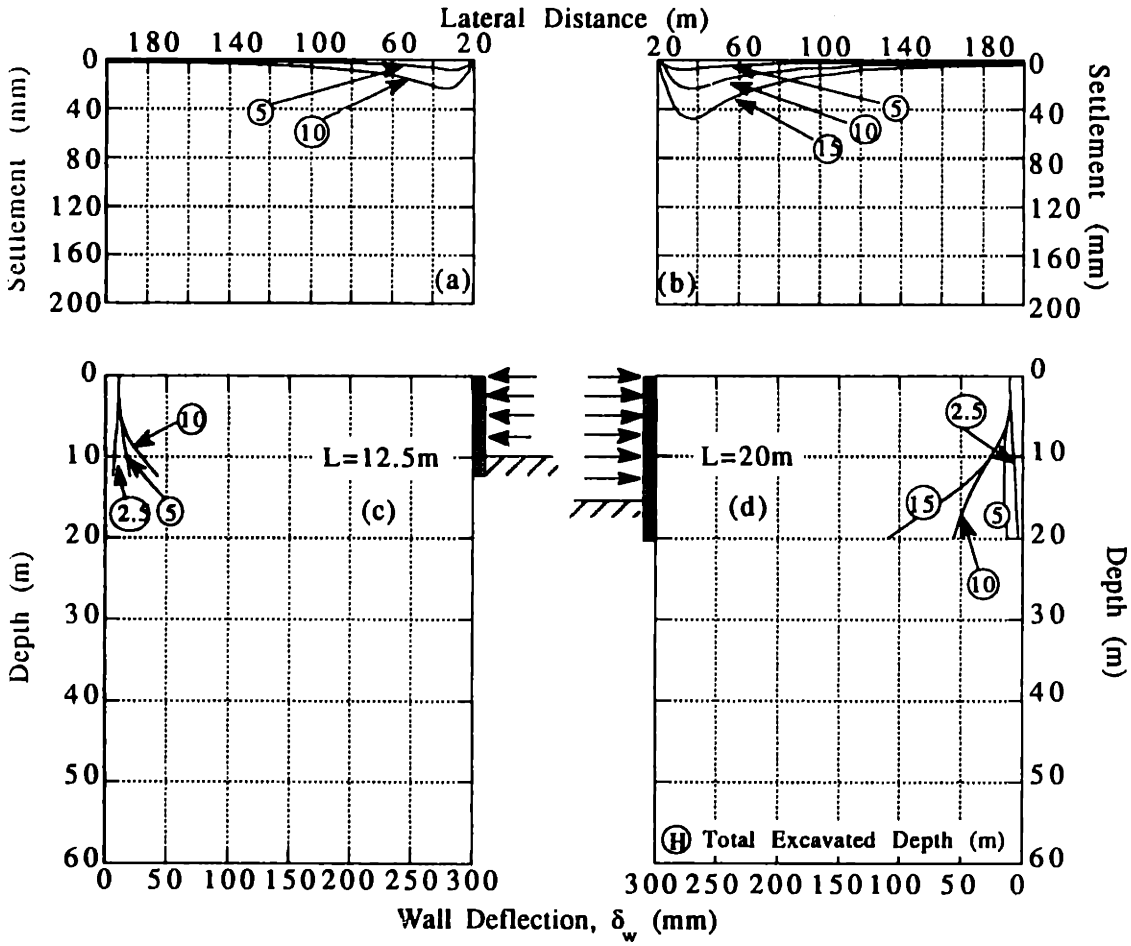

igure 4.4-1 Lateral Wall Deflections and Surface Settlements for L=12.5m and L=20m Wall Analyses (h_u=2.5m, h=2.5m, MIT-E3, OCR=1)

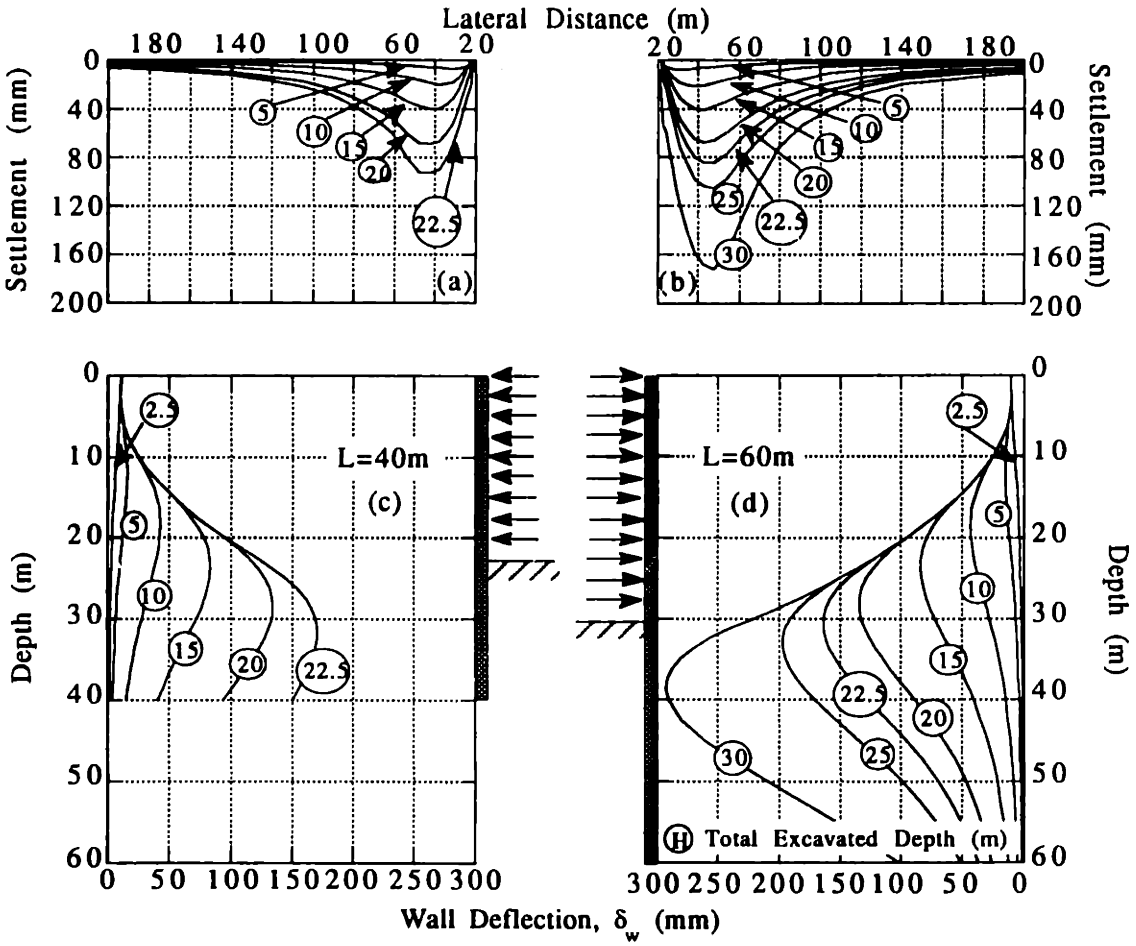

Figure 4.4-2 Lateral Wall Deflections and Surface Settlements for L=40m and L=60m Wall Analyses (h_u=2.5m, h=2.5m, MIT-E3, OCR=1)

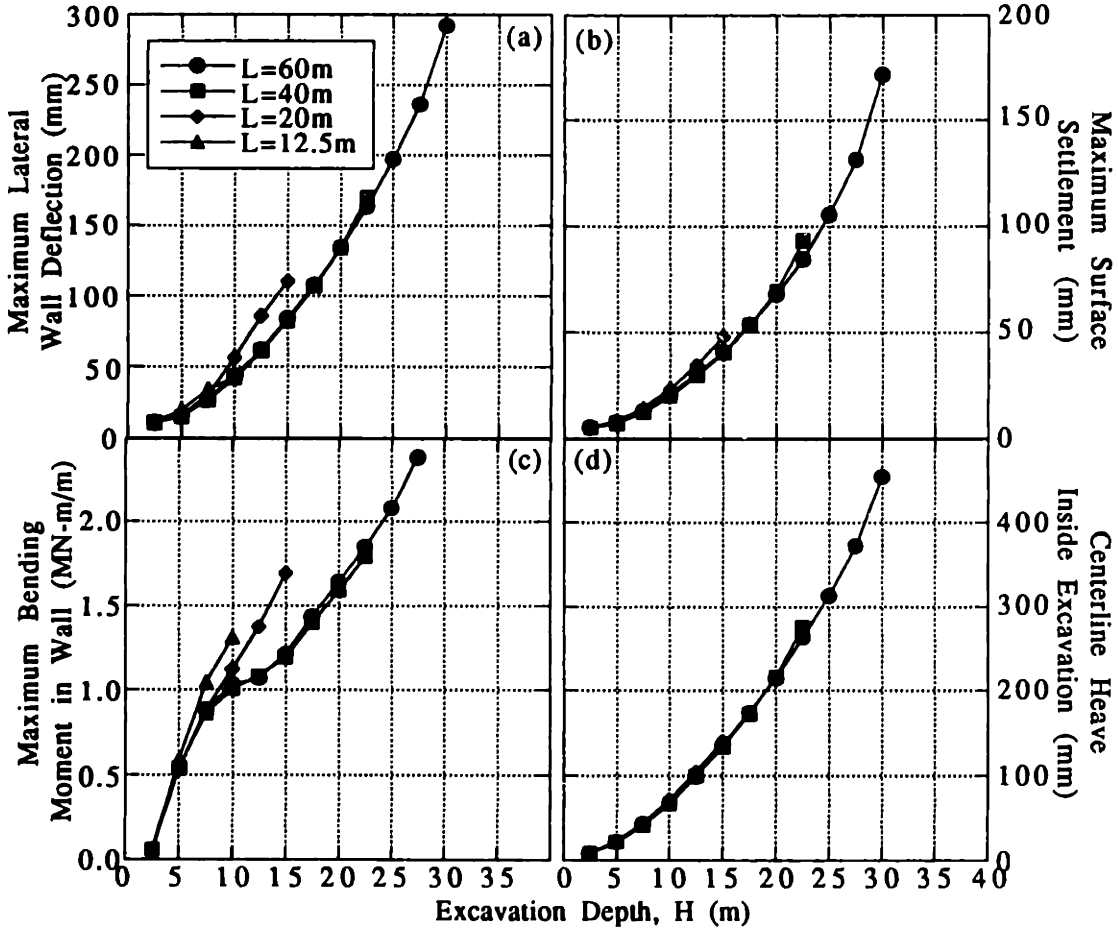

Figure 4.4-3 Effect of Wall Length on Maximum Deformations and Moments (h_u=2.5m, h=2.5m, MIT-E3, OCR=1)

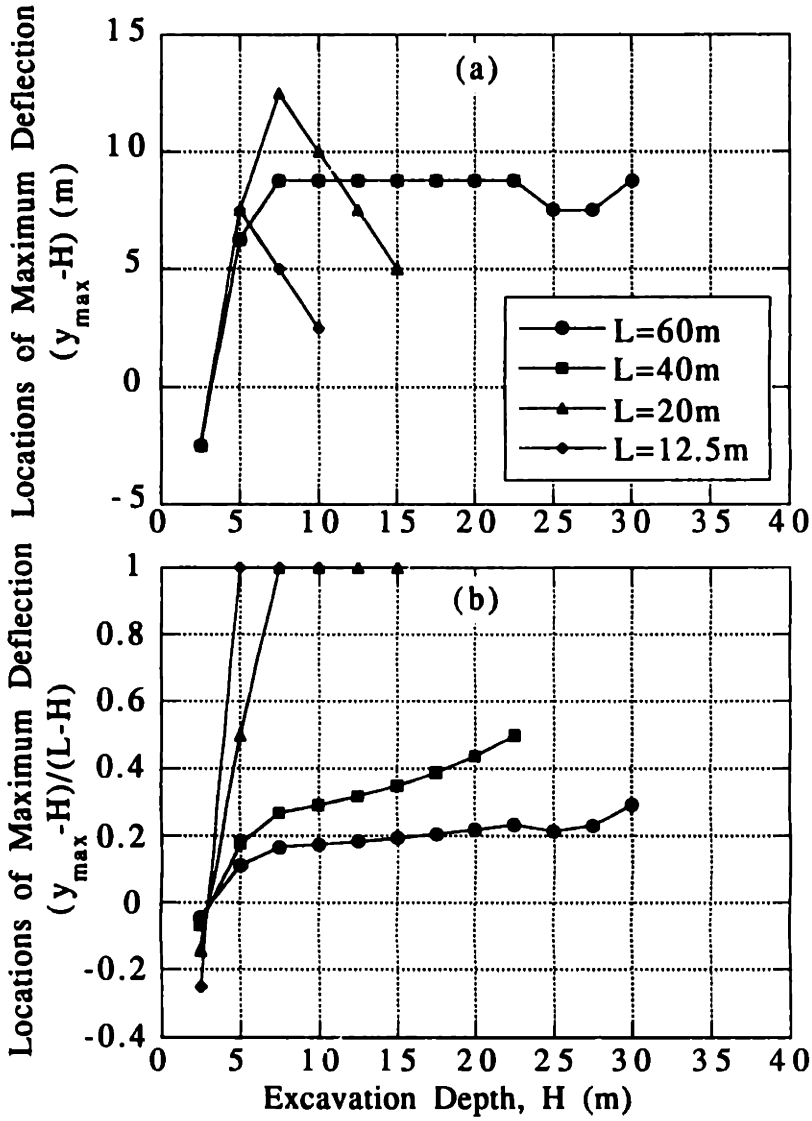

Figure 4.4-4 Effect of Wall Length on Location of Normalized Maximum Deflections (h_u=2.5m, h=2.5m, MIT-E3, OCR=1)

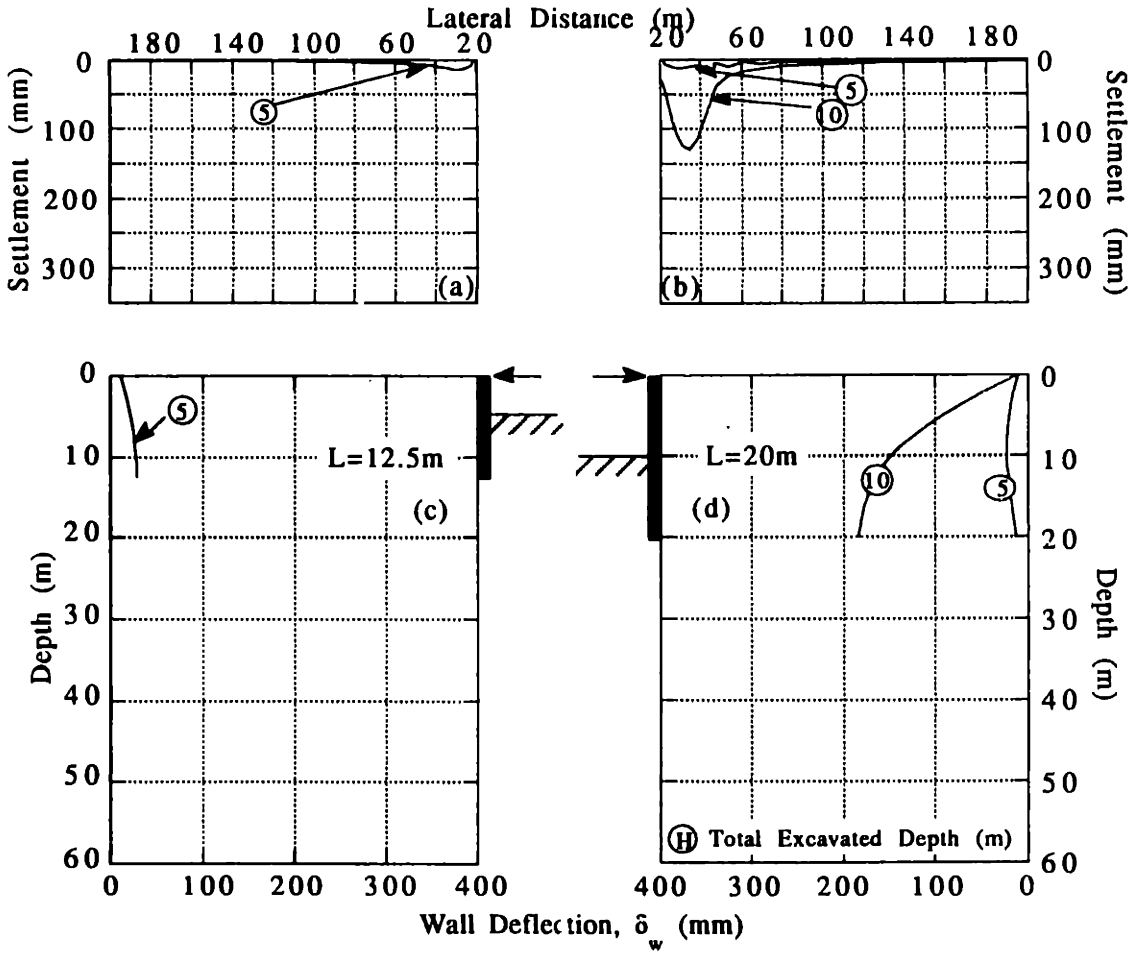

Figure 4.4-5 Lateral Wall Deflections and Surface Settlements for L=12.5m and L=20m Wall Analyses (h_u=2.5m, h=10m, MIT-E3, OCR=1)

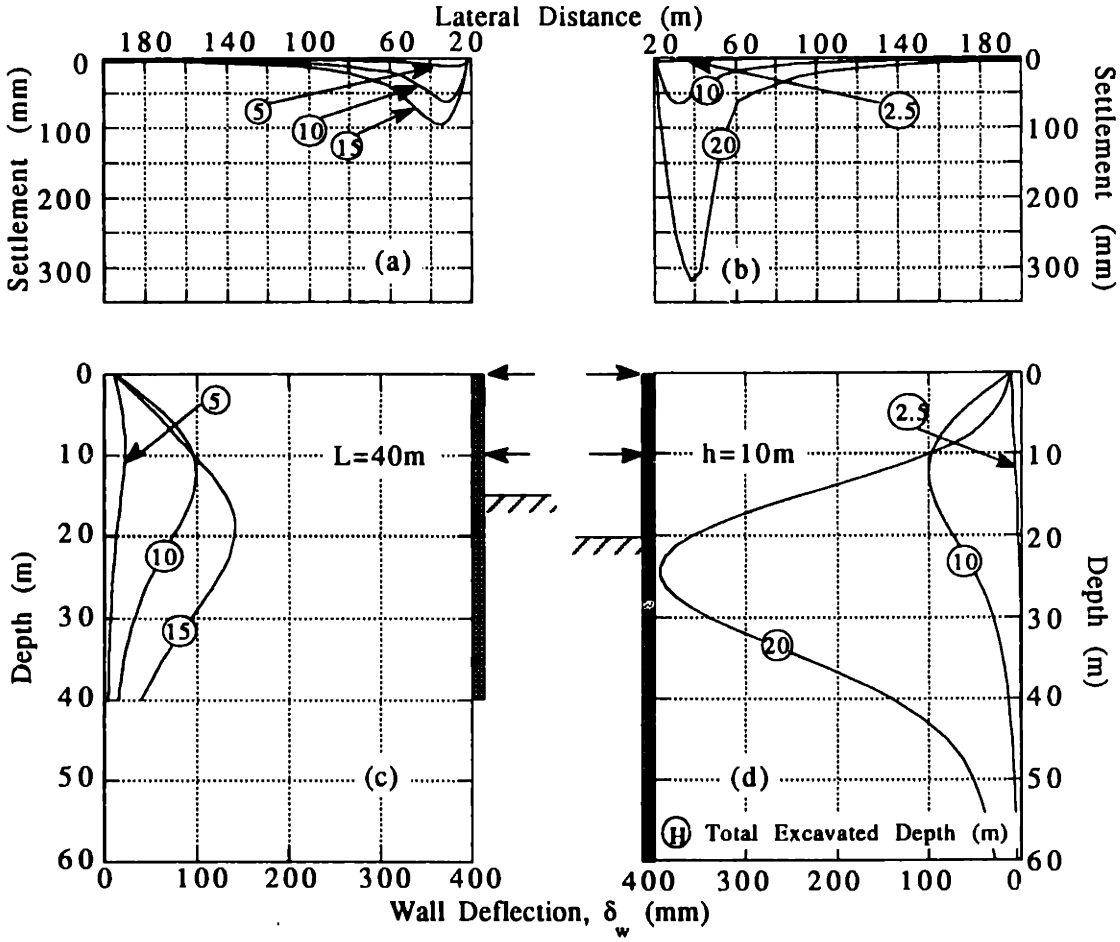

Figure 4.4-6 Lateral Wall Deflections and Surface Settlements for L=40m and L=60m Wall Analyses (h_u=2.5m, h=10m, MIT-E3, OCR=1)

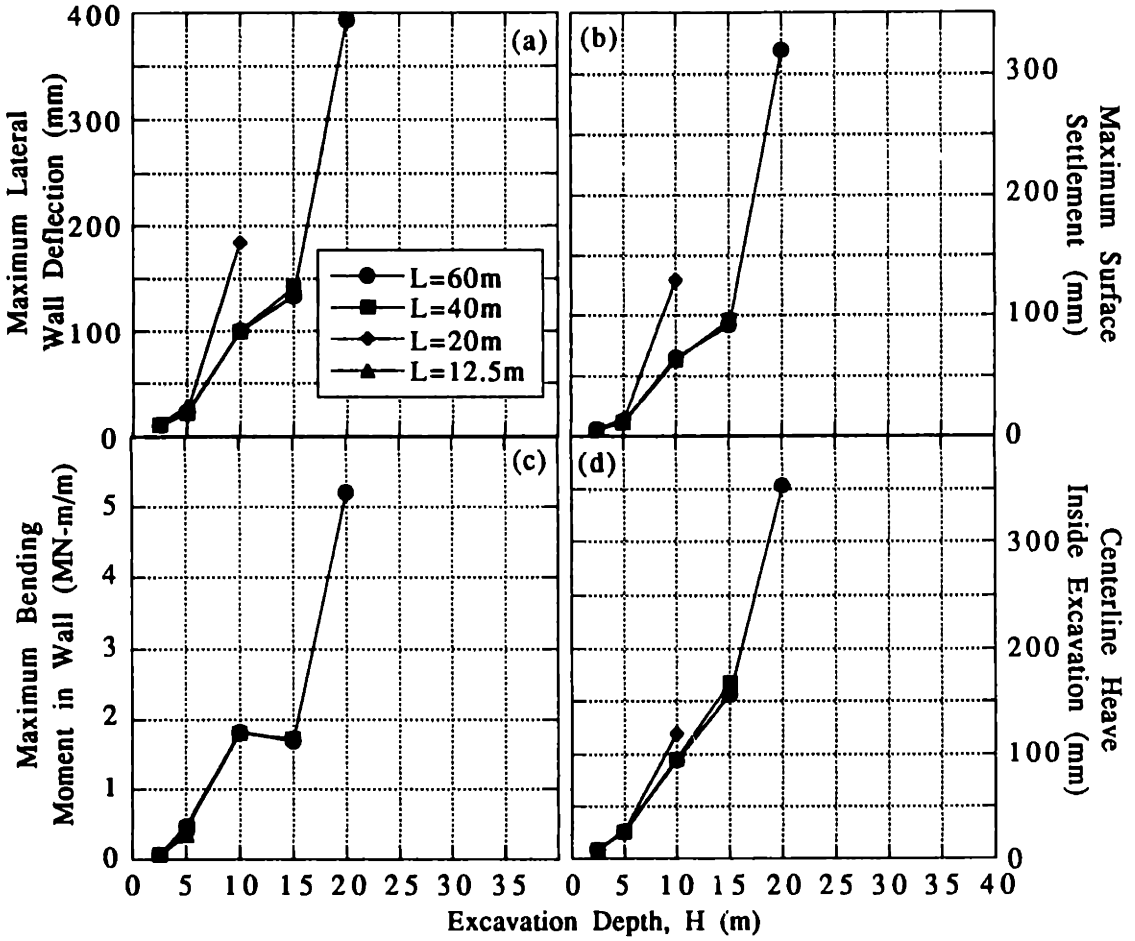

Figure 4.4-7 Effect of Wall Length on Maximum Deformations and Moments (h_u=2.5m, h=10m, MIT-E3, OCR=1)

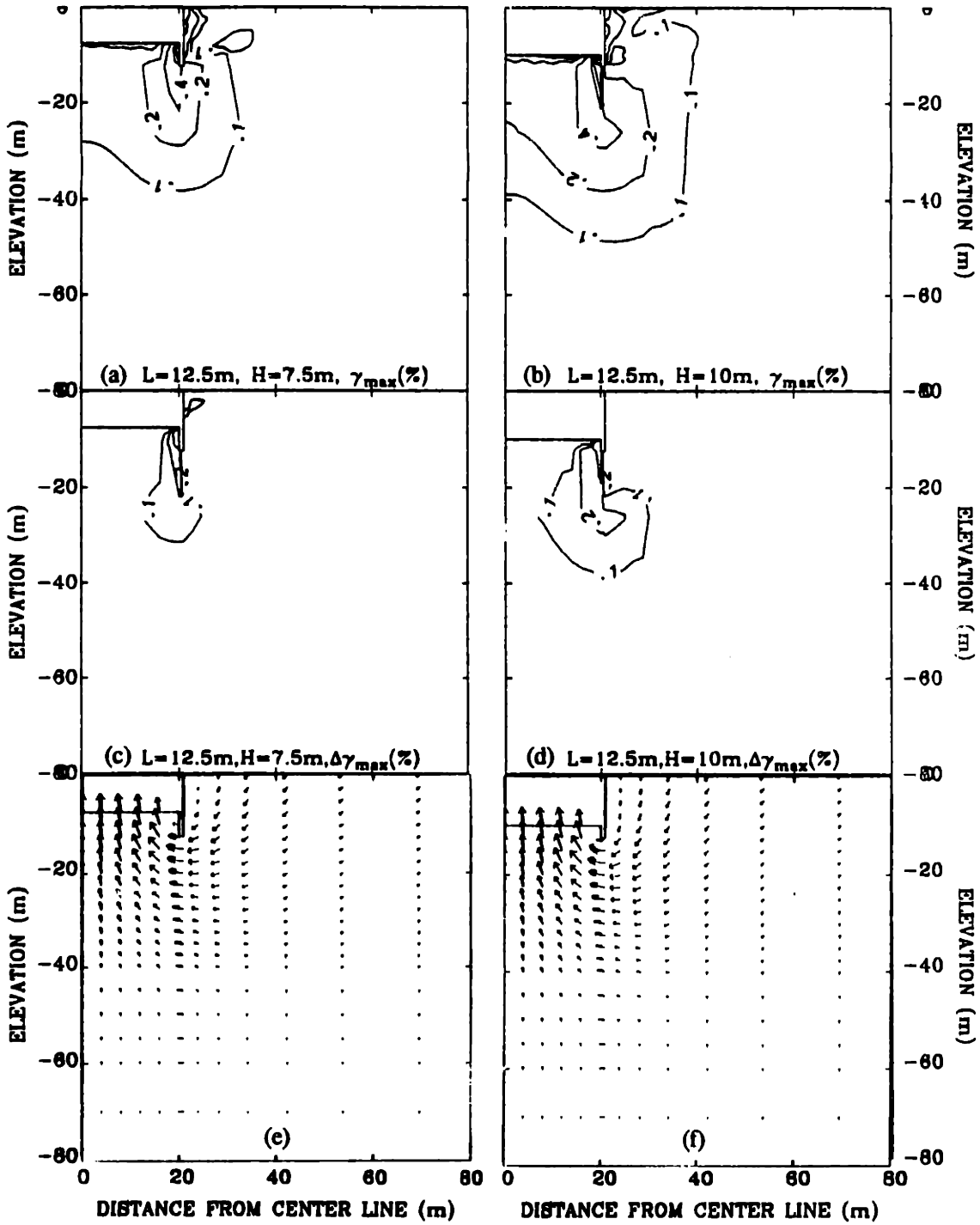

Figure 4.4-8 Maximum and Incremental Maximum Shear Strain Contours, and Incremental Displacement Vector Field for L=12.5m Analysis (h_u=2.5m, h=2.5m, MIT-E3, OCR=1)

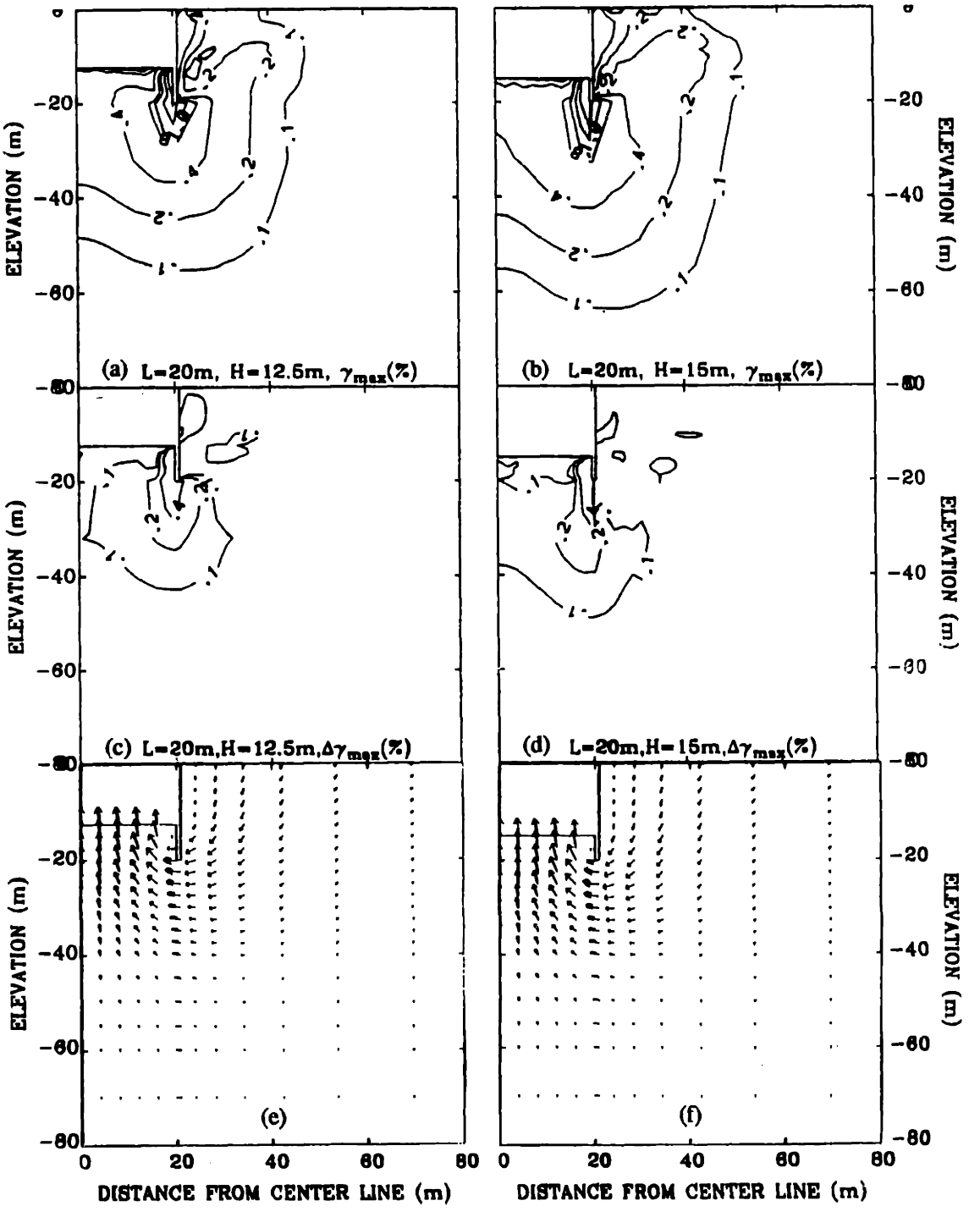

Figure 4.4-9 Maximum and Incremental Maximum Shear Strain Contours, and Incremental Displacement Vector Field for L=20m Analysis (h_u=2.5m, h=2.5m, MIT-E3, OCR=1)

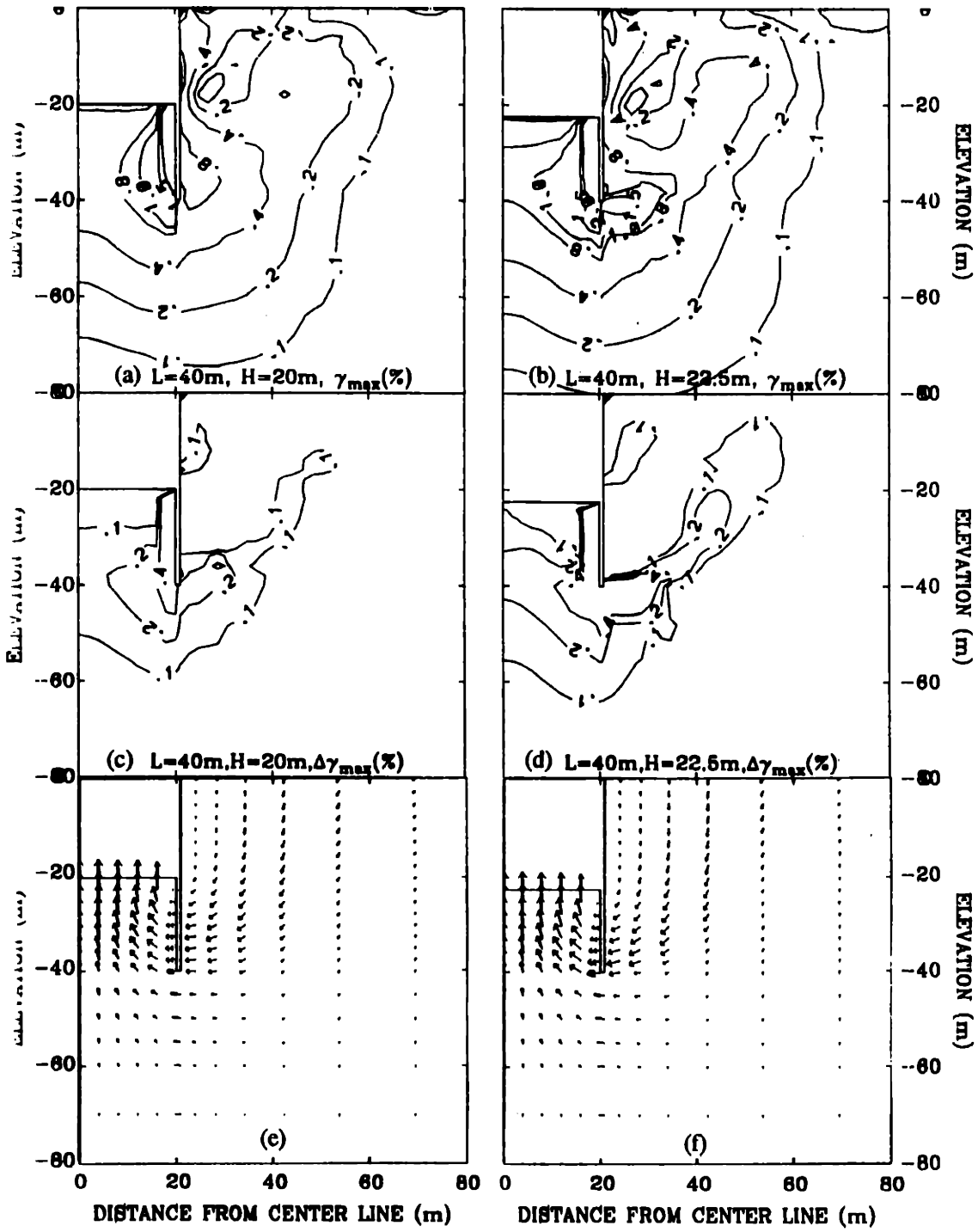

Figure 4.4-10 Maximum and Incremental Maximum Shear Strain Contours, and Incremental Displacement Vector Field for L=40m Analysis (h_u=2.5m, h=2.5m, MIT-E3, OCR=1)

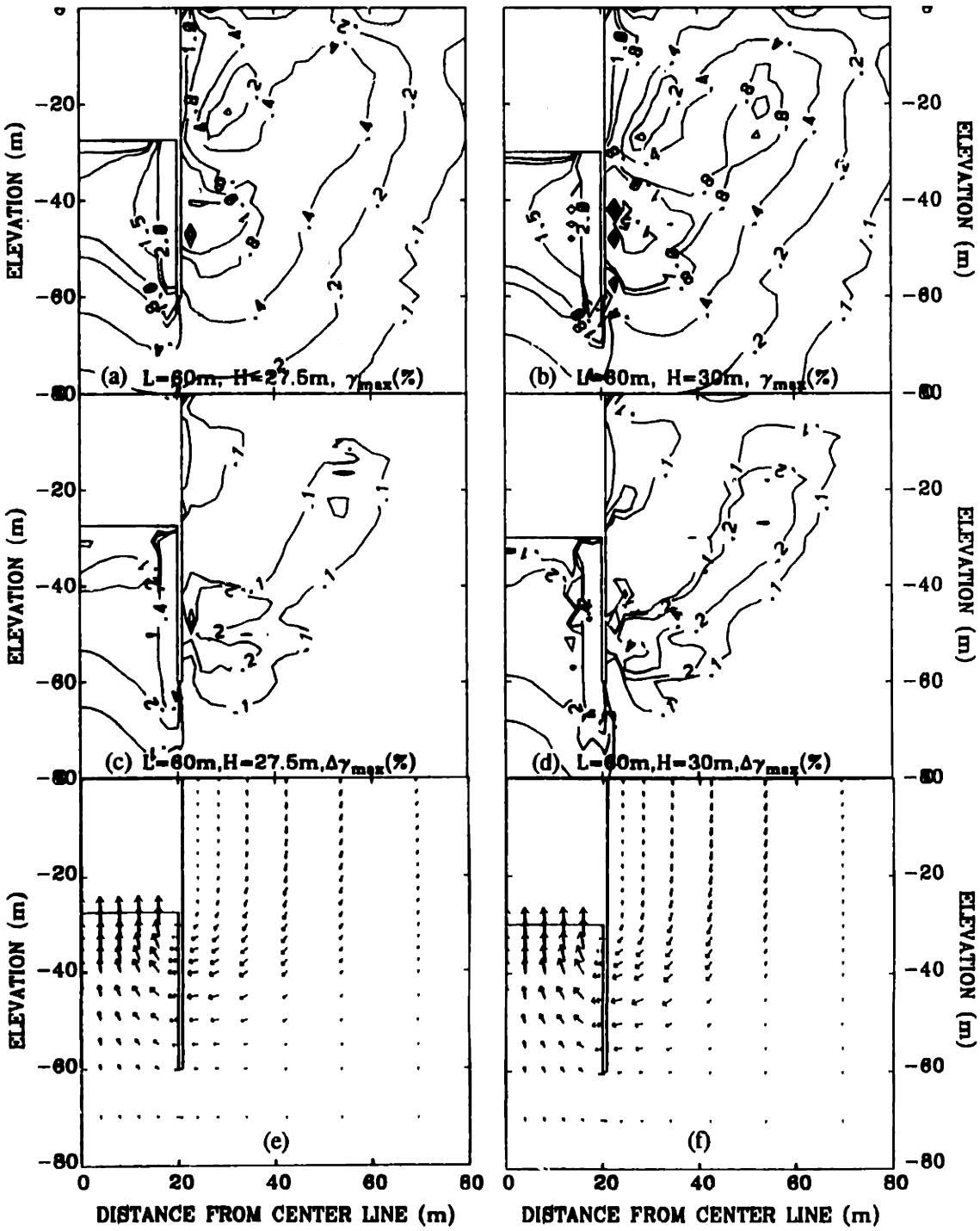

Figure 4.4-11 Maximum and Incremental Maximum Shear Strain Contours, and Incremental Displacement Vector Field for L=60m Analysis (h_u=2.5m, h=2.5m, MIT-E3, OCR=1)

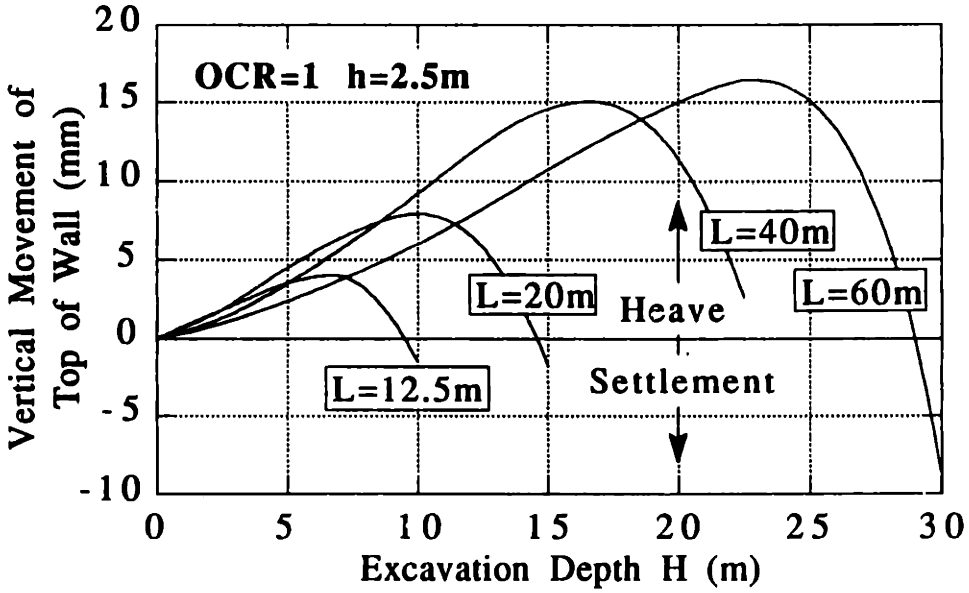

Figure 4.4-12 Effect of Wall Length on Vertical Wall Displacement (h_u=2.5m, h=2.5m, MIT-E3, OCR=1)

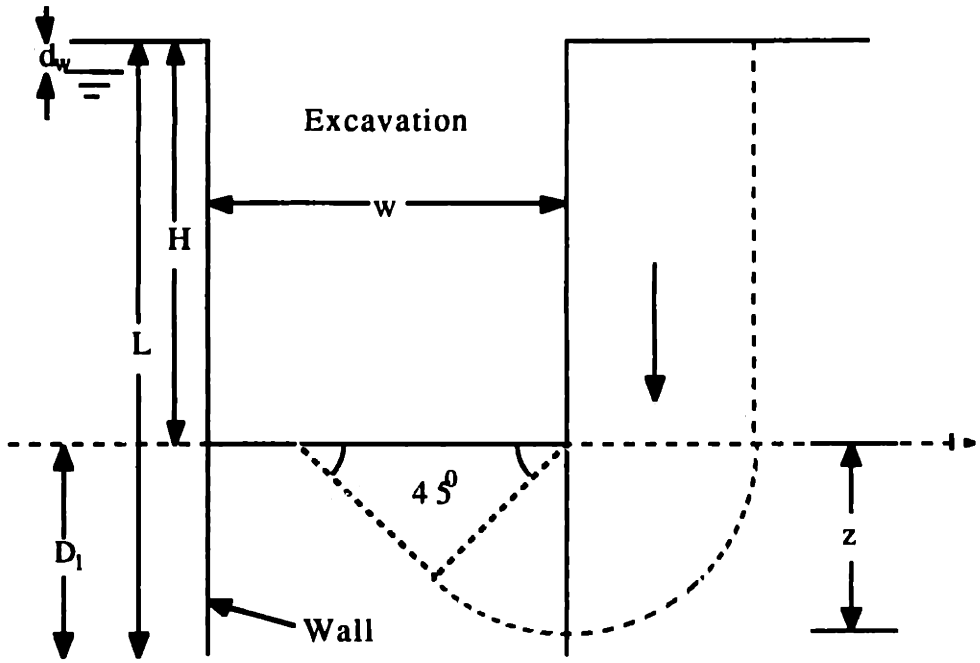

a) Failure Mechanism

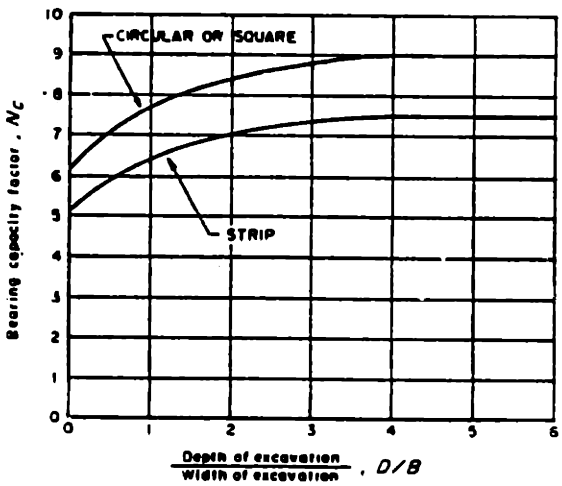

b) N_c Factor (Bejrrum & Eide 1956)

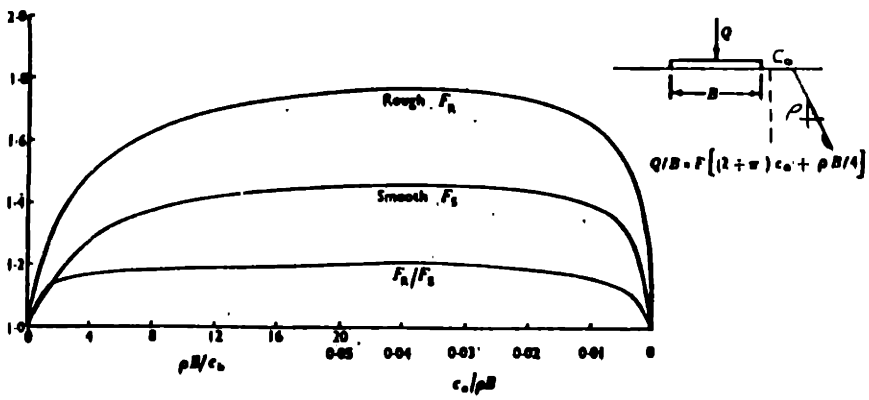

b) F_s Correction Factor (Davis & Booker 1973)

Figure 4.4-13 Definitions of Factor of Safety Against Basal Heave
(continued on next page).

Method	Reference	Factor of Safety Against Basal Heave, FS:
1	Terzaghi (1943)	$\dfrac{5.14\,\frac{\tau_{DSS}}{\sigma'_{v0}}\left[\gamma_t\left(H+\frac{w/\sqrt{2}}{2}\right)-\gamma_b\left(H+\frac{w/\sqrt{2}}{2}-d_w\right)\right]}{\gamma_t H-\frac{\tau_{DSS}}{\sigma'_{v0}}\frac{H}{w/\sqrt{2}}\left[\gamma_t\left(\frac{H}{2}\right)-\gamma_b\left(\frac{H}{2}-d_w\right)\right]}$
2	Ladd	$\dfrac{5.14\,\frac{S_{u,A}}{\sigma'_{v0}}\left[\gamma_t\left(H+\frac{z}{2}\right)-\gamma_b\left(H+\frac{z}{2}-d_w\right)\right]}{\gamma_t H-\frac{\tau_{DSS}}{\sigma'_{v0}}\frac{H}{z}\left[\gamma_t\left(\frac{H}{2}\right)-\gamma_b\left(\frac{H}{2}-d_w\right)\right]}$
3	Bejrrum & Eide	$\dfrac{N_c\,\frac{\tau_{DSS}}{\sigma'_{v0}}\left[\gamma_t\left(H+\frac{w/\sqrt{2}}{2}\right)-\gamma_b\left(H+\frac{w/\sqrt{2}}{2}-d_w\right)\right]}{\gamma_t H}$
4	Davis & Booker	$\dfrac{F_s\left[(2+\pi)\left(\frac{\tau_{DSS}}{\sigma'_{v0}}d_w\gamma_w+H\frac{\tau_{DSS}}{\sigma'_{v0}}\gamma_b\right)+\gamma_b\frac{\tau_{DSS}}{\sigma'_{v0}}\frac{w}{4}\right]}{\gamma_t H-\frac{H}{w/\sqrt{2}}\frac{\tau_{DSS}}{\sigma'_{v0}}\left[\gamma_t\frac{H}{2}-\gamma_w\left(\frac{H}{2}-d_w\right)\right]}$
5	Davis & Booker with Wall Length Effect	$\dfrac{\left\langle F_s\frac{\tau_{DSS}}{\sigma'_{v0}}\left[(2+\pi)(d_w\gamma_w+L\gamma_b)+\gamma_b\frac{w}{4}\right]+(L-H)\left\{\gamma_t+\frac{1}{w}\frac{\tau_{DSS}}{\sigma'_{v0}}\left[\gamma_t\frac{L+H}{2}-\gamma_w\left(\frac{L+H}{2}-d_w\right)\right]\right\}\right\rangle}{\gamma_t L-\frac{L}{w/\sqrt{2}}\frac{\tau_{DSS}}{\sigma'_{v0}}\left[\gamma_t\frac{L}{2}-\gamma_w\left(\frac{L}{2}-d_w\right)\right]}$

Note 1: The classical Terzaghi equation for the factor of saftey against basal heave was developed for a constant strength with depth profile:

$$FS=\frac{S_{ub}N_c}{\gamma_t H-S_{ut}\left(\frac{H}{z}\right)} \qquad S_{ub}=S_{ut}=S_u$$

For a profile with increasing strength with depth, S_{ut} is the average strength over H, and S_{ub} is the average strength over z. This is reflected in the table above. N_c=5.14 for a 'smooth footing', N_c=5.7 for 'rough footing'.

Note 2: Method 4 is developed from the bearing capacity formula proposed by Davis and Booker (1973) using the same technique that Terzaghi (1943) adopted in deriving his original equation.

Note 3: In methods 1, 3 and 4; z=w/2. In method 2, z is varied until the minimum FS is obtained.

Note 4: In methods 1, 3 and 4 the undrained shear strength measured in DSS shearing mode (τ_{DSS}) is used (Table 4.2-2d).

Note 5: In method 2; $S_{u,A}=\frac{1}{3}(S_{u,PSA}+\tau_{u,DSS}+S_{u,PSP})$ (Table 4.2-2d).

Figure 4.4-13 Definitions of Factor of Safety Against Basal Heave
(continued from previous page).

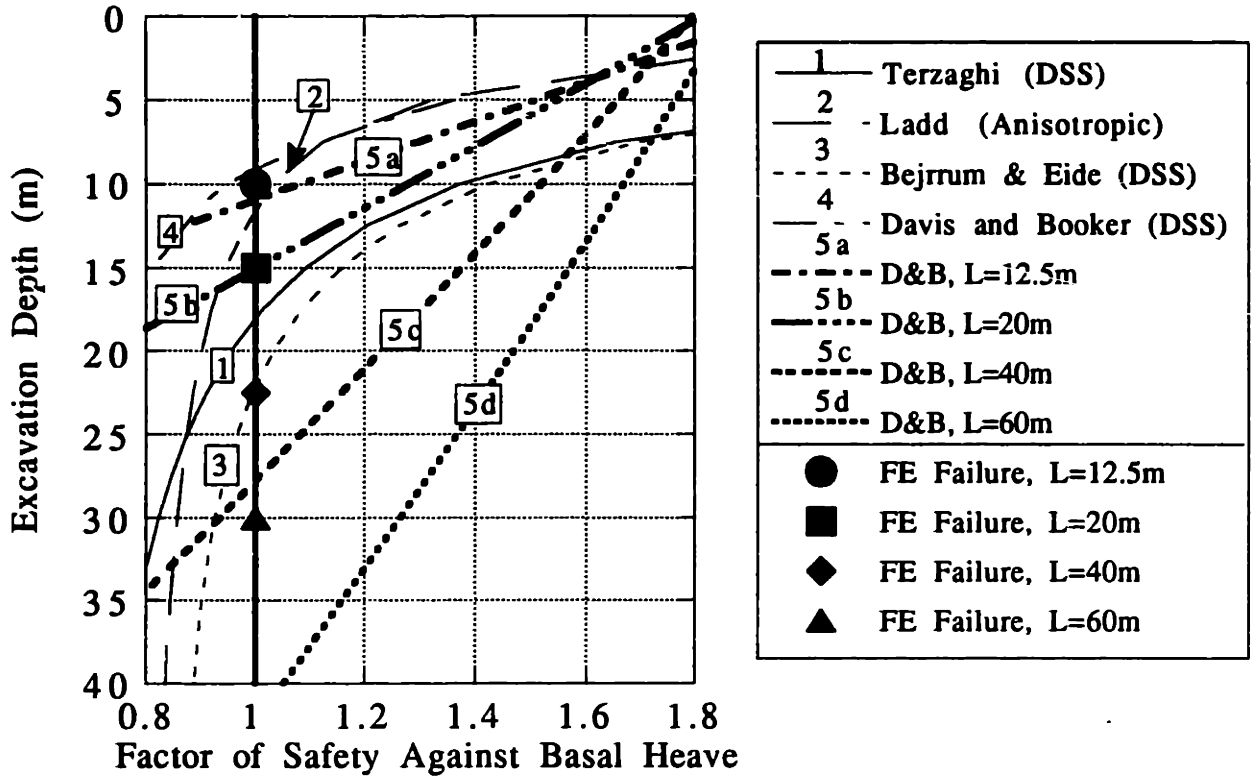

Figure 4.4-14 Factor of Safety Against Failure for the FE Analyses (h_u=2.5m, h=2.5m, MIT-E3, OCR=1)

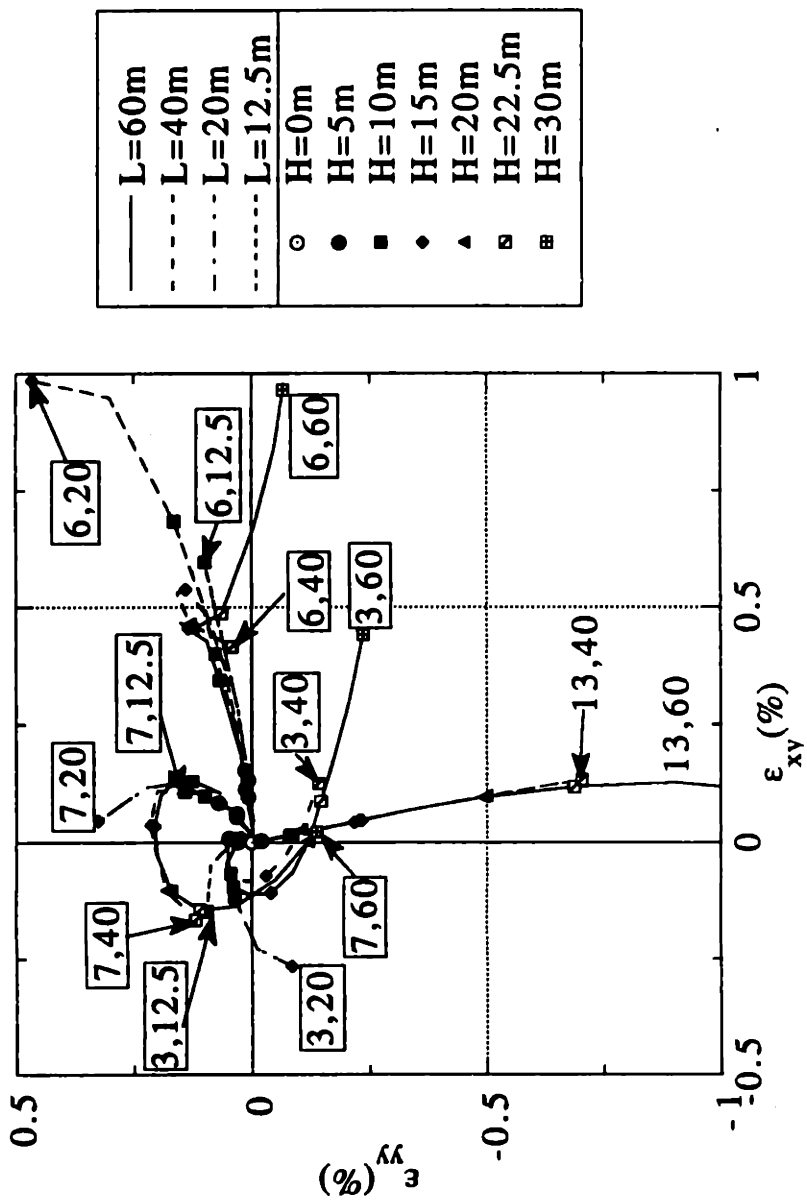

Figure 4.4-15 Effect of Wall Length on Soil Strain Paths (h_u=2.5m, h=2.5m, MIT-E3, OCR=1)

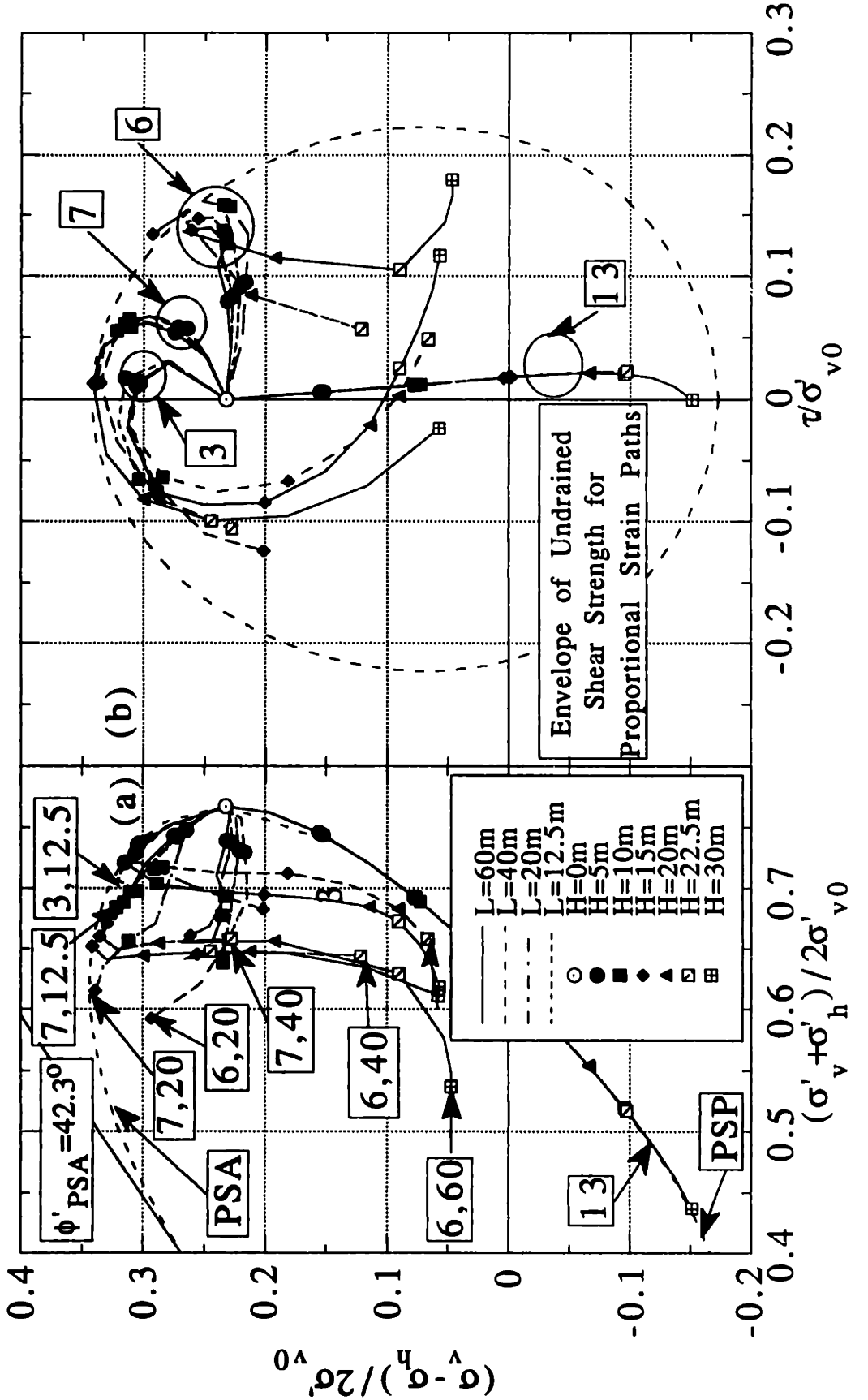

Figure 4.4-16 Effect of Wall Length on Normalized Soil Stress Paths (h_u=2.5m, h=2.5m, MIT-E3, OCR=1)

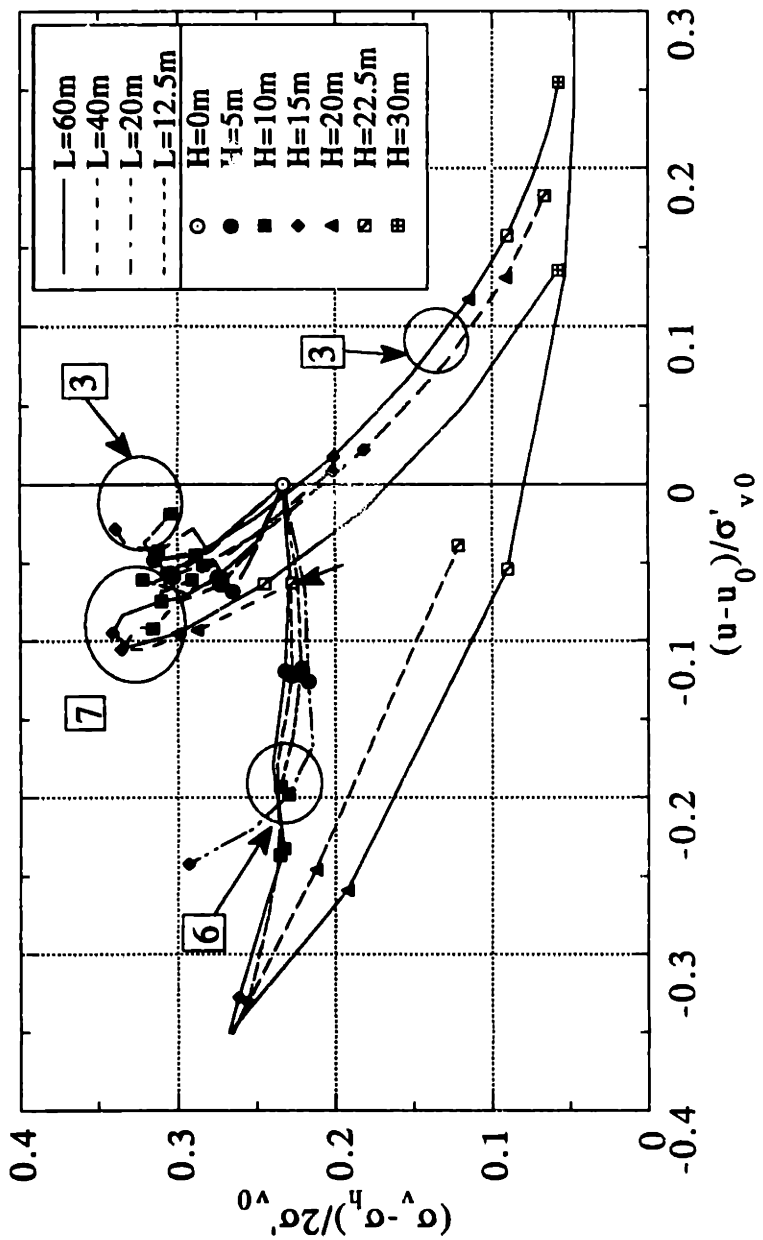

Figure 4.4-17 Effect of Wall Length on Normalized Pore Pressure Change Paths in the Retained Soil (h_u=2.5m, h=2.5m, MIT-E3, OCR=1)

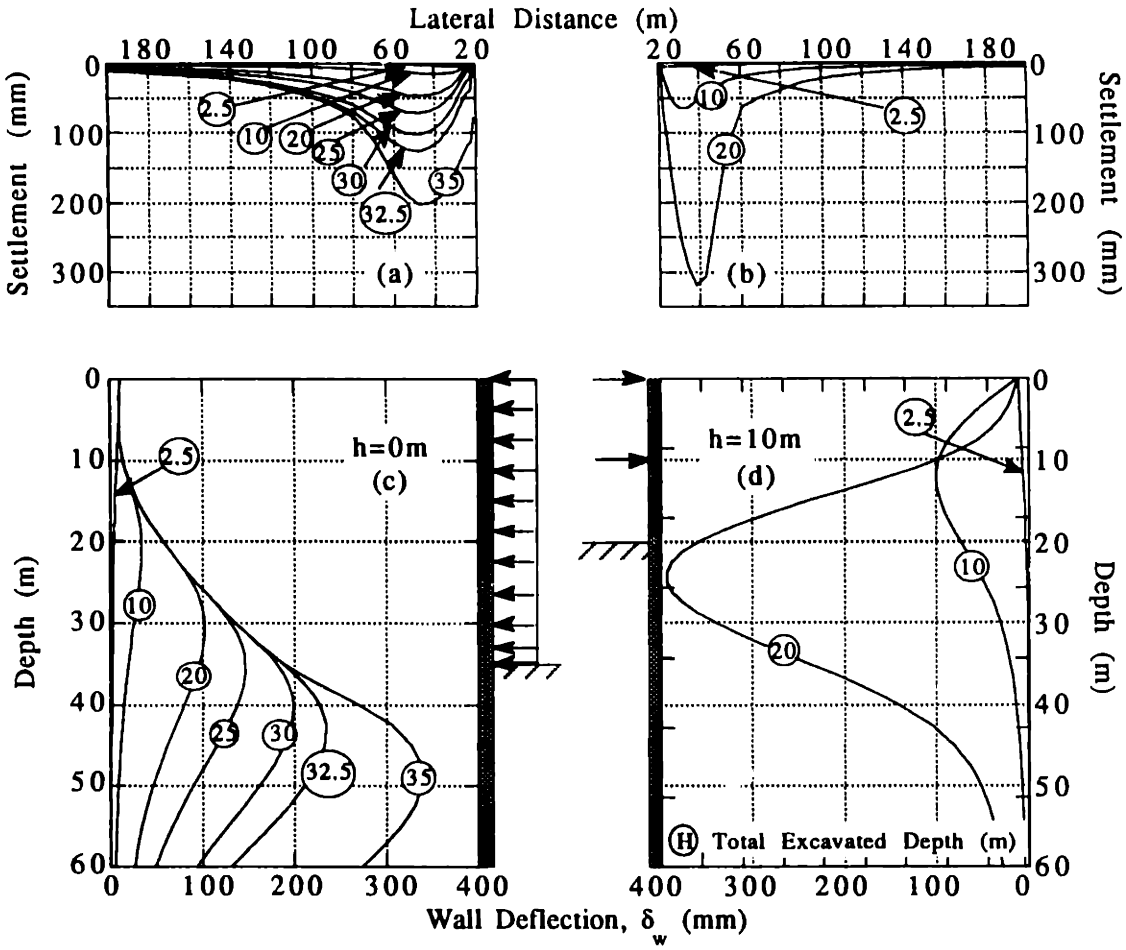

Figure 4.5-1 Wall Deflections and Surface Settlements for h=0m and h=10m Analyses (h_u=2.5m, L=60m, MIT-E3, OCR=1).

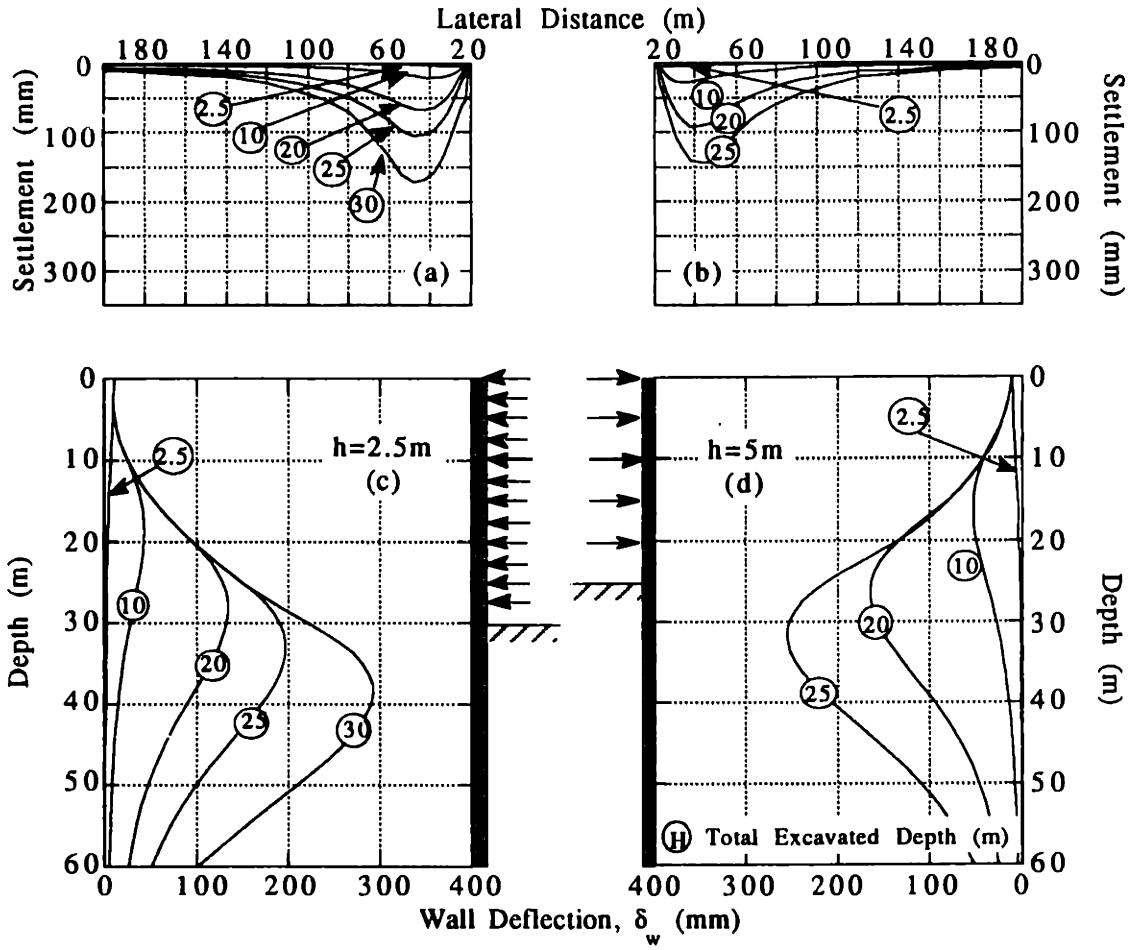

Figure 4.5-2 Wall Deflections and Surface Settlements for h=2.5m and h=5m Analyses (h_u=2.5m, L=60m, MIT-E3, OCR=1).

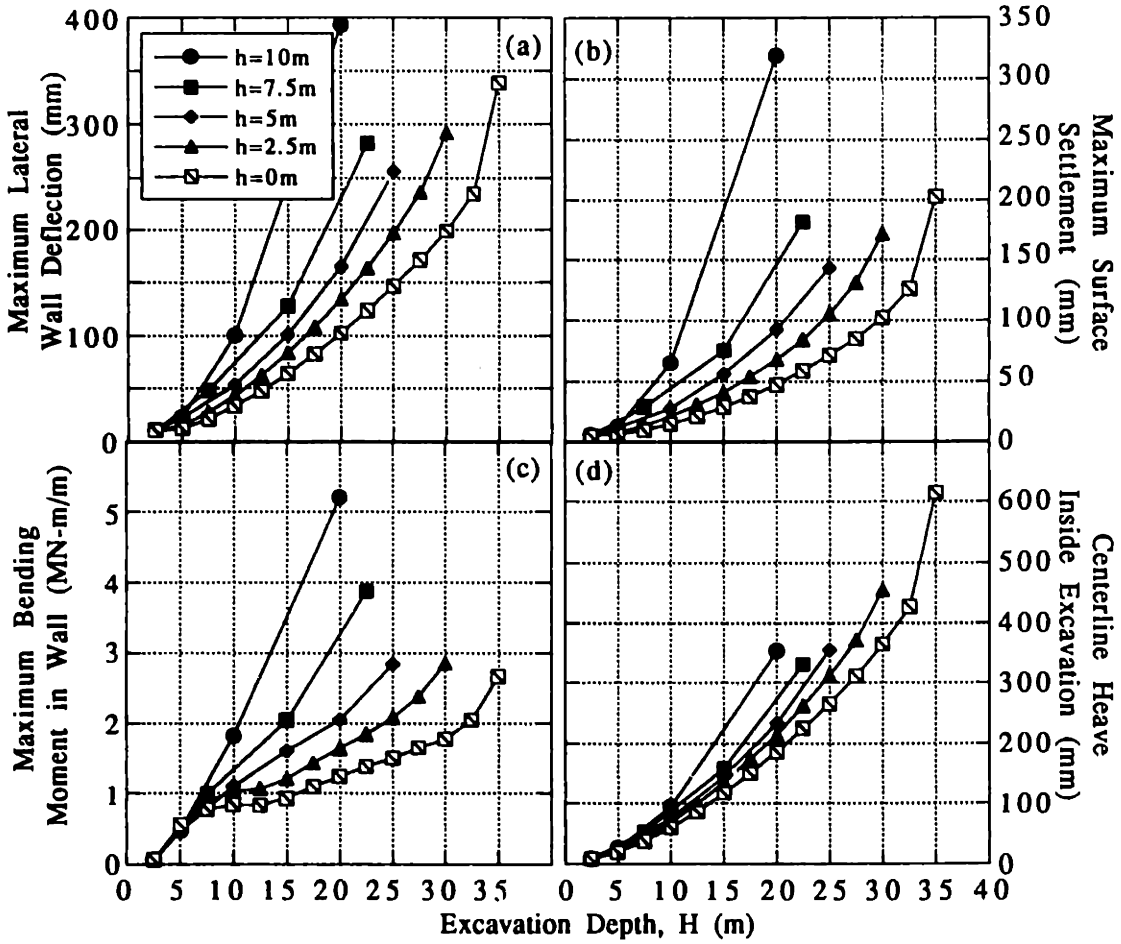

Figure 4.5-3 Effect of Vertical Support Spacing on Maximum Deformations and Moments (h_u=2.5m, L=60m, MIT-E3, OCR=1).

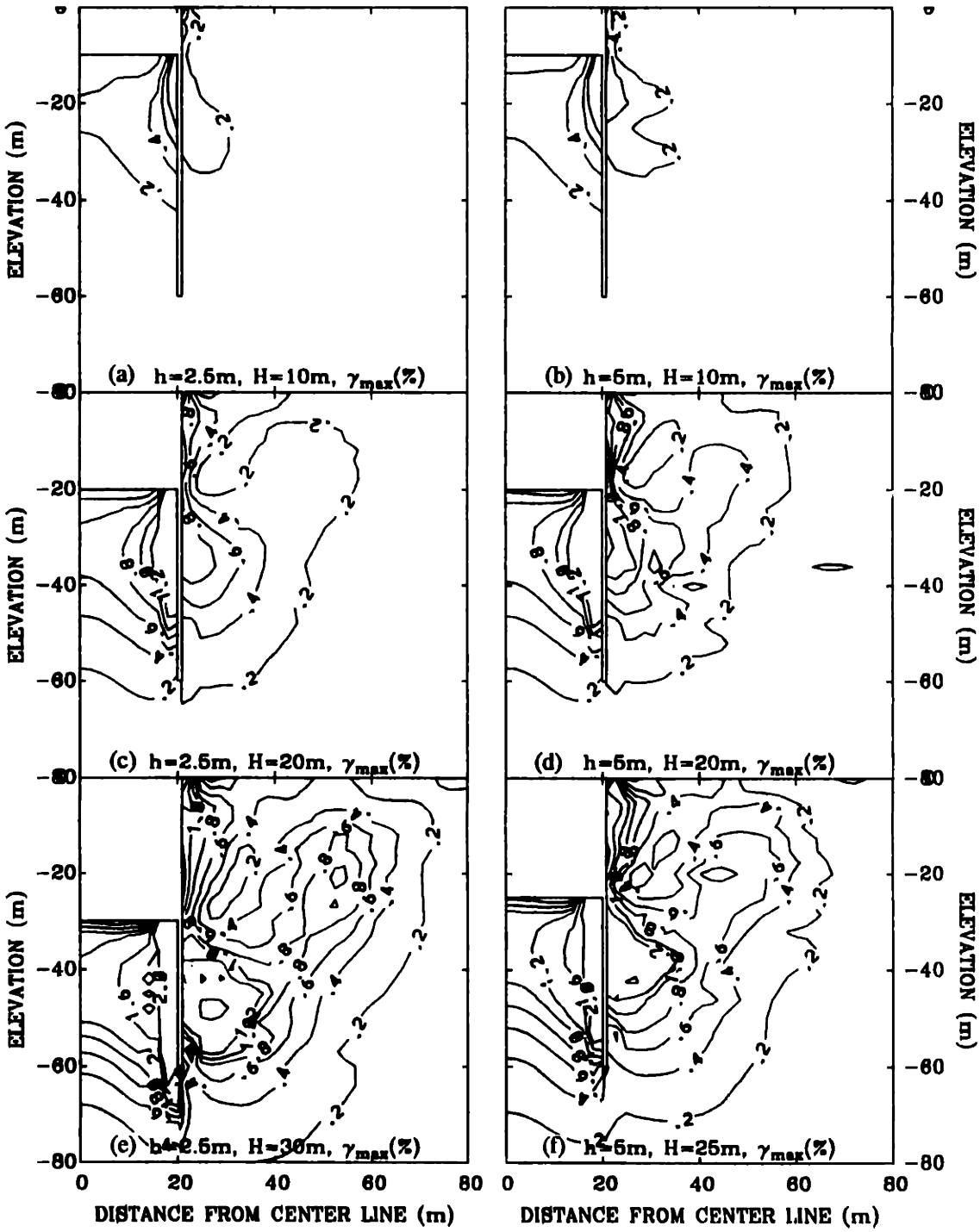

Figure 4.5-4 Maximum Shear Strain Contours for h=2.5m and 5m Analyses (h_u=2.5m, L=60m, MIT-E3, OCR=1).

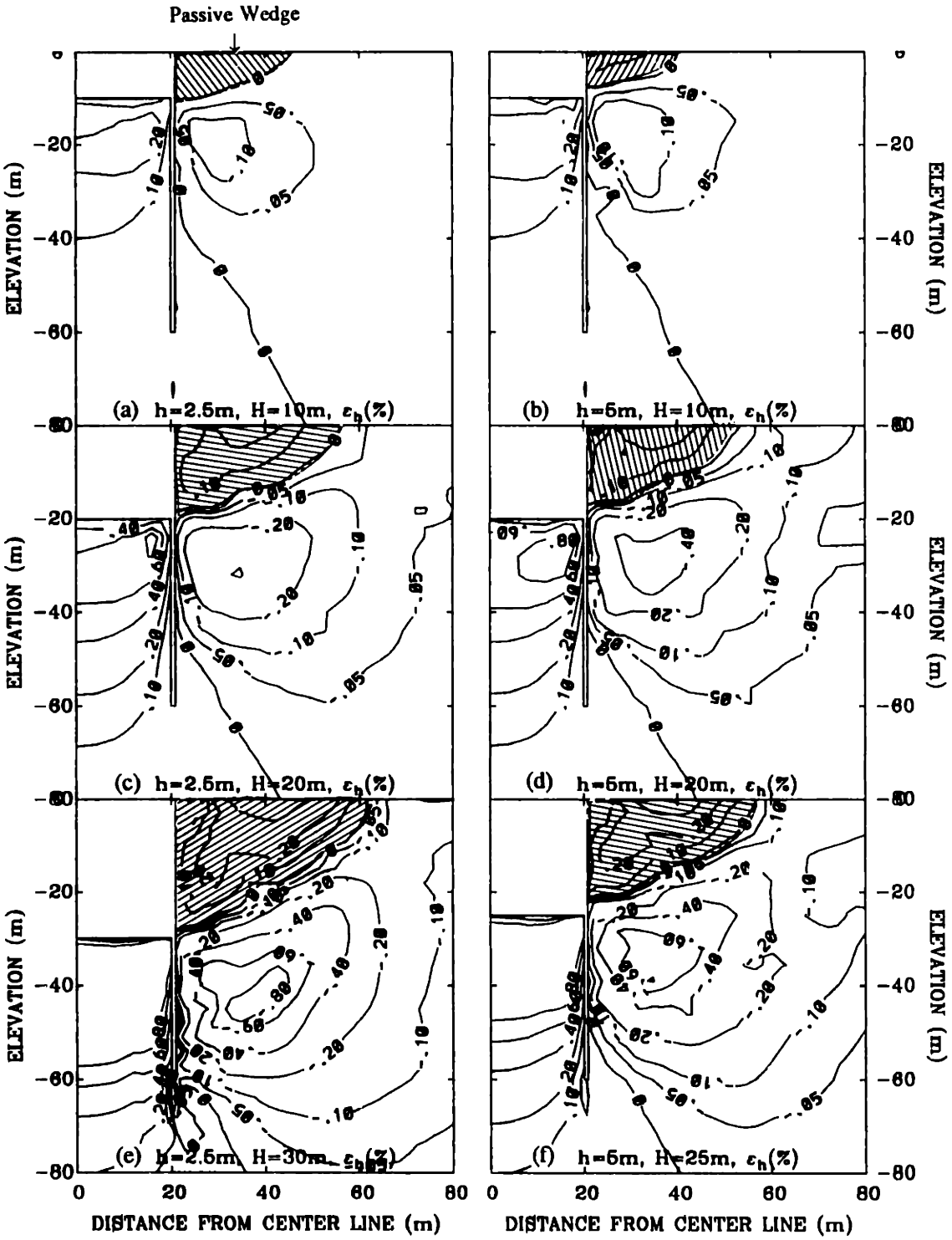

Figure 4.5-5 Horizontal Strain Contours for h=2.5m and 5m Analyses (h_u=2.5m, L=60m, MIT-E3, OCR=1).

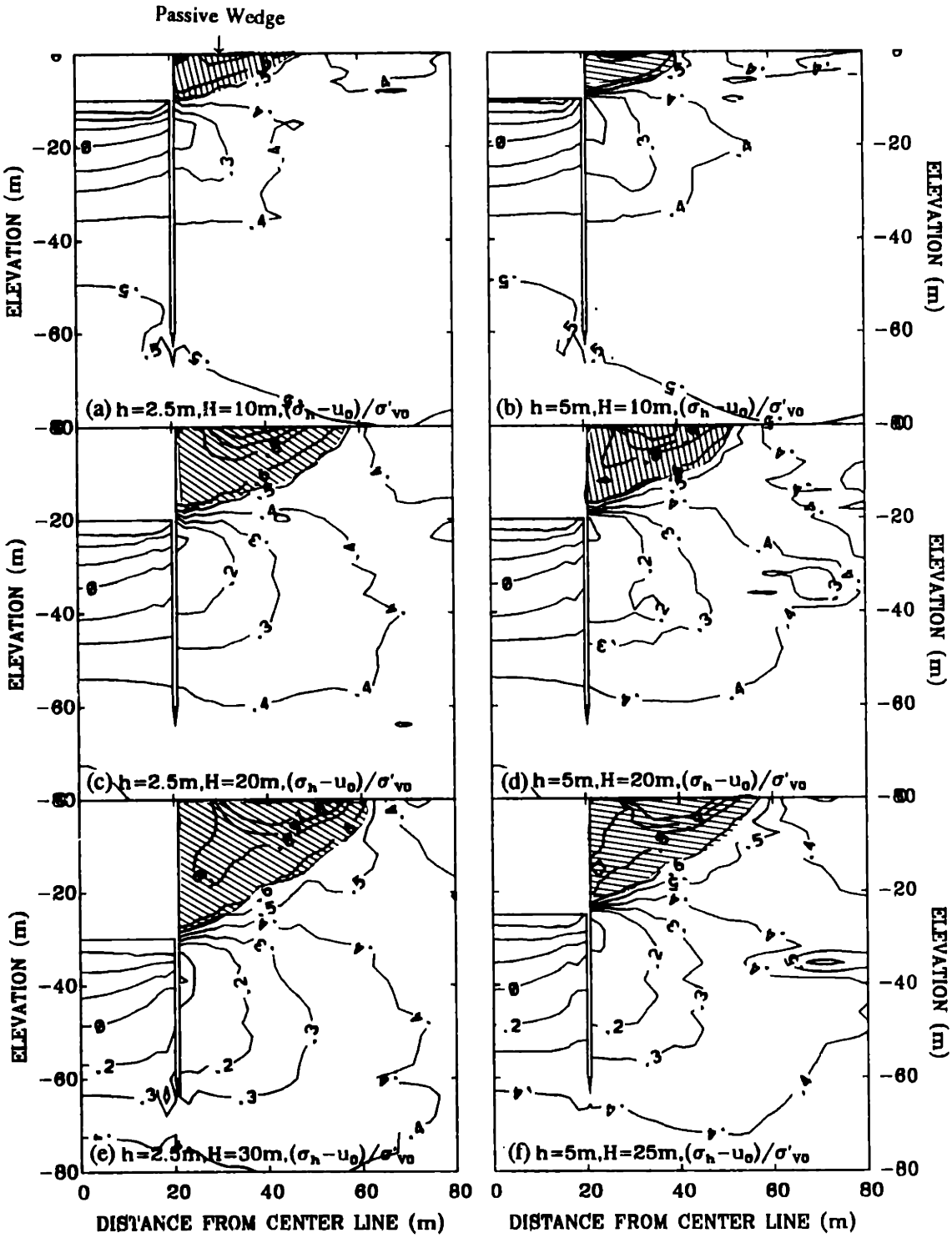

Figure 4.5-6 Normalized Horizontal Stress Contours for h=2.5m and 5m Analyses (h_u=2.5m, L=60m, MIT-E3, OCR=1).

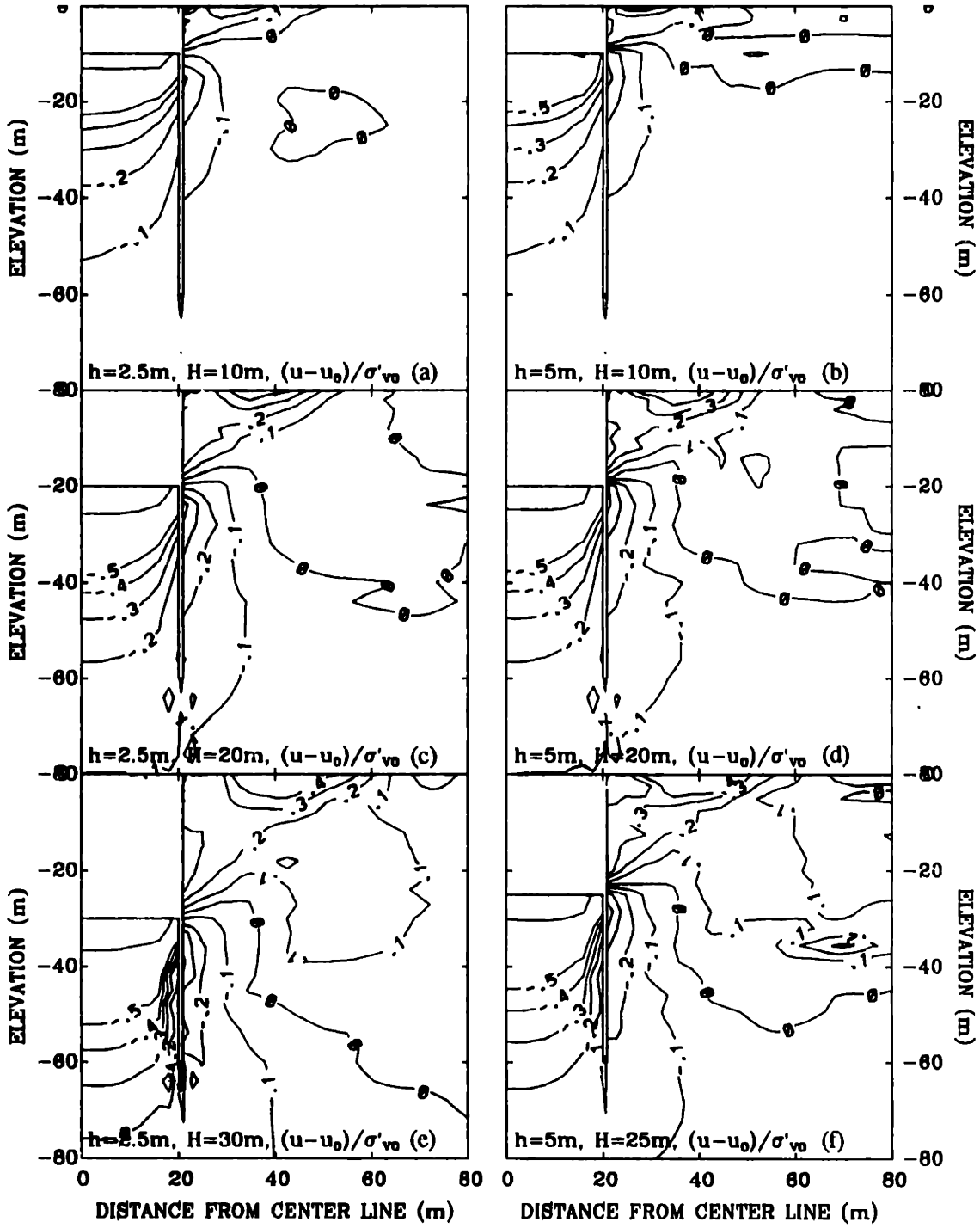

Figure 4.5-7 Normalized Excess Pore Pressure Contours for h=2.5m and 5m Analyses (h_u=2.5m, L=60m, MIT-E3, OCR=1).

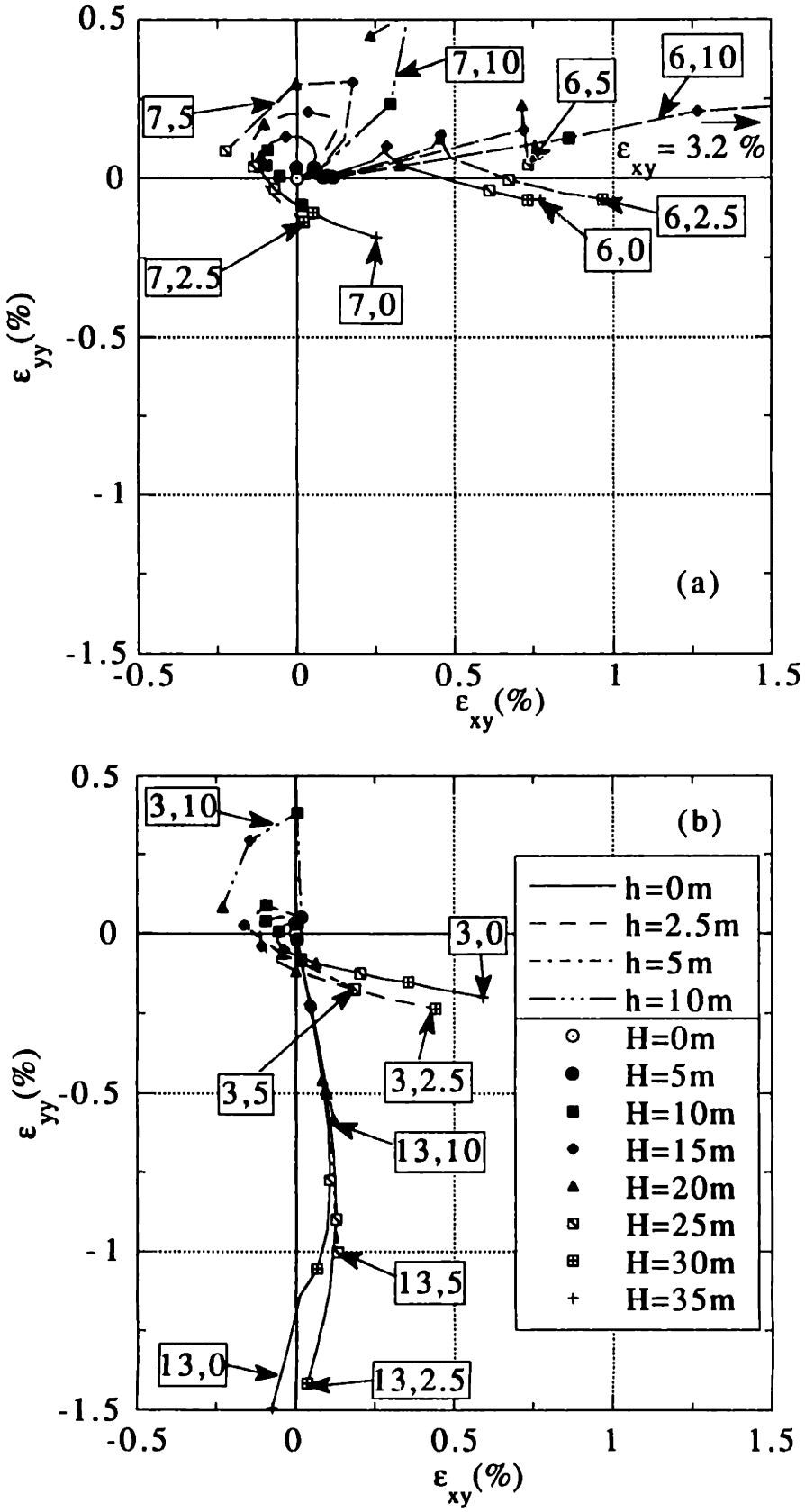

Figure 4.5-8 Effect of Vertical Support Spacing on Soil Strain Paths (h_u=2.5m, L=60m, MIT-E3, OCR=1).

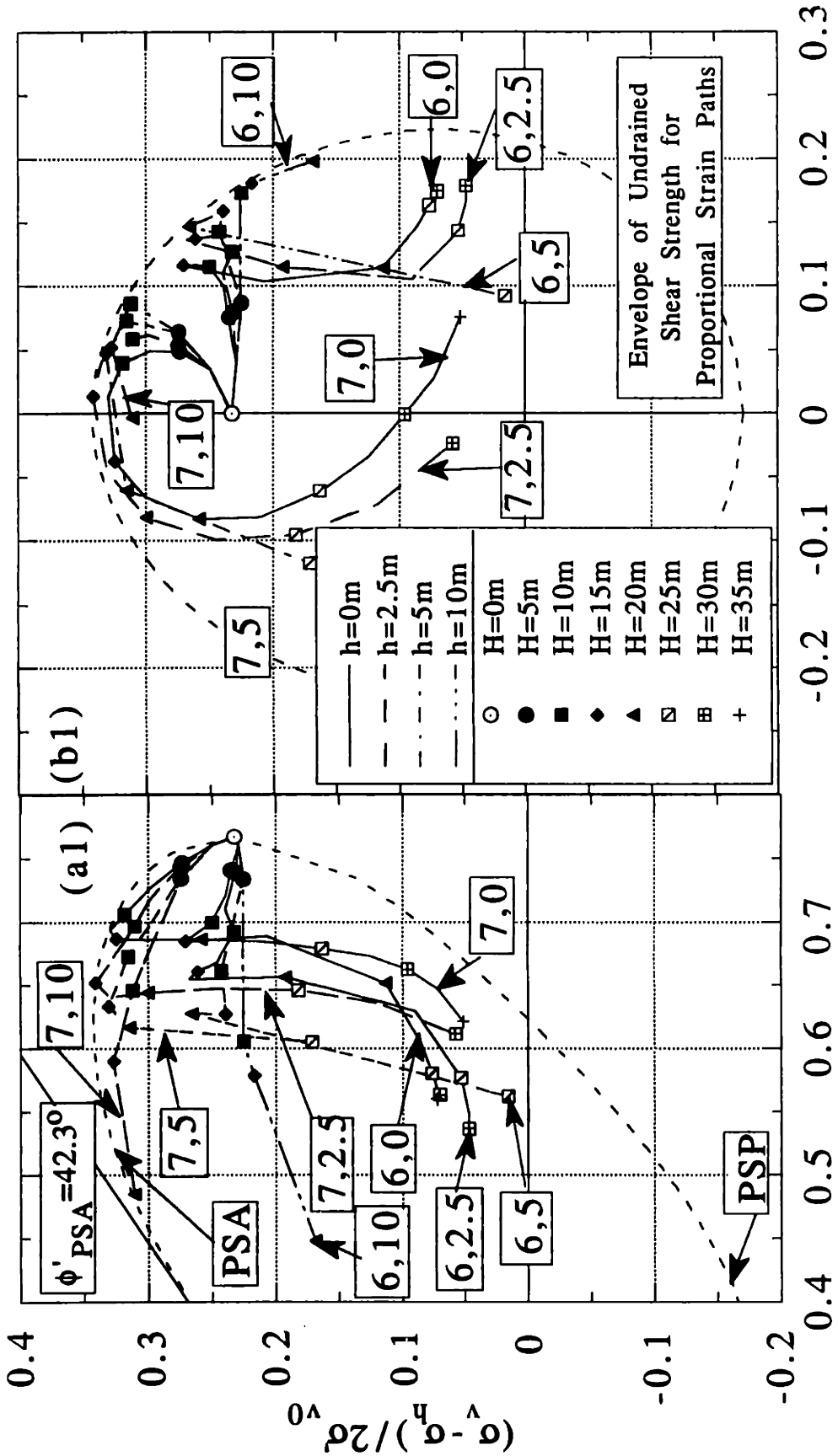

Figure 4.5-9 Effect of Vertical Support Spacing on Normalized Soil Stress Paths (h_u=2.5m, L=60m, MIT-E3, OCR=1).

(continued on next page)

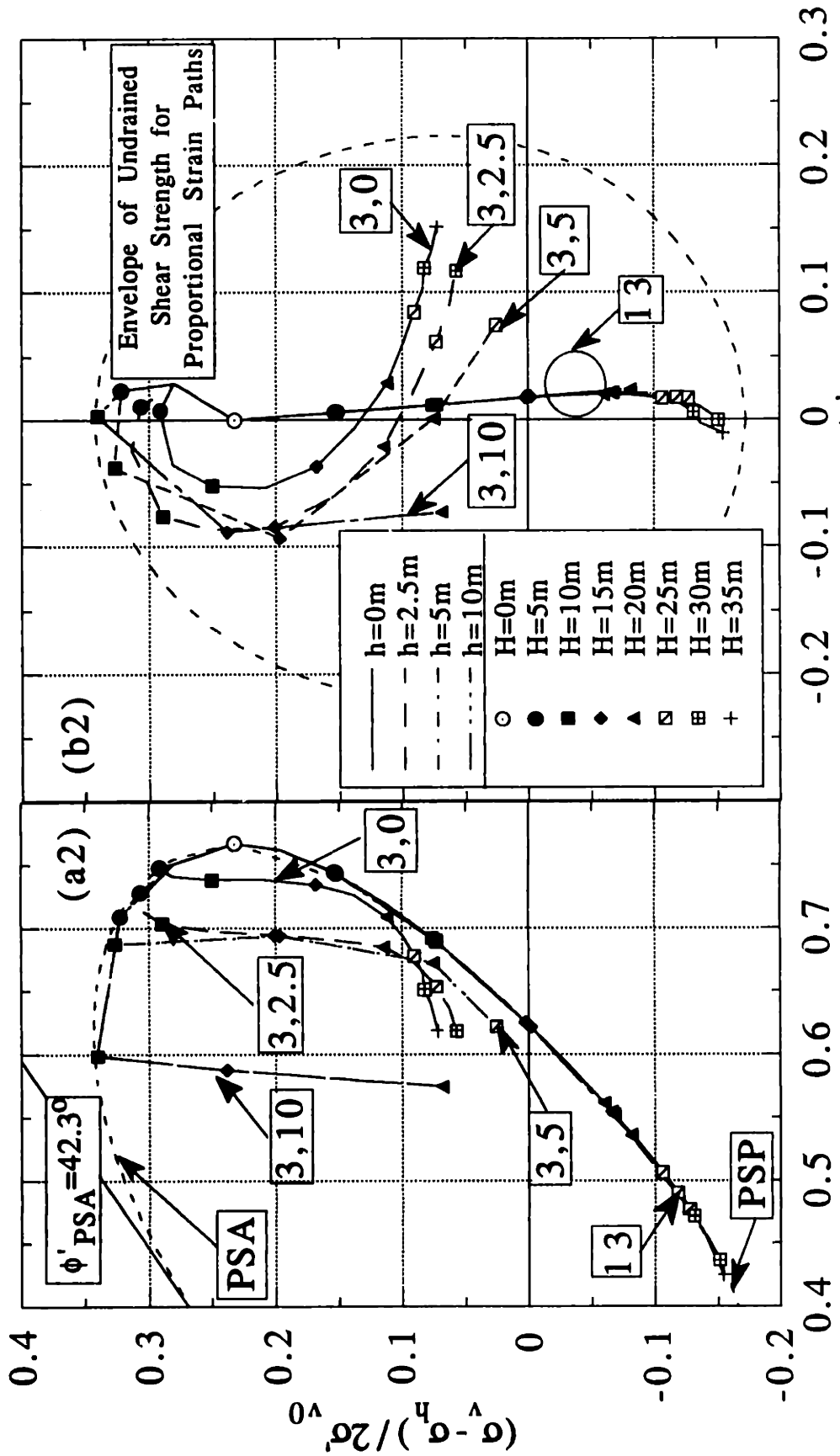

Figure 4.5-9 Effect of Vertical Support Spacing on Normalized Soil Stress Paths (h_u=2.5m, L=60m, MIT-E3, OCR=1).
(continued from previous page)

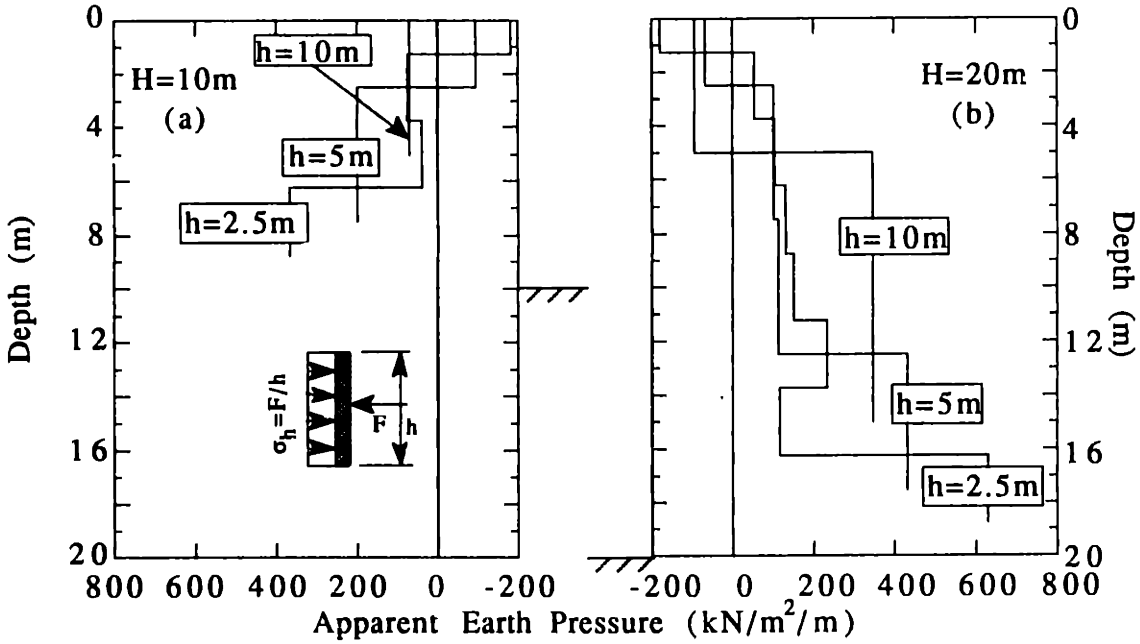

Figure 4.5-10 Effect of Vertical Support Spacing on Apparent Earth Pressures (h_u=2.5m, L=60m, MIT-E3, OCR=1).

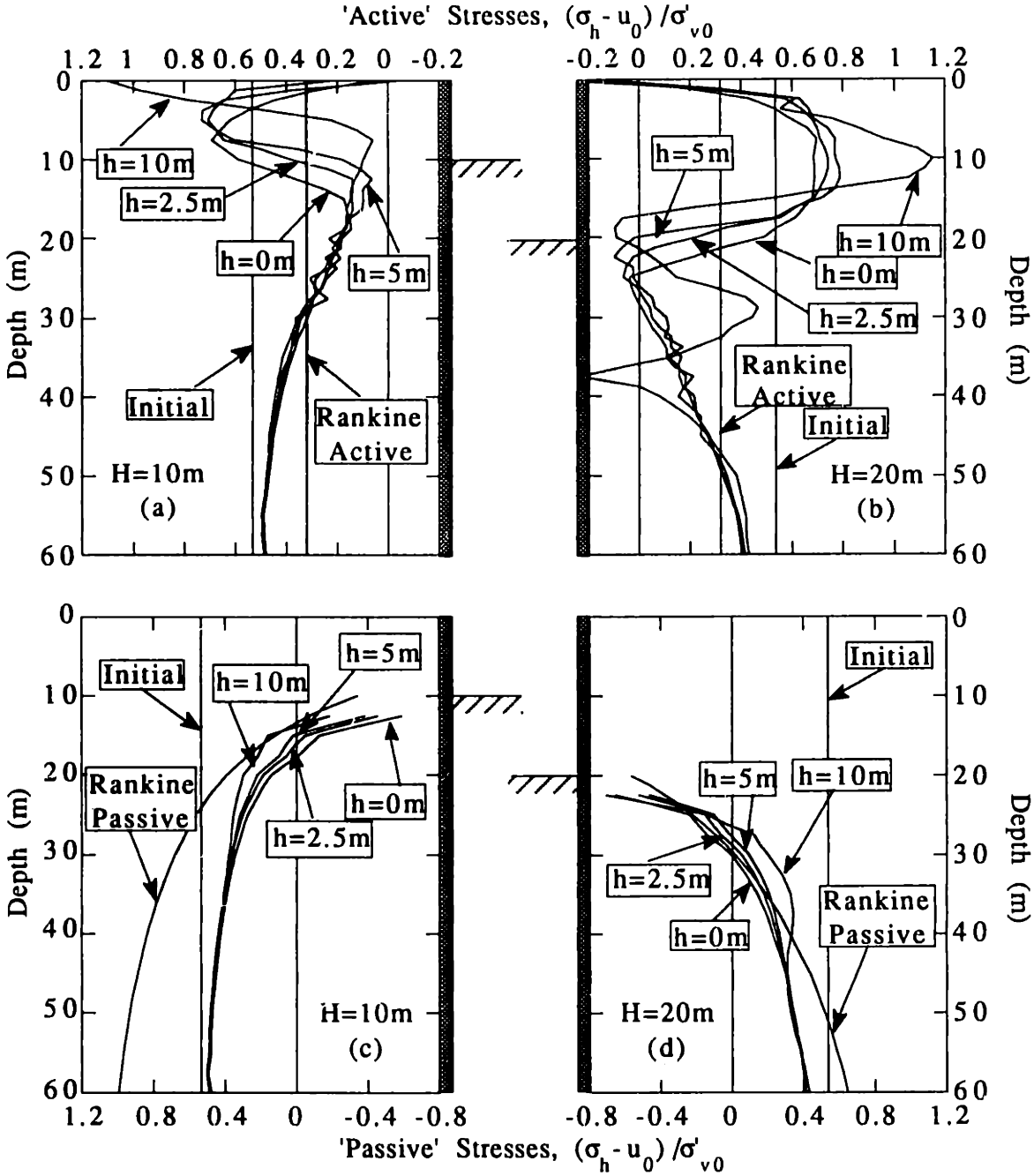

Figure 4.5-11 Effect of Vertical Support Spacing on Normalized Earth Pressures Acting on Both Sides of the Wall (h_u=2.5m, L=60m, MIT-E3, OCR=1).

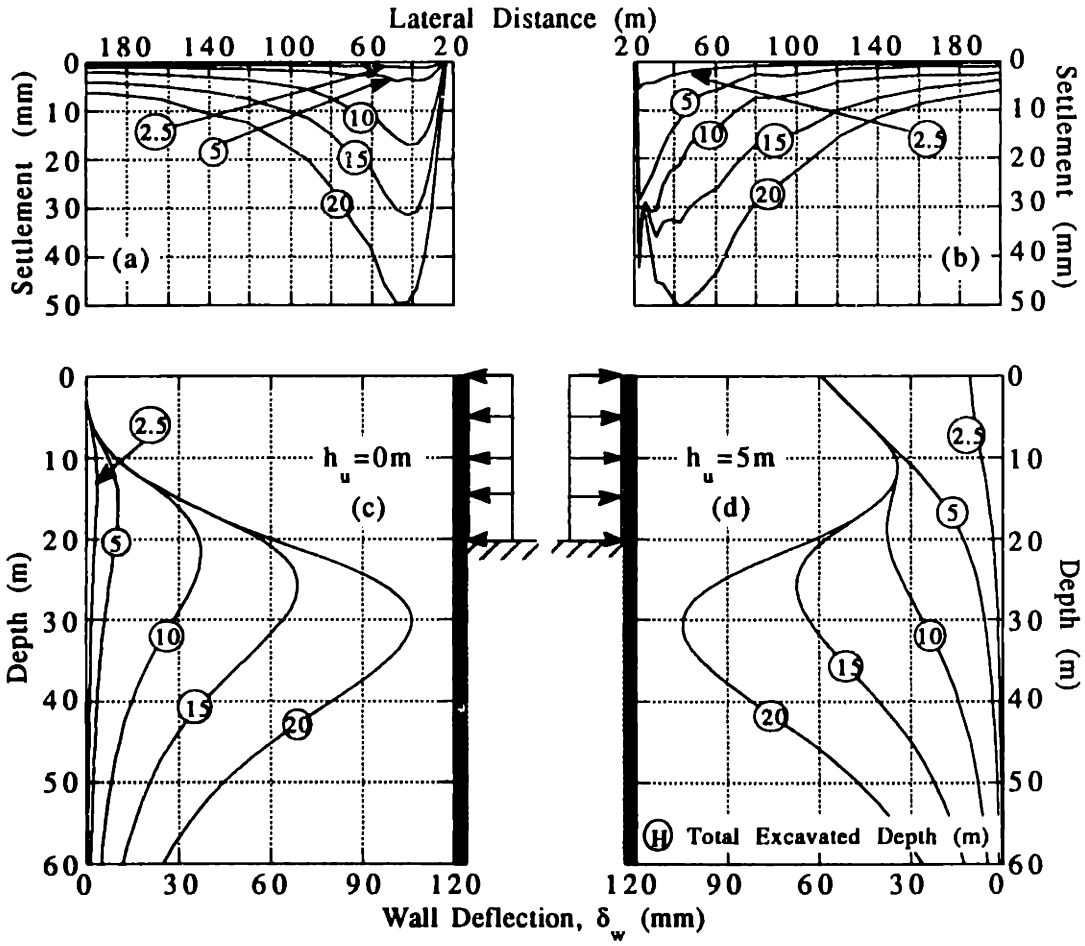

Figure 4.5-12 Wall Deflections and Surface Settlements for h_u=0m and h_u=5m Analyses (h=0m, L=60m, MIT-E3, OCR=1).

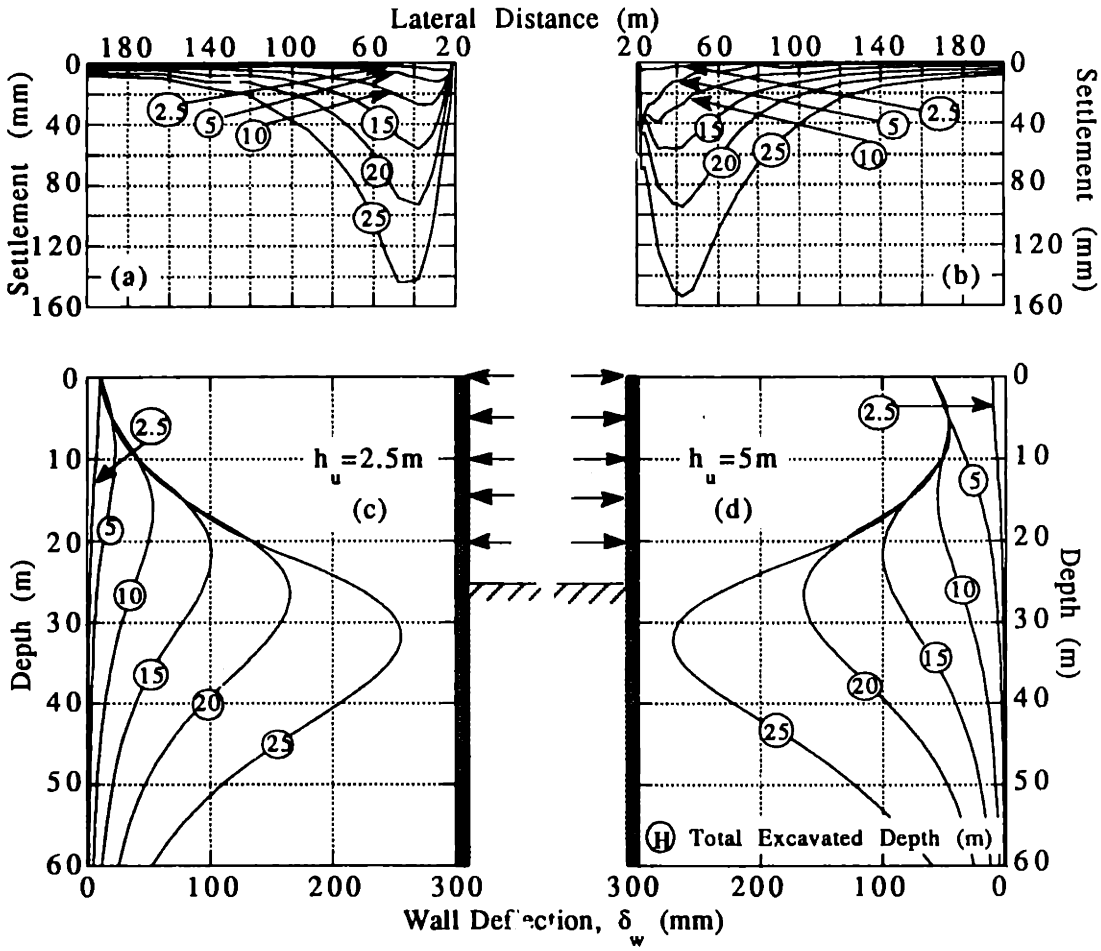

Figure 4.5-13 Wall Deflections and Surface Settlements for h_u=2.5m and h_u=5m Analyses (h=5m, L=60m, MIT-E3, OCR=1).

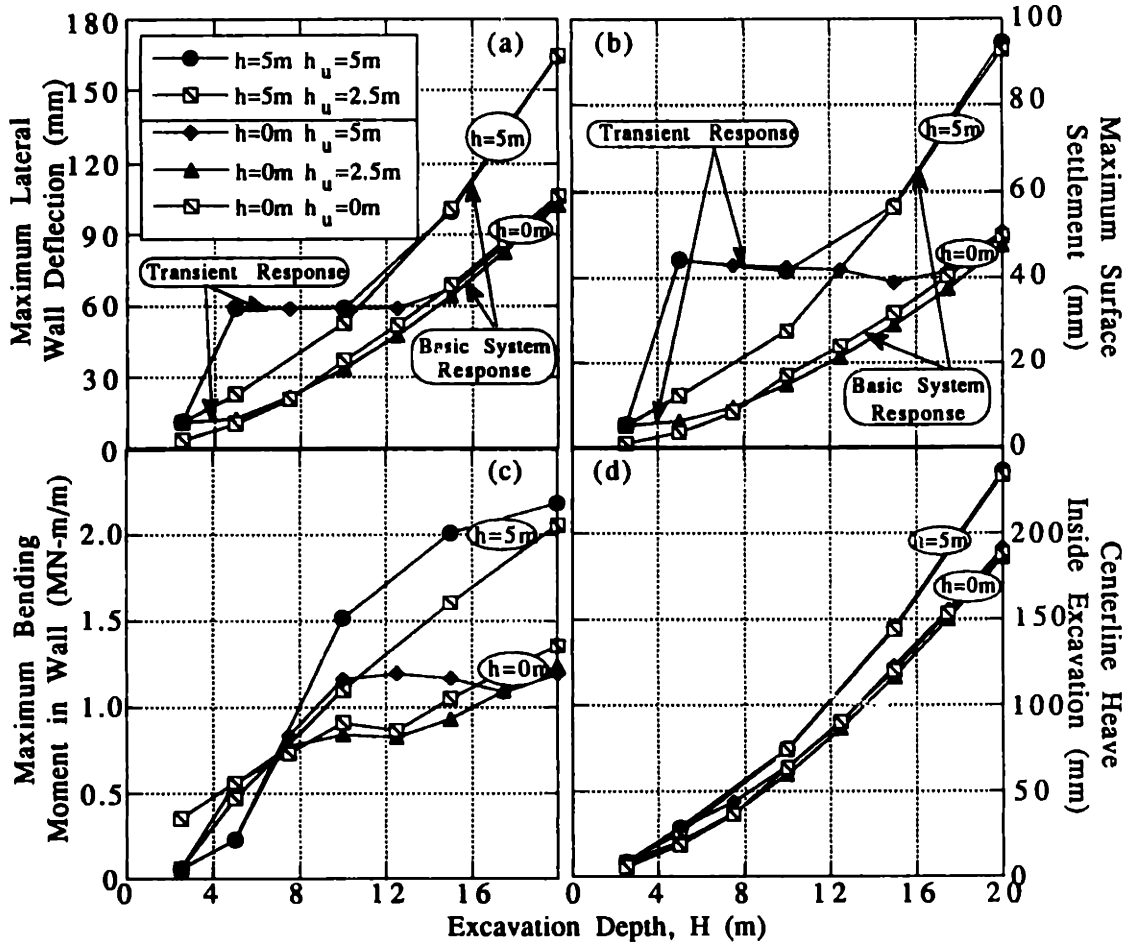

Figure 4.5-14 Effect of Unsupported Excavation Height on Maximum Deformations and Moments (h=0 and 5m, L=60m, MIT-E3, OCR=1).

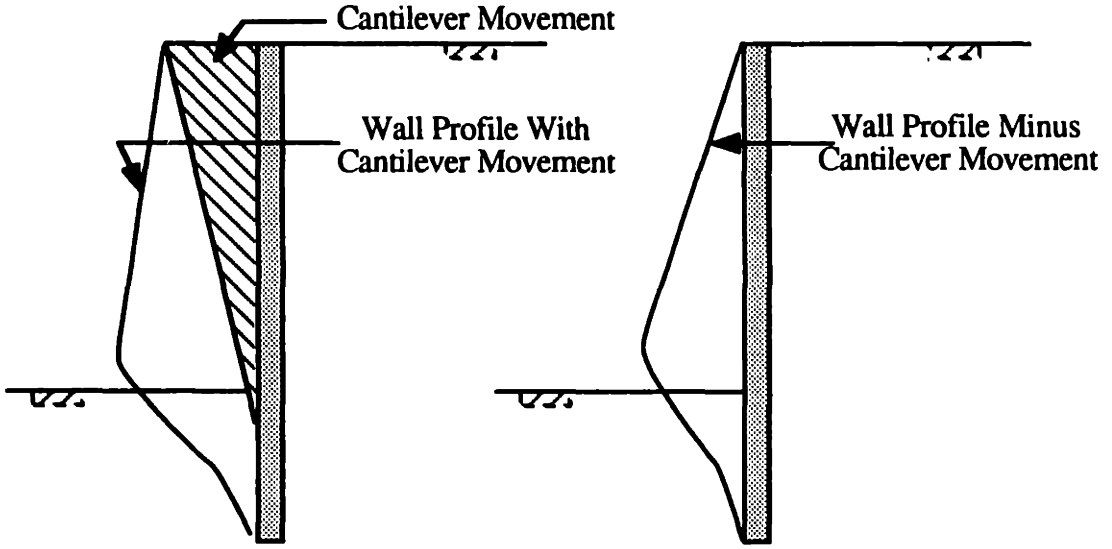

Figure 4.5-15 Effect of Cantilever Stage Movements on System Displacements (Clough et al, 1989).

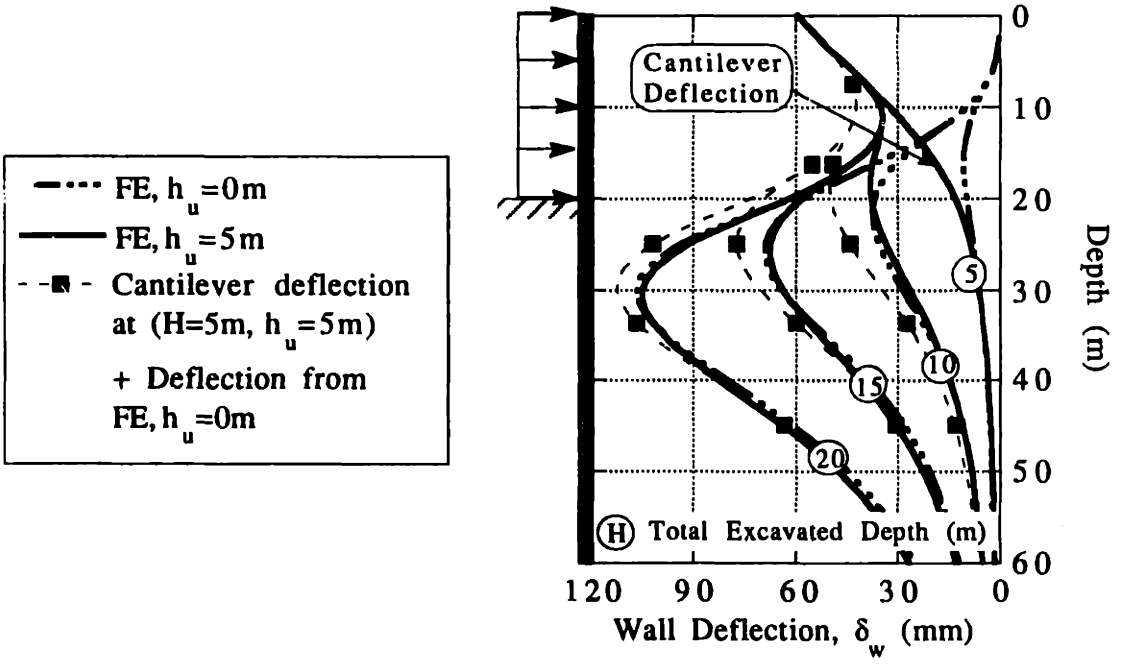

Figure 4.5-16 Effect of Cantilever Stage Movements on System Displacements, Clough et al. (1989) Method versus FE Analysis Results.

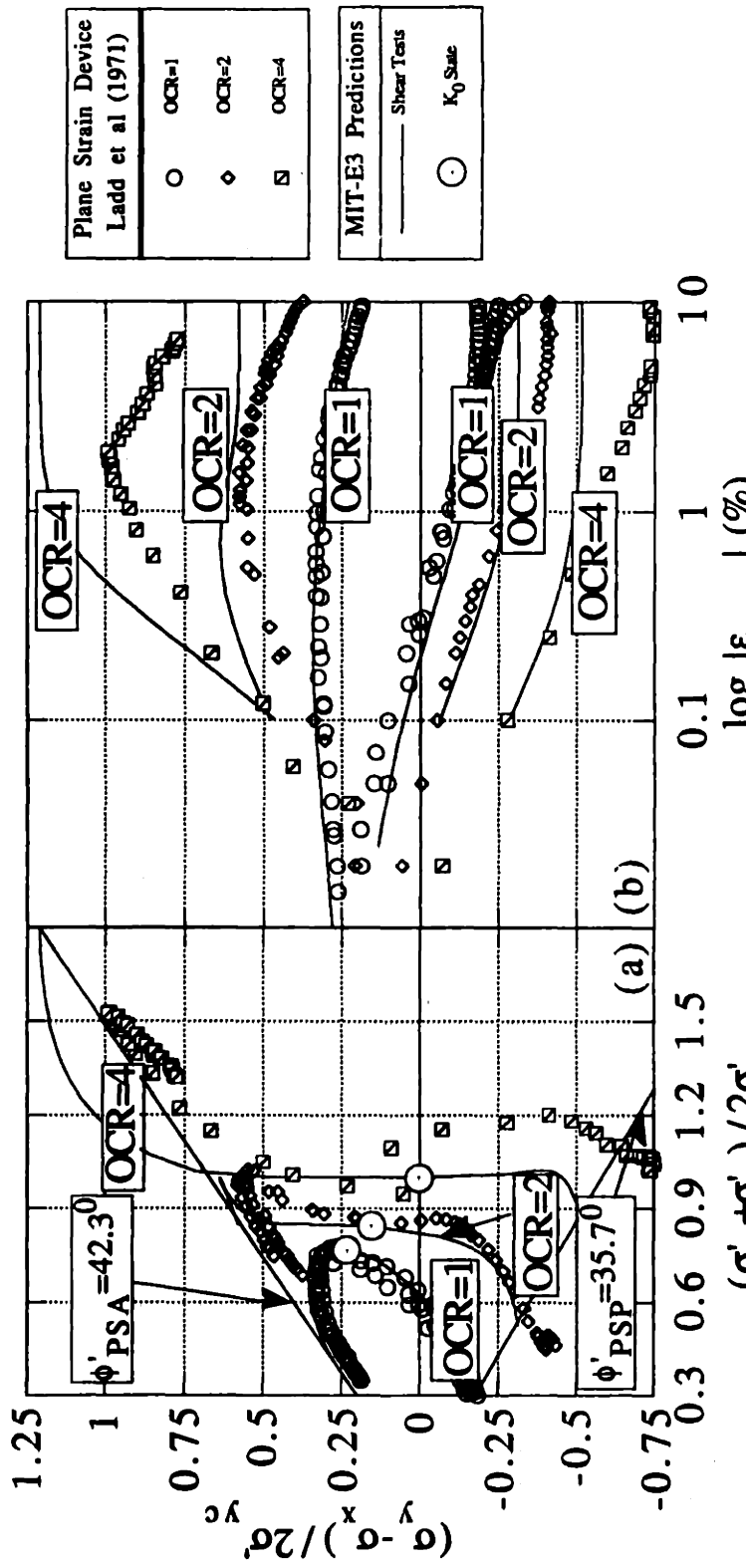

Figure 4.6-1 Comparison of MIT-E3 Predictions and Measured Laboratory Behavior for Boston Blue Clay at OCR = 1, 2 and 4.

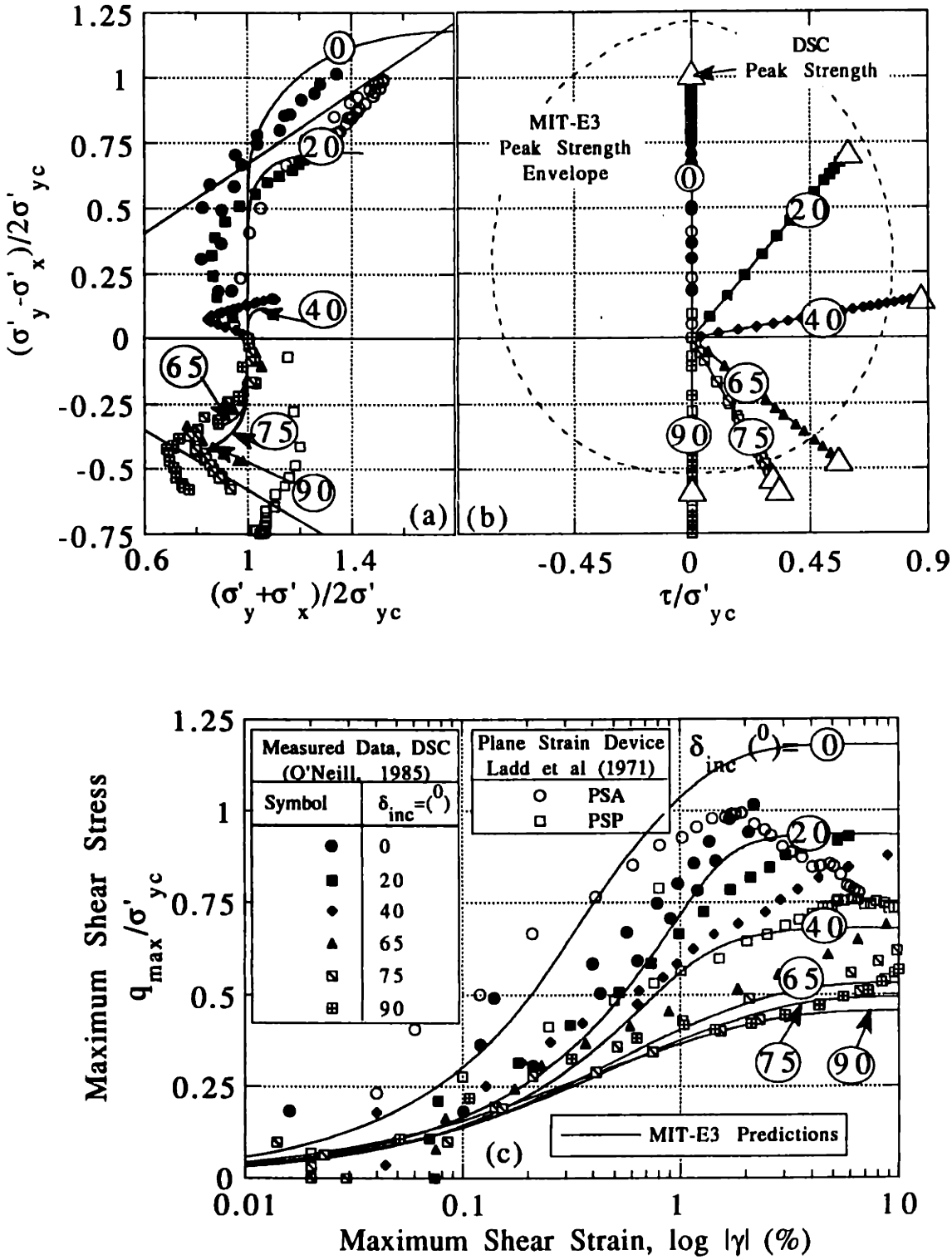

Figure 4.6-2 Evaluation of MIT-E3 Predictions versus DSC Measurements (OCR=4).

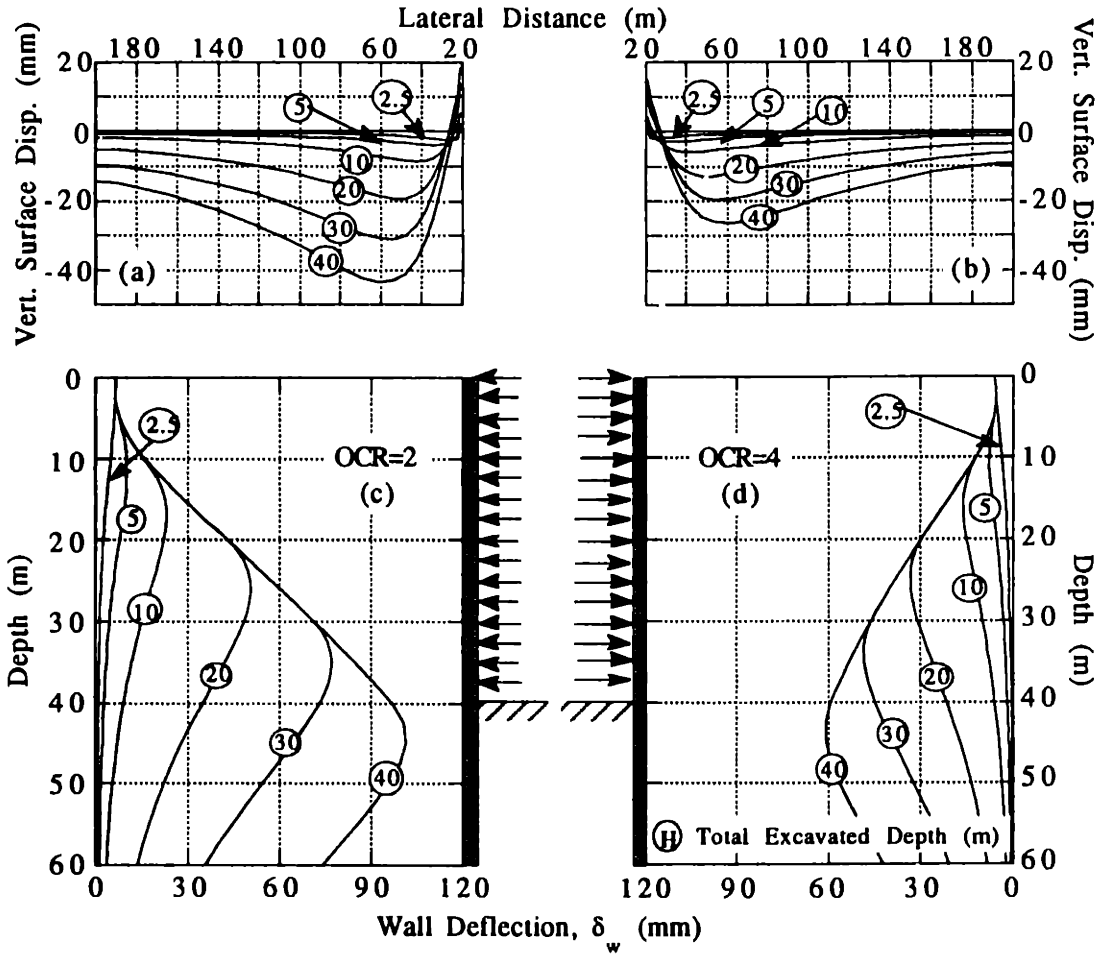

Figure 4.6-3 Wall Deflections and Surface Settlements for OCR=2 and 4 analyses (h_u=2.5m, h=2.5m, L=60m, MIT-E3).

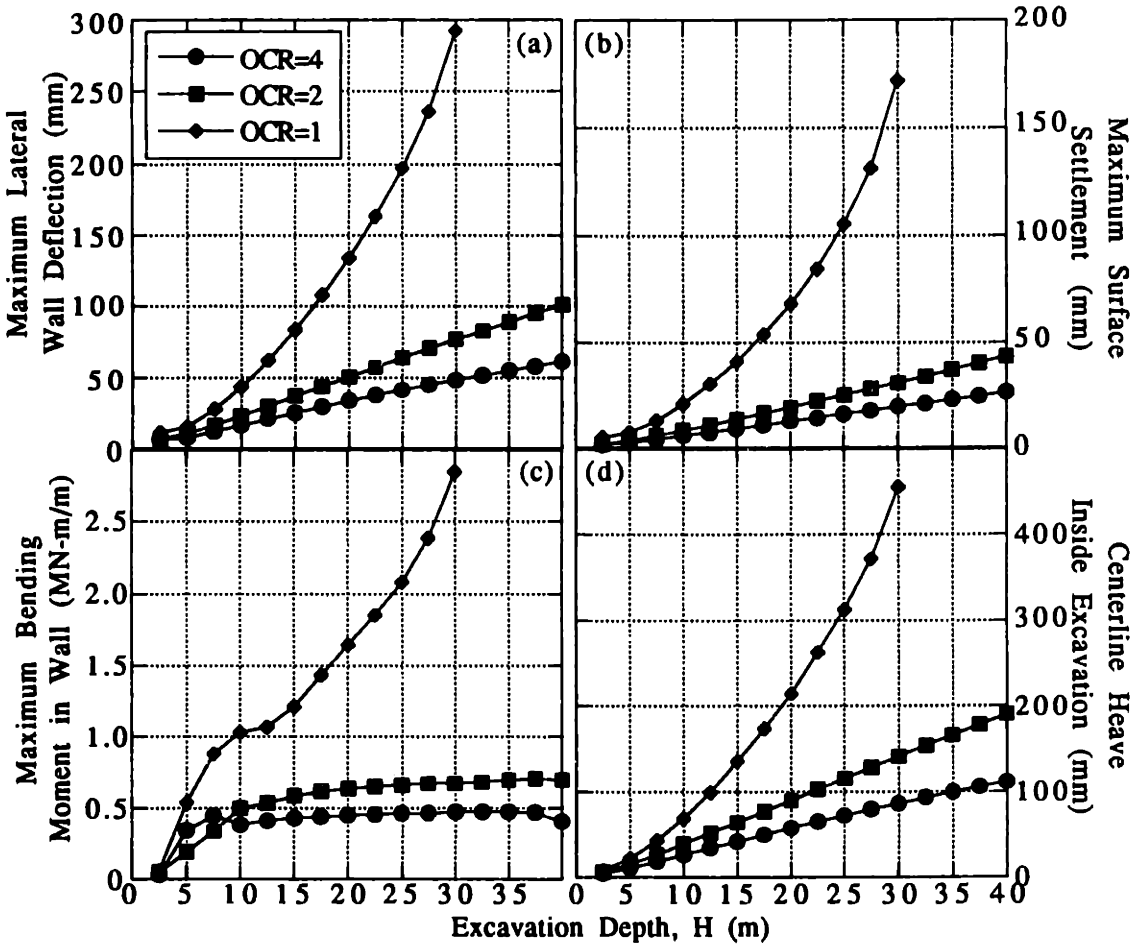

Figure 4.6-4 Effect of Soil Stress History on Maximum Deformations and Moments versus Excavation Depth (h_u=2.5m, h=2.5m, L=60m, MIT-E3).

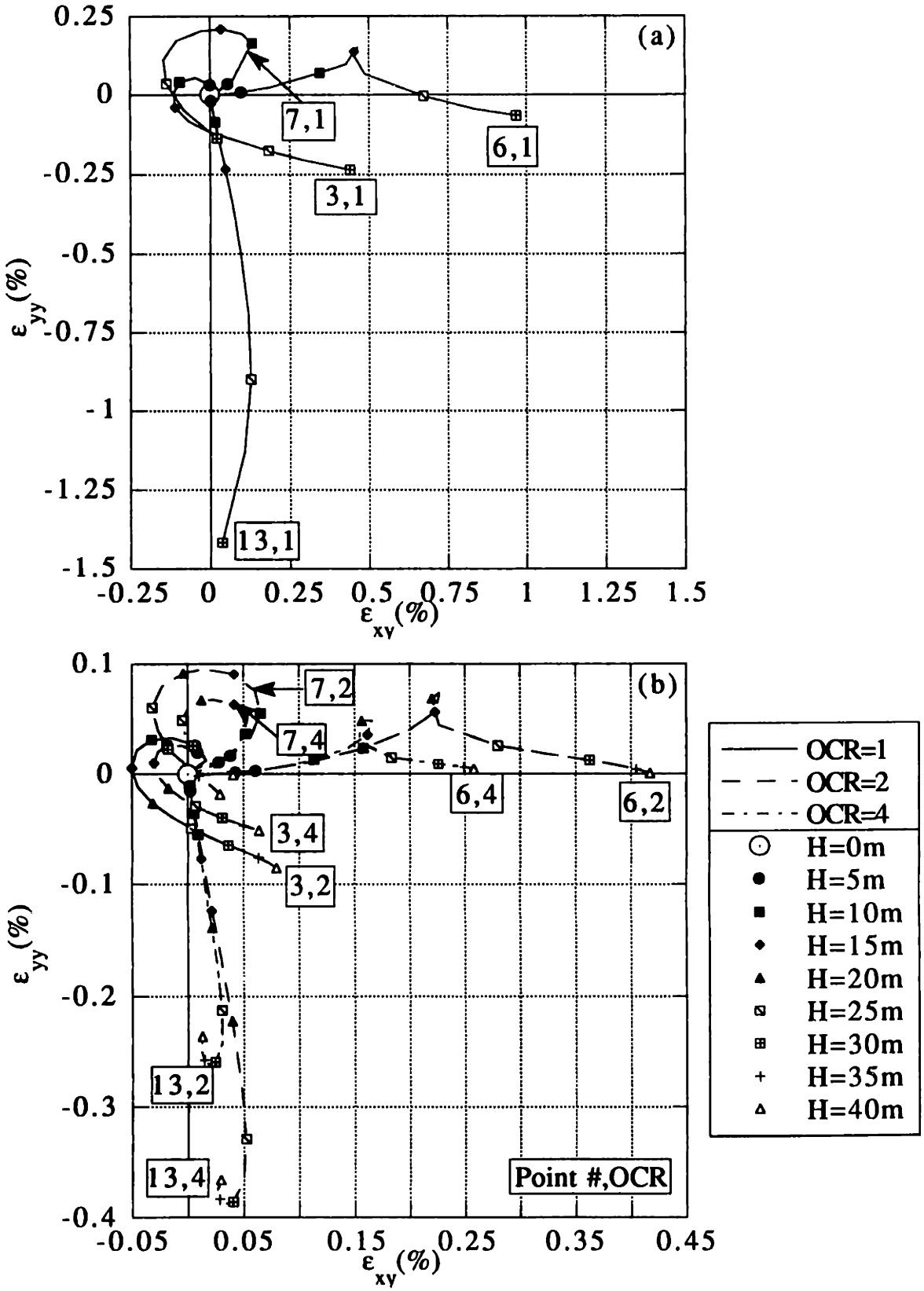

Figure 4.6-5 Effect of Soil Stress History on Soil Strain Paths (h_u=2.5m, h=2.5m, L=60m, MIT-E3).

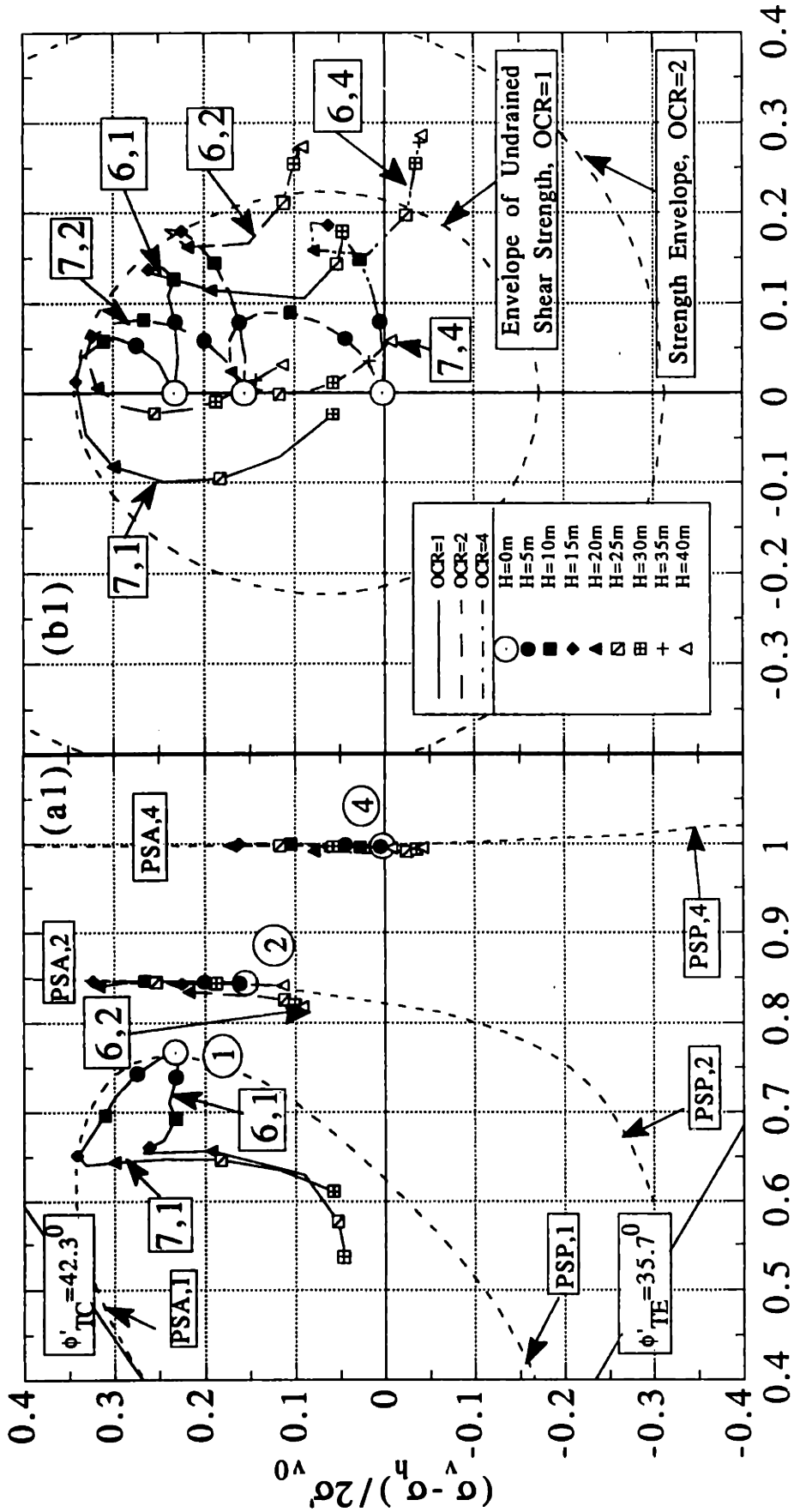

Figure 4.6-6 Effect of Soil Stress History on Normalized Soil Stress Paths (h_u=2.5m, h=2.5m, L=60m, MIT-E3).

(continued on next page)

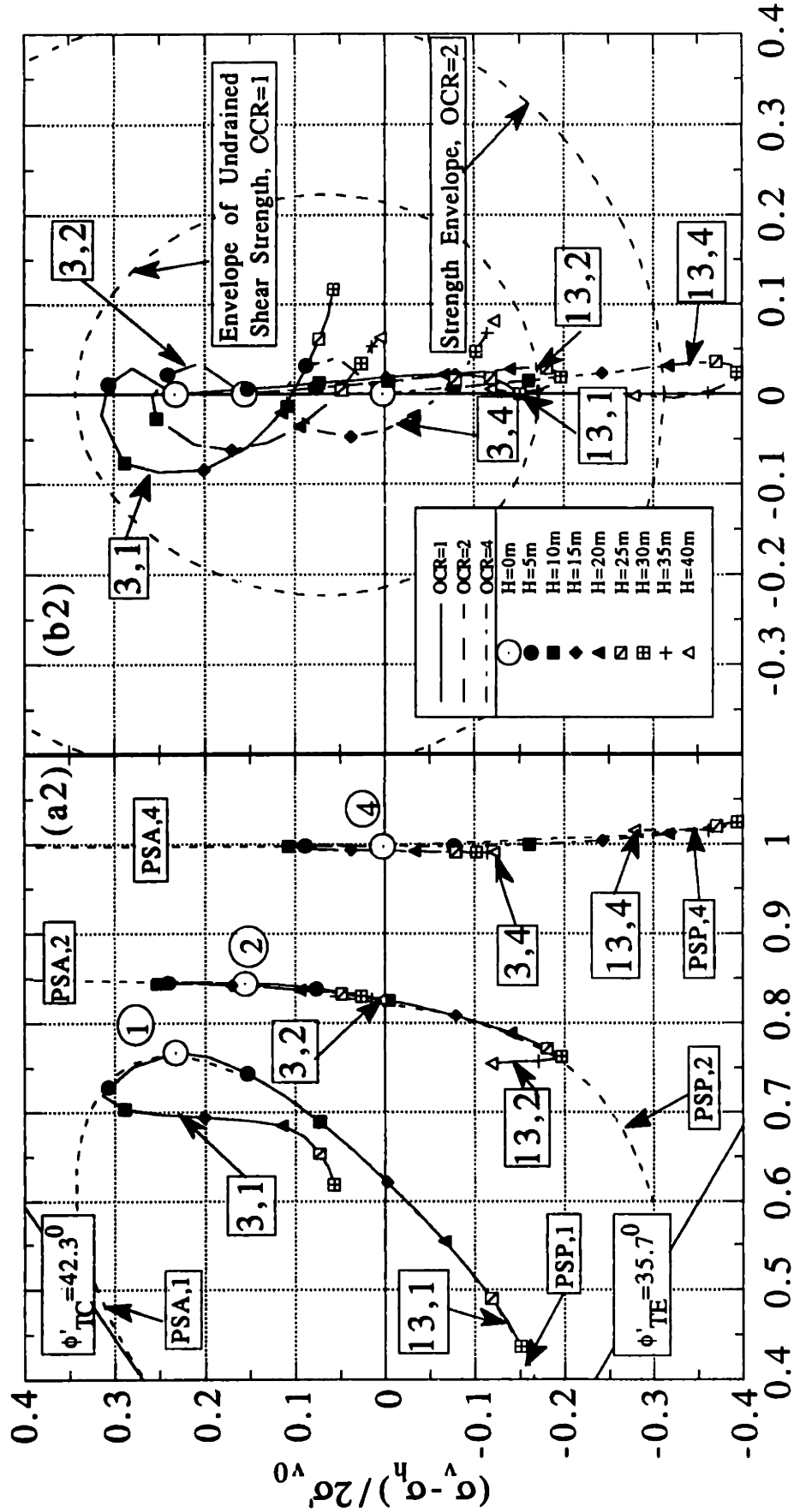

Figure 4.6-6 Effect of Soil Stress History on Normalized Soil Stress Paths (h_u=2.5m, h=2.5m, L=60m, MIT-E3).

(continued on next page)

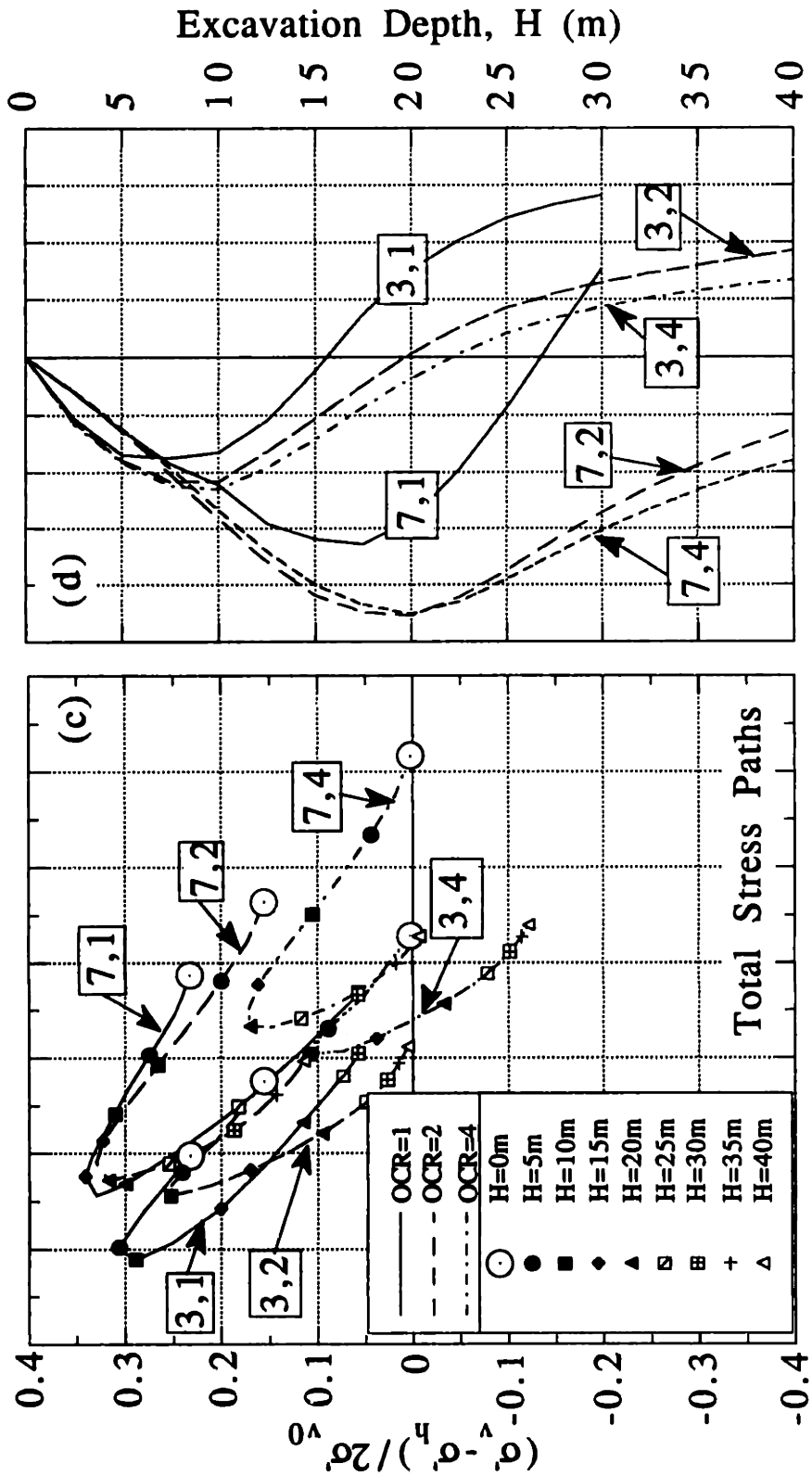

Figure 4.6-6 Effect of Soil Stress History on Normalized Soil Stress Paths (h_u=2.5m, h=2.5m, L=60m, MIT-E3).
(continued from previous page)

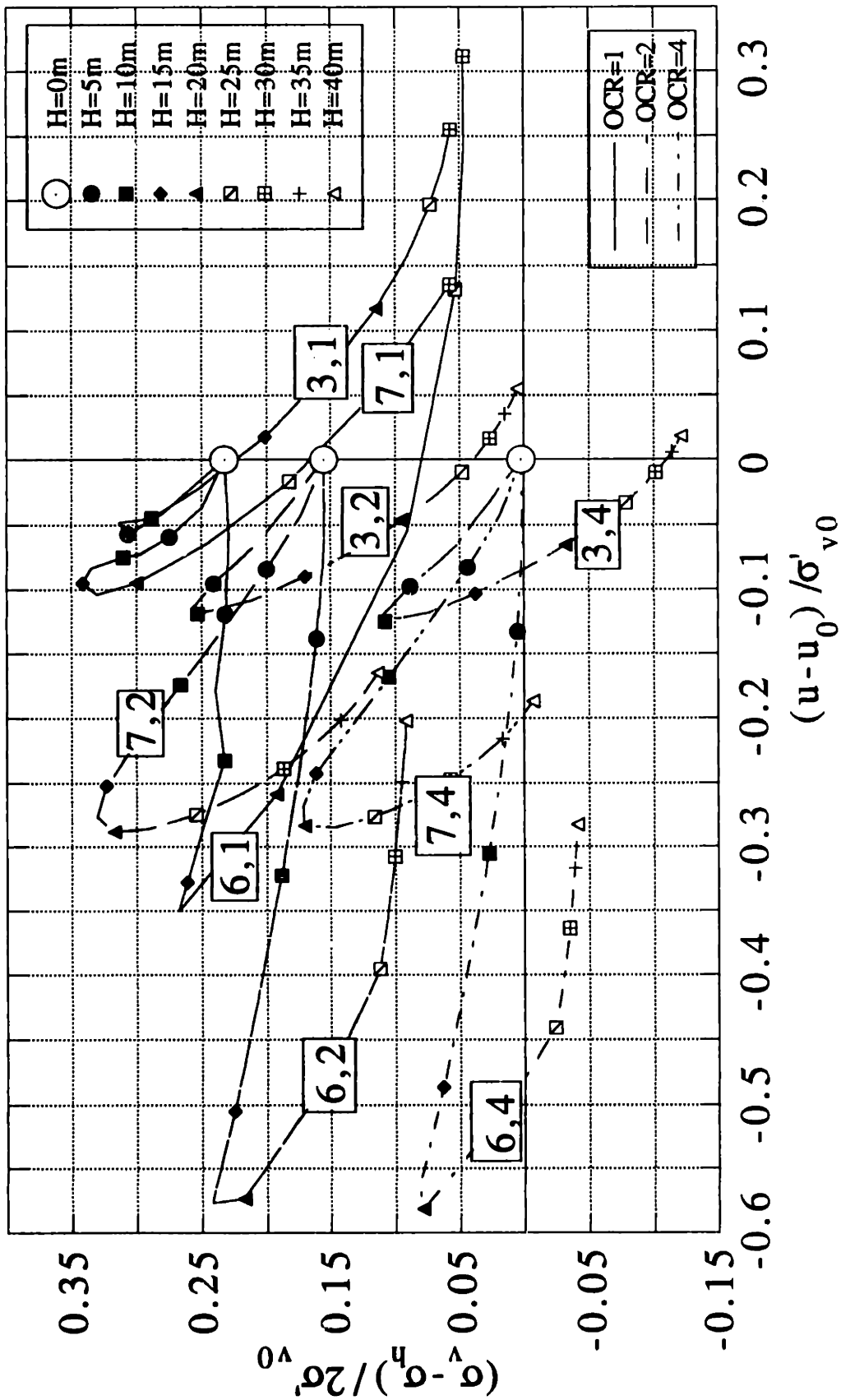

Figure 4.6-7 Effect of Soil Stress History on Normalized Excess Pore Pressure Paths (h_u=2.5m, h=2.5m, L=60m, MIT-E3).

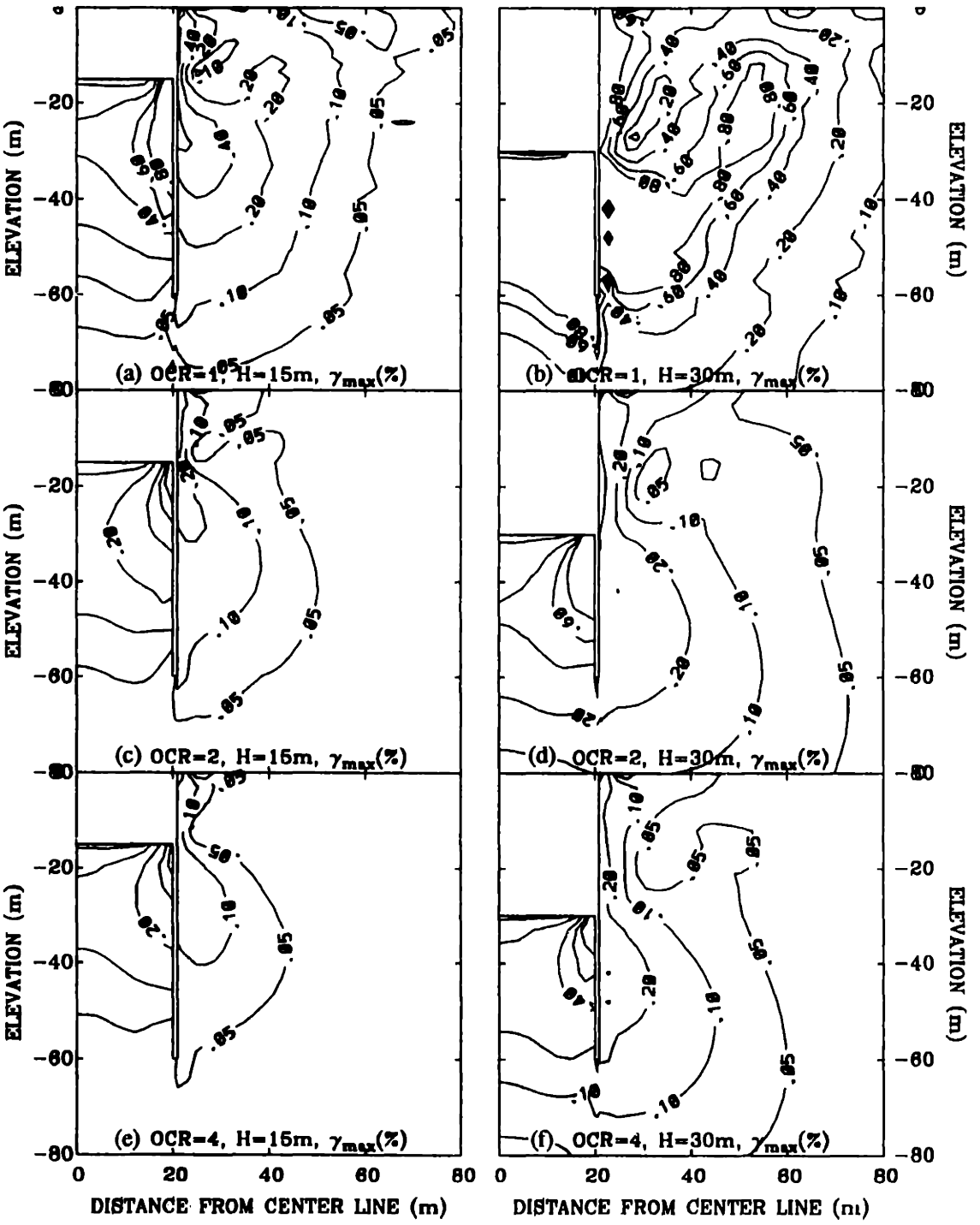

Figure 4.6-8 Effect of Soil Stress History on Maximum Shear Strain Contours (h_u=2.5m, h=2.5m, L=60m, MIT-E3).

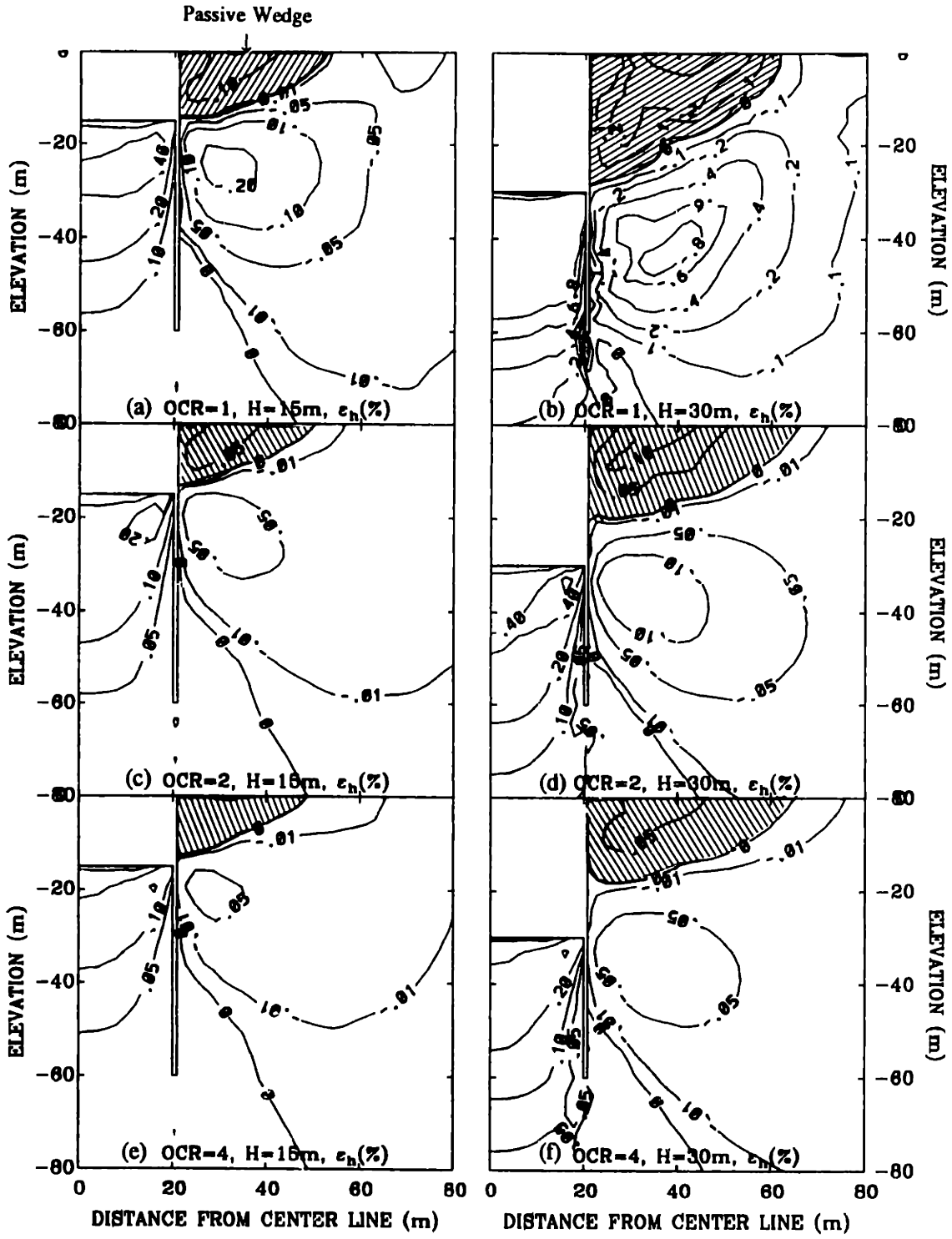

Figure 4.6-9 Effect of Soil Stress History on Horizontal Strain Contours (h_u=2.5m, h=2.5m, L=60m, MIT-E3).

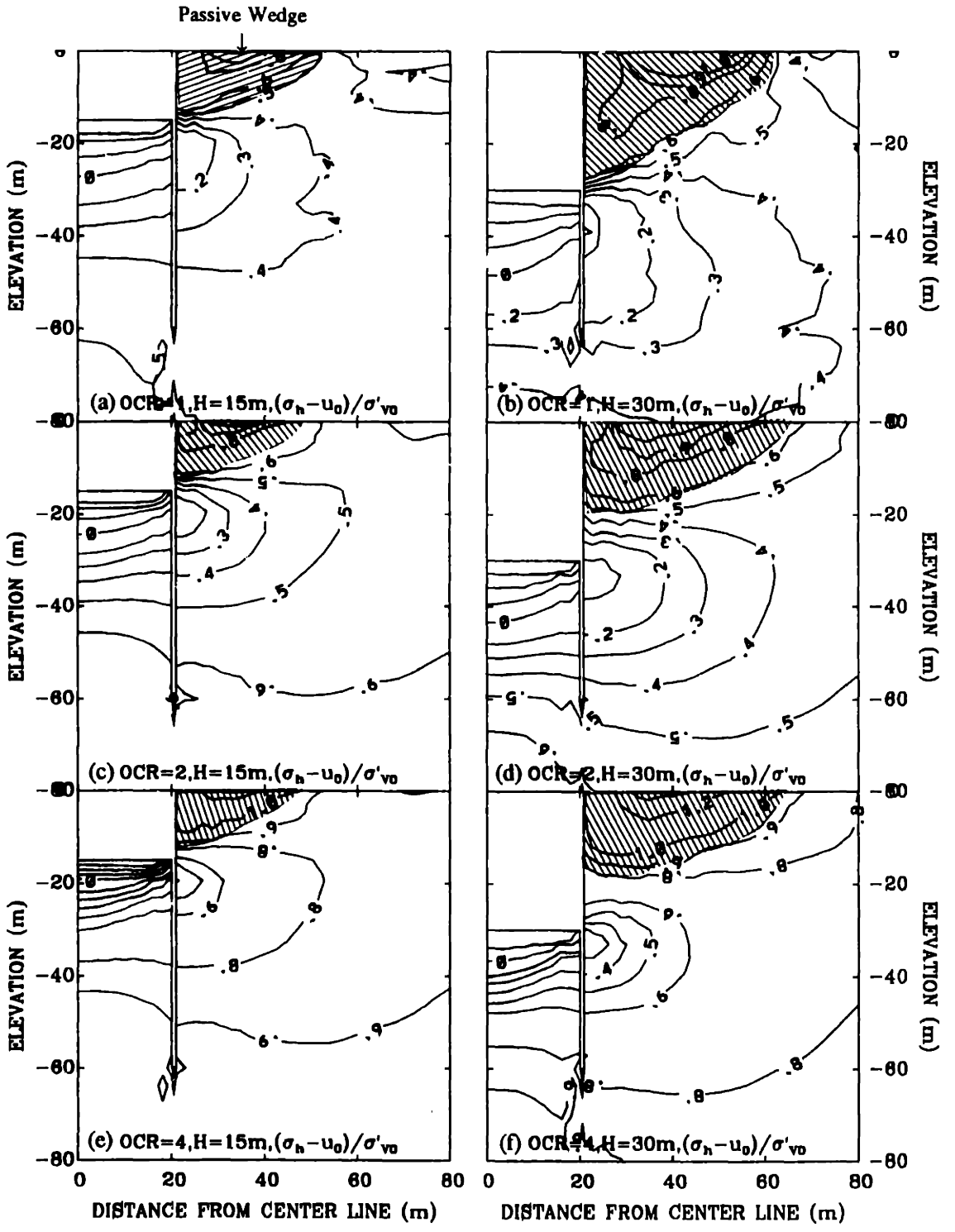

Figure 4.6-10 Effect of Soil Stress History on Normalized Horizontal Stress Contours (h_u=2.5m, h=2.5m, L=60m, MIT-E3).

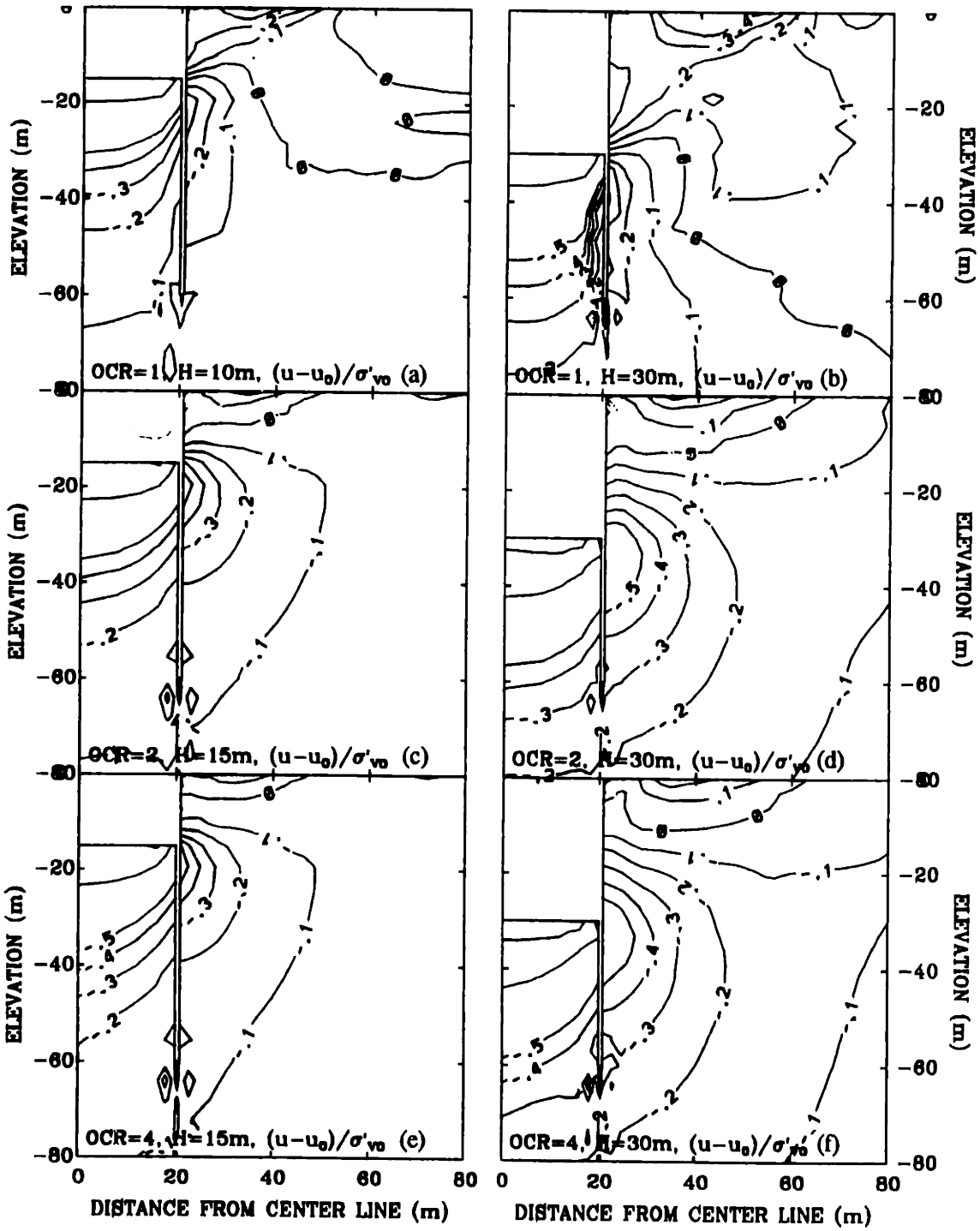

Figure 4.6-11 Effect of Soil Stress History on Normalized Excess Pore Pressure Contours (h_u=2.5m, h=2.5m, L=60m, MIT-E3).

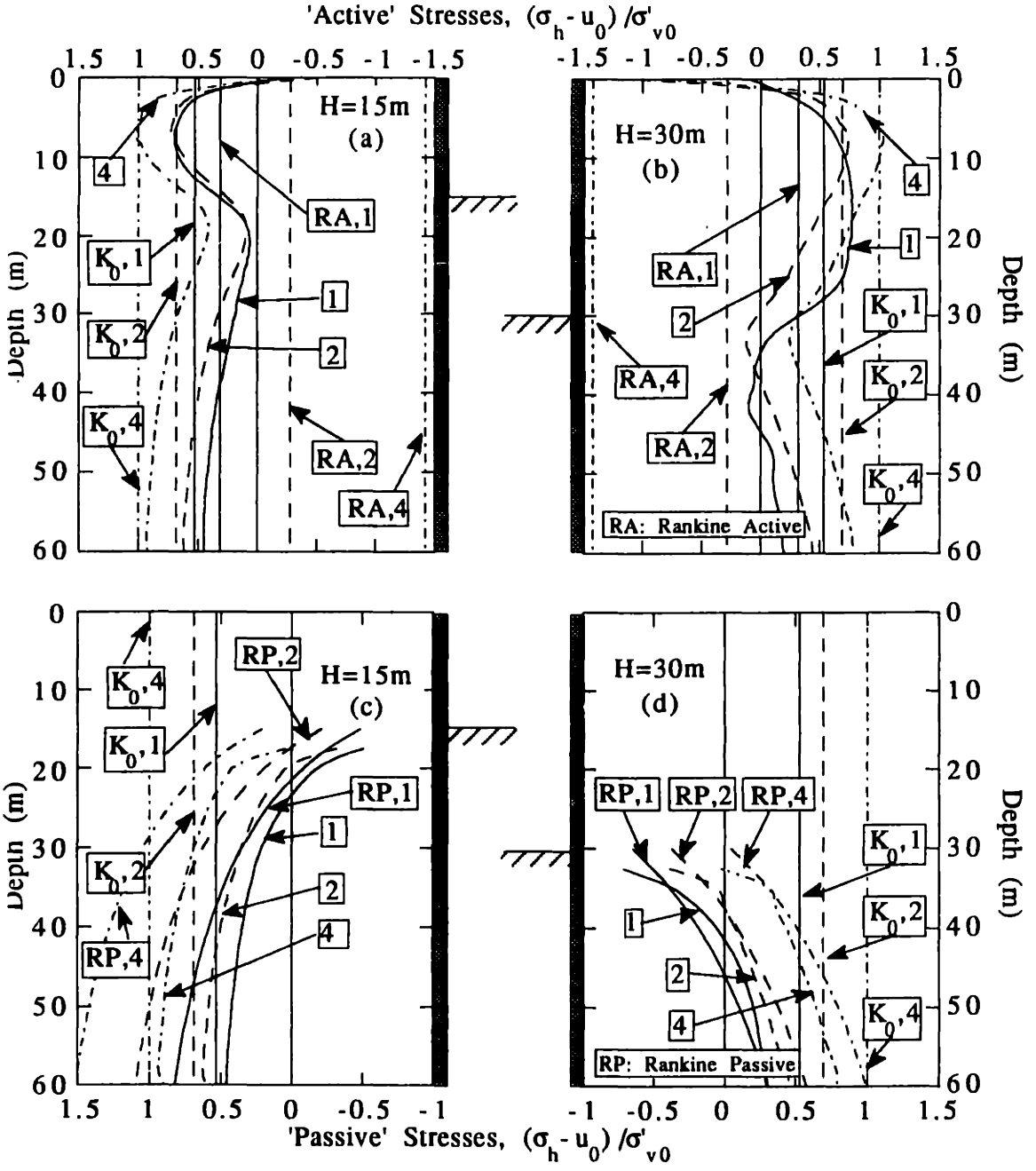

igure 4.6-12 Effect of Soil Stress History on Normalized Earth Pressures Acting on Both Sides of the Wall (h_u=2.5m, h=2.5, L=60m, MIT-E3).

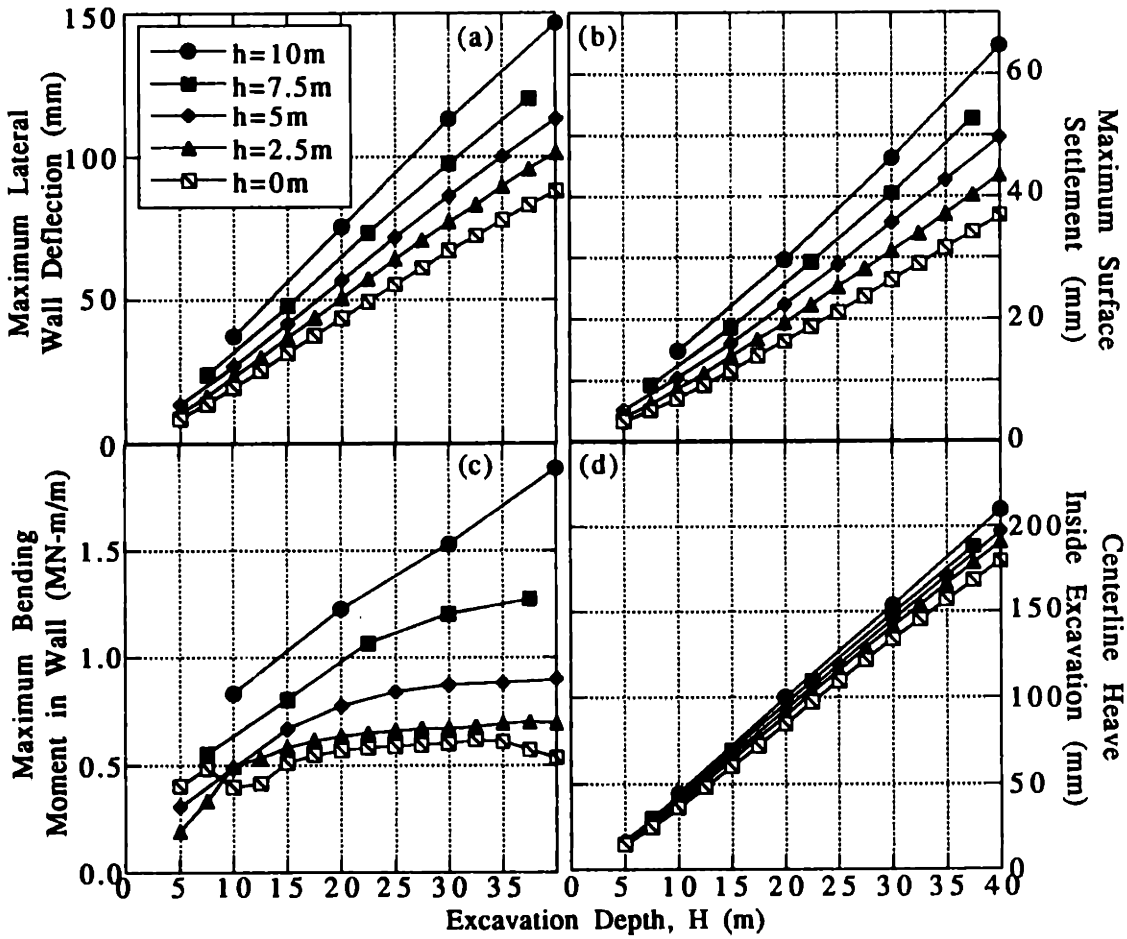

Figure 4.6-13 Effect of Vertical Support Spacing on Maximum Deformations and Moments in an OCR=2 Soil Profile (h_u=2.5m, L=60m, MIT-E3).

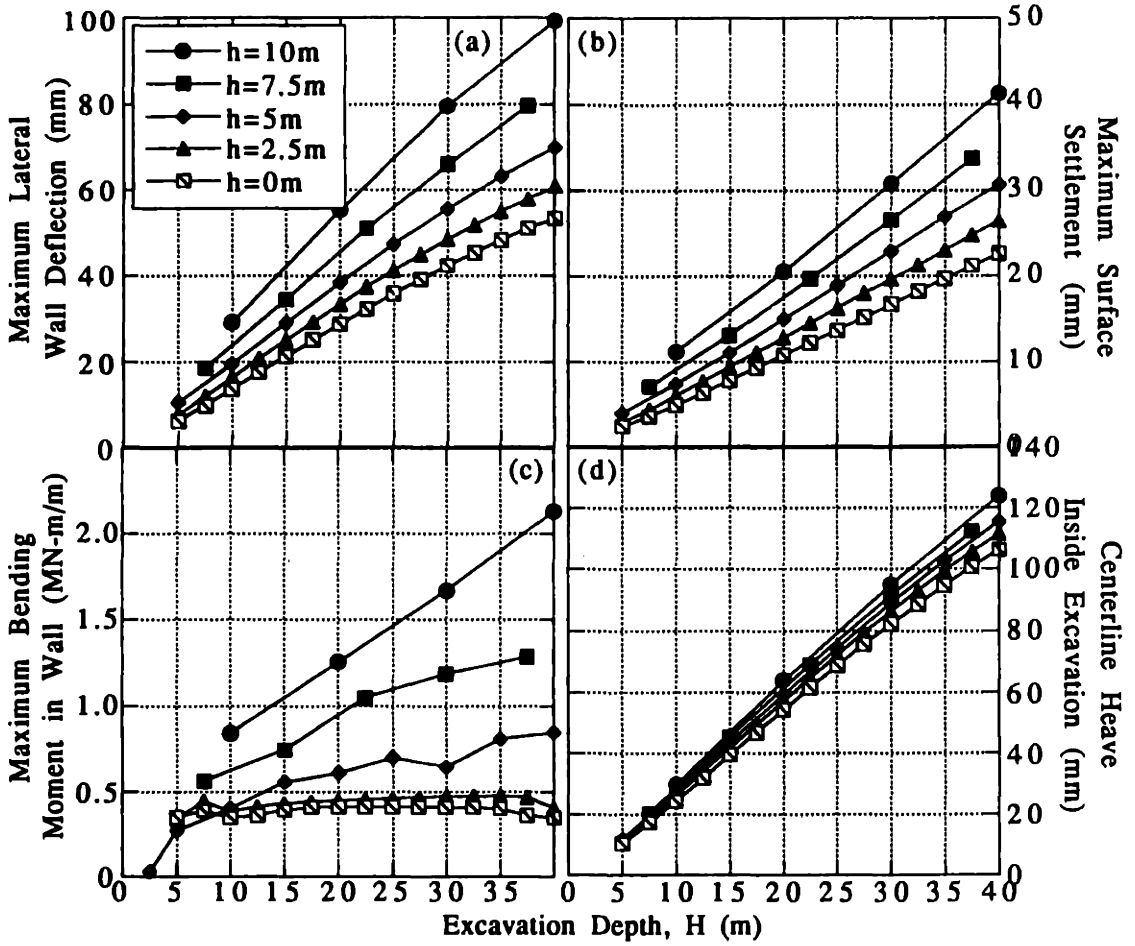

Figure 4.6-14 Effect of Vertical Support Spacing on Maximum Deformations and Moments in an OCR=4 Soil Profile (h_u=2.5m, L=60m, MIT-E3).

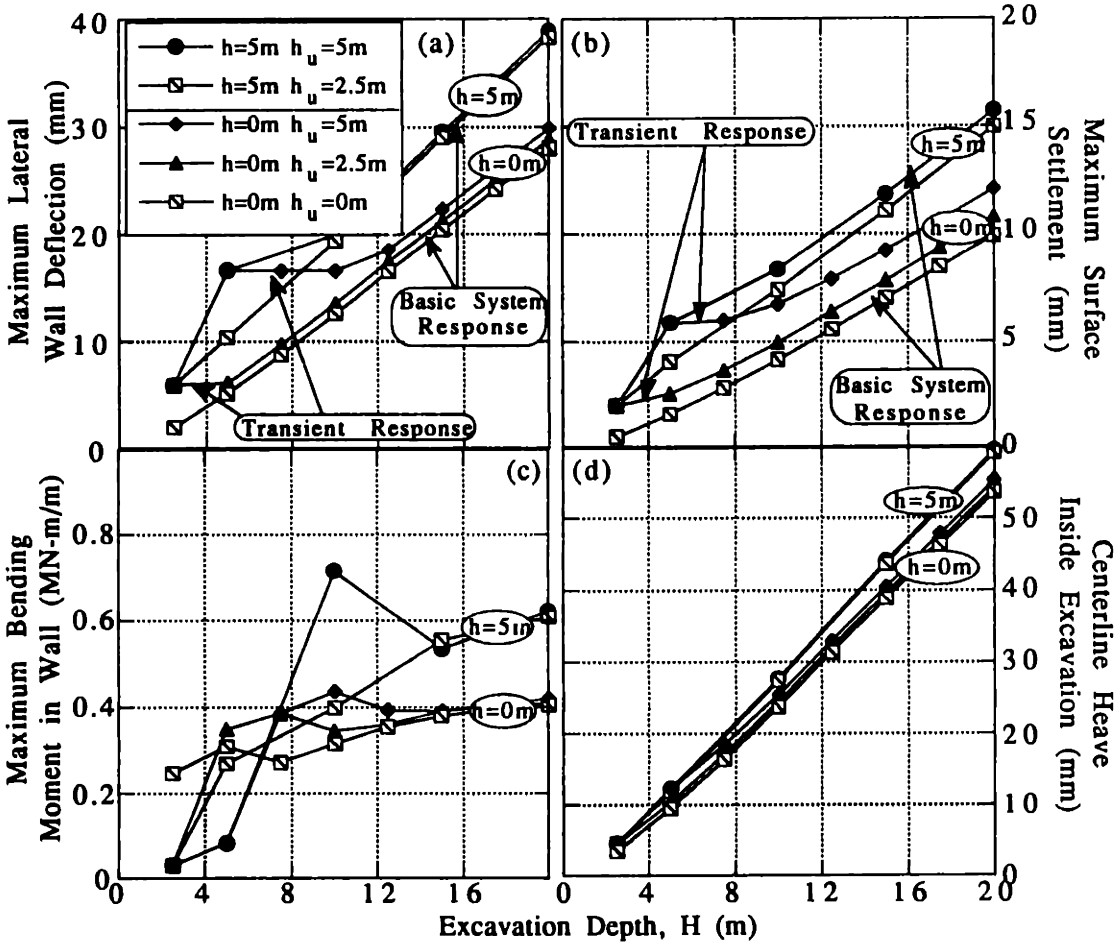

Figure 4.6-15 Effect of Unsupported Excavation Depth on Maximum Deformations and Moments in an OCR=4 Soil Profile (h_u=2.5m, h=2.5m, L=60m, MIT-E3).

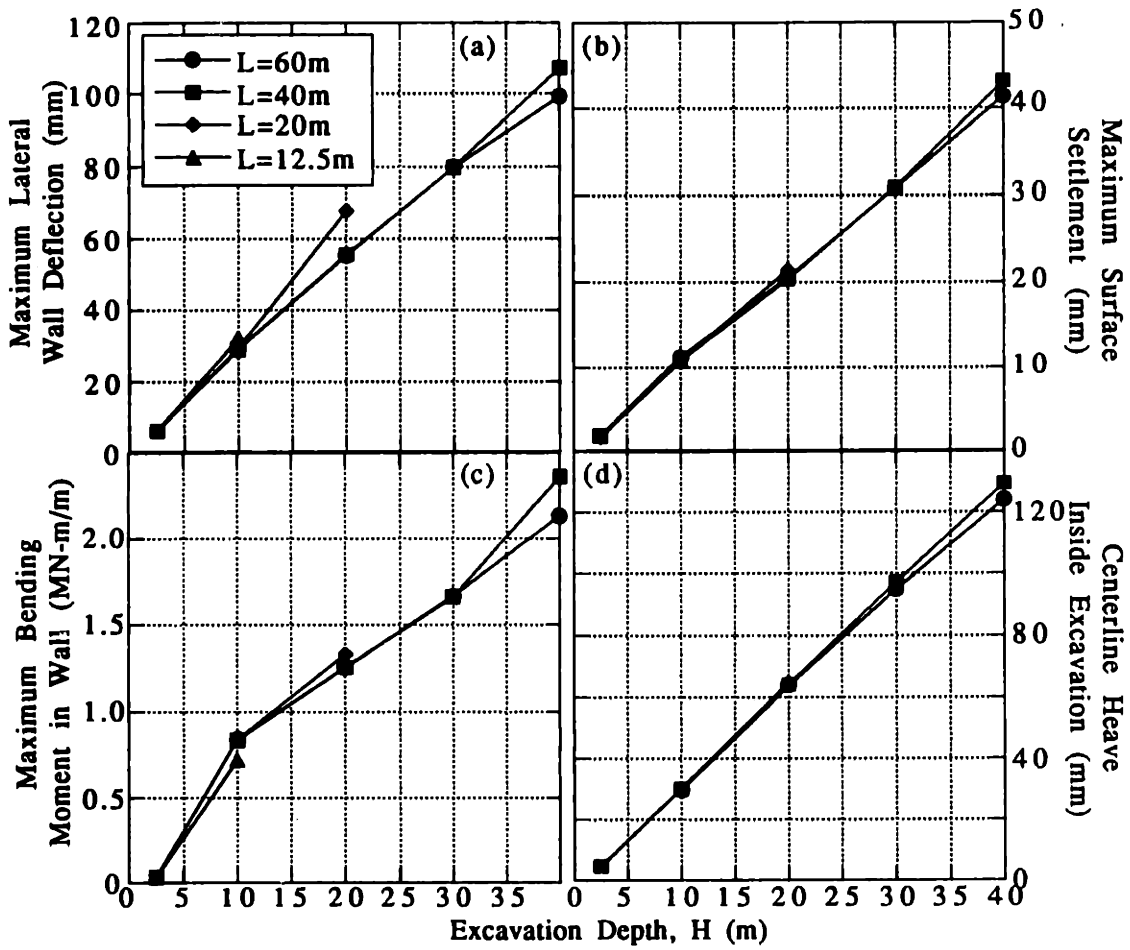

Figure 4.6-16 Effect of Wall Length on Maximum Deformations and Moments in an OCR=4 Soil Profile (h_u=2.5m, h=10m, L=60m, MIT-E3).

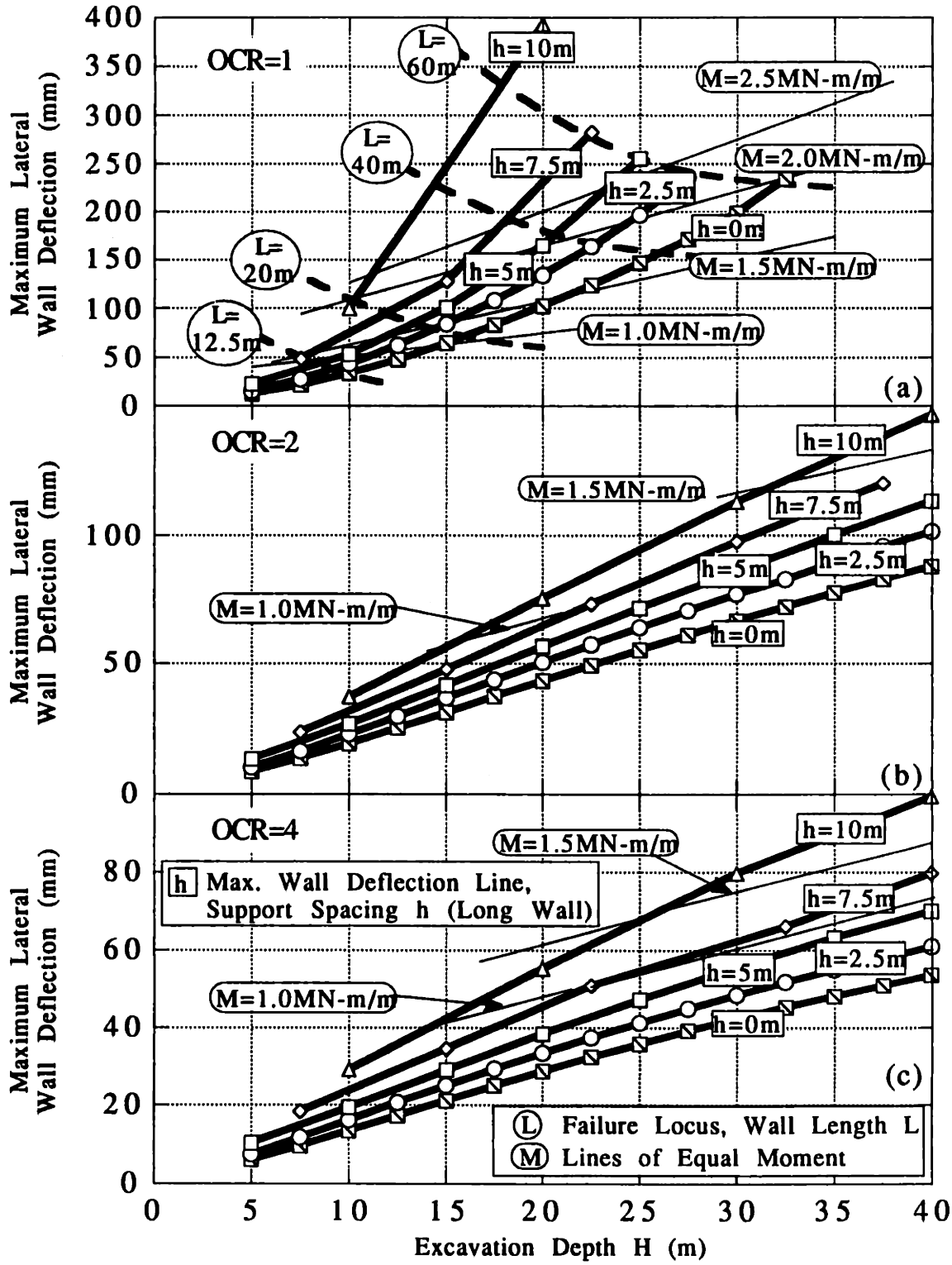

Note: Different Vertical Scales in these figures.

Figure 4.7-1 Simplified Framework for Interpreting Excavation Behavior (OCR=1,2 and 4)

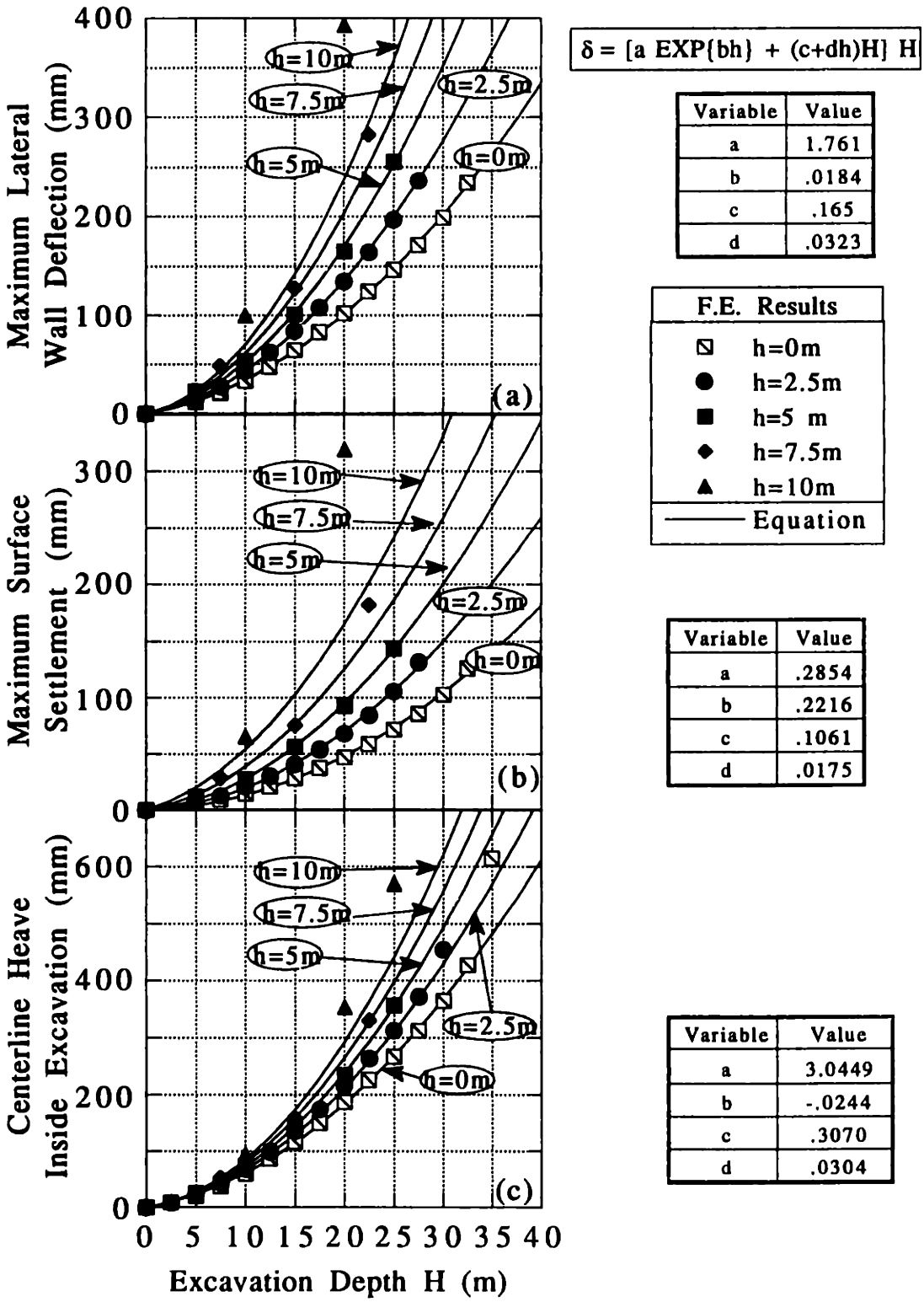

Figure 4.7-2 Curve Fit of Maximum Deformation Data (OCR=1)

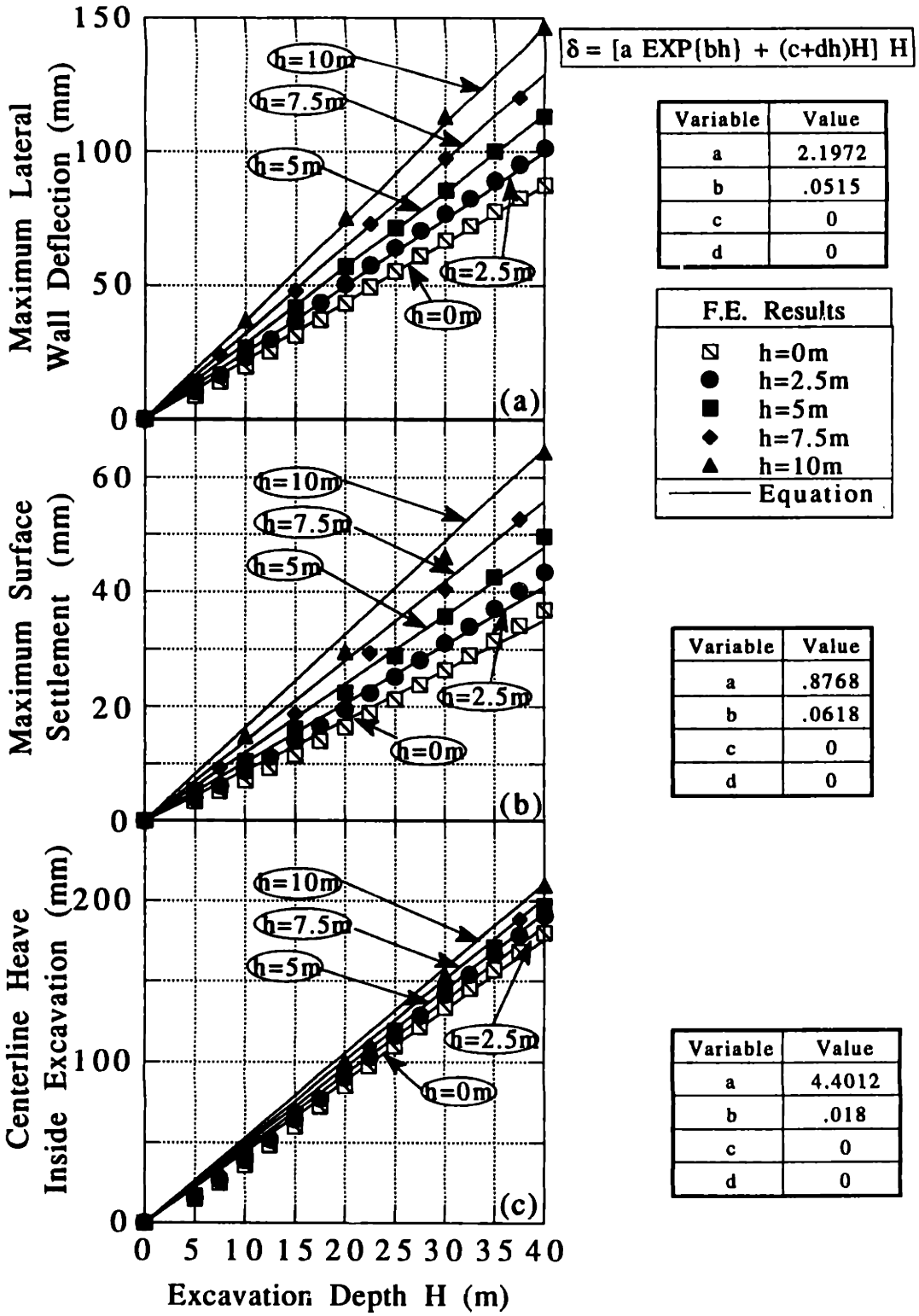

Figure 4.7-3 Curve Fit of Maximum Deformation Data (OCR=2)

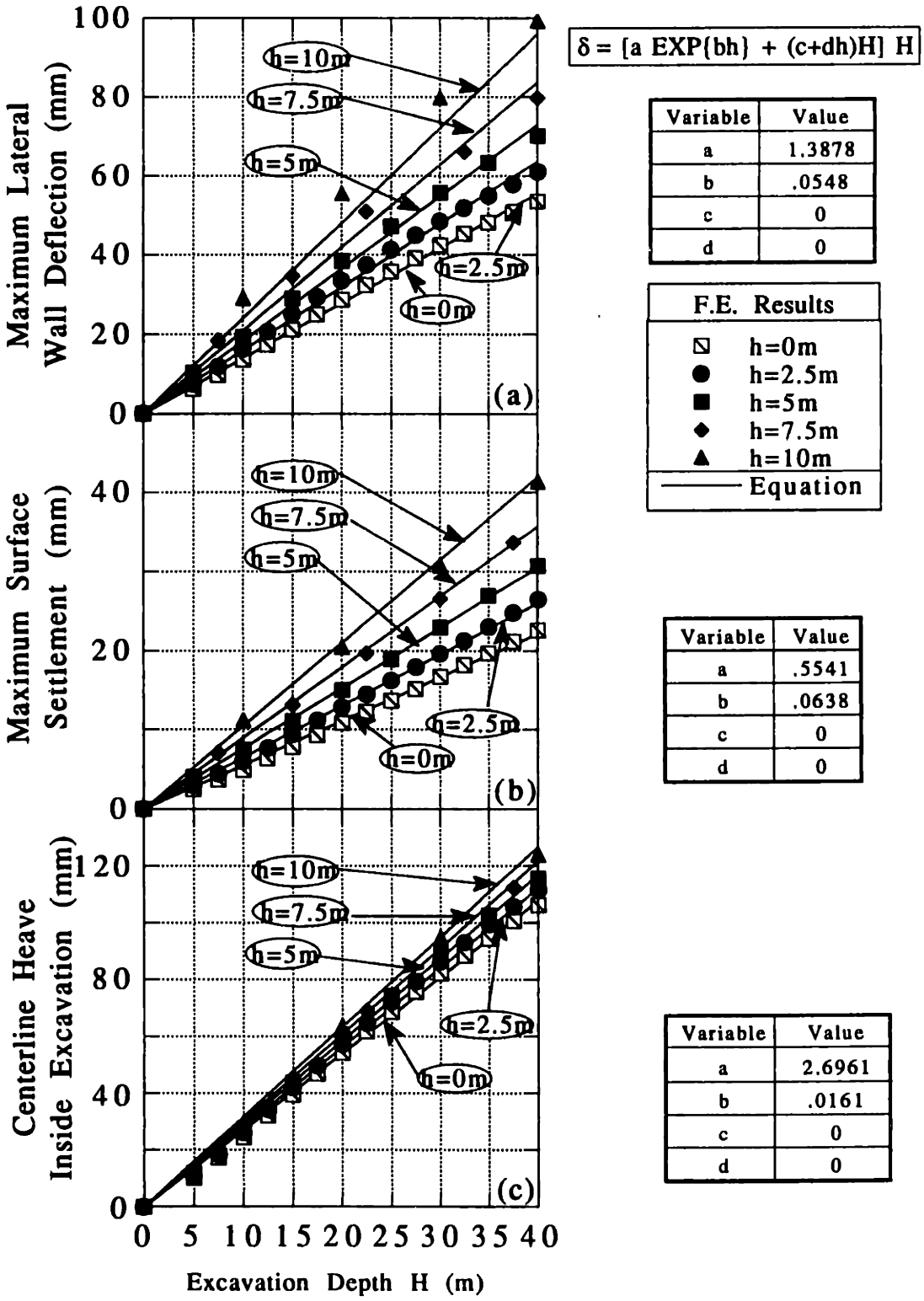

Figure 4.7-4 Curve Fit of Maximum Deformation Data (OCR=4)

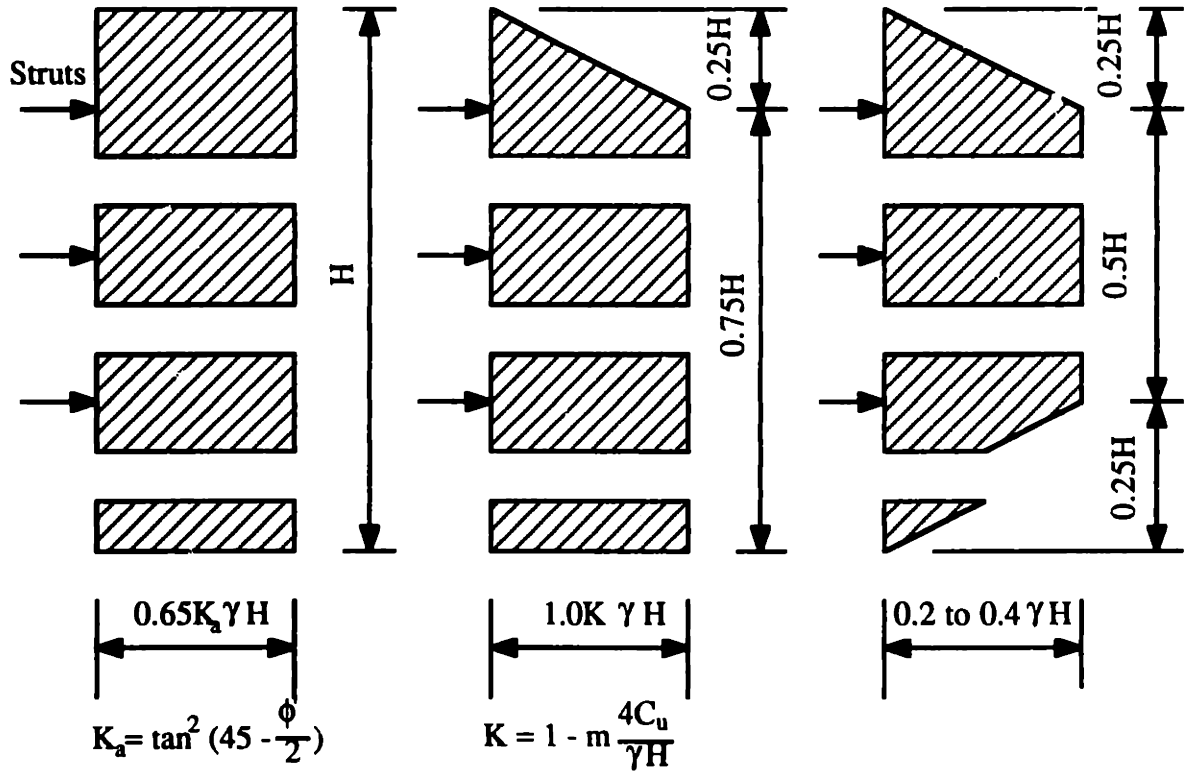

Figure 4.8-1 Apparent Earth Pressure Diagrams for Computing Strut Loads in Strutted Excavations (Peck, 1969).

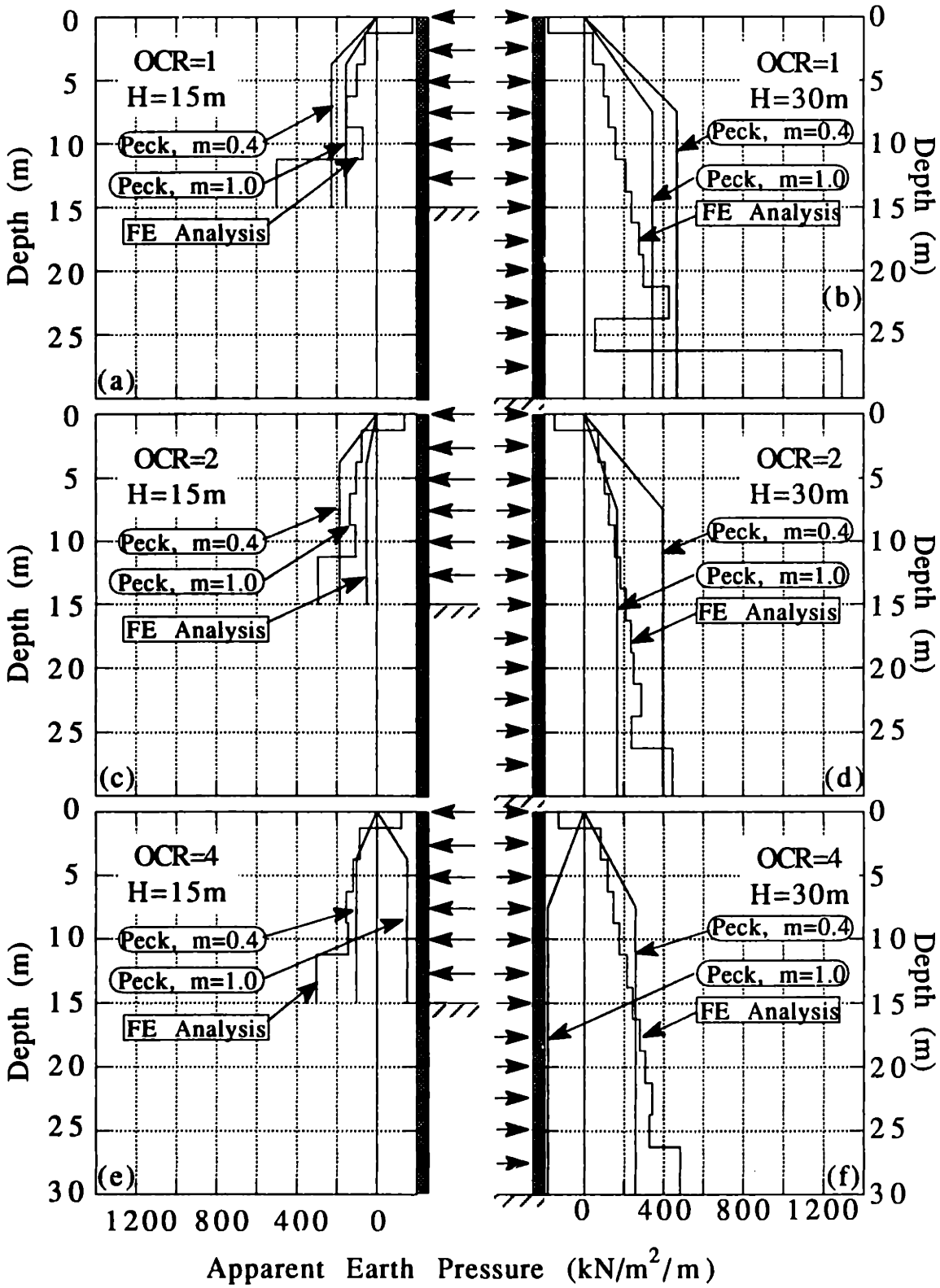

Figure 4.8-2 FE Model Apparent Earth Pressure Diagrams (h_u=2.5m, h=2.5m, L=60m, MIT-E3).

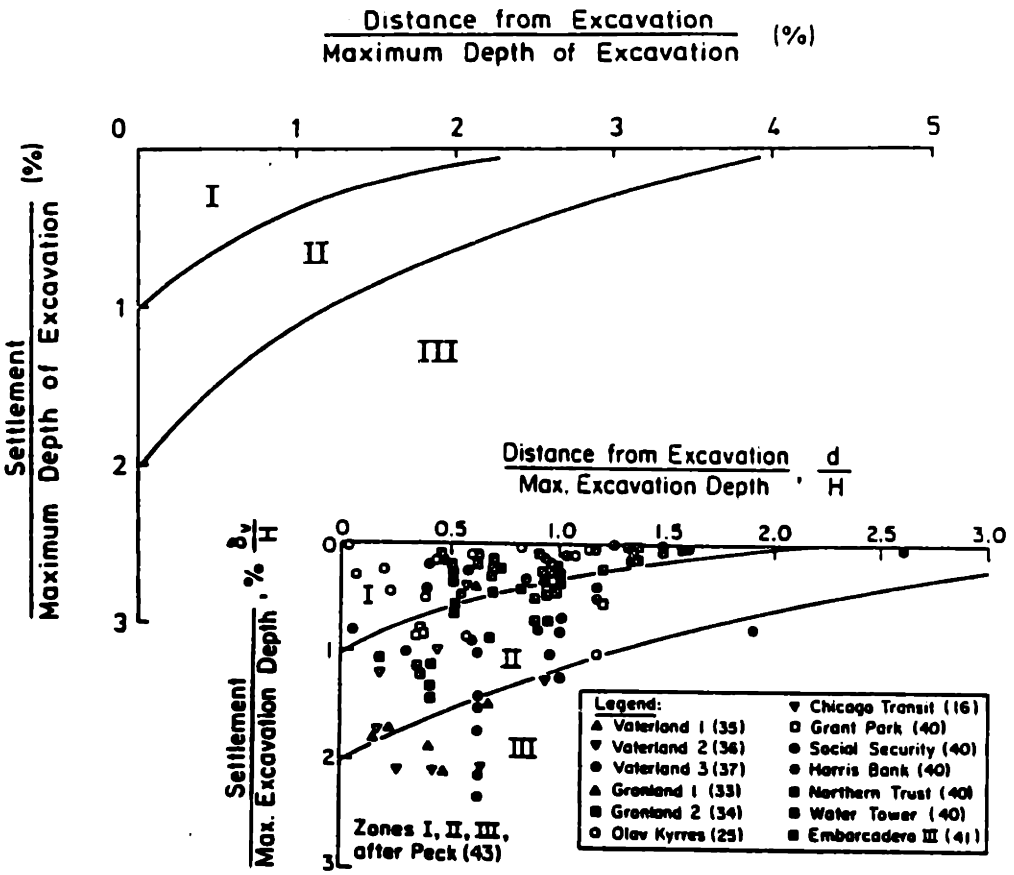

Notes:
(1) Zone I - Sand and soft to hard clay, average workmanship.
(2) Zone II - (a) Very soft to soft clay.
(i) Limited depth of clay below bottom of excavation.
(ii) Significant depth of clay below bottom of excavation but $N_b < 5.14$.
(b) Settlements affected by construction difficulties.
(3) Zone III - Very soft to soft clay to a significant depth below bottom of excavation and with $N_b > 5.14$,
where $N_b = \frac{\gamma H}{C_{ub}}$
(4) The data used to derive the three zones shown in this figure are taken from excavations supported by soldier piles or sheet piles with cross-lot struts or tie-backs.

*Adopted, in part, from GCO (1990)

Figure 4.8-3 Summary of Settlements Adjacent to Strutted Excavations in Soft to Medium Clays (Clough and O'Rourke, 1990).

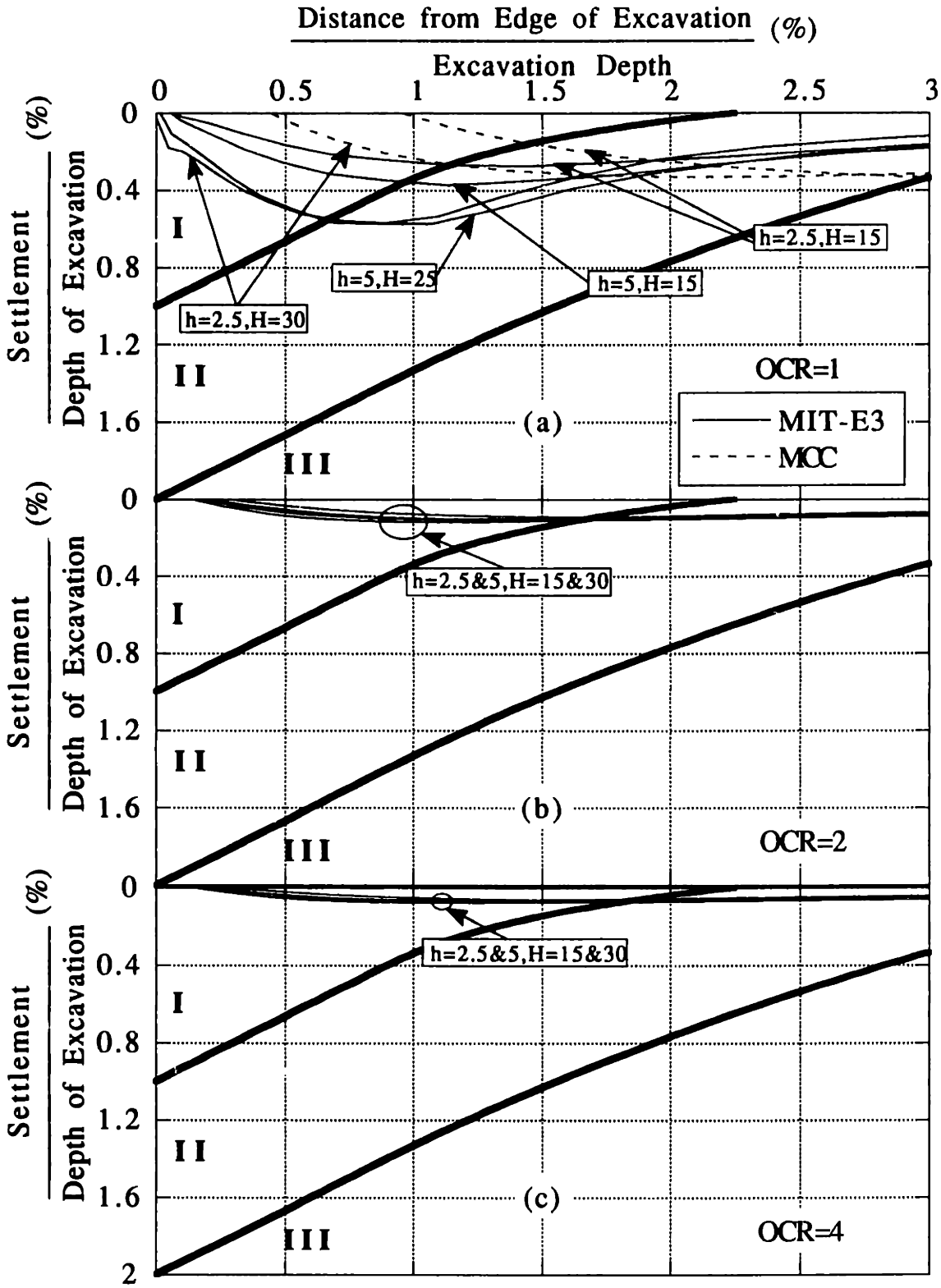

Figure 4.8-4 FE Model Normalized Settlement Profiles (h_u=2.5m, L=60m).

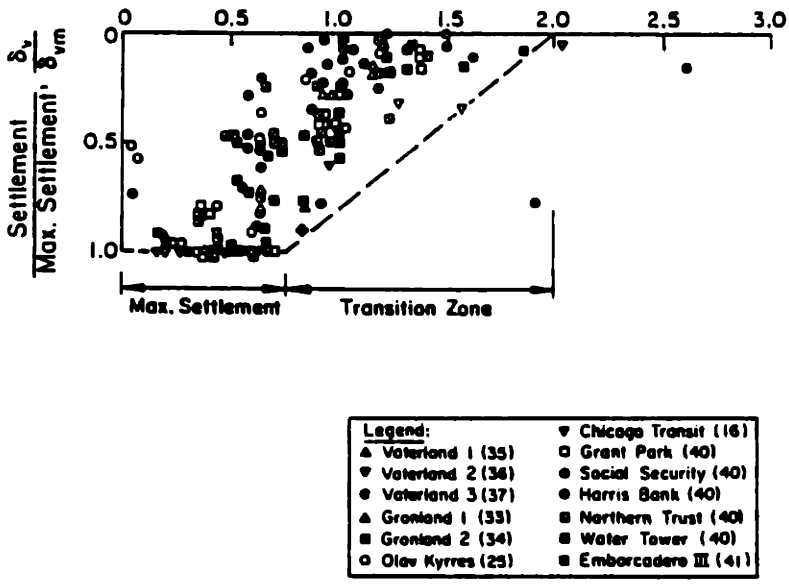

Figure 4.8-5 Summary of Measured Settlements Adjacent to Excavations in Soft to Medium Clay (Clough and O'Rourke, 1990).

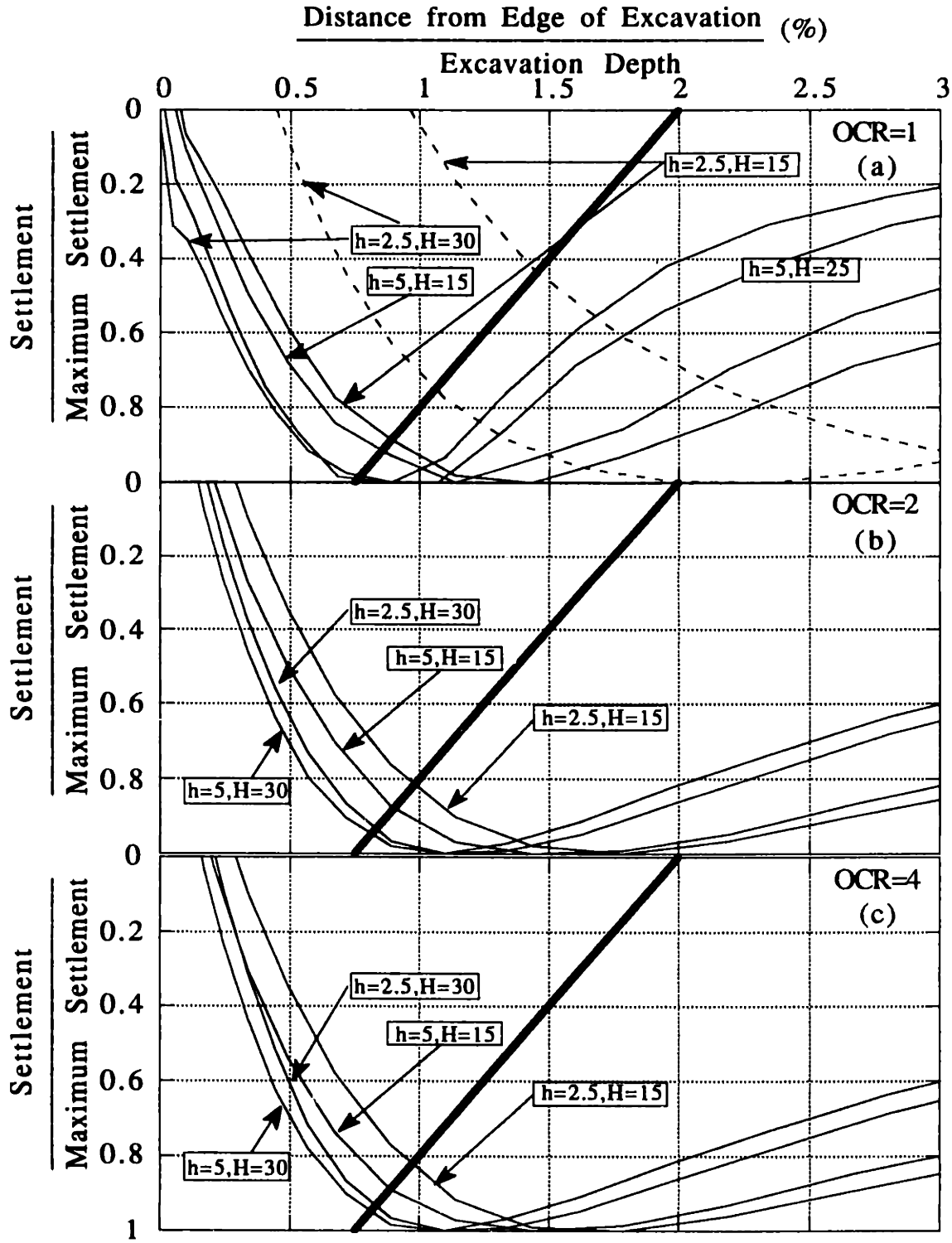

Figure 4.8-6 FE Model Settlement Profiles Normalized by Maximum Settlements (h_u=2.5m, L=60m).

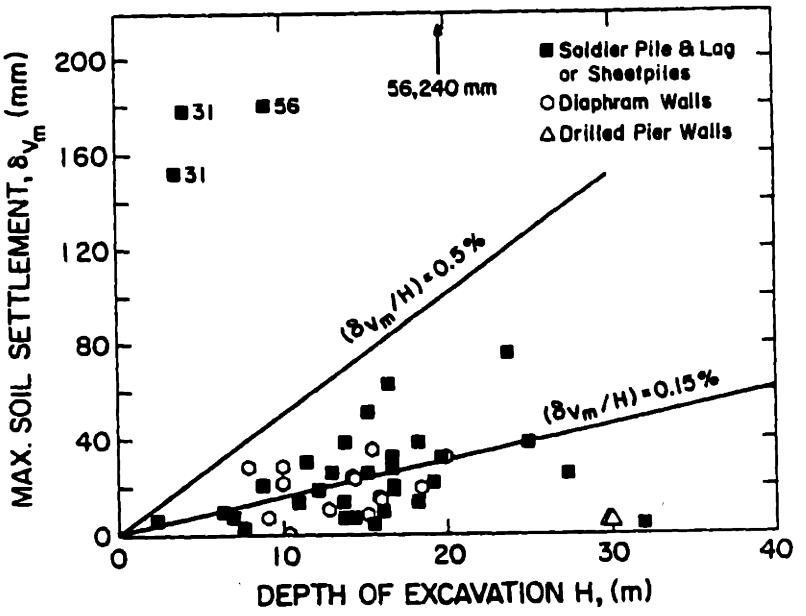

Figure 4.8-7 Observed Maximum Soil Settlements in the Soil Retained by Insitu Walls (Clough and O'Rourke, 1990).

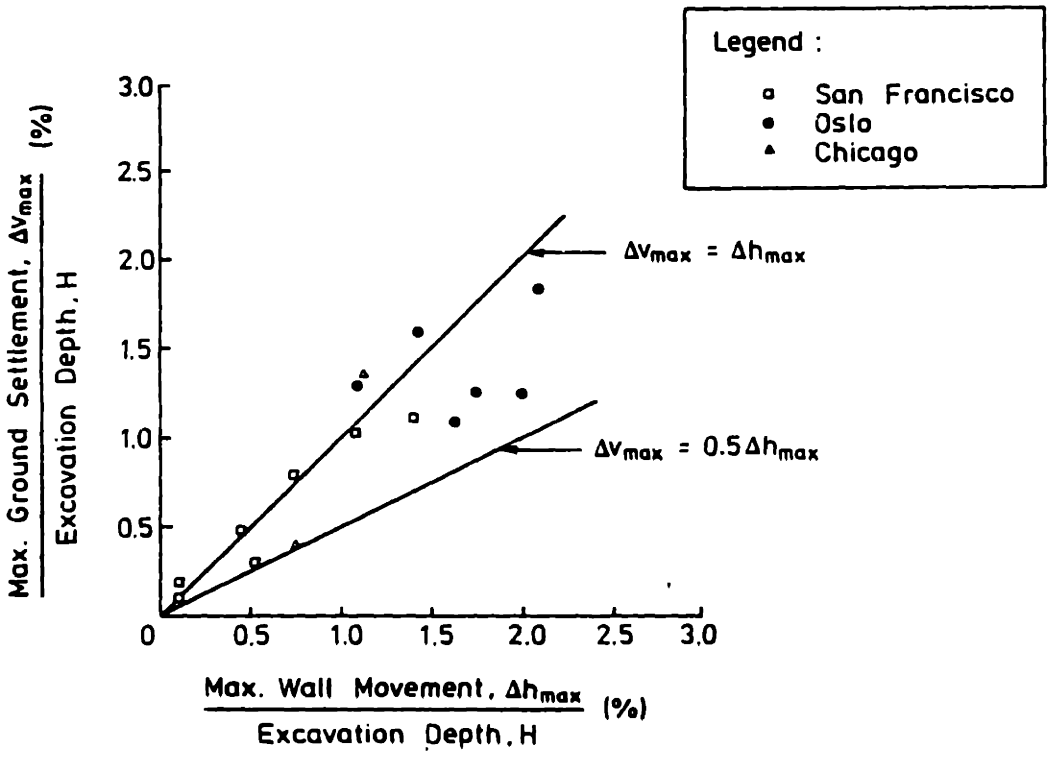

Figure 4.8-8 Relationship between Maximum Ground Settlements and Maximum Lateral Wall Movements for Case History Data (Mana and Clough, 1981).

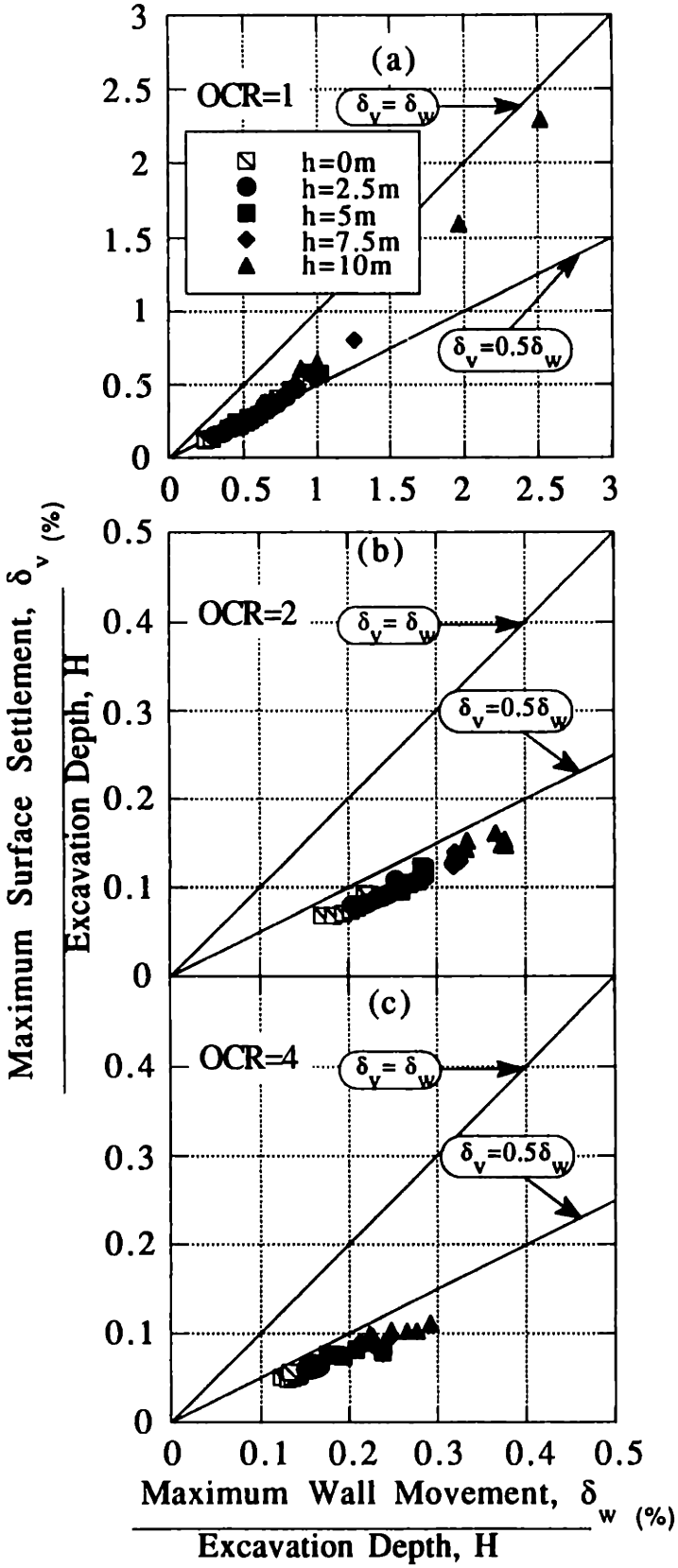

igure 4.8-9 FE Model Maximum Ground Settlements and Maximum Lateral Wall Movements (h_u=2.5m, L=60m, MIT-E3).

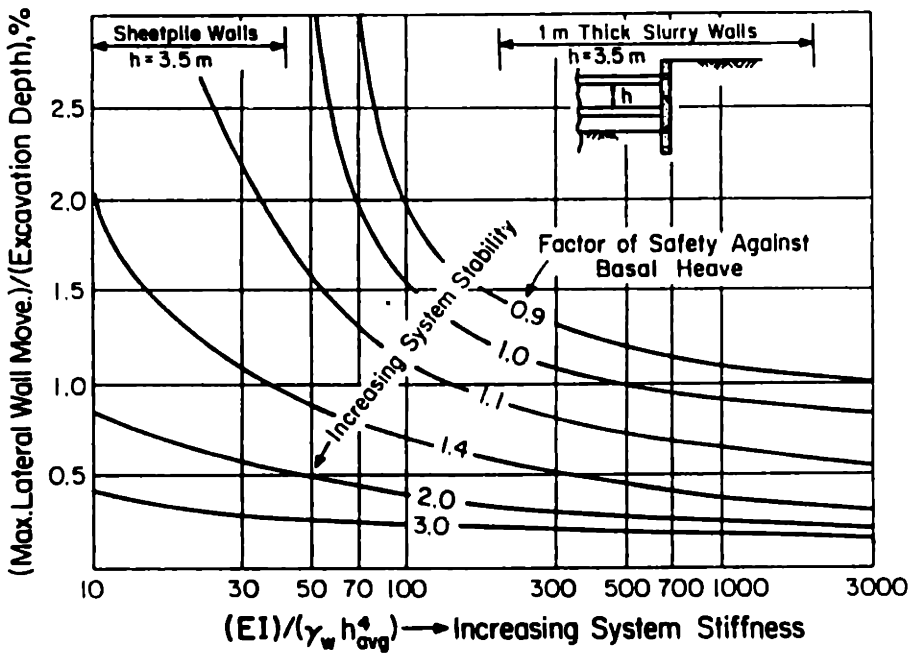

Figure 4.8-10 Chart for Estimating Maximum Lateral Wall Movements and Ground Surface Settlements for Support Systems.

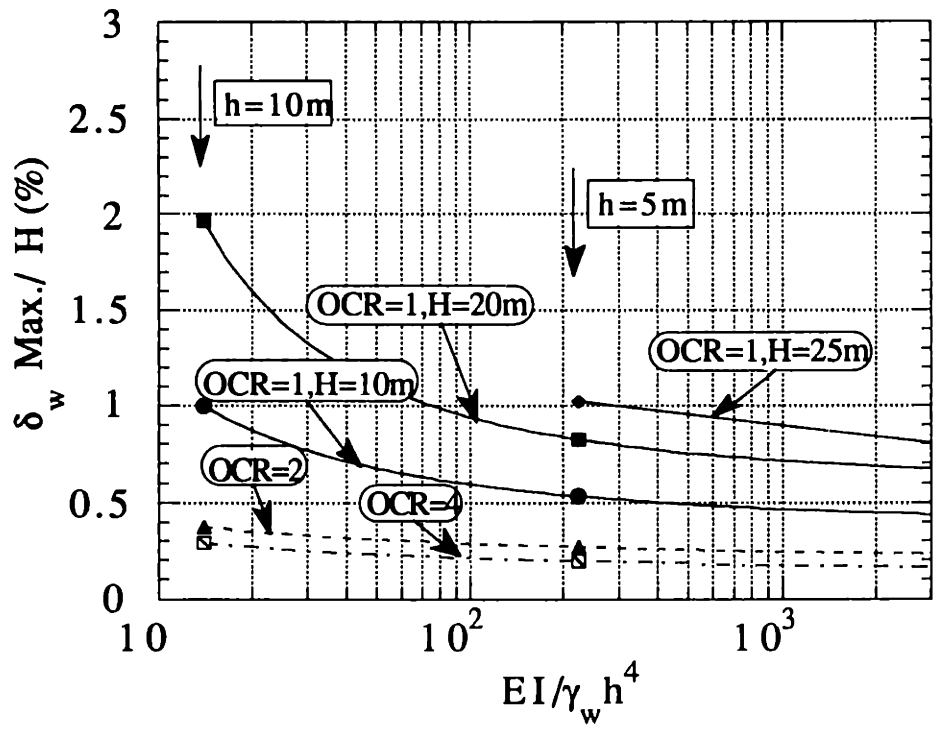

Figure 4.8-11 FE Model Normalized Maximum Deflections versus System Stiffness (h_u=2.5m, L=60m, MIT-E3).

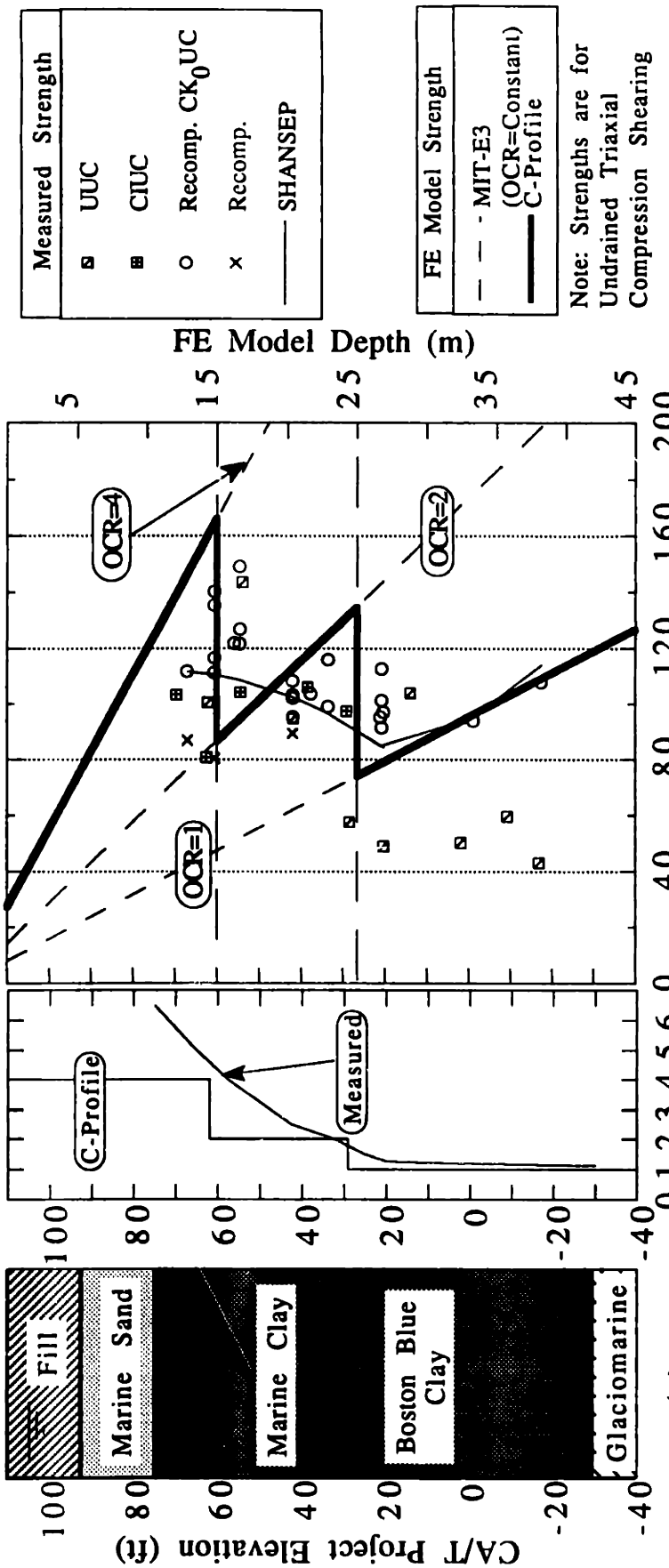

Figure 4.9-1 Soil Strength Profile for the South Boston Test Site (Data from Estabrook, 1991).

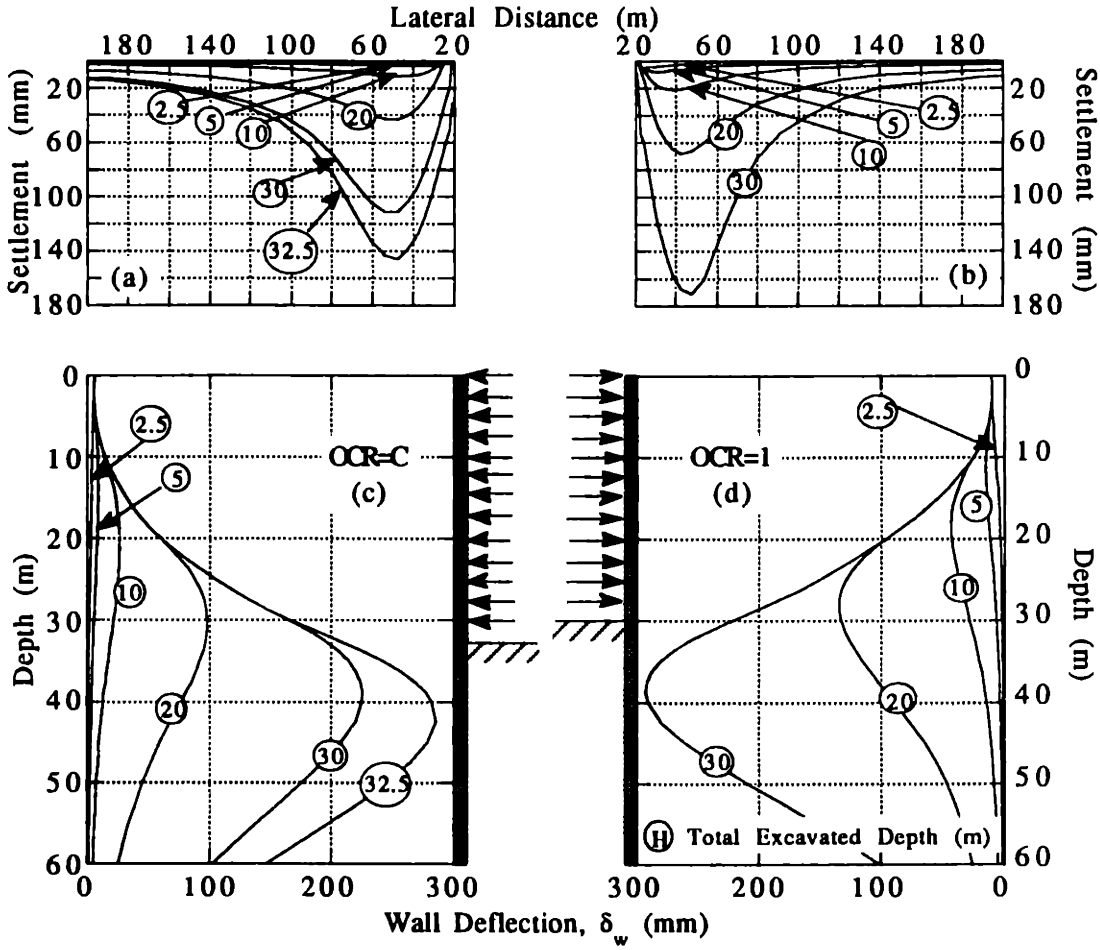

Figure 4.9-2 Wall Deflections and Surface Settlements for OCR=1 and OCR=C Analyses (h_u=2.5m, h=2.5m, L=60m, MIT-E3).

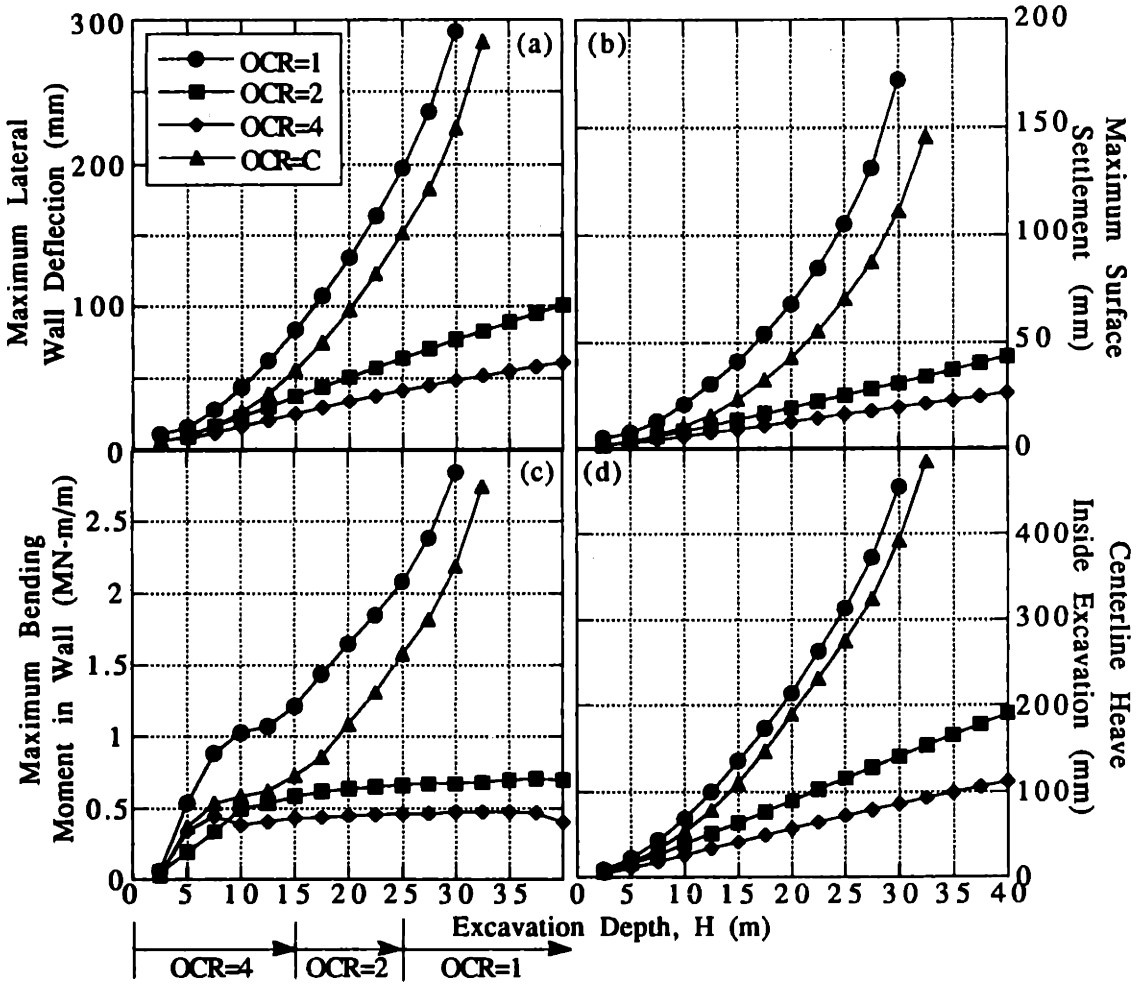

Figure 4.9-3 Effect of Soil Profile Stress History on Maximum Deformations and Moments (h_u=2.5m, h=2.5m, L=60m, MIT-E3).

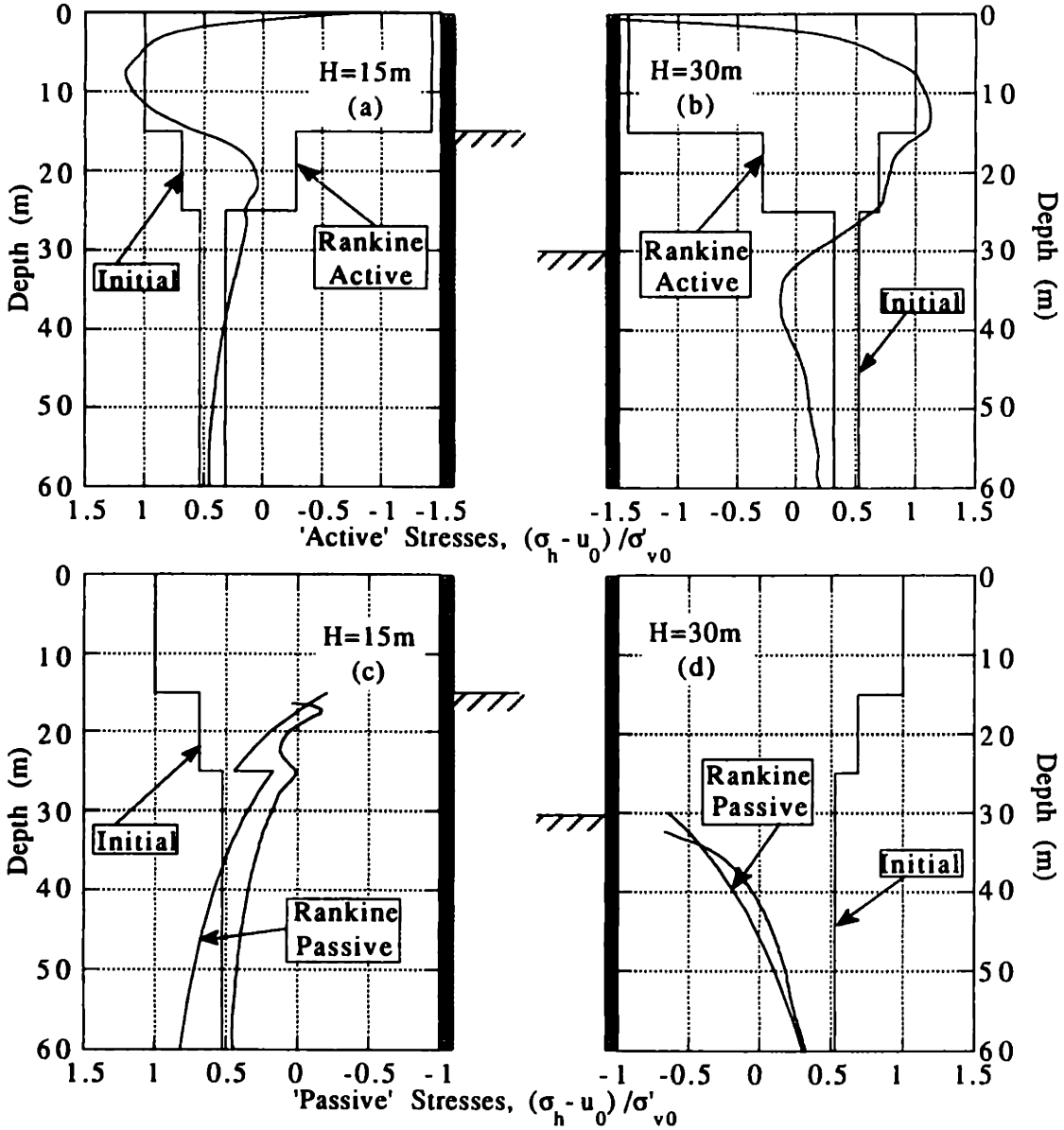

Figure 4.9-4 Normalized Earth Pressure Acting on Both Sides of the Wall for OCR=C Soil Profile (h_u=2.5m, h=2.5, L=60m, MIT-E3).

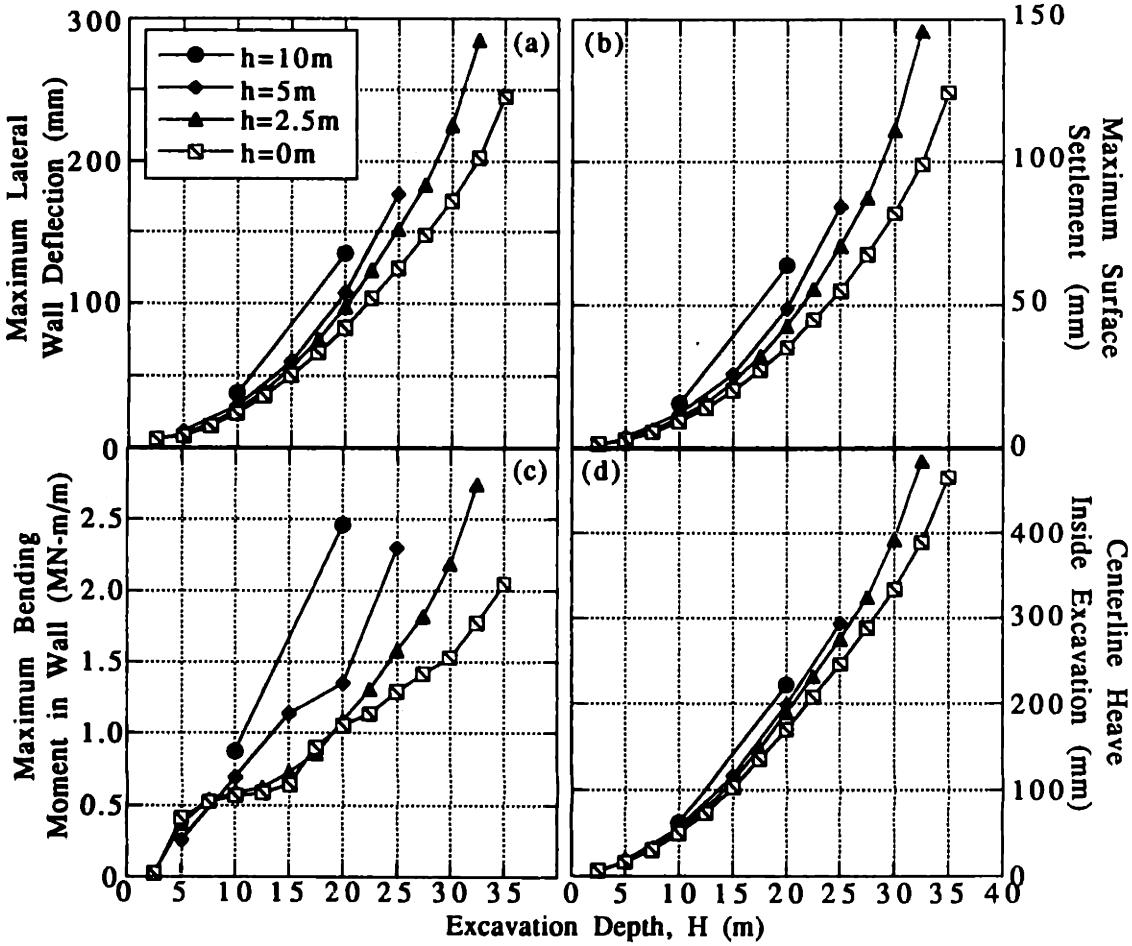

Figure 4.9-5 Effect of Vertical Support Spacing on Maximum Deformations and Movements for OCR=C Soil Profile (h_u=2.5m, L=60m, MIT-E3).

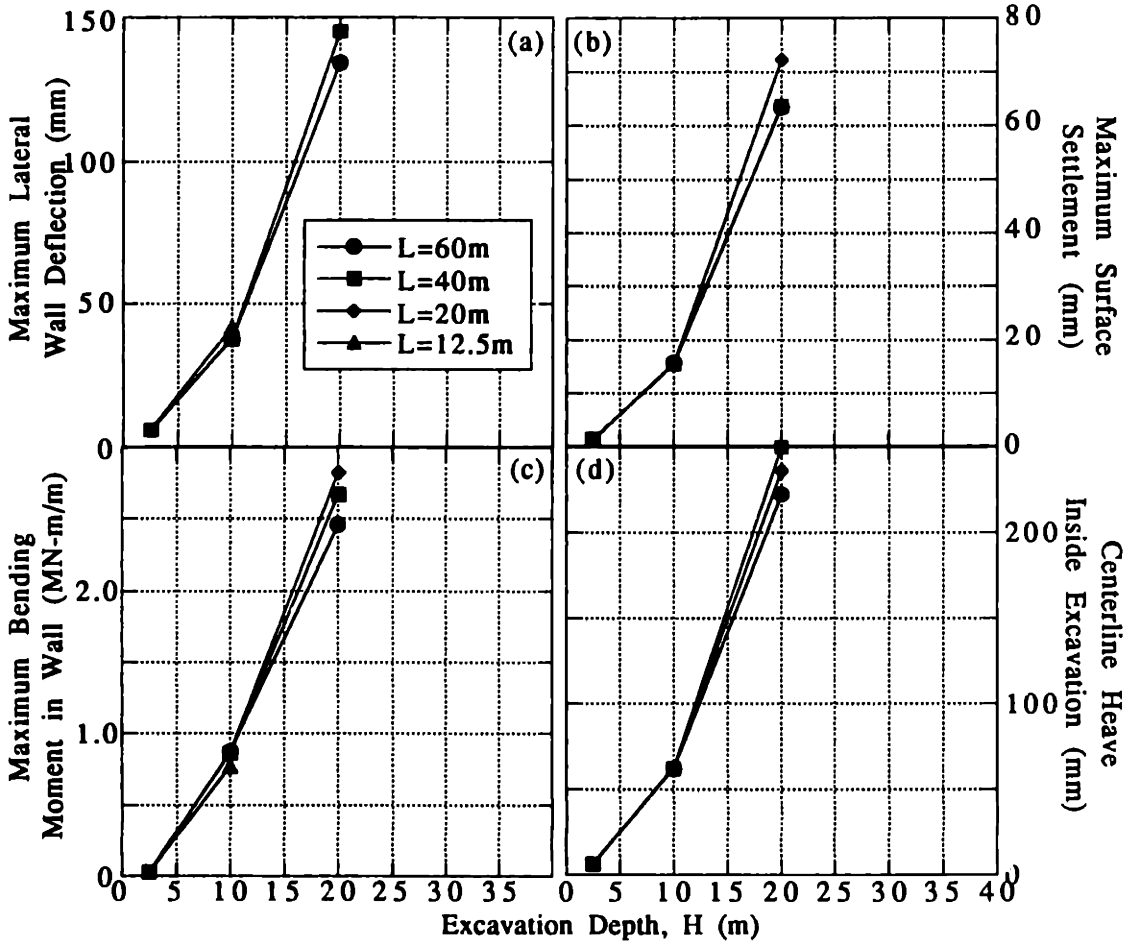

igure 4.9-6 Effect of Wall Length on Maximum Deformations and Movements for OCR=C Soil Profile (h_u=2.5m, h=10m, MIT-E3).

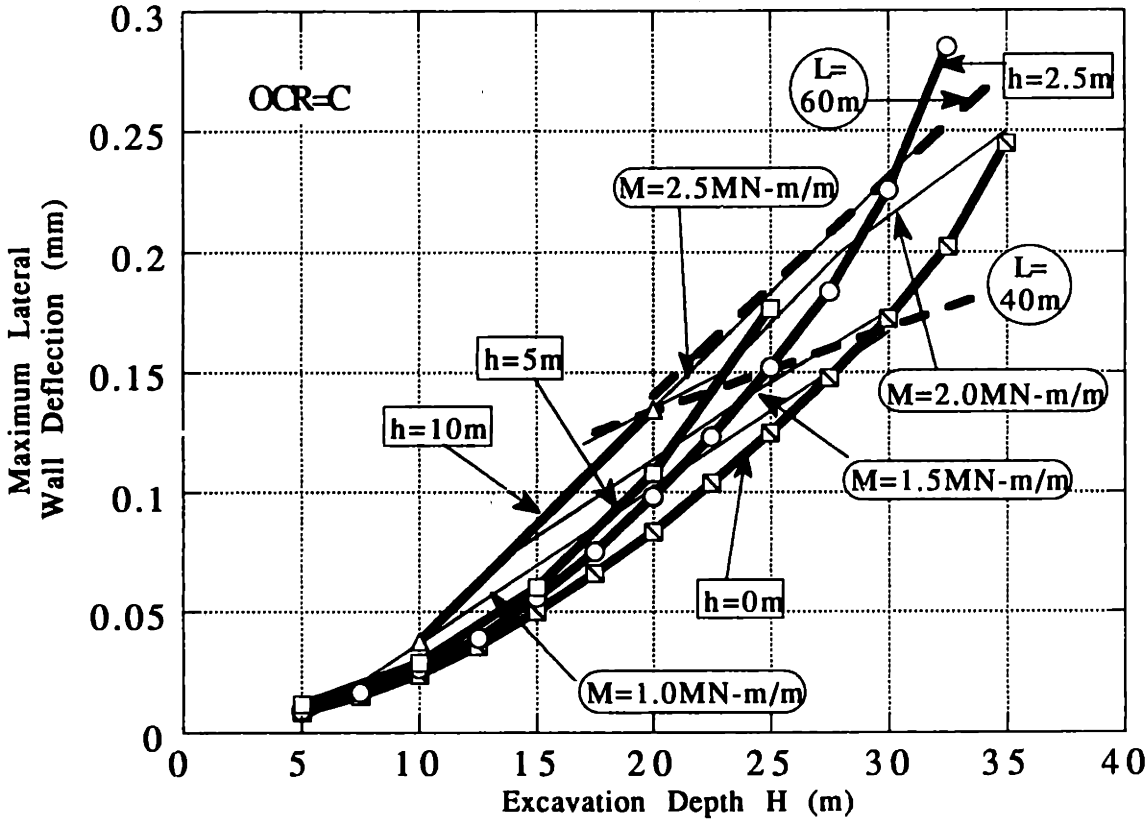

Figure 4.9-7 Simplified Framework for Interpreting Maximum Deflections, OCR=C Soil Profile.

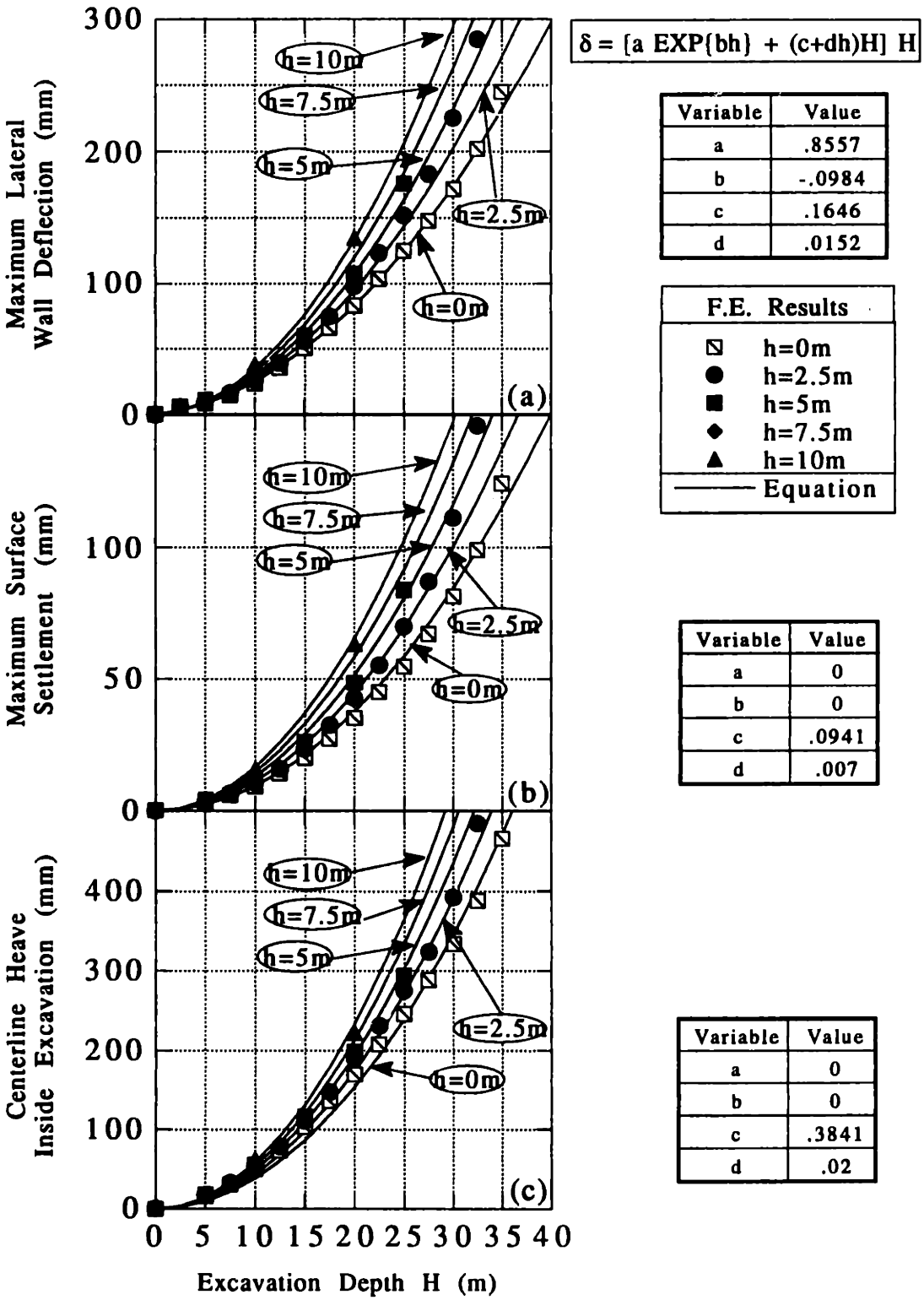

Figure 4.9-8 Curve Fit of Maximum Deflection Data, OCR=C Soil Profile.

5. Analysis of a Deep Excavation in Boston

5.1. Introduction

For deep excavations in congested urban environments, designers are particularly interested in making reliable predictions of the magnitudes of movements in the surrounding soil (Peck, 1969; Clough et al., 1989; O'Rourke, 1981); and then estimating the effects of these movements on adjacent structures and facilities (Burland and Wroth, 1974; Boscardin and Cording, 1989). In principle, these predictions can be achieved using powerful numerical methods such as finite element analyses. However, although there are a number of well documented case studies published in the literature, most of the reported comparisons between computed soil deformations and measured data are more properly classified as 'back analyses'. In these cases, input parameters for the numerical model are calibrated against the measured data using parametric studies based either on engineering judgement or simplified theories (e.g., Gioda and Sakurai, 1989). The widespread use of back analyses reflects the difficulties in achieving reliable analytical predictions of soil deformations (i.e., to within the accuracy required by the design engineer) which can be attributed to a variety of factors:

1. Initial conditions in the ground; including stratigraphy, initial stress state and groundwater flow regime can play a dominant role in the modes of deformation which occur (e.g., Chan and Morgenstern, 1987; Potts and Fourie, 1984). Limitations in the site investigation and geometric approximations used in the analytical model introduce uncertainties in the predictions that are often difficult to quantify.
2. Uncertainties in the selection of engineering properties (strength, stiffness, flow and consolidation) are generally cited as the major source of inaccuracy in numerical predictions of soil deformations. In practice, these uncertainties arise from two sources: a) inadequate laboratory and field characterization of relevant engineering properties for all soil layers; and b) approximate representations of constitutive behavior used in the finite element model (Christian, 1989). While it is widely recognized that soil behavior is controlled by effective stresses, the vast majority of analyses rely on total stress methods of analysis. As a result, predictions of soil deformations are limited to simplified drainage conditions (fully drained or undrained), while separate analyses must be used to calculate groundwater flow.
3. The precise history of construction processes can be highly complex and involves activities which are not easily analyzed using finite element methods

(e.g., O'Rourke and Jones,1989). For example, the installation of diaphragm walls, sheet pile walls or soldier piles can induce significant movements in the surrounding soil (e.g. Cowland and Thorley, 1984, Finno and Harahap, 1991), which are rarely considered in analyses. Other activities such as construction dewatering can only be properly considered using real time simulation of the coupled flow and deformation in the soil.

4. Although correct analytical procedures for simulating the incremental excavation have been described by a number of authors (Ghaboussi and Pecknold, 1984; Brown and Booker, 1986), many finite element programs used in geotechnical practice still do not satisfy the principle of uniqueness for unloading in an elastic medium (Ishihara, 1970; Christian and Wong, 1973; Christian, 1989). This introduces an important, but wholly unnecessary, error in the numerical predictions.

This chapter describes the application of the finite element model, developed in Chapters 2, 3 and 4, for predicting soil deformations and ground water flow associated with the top-down construction of a seven storey, underground parking garage in downtown Boston. The model incorporates a number of advanced features of analysis including: a) a mixed finite element formulation for describing (coupled) flow and deformation in the soil, and hence modeling the effect of partial drainage during construction; b) a numerically accurate algorithm for simulating excavation in non-linear soil (Chapters 2 and 3); and c) an advanced constitutive model (MIT-E3; Whittle, 1990, 1991) for describing the non-linear and inelastic behavior of clays. Site stratigraphy, material properties and initial ground water conditions are all selected using information provided prior to construction. However, the simulation of the construction sequence is based on the actual record of site activities. The numerical predictions are evaluated directly by comparison with data obtained from an extensive field instrumentation and monitoring program (Whitman et al., 1991).

5.2. Site Description

The underground parking garage at Post Office Square (POS) occupies a plan area of 6880 m^2 (approx. 116 x 61m) in the heart of financial district of Boston, and is bounded by the intersections of Pearl, Congress, Milk and Franklin Streets (Figure 5.1). Existing buildings up to 40 storeys tall are located adjacent to the site (Figure 5.1). The majority of these structures are supported on shallow foundations (mats and footings) and contribute negligible net surcharge to the foundation soils. The site was previously occupied by a parking garage (two storeys above, and one storey below ground) that was

demolished in October 1988.

The garage design uses a cast-in-situ, reinforced concrete, diaphragm wall (0.9m thick) extending down into the bedrock (to an elevation, El. -21m, with respect to the Boston City Basin datum) as the permanent lateral earth pressure support (Figure 5.2). This perimeter wall is braced internally by the floor slabs, which are in turn supported by interior columns (steel H-section) founded on the bedrock (at depths 26 to 29m below ground level). Both the diaphragm wall and interior columns are installed prior to excavation using slurry trench methods. The interior columns are concreted into the rock to form Load Bearing Elements (LBE). The slurry trench, in which a column is placed, is then infilled with a cement-bentonite mix over the excavated height of the columns. The roof and seven floor levels are cast in sequence from the top-down, by excavating the soil from beneath the most recently constructed slab. During excavation, dewatering is accomplished using a combination of sump pumps and deep well points located inside the excavation area.

Figure 5.2 shows an 'averaged' profile of subsurface stratigraphy interpreted from a series of 15 borings conducted at the site (H&A, 1987). It should be noted that the boring logs actually show significant variations in the thickness of the individual strata across the site, reflecting the complexity of the glacial geology in the Boston area (Johnson, 1989). The assumption of an average profile is consistent with limited data and uncertainties in engineering properties of individual strata:

1. The fill layer comprises a heterogeneous mixture of sand, sandy gravel and construction debris with thickness ranging from 0.6 to 4.0m.
2. Underlying the fill is a 10-15m thick deposit of low plasticity (I_p=20-30%), moderately sensitive (s_t=3-6) clay containing numerous lenses or layers of sand. Laboratory estimates of the preconsolidation pressure, σ'_p, obtained from a small number of oedometer tests (Figure 5.2c) show that the clay has an in-situ overconsolidation ratio decreasing with depth in the deposit and ranging from OCR=6 to 2. The index properties, stress history and compressibility of the clay compare closely with data reported previously for deposits of 'upper' Boston Blue Clay (BBC) reported at other well documented sites in the Boston area (e.g. Baligh and Vivatrat, 1979; Morrison, 1985; Ladd, 1990). Hence, the selection of engineering properties and modeling of clay behavior are based on results of previous studies (Whittle, 1990).
3. Beneath the clay is a layer of dense to very dense sand whose thickness varies from 0.3 to 5.8m at locations within the excavation. The sand layer is not present at locations north and east of Pearl Street.

4. The soil deposits overlying the bedrock are classified as glacial till (these units have recently been re-classified as 'glaciomarine' by Humphrey, 1990) and comprise a very heterogeneous mixture of particles, ranging from silt-size to cobbles and boulders, embedded in a compact silty-clay matrix (N=50-100 blows/ft from SPT tests). The material is very difficult to sample and results from in-situ Ménard pressuremeter tests show considerable scatter in properties (E_m=10-40 MPa, P_L=2-6 MPa). The till deposits range in thickness from 1.5 to 11.6m across the site.
5. The bedrock is a moderately to severely weathered (kaolinized) argillite deposit containing discontinuous layers of sandstone and quartzite. The surface of the bedrock is located at elevations ranging from El. -16 to -20m. The depth and extent of weathering is highly erratic and the transition to 'sound rock' is assumed at El.-24 m.

The groundwater level in the upper fill exhibited small fluctuations between elevations, El. +2.3 to 2.9m over a period of three months prior to construction. Piezometric levels were also measured in the underlying strata using pneumatic piezometers. In these layers, there is a significant decrease in the piezometric head, ranging from El.+0.9m at the bottom of the clay to El.-1.5m at the top of the bedrock (Figure 5.3c). The site investigation was not able to determine the cause of these deviations from expected hydrostatic conditions. Flow properties of the individual strata were estimated from in-situ permeability tests which included: a) falling head tests in the clay, sand and till; and b) pumping tests from screened wells in the argillite.

5.3. Base Case Analysis

The main aim of the base case analysis is to estimate the capabilities of a 'comprehensive' finite element model for predicting geotechnical parameters of practical importance in the design of the Post Office Square garage including: 1) magnitudes of wall movements and soil deformations associated with the excavation sequence, 2) consolidation settlements due to pore pressure changes in the clay layer; and 3) the quantity of water flowing into the excavation (both during construction and throughout the design life of the structure). The analysis is performed using the ABAQUS finite element code that has well documented capabilities for solving non-linear problems involving coupled flow and deformation in soils (HKS, 1989). The analysis assumes a two-dimensional, plane strain geometry based on the averaged soil profile shown in Figure 5.2. This simplification is a practical necessity in view of the very large additional computational effort involved in performing a complete three-dimensional, non-linear

analysis. The plane strain approximation is also reasonable in view of other uncertainties in site conditions and soil properties described above. The following paragraphs summarize the main features of the base case analysis.

5.3.1. Soil Models

Constitutive modeling of soil behavior and selection of input parameters represent a major source of uncertainty in finite element analysis. For the Post Office Square garage, strength and deformation properties are especially difficult to estimate due to the lack of laboratory test data on intact/undisturbed material in all layers except for the clay. For these materials (i.e. fill, sand, till and argillite), the effective stress-strain-strength properties are described by an elasto-plastic model using a Drucker-Prager failure criterion with a non-associated flow rule (EP-DP model). In order to model realistically the depth variations in properties, the elastic shear and bulk moduli are assumed to be proportional to the mean effective confining stress, σ', in accordance with observed soil behavior (e.g., Gens and Potts, 1988). Initial stress (K_0), deformation (G/σ', ν') and strength parameters (c', ϕ') are estimated from laboratory test data on similar materials reported in the literature, as shown in Table 5.1.

The behavior of the clay layer is described using the MIT-E3 effective stress soil model, developed by Whittle (1990, 1991), using input parameters previously selected for Boston Blue Clay. The MIT-E3 model describes many aspects of the observed behavior of K_0-normally and lightly overconsolidated (OCR≤8) clays including: a) small-strain non-linearity; b) anisotropic stress-strain-strength; and c) hysteretic and inelastic behavior due to cyclic loading. The model has been extensively validated at the element level through comparisons with laboratory test data. Table 5.2 summarizes the input parameters used by the model together with values selected for Boston Blue Clay (Whittle, 1990). The model has been integrated in the ABAQUS code (Chapter 2) and used in parametric studies of the performance of braced excavations in a deep layer of clay (Chapter 4). In the current analysis, properties of the clay layer are established from the stress history (σ'_p, σ'_{v0} ; Figure 5.2) assuming normalized behavior. Table 5.1 summarizes pertinent engineering properties of the clay used by the MIT-E3 model.

5.3.2. Construction Sequence

Figure 5.3 summarizes the sequence of events used in the finite element simulation for a typical section of the garage structure, based on the actual record of site activities. Each 'stage' in the analysis represents a distinct change in either the geometry,

boundary conditions or time elapsed between events. In practice, the top-down construction of the roof and floor slabs is achieved by over-excavating the soil (the mined material is removed through three centrally located glory holes) and then casting the concrete on mobile forms that are supported by the internal columns. In the analysis, this process is simulated by three 'stages' (10-13, 13-16 etc.; Figure 5.3): 1) an undrained excavation, to the appropriate ground elevation; 2) a time delay to account for the curing of the concrete and partial drainage; and 3) installation of a structural prop, (with axial stiffness per unit width Eb/L, where L= 30 m is the half-width of the excavation) corresponding to the completed floor slab (e.g. stages 7, 10, 13, 16 etc.; Figure 5.3).

The numerical simulation assumes that the construction of the diaphragm wall has no effect on the surrounding soil (i.e. the wall is wished-in-place) and does not consider the installation of load bearing elements (LBE's) used to support the internal columns (Figure 5.2). All computed deformations in the analysis are reported relative to an initial equilibrium state ('reference configuration', stage 5; Figure 5.3) wherein: a) the diaphragm wall is installed; b) the ground elevation is excavated inside the perimeter wall (El.4.9m), due to the removal of the pre-existing structure; and c) non-hydrostatic pore pressure conditions are assumed (based on piezometer data, Figure 5.2b).

Dewatering of the site is simulated by controlling the pore pressures at specific locations in the finite element model. At early stages of the construction (e.g. stages 12-15; Figure 5.3) the records show pumping from a limited number of wells, while at later stages (stage 18 onwards; Figure 5.3) more extensive dewatering is conducted. Stage 32 in the analysis represents final conditions corresponding to steady state flow with a permanent dewatering system installed beneath the basement (floor 7) slab.

Figure 5.4 compares the time history of the excavation geometry used in the finite element simulation with the field records of excavation. At any given time, variations in the measured ground elevation are due to stabilizing berms (also included in the simulation, Figure 5.3) and spatial variations in the progress of the construction. The model simulation matches closely the changes in geometry, except at stages 16-19 during which times the simulation underestimates the rate of excavation.

5.3.3. Finite Element Model

Chapters 2 and 3 describe in detail the finite element procedures used to perform numerically accurate, effective stress analysis of excavation in non-linear soils using ABAQUS. Figure 5.5 shows the finite element mesh and boundary conditions used for the analysis of the POS garage. Important features of the model can be summarized as follows:

1. Coupled analysis of fluid flow and deformation in the soil is performed using mixed isoparametric elements with 8-displacement nodes and 4-corner pore pressure nodes. These elements provide quadratic interpolation of displacements, strains and effective stresses; and bi-linear interpolation of pore pressures. The calculations are performed with full integration of element stiffness matrices. Solid, 8-noded, isoparametric elements are used to model the concrete diaphragm wall and dry fill materials. Floor slabs are represented by one-dimensional spring elements. The overall mesh for the base case analysis comprises 611 elements with 4,410 nodal degrees of freedom.
2. The finite element model extends far beneath the base of the excavation (to 60m depth) and laterally a distance of 120m beyond the perimeter wall where soil displacements, due to the simulation of garage construction, are negligible. Boundary conditions inside the excavation are shown schematically in Figure 5.3. Boundaries of the groundwater flow regime are more difficult to estimate. In the farfield, the distribution of (non-hydrostatic) initial pore pressures are maintained (along A-B'; Figure 5.5); while a perched water table is assumed in the fill at El.+2.7m (B'C'; Figure 5.5). Along the lower boundary, there are no data for estimating the permeability of the intact rock. Thus the boundary (O-A; Figure 5.5) can be treated either as a no flow boundary ($\partial u/\partial y=0$) assuming that the intact rock has very low permeability or as a line of constant piezometric head (constant pore pressure). The former of these assumptions is used in the base case analysis.
3. The floor slabs are joined to the diaphragm wall assuming simple pinned connections. Vertical reaction forces are added to the wall to simulate the self weight of the floor slabs. It is assumed that the slabs are simply supported by the wall and the internal columns.
4. The total computation time required for the complete excavation sequence was 30 CPU hours using a VAX 3200 series workstation (subsequent calculations were performed on a Cray-2 supercomputer in 2 CPU hours).

5.4. Comparison of Predictions and Measurements

Whitman et al. (1991) have described the important role of the field and monitoring program in refining the design and construction schedule of the Post Office Square garage. The field data include: a) lateral movements of the diaphragm wall, measured by a series of 13 inclinometers cast within the wall; b) lateral soil displacement from a further 11 inclinometers strategically located either in front of adjacent buildings

or in close proximity to the diaphragm wall; d) surface settlements and vertical movements of the surrounding buildings, monitored by optical survey; c) relative vertical displacement of the clay, till and rock, obtained at 6 locations using multiple position borehole extensometers (MPBX); and e) groundwater and piezometric levels from 5 observation wells and 30 piezometers installed approximately one year prior to construction.

In the following paragraphs, the measured data are compared with predictions from the base case analysis at three reference geometries used in the idealized construction sequence (Figure 5.3) and corresponding to installation of the roof slab (stage 10), the third floor (stage 19), and the sixth floor (stage 28). The measured data are selected from the continuous monitoring records by matching the actual excavation history to the reference configurations at individual sections around the site. Although there is some subjective judgement in this procedure, the methodology greatly simplifies the interpretation of field data (c.f. Figure 5.4) and is consistent with other approximations used in the analysis.

5.4.1. Lateral Wall Movements

Figure 5.6 presents measurements of lateral deflections of the diaphragm wall obtained from 10 inclinometers distributed around the perimeter of the site (Figure 5.6d). The inclinometers casings extend below the base of the wall to an elevation El.-35±1m, within the argillite, in order to provide a fixed datum in computing lateral deflections. The following points should be noted from the data:

1. Prior to stage 10 (roof slab construction) the excavation is unsupported (with maximum depth of 6m) and the diaphragm wall deforms in a cantilever mode. Maximum inward movements (15 to 28mm) occur at the top of the wall, while the base displaces less than 2mm. Measurements from 2 inclinometers at the Milk St. end of the site show significantly less movement at the top of the wall (5mm). This behavior can be explained by differences in the construction sequence at these locations where the roof slab is cast on-grade prior to excavation (unsupported depth is 0 m).
2. As construction proceeds from the roof slab down to floor level 3 (stage 10 to 19), the majority of the data show small additional inward movements at the top of the wall, while the point of maximum deflection moves down to the third floor elevation (El.-4.6m). The data from two inclinometers along Pearl St. show much larger inward movements (up to 50 mm). Schoenwolf et al (1991) suggest possible reasons for this behavior associated with details of berm construction,

temporary support for an access ramp and specification of backfill materials used in LBE construction.

3. After stage 19 there are only small changes in the maximum lateral wall movement; however, the point of maximum movements progresses downwards to an elevation corresponding to the bottom of the clay layer (i.e. El.-10.7±1.5m, at stage 28). Maximum lateral movements are in the range 40 to 50 mm, while the base of the wall moves less than (±)3mm throughout the construction.

Predictions from the base case analysis are also included in Figure 5.6. At stage 10, predictions of the cantilevered deflection mode, with maximum movements of 20mm at the top of the wall, match closely the measured data. However, by the time of third floor construction (stage 10), the analysis underpredicts significantly the maximum deflections (20mm versus 30 to 40 mm) for the majority of inclinometers. Nor does the base case analysis predict the downward progression of the point of maximum displacement (stages 10 to 28) described above. Other aspects of the predictions, such as the fixity of the base of the wall, and the small incremental displacements at later stages of construction (stages 19 to 28) are in accordance with the measurements.

One possible reason for the discrepancy between predicted and measured lateral wall movements is the post-construction behavior of the roof and floor slabs. In the finite element model, these supports are represented by spring elements whose stiffness is controlled by the modulus of the fully cured concrete. The net effect on the predictions is that, at the elevation of a given floor level, practically no lateral wall deflection occurs after the floor is installed (see Figure 5.6). In reality, the effective stiffness of the roof/floors is affected by processes of shrinkage and expansion, due to curing of the concrete and seasonal variations in the ambient temperature. Figure 5.7 summarizes the inclinometer measurements of incremental (i.e. post roof/floor slab construction) lateral wall deformations at the elevations of the roof and five floor levels. Although there is significant scatter in the data, average inward wall movements, ranging from 5 to 10mm occur after floor construction at all six elevations. These trends are later reversed in the upper floors (roof, 1st and 2nd floor levels), such that at the end of construction (stage 28), the net displacements are negligible. The initial inward movements are most probably due to shrinkage associated with the casting of the floor slabs, while the later expansion correlates closely with a marked rise of 25^{0}C in the ambient temperature between the end of February 1990 (stages 16 to 19) and July 1990 (stage 28), as shown in Figure 5.4.

5.4.2. Lateral Movements in the Soil

Figure 5.8 compares predictions of lateral soil deformations with data from inclinometers located at distances of 4, 9 and 14m behind the diaphragm wall. These results show the following:

1. For inclinometers installed close to the wall (4m behind the wall), the maximum lateral deformations occur in the clay layer (20 to 35 mm; Figure 5.8) and are significantly less than those measured in the wall. However, the development of the displacement profile (stages 10 through 28) is very similar to that described previously for inclinometers within the wall.
2. At locations further from the wall, the measurements show much smaller maximum lateral deformations (20-30mm at 9m, 5-6mm at the 14m section) which occur in the upper layer of fill material.
3. The finite element predictions are in good agreement with measured lateral soil deformations at stage 10, when the roof slab is installed. However, as excavation progresses, the analysis underpredicts soil displacements in the section closest to the wall (at 4m), while overpredicting movements at locations further away (at 14m; Figure 5.8). This trend is most clearly observed from the deformations of the till and sand layers (i.e. Els.-18.3 to -12.2m) at stage 28 (Figure 5.8). As both the measurements and predictions show minimal lateral movements at the top of the (weathered) argillite (at El. -18.3m), the deformations beneath the clay layer (at El -12.2m) are primarily due to the shear modulus of the sand and till layers. Thus, the results in Figure 5.8 illustrate limitations in the modeling of these lower soil layers in the base case analysis. Trends in the measured data imply that small strain non-linearity (i.e., variation in the secant shear modulus at strain levels less than 0.1 %) is an important aspect of soil behavior that should be considered in future modeling of sand and till.

5.4.3. Settlements

Regular surveys of surface elevations from a network of reference points in the surrounding streets, produced the settlement profiles in Figure 5.9. The data obtained at locations adjacent to the excavation (i.e. less than 12m behind the wall), show a wide scatter with isolated measurements of up to 60 mm. Further away from the site, settlements taper off rapidly with maximum values ranging from 12mm at a distance of 15m to less than 3mm at 40m.

In addition to surface settlements a series of six multiple position borehole extensometers (MPBX) were installed at locations along Congress and Pearl St.

(approximately 12m behind the diaphragm wall) to measure vertical deformations in the clay layer. These data (Figure 5.10) also show significant scatter (including some measurements of heave), but generally indicate settlements considerably less than 15mm within the clay layer. Based on this evidence, 'large' surface settlements (i.e. greater than 20-25mm, Figure 5.9), close to the excavation, are most probably associated with the behavior of the near-surface fill or pavement materials.

Base case predictions give reasonable estimates of the surface settlements at early stages of construction (stage 10; Figure 5.9). At later stages (19 and 28), the predicted settlements are significantly larger than the measured data. It is particularly noticeable that the analysis does not predict the measured rapid decrease in surface settlements with distance beyond the perimeter wall, and hence exaggerates the effect of the excavation on the adjacent buildings. Average vertical settlements predicted in the clay layer (Figure 5.10) increase significantly during construction. Approximately 40% of the predicted surface settlements at stage 28 are due to compression of the underlying sand, till and argillite layers.

5.4.4. Groundwater Conditions

Measurements from piezometers installed prior to construction of the garage establish that initial groundwater conditions at the site are not hydrostatic (Figure 5.2). Further measurements of piezometric elevations inside the excavation are used to model the dewatering of the site in the finite element simulation (Figure 5.3). Figure 5.11 shows the measurements of piezometric elevation at stages 10, 19 and 28 obtained from piezometers located at distances of 14, 46 and 95m outside the diaphragm wall. Overall, these data show very small changes in piezometric level compared to the initial conditions. In contrast, the base case analysis predicts reductions of up to 15m in the piezometric elevations at the base of the clay layer (at locations 14m behind the wall). This large difference between predictions and measurements can be attributed to a number of factors including the selected permeability properties (especially that of the argillite; Table 5.1) and simulation of dewatering used in the analysis. However, it is also apparent that the 'no flow' boundary condition (O-A; Figure 5.5) used in the finite element model allows unrealistic changes in piezometric elevations in the rock.

The predictions of large decreases in pore pressures (Figure 5.11) have a number of practical implications on the soil and wall deformations described above:

1. In the low permeability clay layer, there is little drainage of excess pore pressures (i.e., $u-u_0$) during the construction of the garage. As a result, vertical deformations within the clay layer are not significantly affected by the drawdown

in pore pressures. However, the total lateral stress acting on the back of the wall is reduced and hence smaller movements of the wall occur.

2. In the sand and till layers, drainage of excess pore pressures causes large increases in the (vertical) effective stresses. As a result, the model overpredicts vertical deformations in these layers.

5.5. Modified Analysis

The previous section has presented direct and comprehensive comparisons between finite element predictions and field data measured during the construction of the Post Office Square garage. From these studies, it is clear that the base case analysis can be improved significantly by the following modifications 1) simulation of floor slab shrinkage, and 2) specification of a constant pore pressure boundary condition in the intact argillite (i.e., along the baseline of the finite element model, Figure 5.5). A highly simplified model of floor shrinkage, which assumes a gap of 13mm between the roof/floor slabs and diaphragm wall (based on data presented in Figure 5.7), was implemented in the analysis. Results of this modified analysis (which should be classified as 'class c' predictions, according to Lambe, 1973) are included in Figures 5.6 through 5.11 and show the following:

1. Piezometric levels from the modified analysis (Figure 5.11) match the field data at locations far from the excavation (46m and 95m behind the wall). However, the analysis 'predicts' a 9m drawdown at the base of the clay layer 14 m behind the wall. This result suggests that other factors, such as the estimated permeability properties and simulation of dewatering are also important in the predictions of the pore pressures.
2. Figure 5.11 also shows computed piezometric levels for steady state flow conditions (stage 32, Figure 5.3), associated with permanent dewatering beneath floor 7. The total flow rate into the basement, computed from the steady state analysis, is 27 l/min. In comparison, measured pumping rates decreased from a maximum of 76 l/min at the early stages of construction, to 38 l/min at stage 28.
3. Modifications in the analysis reduced significantly surface settlements computed at locations 14 to 40 m behind the wall (Figure 5.9). This behavior can be attributed primarily to a reduction in the compression of the sand and till layers, as indicated by the vertical displacements shown in Figure 5.10. After construction is completed, the analysis predicts very small incremental heave movements (less than 5mm) at the ground surface due to increases in pore pressures in the clay, sand and till layers (stages 28 to 32, Figure 5.11).

4. The modified and base case analyses predict very similar lateral wall movements prior to roof slab installation (stage 10; Figure 5.6). However, by the time of third floor construction (stage 19), the modified analysis gives much better agreement with the measured data. At later stages of the construction (stages 19 to 28), the magnitude and point of maximum wall movements are well described by the analysis, while displacements at the top of the wall are overestimated. These patterns of behavior are consistent with post-construction movements of the floor levels from the modified analysis (Figure 5.7) which show that: a) the '13mm shrinkage gap' overestimates initial inward movements; while b) further refinements of the analysis are needed to account for subsequent expansion movements of the floor system (after stage 19).
5. The analyses predict very small post construction movements of the wall (stages 28 to 32; Figure 5.6).
6. Modifications in the analysis generate larger inward lateral displacements in the soil (Figure 5.8). At locations 4 and 9m behind the wall, these effects are masked by the scatter in the measured data; while at 14m, the modified analysis increases the discrepancy reported previously. This difference can be attributed to small strain stiffness properties of the sand and till (as above) which have not been considered in either analyses.

5.6. Discussion

The main advantage of the finite element analyses performed in this study is their capability to describe; a) time dependent (consolidation) deformations associated with transient groundwater flow, and b) non-linear and inelastic effective stress-strain-strength properties of soils. However, there are important approximations in applying the finite element analysis to model a complex soil-structure interaction problem such as the construction of the garage at Post Office Square. For example, the base case analysis assumes a two-dimensional, plane strain geometry together with a simplified representation of site stratigraphy. These approximations preclude the interpretation of movements due to three dimensional construction activities (such as the concurrent curing and casting of floors slabs). Other assumptions implying that diaphragm wall installation does not affect the surrounding soils are partially supported by field data (Schoenwolf et al., 1991).

The representation of soil behavior in the finite element model is severely constrained by the lack of laboratory test data from which to estimate material properties. Accordingly, the base case analysis uses very simple constitutive equations (EP-DP

model), requiring a small number of input parameters, to describe these materials (i.e., fill, sand, till and argillite). A much more elaborate elasto-plastic model (MIT-E3) is introduced for Boston Blue Clay, whose properties have been extensively investigated (at other sites).

The construction sequence used in the analysis attempts to account for all site activities which affect deformations in the surrounding soil, including a) excavation geometry (with berms) and rates, b) floor slab installation, and c) dewatering. However, field measurements show that factors not considered in the analysis, such as post-construction shrinking and expansion of the floor slabs, have a significant effect on wall movements. The data also shows that model simulation of dewatering (Figure 5.3) exaggerates the drawdown in piezometric elevations in the surrounding soil.

The main aim of this finite element model is to provide a comprehensive framework for a) forecasting the effects of the various excavation-related activities on soil deformations, and b) interpreting the performance of the structure from construction monitoring measurements. For the Post Office Square garage, the predictive capabilities and limitations of the base case analysis were evaluated by comparison with extensive field data, including wall deflections, soil deformations, surface settlements and piezometric levels. Differences between predicted and measured wall movements were attributed, in large part, to post-construction deformations of the roof slab and floor slabs; while predicted settlements were affected by unrealistic modeling of piezometric elevations in the argillite. Incorporating these factors into a modified analysis greatly improved agreement with field data. At this stage, remaining differences between 'predictions' and measurements (especially lateral soil deformations) have been linked to properties of the sand and till layers. While it is interesting to speculate on parametric studies to refine the analysis, the only rational basis for such calculations is through improved laboratory characterization of the deformation properties of these materials.

5.7. Conclusions

This chapter has documented the assumptions used to develop a finite element model for simulating the top-down construction of an underground parking garage at Post Office Square in Boston. Model predictive capabilities and limitations have been evaluated through comparisons with field data from an extensive construction monitoring program. The main conclusions of this study are that it is possible to make detailed and useful predictions of deformations occurring during top-down construction. More specifically:

1. Measurements of spatial variation in (vertical and lateral) soil deformations and

pore pressures provide important information on the effects of excavation procedures on the surrounding soil and are essential for evaluating the consistency of model predictions. Interpretations based exclusively on comparisons of lateral wall deflections are incomplete and can be misleading indicators of model performance.

2. As model complexity increases, it is important to minimize uncertainties associated with representation of soil behavior in the finite element model. More efforts should be invested in characterization of soil properties from well controlled laboratory tests.
3. Concrete shrinkage of the floor system and expansion of the roof slab, due to changes in ambient temperature, contribute significantly to the lateral deflections of the diaphragm wall. These factors should be addressed in future finite element models where lateral support is provided by cast-in-place floor systems.
4. Predictions of changes in piezometric elevations are affected significantly by the boundary conditions imposed in the finite element model including procedures used to simulate dewatering during excavation. In the Post Office Square analysis, overprediction of the pore pressure drawdown increased the predicted settlement and reduced lateral wall movements.
5. Reliable modeling of soil deformation properties is especially important in predicting the performance of a structure, such as the Post Office Square Garage, which induces very small deformations in the surrounding materials. Improved characterization of small strain non-linear behavior of soils can greatly enhance finite element predictive capabilities.

5.8. References

Baligh, M.M. and Vivatrat, V., 1979, "In Situ Measurements in a Marine Clay," *Proc. International Conference on the Behavior of Offshore Structures*, Vol. 1, pp. 151-174.

Boscardin, M.D. and Cording, E.J., 1989, "Building Response to Excavation-Induced Settlement," *ASCE Journal of Geotechnical Engineering*, Vol. 115, No. GT1, pp. 1-21.

Brown, P.T. and Booker, J.R., 1985, "Finite Element Analysis of Excavation," *Computers and Geotechnics*, Vol. 1, pp. 207-220.

Burland, J.B. and Wroth, C.P., 1974, "Allowable and Differential Settlement of Structure Including Damage and Soil-Structure Interaction," *Proc., International Conference on Settlement of Structures*, Cambridge, U.K, pp. 661-654.

Chan, D.H. and Morgenstern, N.R., 1987, "Analysis of Progressive Failure of the Edmonton Convention Centre Excavation," *Canadian Geotechnical Journal*, Vol. 24, No. 3, pp. 430-440.

Christian, J.T., 1989, "Design of Lateral Support System", Design, Construction, and Performance of Deep Excavations in Urban Areas, *Proc. BSCE Symposium on Design, Construction & Performance of Deep Excavations in Urban Areas*, Boston Society of Civil Engineers, 31p.

Christian, J.T. and Wong, I.H., 1973, "Errors in Simulating Excavations in Elastic Media by Finite Elements," *Soils and Foundations*, Vol. 13, No. 1, pp. 1-10.

Clough, G.W., Smith, E.M. and Sweeney, B.P., 1989, "Movement Control of Excavation Support Systems by Iterative Design," *Proc. ASCE Foundation Engineering Congress*, pp. 869-884.

Cowland, J.W. and Thorley, C.B., 1984, "Ground and Building Settlement Associated with Adjacent Slurry Trench Excavation," *Proc. of Third International Conference on Ground Movements and Structures*, pp. 723-738.

Einstein, H.H., Azzouz, A.S., McKown, A.F. and Thompson, D.E., 1983, "Evaluation of Design and Performance - Porter Square Transit Station Chamber Lining," *Proc. Rapid Excavation Tunneling Conference*, Volume 1, pp. 597-620.

Finno, R.J. and Harahap, I.S., 1991, "Finite Element Analysis of the HDR-4 Excavation", *J. Geotechnical Engrg.*, Vol. 117, No. 10, pp. 1590-1609.

Gens, A. and Potts, D.M., 1988, "Critical State Models in Computational Geomechanics," *Engineering Computations*, Vol. 5, pp. 178-197.

Ghaboussi, J. and Pecknold, D.A., 1984, "Incremental Finite Element Analysis of Geometrically Altered Structures," *International Journal of Numerical Methods in Engineering*, Vol. 20, pp. 2051-2064.

Gioda, G. and Sakurai, S., 1987, "Back Analysis Procedures for the Interpretation of Field Measurements in Geomechanics," *International Journal for the Numerical and Analytical Methods in Geomechanics*, Vol. 11, No. 6, pp. 555-583.

H&A, 1987, "Report on Subsurface Investigations and Laboratory Testing, Post Office Square Garage Development, Boston" *Report submitted by Haley & Aldrich Inc.* to Friends of Post Office Square, Boston, MA.

HKS, 1989, "ABAQUS Version 4.8 User's Manual," Hibbitt, Karlsson & Sorensen, Inc., Providence, RI.

Humphrey, J., 1990, *Presentation* to Boston Society of Civil Engineers.

Ishihara, K., 1970, "Relations between Process of Cutting and Uniqueness of Solution" *Soils and Foundations*, Vol.10, No.3, pp. 50-65.

Johnson, E.G., 1989, "Geotechnical Characteristics of the Boston Area," *BSCE Journal of Civil Engineering*, Vol. 4, No. 1 pp. 53-65.

Ladd, C.C., 1990, Personal Communication.

Lambe, T.W., 1973, "Predictions in Soil Engineering," *Géotechnique*, Vol. 23, No. 2, pp. 149-202.

Lutenegger, A.J., Kemmis,T.J. and Hallberg,G.R., 1983, "Origin and Properties of Glacial Till and Diamictons," *Geological Environment and Soil Properties*, pp. 310-331.

Morrison, M.J., 1985, "In Situ Measurements on a Model Pile in Clay," PhD Thesis, MIT, Cambridge, MA., 700p.

O'Rourke, T.D., 1981, "Ground Movements Caused by Braced Excavations," *ASCE Journal of Geotechnical Engineering*, Vol 107, No. GT9, pp1159-1178.

O'Rourke, T.D. and Jones, C.J.F.P., 1990, "Overview of Earth Retention Systems: 1970-1990," *Proc. ASCE Specialty Conf. on Design and Performance of Earth Retaining Structures*, Ithaca, NY., pp. 22-51.

Peck, R. B., 1969, "Deep Excavations and Tunneling in Soft Ground," State-of-the-Art Paper, *Proc. of the Seventh International Conference on Soil Mechanics and Foundation Engineering*, Mexico City, pp. 225-290.

Potts, D.M. and Fourie, A.B., 1984, "The Behavior of a Propped Retaining Wall: Results of a Numerical Experiment," *Géotechnique*, Vol. 34, *No. 3*, pp. 383-404.

Schoenwolf, D.A., Whitman, R.V., Abbott, E.L. and Becker, J.M., 1991, "Post Office Square Garage Project - A Case History of Instrumented Wall Performance," *ASTM STP 1129, in press.*

Whitman, R.V., Johnson, E.G., Abbot, E.L., and Becker, J.M., 1991, "Field Instrumentation Program Plays Vital Role in Deep Excavation Project," *Proc. ASCE Geotechnical Engineering Congress 1991*, Boulder, CO., Vol. 1, pp. 173-184.

Whittle, A.J., 1990, "A Constitutive Model for Overconsolidated Clay," *MIT Sea Grant Report*, MITSG90-15.

Whittle, A.J., 1991, "Evaluation of a Constitutive Model for Overconsolidated Clays," *to be published*, Géotechnique.

Young, G.A., 1990, Personal Communication.

Stratum	Soil Model	Total Unit Weight	Initial Conditions		Deformation Properties		Shear Strength[1]		Permeability	References
		γ_t (kN/m^3)	K_0	OCR	G/σ' [2] [at γ=0.1%]	ν'	c' (kPa) [s_u/σ'_{v0}]	ϕ'_{PSC} (^{0})	k (cm/sec)	
Dry Fill Wet	EP-DP	19.6 22.0	0.5	-	35	0.3	0	30	$1x10^{-4}$	-
Boston Blue Clay	MIT-E3[3]	19.6	1.22 0.6	6.0 2.0	1100[4] [150]	0.28	[1.6][5] [0.62][5]	42[5]	$5x10^{-8}$	Whittle (1990)
Sand	EP-DP	19.6	0.4	-	170	0.3	0	37	$1x10^{-5}$	-
Till	EP-DP	20.4	1.0	-	110	0.3	0	43	$1x10^{-5}$	Lutenegger et al.(1983)
Weathered Argillite	EP-DP	22.0	1.0	-	1160	0.3	1720	32	$1x10^{-5}$	Einstein et al. (1983) Young (1990)
Intact Argillite	EP-DP	23.6	1.0	-	4900	0.3	1720	32	$1x10^{-5}$	Einstein et al. (1983)

Notes:

1. All strength properties refer to plane strain compression conditions.
2. $\sigma'=1/3(\sigma'_{xx}+\sigma'_{yy}+\sigma'_{zz})$
3. Complete input properties for MIT-E3 are shown in Table 5.2.
4. Small strain stiffness, G_{MAX}/σ'.
5. The undrained shear strength ratio and large strain (critical state) friction angles are predicted by the model.
6. Elastic properties of concrete: $E=2.3x10^4$MPa; ν=0.15.

Table 5.1. Input Properties used in Finite Element Analysis

Test Type	Parameter / Symbol	Physical contribution/ meaning	Boston Blue Clay
1-D Consolidation (Oedometer, CRS etc.)	e_0	Void ratio at reference stress on virgin consolidation line	1.12
	λ	Compressibility of virgin normally consolidated clay	0.184
	C	Non-linear volumetric swelling behaviour	22.0
	n		1.6
	h	Irrecoverable plastic strain	0.2
K_0 -oedometer or K_0 -triaxial	K_{0nc}	K_0 for virgin normally consolidated clay	0.48
	2G/K	Ratio of elastic shear to bulk modulus (Poisson's ratio for intial unload)	1.05
Undrained Triaxial Shear Tests: OCR=1; CK_0UC OCR=1; CK_0UE OCR=2; CK_0UC	ϕ'_{TC}	Critical state friction angles in triaxial compression and extension (large strain failure criterion)	33.4^0
	ϕ'_{TE}		45.9^0
	c	Undrained shear strength (geometry of bounding surface)	0.866
	s_t	Amount of post-peak strain softening in undrained triaxial compression	4.5
	ω	Non-linearity at small strains in undrained shear	0.07
	γ	Shear induced pore pressure for OC clay	0.5
Resonant Column*	κ_0	Small strain compressibility at load reversal	0.001
Drained Triaxial	ψ_0	Rate of evolution of anisotropy (rotation of bounding surface)	100.0

* Alternatively use shear wave velocity from cross-hole tests.

Table 5.2 Input Parameters for Boston Blue Clay using the MIT-E3 Model (Whittle, 1990)

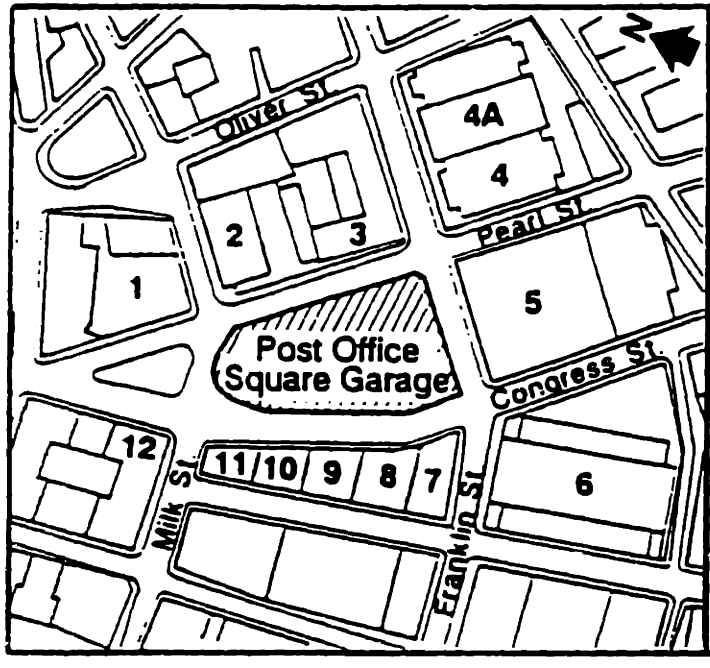

Key	No. of stories	Foundation type	Bearing soil
1	14	Piers/caissons	Till
2	40	PIF's	Till
3	5	Footings	Clay
4	12	Footings/caissons	Clay
4A	34	Mat	Till
5	21	Mat	Till
6	38	Mat	Till
7	7	Mat/footings	Clay
8	11	Footings	Clay
9	7	Footings (?)	Clay (?)
10	12	Strip footings	Clay
11	11	Mat/footings	Clay
12	17	Mat	Clay

Figure 5.1 Site Location and Adjacent Buildings (Whitman et al. 1991)

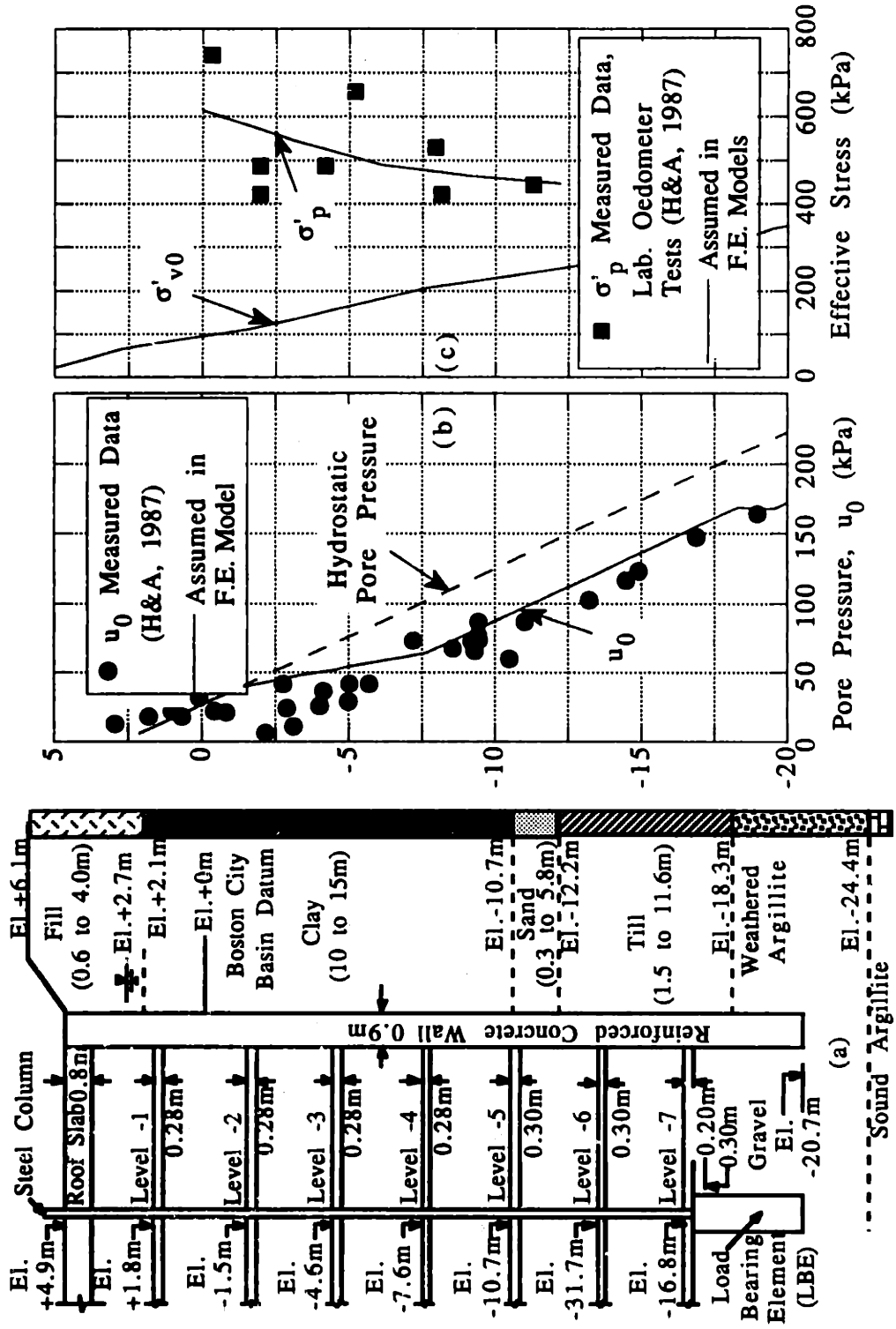

Figure 5.2 Garage Structure and Initial Soil Conditions, Post Office Square

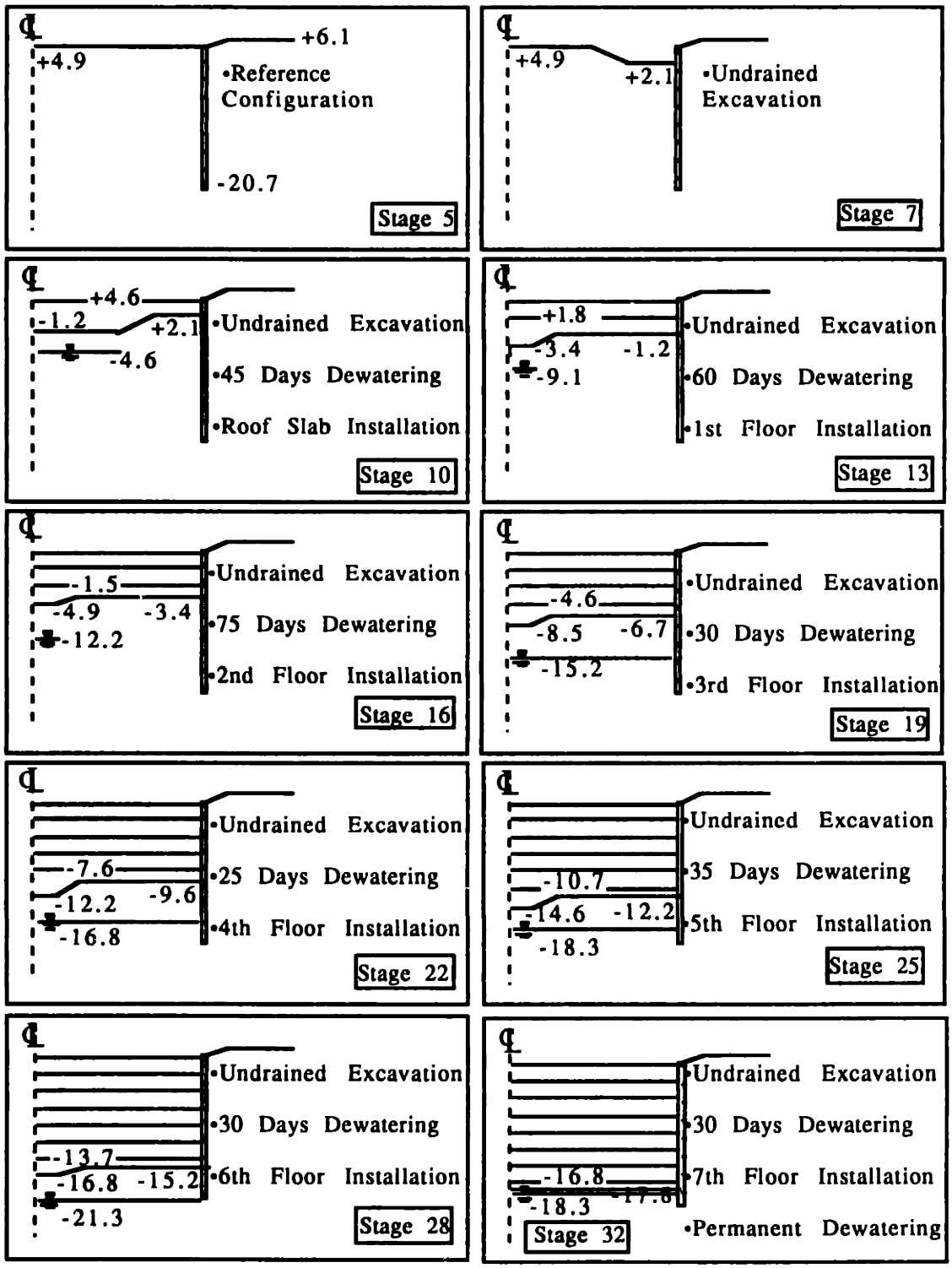

Figure 5.3 Construction Sequence used in Finite Element Model

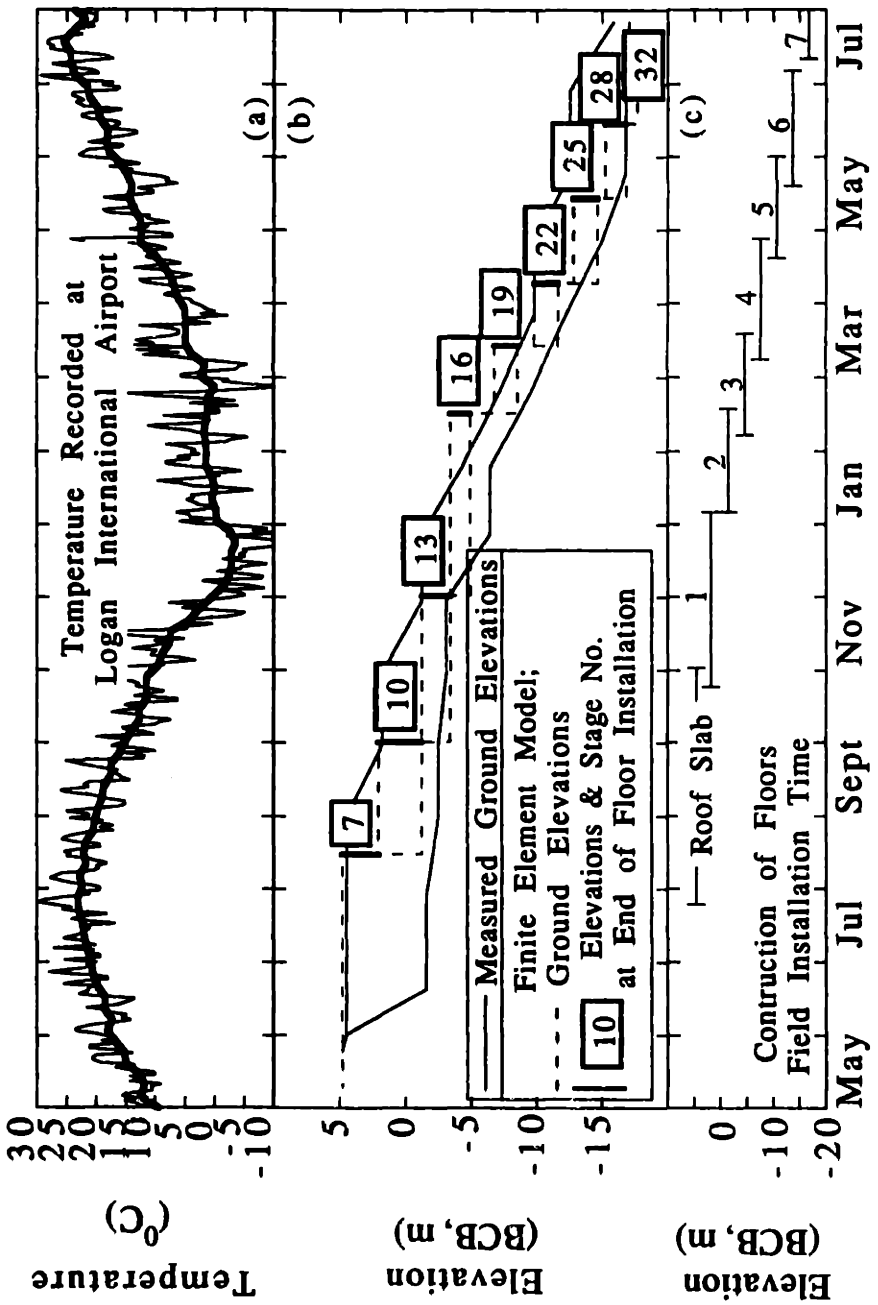

Figure 5.4 Time History of Construction Activities and Ambient Temperatures

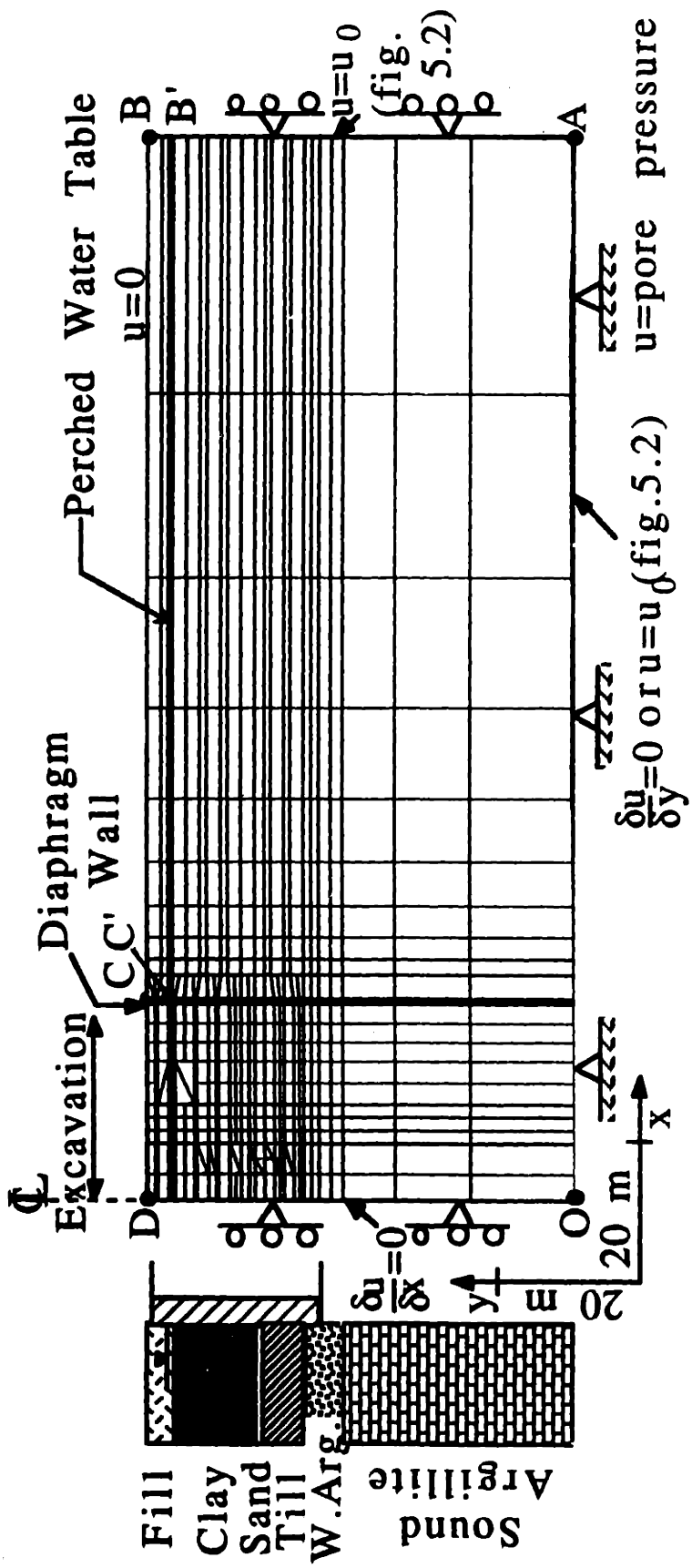

Figure 5.5 Finite Element Mesh and Boundary Conditions, Post Office Square

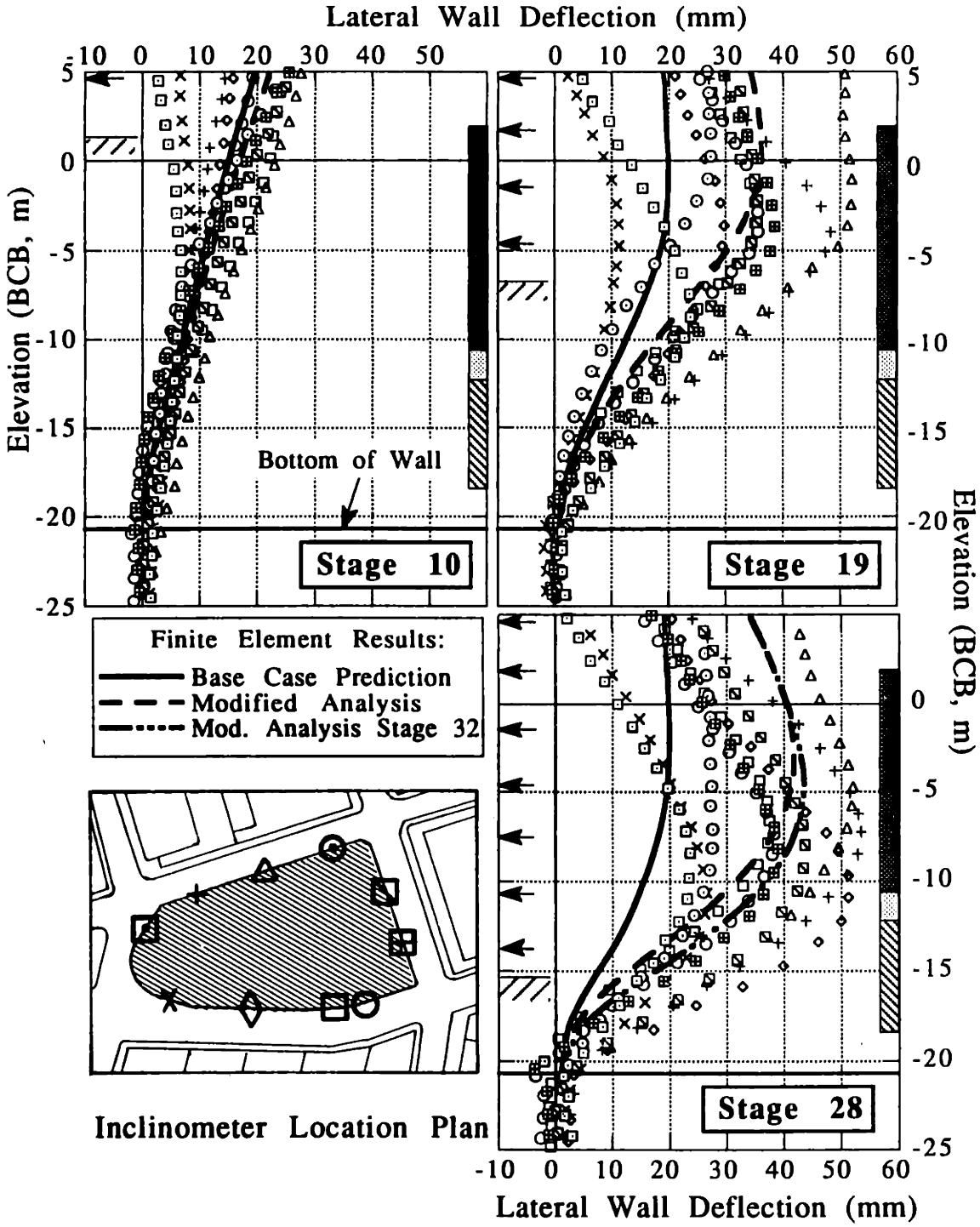

Figure 5.6 Comparison of Predicted and Measured Lateral Wall Deflections

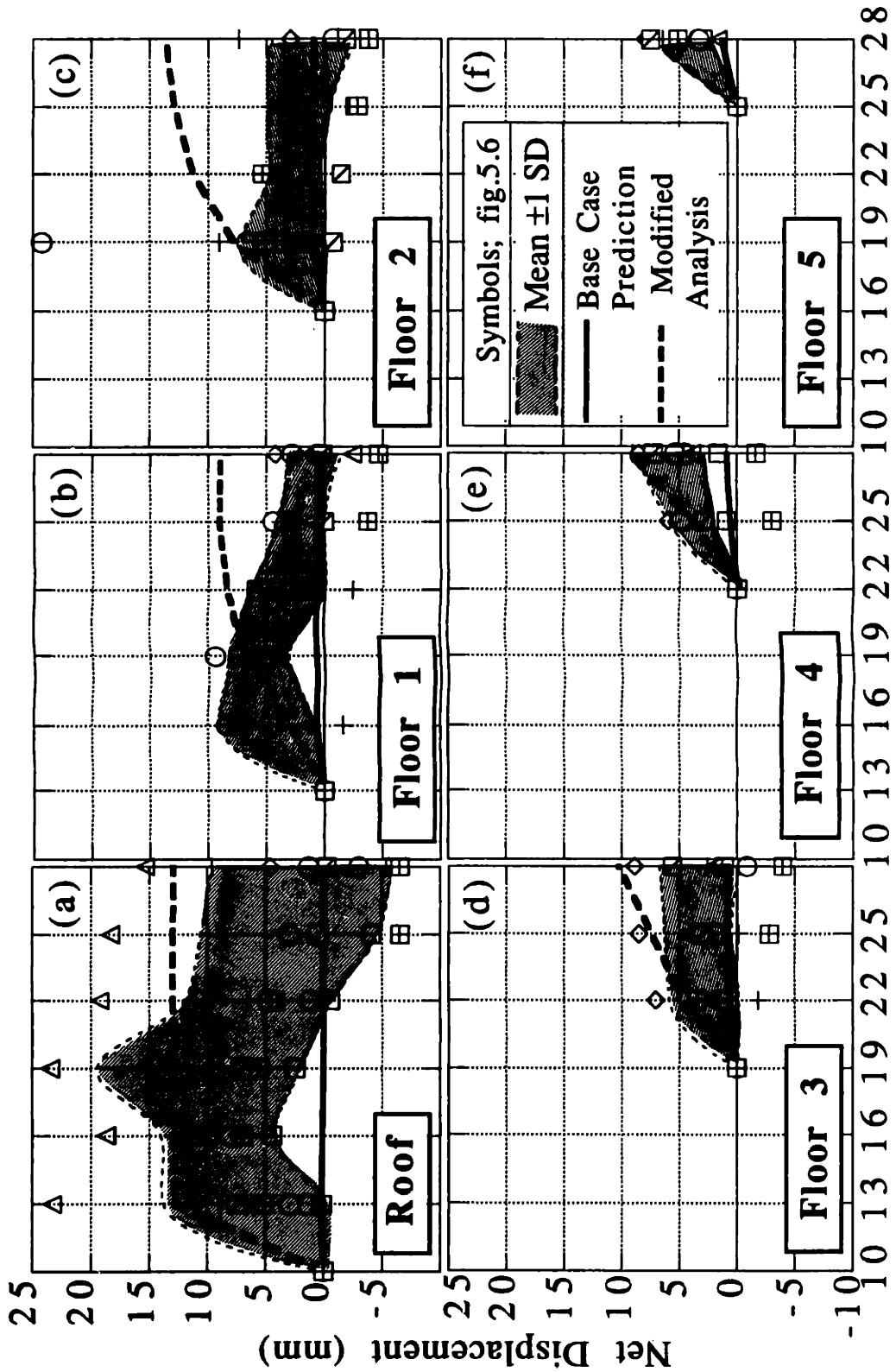

Figure 5.7 Comparison of Predicted and Measured Post-Construction Wall Deflections at Roof and Floor Levels.

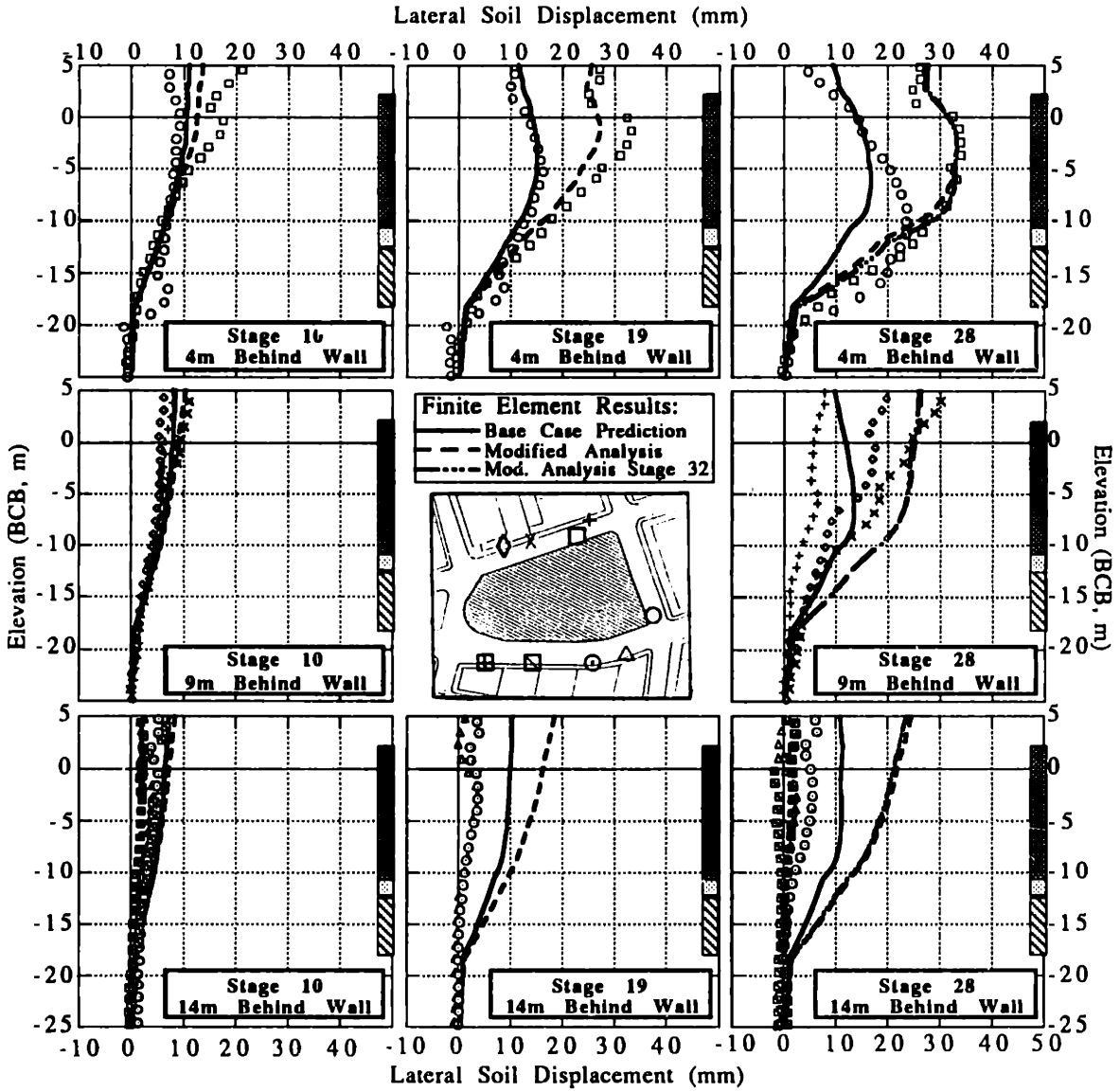

Figure 5.8 Comparison of Predicted and Measured Lateral Soil Deformations.

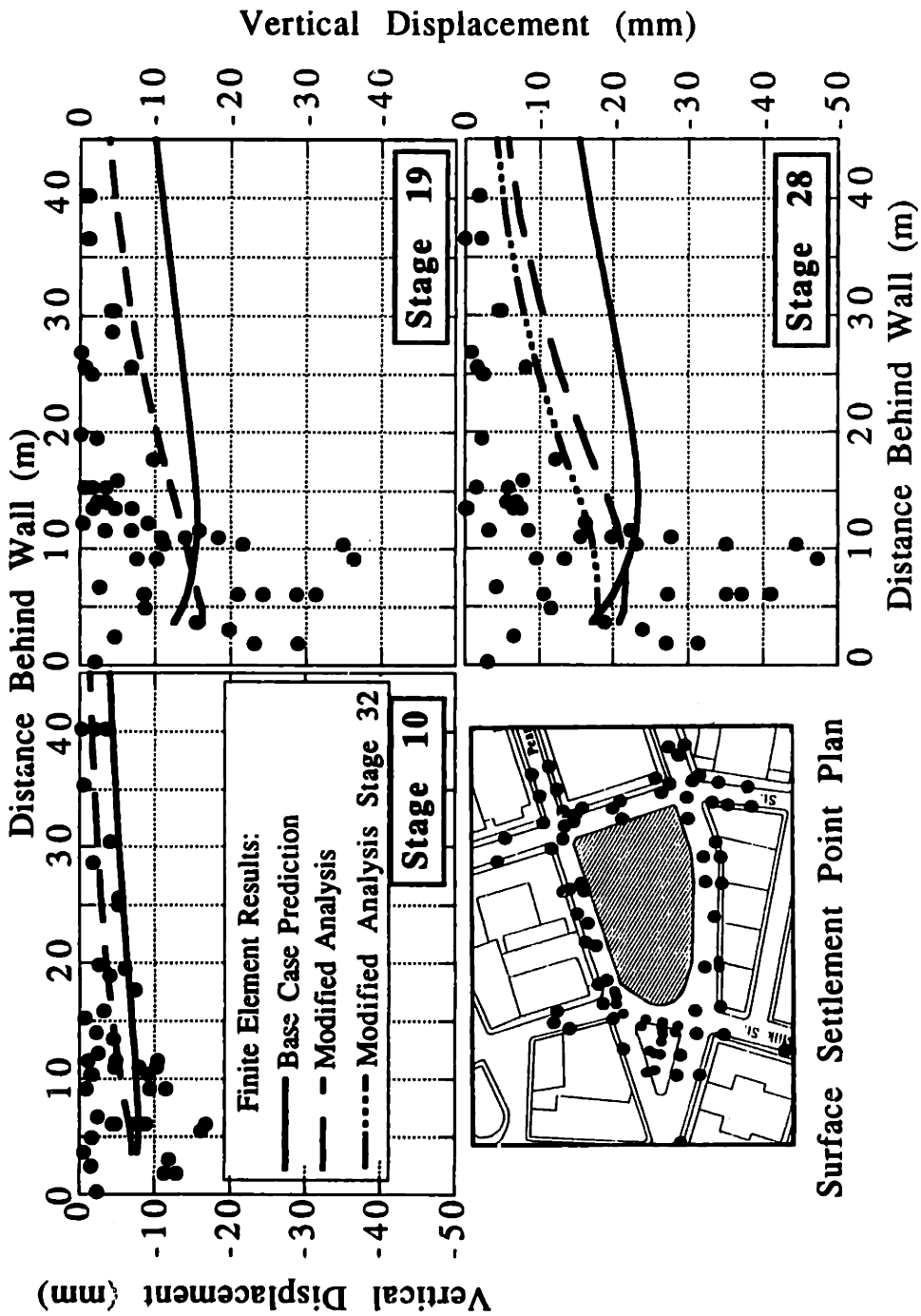

Figure 5.9 Comparison of Predicted and Measured Surface Settlements

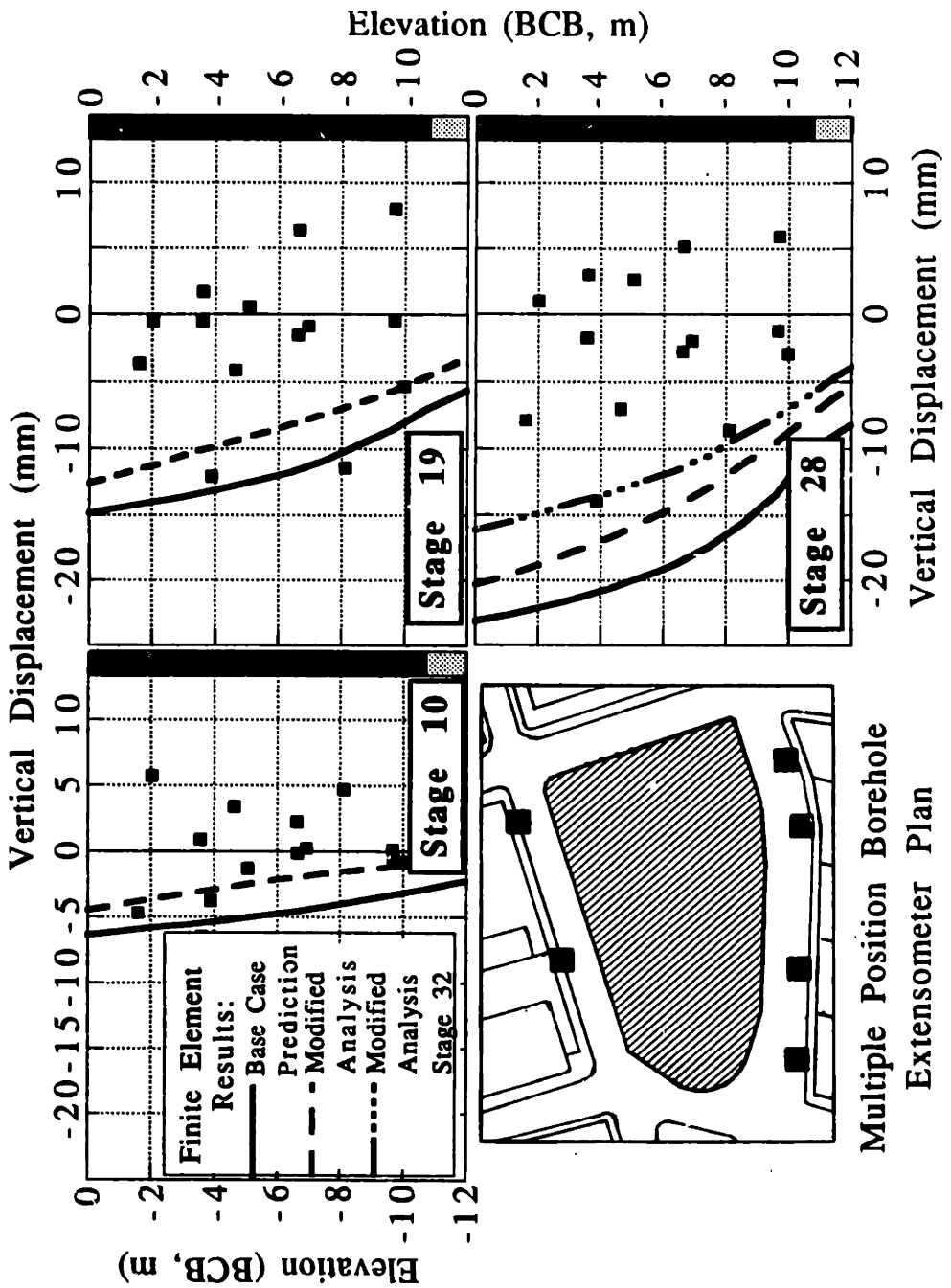

Figure 5.10 Comparison of Predicted and Measured Vertical Displacements in the Soil

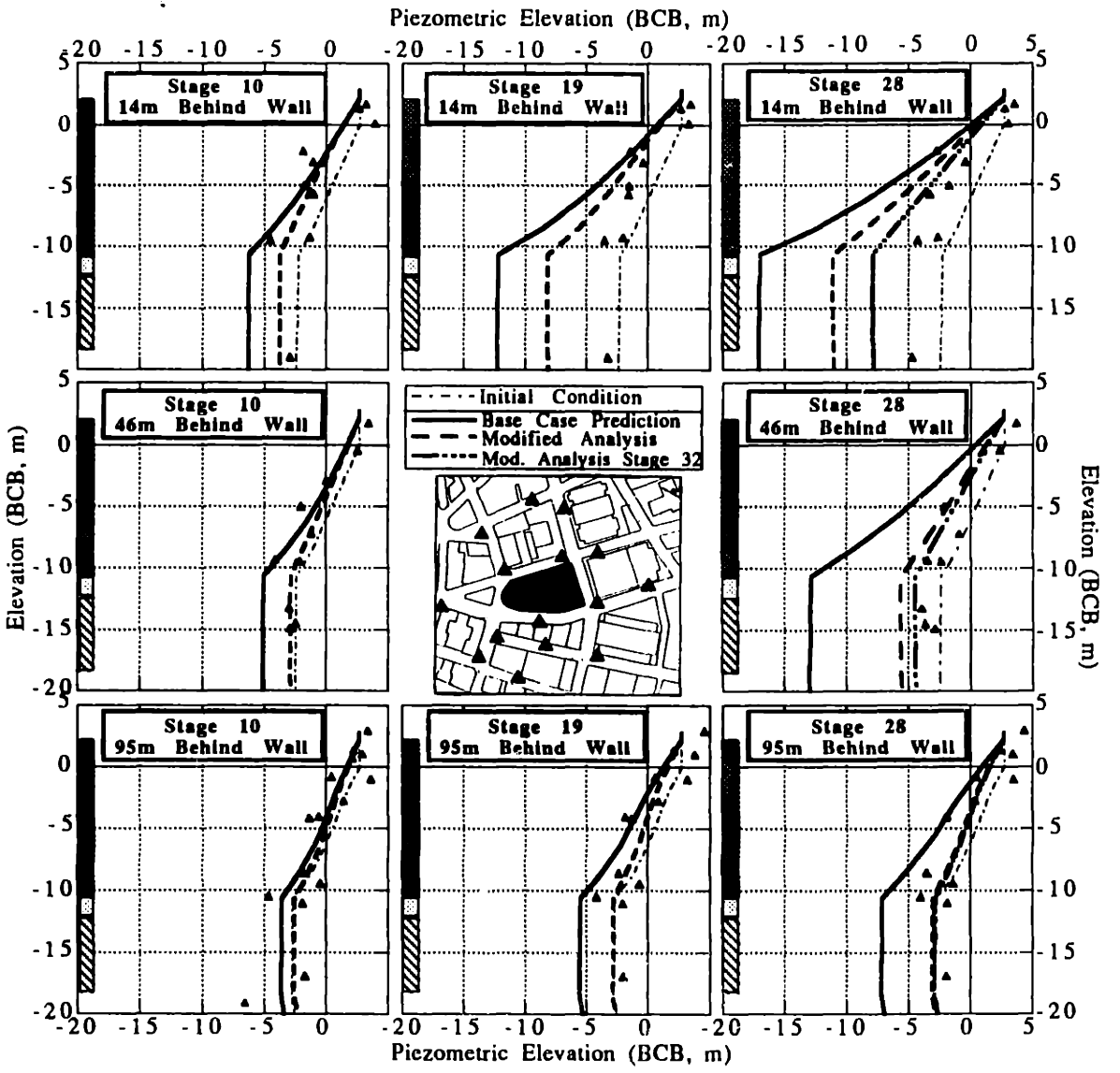

Figure 5.11 Comparison of Predicted and Measured Piezometric Elevations

6. Summary, Conclusions and Recommendations

The research presented in this thesis contributes towards: 1) the use of more realistic soil models in the analysis of complex geotechnical boundary value problems, 2) the understanding of some of the fundamental mechanisms controlling the performance of deep excavations in clays, and 3) the development of systematic procedures for predicting and evaluating field excavation response.

The research is motivated by the practical problem of predicting the performance of proposed deep excavations (excavation depths up to 30m) in soft clays associated with the construction of the Central Artery/Tunnel project in Boston and the Taipei Rapid Transit system in Taiwan. In these situations accurate predictions of ground movements are an important design criterion in order to avoid damage to adjacent facilities. Non-linear finite element methods represent the only rational analytical techniques which can incorporate both realistic constitutive behavior of the surrounding soils and simulate the complex construction history for staged excavations. This research applies the non-linear finite element method in order to predict soil response due to excavation. The study includes the following main tasks:

1. The development of numerical techniques to implement the Modified Cam Clay (MCC; Roscoe and Burland 1968) and MIT-E3 (Whittle 1990) effective stress soil models in the finite element code ABAQUS (Chapter 2). Chapter 3 describes numerical procedures used to model excavation activities including soil removal and support installation.
2. A fundamental study of the short term (undrained) performance of deep excavations (Chapter 4). Principal parameters considered in the study are the soil model, stress history profile, wall length and vertical support spacing. The study interprets soil response at the element level, as well as global performance variables such as wall deflection and ground settlements.
3. Predictions for the top-down construction of a seven story (23m deep) underground parking garage at Post Office Square in Boston, Massachusetts. The predictions are evaluated through comparisons with field measurements during construction. Chapter 5 demonstrates the predictive capabilities and limitations in analyzing a complex construction sequence.

6.1. Implementation of Elasto-Plastic Models in the Finite Element Method

6.1.1. Summary and Conclusions

Significant research efforts over the last twenty years have attempted to develop constitutive models which describe complex aspects of real soil behavior. In order to apply these models in the solution of boundary value problems, the constitutive equations must be implemented in non-linear finite element analyses. In general, elasto-plastic soil models describe material behavior which is path dependent and hence is characterized by 'rate constitutive equations' (relating infinitesimal increments of strains and effective stresses). However, when the constitutive model is used in non-linear finite element analysis, the constitutive equations must be integrated numerically over a discrete sequence of time steps. The procedures used to integrate the constitutive equations have a direct impact on the overall accuracy, stability and convergence properties of the non-linear finite element analysis.

Chapter 2 describes numerical algorithms used to integrate the constitutive relations and introduces the concept of consistent linearization in estimating the tangent stiffness matrix in the finite element equilibrium equations.

Section 2.3 describes the implementation of the MCC model in the general purpose finite element code ABAQUS using a fully implicit integration scheme and a consistent constitutive matrix. The procedure does not require subincrementation at the local level. Examples presented in Section 2.3.4 show that the numerical implementation is very efficient, robust and accurate. The use of a consistent stiffness matrix provides for a highly improved convergence rate of the global finite element iteration.

Section 2.4 presents the algorithm used to implement the MIT-E3 model in ABAQUS. The complexity of the model, including a) the non-linear elastic formulation, and b) complex isotropic and kinematic hardening functions preclude the use of the efficient implicit integration scheme. Section 2.4.2 describes the implementation of MIT-E3 using an explicit integration scheme, with correction for drift from the bounding surface, and local subincrementation. The scheme uses a 'quasi-consistent' tangent stiffness matrix which represents a corrected average of the continuum stiffness matrix over the subincrements. Section 2.4.3 presents examples that demonstrate the accuracy and convergence characteristics of the procedure. However, the implementation is less robust and more computationally expensive than the implicit integration scheme used for the MCC model.

6.1.2. Recommendations for Future Work

The numerical procedures developed for implementing MCC and MIT-E3 in ABAQUS (Chapter 2) and for modelling excavation activities (Chapter 3) provide a versatile capability to analyze many geotechnical boundary value problems using a realistic soil model. The capability, though powerful, has its limitations. Further work to extend these capabilities should focus on the following areas:

1. The constitutive equations of the MIT-E3 model should be reformulated to make them amenable to implicit integration without local subincrementation. Implicit integration is advantageous as it enables the determination of a linearized consistent stiffness matrix which improves significantly the convergence characteristics of the global finite element iteration.
2. The implemented effective stress models assume a rate-independent normalized soil behavior and are mostly limited to lightly overconsolidated clays (OCR≤8). There is a need to extend models capabilities to incorporate rate effects and to model highly overconsolidated clays, sensitive and cemented clays, as well as sands. Current work by Pestana (1992) focuses on improving the modelling of clays and developing a model for sands.

6.2. Fundamental Excavation Study

6.2.1. Developments in this Research

The understanding of the behavior of deep diaphragm wall supported excavations in soft clays is necessary for the design of proposed excavations associated with the construction of the Central Artery project in Boston and the Taipei Rapid Transit system in Taiwan. The numerical tools developed in Chapter 2,3 are used to conduct a series of experiments to understand fundamental mechanisms controlling soil and wall movements in this type of excavation (Chapter 4). The analyses focus on a simplified excavation geometry, soil profile and construction sequence using the following assumptions:

1. For deep layers of low permeability clay, the excavation process occurs sufficiently rapidly that there is no migration of pore water, hence the soil is subject to undrained shearing.
2. The numerical experiments use plane strain geometry with a fixed excavation width (40m) and a constant wall thickness (0.9m). It is assumed that wall installation does not disturb the surrounding soil.
3. The clay is saturated and exhibits normalized engineering properties. The numerical experiments focus on simplified soil profiles in which the

overconsolidation ratio, OCR, of the clay is constant with depth.

4. The effective stress-strain behavior of the soil is described by the MIT-E3 model with input parameters corresponding to properties of Boston Blue Clay. The experiments evaluate the importance of clay behavior on the predicted performance by comparing results obtained using elastic, MCC and MIT-E3 soil models.
5. The excavation is braced by incompressible (rigid) supports spaced at equal intervals. Installation of rigid bracing represents an ideal condition in which there is no further lateral deflection of the wall at the elevation of the support.
6. The analyses assume a simplified top-down construction sequence where all supports are constructed 'on-grade', except for the first (top) support level where a layer of soil is initially excavated without lateral supports.

The analyses focus on studying the effect of the following parameters on excavation performance:

1. The constitutive soil model (Elastic, MCC and MIT-E3; Section 4.3).
2. Wall length and embedment (Section 4.4).
3. The vertical support spacing (Section 4.5.1).
4. The initial unsupported excavation height, prior to installation of top bracing (Section 4.5.2).
5. The soil stress history (Section 4.6, 4.9; OCR=1,2,4, Combined[1]).

Detailed examination of the effects of these parameters on excavation response leads to the following main observations:

1. The analyses show that excavation response using the MCC and Elastic models is similar. The experiments show that MIT-E3 gives a more accurate and realistic prediction of deformation patterns, particularly surface settlements and describes the development of failure for deep excavations (not observed in the MCC analysis). The analyses show the need for reliable soil models in the prediction of deep excavation behavior.
2. Wall length and hence embedment has a minimal effect on the predicted pre-failure deformations. However, wall length does affect the failure depth of the excavation. Failure mechanisms observed for OCR=1 soil profile include: 1) a basal heave mechanism for short to medium length walls; 2) a deep seated mechanism for long walls. Basal heave calculations based on plasticity solutions of Davis and Booker (1973), which incorporate wall length effect, give good estimates of the safety factor for shallow walls (L≤20m) but do not predict

[1]The combined profile consists of clay layers with decreasing OCR with depth.

collapse for long wall embedment.

3. The support spacing has a very significant impact on predicted deformations (all OCR values) and failure (OCR=1 and C) and controls the 'basic system response'. The initial unsupported excavation depth has only a 'transient' effect on the 'basic system response'. However, this transient effect may produce large deformations in shallow excavations.
4. The soil stress history has a major impact on predicted deformations and failure. As the OCR increases, the magnitudes of deformations reduce significantly and failure mechanisms do not develop even for very deep excavations (for OCR=2 and 4 analyses). For a combined soil profile (OCR value decreasing with depth), wall movements are significantly influenced by deep seated movements in the clay which are controlled by soil properties below the current excavation depth.
5. The analyses predict large total lateral stresses acting against the wall behind the excavation. The stresses are in some cases equal to or larger than the initial in-situ total lateral stresses. The large stresses are related to the development of a passive wedge in the retained soil above the excavation level. This wedge is associated with reversal in loading direction for soil elements in that region. The predicted behavior is qualitatively in agreement with field measurements but has not been explained in previous finite element studies. Total vertical stresses in this wedge are generally smaller than the initial in-situ stresses due to the development of shear stress along the back of the wall.
6. The trends observed in the analyses are summarized in a simplified framework that accounts for different failure modes in the excavations (Figure 4.7-1, 4.9-7). In addition to soil failure, the framework includes estimates of structural failure of the diaphragm wall which is a significant factor for excavations with long walls or walls which are lightly braced. The framework can be used to estimate/interpret deformations for a wide range of support conditions and wall lengths but is restricted to the standard size diaphragm wall considered in this study. A simple four parameter equation (Equation 4.7-1) matches the trends in the maximum movements and hence, a procedure is described in order to reduce the number of analyses required for a given soil profile.

The results of the numerical experiments have some significant practical implications that should be considered in the design of deep excavations in soft clays:

1. Wall embedment has a very limited impact on pre-failure deformations, but has a large effect on excavation stability (for OCR=1,C). This implies that during the construction of an excavation, measurements of deformations may not give a clear

warning of possible failure in the system. In addition, deformations observed at early excavation stages do not necessarily give an indication of movements at later excavation stages (See for example the transient effects observed in Section 4.5.2, or the early movements observed in the OCR=C analysis, Section 4.9). Therefore, care should be used in extrapolating deformation data and in adjusting predictions of movements based on early excavation behavior. However, the observational method (Peck, 1969) is still a very important tool for monitoring excavation performance.

2. The conventional factor of safety against basal heave does not represent fully the failure modes observed in the FE analyses. The basal heave mechanism is valid for short and medium well supported walls.
3. The wall and support system may need to be designed to withstand large lateral stresses. In the analyses, a passive wedge with stresses equal to or higher than in-situ stresses is predicted in the retained soil. Stresses equal to or higher than the initial in-situ stresses have been measured in the retained soil of some excavations in soft clays (e.g., Aas 1984).
4. Extensive site characterization is required to predict accurately excavation response. Conventional triaxial compression and extension tests do not characterize the stress paths experienced by soil elements during excavation. The analyses have shown clearly the importance of modelling complex aspects of soil behavior including stress-strain response for a) reversals in stress paths, b) rotations of principal stresses, and c) non-linearity for shearing at small strain levels ($\gamma<0.1\%$).

This is the first fundamental study of its kind that uses an advanced realistic clay material model in analyzing deep excavation behavior (and represents the first use of the MIT-E3 model in the solution of 2-D boundary value problems). The numerical experiments provide valuable insight into deformation and failure mechanisms not reported previously in the literature.

6.2.2. Recommendations for Future Work

The numerical experiments performed in this fundamental study deal with a limited number of parameters. While the results of this study provide significant insights into excavation behavior, further studies are needed to extend the results from this study to more general field situations. Future work should focus on the following issues:

1. The influence of support flexibility, preloading and shrinkage on excavation response, including resulting lateral earth pressures acting on the wall and the

extent of stress and strain reversal in the retained soil.

2. The effect of excavation width on deformations and failure, particularly for excavations with long walls.
3. The use of a more realistic model for the wall that includes reinforcement, yielding and failure. In many of the analyses in the current study, wall yielding is predicted to occur prior to general failure in the excavation. By including the possibility of wall failure in the numerical model the analyses will give greater insights into excavation response, particularly in cases where failure is now predicted to occur due to the development of a shear surface that intersects very deep diaphragm walls.
4. The effect of overexcavation prior to support installation at all excavation stages. In the current study it is assumed that supports are installed on grade (except for the first support). The framework proposed in Chapter 4 can account for the effects of overexcavation. However, it is of interest to compare a limited number of analyses that include overexcavation with the framework.
5. The effect of a limited depth of clay below the bottom of the excavation. In many field situations this condition should result in smaller deformations and greater safety against failure for an excavation.
6. The effect of drainage (including partial drainage). Appendix C presented preliminary results of the effect of drainage on excavation response. These calculations show that the depth and lateral extent of the clay layer are significant in a drained analysis. Studying the effect of drainage in a clayey soil should focus on: a) effects of partial drainage during construction (variables include the permeability of the system, dewatering conditions, and construction time); and b) effects of long term drainage after completion of the excavation (i.e, steady state conditions).

6.3. Prediction of Field Excavation Response

Chapter 5 describes the application of the non-linear finite element method for predicting soil deformations and ground water flow associated with the top-down construction of a seven storey, underground parking garage in downtown Boston.

The garage design uses a cast-in-situ, reinforced concrete, diaphragm wall extending down into the bedrock as the permanent lateral earth pressure support. This perimeter wall is braced internally by the floor slabs, which are in turn supported by interior columns (steel H-section) founded on the bedrock. Both the diaphragm wall and interior columns are installed prior to excavation using slurry trench methods. The roof and seven floor levels are cast in sequence from the top-down, by excavating the soil from

beneath the most recently constructed slab. During excavation, dewatering is accomplished using a combination of sump pumps and deep well points located inside the excavation area. The subsurface stratigraphy includes layers of fill, clay, sand, till and argillite of varying thicknesses across the site, reflecting the complexity of the glacial geology in the Boston area. An extensive instrumentation program was implemented on this project to monitor construction performance

The finite element model of the POS garage assumes a simplified geometry and discretizes the construction sequence. Model predictive capabilities and limitations are evaluated through comparisons with field data from an extensive construction monitoring program. The main aim of the finite element model is to provide a comprehensive framework for a) forecasting the effects of the various excavation-related activities on soil deformations, and b) interpreting the performance of the structure from construction monitoring measurements. The predictive capabilities and limitations of the base case analysis (Class A predictions) are evaluated by comparison with extensive field data, including wall deflections, soil deformations, surface settlements and piezometric levels. Differences between predicted and measured wall movements are attributed, in large part, to post-construction deformations of the roof slab and floor slabs; while predicted settlements are affected by unrealistic modeling of piezometric elevations in the argillite. Incorporating these factors into a modified analysis greatly improved agreement with field data.

The main conclusions of this study are that it is possible to make detailed and useful predictions of deformations occurring during top-down construction. More specifically:

1. Measurements of spatial variation in (vertical and lateral) soil deformations and pore pressures provide important information on the effects of excavation procedures on the surrounding soil and are essential for evaluating the consistency of model predictions. Interpretations based exclusively on comparisons of lateral wall deflections are incomplete and can be misleading indicators of model performance.
2. As model complexity increases, it is important to minimize uncertainties associated with representation of soil behavior in the finite element model. More efforts should be invested in characterization of soil properties from well controlled laboratory tests.
3. Concrete shrinkage of the floor system and expansion of the roof slab, due to changes in ambient temperature, contribute significantly to the lateral deflections of the diaphragm wall. These factors should be addressed in future finite element

models where lateral support is provided by cast-in-place floor systems.

4. Predictions of changes in piezometric elevations are affected significantly by the boundary conditions imposed in the finite element model including procedures used to simulate dewatering during excavation. In the Post Office Square analysis, overprediction of the pore pressure drawdown increased the predicted settlement and reduced lateral wall movements.
5. Reliable modeling of soil deformation properties is especially important in predicting the performance of a structure, such as the Post Office Square Garage, which induces very small deformations in the surrounding materials. Improved characterization of small strain non-linear behavior of soils can greatly enhance finite element predictive capabilities.

Further predictions and analyses of more excavation case studies should be performed using the tools and approaches developed in this thesis. These studies are required for the following reasons:

1. Further validate the modelling techniques proposed regarding the simulation of construction sequence and soil modelling.
2. Compare the factors that contribute to the development of deformations and failure with the mechanisms and interpretation frameworks proposed in this research.
3. Identify the limitations of current modelling techniques and methods for understanding excavation behavior, and hence, suggest areas where further developments are needed.

6.4. References

Aas, G., 1984, "Stability Problems in a Deep Excavation in Clay." *Proc. Int. Conf. Case Histories in Geotechnical Engineering*, St. Louis, Vol. 1, pp. 315-323

Davis, E.H., and Booker, J.R., 1973, "The Effect of Increasing Strength with Depth on the Bearing Capacity of Clays." *Géotechnique*, 23, No.4 , pp. 551-563.

Pestana-Nascimento, J., 1992, *ScD thesis in progress*, MIT.

Roscoe, K.H., and Burland, J.B., 1968, On the Generalized Stress-Strain Behavior of 'Wet' Clay. *Engineering Plasticity*, pp. 535-609.

Whittle, A.J., 1990, "A Constitutive Model for Overconsolidated Clay," *MIT Sea Grant Report*, MITSG90-15.

A. Evaluation of Scalar Properties r_c and r_x in MIT-E3

The formulation of the MIT-E3 model (Section 2.4.1) includes definitions of two scalar parameters r_x and r_c (Equations 2.46b and 2.49) which describe the position of the current stress state relative to the (critical state) failure condition. Figure A.1 shows the geometry of the MIT-E3 model and defines the following stress states:

P - Current stress point (σ', S)

C - Central axis of the yield surface ($S=\sigma'\mathbf{b}$)

R_c - Projected intersection of CP with failure surface $(\hat{\sigma}', \hat{S})$.

O' - Central axis of failure surface ($S=\sigma\underset{\sim}{\xi}$)

R_x - Projected intersection of O'C with failure surface (h=0).

1. The scalar r_c is defined as follows:

$$\overrightarrow{PR_c} = r_c \overrightarrow{CR_c} \tag{A.1}$$

A subsidiary definition can be written,

$$\overrightarrow{CR_c} = y \overrightarrow{CP} \tag{A.2}$$

where $\overrightarrow{CP} = (S - \sigma' \mathbf{b})$

and, $\overrightarrow{PR_c} = (y - 1)\overrightarrow{CP}$, $r_c = (y - 1)/y$.

At R_c;

$$y(S - \sigma' \mathbf{b}) + \sigma' \mathbf{b} = \hat{S}$$

$$\sigma' = \hat{\sigma}' \tag{A.3}$$

and R_c is also located on the failure surface such that::

$$(\hat{S} - \hat{\sigma}' \xi) : (\hat{S} - \hat{\sigma}' \xi) - k^2 \hat{\sigma}' = 0 \tag{A.4}$$

Substitute A.3 in A.4, and solving for y enables r_c to be found as follows:

$$r_c = \frac{A \cdot B - D}{B - D} \tag{A.5}$$

where $A = c^2(2\alpha - \sigma)$ $B = (\mathbf{b} - \xi) : (\mathbf{s} - \sigma\mathbf{b})$

$C = \sigma(k^2 - (\mathbf{b} - \xi) : (\mathbf{b} - \xi))$ $D = \sqrt{B^2 - AC}$

r_c has a maximum value of, $r_c=1$, when the stress state is located at the tip of the yield surface and decreases to a minimum, $r_c=0$, at the critical state.

2. The parameters r_x describes the relative orientation of the yield surface to the critical state cone (Figure A.1):

$$\overrightarrow{CR_x} = r_x \overrightarrow{O'R_x} \tag{A.6}$$

One can repeat the same exercise but now assume that $R_x(\hat{\sigma}', \hat{S})$:

$$\begin{cases} \overrightarrow{O'R_c} = y\,\overrightarrow{O'C} \\ \overrightarrow{CR_x} = (y-1)\,\overrightarrow{O'C} \end{cases} \tag{A.7}$$

where $\overrightarrow{O'C} = \sigma'\left(\mathbf{b} - \underset{\sim}{\xi}\right)$.

Hence, $r_x=(y-1)/y$. At R_x:

Find y, but at R_x

$$\begin{cases} y\,S : \left(\mathbf{b} - \underset{\sim}{\xi}\right) + \sigma'\,\underset{\sim}{\xi} = \hat{S} \\ \sigma' = \hat{\sigma}' \end{cases} \tag{A.8}$$

But R_x is also located on the failure surface. Therefore, substituting A.6 and A.7 in A.8, y can be found and rearranged to solve r_x:

$$r_x = \frac{k - \sqrt{\left(\mathbf{b} - \underset{\sim}{\xi}\right) : \left(\mathbf{b} - \underset{\sim}{\xi}\right)}}{k} \tag{A.9}$$

$r_x = 1$ when $\mathbf{b}=0$ and $\xi_1=0$ (isotropic material or when $\mathbf{b}=\xi$ (when the orientation of the yield surface overlaps with the critical state cone).

$r_x = 0$ when point C on the central axis of the yield surface is on the critical state cone.

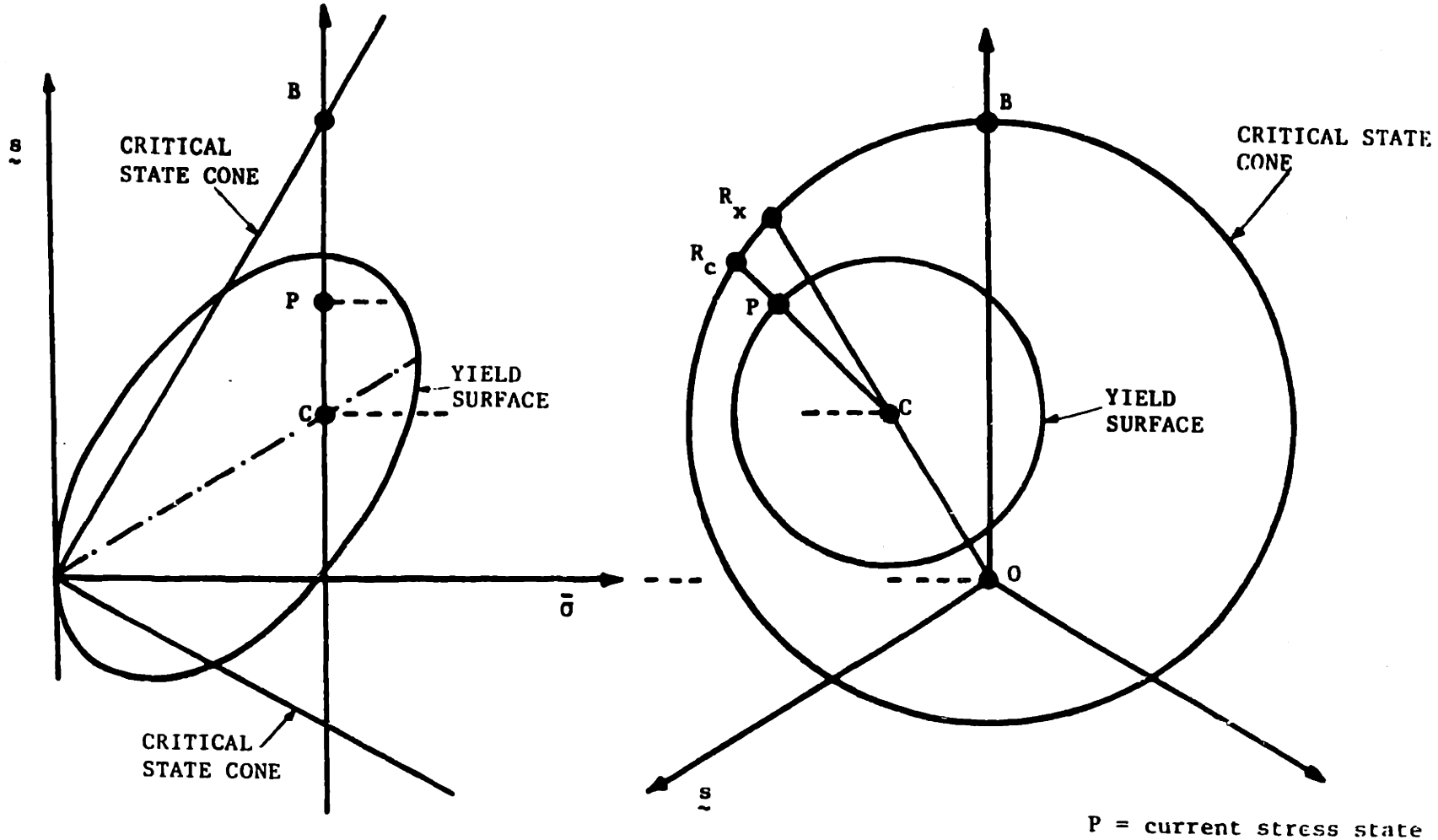

$$\vec{PR}_c = r_c . \vec{CR}_c$$
$$\vec{CR}_x = r_x . \vec{OR}_x$$

Figure A.1 Definition of Parameters r_c and r_x (Whittle 1987)

B. Analysis of the Stability of a Vertical Cut in ABAQUS

B.1. Introduction

This appendix summarizes analyses of stability of unsupported vertical cuts in cohesive soil using the finite element code ABAQUS. The analyses have limited objectives, and are not reported with the intent of investigating all aspects of the behavior of unsupported vertical cuts. The analyses described in this section have two main objectives:

1. Compare numerical predictions of failure depth with those described in the literature and available closed form solutions. An Elastic Perfectly Plastic soil model is used for this purpose. This set of analyses provides a check on the validity of some of the excavation procedures proposed in Chapter 3.
2. Use MCC and MIT-E3 soil models and compare failure depths for the two analyses.

B.2. Previous Work Regarding Stability of Vertical Cuts

Given a deep layer of clay with constant shear strength with depth. Then, under plane strain conditions, the maximum height of unsupported vertical excavation that could be achieved is H, Figure B.1. The stability number, N, is defined as:

$$N = \frac{\gamma H}{C_u} \qquad \text{B.1}$$

Using the upper and lower bound theory of plastic limit analysis (e.g., Atkinson 1981, Chen 1975):

$$3.635 < N < 3.835 \qquad \text{B.2}$$

A variety of numerical techniques have been reported in the literature for performing limit calculations for geotechnical engineering problems (e.g., Tamura et al 1984, Griffith and Koutsabeloulis 1985, Arai and Jinki 1990, Arai and Nakagawa 1988, Arai and Tagyo 1985, Asaoka et al 1990, Vermeer and van Langen 1989, Asaoka and Ohtsuka 1986, De Borst and Vermeer 1984, Toh and Sloan 1980, Tamura et al 1987). The technique described by Toh and Sloan (1980), which uses a mixed variational approach in conjunction with the finite element method, gives very good estimate of upper and lower bound limit calculations.

The displacement based finite element method has been used by Griffith and Koutsabeloulis (1985) to estimate the stability number for a vertical cut. The analyses

show (Figure B.2) that the FE method gives a stability number slightly higher than that obtained from an upper bound calculation. The calculated stability number is dependent on the mesh coarseness.

B.3. Prediction of Failure of a Vertical Cut in ABAQUS

As part of exploring the capability of the procedures developed in Chapters 2 and 3 for the simulation of various aspects of excavation analysis, this section presents numerical simulations of the vertical cut problem using ABAQUS.

B.3.1. Unsupported Vertical Cut in Elastic-Perfectly Plastic Soil

In this set of simulations, the stability number of a vertical cut is calculated using ABAQUS with an elastic perfectly plastic model for the soil. Soil strength is assumed to be constant with depth. Four numerical simulations are performed:

Simulation #1:

In this simulation the mesh shown in Figure B.3 is used. The analysis performed is a total stress analysis (total stresses are equal to effective stresses). Initially the state of stress and the unit weight (body forces) of the material are given as zero. Loading of the mesh is performed by incrementally increasing the unit weight of the material. This loading situation is similar to tests performed using a centrifuge. Failure in the system is reached when very large deformations occur in the mesh due to a small incremental increase in the unit weight. The calculated stability number in this analysis is 4.0. This number can be improved by increasing the number of elements in the FE mesh and reducing the analysis step size. Figure B.4 shows the deformed mesh at failure. Figure B.5 shows displacement vectors plot at failure.

Simulation #2:

This analysis is the same as the above analysis. However, in this case, the analysis is performed using coupled (stress-pore pressure) elements (i.e effective stress analysis). The elastic perfectly plastic model is assumed to describe the solid phase of the material. The unit weight of the material is increased under undrained condition (quick loading). Again, the stability number calculated from this analysis is 4.0.

Simulation #3:

In this analysis we try to simulate more closely a real field situation. Mesh of Figure B.6 is used. Assuming an initial isotropic state of stress, and a unit weight for the

material, the soil is excavated incrementally. The analysis is a total stress analysis. Again, in this situation the stability number obtained is 4.0.

Simulation #4:

This analysis is similar to the previous analysis. However, the analysis is performed using coupled formulation (effective stress analysis), and the excavation procedure described in Chapter 3. Again, the stability number obtained is 4.0.

All four analyses give consistent results regarding the failure load computed in the system. The stability number computed is 4 which is about 4% larger than the upper bound solution give by Chen (1975). This is an acceptable result given all other numerical considerations of the problem. The simulations where coupled analyses is performed indicate that the procedures proposed in Chapter 3 give correct results.

B.3.2. Unsupported Vertical Cut in MCC & MIT-E3 Soil

In this section two analyses are performed using MCC and MIT-E3 models. The soil is assumed to be normally consolidated with a K_0=0.48. The material properties for both models used are listed in Table B.1 Note that the two models have the same peak friction angle in triaxial compression and very similar strength ratios in undrained plane passive shearing. In this set of analyses the soil profile has an increasing strength with depth (Figure B.7).

Figure B.8 shows a plot of the maximum deflection vs. excavation depth for the two models (The excavation is conducted under undrained conditions). Failure in both analyses is detected beyond an excavation depth of 4m. The MIT-E3 model shows a stiff nonlinear response. MCC shows a soft linear response (elastic unloading is dominant) up to failure. The difference in response is due to the difference in the constitutive formulation of the two models At failure, H>4m, the numerical solution for MCC is stable, but for MIT-E3 it is completely unstable because of strain softening.

MIT-E3 and MCC fail at about the same excavation depth. The analyses indicate that the controlling parameter for the failure of the unsupported cut is the peak undrained strength in plane strain active shearing. Other aspects of the models appear to only affect the magnitude of deformations prior to failure.

.4. References

.rai, K. and Jinki, R., 1990, " A Lower-Bound Approach to Active and Passive arth Pressure Problems." *Soils and Foundations*, Vol. 30, No. 4, pp. 25-41.

.rai, K. and Nakagawa, M., 1988, "A New Limit Equilibrium Analysis of lope Stability Based on Lower-Bound Theorem." *Soils and Foundations*, Vol. 28, o. 1, pp. 1-15.

.rai, K. and Tagyo, K., 1985, "Limit Analysis of Geotechnical Problems by .pplying Lower-Bound Theorem." *Soils and Foundations*, Vol 25, No. 4, pp. 37-8.

.saoka, A. and Ohtsuka, S., 1986, "The analysis of Failure of a Normally onsolidated Clay Foundation Under Embankment Loading." *Soils and oundations*, Vol 26, No. 2, pp. 47-59.

.saoka, A. and Ohtsaka, S., 1987, "Bearing Capacity Analysis of a Normally onsolidated Clay Foundation." *Soils and Foundations*, Vol. 27, No. 3, pp. 58-70.

.saoka, A., Ohtsuka, S. and Matsuo, M., 1990, "Coupling Analysis of imiting Equilibrium State for Normally Consolidated Soils", *Soils and Foundations*, ol. 30, No. 3, pp. 109-123.

.tkinson, J.H., 1981, *Foundations and Slopes, An Introduction to Applications of Critical State Soil Mechanics.*

Chen, W-F., 1975, "Limit Analysis and Soil Plasticity." *Developments in Geotechnical Engineering*, 7.

De Borst, R. and Vermeer, P.A., 1984, "Possibilities and Limitations of Finite Elements for Limit Analysis." *Géotechnique*, 34, No. 2, pp. 199-210.

riffiths, D.V. and Koutsabeloulis, N., 1985, "Finite Element Analysis of ertical Excavations." *Computer and Geotechnics*, Vol. 1, pp. 221-235.

eyman, J., 1973, "The stability of a Vertical Cut." *International Journal of echanical Sciences*, Vol. 15, pp. 845-854.

amura, T, Kobuyashi, S. and Sumi, T., 1984, "Limit Analysis of Soil tructure by Rigid Plastic Finite Element Method." *Soils and Foundation*, Vol. 24, o. 1, pp. 34-42.

amura, T, Kobuyashi, S. and Sumi, T., 1987, "Rigid-Plastic Finite Element ethod for Frictional Materials." *Soils and Foundations*, Vol. 27, No. 3, pp. 1-12.

oh, C.T. and Sloan, S.W., 1980, "Finite Element Analysis of Isotropic and nisotropic Cohesive Soils with a View to Correctly Predicting Impending Collapse." *ternational Journal for Numerical and Analytical Methods in Geomechanics*, 4, pp. 1-3.

ermeer, P.A. and Van Langen, H., 1989, "Soil Collapse Computations with inite Elements." *Ingenieur-Archiv* 59, pp. 221-236.

Input Parameters	MIT-E3	MCC
OCR	1	1
e_0	0.9	0.9
K_{0NC}	0.48	0.48
κ_0	0.001	0.034
λ	0.184	0.184
2G/K	1.05	1.05
ϕ'_{TC}	33.4^o	33.4^o
ϕ'_{TE}	45.9^o	
c	0.86	
S_t	4.5	
C	22.0	
n	1.60	
ω	0.07	
h	0.2	
γ	0.5	
ψ_o	100	

Model	$S_{u,TC}/\sigma'_{vo}$	$S_{u,PSA}/\sigma'_{vo}$
MCC	0.32	0.37
MIT-E3	0.34	0.36

Table B.1 Input Parameters for MCC and MIT-E3 models

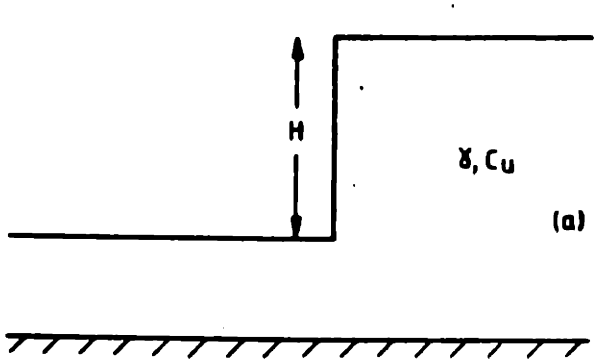

Figure B.1 Unsupported Excavation

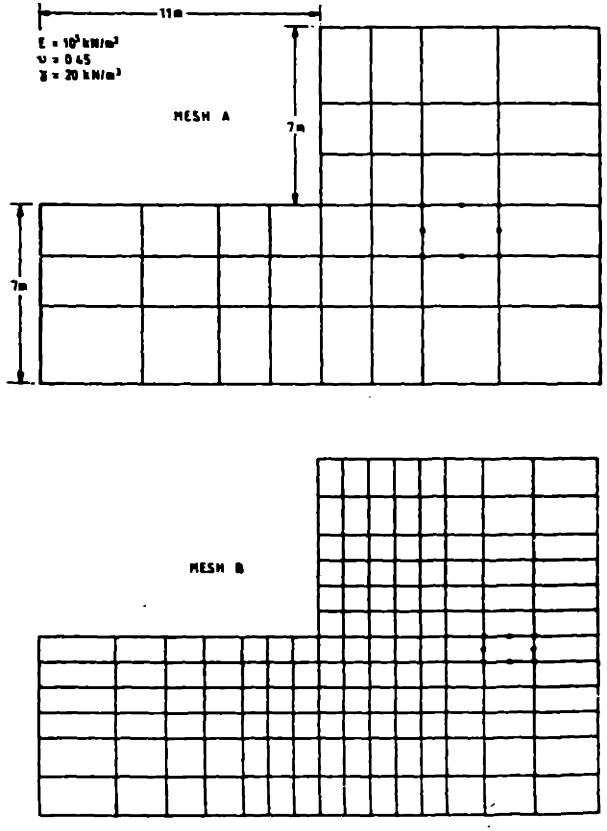

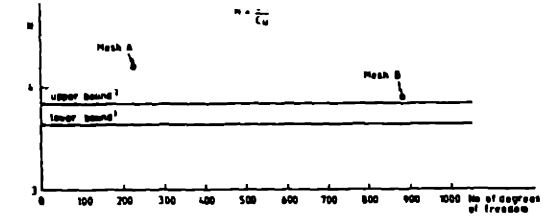

Fig.5 Effect of mesh coarseness on computed stability number

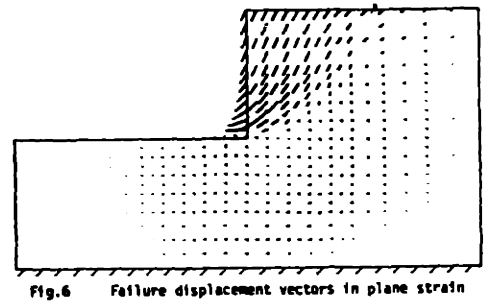

Fig.6 Failure displacement vectors in plane strain

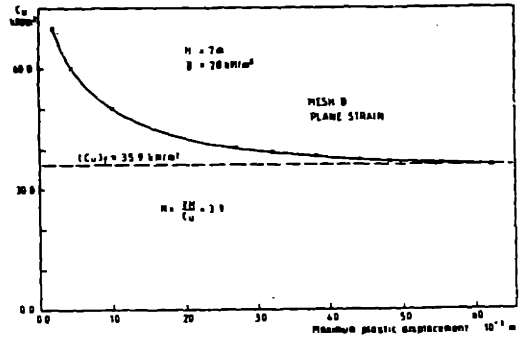

Figure B.2 Effect of Cohesion on Plastic Displacement (Griffith and Koutsabeloalis, 1985)

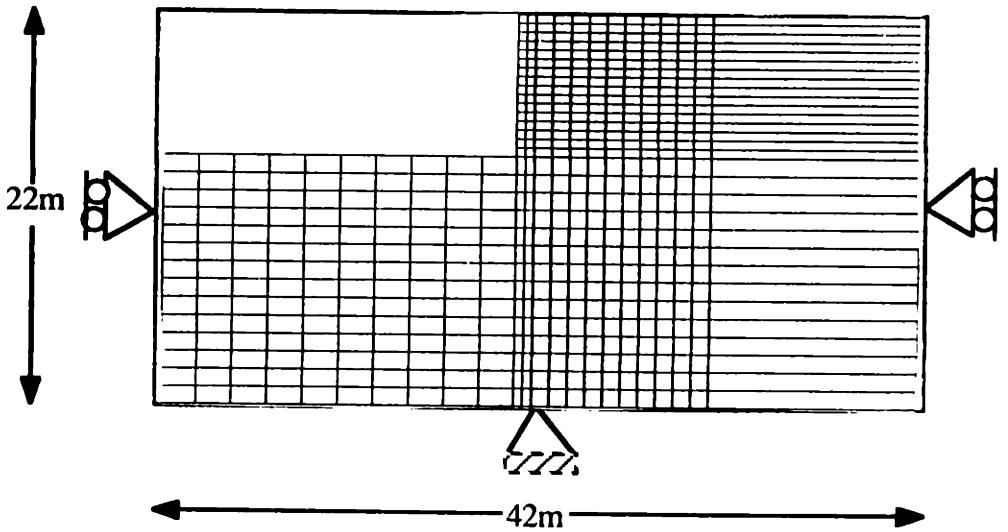

Finite Element Model:

426 Elements

1369 Nodes

2738 Degrees of Freedom (Total Stress Analysis, TSA)

3210 Degrees of Freedom (Effective Stress Analysis, ESA)

Material Properties:

Elastic Perfectly Plastic Model

$E=14.7x10^3$ kN/m^2

ν=0.5 (TSA), 0.3 (ESA)

$\gamma_t=gx19.6kN/m^3$

$\gamma_w=gx9.8kN/m^3$

g, Gravitational Field, Increased Incrementally in the Analysis

Cu=29.4 kN/m^2

Figure B.3 Finite Element Mesh (Failure Achieved by Increasing Body Forces)

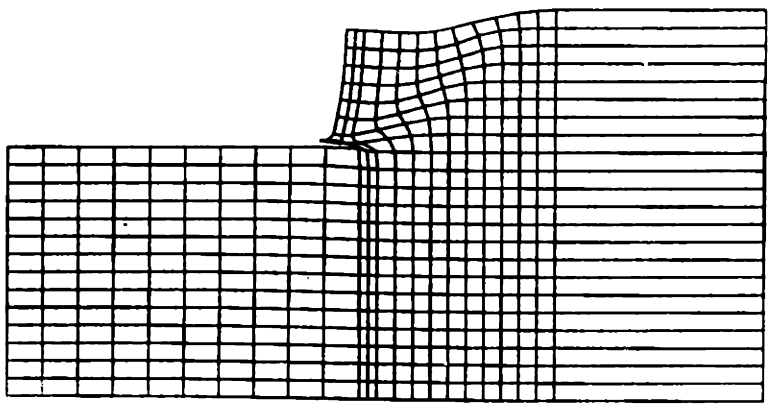

Figure B.4 Deformed Mesh, Simulation #1

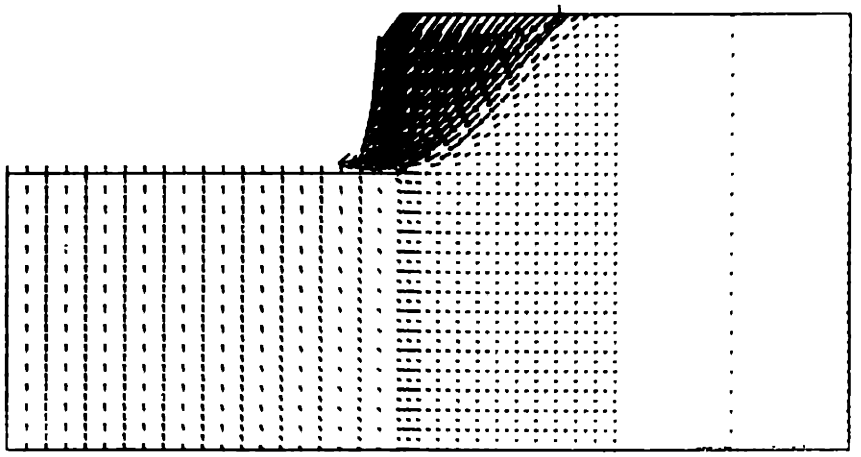

Figure B.5 Displacement Vectors, Simulation #1

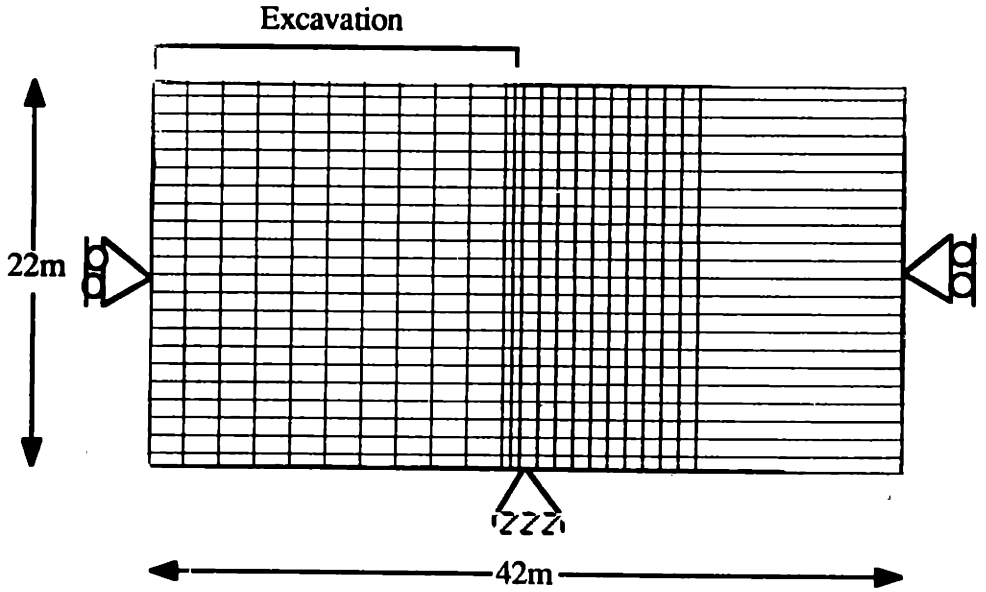

Finite Element Model:

506 Elements

1609 Nodes

3218 Degrees of Freedom (Total Stress Analysis, TSA)

3770 Degrees of Freedom (Effective Stress Analysis, ESA)

Material Properties:

Elastic Perfectly Plastic Model

$E=14.7x10^3$ kN/m^2

ν=0.5 (TSA), 0.3 (ESA)

$\gamma_t=19.6$kN/m^3

$\gamma_w=9.8$kN/m^3

g, Gravitational Field, Unity (g=1) for Analyses with Soil Removal

$C_u=29.4$ kN/m^2

Figure B.6 Finite Element Mesh (Failure Achieved by Soil Removal)

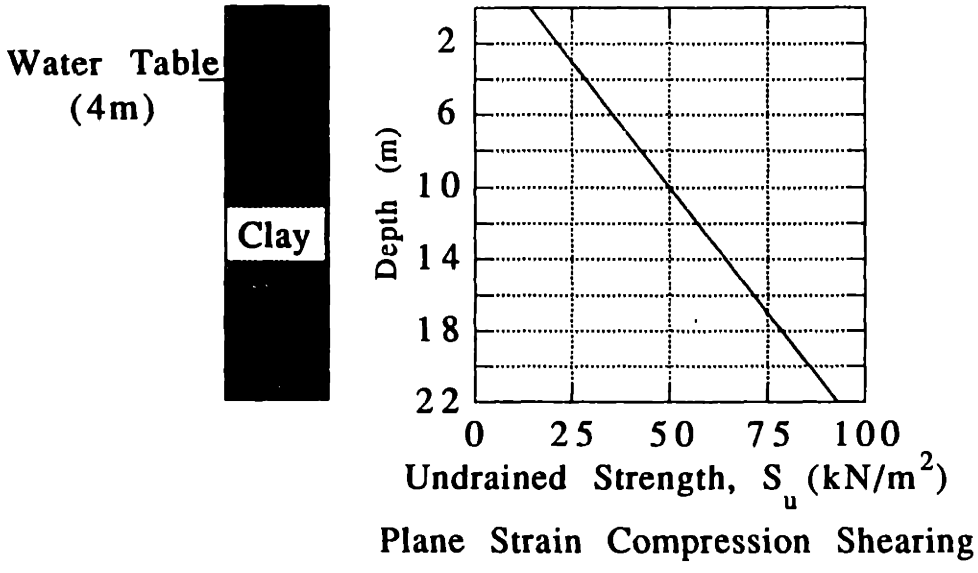

Figure B.7 Strength Profile, MCC and MIT-E3 Analyses

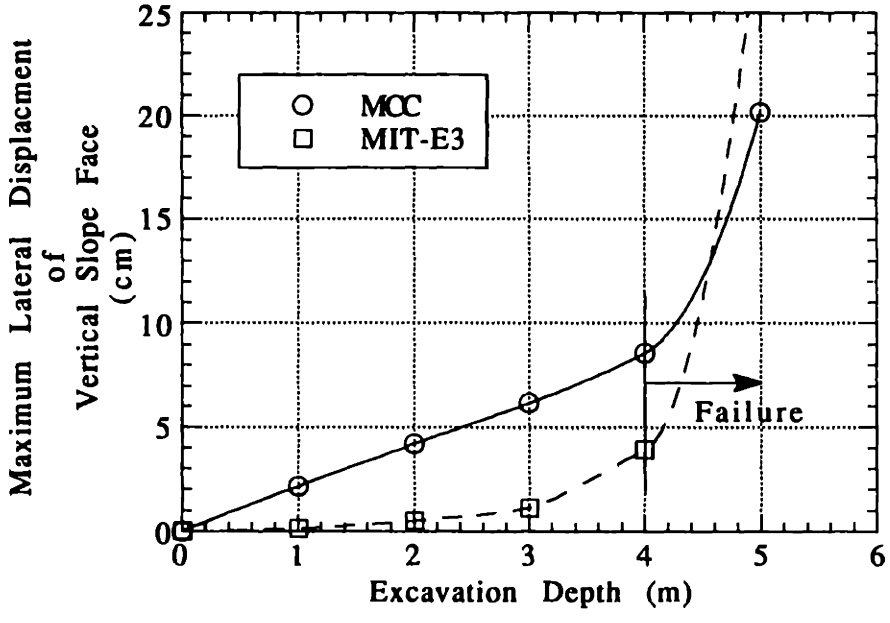

Figure B.8 Maximum Displacement versus Excavation Depth for MCC and MIT-E3 Analyses.

C. Effect of Drainage on Excavation Movements

The discussion presented in Chapter 4 focused on the study of undrained excavation behavior. Undrained conditions prevail in many low permeability clays. However, in areas where the clay becomes silty (hence leading to an increase in permeability) or where construction steps are carried over long periods of time, partial drainage is expected to occur in the soil. In this section the effect of drainage on movements due to excavation is briefly examined.

Incorporating drainage effects into an excavation analysis adds several parameters to the problem. The following issues become important:

1. Length of Wall

   The length of the wall in a drained excavation can significantly affect prefailure deformations. The penetration of the wall beneath the excavation level affects the degree of water table drawdown behind the wall, and consequently soil settlements. In contrast, in Chapter 4, it was shown that wall length had a very limited impact on undrained prefailure deformations in an excavation. If the wall penetrates into an impermeable layer, dewatering inside the excavation will cause little reduction in pore pressures behind the wall. In this section, a wall length L=60m will be used.

2. Bottom Pore Pressure Boundary Condition

   The boundary condition deep beneath the surface affects the flow pattern in an excavation. The boundary condition can be either a flow line (impermeable layer) or a constant head line. Based on results of Post Office Square Garage analysis (Chapter 5) a constant head line is assumed. The head is equal to the initial hydrostatic head in the soil. The location of this boundary (distance y in Figure 4.2-1) will have an important effect on the pore pressure distribution and consequently movements in the excavation. In this section x is kept constant.

3. Ground Surface Pore Pressure Boundary Condition

   The surface boundary condition can be either a no-flow boundary condition which would allow for a lowering of the water table, or a constant head (fixed water table) condition. In the analysis, the water table is fixed at a depth of 2.5m below ground surface.

4. Far Field Pore Pressure Boundary Condition

   It is commonly assumed that initial hydrostatic conditions prevail far behind the excavation. The distance x, Figure 4.2-1, is now an important variable and will control the extent of the pore pressure drawdown due to dewatering. Y is taken as

a constant. In an undrained analysis, it is desirable to make the distances x and y as large as possible to reduce the impact of displacement boundary conditions on predicted movements due to excavation. However, large x and y distances will lead to a larger zone of soil being affected by dewatering in the drained analysis. This may not be the case in many field situations. The problem can be limited if the pumping rate inside the excavation is controlled.

5. Excavated Surface Pore Pressure Boundary Condition

Depending on the particular situation, a dewatering system or a pressure resistant slab (hydrostatic condition) can be used. Allowing the pore pressures to recover to their initial conditions can cause substantial heave and requires installation of a heavy slab to resist the upward pore pressure. In this analysis, at any excavation step, the water table is maintained at a distance of 2.5m below the surface of the excavation. This assumption is made to avoid a condition of zero effective stress along the excavated surface that may lead to numerical instabilities (infinite heave of the surface).

6. Wall Permeability

In this analysis, the wall is assumed to be impermeable. In field situations, this may not be true due to the presence of joints or cracks in the wall.

A single analysis is performed in this section assuming excavation under fully drained conditions. Pore pressure boundary conditions are shown in Figure C.1. A combined soil profile (OCR=C) is used with vertical support spacing h=2.5m and an unsupported excavation depth h_u=2.5m. The analysis is carried to a maximum depth of 27.5m beyond which it was not possible to continue the analysis due to numerical difficulties. Significant strain softening develops in large parts of the OCR=1 layer. It is not clear whether the difficulties arose due to pure numerical instabilities caused by strain softening or whether genuine failure occurred in the soil.

C.1. Wall Deflections and Surface Settlements

The drained excavation behavior is compared to the equivalent undrained analysis presented in Section 4.9. Figure C.2 compares wall deflections and surface settlements from the two analyses. The last excavation analysis prior to failure in the drained analysis is 27.5m while in the undrained analysis it is 32.5m.

Wall deflections, at all excavation stages (Figure C.2c), in the drained analysis are larger than those in the undrained analysis (Figure C.2d). This is most likely due to the increased water pressure on the back of the wall.

Initially settlements in the drained analysis, Figure C.2a, are smaller than those in

the undrained analysis (Figure C.2b). Beyond H=15m, drained settlements exceed undrained settlements. Under undrained conditions, negative pore pressures initially develop due to excavation. When these pore pressures are allowed to dissipate, the soil behind the wall will heave and, therefore, drained settlements will be smaller than undrained settlements. As the excavation depth increases, positive excess pore pressures develop, particularly in the normally consolidated clay, in the undrained analysis. In the drained analysis, these pore pressure are reduced to result in negative excess pore pressures (water level drawdown), causing large settlements in the soil.

C.2. Maximum Deformations and Moments

Figure C.3 shows plots of maximum deformations and moments versus excavation depth for the drained and undrained analyses. Drained maximum wall deflections, Figure C.3a, and center line heave, Figure C.3d are consistently larger than corresponding undrained quantities. Initially drained maximum settlements, Figure C.3b, are smaller than undrained maximum settlements, but eventually exceed them. Drained wall moments, Figure C.3c, are consistently larger than undrained wall moments.

C.3. Lateral Stresses in the Wall

Figure C.4 plots lateral stresses acting on both sides of the wall for the drained an the corresponding undrained analysis. Stresses acting along the back of the wall are slightly larger for the drained analysis than the undrained one. Stresses acting along the wall inside the excavation are similar for both analysis.

C.4. Discussion

In this section a comparison is made between drained and undrained excavation behavior in an OCR=C soil profile. The following observations are made:

1. The excavation under drained conditions fails at a smaller excavation depth compared to an excavation under undrained conditions.
2. Drained wall movements are larger than those in the undrained analysis.
3. Drained settlements are smaller than undrained settlements when the excavation is in the OCR>1 material. Drained settlements exceed undrained settlements once the excavation penetrates the OCR=1 layer.
4. Drained lateral stresses acting along the back side of the wall are slightly larger than corresponding undrained stresses. Passive stresses inside the excavation are similar for both analyses.

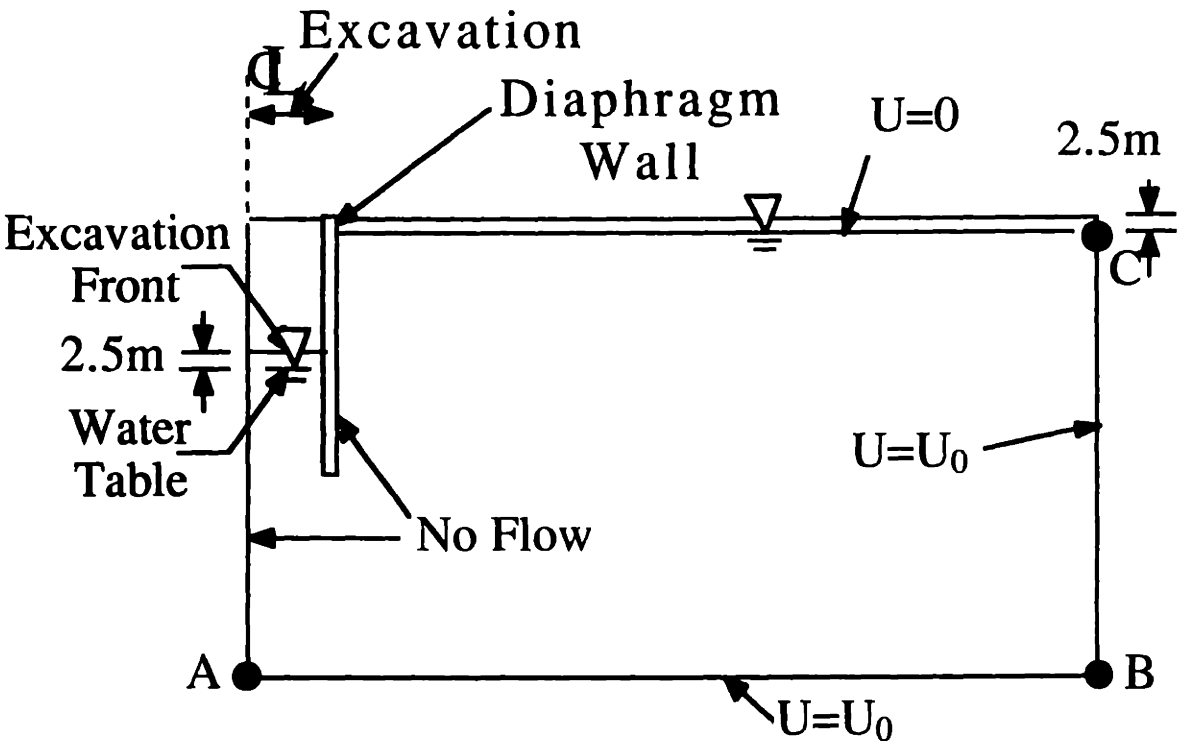

Figure C.1 Pore Pressure Boundary Conditions, Drained Analysis.

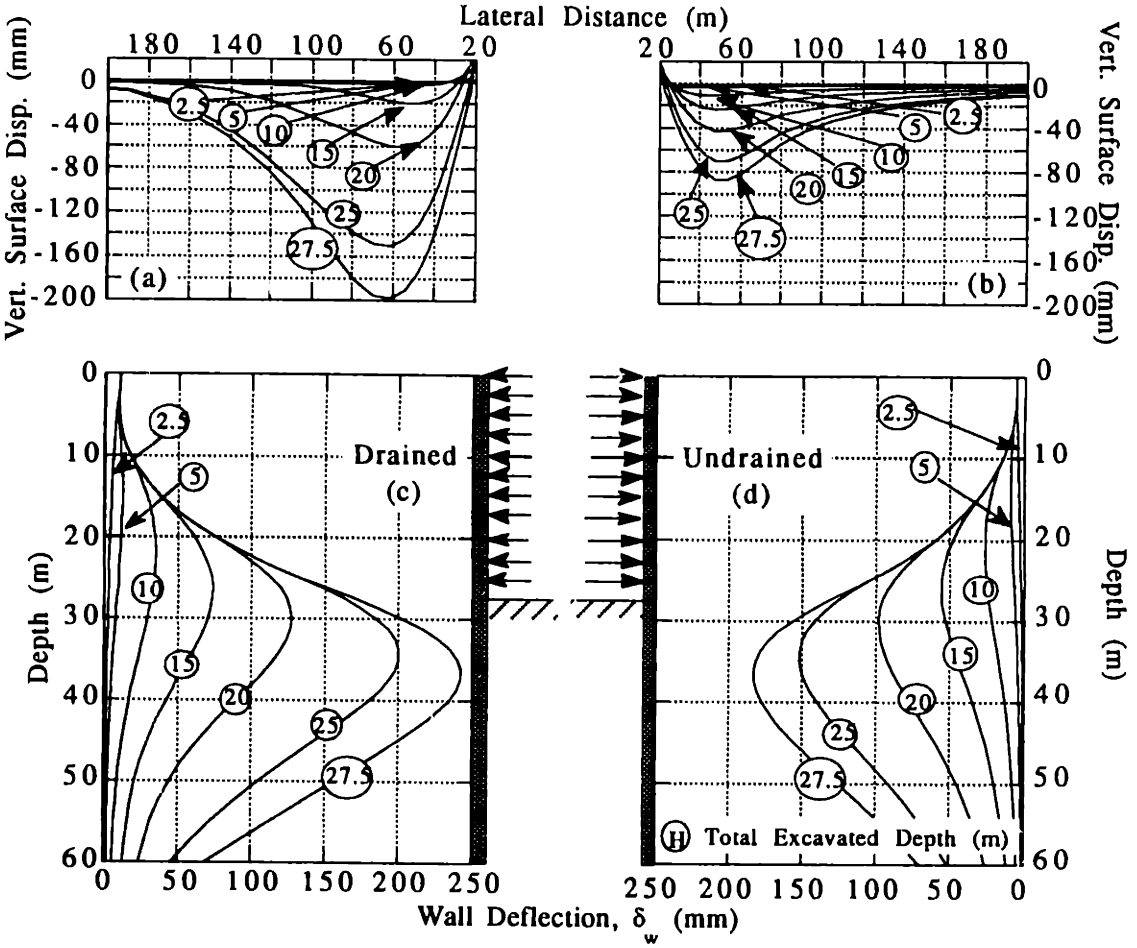

Figure C.2 Effect of Drainage Condition on Lateral Wall Deflections and Surface Settlements (h_u=2.5m, h=2.5m, L=60m, MIT-E3, OCR=C).

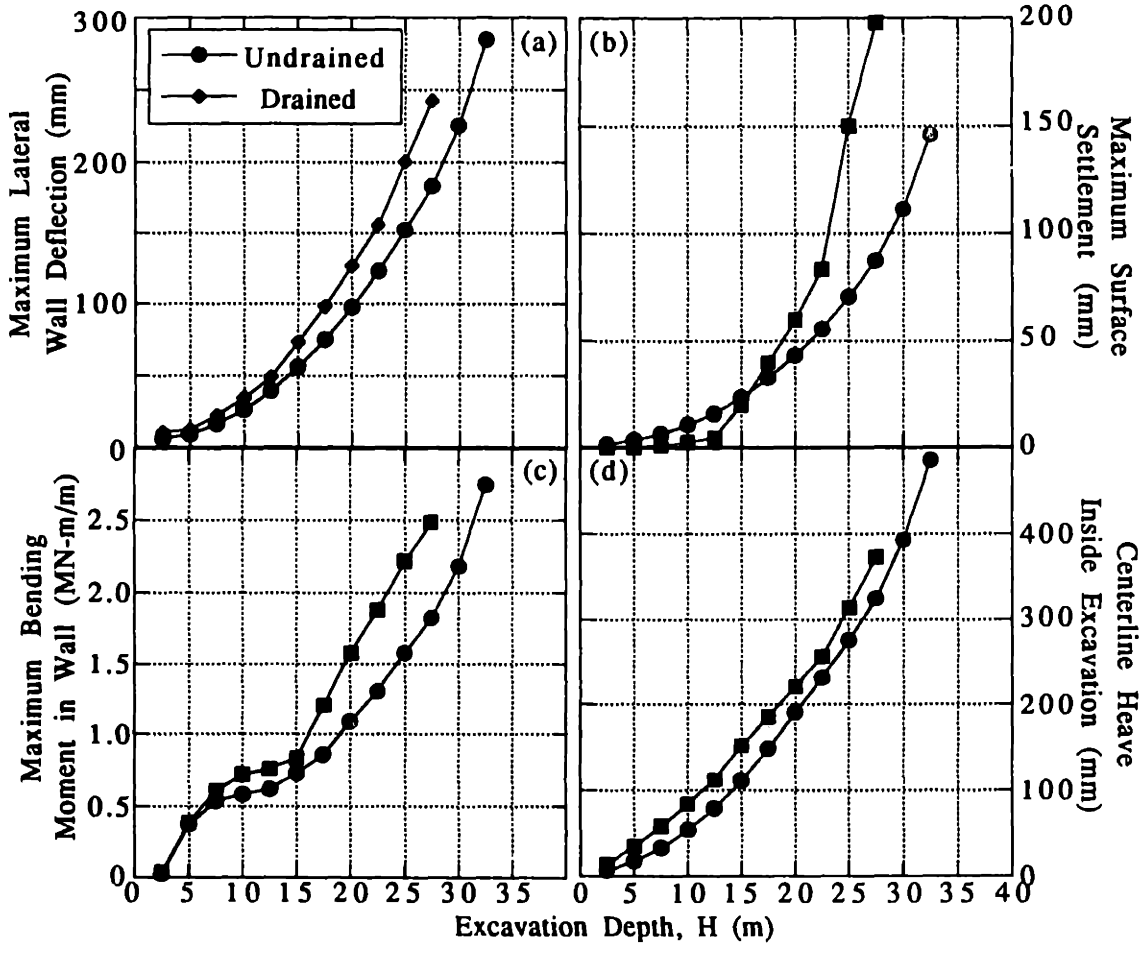

Figure C.3 Effect of Drainage Condition on Maximum Deformations and Moments (h_u=2.5m, h=2.5m, L=60m, MIT-E3, OCR=C).

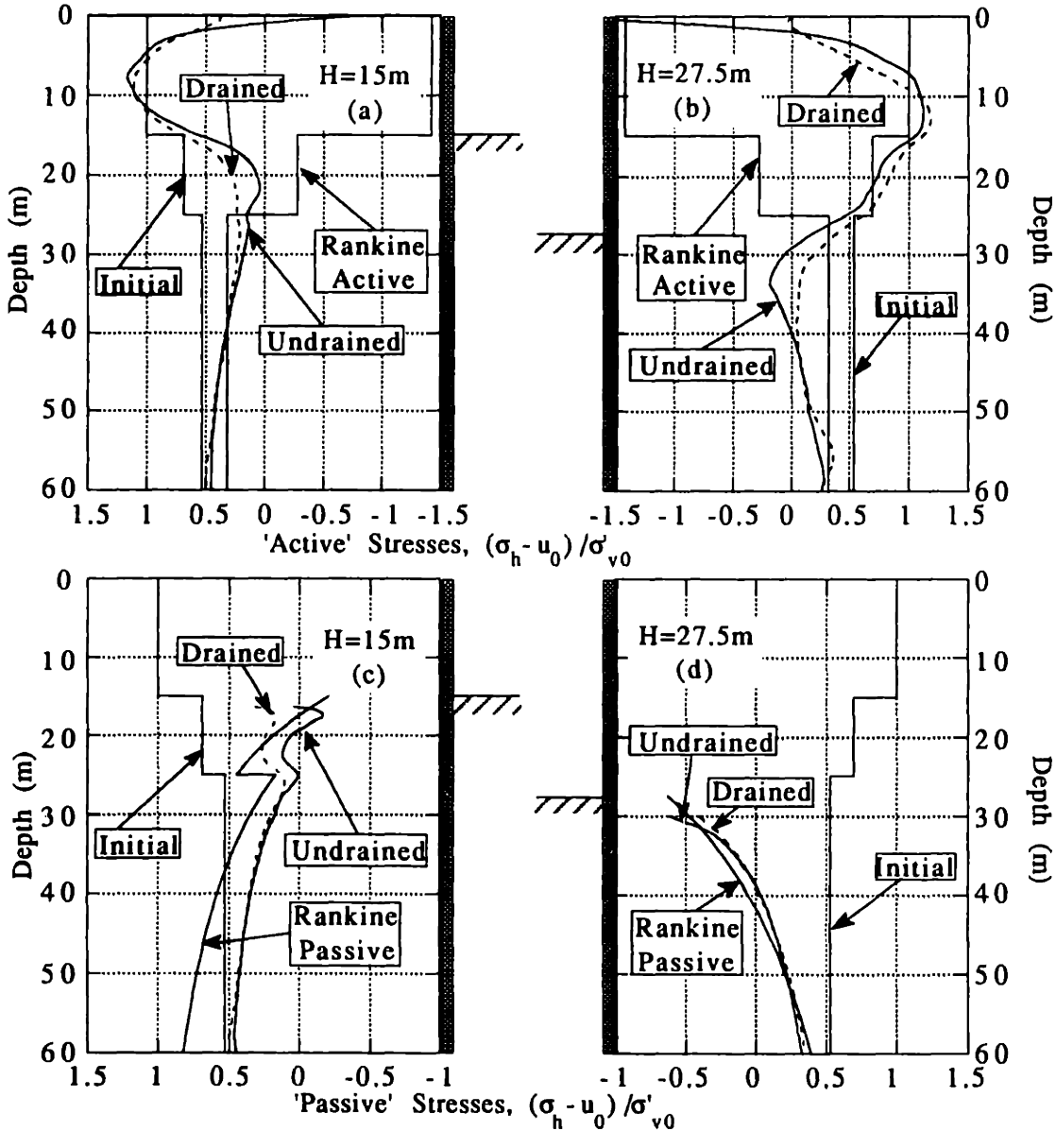

Figure C.4 Effect of Drainage Condition on Normalized Earth Pressures acting on the Wall (h_u=2.5m, h=2.5m, L=60m, MIT-E3, OCR=C).

D. Analysis of the Behaviour of Propped Diaphragm Walls in a Deep Clay Deposit*

D.1 Abstract

Modern techniques of excavation, including the use of structural diaphragm walls and top-down construction, provide effective methods to minimize deformations in the surrounding soil. However, for deep excavations and walls embedded in deep layers of soft clays, it is difficult to control soil movements. In these situations, reliable predictions of deformations are an important consideration in the design of the earth support system. This paper describes results of numerical experiments, based on non-linear finite element analyses and incorporating an effective stress soil model which describes observed aspects of soft clay behaviour including small strain non-linearity and anisotropic stress-strain-strength. The analyses consider the undrained deformations around a braced diaphragm wall in a soft clay deposit. Principal parameters considered in the study are the wall embedment depth and support spacing. A simplified framework is developed to interpret wall deflections and ground movements with excavation depth.

D.2 Introduction

Excavations up to 20 to 25m deep, for an underground highway through downtown Boston (referred to as the Central Artery/ Tunnel project, CA/T), will be supported by structural diaphragm walls using techniques of top-down construction. In some locations, the soil conditions include very deep layers of soft Boston Blue Clay and it is not economical to extend the diaphragm walls down to the underlying till and rock layers. Reliable predictions of soil deformations are particularly important in the design of the lateral earth support at these sections especially due to the proximity of adjacent structures. Previous observations (ref.1) show that large lateral wall deflections and surface settlements, in the range of 2 to 3% of the excavation depth, can be expected for walls embedded in soft clays. However, most of the existing data were obtained from excavations less than 15m deep, supported by relatively flexible, sheet pile and soldier pile walls. This paper describes results of numerical experiments, using non-linear finite element analyses, which have been performed in order to investigate the effects of wall length and support conditions on predictions of wall deflections and ground movements.

---

*This is a paper accepted for publication at the International Conference on Retaining Structures, 20-23rd July 1992, Cambridge, UK. Authors: Whittle, A.J., and Hashash, Y.M.A.

D.3 Scope of Parametric Study

Compilations of measured data and case studies emphasize the large number of factors, relating to construction activities and soil conditions, which can affect the development of ground movements for braced excavations. In contrast, the design of numerical experiments attempts to limit the number of parameters in order to facilitate the interpretation of the analyses, while still maintaining sufficiently realistic conditions that the results can have practical application. The following assumptions have been used in this study:

1. For deep layers of low permeability clay, the excavation process occurs sufficiently rapidly that there is no migration of pore water, hence the soil is subject to undrained shearing.
2. The study focuses on a plane strain geometry with a fixed excavation half-width, w=20m, and standard diaphragm wall thickness, t=0.9m, (Fig. D.1a) typical of conditions expected for the CA/T project. It is assumed that wall installation does not disturb the surrounding soil (i.e., the wall is wished-in-place) and that the full shear strength of the soil can be mobilized at the soil-concrete interface.
3. The excavation is braced by incompressible (rigid) supports spaced at equal intervals, h, as shown in Figure D.1b. Installation of rigid bracing represents an ideal condition in which there is no further lateral deflection of the wall at the elevation of the support. The analyses do not consider support compressibility or other complex aspects of soil-structure interaction associated with different bracing systems, such as shrinkage and expansion of cast in-situ floor systems (ref.7) or prestressing of cross-lot bracing (ref.3).
4. The analyses assume a simplified construction sequence (fig. D.1b) comprising *the following steps: 1) soil is initially excavated to a depth, h_u, without lateral* support; 2) the wall is propped at the surface and excavation proceeds to a depth, h_e; 3) a second level of support is installed at a spacing, h, and soil is then removed over a further interval, h_e; 4) step 3 is repeated until failure occurs. By varying the parameters h, h_e and h_u it is possible to study a wide range of top-down construction sequences.
5. The clay is saturated and exhibits normalized engineering properties. The numerical experiments then focus on simplified soil profiles in which the overconsolidation ratio ($OCR = \sigma'_p/\sigma'_{v0}$) is constant with depth, and hence the engineering properties are proportional to the initial overburden stress, σ'_{v0}. It is

assumed that the pore pressures are initially hydrostatic with the groundwater table located at a depth, d_w = 2.5m (typical of conditions in Boston) and full capillarity in the overlying clay.

The effective stress-strain-strength properties of the soil are characterized by the MIT-E3 model (refs 5-6) using input parameters previously selected for Boston Blue Clay. The MIT-E3 model describes many aspects of the observed behavior of K_0-normally and lightly overconsolidated ($1 \leq OCR \leq 8$) clays including a) small strain non-linearity, b) anisotropic stress-strain-strength; and c) hysteretic and inelastic behavior due to cyclic loading. The model has been extensively validated at the element level through comparisons with laboratory test data (refs 5-6). Figure D.2 compares model predictions with laboratory data from undrained plane strain shear tests on K_0-normally consolidated Boston Blue Clay measured in the Directional Shear Cell (DSC; ref.4). In these tests (Fig. D.2a) the sample is sheared by applying incremental principal stresses oriented at an angle δ_{inc} to the direction of the principal consolidation stress (σ'_{yc}). The data at $\delta_{inc}=0^0,90^0$ correspond to plane strain 'active' and 'passive' modes of shearing, while intermediate values of δ_{inc} produce continuous rotations of principal stresses (σ'_1 is oriented at δ to the y-axis). Figure D.2b shows that the model predicts accurately the measured changes in undrained shear strength ratio (i.e., q_{MAX}/σ'_{yc}) with the direction of the major principal stress. The predicted strength ratio ranges from $q_{MAX}/\sigma'_{yc}=0.34$ at $\delta=0^0$ to 0.17 at 90^0 and illustrates the importance of anisotropic undrained strength properties for K_0-consolidated Boston Blue Clay.Measurements of the secant modulus (defined in Fig. D.2c) show that the clay exhibits non-linear stress-strain behavior for shear strains, $\gamma \geqq 0.05\%$. Model predictions agree well with the data for tests with $\delta_{inc}=60^0$, 75^0 and 90^0 but generally overpredict the stiffness at $\delta_{inc}=0^0$, 45^0. These results illustrate that MIT-E3 is well suited to modelling the complex stress-strain history of the soil induced by excavation processes, including principal stress rotations.

Reference 2 describes the incorporation of MIT-E3 in the finite element code ABAQUS and gives details of the procedures used to perform numerically accurate, effective stress analyses of excavations in non-linear soils.

D.4 Typical Results

Figure D.3 and D.4 show typical predictions of lateral wall defections and surface settlements for excavations in a deep layer of normally consolidated Boston Blue Clay. Figure D.3 compares results for two walls with lengths, L=20m and 40m, which are both braced at intervals h=2.5m over the full depth of the excavation (the initial

unsupported depth h_u=2.5m in both cases). The effect of length on the deflected shapes of the walls is immediately apparent: For the short wall (L=20m), the maximum lateral deflection develops at the toe even for relatively shallow excavation depths (H≤10m). In contrast, for the 40m long wall, the maximum deflection is associated with a point of contraflexure which occurs 8 to 10m below the base of the excavation.

Figure D.3 also includes the excavation geometry and deflected wall shapes at the stage immediately prior to failure (i.e., at H=15m and 22.5m for the 20m and 40m long walls, respectively). The actual failure depths are difficult to estimate precisely as the analysis models finite excavation increments of 2.5m. However, detailed interpretations of the data (ref.2) show that the mechanism of failure can be well defined from the development of shear strains in the soil and is controlled by anisotropic properties of the MIT-E3 model. The failure mechanism is affected both by the embedment of the wall and by the assumed excavation width (w= 20m; Fig. D.1a). The results in Figure D.3 show that as the wall length increases from L = 20m to 40m, the failure depth increases by 50%. This additional stability is not considered in conventional calculations of base heave used for braced excavations.

Although there are significant differences in the deformed shapes of the two walls, the maximum lateral wall deflections, δ_{MAX}, are very similar at early stages of excavation, and differ by less than 30%, even for conditions close to failure (i.e. at H=15m for the L=20m wall). The results in Figure D.3a also show that wall length has practically no effect on the development of surface settlements. In both cases, the maximum settlement occurs at a lateral distance 15m to 20m behind the wall, with magnitudes approximately 40 to 60 percent of δ_{MAX}. The lateral distribution of settlement is strongly influenced by non-linear properties of the soil at small strain levels.

Figure D.4 compares the behaviour of 'perfectly supported' (h=0m) and 'minimally supported' (h=10m), 60m long walls. For the perfectly supported case, wall deflections only occur below the current excavation level. The deflected shape is similar to that reported in Figure D.3b for a 40m long wall, with maximum lateral deflections occurring approximately 10m below the base of the excavation. Failure of the perfectly supported wall at H=35m is associated both with a deep seated mechanism in the soil (H= 32.5m to 35m; Fig. D.4b) and with a vertical 'bearing' failure of the wall itself (observed from the wall settlements; Fig. D.4a). Large deformations (in the range 100 to 150 mm) develop in the soil prior to failure. In contrast, for the minimally supported wall, large lateral deflections develop over the excavated height, with maximum deformations located close to the base of the excavation. Failure in the soil is resisted by the bending of the wall. At the computed failure depth (H=20m; Fig. D.4), the wall

sustains a maximum bending moment, M_{MAX}=5MNm/m, which is significantly larger than the ultimate moment (M_u) for even a heavily reinforced diaphragm wall of these dimensions (typically, M_u=1.5 to 2.0MNm/m for t=0.9m walls). Overall, the results demonstrate the importance of support conditions on the development of lateral wall deflections, and their corresponding implications for control of soil deformations induced by excavations in deep clay layers.

D.5 Framework for Interpreting Maximum Wall Deflections

Extensive parametric studies described in ref.2 confirm that wall length has a very minor effect on the pre-failure soil deformations and maximum lateral wall deflections (δ_{MAX}). Figure D.5 then summarizes the numerical predictions of δ_{MAX} for excavations in normally consolidated BBC as a function of the excavation depth, H, and support spacing, h. The figure includes loci of failure conditions obtained for walls of different lengths, L, ranging from 12.5 m to 60m, and implicitly incorporates observations of different failure mechanisms in the soil. Failure of the diaphragm wall can be evaluated from contours of the maximum moment compared to the capacity of the section (M_u).The figure shows the following:

1. For excavations which are perfectly supported, the deflection to depth ratio, (δ_{MAX}/H)≥0.5%. For minimally supported walls, this ratio increases to (δ_{MAX}/H)=1.5 to 2.0%.
2. Excessive bending moments in the wall are the most critical design condition for long walls (L≥40m) and lightly braced walls (h≥5m).

The results in Figure D.5 should be used with caution for shallow excavations (H≤10m), where wall deflections are significantly affected by details of the top-down construction sequence (e.g., initial unsupported height, h_u; ref.2).

D.6 Conclusions

Predictions of wall deflections and soil deformations are an important consideration in the design of lateral earth support systems for excavations in deep deposits of soft clay. This paper has demonstrated the use of parametric studies, based on non-linear finite element analyses and incorporating effective stress modelling of soil behaviour, for interpreting the performance of braced diaphragm walls embedded in Boston Blue Clay. Results of the study indicate that support spacing is critical in controlling the development of soil deformations, while embedment length primarily affects the excavation stability. For these analyses, predictions of maximum wall

deflections can be summarized as functions of the excavation depth and support spacing.

D.7 References

1. **Clough, G.W. and O'Rourke, T.D**, 1990, "Construction induced movements of insitu walls." *Proc. ASCE Conference on Earth Retaining Structures*, Ithaca, NY, pp. 439-470.

2. **Hashash, Y.M.A.**, 1992, "Analysis of Deep Excavations in Clay.", *PhD Thesis*, MIT, Cambridge, MA.

3. **Mana, A.I., and Clough, G.W.**, 1981, "Prediction of movements of braced cuts in clay." *ASCE Journal of Geotechnical Engineering*, Vol. 107, No. 4, pp. 759-778.

4. **Seah, T.H.**, 1990, "Anisotropy of resedimented Boston Blue Clay." *PhD Thesis*, MIT, Cambridge, MA.

5. **Whittle, A.J.**, 1990, "A constitutive model for overconsolidated clays." *MIT Sea Grant Report*, MITSG 90-15.

6. **Whittle, A.J.**, 1991, "Evaluation of a constitutive model for overconsolidated clays." *to be published*, Géotechnique.

7. **Whittle, A.J., Hashash, Y.M.A. and Whitman, R.V.**, 1991, "Analysis of a deep excavation in Boston." *submitted for publication*, ASCE Journal of Geotechnical Engineering.

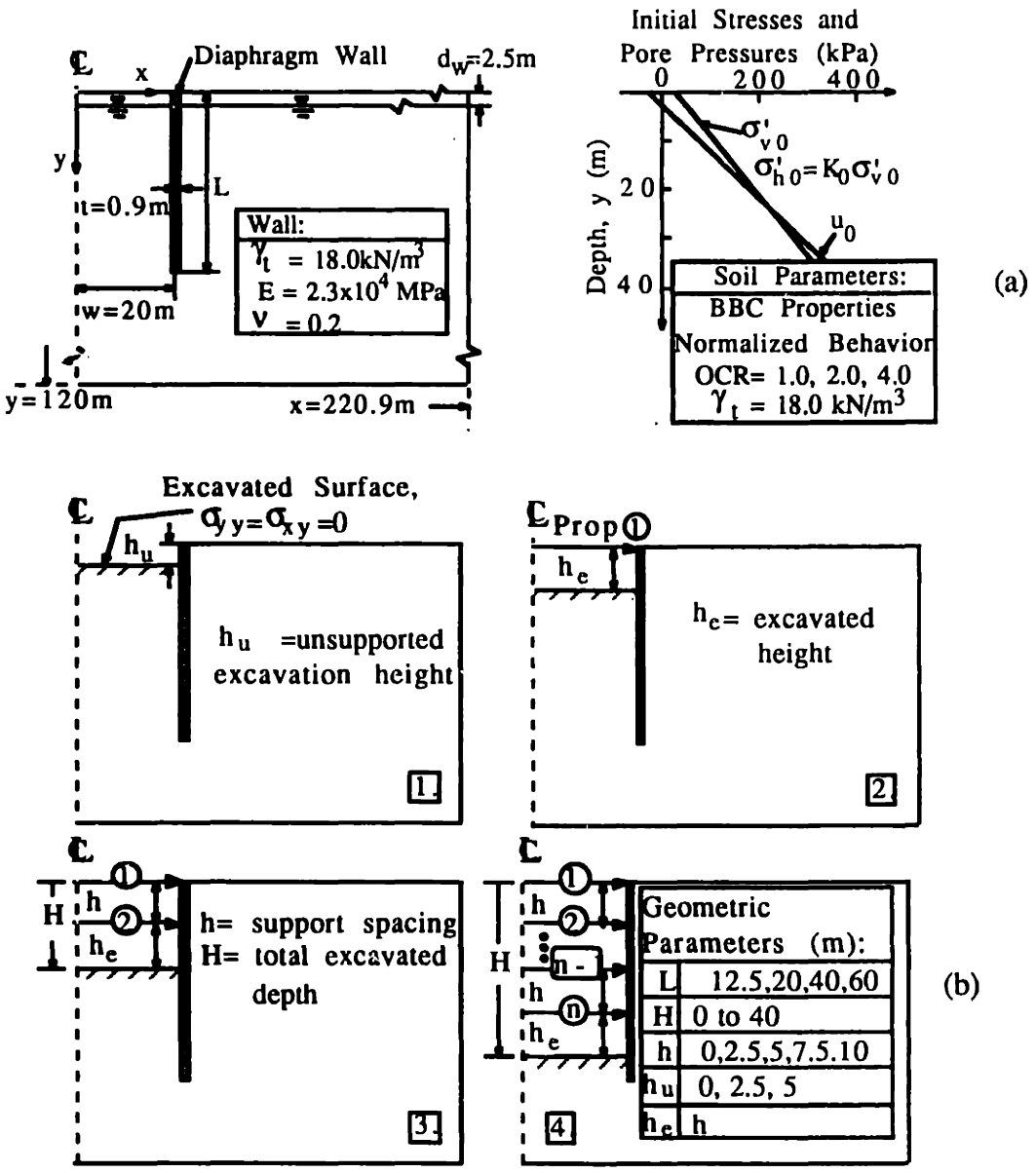

Figure D.1 Initial Conditions and Model Excavation Sequence

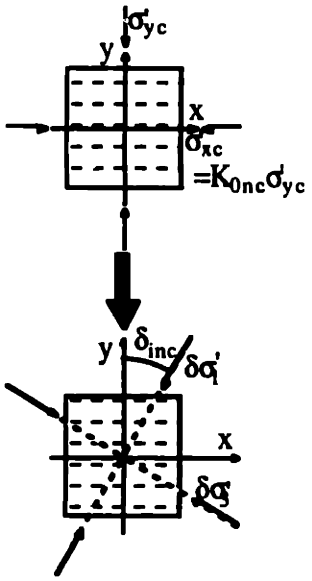

a) Test Procedure

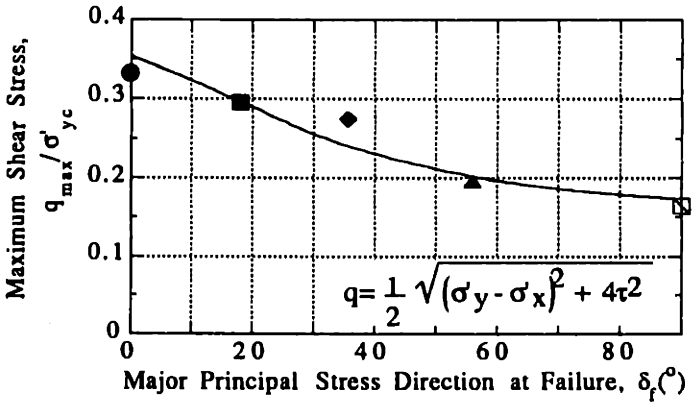

b) Undrained Shear Strength

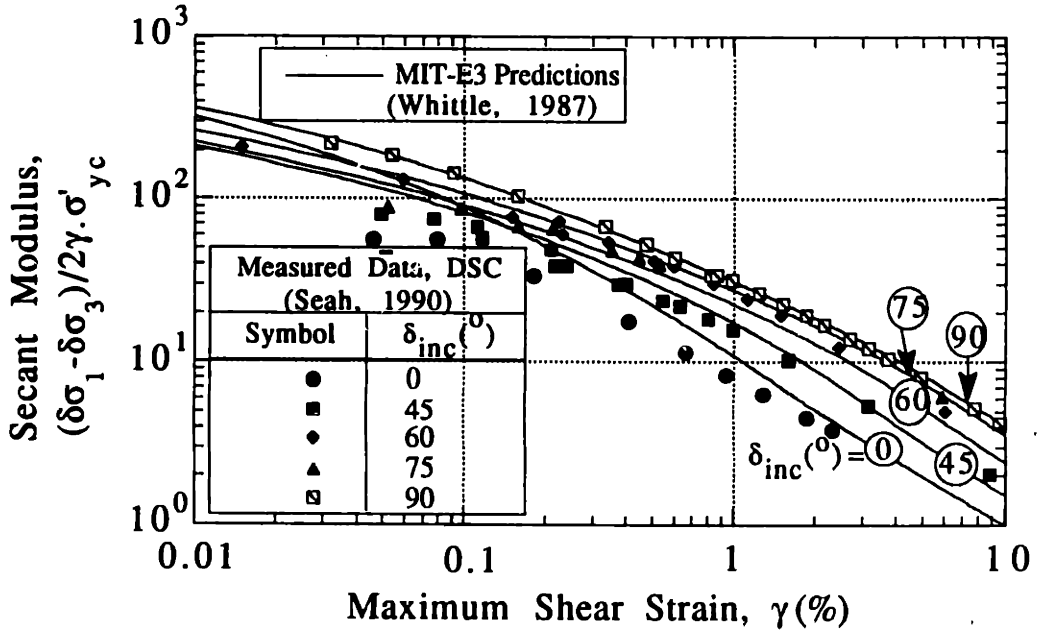

c) Variation of Modulus with Strain

Figure D.2 Evaluation of MIT-E3 Model for Undrained Plane Strain Shearing with Principal Stress Rotations

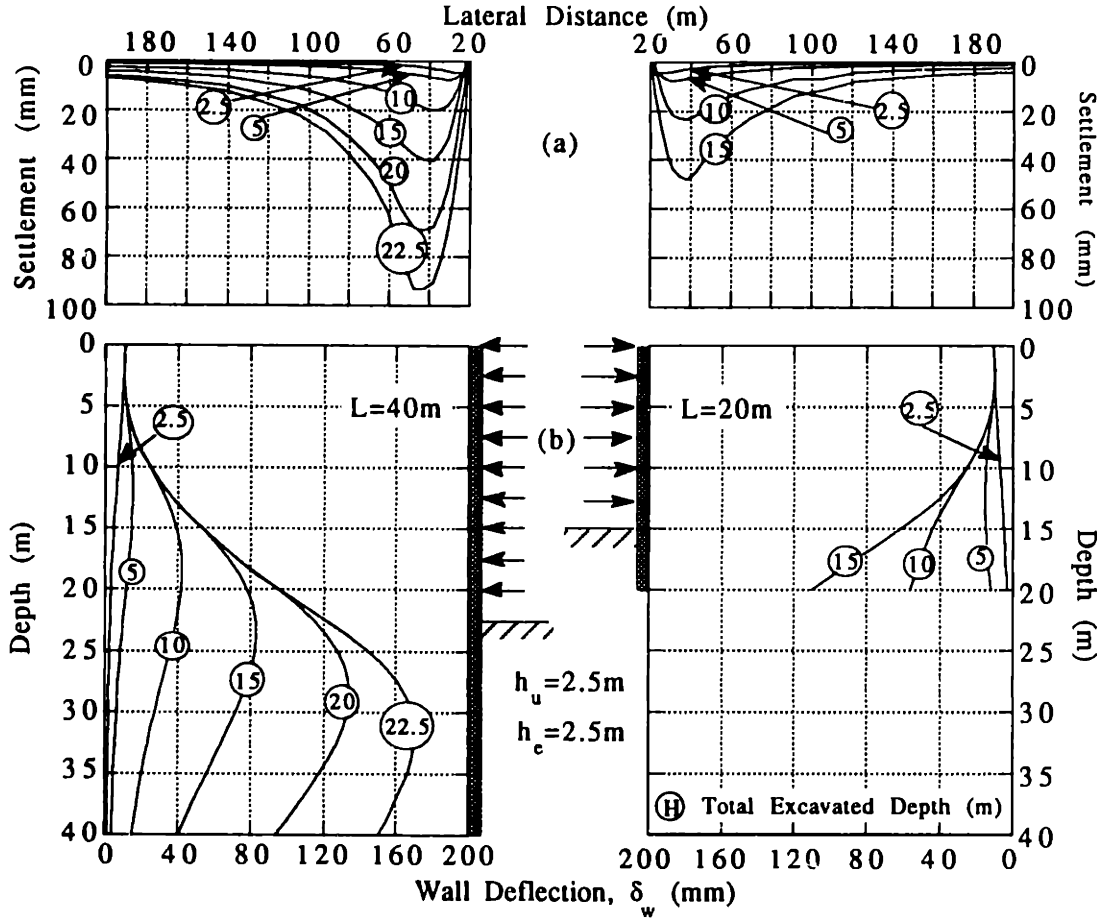

Figure D.3 Effect of Wall Length on Predicted Ground Movements

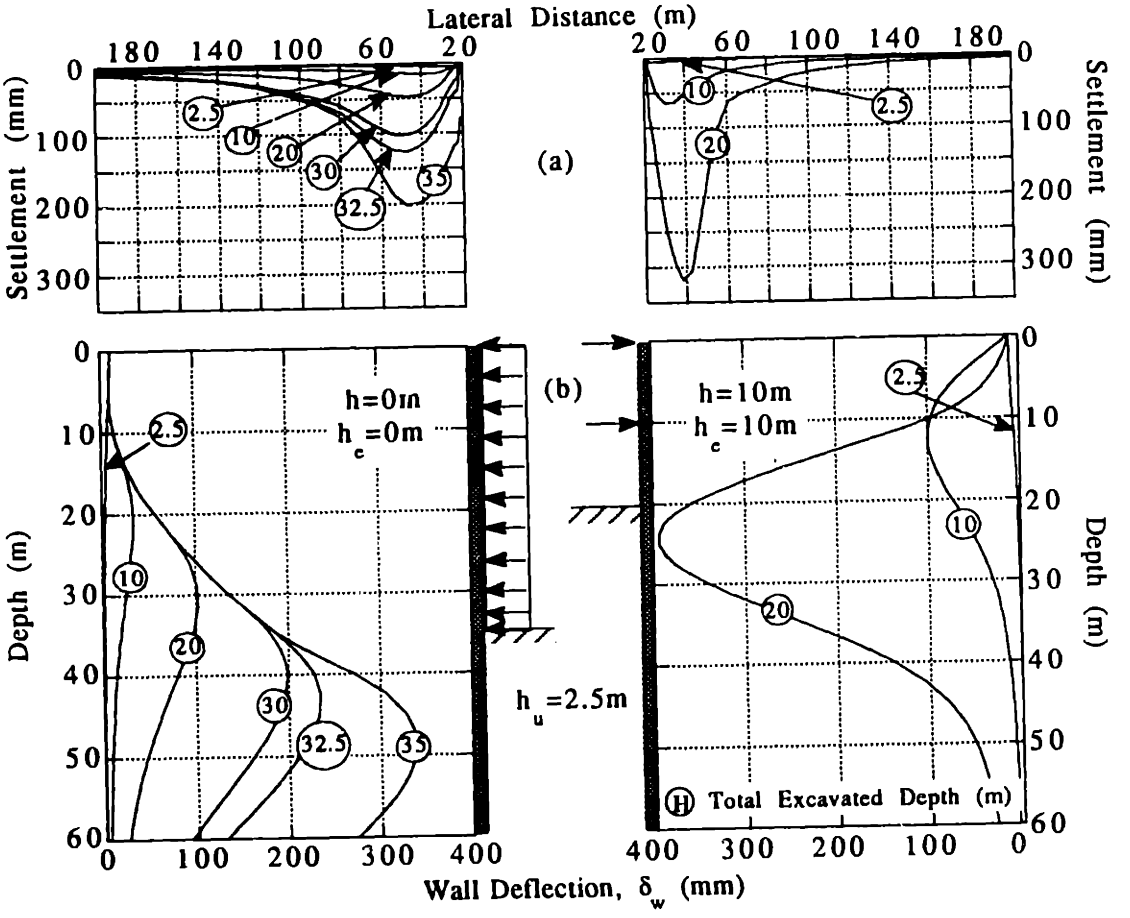

Figure D.4 Effect of Support Spacing on Predicted Ground Movements

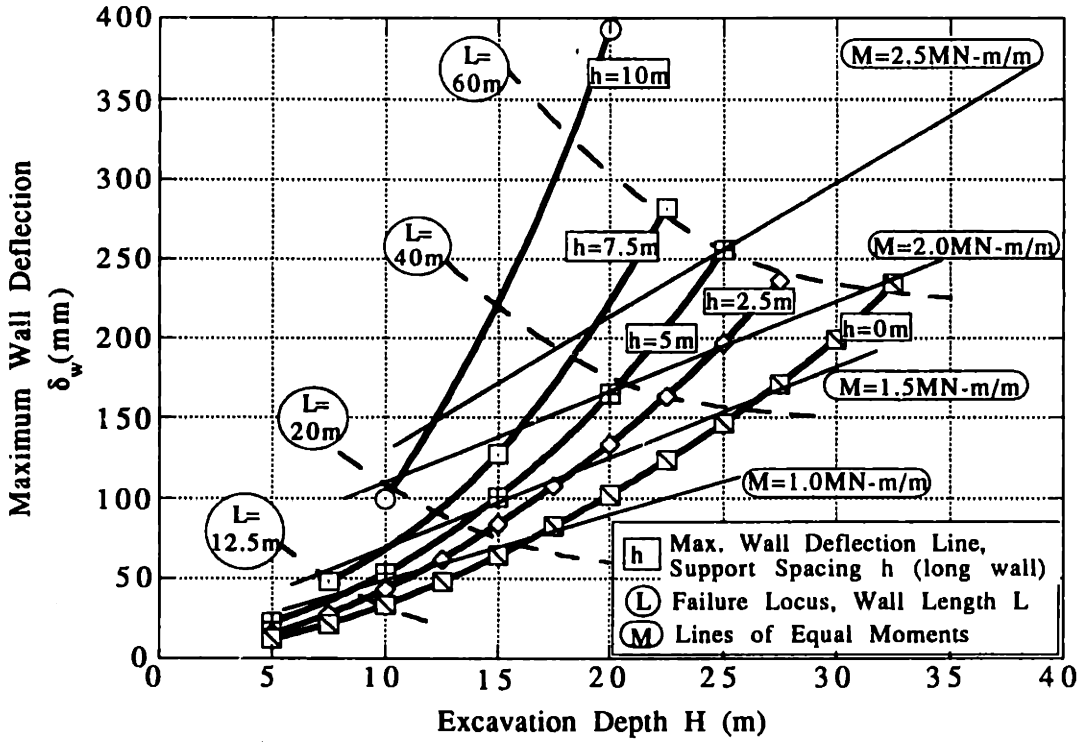

Figure D.5 Interpretation of Maximum Wall Deflection from Analyses